35th European and 10th International Conference on Acoustic Emission Testing

EWGAE 35 & ICAE 10

13th - 16th September 2022 - Ljubljana, Slovenia

CONFERENCE PROCEEDINGS

Editors:
Roman Šturm, Tomaž Kek
Faculty of Mechanical Engineering, University of Ljubljana

13th - 16th September 2022 - Ljubljana, Slovenia

Title: "35th European and 10th International Conference on Acoustic Emission Testing"

ORGANIZATION

ORGANIZING COMMITTEE
(University of Ljubljana, Faculty of Mechanical Engineering)

Roman Šturm (Chairman)
Tomaž Kek (Co-Chairman)
Dušanka Grubor Železnik (Secretariat)

EWGAE AWARDS COMMITTEE

Irek Baran (President)
Alexei Vinogradov
Gerd Manthei
Antolino Gallego (Secretary - no voting)

SCIENTIFIC COMMITTEE

- D. Aggelis (Greece)
- A. Anastasopoulos (Greece)
- V. Barat (Russia)
- A. Brunner (Switzerland)
- M. Chlada (Czech Republic)
- M. Enoki (Japan)
- S. Elizarov (Russia)
- A. Gallego (Spain)
- N. Godin (France)
- V. Godinez (USA)
- M. Gómez (Argentina)
- C. Grosse (Germany)
- M. Hamstad (USA)
- C. Hervé (France)
- T. Kek (Slovenia)
- G. Locidogna (Italy)
- I. Lyasota (Poland)
- P. Mazal (Czech Republic)
- Y. Mizutani (Japan)
- B. Muravin (Israel)
- M. Nowak (Poland)
- K. Ono (USA)
- D. Ozevin (USA)
- R. Piotrkowski (Argentina)
- A. Proust (France)
- R. Pullin (UK)
- F.J. Rescalvo (Spain)
- C. Rowland (UK)
- M. Sause (Germany)
- H. Schoorlemmer (Netherlands)
- T. Shiotani (Japan)
- E. Suárez (Spain)
- R. Šturm (Slovenia)
- H. Vallen (Germany)
- E. Verstrynge (Belgium)

TECHNICAL EDITORS

Bor Mojškerc, Zoran Bergant

PREFACE

The rapidly growing importance of non-destructive testing and evaluation (NDT & NDE) methods applied in the manufacturing, energy, construction, and maintenance industries, as well as in basic research and development, has created a great need for practitioners, engineers, and scientists with knowledge in this field. Non-destructive testing of materials is becoming increasingly important, during the production process before individual parts are incorporated into individual pieces of equipment and machinery. Testing during operation is becoming even more important in in-service inspection where the condition of the material is checked, and further safe operation of the equipment or machine is confirmed. Acoustic emission testing (AE) is an important part of non-destructive testing. AE is a non-invasive technique that makes it possible to detect damage in materials and follow their evolution in real time. AE signals resulting from the detection of elastic waves in the material can provide comprehensive information on the origin of different sources of damage in a stressed material, and also provide information on the development of discontinuities when the material is subjected to different types of loading.

To promote the use and development of AE testing, the Faculty of Mechanical Engineering at the University of Ljubljana has organised the EWGAE 35 & ICAE 10 conference. The three-day event provides a forum for scientists, engineers, and practitioners to discuss the latest developments, identify particular needs and opportunities for further progress, share knowledge and experiences with other well-known experts, and outline milestones for further progress in the fields.

The editors would like to thank the authors of these proceedings and the members of the International Scientific Committee for their work, collaboration, and constructive evaluations in selecting the final contributions. We are proud to welcome all well-known experts in the field to share their scientific knowledge in formal and informal discussions at the meeting. This proceeding comprise papers presented at the EWGAE 35 & ICAE 10 conference held in Ljubljana, Slovenia from 13th to 16th September 2022. The conference is supported by the Slovenian Society for NDT. The co-organisers of the event are the European Working Group on Acoustic Emission (EWGAE) and the International Institute of Innovative Acoustic Emission (IIIAE).

Editors
Prof. Dr. Roman Šturm
Assist. Prof. Dr. Tomaž Kek

TABLE OF CONTENTS

A GLIMPSE AT FIFTY-ONE YEARS IN ACOUSTIC EMISSION

Marvin A. Hamstad[1]

[1]University of Denver, Daniel Felix Ritchie School of Engineering and Computer Science, Dept. of Mechanical and Materials Engineering, Denver, CO, USA; mhamstad@du.edu

ABSTRACT

After 51 years continuously involved in acoustic emission (AE) testing and research, it has been interesting to look back over five decades. The equipment available in the early 1970s was primitive compared to now. At the start of that decade, only one, recently established, commercial company sold AE measurement equipment, and other useful equipment was internally built or adapted from other technologies. Further, the data that came from an AE monitored test was simply the number (counts) of penetrations of a fixed one-volt threshold expressed as an increasing total or a rate and recorded on an x-y plotter. The purpose of this "glimpse" is to present advances both within the author's research as well as those that were adopted from others research that were viewed as moving AE technology forward. This "glimpse" is not intended to be comprehensive, instead it is limited to aspects the author was involved in. Among the topics to be covered are advances such as understanding hydraulic test machine continuous noise, true root-mean-square (RMS) voltage measurements, inclusion particle fracture or decohesion, tension versus compression testing for unflawed metal samples, the pencil lead break, an acoustic emission signal simulator, broadband sensors, digital waveform recorders, large transverse-dimensioned plates, absolutely calibrated flat-with-frequency AE sensors, finite element modeling (FEM) in isotropic materials, validation of FEM, computer-based digital AE systems, intensity of frequency versus time of AE signals, superposition of group velocity results and FEM beyond the case of dipoles in an isotropic plate.

Keywords: Acoustic emission, technology advances, historical perspective, key contributions.

1. Introduction

During a career of 51 years (to-date), the positions have been at three organizations. The initial years were at Lawrence Livermore National Laboratory (LLNL), where rather than being in a nondestructive testing group, the position was in a material testing group. Then in 1984 a move was made to the University of Denver, CO as a professor and, in parallel, from 1992 various roles at the National Institute of Standards and Technology (NIST) Boulder, CO. The purpose of this paper is not to review in a comprehensive way what has occurred in the acoustic emission (AE) field over the five plus decades. Instead, the goal is to provide a "glimpse" of some aspects of the technology, where, progress was made that moved the technology to a more mature level. This "glimpse" includes self-research progress, as well as, research by others that impacted these AE projects. Up front, it should be clarified that there have been multiple contributors. A review of publications (the majority relating to AE) showed a total of 49 co-authors. A few (Prof. Amiya

Mukherjee, Mr. Jerry Whittaker, Ms. Karyn Downs, Dr. John Gary, Ms. Abbie O'Gallagher and Prof. Markus Sause) of these had the most involvement. Finally, one other contributor was Mr. Tom Drouillard who provided multiple references and/or papers that prevented reinventing AE results. This information came from the extensive collection of papers (some 1,996) on AE that eventually was published in the late 1970s [1].

2. Initial AE involvement

Until being hired, with *no prior AE experience,* to work in the field of AE only the AE name was familiar. The initial task, in 1971, was to repeat the recent experiment that Dr. Clem Tatro (supervisor and one of the initial persons in the US doing research in the AE field; starting in the late 1950s) had done [2]. The experiment was an AE-monitored tensile test of an unflawed 7075 aluminum sample. Carefully, all the same test conditions (material batch, same extensometer, same crosshead rate and pin-loading of the sample) were repeated, as well as, the AE related settings (gain, preamplifier, couplant and sensor). The previous result of count rate and load versus strain had a rapid rise in the continuous AE that started after the yield and increased until reaching a peak at about 2% strain. That was followed by a gradual decline until about 10% strain. The new result did not repeat the previous one, nor was any of the continuous AE even detected in the experiment. This result was not a very successful start to an AE career! In seeking the reason for the lack of AE in the attempted duplication, the only difference was the use of a different tensile test machine. The previous experiment was done on a hydraulic machine, while the new test was done on an older screw-driven (via a DC motor) machine. As the analysis progressed, the conclusion was that the sensitivity was effectively different in the two tests. In the previous case, the gain (relative to the fixed one-volt threshold) was set so as to exclude continuous background noise. In this case, the continuous background noise was both the electronic noise of the preamplifier *plus* the noise that came from the tensile test machine servo valve. In the new experiment, the screw-driven machine was much quieter, so the continuous background noise was *only* the preamplifier electronic noise. Thus, in the new case the sum of background noise plus the continuous specimen-based AE was below the threshold. So, the *first lesson* in the AE career was the issue of the presence of significant continuous machine noise from a servo valve in a hydraulic test machine. Subsequently, at LLNL, the University of Denver and NIST Boulder, a modification was made to locate the servo valve on an external manifold with connections to the machine actuator by reinforced rubber hoses that provided attenuation of the servo-based noise.

3. Research on unflawed specimens that exhibited continuous AE

The first new research project was to characterize the effect of tensile-test strain rate on the continuous AE from unflawed 7075 aluminum. The initial results using count rate were confusing. This result led to the adoption of true root-mean-square (RMS) voltage as the measurement technique, which removed the effect of a threshold on counts. This change resulted in much more repeatable AE data and was the *second lesson* learned. A significant additional test-technique change was made by use of a screw-driven test machine, where the crosshead rate could be changed by pushing a button to immediately change to a new fixed rate. This procedure removed the major effect of the changes from one sample to the next, since the strain-rate change was for the *same* test specimen. The results of a series of similar tests, established the true RMS (background RMS electronic noise level; correctly subtracted) was proportional to the square root of the plastic strain rate [3,4].

Subsequently the effect of multiple variables (specimen reduced section volume, aluminum manufacturer, orientation relative to rolling direction) on the continuous AE was studied for 7075 under tensile testing. This work proceeded until an *unexpected result* was obtained. In this case,

burst-type AE was superimposed on the continuous AE. Careful and extensive specimen polishing, while keeping track of the orientation of the tensile axis, revealed a very limited number of relatively large, cracked, inclusion particles (some 20 μm to 60 μm) with the cracks approximately perpendicular to the tensile axis [5]. Analysis of these large inclusions showed the element content was largely chromium [5]. Later, discussion with an aluminum manufacturer indicated a filter intended to remove them when the melt was poured had likely failed.

The above *"chance or lucky"* situation led to a significant change in the understanding of the sources of the continuous-type AE in the plastic strain range for 7075. Up to this time, this AE had been assumed to be from dislocation motion [6]. Three factors changed this notion. First, publications [7,8] were discovered on the microstructure of aluminum alloys. These publications revealed there were very large numbers of small inclusion particles in the size range of one to ten μm. Second, information surfaced that the 7075 materials in past testing was T651 (due to a plastic stretching done after the aging treatment) rather than T6. Third, a compression test was done along with tensile testing of 7075 T6 material. Testing real T6 material revealed two peaks in RMS versus strain plots in both the tension and compression tests. The first peak was at the yielding and the second after additional plastic strain. Correcting the RMS levels of both peaks in the compression test result by the previously determined dependence of the RMS level on volume (RMS proportional to the square root of the volume) and strain rate to those of the tension test, the first peak RMS levels of the yield-related AE were found to be very close to each other (tension 0.14 V and compression 0.13 V). For the second peak, the corrected values were very different. In tension the value was 0.44 V and in compression 0.02 V [9]. This situation for the first peak is expected, since dislocation motion during yielding depends on the shear stress, which is the same for both tension and compression loading. The considerably lower second peak RMS levels in the case of compression versus tension led to a conclusion that the AE source after the yield region was from particle fracture and/or decohesion rather than the previously assumed dislocation motion. This result was a *third lesson* in AE. Subsequent testing, in tension, of samples from aluminum alloy plates where the chemical composition had been altered to reduce the number of these very small inclusion particles resulted in a significant drop, as expected, in the second peak RMS values in tensile testing [10].

4.   Use of AE in composite material optimization

At LLNL being a part of a materials testing laboratory, it was possible to add an AE sensor to tests that were routinely made. In the case of proof and/or burst testing of small filament wound rubber-lined S-glass or Kevlar 49/epoxy vessels (studied under a NASA contract), interesting results as to a role for AE in the determination of the best winding pattern were observed. Changing from interspersing the longitudinal and hoop windings to instead placing all the hoop windings outside the longitudinal ones (non-interspersed) resulted in a large difference in the AE-determined accumulation of damage as a function of pressure for S-glass fiber. Early damage in the interspersed case correlated with an approximately 14% to 18% lower burst pressure compared to the non-interspersed vessels [11].

 A similar role was suggested for AE in the determination of best epoxy material for Kevlar 49/epoxy vessels. Eight vessels for each of eight different matrix epoxies were filament wound. The 80-vessel build was selected to statistically find the epoxy(s), which provided the highest burst pressure of the composite pressure vessels (COPVs). Adding an AE sensor to each test provided a damage progression record, via counts versus pressure to failure. The AE data showed a direct correlation of the total counts in an early low-pressure region with the eventual statistical average failure pressure for low failure- and high failure- pressure epoxy systems. The two best epoxy cases were matrix #1 (≈ 1,000 early counts; average burst pressure 18.8 MPa) and matrix #4 (≈ 2,000 early counts; average burst pressure 16.0 MPa). The poorest epoxy #7 had much more damage (≈ 22,000 early counts; average burst pressure 14.8 MPa) [12]. The source of this early

AE peak had been established earlier, when a similar vessel failed in the boss region rather than in the hoop portion [13]. A closeup photo of the hoop portion revealed multiple approximately equally spaced circumferential cracks parallel to the fiber direction. These cracks extended thought the full thickness of the hoop wraps, and they occurred at lower pressures for the biaxial loading due to the relatively low strength of the epoxy. When these cracks formed, they damaged the filaments/fibers (more with poor performing epoxies) in the hoop portion. This damage led to the low-pressure failures in the hoop region, under the hoop stresses (vessels were designed for hoop region failure) in the case of the poorer fiber/epoxy combinations.

5.   The introduction of the pencil lead break in AE

At the AEWG meeting at Williamsburg, VA in 1976, Dr. Nelson Hsu introduced to the attendees the pencil lead break (PLB) technique (known as the Hsu-Nielsen source [14]). This technique was most significant, as it was now possible, on demand, to apply a short-rise-time point source at a known location. This technique was valuable for multiple reasons: source location studies, verification of sensor coupling, effects of changes in sensor types, verification of AE channel operation, wave propagation studies, and checking of sensors that might have been damaged. It also provided the first possibilities for comparisons between different experimenters; if they did similar PLBs. Many PLBs were done over the subsequent years leading to a painful middle right finger "bump" that had to be surgically removed!

6.   Composites and the Felicity ratio

In general, composite structures and coupons generate significant amounts of AE, particularly on virgin loading. Mr. Timothy Fowler made an important observation (1977) relative to a second loading or subsequent loading. Fowler defined the Felicity ratio (FR) based on the load/pressure when significant AE started on this second/subsequent loading compared to the previous peak load/pressure. The fiberglass reinforced plastic (FRP) experimental data [15] showed results that directly tied the FR to the residual strength of the composite item. As is well known today, the FR is a measure of the violation of the Kaiser effect. Felicity ratios for composites can be less that 1.0 (essentially the value when the Kaiser effect is present), and the smaller the ratio, potentially the closer to failure the initial load (usually labelled as a proof loading) was. Fowler's work led to an ASTM standard [16] for AE testing of large low-pressure (internal pressure ≤ 1.73 MPa and for vacuum service 0 to 0.10 MPa) FRP tanks. The result of using the standard was that unexpected failures, resulting in dangerous conditions for workers, of such tanks were not occurring. This was a major advance.
In the case of aerospace-type COPVs, it was not straightforward as to the implementation of the Felicity ratio (FR). The fibers used in aerospace in the 1970s were typically superior to fiberglass (Kevlar and later graphite or carbon), and the fabrication method of filament winding was also used for these types of COPVs, rather than typical hand-layups for FRP tanks. These COPVs were often much smaller in size than the tanks typically used in the chemical process industry, and the working pressures were much higher. Applications of the FR for aerospace-type COPVs initially focused on the effect on burst pressure of impact damage. A project in the 1980s showed direct correlations of the FR with the amount of impact energy (impacted in virgin condition) and the residual strength for Kevlar-49/epoxy vessels [17]. A second project in the 1990s was for carbon fiber/epoxy COPVs that had experienced impact damage (post proof testing). In this study, the final residual strength was correlated with the FR (from a post impact proof test) and on the AE generated during depressurization from that proof level (characterized by the Shelby ratio) [18].

7. Characterization of AE measurement systems providing hit features

As AE measurement equipment progressed from simple counts to providing values for peak amplitude, rise time, duration etc., the question was how comparable were these results from the analog AE systems offered by different commercial companies? In addition, at this time, the AE measurement systems could be characterized as "black boxes" with their details only known to their designers. Dr. Adrian Pollock (*who the award is named after*) with his colleague Mr. T. Kevin Bierney recognized the need to characterize the AE measurement equipment. They developed, produced and sold an AE Simulator. This two-channel instrument could be hardware programmed to provide simulated signals with variable rise time, variable decay time, different carrier frequencies, different peak amplitudes (to either a preamplifier or to the main AE system) as well as spaced-in-time two simulated events, with a known fixed time interval between them to check delta time results from two different hits. In addition, the simulator allowed the measurement of the AE systems threshold, as compared to the "set" value of the threshold. Also, the simulated AE events could be generated at a certain event rate with a counter accessory to count how many had been generated in a certain test time. This allowed one to compare how many events were recorded by the AE system and how many were "lost" during the test. Such measurements were important, since at the time computers built into the AE systems were still very slow compared to those today. At the University of Denver, tests were made on three available systems from different AE manufactures. The same event signals from the simulator were fed into each of the channels of the three systems. A paper comparing the results was published in 1988 [19]. Further, the characterization of event rates (possible with the simulator) that a given AE system could "keep up" with, could be used to properly set loading or pressurization rates for composite AE testing where high event rates are common.

8. Addition of digital waveform recorders

Up to the time when digital waveform recorders were first available, the only view of continuous or burst AE that could be studied was from a Polaroid camera picture made from an oscilloscope screen. Such pictures provided little opportunity to fully analyze the signals. So, when digital signal data could be obtained and inputted to a computer for subsequent analysis, it was a major step forward in the AE field. This was possible as a result of advancements in the electronics world. Initially, such recorders had limited digitization rates, dynamic range and memory. With improved electronics and computers, current AE measurement systems can digitize (including pre-trigger, at high rates, with many bits and large memory) each AE hit on multiple channels even for a higher event rate of composites testing. These systems also have software available for analysis, or the digital information can be exported for other analysis approaches. The important advancement of digital recording opened up many possibilities for analysis of the AE signals and also increased the accuracy of the features of AE hits.

9. Use of large transverse plates and broadband AE sensors for wave propagation studies

Another significant development for the progress of AE, was introduced when visiting Prof. Michael Gorman's, laboratory at the Naval Postgraduate School, Monterey, CA. Gorman demonstrated how the AE signals from PLBs on a 3.1 mm thick aluminum plate with large transverse dimensions could be used to compare with analytical calculations. Gorman used a broadband sensor and in-plane as well as out-of-plane orientations of the pencil. Due to the large size, there were no reflections present in the direct arriving signals. Gorman's ideas developed the concepts of extensional and flexural modes (fundamental Lamb modes) and showed how these modes were present and identifiable in the resulting AE signals [20-22]. Gorman also emphasized

the importance of frequency filtering of certain analytically modeled results to correspond to the frequency range that AE sensors responded to. As many may be aware, Gorman's research results led to starting the company named Digital Wave for AE work; with the equipment based solely on waveform recording. A unique feature was the use of a narrower frequency bandpass for the trigger circuit (to better eliminate noise signals from being digitized) compared to the circuit with a wider bandpass for the digitization of signals. The adoption of large transverse sized plates in subsequent years greatly enhanced PLB-based wave propagation studies in metals, polymers, composites and veneer wood plates.

10.   Absolutely calibrated flat-with-frequency AE sensor

A very significant development came out of a large AE research project at NIST Gaithersburg. There were three parts to this development. First, was the preparation of a large cylindrical steel block with a diameter of 900 mm by height 430 mm and a highly finished top surface. Second, was the use of a capacitive sensor that directly measured the out-of-plane displacement of a surface wave (primarily a Rayleigh wave) generated by the fracture of a glass capillary. The combination of the first two provided the important development of absolute AE sensor calibration [23]. Third, was the design of a conical (tip diameter of 1 mm) piezoelectric element backed by a large shaped brass block (609 g). Combining all three parts, resulted in an absolutely-calibrated out-of-plane displacement sensor (in NIST terminology a Standard Reference Material (SRM)) [24]. These sensors, flat with frequency from about 30 kHz to at least 1.2 MHz, with a matched preamplifier, were essential in the next described development. Dr. Frank Breckenridge (mainly the calibration block) and Mr. Tom Proctor (mainly the conical sensor) were the primary individuals behind this NIST work. Then, for the first time an AE sensor could be sent to NIST for *absolute calibration* (for a charge of $500 in the late 1990s) where the wave passed under the sensor face, rather than the typical face-to-face *characterization* of a sensor's frequency response.

11.   Initial far-field finite element modeling of waves

At the start of 1992, a sabbatical leave commenced at NIST Boulder. The first and probably the most significant advance in the author's career in AE came about upon meeting Dr. John Gary at a seminar. The result of this meeting shaped a significant part of the AE career since then. At NIST, experiments were being done using out-of-plane PLBs on a large aluminum alloy plate (3.1 mm by 1.22 m by 1.52 m) to compare the signals, from pinducers fabricated with different piezoelectric materials, to signals from a NIST SRM absolute sensor. Upon describing the experiments, Gary mentioned a *personal* code (Fortran) for explicit finite element calculations for wave propagation that might model the waves generated from the out-of-plane PLBs. With the code, the signals were modeled at 254 mm from the source on a 3.1 mm thick large aluminum alloy plate (so edge reflections would not be present). In the model, the PLB force of 1 N was shaped in time and magnitude to an experimental result by Breckenridge [25]. The modeled results were compared with the digitally recorded voltage signals from the absolute SRM sensor at 254 mm from the PLB, after modifying them by the sensor calibration constant to change the results to out-of-plane displacement (m). The very close match of the modeled result to the experimental one for both the flexural region as well as the extensional region was at that time the first far-field FEM result for an AE-like signal [26]. This result experimentally validated the code for this 2D axisymmetric case. This result started a collaboration with Gary and Abbie O'Gallagher (coworker) that lasted for many years, even after Gary retired. Next (1995-96) the 3D version of the code was experimentally validated by the close match to the absolute sensor result from in-plane edge PLBs on a steel plate 25 mm by 1.32 m by 0.78 m, again before edge reflections appeared [27,28]. Later, a yearlong visitor from NASA brought plates (3.175 mm thick aluminum

alloy) that by a carefully controlled vertical position of in-plane edge PLBs validated the 3D code when the edge reflections were included [29]. This provided results (never done with analytical calculations) for AE-like signals (multi-mode and multi-frequency) that included edge reflections. Finally, the 3D code was validated for buried self-equilibrated dipole sources as well as muti-dipoles in different directions. This validation used analytical results from Prof. Yih-Hing Pao, and colleagues and students at Cornell University. Ultimately, the modeling conditions required to obtain a converged and validated results were published [30].

Over the succeeding years many studies were made of different variables: depth of sources, dipole orientation, muti-dipoles, radiation patterns, source rise time, plate thickness, propagation distance. An interesting study with buried in-plane dipoles was made of the amplitude reinforcement in the AE signals in a typical laboratory-sized test sample as compared to a large transverse sized sample (like for field testing). The reinforcement was up to 10 to 12 dB in these modeled cases; important when using laboratory tests to determine amplitudes expected for the same sources in field tests [31]. In addition, using the perfect FEM signals, attempts were made to develop source identification methods for different dipole cases [32]. Also, signal-to-noise was studied by superimposing real preamplifier noise on the noise-free FEM modeled data [33]. The ability to carry out the modeling was facilitated by two factors. First, Gary's code was efficient due to the use of a uniform mesh (coupled with an approach that took advantage of this) as contrasted to potential commercial codes with non-uniform meshes. Second, the computer facilities at NIST provided work stations with large memory and multiple processors. Later as computers became even faster with more memory and parallel processing capability, a desktop could be used. FEM provides the means to model AE type experiments on a computer from buried, fully known and self-equilibrated sources at fixed positions with perfect sensors. Thus, it also provides a way to study wave propagation of AE-type signals with perfect conditions. This approach is likely much less costly and provides results even when an experiment could not easily be done (very thick plates [[34]). Further, such modeled data is ideal to develop and test possible signal processing methods, since the data is noise free and is from a perfect sensor. Also, the modeled data can be frequency filtered to correspond to different sensors.

12. A small conical near flat-with-frequency sensor

The conical sensor that Proctor developed was not amendable to being placed on typical laboratory AE test specimens due to the large brass backing mass (609 g). With funding from the US Agriculture Department at the University of Denver, work on an improved broadband sensor for acoustic studies in wood was being done. So, during the continuing involvement at NIST Boulder, a complementary series of experiments was started to determine if the backing mass could be reduced without a serious reduction in the "flatness" with frequency. These experiments examined the changes in the frequency response as the mass of a brass cylinder backing a conical element decreased. The process was done by progressively machining the size of the brass and then repeating out-of-plane PLBs on a large aluminum plate. The signals from the conical element were compared to those from the absolutely calibrated SRM sensor. The experimental results were encouraging, and it was apparent that it might be possible to use a smaller backing mass. After discussions with NIST colleague Dr. Chris Fortunko (an EE), it was decided to adopt a technique used in an AE sensor produced in Japan [35] in the fabrication of small sensors. This involved placing a very low-noise field-effect transistor (FET) very close to the conical element (along with a bias resistor). The special preamplifier needed for this approach had been obtained from a commercial source. The purpose of the internal FET was to improve the sensitivity by reducing the voltage division due to the low capacitance of the conical element relative to the parasitic capacitance of a wire to a normal external preamplifier. A series of four conical sensors was fabricated with the brass backing mass changing from 129 g to 3.0 g along with steel sensor cases. The results showed that a complete sensor could be fabricated with a much lower backing mass,

without a large sacrifice frequency response [36]. So, a final design change was made. To potentially reduce waves transmitted to the backing mass from reflecting back to the conical element, it was decided to use a backing mass of 7 g of granite (due to the structure of granite). Two versions, one without the FET and one with the FET were completed and sent to NIST Gaithersburg to be calibrated. They both had approximately flat with frequency response, but the one with the internal FET had much better response (up about 13 dB, based on the NIST absolute calibrations; at zero gain). This was a significant improvement, as now the sensor with internal FET approached the signal-to-noise (S/N) ratio of resonant sensors [37]. Later, a modified commercial version (design modified by Prof. Steve Glaser) has been available, known as the KRN sensor. The NIST-built sensor with internal FET has been used in studies for wave propagation in metal, polymer and composite large-transverse-sized plates as well as during fatigue testing of large transverse sized center-cracked samples at NIST Boulder.

13. AE testing in tensile fatigue of large transverse sized center-cracked plate samples

With a goal to provide "natural" AE signals from a sharpened crack without the complications and reinforcement of amplitude due to reflections from the test sample edges and also allow the radiation pattern to be observed, a large specimen was designed for use with the small conical sensors with internal FET. Specimens (from both steel and an aluminum alloy, all expensive) were fabricated that had a reduced section of 533 mm wide by 483 mm (load direction) for the 6.4 mm reduced section thickness. Large cut-outs in the grip region were designed by application of static finite element modeling to create a near uniform axial stress field in the region of the center crack (verified by strain gages). Electrical discharge machining (EDM) created through center cracks that were sharpened in fatigue. In addition, to the conical sensors at various angles from the center of the sample, in some experiments some resonant sensors were also used along with very small diameter (approximately 6 mm) PICO sensors, one near each crack tip. The signals from these were often used to trigger (greatly reduced recording sources that did not originate at the cracks) the simultaneous waveform recording of up to eight channels, as well as, to identify which crack tip the source came from [38]. Unfortunately, these experiments were only partially completed as the funding from Federal Highway Administration (FHWA) was not renewed for reasons not related to the progress of the research. In the 2024 T651 aluminum alloy during fatigue (tension/tension), some interesting events were observed from crack tip region sources at the peak cyclic loads [39]. First, events with dominant flexural mode were observed as compared to those with dominant extensional mode. FEM results had shown that buried dipole sources near the mid-plane have a dominant extensional mode, while those some distance away from the mid-plane have a dominant flexural mode Second, events with opposite flexural mode polarity were observed. FEM results had shown a change in polarity of the flexural mode indicates the sources being on different sides of the midplane. Thus, a significant advancement was the large sample (so reflections from the specimen edges do not complicate the direct arrival signals or reinforce their amplitude; important relative to possible following field testing) coupled with the reasonably flat-with-frequency, broadband sensors (so the extensional mode can be distinguished from the flexural mode when reflections are not present) to monitor real AE from a sharpened crack and characterize the radiation pattern.

14. Frequency versus time display of intensity of AE signals with superimposed dispersion curves

With the advent of FEM results as well as AE systems with waveform digitization, a useful technique was to view the waveforms intensity in frequency versus time. Prof. Mikio Takemoto (Aoyama Gakuin University, Tokyo) with colleagues had developed a wavelet transform (WT) for

AE signals [40]. At an AE meeting (2000) in Japan, a meeting (facilitated by Prof. Kanji Ono) was held between Prof. Takemoto and Mr. Jochen Vallen to discuss possible implementation of the WT in a form that was easy to use for AE users. The result was the AGU-Vallen Wavelet [41]. To demonstrate and verify the result, it was agreed to use FEM results and create a tutorial. Later, the ability to superimpose the relevant group velocity curves (modified for the relevant propagation distance to the sensor) was added to the software, after Dr. Richard Nordstrom and Dr. Yoshihiro Mizutani provided Vallen with the dispersion coding. These two features were viewed as greatly increasing the understanding of AE signals in plates and solidified the fact that only certain frequency regions in the modes were excited more intensely in the AE signals both for FEM generated and experimentally obtained signals from broadband sensors. An additional important fact is that WT analysis reduces the noise in the AE signals, since it is spread out in time and frequency, whereas the intense regions of the Lamb waves are concentrated at certain times and frequencies. Thus, real events can be viewed in the WT plots, where they may be hard to observe in the time domains [42]. Sometime later Gary coded the Choi William Distribution (CWD), which has some advantages, and passed it to Vallen who implemented it as an alternative in the software.

15. FEM beyond simply the waves in an isotropic plate from a dipole source

Multiphysics commercial software packages with different modules provide opportunities for finite element modeling of additional aspects beyond the waves in a particular domain. In the author's research, these aspects as well as modeling of anisotropic domain cases have been a part of the last 10 years during the collaboration with Prof. Markus Sause. Two studies were completed dealing with anisotropic domains. One dealt with anisotropic hybrid materials, where both isotropic and anisotropic layers made up the same plate thickness. In this case, both full thickness and individual layer thickness propagation were observed. [43]. A second study examined a propagation situation to simulate the hoop region of a metal-lined cylindrical COPV [39]. To simulate the hoop region, the stiffness and thickness of a plate were such that the properties had twice the stiffness in one direction as the other direction. Significant differences were present for both propagation in the different directions as well as for dipole sources in the two directions [44]. The application of different Multiphysics modules has been applied for cases combining propagation domains, piezoelectric sensors and attached electrical circuitry. Studies with Sause were completed in three situations. First, modeling was done for PLBs on an aluminum alloy plate versus different dimensions of conical piezoelectric elements with a fixed backing mass. The electrical circuitry was included for comparison with corresponding experiments [45]. Second, the modules were applied to study four different AE sensor calibration approaches [46]. Third, the same modules were also applied for two studies (including Dr. Zelenyak) with sensors mounted on waveguides that were connected to plates where waves had been excited by pencil lead breaks [47, 48].
Some similar studies were completed with Dr. Brian Burks (a NIST Boulder colleague at that time). First, modules including piezoelectric transducers/sensors were used for a study of a transducer mounted on one surface of a transfer block to drive a signal to the opposite surface where a sensor was mounted at the epicenter position. This study was related to what is called face-to-face characterization of sensors [49]. A second study with Burks examined the effect of the presence of a fluid filled-COPV on the wave propagation. The study included paths through the fluid [50].

16. Conclusions/Future

The reader, of this paper, can likely expect incremental progress over the next five years. Those that continue in AE for a total of 20, 30 or 40 years can expect changes that it might be difficult to currently imagine. In 1976, after the first five years, it was not possible to imagine the changes that would occur over five decades. This fact should encourage individuals with a career in AE to have the view that much more can be accomplished. Your role can be that of a leader or a follower in the future AE advancements. These advancements could be directly in the field of AE, as well, as the incorporation of adjacent technologies that can help to advance AE technology.

17. References

[1] Drouillard, Thomas F. (1979). Acoustic emission a bibliography with abstracts. IFI/Plenum Data Company, New York.

[2] Tatro, C.A. (1972). Design criteria for acoustic emission experimentation. Liptai, R.G., Harris, D.O., Tatro, C.A. (Eds.), Acoustic emission ASTM STP 505, American Society for Testing and Materials. p. 84-99.

[3] Hamstad, M.A., Mukherjee, A.K. (1974). The dependence of acoustic emission on strain rate in 7075-T6 aluminum. Experimental Mechanics, vol. 11, January, p. 33-41.

[4] Hamstad, M.A. (1987). Energy measurement of continuous acoustic emission. Miller, Ronnie, K., McIntire, Paul. (Eds.). Nondestructive Testing Handbook, 2nd ed., vol. 5, Acoustic emission testing, American Society for Nondestructive Testing, Section 16: Special Acoustic Emission Applications, p. 586-591. Originally published, Hamstad, M.A. (1974). Report UCRL-76286, Lawrence Livermore Laboratory, Livermore, California.

[5] Bianchetti, R., Hamstad, M.A., Mukherjee, A.K. (1976). Origin of burst-type acoustic emission in unflawed 7075-T6 aluminum. Journal of Testing and Evaluation, vol. 4, no. 5, p. 167-172.

[6] Dunegan, H., Harris, D.O. (1969). Acoustic emission-a new nondestructive testing tool. Ultrasonics, vol. 7, no. 3, p. 160-166.

[7] Stone, R. H., Psioda, R.H. (1975). Discussion of metallurgical factors affecting fracture toughness of aluminum alloys. Met. Trans. A, vol. 6A, p. 668-670.

[8] Thompson, David S. (1975). Metallurgical factors affecting high strength aluminum alloy production. Met. Trans. A, vol. 6A, p. 671-683.

[9] Hamstad, M.A., Mukherjee, and A.K. (1975). A comparison of the acoustic emission generated by tensile and compression testing of 7075 aluminum. Report UCRL-77502, Lawrence Livermore Laboratory, Livermore, California, 1975

[10] Bunch, R., Hamstad, M.A., Mukherjee, A.K. (1979). Correlation between acoustic emission and microstructure in aluminum alloys. Conference proceedings, Spring Meeting ASNT, 2-5 April, San Diego, CA, American Society for Nondestructive Testing, Columbus, OH, p. 201-208.

[11] Hamstad, M.A. (1972). Acoustic emission from filament-wound pressure bottles. Conference proceedings, 4th National SAMPE Technical Conference and Exhibition, titled: Non-metallic materials, 17-19, October, Palo Alto, CA, p. 321-331.

[12] Hamstad, M.A., Chiao, T.T. (1976). Structural integrity of fiber/epoxy vessels by acoustic emission: some experimental considerations. SAMPE Quarterly, vol. 8, no. 1, p. 31-45.

[13] Hamstad, M.A., Chiao, T.T. (1974). A physical mechanism for the early acoustic emission in an organic-fiber/epoxy pressure vessel. SAMPE Quarterly, vol. 5, no. 2, p. 22-27.

[14] Standard Guide for Determining the Reproducibility of Acoustic Emission Sensor Response, ASTM E976-21, ASTM International, West Conshohocken, PA.

[15] Fowler, T. J. (1977). Acoustic emission testing of fiber reinforced plastics. ASCE Fall Convention and Exhibit at San Francisco, CA., vol. Preprint 3092, American Society of Civil Engineers, Reston, VA.

[16] Standard Practice for Acoustic Emission Examination of Fiberglass Reinforced Plastic Resin (FRP) Tanks/Vessels, ASTM E1067M-18, ASTM International, West Conshohocken, PA.

[17] Whittaker, J.W., Brosey, W.D., Hamstad, M.A. (1989). Correlation of Felicity ratio and strength behavior of impact-damaged spherical composite test specimens. Conference proceedings, Third International Symposium on Acoustic Emission from Composites, titled: AECM-3, 17-21 July, Paris, France, p. 160-167.

[18] Downs, K.S., Hamstad, M.A. (1998). Acoustic emission from depressurization to detect/evaluate significance of impact damage to graphite/epoxy pressure vessels. Journal of Composite Materials, vol. 32, no. 3, p. 258-307.

[19] Hamstad, M.A. (1988). Characterization and measurement accuracy of acoustic emission systems. Conference proceedings, 9th International Acoustic Emission Symposium, titled: Progress in Acoustic Emission IV, 14-17 November, Kobe, Japan, p. 121-132.

[20] Gorman, M. R. (1989). Personal communication.

[21] Gorman, Michael R., Prosser, William H. (1991). AE source orientation by plate wave analysis. Journal of Acoustic Emission, vol. 9 no.4, p. 283-288.

[22] Gorman, Michael R. (1991). Plate wave acoustic emission. The Journal of the Acoustical Society of America, vol. 90, p. 358-364.

[23] Breckenridge, F.R. (1982). Acoustic emission transducer calibration by means of the seismic surface pulse. Journal of Acoustic Emission vol. 1, no. 2, p. 87-94.

[24] Proctor, Jr., T.M. (1982). An improved piezoelectric acoustic emission transducer. Journal of Acoust. Soc. Am., vol. 71, vol. 11, p. 1163-1168.

[25] Breckenridge, F., Proctor, T., Hsu, N., Fick, S., Eitzen, D. (1990). Transient sources for acoustic emission work, Progress in Acoustic Emission V., eds K. Yamaguchi et al, JSNDI, Tokyo, p. 20-37.

[26] Gary, John, Hamstad, Marvin (1994). On the far-field structure of waves generated by a pencil break on a thin plate. Journal of Acoustic Emission, vol. 12, nos. 3-4, p. 157-170.

[27] Hamstad, M.A., Gary, J., O'Gallagher, A. (1995). A comparison of measured and computed acoustic emission waves in a thick plate. Conference proceedings, Society of Engineering Science 32nd Annual Technical Meeting, titled: SES'95, 29 October-2 November, New Orleans, LA, p. 171-172.

[28] Hamstad, M.A., Gary, J., O'Gallagher, A. (1996). Far-field acoustic emission waves by three-dimensional finite element modeling of pencil breaks on a thick plate. Journal of Acoustic Emission, vol. 14, no. 2, p. 103-114.

[29] Prosser, W.H., Hamstad, M.A., Gary, J., O'Gallagher, A. (1999). Reflections of AE waves in finite plates: finite element modeling and experimental measurements. Journal of Acoustic Emission, vol. 17, nos. 1-2, p. 37-47.

[30] Hamstad, M.A., O'Gallagher, A., Gary, J. (1999). Modeling of buried acoustic emission monopole and dipole sources with a finite element technique. Journal of Acoustic Emission, vol. 17, nos. 3/4, p. 97-110.

[31] Hamstad, M.A., O'Gallagher, A., Gary, J. (2001). Effects of lateral plate dimensions on acoustic emission signals from dipole sources. Journal of Acoustic Emission, vol. 19, p. 258-274.

[32] Downs, K.S., Hamstad, M.A., O'Gallagher, A. (2003). Wavelet transform signal processing to distinguish different acoustic emission sources. Journal of Acoustic Emission, vol. 21, p.52-69.

[33] Hamstad, M.A., O'Gallagher, and A. (2005). Effects of noise on Lamb-mode acoustic-emission arrival times determined by wavelet transform. Journal of Acoustic Emission, vol. 23, p. 1-24.

[34] Hamstad, Marvin, Sause, Markus (2022). On trailing waves rather than Lamb waves being generated by buried in-plane dipoles in thick plates. Conference proceedings, EWGAE 35 and ICAE 10, 13-16 September, Ljubljana, Slovenia.

[35] Shiwa, M., Inaba, H., Carpenter, S.H., Kishi, T. (1992). Development of high-sensitivity and low-noise integrated acoustic emission sensor. Mat. Eval., vol 50, no. 7, p. 868-874.

[36] Hamstad, M.A., Fortunko, and C.M. (1995). Development of practical wideband high fidelity acoustic emission sensors. Conference proceedings, titled: Nondestructive Evaluation of Aging Bridges and Highways, 6-7 June, Proc. SPIE 2456, p. 281-288.

[37] Hamstad, M.A. (1997). Improved signal-to-noise wideband acoustic/ultrasonic contact displacement sensors for wood and polymers. Wood and Fiber Science, vol. 29, no. 3, p. 239-248.

[38] Hamstad, M.A., McColskey, J.D. (1999). Detectability of slow crack growth in bridge steels by acoustic emission. Materials Evaluation, vol. 57, no. 11, p. 1165-1174.

[39] Hamstad, M.A. (2001). Some key advances in wideband acoustic emission technology. Tenth Annual Research Symposium of ASNT, 26-30 March, Denver Colorado.

[40] Suzuki, H., Kinjo, T., Hayashi Y., Takemoto, M., Ono, K., Appendix by Hayashi Y. (1996). Wavelet transform of acoustic emission signals. Journal of Acoustic Emission, vol. 14, no.2, p. 69-84.

[41] Vallen, J. (2005) "AGU-Vallen Wavelet transform software version R2005.1121," Vallen-Systeme GmbH, München, Germany. Available at http://www.vallen.de/wavelet/index.html.

[42] Hamstad, Marvin A. (2004). Electronic noise effects on fundamental Lamb-mode acoustic emission signal arrival times determined using wavelet transform results. Conference proceedings, 26th European Conference on Acoustic Emission Testing, titled: EWGAE 2004, 15-17 September, Berlin, Germany, p. 613-621.

[43] Sause, M.G.R., Hamstad, M.A., Horn, S. (2013). Finite element modeling of Lamb wave propagation in anisotropic hybrid materials. Composites: Part B Engineering, vol. 53, p. 249-257.

[44] Hamstad, Marvin A., Sause, Markus G. R. (2014). Acoustic emission signals versus propagation direction for hybrid composite layup with large stiffness differences versus direction," Conference proceedings, 31st Conference of the European Working Group on Acoustic Emission, titled: EWGAE, 3-5 September, Paper We.1. A.1, p. 1-9, Dresden, Germany.

[45] Sause, Markus G.R., Hamstad, Marvin A., Horn, Siegfried (2012). Finite element modeling of conical acoustic emission sensors and corresponding experiments. Sensors and Actuators A: Physical 184, p. 64-71.

[46] Sause, Markus, Hamstad, Marvin (2018). Numerical modeling of existing acoustic emission sensor absolute calibration approaches. Sensors and Actuators A: Physical 269, p. 294-307.

[47] Zelenyak, Andreea-Manuela, Hamstad, Marvin A., Sause, Markus G. R. (2014). Finite element modeling of acoustic emission signal propagation with various shaped waveguides. Conference proceedings, 31st Conference of the European Working Group on Acoustic Emission, titled: EWGAE, 3-5 September, Paper We.1. A.4, Dresden, Germany.

[48] Zelenyak, Andreea-Manuela, Hamstad, Marvin A., Sause, Markus G. R. (2015). Modeling of acoustic emission signal propagation in waveguides. Sensors 15, p.11805-11822; doi:10.3390/s150511805.

[49] Burks, Brian, Hamstad, M.A. (2015). An experimental-numerical investigation of the face-to-face sensor characterization technique. Materials Evaluation, p. 414-423.

[50] Burks, Brian, Hamstad, M.A. (4014). The impact of solid–fluid interaction on transient stress wave propagation due to acoustic emissions in multi-layer plate structures. Composite Structures, vol. 117, p. 411-422.

Measurement Equipment and Customized Solutions for Acoustic Emission Testing

We develop and produce innovative technology that makes a true difference for the safety of humans, the environment and the preservation of infrastructure. This commitment differentiates us from other suppliers and defines who we are: Vallen Systeme – The Acoustic Emission Company

AMSY-6 System

The AMSY-6 System is a fully featured, multi-channel Acoustic Emission measurement system. It forms a flexible basis that can be customized, extended and configured to the needs of an application.

The field of applications ranges from various inspection tasks such as pressure vessel testing, leakage testing to research and structural health monitoring of large objects

spotWave Device

The spotWave device is a portable single channel AE-measurement unit that can be controlled by a Laptop, Tablet PC, Smartphone or IoT device. It is a fully featured AE measurement device. The software supports the Vallen pridb and tradb data file format.

Typical applications are leakage detection, hot spot monitoring, AE research, etc.

Acoustic Emission Sensors

A wide range of sensors is offered covering any AE testing application.

Sensors are available for standard environments, explosion hazardous areas, for underwater applications, high temperature surfaces and harsh environments.

Sensors supporting the SmarLine™ protocol register themselves with an AMSY-6 system and minimize the configuration effort.

Vallen AE Suite Software

Unmatched flexibility and transparency at all times makes the Vallen AE Suite Software the preferred tool of choice for all acoustic emission applications.

Its modular architecture can be configured and extended to match any requirement of an application.

It offers everything from simple data visualization over complex analysis and pattern recognition to automation and web-based dashboards.

Measurement data is written to a database structure that complies with SQLite3 standard. It can be accessed from any application supporting SQLite3 which includes Matlab, Python and many more fast development environments.

CONTRIBUTION OF ELASTIC WAVE APPROACHES TO CIVIL ENGINEERING DIGITAL TRANSFORMATION

Tomoki Shiotani[1]

[1]Kyoto University; shiotani.tomoki.2v@kyoto-u.ac.jp

ABSTRACT

As for DX for civil infrastructures, digital twin of point-clouds of spillway of a rock fill dam is demonstrated. Reproduction of existing structures with point-clouds from still or movie images are shown. Necessary information in addition to the point-clouds such as surface and internal condition of the structure are depicted. As for the diagnosis methods for internal condition, brief history with elastic wave approaches is reviewed. Information such as surface deterioration condition as well as internal condition composed of elastic wave velocities, which will be crucially important to realize life-cycle-oriented design, construction, and maintenance, is incorporated into the digital twin. Through the suggested model, overall damage of the spillway is discussed in combination with the pin-point excavations for the verification. Through the life cycle of the civil engineering structures roles of elastic wave approaches including AE techniques will be suggestively indicated.

Keywords: Civil engineering DX, point-clouds, elastic wave approaches, tomograms.

1. Introduction

Digital transformation (abbreviated DX at present) is first introduced by Stolterman and Fors in Information System Research [1]. They describe that the ongoing development of information technology intertwined in our daily life, raising new issues concerning the possibility of understanding new configurations. Upon this paradigm, METI (Ministry of Economy, Trade and Industry) in Japan, e.g., made a guideline for DX, and defined that "To respond to drastic changes in the business environment, companies revolve products, services and business models, and establish a competitive advantage to transforms its business, organization, process, corporate culture and culture". As shown DX does not mean to transfer analogue data to digital data, but transform the peoples' daily life into better direction, utilizing IT (Information Technology) or ICT (Information Communication Technology). Here one question arises 'what is the DX for civil infrastructures?'. There is no decisive definition; however, the author would like to propose that it is realization of life-cycle-oriented design, construction and maintenance with IT and ICT.

2. Reproduction of existing structures

Digital twin/tandem of civil structures is mandatory to start the DX for civil infrastructures. Reproduction of existing civil structures on the computer display is the first step to manage them

through the life. This is well implemented by using point-clouds generated from still images and videos as shown in Fig.1.

| a) Bridge | b) Spill way of rock fill dam |
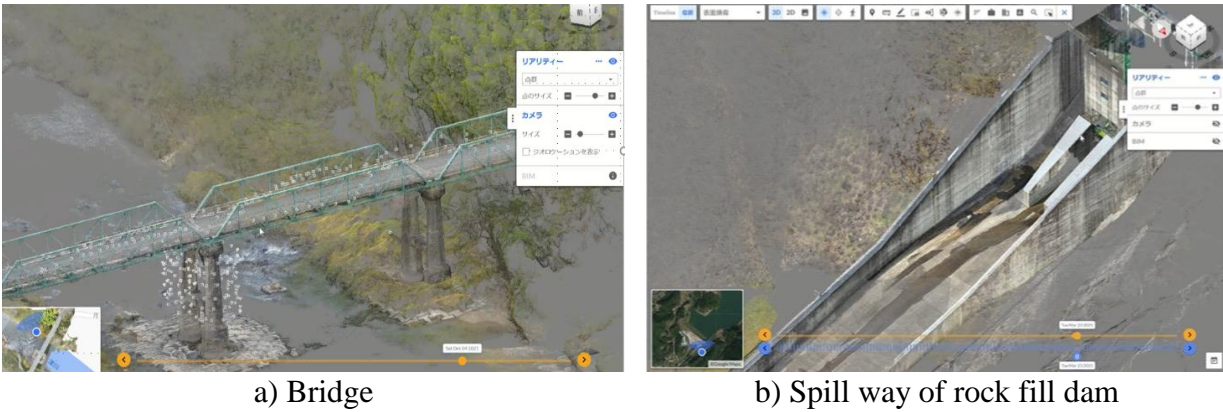
Fig. 1: Three-dimensional image of civil structures reproduced by point-clouds from images taken by drone.

Surface condition shall be incorporated into the reproduced digital twin linking to real images as shown in Fig. 2.
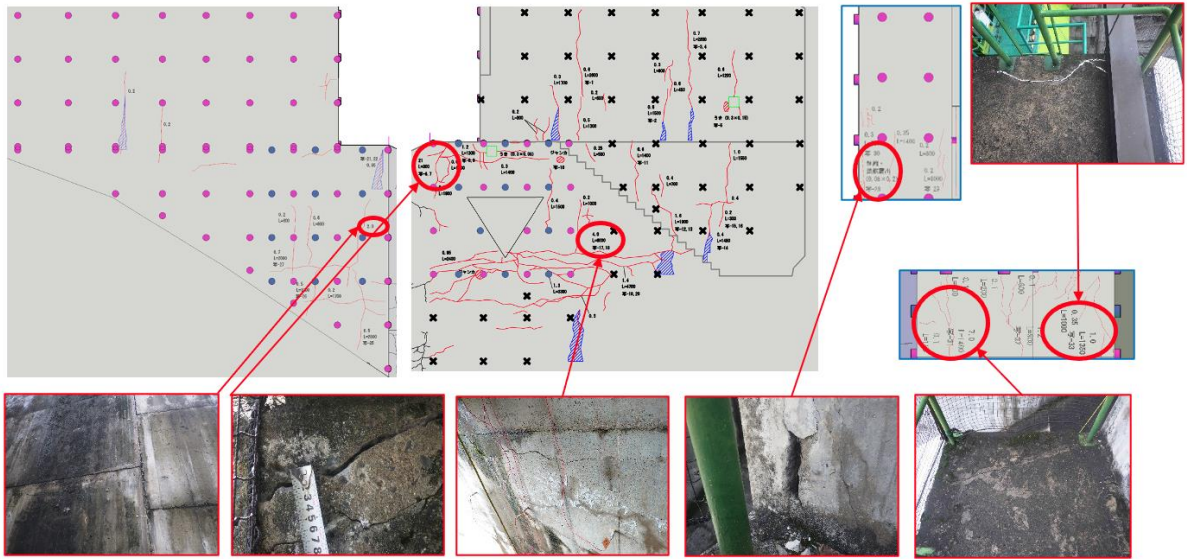
Fig. 2: Side wall concrete of orifice gate of Fig. 1b.

Currently reproduction of the existing structures with point-clouds and incorporating surface condition are thus enthusiastically studied elsewhere. As known, an urgent matter to tackle in existing infrastructure is to establish rational countermeasure against ones rated to be seriously ill and therefore the digital twin with surface condition will suffice the requirement to make a decision; however, to propose the reasonable maintenance program or establish a proactive maintenance program for the future, internal information of the structures will be essentially obtained. In this paper, the internal condition will be visualized by elastic wave parameters as velocities through elastic wave tomography approaches.

3. Elastic wave approaches for concrete structures
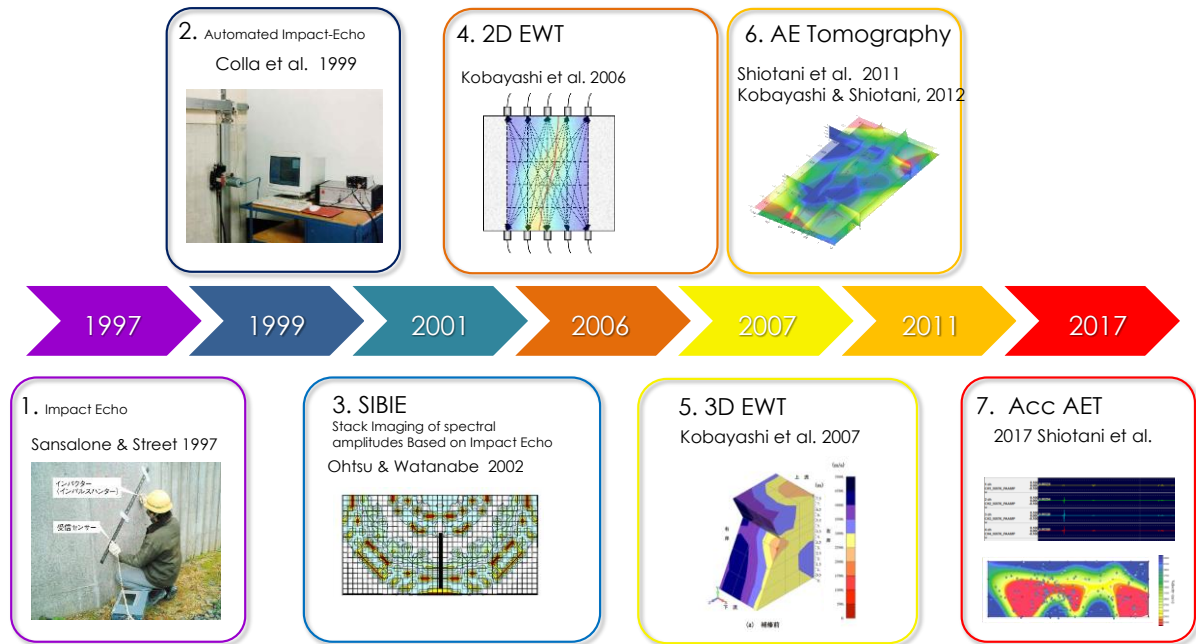
Fig. 3: Brief history of elastic wave techniques for engineering concrete.

In 1990s, an early period of applications of elastic wave techniques for concrete, the evaluation is utilizing impact-generated waves from one surface, propagated through concrete, and reflected by internal flaws and other surfaces [2]. A pair of transmitter and receiver of ultrasonic sensors installed on the same surface are employed, and internal defects can be identified for the depth based on the propagation time. With this one-dimensional evaluation was possible with a pin-point measurement, and to draw two-dimensional pictures, scanning of the measurement points are automated with a manner of a X-Y plotter [3]. Corresponding to plural numbers of defects inside concrete as well as to visualize internal information, SIBIE (Stack Imaging of spectral amplitude Based on Impact Echo) is presented [4]. As this still use a pair of sensors, the resulted 2D image could be virtual i.e., only the information in the depth direction could be obtained. To realize real 2D images of defect inside concrete, a tomographic approach using through the thickness elastic waves is developed for concrete [5]. In this approach multiple numbers of ultrasonic sensor are to be attached on a surface, and excitations are carried out from the opposite side surface. A ray-trace algorithm supposing the wave-radiation to multiple directions is considered with using SIRT (simultaneous iterative reconstruction technique). This tomographic approach was followed to expand to three dimension and used to evaluate the repair effectiveness in concrete dam piers [6]. As shown, general tomographic approaches require the artificial excitations of elastic wave i.e., as it uses through the thickness waves minimal two surfaces should be accessible, limiting in the scope of applications. Therefore, the author idealized the AE tomography [7] and coded [8], it was confirmed afterward that the AE tomography was first presented by Schubert [9], earlier than our study. It is noted that there were no acoustic emission techniques in Fig. 3 demonstrating elastic weave techniques for concrete. Acoustic emission is a very powerful method to know real-time evolution of crack assuming installation of AE sensors; however, the time span of deterioration or ageing of engineering concrete namely concrete structure takes a decade of years in minimum, meaning that there was no application of AE technique to install/ monitor the concrete structures for that long period, leading only a short time continuous monitoring in a level of laboratory by AE techniques. AE techniques shall be thus considered and applying only for unique cases such as experimental in-situ monitoring and safety confirmation monitoring when serious damages became obvious but shall be in-service until ultimate countermeasures [10]. Again in AE tomography, artificial excitations of elastic waves are not needed but source location algorithm of

AE technique is applied to identify the naturally produced AE sources due to reversable motions of existing defects as fritting and friction among crack interfaces. By regarding the located AE sources as excitations of elastic wave, distributions of elastic wave velocity are calculated. Based on the obtained velocity distributions, AE sources are again identified, and velocity distributions are renewed by re-identified AE sources. This procedure is repeatedly implemented and most-likely AE sources as well as velocity distributions reflecting internal damage are finally determined. To enlarge monitoring area of a sensor as well as to focus first on serious damage, AE tomography has been subsequently expanded to the frequency of acceleration namely smaller than 20 kHz [11]. So far, a group of author has been applying the AE tomography to buildings' piers, bridge slabs, concrete dam piers, and spillway of rockfill dam. In the following part of the paper, the application of spillway of concrete in a rockfill dam is demonstrated, followed by incorporation into reproduced digital image of point-clouds.

4. Spillway of rock fill dam

4.1 Condition of damage

A 40 year-old spillway of a rock fill dam is composed by orifice gate of concrete side walls (see Fig. 3a) is investigated for the damage by elastic wave tomography. As shown in Fig. 2, cracks along steel reinforcement and precipitation of efflorescence, seemed to be led by ASR (alkaline silica reaction), were observed. Substantial crack widths are 4 mm in bank side walls, 7 mm in lower current side wall, respectively. At present structural integrity due to ASR seems to be attributed only to these crack widths information without internal deterioration information. Tomographic reconstruction with elastic wave velocity is thus expected to replace those conventional idea only from surface condition.

a) Overall view of orifice gate and illustration   b) Sensor arrangement
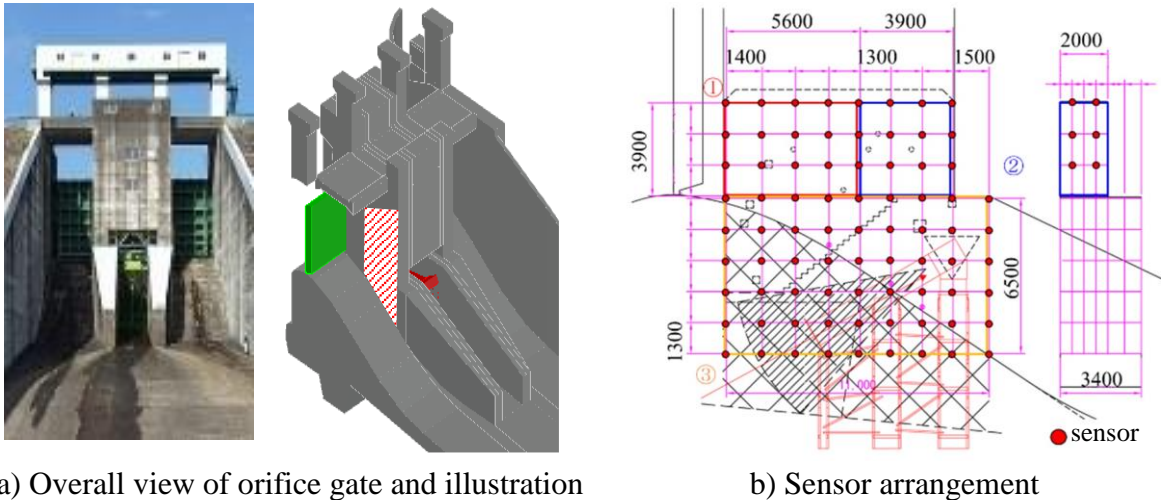
Fig. 4: Configuration of elastic wave tomography monitoring.

4.2 Measurement of elastic wave tomography

Sensor arrangement of accelerometers is depicted as in Fig.4b. A 30 kHz resonant accelerometer of TEAC 707IS is employed and arrayed in a space of 1.3-1.5 m. A spherical steel ball of 30 mm in diameter is used to excite the elastic waves. The excitations are made on the opposite side of sensor installation side. 10 times excitations in every designated point are made and stacked to eliminate noises, then recorded with a 200 kHz sampling rate. As resolution of the velocity distributions is highly dependent on the sensor array i.e., space between sensors and regarded as a half of it, 0.65 - 0.75m is a minimal resolution of this measurement. Analytical mesh size of this case is thus set at 1.0 m. Monitoring is carried out three areas separately as demonstrating 1, 2 and 3 in Fig. 4b.

4.3 Results and discussions
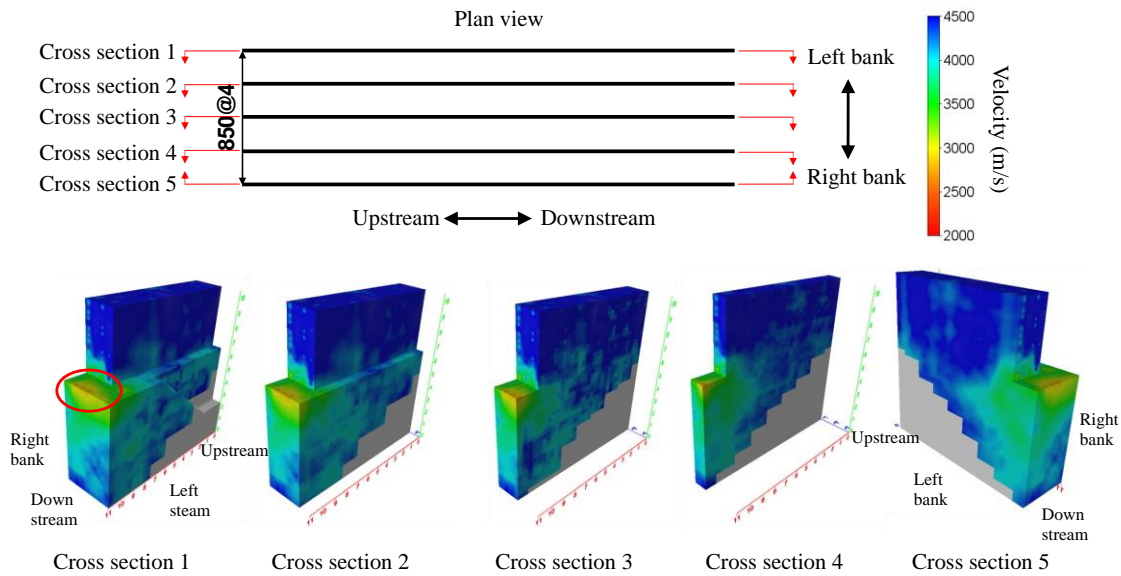
Fig. 5: Distributions of elastic wave velocity (Tomogram).

Tomogram when the measurement was conducted in the shadow area of Fig. 4a right is demonstrated as in Fig. 5. In Fig. 5, 2D sectional tomograms from section 1-5 are depicted. A good agreement of the location of serious surface cracks and areas showing small velocity as less than 3000 m/s is obvious indicated by a red circle in section 1 of Fig. 5.
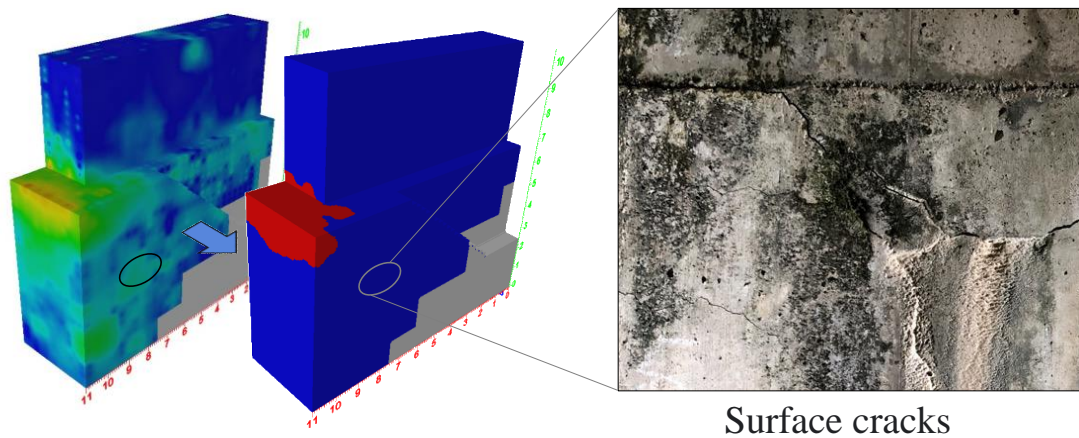
Surface cracks

Fig. 6: Comparison between tomogram and surface cracks of left bank side.

The surface crack condition of left bank side and 3D tomogram are shown in Fig. 6, where the binarized image based on the velocity of 3500 m/s is demonstrated in the middle of Fig. 6. Red areas show the velocity less than 3500m/s while the blue shows it larger than 3500 m/s. It is obvious that serious crack locations are well identified with red areas. It is noted that the area where surface cracks are observed on the left bank side (see the right photo of Fig. 6), there was no area of red, showing the velocity less than 3500 m/s, suggesting that the crack on this left bank surface will not be expanded into a deeper area of the wall. This estimation was subsequently verified by borehole cameras' observation after excavating holes up to 50 cm depth (see Fig. 7 & 8). The deepest cracks could be observed up to 13 cm depth in No. 5 drilling point. This result are well accorded to the estimation by the tomography.
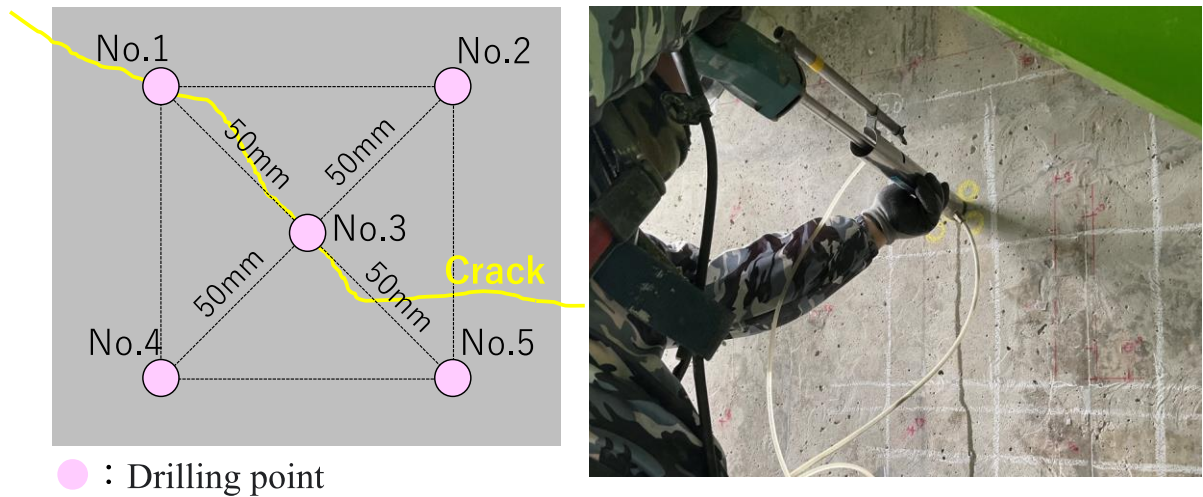
Fig. 7: Excavating five points from #1-5 on the cracked area (left) and a photo when fluorescent epoxy impregnation was carried out (right).
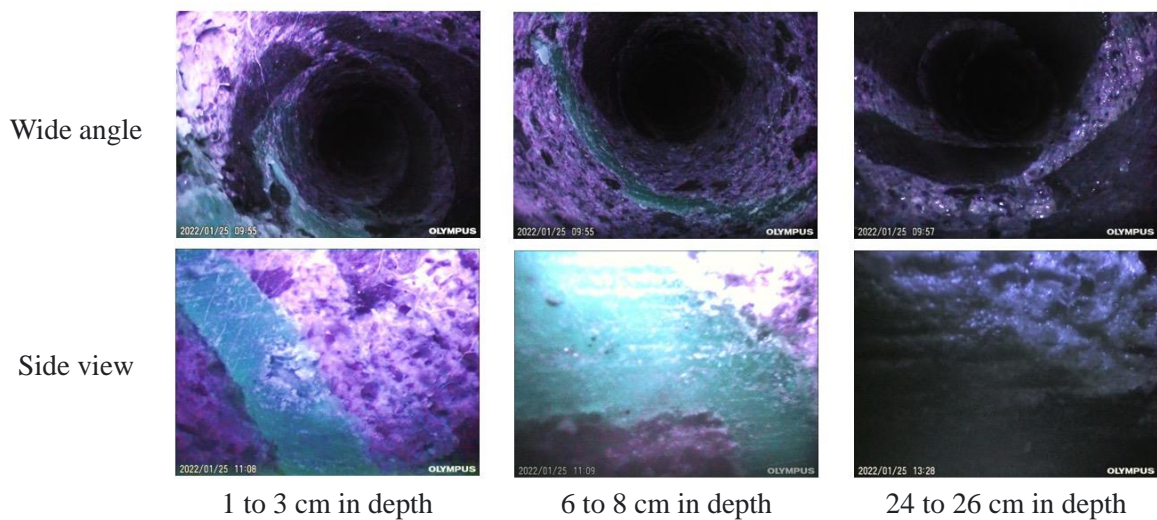
Fig. 8: Still images under ultraviolet light of the borehole in No. 5 in the depth direction.

4.4 Incorporating velocity distributions into digital twin

As aforementioned in chapter 2, for the reasonable maintenance program as well as to establish a proactive maintenance program, internal information of the structures will be essentially obtained and needed to be incorporated into digital twin. In this study as a collaboration project with University of Illinois at Urbana-Champaign, the spillway is reproduced by 3D point-clouds using still and video images, tomograms namely internal velocity distributions, 2D surface observations and design drawing. The configuration of integration procedures (see Fig. 9) and finally obtained integrated model (see Fig. 10) and details of superposition of surface and internal information (see Fig. 10) are demonstrated. By using Fig. 10, the structure of interest can be visualized in 360 degrees in all directions. Damage specifications such as crack width, length as well as density can be visually quantified and overall internal damage can be confirmed by the tomograms. Classification of damages and interpretation of structural performance will be automatically implemented with using AI near future.
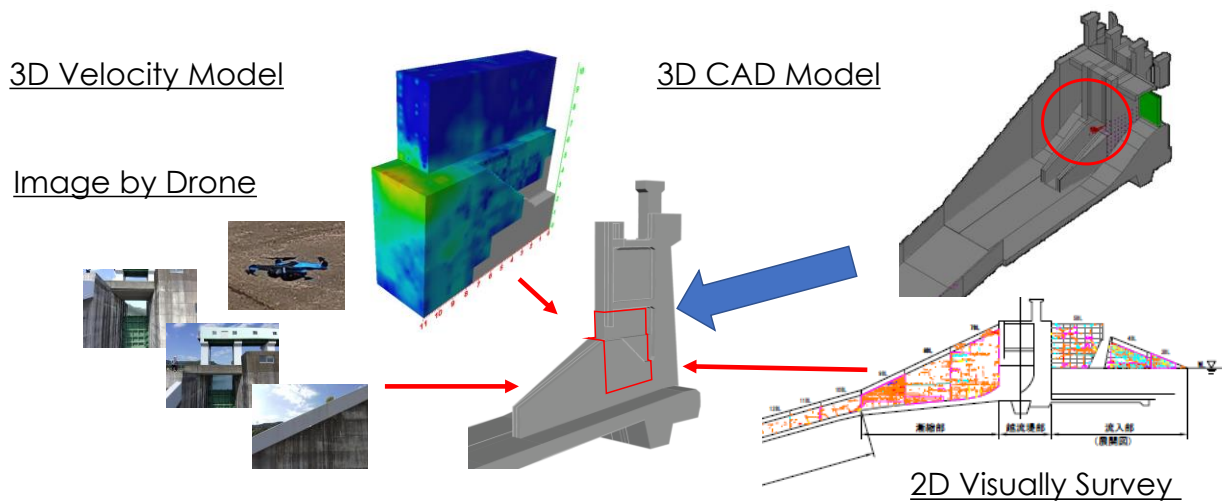
Fig. 9: Configuration of integration procedures for real digital twin.
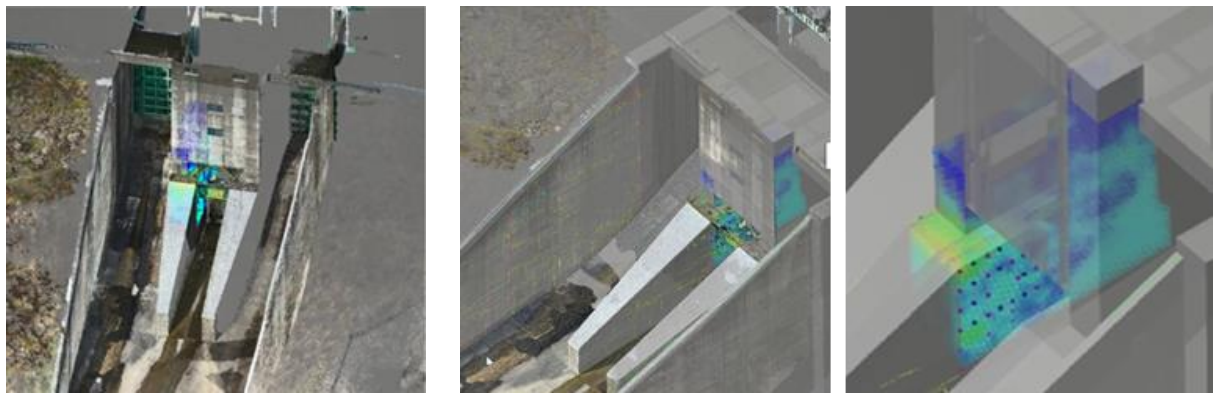
Fig. 10: Resulted digital twin incorporated point-clouds, surface condition and internal elastic wave velocities.

5.   Conclusions

As for DX for civil infrastructures, digital twin of point-clouds of spillway of a rock fill dam is demonstrated. Information such as surface deterioration condition as well as internal condition composed of elastic wave velocities, which will be crucially important to realize life-cycle-oriented design, construction, and maintenance, is incorporated into the digital twin. From the resulted digital twin, the overall damage of the structure can be readily visualized. When these inspections are periodically carried out and visualized with the proposed integration procedure, rational maintenance program through the life cycle of the structures will be reasonably proposed. Reduction of measurement time and cost of sensing, suggesting development of remote sensor installation and excitations, with wireless sensor network will be necessary. Unfortunately, AE techniques has been using principally for experimental purpose in civil engineering as there was no demand for long-term monitoring for the structures, taking a huge cost; however, impending failure monitoring for important structures damaged seriously will be increasing as there is no diversion route of road or taking a time for replacing new ones. AE techniques will definitely contribute to these cases. To prepare these occasions, usefulness of elastic wave approaches including AE techniques shall be demonstrated through the suggested DX in civil engineering.

6. Acknowledgements

7. References

[1] Stolterman, E., Fors, A.C. (2004) . Information technology and the good life, Information System Reseach, pp.693-697.

[2] Sansalone, M.J., Street, W.B. (1997). Impact echo, Bullbrier Press, ISVBN: 0-9612610-6-4.

[3] Colla, C., Schneider, G., Wiggenhauser, H. (1999). Automated impact-echo: method improvement via 2- and 3-D imaging of concrete elements. In Proc. 8th Int. Conf. Structural Faults and Repair-1999, M. Forde (Eds.) CD-ROM, Engineering Technics Press, UK

[4] Ohtsu, M., Watanabe, T. (2002). Stack imaging of spectral amplitudes based on impact-echo for flaw detection, NDT & E International, Vol. 36, No.3, p. 189-196.

[5] Kobayashi, Y., Shiotani, T., Shiojiri, H. (2006). Damage identification using seismic travel time tomography on the basis of evolutional wave velocity distribution model," In Proc. 11th Int. Conf. Structural Faults and Repair-2006, M. Forde (Eds.) CD-ROM, Engineering Technics Press, UK

[6] Kobayashi, Y., Shiotani, T., Aggelis, D.G., Shiojiri, H. (2007). Three-dimensional seismic tomography for existing concrete structures, In Proc. Second Int. Operational Analysis Conference, 2, p. 595-600.

[7] Shiotani, T., Okude, N ., Momoki, S., Kobayashi, Y. (2011). Proposal of assessment method for infrastructures by AE tomography, Proceedings of 2011 National Conference on Acoustic Emission, p. 39-42 (in Japanese).

[8] Kobayashi, Y., Shiotani, T. (2012). Seismic tomography with estimation of source location for concrete structure, In Proc. 14th Int. Conf. Structural Faults and Repair-2012, M. Forde (Eds.) CD-ROM, Engineering Technics Press, UK.

[9] Schubert, F. (2004). Basic principles of acoustic emission tomography, Journal of Acoustic Emission, Vol. 22, p. 147-158.

[10] Johnson, M.B., Ozevin, D., Washer, G., Ono, K. Gostautas, R., Tamutus T. (2012). Acoustic emission method for real-time detection of steel fatigue crack in eyebar, National Academy of Science, Washington, DC, USA, p.72-79.

[11] Shiotani, T., Asaue, H., Nishida, T., Maeshima, T., Tanaka, Y. (2017) Evolution of fatigue damage in wheel-loading tests evaluated by 3D elastic-wave tomography, Journal of Disaster Research Vol.12, No. 3, p.487-495.

ACOUSTIC EMISSION TESTING FOR MULTI-SCALE ASSESSMENT OF REINFORCEMENT CORROSION IN CONCRETE STRUCTURES

Els Verstrynge[1], Charlotte Van Steen[2] and Martine Wevers[3]

[1]KU Leuven, Department of Civil Engineering, Leuven, Belgium; els.verstrynge@kuleuven.be
[2]KU Leuven, Department of Civil Engineering, Leuven, Belgium; charlotte.vansteen@kuleuven.be
[3]KU Leuven, Department of Materials Engineering, Leuven, Belgium; martine.wevers@kuleuven.be

ABSTRACT

Degradation of existing structures poses a serious threat to our built environment. The aim of this paper is to investigate the use of acoustic emission monitoring in degradation assessment of existing structures, focusing specifically on corrosion damage detection in reinforced concrete structures. Reinforcement corrosion is seen as one of the most significant and costly degradation mechanisms that impact the durability and structural safety of our built infrastructure and Modern heritage buildings. The paper presents a multi-scale experimental approach, from material to structure, focusing on two challenges: (i) monitoring the evolution of the corrosion process itself and the consequential concrete cracking during accelerated corrosion, and (ii) identifying the different AE sources in this complex process. The application of AE testing for rebar corrosion monitoring is investigated on various sample types and scales under accelerated conditions in a lab environment, and from on-site monitoring of a concrete girder bridge. Results show that the developed test setups, data filtering and processing procedures substantially improve AE-based corrosion damage monitoring, and provide a valuable contribution towards on-site application.

Keywords: Reinforcement corrosion, concrete, passive acoustic emission sensing, multi-scale experimental program.

1. Introduction

In structural engineering, the acoustic emission (AE) technique is particularly useful for degradation assessment in existing structures. Typical degradation processes, such as reinforcement corrosion and time-dependent crack formation start at the material level in the form of micro-cracking which cannot be monitored with common techniques. Additionally, such processes often start internally and degradation may already be substantial before being noticed in visual inspection or structural health monitoring (SHM). Yet, such degradation mechanisms cause a serious threat to the durability and structural safety of existing structures, from civil infrastructure to heritage buildings. The aim of this paper is to show how acoustic emission monitoring can make a major contribution to the degradation assessment of existing structures.

As degradation phenomena are complex time-dependent processes, the way to tackle them is through careful validation with other techniques, with dummy samples, and through upscaling from material to structure within a multi-scale framework.

In concrete structures, acoustic emission sensing is frequently used during lab testing to detect and identify crack formation in various cementitious composites, from reinforced concrete (RC) beams under bending and shear [1] to fiber reinforced concrete (FRC) under fatigue loading [2]. Also the study of reinforcement corrosion with AE testing has been subject of various test programs [3, 4], and even on-site monitoring of corroded concrete bridges [5]. However, most research has focused on AE testing of corroded RC elements rather than the monitoring of corrosion damage. In addition, test repeatability has proven to be rather low and even contradictory findings have been reported [15]. Hence, a profound study on AE monitoring of reinforcement corrosion and related concrete damage that addresses the challenges within a multi-scale approach, from a fundamental understanding of the corrosion process to the structural behavior of damaged RC elements, is needed.

This paper presents an overview of our recent work on corrosion detection in reinforced concrete (RC) structures, within a multi-scale approach, while focusing on two specific challenges:

- Monitoring the evolution of the corrosion process itself and the consequential concrete cracking, and
- Identifying the different AE sources in this complex process.

In the first section of this paper, the process of reinforcement corrosion in concrete structures and use of AE testing during this damage process are elaborated. In the next section, an overview of the multi-scale experimental test program is presented, focusing on the specific AE testing objectives and complementary techniques that were applied for AE validation. Hereafter, the most important results of the experimental tests are elaborated, with focus on the two challenges enlisted above. The paper concludes with a brief recap of the research highlights and outlook.

2.   Reinforcement corrosion and the use of AE testing

In normal conditions, steel reinforcement is passivated and hence protected from corrosion due to the high-alkaline environment created by the surrounding concrete. When the concrete carbonation depth reaches the rebars or a critical chloride concentration is present, e.g. due to ingress of de-icing salts, the alkalinity drops and the steel may start corroding in the presence of water and oxygen. Chloride-induced corrosion is generally considered most detrimental for an RC structure as it leads to a faster corrosion process with localized macro-cells, causing corrosion pits in the steel reinforcement. Regardless of the cause of corrosion initiation, the corrosion process of reinforcement bars (rebars) is generally described as a two-phase process, see Fig. 1 [6]. In the initiation phase, the concrete carbonation front and/or chloride ions progress towards the rebars. At the end of the initiation phase, the critical chloride content or carbonation depth is reached and the corrosion process may start. The second phase, corrosion propagation, is divided into sub-phases in the fib model; before and after concrete surface cracking.

Most processes involved in this corrosion process will result in acoustic emissions, be it with different strength and signal characteristics. As indicated on the left hand side of Fig. 1, it is generally expected that AE activity (amount of AE events and strength of each event) increases towards the later stages of the corrosion process. Steel corrosion, absorption and hydration are known to produce rather low-energy AE events. Also stress build-up by the expansive corrosion products and micro-cracking in the concrete will cause AE activity. Towards the later damage stages, concrete cracking and spalling induce high-energy AE events. However, it should be noted that the presence of concrete cracks in later stages of the corrosion process might hinder the wave propagation, leading to an apparently reduced AE activity. Hence, AE energy is not always a good indicator of the source type as it depends on source-sensor distance and attenuation which increases during crack formation.

In addition, the different types of AE sources cannot be spatially separated. Pressure build-up, concrete cracking and steel corrosion all start internally and in close proximity of the corrosion

hot-spot. This means that an AE activity analysis is not always a reliable method for studying reinforcement corrosion in concrete. Thus, a more in-depth analysis is required to identify the different AE sources to ensure reliable AE-based corrosion monitoring methods for RC structures.
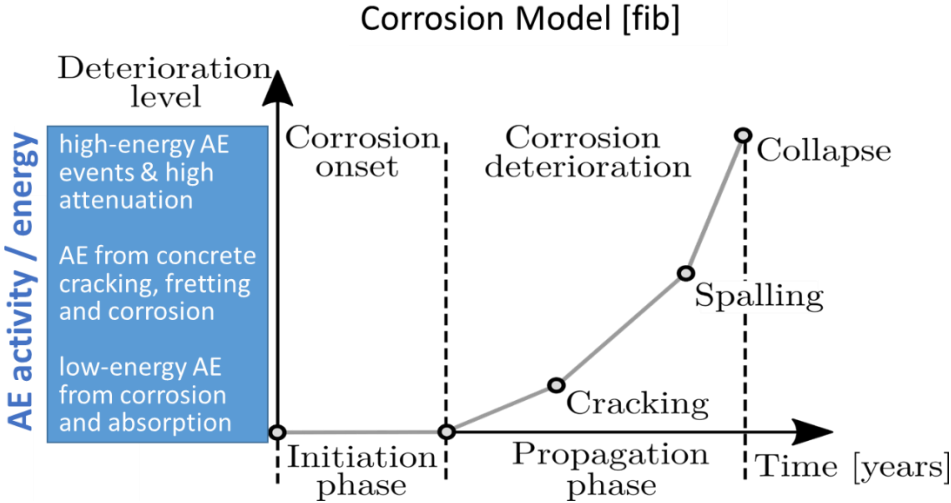
Fig. 1: Increase in AE activity as a function of the corrosion process in reinforced concrete.

Corrosion experiments are usually performed under accelerated conditions to obtain results within a limited time frame. The corrosion process is often accelerated by means of an imposed direct current (DC), where the corroding rebar is the anode and an external cathode is provided. It should be noted that in such setup, the initiation phase is skipped as the corrosion onset is forced. To avoid unnatural corrosion effects, corrosion currents should be limited, e.g. typically to a maximum of 100 μA/cm². This value was also used as a maximum limit in this study. Few studies focus on more natural corrosion processes in which case chlorides are added and/or wet-dry cycling is used instead of an impressed current.

3. Multi-scale experimental test program

The test program presented here was executed in the framework of the KU Leuven project "Multi-scale assessment of residual structural capacity of deteriorating reinforced concrete structures" (KU Leuven internal funds (3E170431)). It should be noted that only the AE data sets and results are discussed here, while interested readers are referred to the literature for a discussion on the structural analysis of the corroded RC elements [7]-[9].

Table 1 presents an overview of the test program, including sample type, sample sizes, number of samples monitored with AE (out of the total number of samples), type of corrosion process (impressed current or natural conditions), corroding length of the rebar (C_L), duration of the AE-based corrosion monitoring, the number of AE sensors per sample and their layout (1D, 2D or 3D), AE sensor type (flat or peak response spectrum, frequency range or peak frequency), and other techniques used for validation of the AE results. A picture for each of the test series that is included in detail in this paper is presented in Fig. 2.

Table 1: Overview of all test series included in the corrosion test program with AE monitoring.

	MATERIAL		*STRUCTURAL COMPONENT*		*STRUCTURE / CASE STUDY*	
Test series	Test A1 (XCT samples)	Test A2 (Pull-out samples)	Test B1 (RC beams)	Test B2 (RC beams)	Case C1 (RC building pilotis)	Case C2 (PC bridge girders)
sample size [m]	cylinder, diam. 0.036	prism 0.15 x 0.15 x 0.25	RC beams length 1.8	RC beams length 3.0	RC columns, section 0.3x0.5	PC I-beams, length 22.9
#AE test (total)	3 (7)	8 (117)	2 (25)	2 (4)	2	3
corrosion process	100 µA/cm² DC	100 µA/cm² DC	50-100 µA/cm² DC	50 µA/cm² DC	natural (carbonation)	natural (chlorides)
C_L [m]	0.02	0.042-0.100	1.4-1.5	0.4	unknown	unknown
test duration	up to 25 days	up to 90 days	up to 30 days	21 days	3 x 6 hours	12 days & 8 days
# AE sensors	2 (1D) & 6 (3D)	2 (1D) & 6 (3D)	4 (2D)	6 (2D)	6 (3D)	2 (1D) & 6 (3D)
type AE sensor	flat, 50-2000 kHz	flat, 100-400 kHz	flat, 100-400 kHz	flat, 100-400 kHz	flat, 100-400 kHz	peak, 75 kHz & flat, 100-400 kHz
other NDT	XCT	surface crack size	surface crack size, UPV	surface crack size, UPV	surface crack size, concrete tests	surface crack size, UPV, concrete tests

Test series A1 (XCT samples)

Test series A2 (RC prisms)
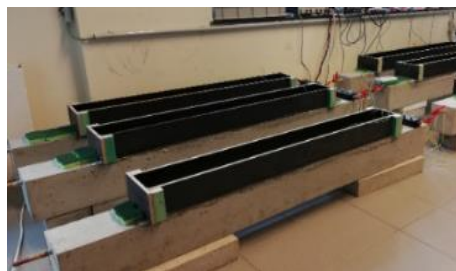
Test series B1 (RC beams)

Case study C2 (PC girder bridge)

Fig. 2: Overview of test series.

Following remarks are noted regarding the test programs (Table 1):
- From "material" to "structure", sample sizes increase. Hence the response spectrum of the chosen AE sensors decreases to allow for larger source-sensor distances. However, it should be noted that a flat response AE sensor (100-400 kHz frequency range) was applied for most test series, enabling a signal-based AE analysis and upscaling of developed processing algorithms.
- The number of samples that was monitored with the AE technique during corrosion in each test series is limited by the availability of AE equipment and length of the test. Hence, not all corroding samples have been monitored with AE.

- The maximum number of AE sensors per sample is indicated in Table 1. For the smaller samples, a 3D setup was used, while for the beams, the AE sensors were positioned on the side of the beams in a plane (2D setup). For the bridge girders of case study C2, both a 1D setup on three beams simultaneously, as well as a 3D setup on one beam were used.
- On test series A2 (prisms), additional resonance sensor types (peak frequency 150 kHz) were applied during corrosion monitoring for validation purposes. For brevity, these tests are not included in current paper, but a description can be found in the literature [10].
- For all experiments in the lab, corrosion was accelerated by an impressed direct current (50-100 µA/cm² DC). Samples of Test series A1 and A2 were partly submerged in a salt solution during corrosion, while beams of Test series B1 and B2 were positioned upside-down (tensile reinforcement near top surface) with a bottomless water tank on top that contained the cathode and salt solution. A schematic representation of the corrosion setup during Test series B1 is presented in Fig. 3.
- The RC beams of test series B1 contained one corroding rebar (corroding length 1.4-1.5 m), while the beams of test series B2 had stirrups and two corroding rebars that were only locally corroded (corroding length $C_L = 0.4$ m). Uncorroding parts of rebars were protected with anti-rust paint.
- The two case studies were subjected to natural corrosion: in Case C1, corrosion was caused by severe concrete carbonation due to poor concrete quality of in-situ cast members, in Case C2, some evidence of chloride-induced corrosion was found, probably due to de-icing salts and water infiltration in the post-tensioning ducts.
- To evaluate the AE results, samples were also monitored with X-ray scanning Computed Tomography (XCT), see [11] for a detailed description, ultrasonic pulse velocity measurements (UPV), and monitoring of the crack widths and patterns on the concrete surface. In addition, for case studies C1 and C2, small cores were investigated to test carbonation depth and chloride content (referred to in Table 1 as "concrete tests").
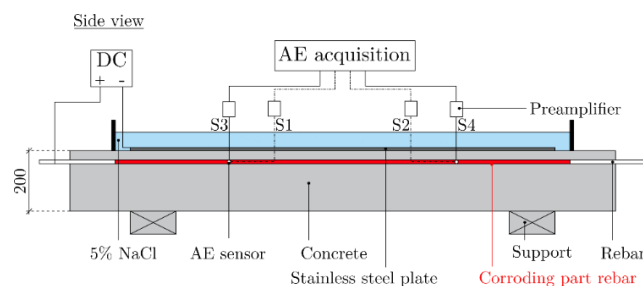
Fig. 3: Corrosion setup and AE sensor setup for RC beams of Test series B1, picture from [12].

The objectives of AE monitoring vary for the different corrosion test series. At the *MATERIAL* scale, a protocol for AE monitoring of corroding reinforced concrete was developed, including: data filtering, improved arrival time picking, AE source localization, and source identification through hierarchical clustering. AE results as obtained from this data-processing protocol were validated in Test series A1 with 3D imaging of steel corrosion and mortar cracking from XCT scanning [11]. Secondly, AE-based corrosion monitoring, AE source localization and identification were upscaled to RC prisms in Test series A2, and validated by means of surface crack monitoring, rebar extraction at the end of testing, and the use of dummy samples to spatially differentiate different AE sources and validate the source clustering protocol. The latter study is described in detail in [10]. At the *STRUCTURAL COMPONENT* scale, RC beams were monitored during corrosion to upscale the developed AE protocols, and provide a valuable link between small-scale testing and real-scale structures. AE results were validated by means of surface crack monitoring and rebar extraction at the end of testing. Finally, at the structure level, two *CASE STUDIES* were investigated to apply the gained knowledge in practice and define further challenges for AE-based corrosion damage monitoring of existing RC structures.

The following sections provide an overview of the most important results in relation to the objectives discussed above. For sake of brevity, description of the data processing is kept limited to enable an understanding of the major advancements made in the project, yet for a more detailed description of test setups and data processing, we make reference to the literature.

4. Results and discussion

4.1 Monitoring of rebar corrosion and concrete cracking

As reinforcement corrosion monitoring is a test with long duration and various influencing factors, many noise data can be expected, especially during in-situ monitoring of bridges in operational conditions, but even during controlled lab tests. Therefore, a first step is a proper design and calibration of the AE test setup to ensure:

- proper choice of AE sensor types and frequency range in function of expected source-sensor distance and attenuation, which can be done by means of pencil lead breaks (PLB).
- deciding on threshold values and hardware filters, aiming at filtering as much noise signals as possible without any relevant loss of valuable AE data.

Secondly, as not all noise signals can be avoided during testing, further data analysis requires the development of a reliable filtering protocol. In [13], details can be found on a two-step filtering protocol that was developed specifically for use during AE-based corrosion monitoring. However, it is generally applicable to tests in which internal damage sources are captured through monitoring of AE bulk waves, e.g. in concrete and masonry structures. It consists of following steps:

- step 1: signal-based filtering, using the Signal to Noise Ratio (SNR) and the obtained accuracy of the Time Of Arrival picking (TOA).
- step 2: location-based filtering: using the estimated Source Location Error (SLE) and omitting sources located outside of sample boundaries (reflections).

Fig. 4 presents the evolution of the unfiltered (left) and filtered (right) cumulative AE data for the on-site monitoring on the bridge girders (Case C2). The unfiltered data present higher AE activity, especially during the week when the bridge carries more traffic. It can also be seen that a non-negligible amount of noise signals are filtered out by the two-step filtering protocol.
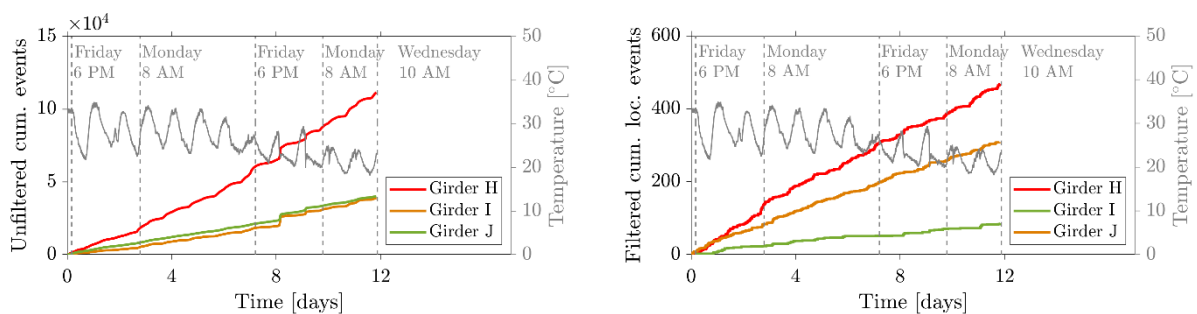
Fig. 4: Cumulative AE events and temperature as a function of time captured during on-site monitoring on three PC bridge girders (Case C2): unfiltered (left) and filtered (right) data.

In Figs. 5 and 6, the cumulative AE events or energy are related to the average corrosion crack width measured on the concrete surface during corrosion of a representative RC prism and RC beam, respectively. Both test samples had one longitudinal corroding rebar, yet with a different concrete cover depth and corroding length. Despite the difference in sample size and test setup, see Table 1, a good agreement is observed between the cumulative AE data and the concrete surface crack growth for each of the test series. This is an indication that AE monitoring is well able to capture damage progress during an accelerated corrosion experiment.

However, there is no evidence that this relation can be extended towards real-life natural corrosion processes, and hence towards long-term on-site AE monitoring of reinforcement corrosion in RC structures. Although it should be mentioned that promising results were obtained for AE monitoring of wire rupture in prestressing strands [5]. In addition, comparison between AE results and corrosion levels or pit locations have shown limited agreement between such data, as a majority of AE events is caused by concrete cracking rather than the corrosion process itself [7]. Much more information about the corrosion process can be obtained when looking beyond the cumulative AE activity, and using AE results to observe the internal damage processes by means of 3D source localization and identification. Distinguishing between different AE sources potentially allows to identify AE events coming from steel corrosion on one hand and from concrete cracking on the other hand. These aspects are discussed in the next section.
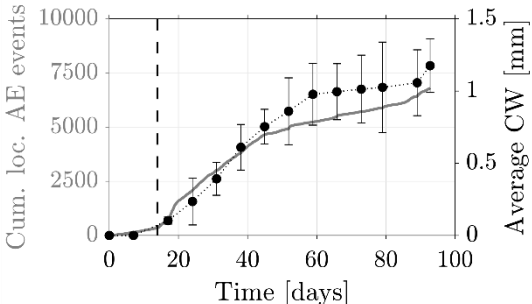
Fig. 5: Crack width versus cumulative AE events during corrosion of RC prism (Test series A2), figure adapted from [7].
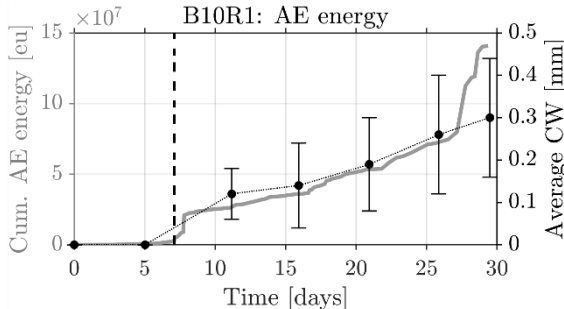
Fig. 6: Crack width versus cumulative AE energy (eu = 10-14 V²s) during corrosion of RC beam (Test series B1).

4.2 AE source localization and identification

Corrosion of steel reinforcement in concrete is a complex process in which many AE sources are active. Besides the corrosion itself, also the absorption and drying of salt water, the formation of hydrogen bubbles at the cathode, the pressure exerted by the expansive rust products and the cracking of the concrete may cause AE events. An overview of possible AE sources during an accelerated corrosion test with indication their probability of detection is indicated in Fig. 7.
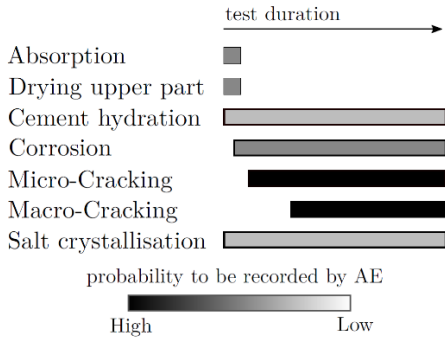
Fig. 7: Overview of possible AE sources during accelerated corrosion testing of RC.

In a first step, 3D AE source localization is performed to spatially identify the corrosion damage. Figs. 8 and 9 present results of 3D AE source locations in corroding RC prisms (test series A2). Although the six AE sensors can only be positioned on the upper half of the prisms, due to the salt bath in which they are partly submerged, a very good agreement between the corroding parts of the rebar or stirrup and the AE source locations is obtained.

From Fig. 8, it can be observed that the first step of the filtering protocol, being the application of the SNR filter and enhanced TOA picker also have a significant effect on the quality of the AE source localization; As source locations are calculated using the arrival time of the wave at multiple sensors, a correct TOA is essential. Further, the AE source locations were determined by assuming a homogeneous wave velocity. This assumption is justified as all AE sensors are positioned on the (thick) concrete cover. However, when a denser grid of steel rebars is used, or sensors are positioned on or near the rebar, one should take into account the increased wave velocity in the steel by application of a non-homogeneous wave velocity field [14].
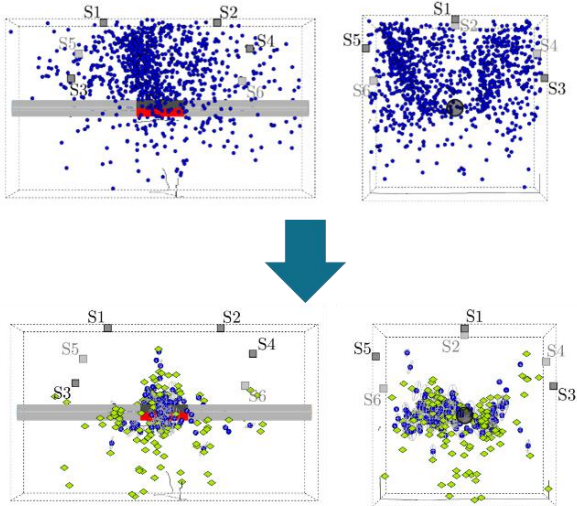
Fig. 8: 3D AE source localization in corroding RC prism without (top) and with (bottom) filtering and improved TOA picker [13].
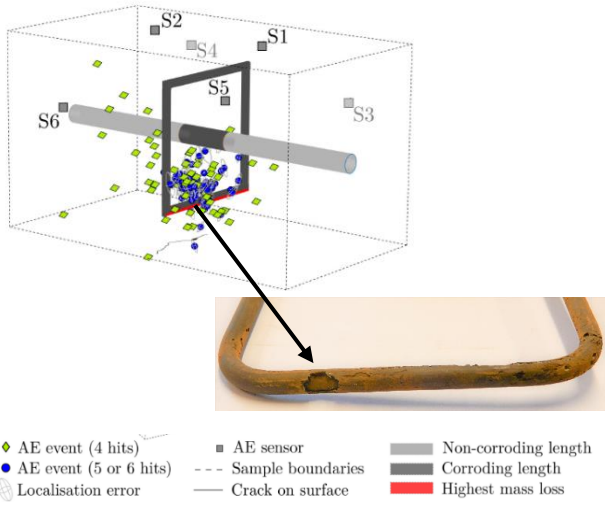
Fig. 9: 3D AE source localization in RC prism with corroding stirrup, and comparison with pit location in stirrup at the end of the test [13].

During reinforcement corrosion in concrete, AE sources such as steel corrosion and concrete cracking are difficult to differentiate spatially, as they are located in close vicinity. To differentiate the various AE sources, the AE signal characteristics can be used. This can be done using a parameter- or a signal-based approach, applying manual or unsupervised clustering. AE parameters such as amplitude, energy and average frequency may be biased through signal alterations during wave propagation in (heterogeneous) concrete and the use of resonance sensors. In [10], a signal-based hierarchical clustering algorithm was developed and applied on corroding RC prisms that were monitored with flat response (100-400 kHz) and resonance (150 kHz) AE sensors. The algorithm was evaluated by means of dummy samples in which AE sources such as rebar corrosion, absorption and concrete cracking were isolated. Fig. 10 shows an application of this clustering approach on a dummy RC prism, concrete prism, steel rebar and RC beam [12]. AE events belonging to the first cluster (blue) are found in each dummy sample. AE events from the second cluster (red) are mainly found in the uncorroded RC beam that was subjected to bending. Hence this cluster can be attributed to concrete cracking. A decrease of the cluster dissimilarity threshold did not allow for a further differentiation between the other sources such as micro cracking, absorption and steel corrosion [12]. Fig. 11 presents the results of AE signal clustering on both corroding beams of test series B2. Again, two clusters are found, from which cluster 1 (blue) can be attributed to the corrosion process and related effects, and cluster 2 (red) is assigned to concrete cracking. This latter cluster has a lower peak frequency and shows a significant increase in AE events a few days into the corrosion test when the concrete surface cracks are appearing. Results indicate that the developed AE clustering algorithm is able to distinguish the initiation of corrosion-induced concrete macro-cracking.
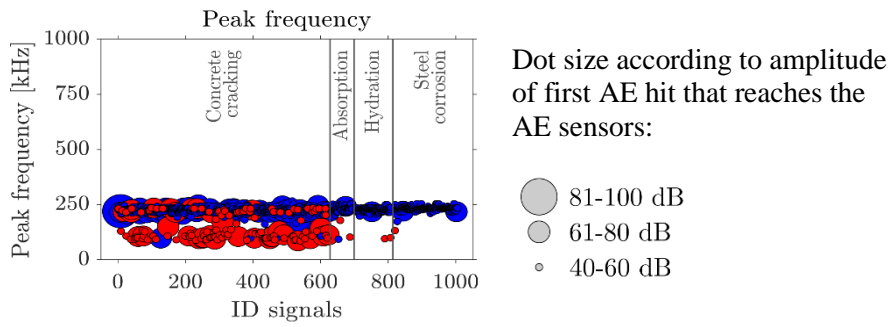
Fig. 10: Results of AE signal clustering on dummy samples showing peak frequency versus ID number of the AE signals. Expected AE sources are indicated for each group of signal IDs [12].
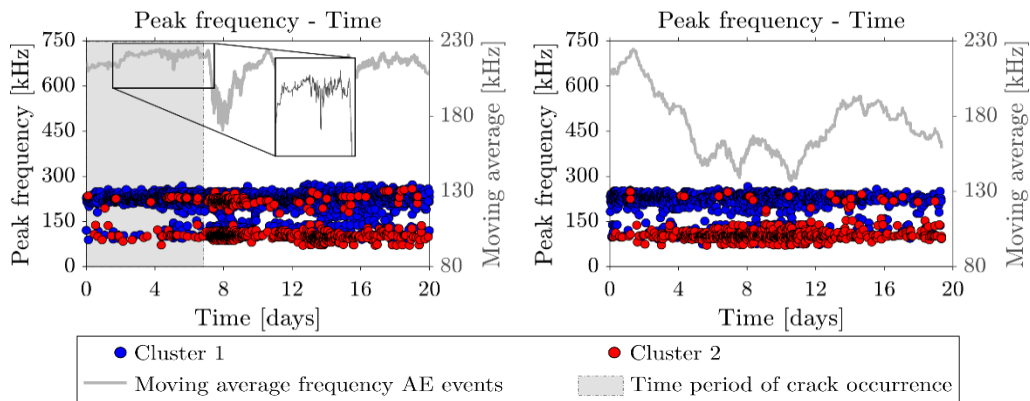
Fig. 11: AE signal clustering on corroding RC beams (test series B2), showing peak frequency versus elapsed corrosion time. Figures adopted from [12].

It can also be observed from Fig. 11 that the typical accelerated corrosion setup aims at obtaining very high corrosion levels in a short time interval, resulting in early concrete cracking and high damage rates that might not be representative for on-site corrosion damage processes. Therefore, a further validation of the clustering algorithm on samples with slower or natural corrosion rates will be done in future work as a next step towards on-site AE monitoring.

5.   Conclusions and outlook

AE monitoring has several important features that makes it particularly interesting for RC corrosion monitoring. Appropriate filtering and time of arrival (TOA) picking are essential to obtain qualitative AE data from corrosion tests on RC samples. Although a good correlation was obtained between cumulative AE activity and other damage indicators, such as crack width, such relations are difficult to extrapolate to other setups and non-accelerated corrosion conditions. Therefore, further analysis included 3D AE source localization and identification. Accurate source location results were obtained from AE data with improved TOA picking. Signal-based hierarchical clustering enabled distinguishing corrosion-induced concrete macro cracking from other AE sources related to the corrosion process. Our past research has focused on establishing a fundamental basis for reliable AE testing of complex damage processes such as reinforcement corrosion, using accelerated degradation tests. Future research will aim at on-site application of AE monitoring, where specific challenges are the detection of non-accelerated degradation and the value of AE for structural damage assessment.

6.   Acknowledgements

7.   References

[1]   Grosse C.U., Ohtsu M., Aggelis D.G., Shiotani T., eds. (2022) Acoustic emission testing - basics for research - applications in civil engineering. 2 ed. Springer.

[2]   De Smedt M., Vandecruys E., et al. (2022) Acoustic emission-based damage analysis of steel fibre reinforced concrete in progressive cyclic uniaxial tension tests. Construction and Building Materials 321: p. 126254.

[3]   Zaki A., Chai H.K., Aggelis D.G., Alver N. (2015) Non-Destructive Evaluation for Corrosion Monitoring in Concrete: A Review and Capability of Acoustic Emission Technique. Sensors 15(8): p. 19069-19101.

[4]   Kawasaki Y., Wakuda T., Kobarai T., Ohtsu M. (2013) Corrosion mechanisms in reinforced concrete by acoustic emission. Construction and Building Materials 48: p. 1240-1247.

[5]   Fricker S., Vogel T. (2007) Site installation and testing of a continuous acoustic monitoring. Construction and Building Materials 21(3): p. 501-510.

[6]   Fédération international du béton (2006) Model code for service life design, fib bulletin 34.

[7]   Van Steen C., Verstrynge E., Wevers M., Vandewalle L. (2019) Assessing the bond behaviour of corroded smooth and ribbed rebars with acoustic emission monitoring. Cement and Concrete Research 120: p. 176-186.

[8]   Nasser H., Van Steen C., Vandewalle L., Verstrynge E. (2021) An experimental assessment of corrosion damage and bending capacity reduction of singly reinforced concrete beams subjected to accelerated corrosion. Construction and Building Materials 286: p. 122773.

[9]   Vrijdaghs R., Verstrynge E. (2022) Probabilistic structural analysis of a real-life corroding concrete bridge girder incorporating stochastic material and damage variables in a finite element approach. Engineering Structures 254: p. 113831.

[10] Van Steen C., Nasser H., Verstrynge E., Wevers M. (2021) Acoustic emission source characterisation of chloride-induced corrosion damage in reinforced concrete. Structural Health Monitoring 21(3): p. 1266-1286.

[11] Van Steen C., Pahlavan L., Wevers M., Verstrynge E. (2019) Localisation and characterisation of corrosion damage in reinforced concrete by means of acoustic emission and X-ray computed tomography. Construction and Building Materials 197: p. 21-29.

[12] Van Steen C., Verstrynge E. (2022) Signal-Based Acoustic Emission Clustering for Differentiation of Damage Sources in Corroding Reinforced Concrete Beams. Appl. Sciences 12(4).

[13] Van Steen C., Verstrynge E. (2021) Degradation Monitoring in Reinforced Concrete with 3D Localization of Rebar Corrosion and Related Concrete Cracking. Appl. Sciences 11(15).

[14] Gao Y., Suryanto B., Chai H.K., Forde M.C. (2021) Evaluating the effect of corrosion on shear-critical RC beams by integrated NDT. Developments in the Built Environment 7: 100050.

[15] Verstrynge E., Van Steen C., Vandecruys E., Wevers M. (2022) Steel corrosion damage monitoring in reinforced concrete structures with the acoustic emission technique: a review. Construction and Building Materials (in revision).

ACOUSTIC EMISSION FOR IDENTIFICATION OF THE DOMINANT STRESS COMPONENT IN POLYMER COMPOSITES AT EARLY LOADS

Kalliopi-Artemi Kalteremidou[1,*], Dimitrios G. Aggelis[1], Danny Van Hemelrijck[1] and Lincy Pyl[1]

[1]Vrije Universiteit Brussel (VUB), Department of Mechanics of Materials and Constructions (MeMC), Pleinlaan 2, 1050 Brussels, Belgium;
Kalliopi-Artemi.Kalteremidou@vub.be, Dimitrios.Aggelis@vub.be, Danny.Van.Hemelrijck@vub.be, Lincy.Pyl@vub.be
*Correspondence: Kalliopi-Artemi.Kalteremidou@vub.be

ABSTRACT

Carbon Fiber Reinforced Polymer (CFRP) composites are broadly used in engineering applications. Their inherent anisotropy due to different fiber orientations can be considered an advantage since the strength of the component can be designated in preferential loading directions. However, this anisotropy leads to multiaxial stress conditions, complicating their damage sequence and mechanical response. Identification of these multiaxial conditions at early loading stages is of paramount importance to predict the upcoming structural response of the material. Acoustic Emission (AE) is applied in this study to CFRP laminates with different stacking sequences, in which different multiaxial conditions are generated. Laminates consisting of 30º plies are characterized by dominant shear stresses, whereas in laminates with 60º layers transverse normal stresses govern the stress state. Through quasi-static and incremental loading, it is shown that certain AE features can be used to identify the dominant stress component rather than just the occurring damage mode even at early loads, before severe fracture influences the mechanical capacity. This is of great importance in cases that detrimental shear stresses are generated, leading to delaminations and mechanical deterioration. AE can be used in this direction to predict the upcoming damage and to take necessary measures to avoid final failure.

Keywords: Polymer composites, acoustic emission, multiaxiality, shear, Kaiser effect.

1. Introduction

Acoustic Emission (AE) is a non-destructive method which has been widely used for damage studies in composites. In practice, piezoelectric sensors are mounted on the surface and record the elastic waves generated in a material undergoing irreversible changes. The wave magnitude and further features are correlated to emission sources. Firstly, the total AE activity can be examined, giving information on the "amount" of damage [1]. Secondly, analysis of waveform features in the time domain can be used as damage indicator [2, 3]. In other studies, waveform analysis in the frequency domain is performed and clustering approaches for identification of damage modes have been many times reported [4, 5]. However, to the authors' best knowledge, no direct correlation of AE features with the stress/strain states in polymer composites has been performed in literature. Due to the intrinsic anisotropy of composites, multiaxial stresses occur even in flat laminates under

simple tensile loads, because of the different fiber orientations in their individual layers [6]. However, the AE response of composites has been mostly investigated for conventional lay-ups (i.e. [0°/90°], [±45°]) [7, 8] or for representative specimens with specified model damage sources (double cantilever beam specimens [9] or single fiber filaments [10]). Certain correlations between AE parameters and specific fracture modes have been established, like delaminations resulting in longer duration and lower frequencies than matrix cracks or fiber rupture. Despite the fact that multiaxial stress conditions occur in all composite structures in the microscale due to their anisotropic nature, in conventional lay-ups the dominant stress state remains largely uniaxial in the lamina level. Thus, it would be of great interest to study the potential of AE to indicate the dominant stress/strain component rather than just the occurring damage mode when the stress state is multiaxial and especially during the very early loading stages.

A thorough experimental campaign was performed in this study to obtain a successive AE analysis of carbon/epoxy laminates, in which different multiaxial stresses are developed. Two laminates, namely [0°/30°]$_{2s}$ and [0°/60°]$_{2s}$, were tested under quasi-static and incremental tensile loading. Due to the different fiber orientations, shear stresses govern the stress state in the 30° plies, while normal transverse stresses are the dominant ones in the 60° plies [11]. It is shown through this study that certain AE features can be used to identify the dominant stress/strain component at the early loading stages, before the occurrence of severe damage. At a later stage, damage modes can be also identified through AE feature analysis. One of the most beneficial aspects of the employed methodology is that the AE findings are correlated to real-time fracture scans and not to just theoretical damage modes [12].

2. Materials and methods

The material used was a pre-preg carbon fiber/epoxy matrix composite, manufactured by Mitsubishi Chemical Corporation and Honda R&D Co., Ltd. Samples were cut following ASTM D3039 [13] and had a length of 250 mm, a width of 25 mm and a thickness of 1.83 mm. Two angle-ply unbalanced laminates, [0°/30°]$_{2s}$ and [0°/60°]$_{2s}$, were tested during this work. The lay-ups were selected in such a way that different multiaxial stresses are developed in their off-axis layers. By using the classical laminate theory, it can be calculated that the λ_{12} ratio, defined as:

$$\lambda_{12} = \frac{\sigma_6}{\sigma_2} \tag{1}$$

is equal to 2.02 in the off-axis layers of the [0°/30°]$_{2s}$ laminates and equal to 0.64 in the [0°/60°]$_{2s}$ laminates. This shows that the shear stress component σ_6 is the dominant one in the off-axis layers of the [0°/30°]$_{2s}$ laminates whereas the transverse stress σ_2 dominates in the [0°/60°]$_{2s}$ laminates. In order to highlight the AE findings related to the identification of multiaxiality in the angle-ply laminates, the results are also compared with those from more conventional [0°/90°]$_{2s}$ and [±45°]$_{2s}$ laminates from the same material.

An MTS servo-hydraulic test bench with a load capacity of 100 kN was used to perform the tensile tests. Initially quasi-static tests were performed at a displacement rate of 1 mm/min to capture the AE activity of the samples. Apart from continuous tests, interrupted tests were also performed at specific load intervals, during which through-thickness microscopic inspection was carried out. Afterwards, incremental loading tests were performed. During these, the Kaiser effect and the Felicity Ratio (*FR*) and Calm Ratio (*CR*) were studied. For each loading condition at least three samples from both laminates were tested for statistically acceptable results.

The elastic waves (AE hits) were captured using a Mistras Group system equipped with the AEwin software. Two Pico sensors (with peak frequency at 450 kHz) were placed on the specimen with a distance of 80 mm. Vaseline was applied between the sensors and the sample to guarantee the acoustic coupling. An amplitude threshold of 35 dB was applied and the signals were amplified with a gain of 40 dB using pre-amplifiers. Prior to testing, pencil lead breaks were performed to

assess the wave velocity (5962 m/s and 5479 m/s for the $[0^\circ/30^\circ]_{2s}$ and $[0^\circ/60^\circ]_{2s}$ lay-ups respectively). By using the distance between the sensors and the automatic onset time as recorded by the acquisition channels, linear localization of hits was obtained (AE events).

Among the most regularly studied AE features, also investigated in this work, are the absolute energy of the signal, expressed in aJ (10^{-18} J), indicative of the wave intensity, and the Rise Time (*RT*), expressed in μs, defined as the time from the first threshold crossing of a signal until the time it reaches its maximum amplitude. The Average Frequency (*AF*), expressed in kHz, is also examined in this analysis. *AF* is measured in the time domain by the number of threshold crossings over the signal duration and is a representative parameter for the main frequency content of the waveform (Fig. 1a)) [14]. After having performed thorough data analysis, it was concluded that the *RT* and *AF* were the most sensitive descriptors to realize differences between the considered cases. Moreover, during incremental loading the Kaiser and Felicity effects were investigated. The Kaiser effect occurs when AE activity initiates during a loading cycle only at a stress level equal to or higher than the maximum stress of the previous loading cycle. In order to demonstrate the Felicity effect, the *FR* is defined from the following equation:

$$FR(i+1) = \frac{AE\ onset\ stress\ level\ [Cycle(i+1)]}{Maximum\ stress\ level\ [Cycle\ (i)]} \qquad (2)$$

FR values equal to or higher than unity indicate that negligible or no damage has occurred in the material and that the Kaiser effect is noticed. When *FR* drops below unity, the Kaiser effect does not appear anymore, indicating that damage has been nucleated during the previous loading cycle (Fig. 1b)). In this case the Felicity effect appears, designating that AE activity initiates earlier than the maximum stress level of the previous cycle. Another parameter that can be used in order to study the structural integrity of the material under incremental loading is the *CR*, pointing out the AE activity emitted during the unloading stages of the successive cycles. The *CR* is defined as:

$$CR(i) = \frac{AE\ activity\ (unloading)\ [Cycle(i)]}{AE\ activity\ (loading+unloading)\ [Cycle\ (i)]} \qquad (3)$$

In a sound material *CR* is close to zero. With the accumulation of damage *CR* increases, indicating AE activity also during the unloading stages.

Regarding optical damage monitoring, a Leica MZ125 stereomicroscope was mounted on the test bench to scan the free edge of the specimen. This allowed damage observations by stopping the test at certain load intervals while still keeping the sample loaded. To obtain strain measurements a DIC system, VIC-3D by Correlated Solutions, was utilized [12].
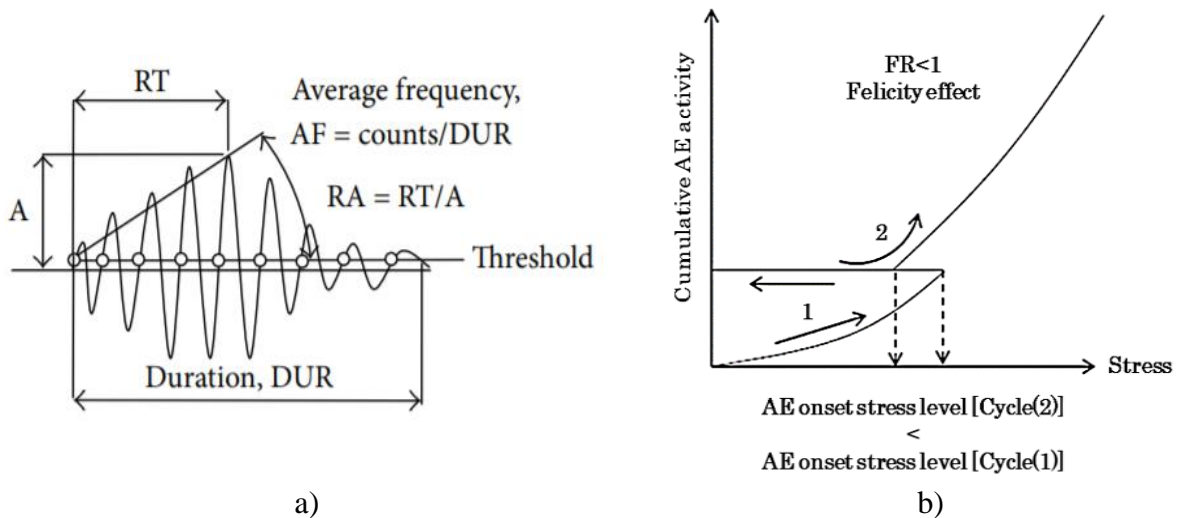
Fig. 1: a) Typical AE waveform and b) AE representation of Felicity effect [12].

3. Results and discussion

3.1 AE results during quasi-static loading

The initial important finding during the quasi-static tests was the potential of AE to differentiate between laminates with dissimilar multiaxial stress states from early loading stages (even before reaching 20-25% of the ultimate load) based on analysis of certain signal features, such as the *RT* and the *AF*. Since the different multiaxiality is expressed through the λ_{12} ratio, in Fig. 2 the link between the *RT* values and the λ_{12} ratio is plotted. This is done by taking into account the λ_{12} ratios of the $[0^o/30^o]_{2s}$ and $[0^o/60^o]_{2s}$ laminates, which are equal to 2.02 and 0.64 respectively, and by calculating that the same ratio equals 0 in the cross-ply $[0^o/90^o]_{2s}$ laminates and 5.78 in the shear dominated $[\pm45^o]_{2s}$ laminates. The points depict the average *RT* values recorded between 0% and 50% of the testing time for each case. This way the AE feature comes from a relatively early state before severe damage influences the original λ_{12} ratios. The values of five specimens for each case are shown. A good repeatability is observed, allowing a separation between the considered cases. Specifically, when shear stresses are negligible, *RT* averages at approximately 70 μs, while gradually and as λ_{12} becomes 5.78, *RT* climbs to 150 μs. It is evident that higher λ_{12} ratios corresponding to higher shear stresses lead to higher *RT* values, allowing estimation of the dominant stress component in the composite layer from a relatively early point.
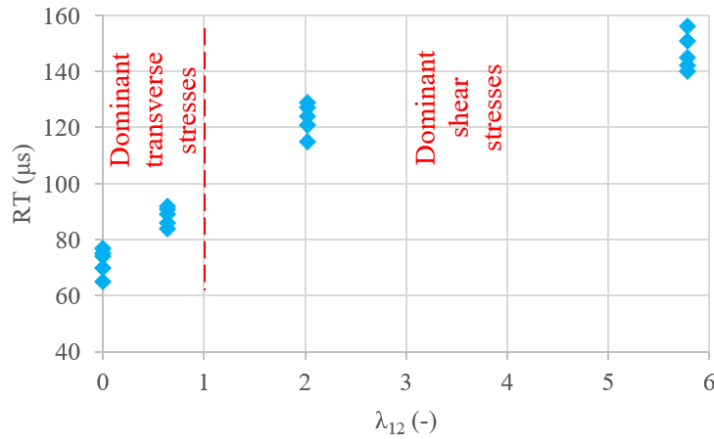
Fig. 2: Dependence of *RT* on the λ_{12} ratio as obtained from the moving average curves of different laminates at a time range equal to 0-50% of the testing time [12].

Apart from correlations of the AE features with the multiaxial stress conditions, associations with the captured strain field throughout the test could be further obtained. Strains in the material coordinate system of a laminate can only be obtained analytically. Nevertheless, in the angle-ply unbalanced $[0^o/\theta]_{2s}$ composite laminates, a shear coupling exists also in the geometrical axes owing to the non-zero terms A_{xs} and A_{ys} of the extensional stiffness matrix A. This leads to the appearance of shear strains γ_{xy} under the application of any normal extensional force N_{xx}, which can be measured by DIC on the surface of the specimens. In order to exhibit the correlation between the AE signal features and the different shear strains owing to changes of the angle θ, the evolution of the *RT* as a function of the stress and γ_{xy} (shear strain as measured by DIC) is plotted in Fig. 3 for both the angle-ply laminates and the cross-ply laminates (with the period of the moving average curve corresponding to 5% of the data points in each case).

It is clear that for the $[0^o/30^o]_{2s}$ laminates the *RT* presents a continuously increasing trend from an early stage of the test, following a steady increase of γ_{xy} and the corresponding shear damage. The average *RT* values initiate from around 100 μs and they arise to high values, close to 250 μs, following the appearance of delaminations between the laminate layers. These delaminations were the first visible damage incidents microscopically observed in the $[0^o/30^o]_{2s}$ laminates at around 1000 MPa of the global stress, before any visible matrix cracks in the off-axis plies (Fig. 4a)). On

the other hand, in the $[0^o/90^o]_{2s}$ laminates, γ_{xy} shows negligible increasing trends, similarly to the *RT* trendline, which remains at low levels of around 70 µs, before rising at the end due to the occurrence of delaminations. The shear strain of the $[0^o/60^o]_{2s}$ laminates presents a behavior in between the two previous cases, being initially low but starting to increase at around 600 MPa, clearly deviating from the $[0^o/90^o]_{2s}$ case. Interestingly, the same applies for the *RT* curve which is constantly higher than the one from the $[0^o/90^o]_{2s}$ laminates, leading again to a sudden increase due to the emergence of delaminations. Matrix cracking was the first damage mode recorded in the $[0^o/60^o]_{2s}$ laminates from a stress equal to 600 MPa on average. Delaminations occurred late in the test, at a stress greater than 90% of the ultimate stress (around 1200 MPa), like indicatively shown in Fig. 4b).
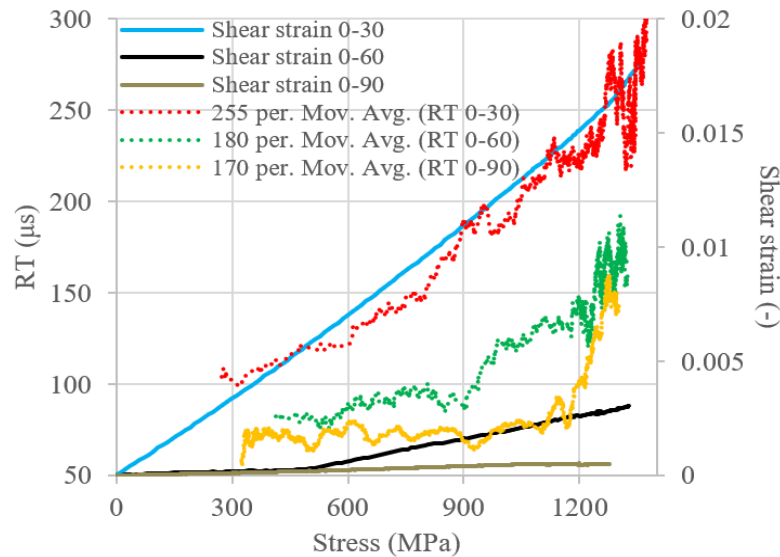
Fig. 3: Evolution of *RT* versus the stress and the shear strain γ_{xy} of the unbalanced angle-ply and the cross-ply laminates [12].
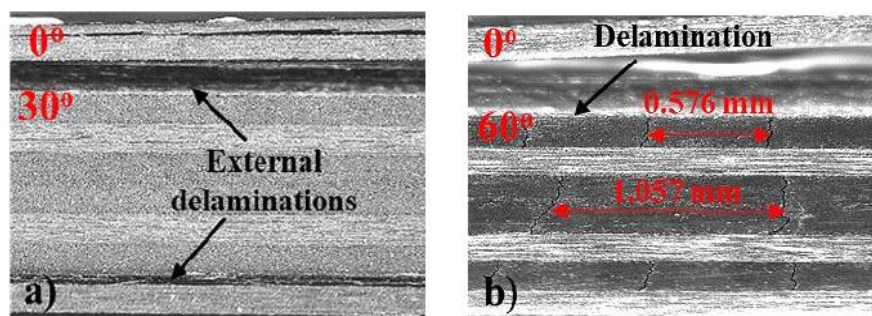
Fig. 4: Damage state in a) $[0^o/30^o]_{2s}$ laminates at 1100 MPa stress and b) $[0^o/60^o]_{2s}$ laminates at 1200 MPa stress [12].

To obtain a quantitative insight into the *AF* and the AE signal energy content of the angle-ply laminates, Figs. 5a) and 5b) plot the average *AF* and absolute energy values at indicative stress stages. Regarding the *AF*, constantly lower values are registered for the $[0^o/30^o]_{2s}$ laminates due to the dominant shear stresses. Especially combination of shear damage with delaminations towards failure leads to very low *AF* values, close to 50 kHz. When transverse stresses and matrix cracking are dominant, higher *AF* values are recorded, as shown for the $[0^o/60^o]_{2s}$ laminates. Regarding the energy values, until 900 MPa the average absolute energy for the $[0^o/30^o]_{2s}$ case remains quite low, possibly due to the appearance of intralaminar shear debondings only. Beyond this stress, the energy increases due to the emergence of delaminations and fiber breaks. In the $[0^o/60^o]_{2s}$

laminates higher energy is observed in the 700-1200 MPa stress range due to the occurrence of matrix cracks. After 1200 MPa, an increase in the absolute energy is registered, due to delaminations and fiber breaks. These results prove that for the same external stress on the two laminates, important differences in the AE features are obtained due to the dissimilar stresses in the material coordinate system even before the occurrence of microscopically visible damage. It is shown that AE is sensitive not only to the actual damage but also to the stress field that will eventually result in a specific damage mechanism. Moreover, despite the fact that damage at early loads is not yet manifested in a form visually observable by the applied monitoring methods, the sensitivity of AE allows detecting phenomena in the scale of aJ [12].
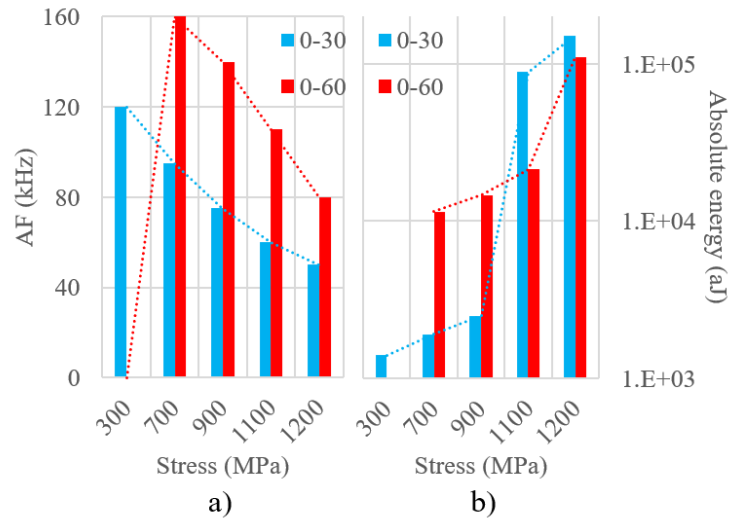
Fig. 5: a) *AF* and b) absolute energy versus the stress of the $[0^o/30^o]_{2s}$ and $[0^o/60^o]_{2s}$ laminates [12].

3.2   AE results during incremental loading

Considering that the failure stress σ_{ult} of the $[0^o/30^o]_{2s}$ laminates was found to be equal to 1375 MPa, whereas for the $[0^o/60^o]_{2s}$ laminates it equaled 1318 MPa on average [11, 15], incremental tests were performed with six successive steps at maximum stress levels of 220, 440, 660, 880, 1100 and 1200 MPa. The last loading step continued until failure. The difference in the AE activity between the $[0^o/30^o]_{2s}$ and $[0^o/60^o]_{2s}$ laminates is indicatively displayed in Fig. 6 for the 0-1200-0 MPa loading-unloading cycle. It is clear that certain differences arise between the two laminates. Apart from the intensity of the AE activity, which is always higher for the shear dominated $[0^o/30^o]_{2s}$ laminates, one of the major differences concerns the onset of AE during the consecutive loading cycles or else the appearance of the Kaiser and Felicity effects. In order to demonstrate the different response during the incremental loading, Fig. 7 plots the evolution of the Felicity ratio *FR* versus the maximum stress of each successive loading step. For calculating the *FR* values, the AE onset was assumed to coincide with the appearance of the very first AE event during the loading regime of each cycle. In cases that the Kaiser effect still appeared, mainly during the initial cycles, the *FR* was assumed equal to one even if greater values were potentially obtained.

Looking initially at the 0-440 MPa loading step, the Kaiser effect is evident for both samples. The forming microdamage is of such a small scale that *FR* values equal to one. The first deviation occurs in the 0-660 MPa cycle. The Felicity effect has appeared for the $[0^o/30^o]_{2s}$ specimens with an *FR* value equal to 0.93, while the $[0^o/60^o]_{2s}$ laminates are still under the Kaiser effect. Until a stress of 1100 MPa the *FR* constantly decreases for the $[0^o/30^o]_{2s}$ laminates, following the increase of shear stresses and the growth of intralaminar debondings. Contrarily, in the $[0^o/60^o]_{2s}$ specimens the Felicity effect appears during the 4th loading step. Comparing the *FR* until 1100 MPa for both laminates, notably lower values can be observed for the $[0^o/30^o]_{2s}$ laminates. This indicates that the internal shear damage in this lay-up is linked to more brittle behavior and to fracture surfaces

being able to generate AE earlier than the matrix cracks in the $[0°/60°]_{2s}$ samples, having a more elastic response and smoother fracture surfaces. In the 0-1200 MPa loading step a significant decrease of the *FR* occurs for the $[0°/30°]_{2s}$ laminates, which reaches a value of 0.63. This corresponds to the formation of delaminations during the previous loading step, showing that the permanent damage caused by the delaminated layers is able to produce early AE activity. This is confirmed in the $[0°/60°]_{2s}$ laminates for which a significant decrease is shown at the last step, corresponding to the growth of delaminations.
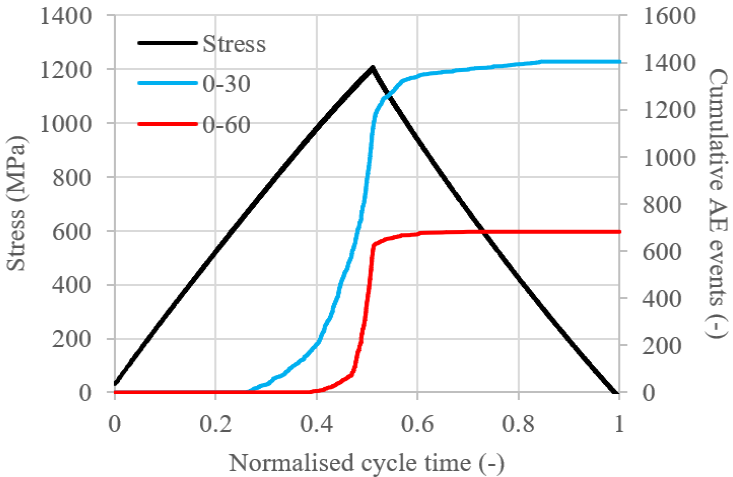
Fig. 6: AE activity versus the stress and the normalized time of the $[0°/θ]_{2s}$ laminates during the 0-1200-0 MPa loading-unloading cycle [12].
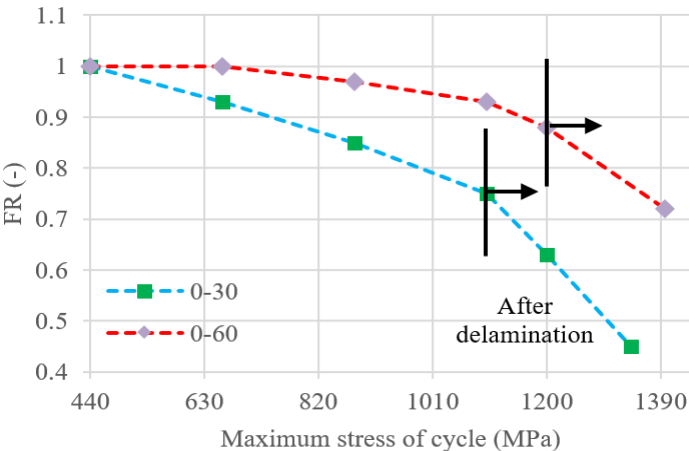
Fig. 7: *FR* evolution versus the maximum stress of succeeding loading-unloading cycles for the $[0°/θ]_{2s}$ laminates [12].

Fig. 8 plots the calm ratio evolution versus the maximum stress of the consecutive cycles for both laminates. It is clear that an increasing tendency appears, related to the developing damage, leading to the release of more and more AE signals during unloading. However, a clear differentiation in the *CR* values between the two laminates can be observed due to the dissimilar multiaxiality. Even from the early loading cycle at 440 MPa, higher *CR* values are recorded for the shear dominated laminates. The shear debondings seem to generate friction not solely when the load increases, but also during the unloading stages. Contrarily, the fracture surfaces developed by the matrix cracks in the laminates with 60° off-axis layers seem to generate less AE activity when the load drops. In all cases, similarly to the *FR* evolution, sudden changes in the *CR* value are captured when severe damage in the form of delaminations occurs [12].
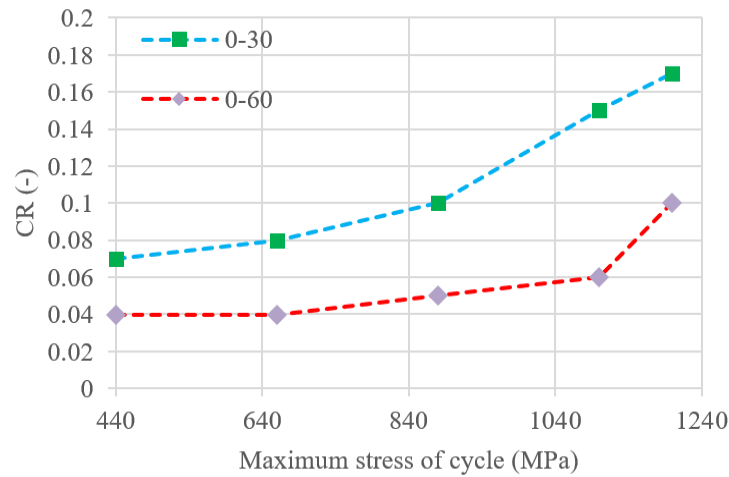
Fig. 8: *CR* evolution versus the maximum stress of succeeding loading-unloading cycles for the $[0^o/\theta]_{2s}$ laminates [12].

4. Conclusions

Two types of carbon/epoxy laminates, namely $[0^o/30^o]_{2s}$ and $[0^o/60^o]_{2s}$, were tested during this experimental campaign. The laminates, characterized by dominant shear and transverse stresses respectively in their off-axis plies, were examined under quasi-static and incremental loading. AE was constantly applied with the aim to examine the potential of the method to indicate the dominant stress/strain component rather than just the appearing damage mode. It was concluded that certain AE features, such as the rise time, the average frequency, the Felicity ratio *FR* and the calm ratio *CR* can be used even from early loading stages for the discrimination between laminates with different stress components. This opens the way for acoustic emission to be used for the prediction of the upcoming response of polymer composites rather than just the post-damage assessment that has been mainly investigated so far in literature.

5. Acknowledgements

6. References

[1] Barré, S., Benzeggagh, M.L. (1994). On the use of acoustic emission to investigate damage mechanisms in glass-fibre-reinforced polypropylene. Composites Science and Technology, vol. 52, no. 3, p. 369-376.

[2] Carvelli, V., D'Ettorre, A., Lomov, S.V. (2017). Acoustic emission and damage mode correlation in textile reinforced PPS composites. Composite Structures, vol. 163, p. 399-409.

[3] Roundi, W., El Mahi, A., El Gharad, A., Rebiere, J.L. (2018). Acoustic emission monitoring of damage progression in glass/epoxy composites during static and fatigue tensile tests. Applied Acoustics, vol. 132, p. 124-134.

[4] Kostopoulos, V., Loutas, T.H., Kontsos, A., Sotiriadis, G., Pappas, Y.Z. (2003). On the identification of the failure mechanisms in oxide/oxide composites using acoustic emission. NDT & E International, vol. 36, no. 8, p. 571-580.

[5] Godin, N., Huguet, S., Gaertner, R., Salmon, L. (2004). Clustering of acoustic emission signals collected during tensile tests on unidirectional glass/polyester composite using supervised and unsupervised classifiers. NDT & E International, vol. 37, no. 4, p. 253-264.

[6] Quaresimin, M. (2015). 50th anniversary article: multiaxial fatigue testing of composites: from the pioneers to future directions. Strain, vol. 51, no. 1, p. 16-29.

[7] Fotouhi, M., Najafabadi, M.A. (2016). Acoustic emission-based study to characterize the initiation of delamination in composite materials. Journal of Thermoplastic Composite Materials, vol. 29, no. 4, p. 519-537.

[8] Brunner, A.J. (2018). Identification of damage mechanisms in fiber-reinforced polymer-matrix composites with acoustic emission and the challenge of assessing structural integrity and service-life. Construction and Building Materials, vol. 173, p. 629-637.

[9] Sause, M.G.R., Müller, T., Horoschenkoff, A., Horn, S. (2012). Quantification of failure mechanisms in mode-I loading of fiber reinforced plastics utilizing acoustic emission analysis. Composites Science and Technology, vol. 72, no. 2, p. 167-174.

[10] R'Mili, M., Moevus, M., Godin, N. (2008). Statistical fracture of E-glass fibres using a bundle tensile test and acoustic emission monitoring. Composites Science and Technology, vol. 68, no. 7-8, p. 1800-1808.

[11] Kalteremidou, K.A., Hajikazemi, M., Van Paepegem, W., Van Hemelrijck, D., Pyl, L. (2020). Effect of multiaxiality, stacking sequence and number of off-axis layers on the mechanical response and damage sequence of carbon/epoxy composite laminates under static loading. Composites Science and Technology, vol. 190, no. 108044.

[12] Kalteremidou, K.A., Aggelis, D.G., Van Hemelrijck, D., Pyl, L. (2021). On the use of acoustic emission to identify the dominant stress/strain component in carbon/epoxy composite materials. Mechanics Research Communications, vol. 111, no. 103663.

[13] ASTM, D3039 (2008). Standard test method for tensile properties of polymer matrix composite materials.

[14] Aggelis, D.G., Dassios, K.G., Kordatos, E.Z., Matikas, T.E. (2013). Damage accumulation in cyclically-loaded glass-ceramic matrix composites monitored by acoustic emission. The Scientific World Journal, vol. 2013, no. 869467.

[15] Kalteremidou, K.A., Murray, B.R., Tsangouri, E., Aggelis, D.G., Van Hemelrijck, D., Pyl, L. (2018). Multiaxial damage characterization of carbon/epoxy angle-ply laminates under static tension by combining in situ microscopy with acoustic emission. Applied Sciences, vol. 8, no. 11, no. 2021.

49

EVALUATION OF THE MECHANICAL BEHAVIOUR OF POPLAR SPECIMENS WITH AND WITHOUT FINGERS SUBJECTED TO TENSILE STRESS BY MEANS OF ACOUSTIC EMISSION AND DIC

Francisco J. Rescalvo[1], María Portela[2], Rafael Bravo[3], Jose Lorenzana[2], Carlos Cruz-Rodríguez[3], Manuel Guaita[3] and Antolino Gallego[3]

[1]University of Granada, Department of Building Construction, Granada, Spain; rescalvo@ugr.es
[2]University of Santiago de Compostela, PEMADE, Lugo, Spain;
maria.portela.barral@usc.es, joseantonio.lorenzana@usc.es
[3]University of Granada, Department of Structural Mechanics, Granada, Spain;
rbravo@ugr.es, carlos.cruz@ugr.es
[4]University of Santiago de Compostela, Department of Agroforestry Engineering, Lugo, Spain;
m.guaita@usc.es
[3]University of Granada, Department of Applied Physics, Granada, Spain; antolino@ugr.es
*Correspondence: rescalvo@ugr.es

ABSTRACT

Engineered wood product (EWP) offers an improvement in performance and mechanical properties over the use of sawn timber. This is mainly due to the fact that these products can eliminate defects such as knots, splits, etc. The removal of these defects has been achieved through the development of the finger-joint technique. This technique makes it possible to merge boards together to produce the desired length or width, making it possible to manufacture, among other products, laminated beams of larger dimensions. Therefore, the evaluation of these joints in a laminated element is vital to ensure a quality final product, as they become the areas with the highest stress concentration. To this end, this work aims to carry out an evaluation of the mechanical behaviour of elements with and without finger-joints made of poplar monitored with acoustic emission and DIC, as well as to obtain parameters to predict the failure in the specimens with finger-joints.

Keywords: Acoustic emission, timber, finger-joint, poplar, DIC, characterization.

1. Introduction

Timber is one of the most important materials used over the centuries withing the construction sector [1]. Due to the increasing demanding of timber, elements with special shapes and higher spans have become overwhelming. Finger-joints are currently used to produce engineered wood products (EWPs) like glued laminated timber (glulam) for different applications such as the construction sector, buildings, bridges, etc. Thanks to the finger-joint connection, it is possible to avoid some types of defects such as high grain deviation, knots, cracks, etc. In addition, the increasing demand of timber makes it highly necessary to use fast-growing species to supply the demand and avoid further pressures on natural forests. In this respect, poplar stands out as an ideal candidate.

Nowadays, the finger-joint technique is highly industrialized and its geometry and gluing process is standardized [2]. Several works have been carried out in order to parametrize both issues in order to achieve the higher strength as possible at the bonding between lamellas. According to Bustos [3], the applied end pressure is likewise a key parameter for the evaluation of a specimen's ultimate tensile strength.

The digital image correlation (DIC) has become a powerful tool to explore full-field displacements and strain measurements in the realm of experimental mechanics. DIC has proven to be an ideal tool for the study of material behaviour for a very different type of products [4].

However, these finger joints are key elements to ensure the quality of the final product, especially when they are subjected to tensile stress. Therefore, it is not only necessary to evaluate the mechanical strength but also the quality of the bonding and its possible deterioration over the lifetime of the element (overloading, unwanted moisture, etc.).

In order to monitoring these critical points, acoustic emission (AE) is the ideal non-destructive method, as it allows a real time evaluation and can allows to discern between different failure mechanisms. However, there is few literature on the monitoring of finger joints using this technique. In Ayarkawa [5], a prediction of the ultimate tensile strength by means of the acoustic Emission technique is performed. However, the do not address the quality of the bonding.

This work aims to evaluate the quality of bonding in specimens with and without finger-joint specimens that mechanically comply with current standards, as well as to establish future parameters that could allow the assessment of deterioration in a finger-joint before final failure.

2. Materials and methods

2.1 Poplar wood and adhesive

For this work, 9-year-old-poplar timber of the cultivar I-214 (*Populus X Euroamericana* [Dode] Guinier) was used. It was extracted from a plantation located nearby the city of Granada, Spain. From the logs, boards of 2000 mm length and with a section of 35 x 75 mm were sawn and dried for 6 months in natural conditions ensuring a proper ventilation and avoiding direct exposure to the sun or rain. The final Moisture Content (MC) of the boards was 10±2%.

2.2 Sample description and manufacturing of the finger-joints

The 20 poplar specimens prepared to be subjected to tension in the grain direction were divided into two batches of 10 specimens each, one without finger-joints (TT) and another with finger-joints (TF), respectively. Two samples were randomly selected from each batch to be monitored with acoustic emission and DIC. This work presents the results of one sample with and without finger-joint. All the specimens were sawn to a length of 586 mm, with a general cross-section of 50 x 17 mm. In order to induce the failure in the central area of the specimen and to avoid breakage at the clamp areas, the width of the central part of the specimen was narrowed to 20 mm. This results in a mid cross-section of 20 x 17 mm with a length of 120 mm (Fig. 1).
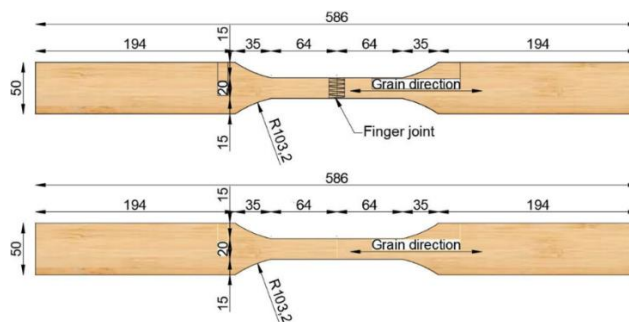
Fig. 1: Sample geometry description for specimens with (TF) and without finger-joints (TT). Dimensions in mm.

The finger-joints were manufactured using a standardized milling cutter. A mono-component polyurethane adhesive was used for the bonding. The adhesive was applied at 20±2°C and the moisture content of the wood was controlled during the whole process resulting in an average MC of 9.8±1.5%. The adhesive rate was of 250 g/m^2 and the samples were conditioned before the test following the recommendations of the EN 408:2010 + A1:2012 standard. More details of the manufacturing process are given in [6].

2.3 Acoustic emission monitoring and data analysis

A Vallen Systeme AMSY-6 equipment was used to acquire the AE signals. In order to have sensitivity within the frequency range between 25-500 kHz, multi-resonant VS45-H sensors were used. The sampling frequency for the waveforms recorded was established at 5 MHz with 4096 samples per set (pre-trigger of 200 samples), resulting in a page length of 819,2 µs. Fig. 2 shows the AE sensors arrangement for all the samples, including the DIC monitoring area. In particular, two sensors were used for the analysis (Sensors 1 and 2) and two sensors were placed as guard sensors near the clamps areas to avoid undesirable signals coming from friction processes (Sensors 3 and 4, respectively).
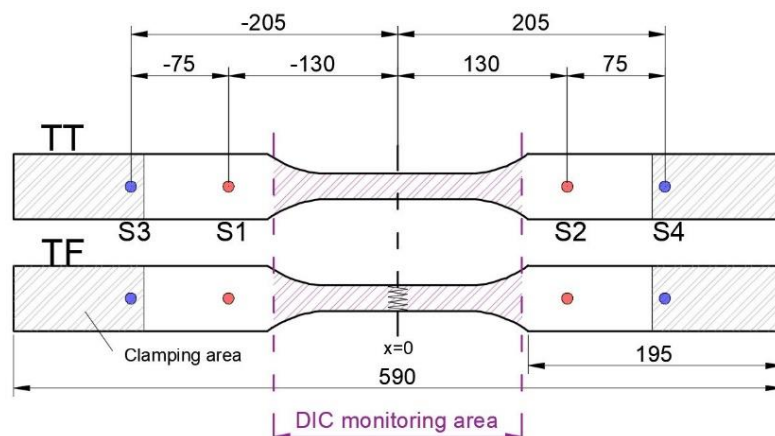
Fig. 2: AE and DIC monitoring arrangement. Sensors 1 and 2 in red: analysis. Sensors 3 y 4 in blue: guard sensors. Dimensions in mm.

Due to the heterogeneity of the wood and the geometry of the sample, for the analysis and evaluation of the AE, two considerations were taken: I) Only located events within Sensors 1 and 2 were used for the analysis. II) Only the initial part of the signal was used in order to avoid distortion effects. For step I, the propagation velocity of the wave was measured using the distance between Sensors 1 and 2 and a PLB (Pencil Lead Break) with a 0.5 mm 2H lead as source. The propagation velocity was measured in both directions, resulting in average of 490 and 500 cm/ms for TT and TF samples, respectively. For step II, in order to establish the analysis window W_0, the mean duration of all the located events was calculated, resulting the following window where the spectral energy was calculated, W_0: [(-30)-300] µs. In this interval, the portion before the FTC (First Threshold Crossing) was used to obtain as far as possible the information of the real onset of the signal. According to previous works and the results observed in these tests, the spectral energy was calculated into the following frequency bands:
- band 1 (B1): low frequencies [80-120] kHz,
- band 2 (B2): medium frequencies [140-180] kHz.

2.4 DIC monitoring

For monitoring the strain field in the central portion of the specimens, a three-dimensional image correlation non-contact optical measurement system was used; the Aramis 3D® (GOM mbH, Braunschweig, Germany). The surface was cleaned, sanded and prepared with a black-on-white

random speckle pattern and the DIC system was calibrated using the specific Aramis 3D calibration protocol. In order to obtain the longitudinal modulus of elasticity and the poisson ratio, different virtual extensometers were placed on the sample [6].

The evolution of strains with respect to the load was obtained in a different way for the specimen with and without finger. The reason for this is that the specimen without a finger does not have a "artificial defect" in which the stresses are mainly concentrated, so the areas with the greatest damage can develop at different points of the specimen and in a superficial pattern (Fig. 3-left). However, for the finger specimens, the highest stresses are located at the tips of the fingers. Furthermore, each tip can develop slight individual variations in the strain field, making necessary to analyze them individually (Fig. 3-right).
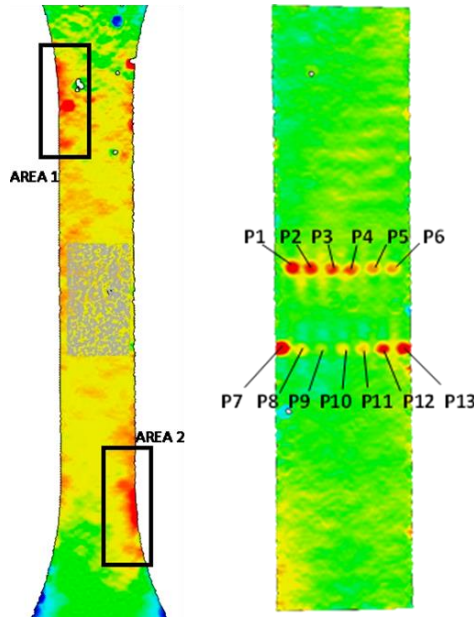
Fig. 3: DIC analysis areas. Left: Sample without finger-joint (TT). Right: Sample with finger-joint (TF).

2.5 Experimental test

The tensile tests were performed in a multi-testing machine, with an electrical actuator with a maximum capacity of 200 kN from the company Microtest S.A. Company. The speed rate was established at 0.5 mm/s. To calculate the maximum tensile strength ($f_{t,0}$), Eq.1 was followed:

$$f_{t,0} = \frac{F_{max}}{A} \tag{1}$$

where F_{max} is the maximum axial load and A is the cross-section at the mid-length. Fig. 4 shows the general arrangement of the tensile test. In order to calculate the modulus of elasticity $E_{t,0}^{ext.100}$, a virtual 100 mm long extensometer in the direction of the grain was placed at the geometrical center of the sample. Furthermore, a perpendicular to the grain direction virtual 20 mm long extensometer was placed at the center of the sample to calculate the poisson ratio (ν).
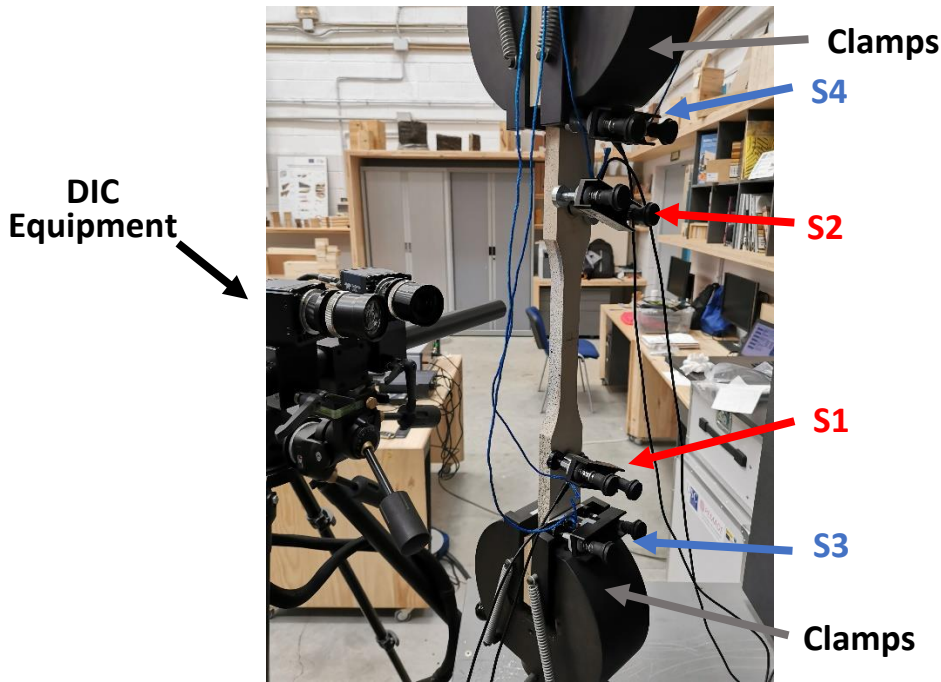
Fig. 4: Tensile test set-up with DIC and AE monitoring.

3. Results

3.1 Mechanical tests

Table 1 shows the average values of the different mechanical properties measured for the 10 specimens of each type (with and without fingers). The mechanical results are presented in more detail in [6]. It can be seen that the presence of the finger reduces the tensile strength along the grain direction by 28% and the longitudinal modulus of elasticity by 15%. However, it is important to note that the tensile strength values achieved for the specimens with finger (TF) exceed the maximum value of 29.3 MPa required by the UNE-EN 14080:2013 standard for glued laminated timber elements [2].

Table 1: Mean values of poisson ratio (v), tensile strength parallel to the grain ($f_{t,0}$), density (ρ) and mean longitudinal modulus of elasticity ($E_{t,0}^{ext.100}$).

SPECIMEN NAME	v	$f_{t,0}$ (Mpa)	ρ (kg/m³)	$E_{t,0}^{ext.100}$(MPa)
TT	0.40	51.0	385	8495
TF	0.40	37.0	375	7256
Variation of TF respect to TT (%)	0.0	-27.5	-2.6	-14.6

3.2 Digital image correlation

Fig. 5 shows the results of the monitoring using the DIC technique for the two specimens monitored with acoustic emission. In order to be able to correlate both techniques, the DIC images have been divided every 10% of the maximum failure load, thus evaluating the evolution of the strains in the direction of the fiber throughout each test.

As can be seen in Fig. 5, in the case of the specimen without finger (TT), from 50% of the maximum failure load, a concentration of strain begins to be observed around -50 mm (Area 2). The strain pattern remains similar until 80% of the maximum load, where a new concentration of strain appears at 50 mm (Area 1), asymmetrically to that generated at 50%. This fact is mainly associated with fiber deviation, which, though it is lower in poplar compared with other species, is a key defect during a tensile test. From 90%, high strains are observed distributed throughout the central zone, where the final failure occurs, with the initial points of failure corresponding to Areas 1 and 2 of the analysis. Fig. 6 shows an image of the failure of the TT specimen.
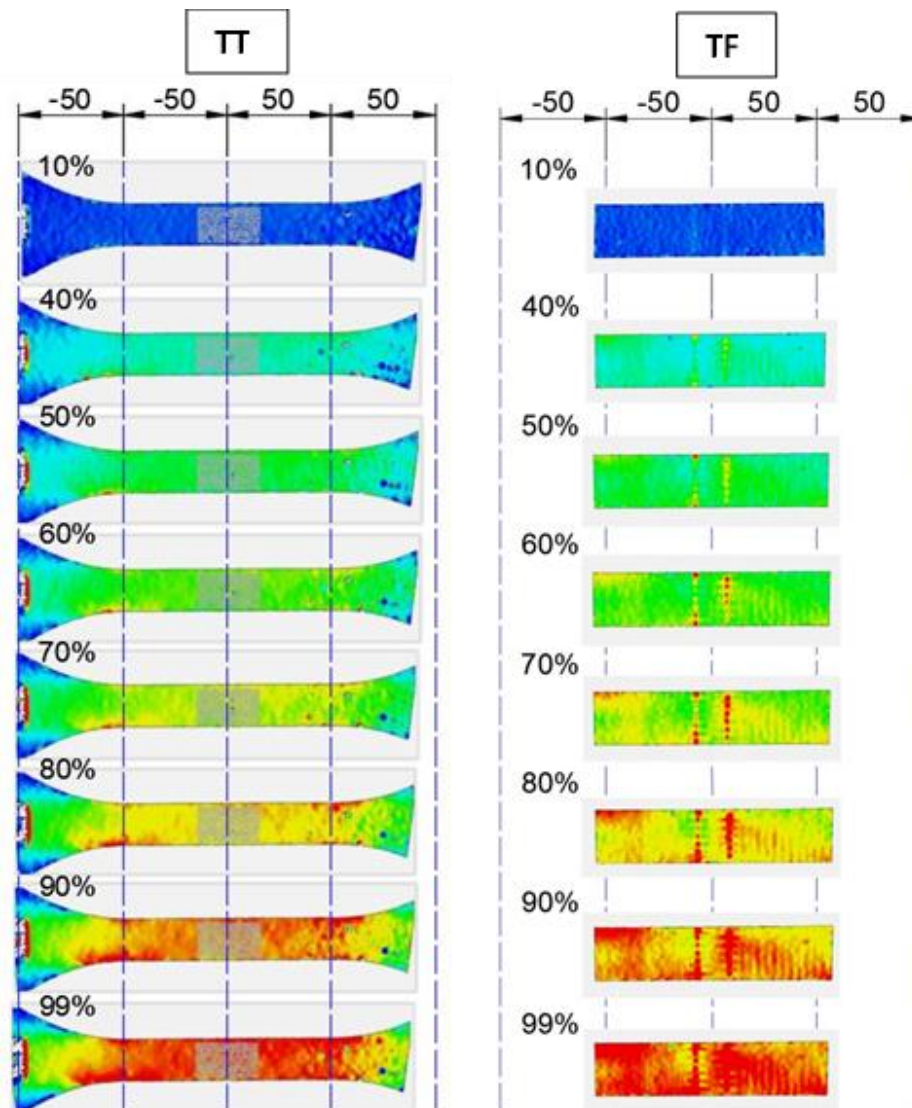
Fig. 5: DIC images of the samples without (TT) and with (TF) samples every 10% of the maximum load. Dimensions in mm.

Regarding the specimen with fingers (Fig. 5-right), as mentioned in Section 2.3, the highest strain concentration occurs in the area of the finger-joint. From 40% of the maximum load, a concentration of strain begins to be observed in the lower part of the fingers (P7). Between 50% and 60%, this strain concentration extends over a large part of the finger tips, with all the tips having high strain concentrations from 70% onwards, as well as the appearance of areas outside the finger with high longitudinal strains. From 90% onwards, the strains extend over the whole of the central area. As it can be seen in Fig. 6-right, the final failure occurs at the finger, mainly in the wood, although the crack passes through one of the fingers, producing a second-order an adhesive failure.
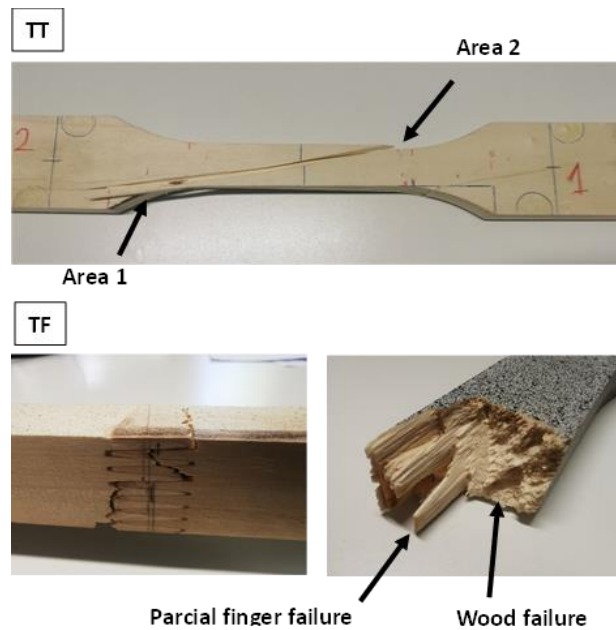
Fig. 6: Image of the failure pattern of the samples. Left: without finger (TT). Right: with finger (TF).

3.3 Acoustic emission and longitudinal strain correlation

Fig. 7 and 8 represent the mean longitudinal strain and acoustic emission results for the specimen without fingers (TT), respectively. In the case of Fig. 8, the results are represented only for the events located between Sensors 1 and 2. As it can be seen, no AE signals were recorded up to 30% of the maximum failure load, when point variations in the strains of Area 2 are registered. Around 50%-60%, high fluctuations are observed in the Area 2 strains (Fig. 7), which are corroborated by the DIC images in Fig. 5. Between these percentages, a significant increase in the cumulative energy can be observed (Fig. 8-top-left), just when a noticeable change in the trend of the curve for signals whose maximum frequency is lower than 130 kHz (low frequencies), as shown in Fig. 5 (DIC images). Between 70%-80% there is a noticeable increase in the strain concentration, with high concentrations appearing in Area 1. This is corroborated by both the longitudinal mean strains (Fig. 7) and the change in trend observed for the located cumulative AE events (Fig. 8-top-right) as well as the changes of the cumulative RMS curves for both frequency bands (B1 and B2). In addition, it is important to note that signals with a maximum frequency higher than 130 kHz begin to be slightly recorded. Around 90%, the number of these signals increases, which could be an indicator that signals medium-high frequencies (>130 kHz) are produced by mechanisms close to material failure, such as fiber breakage.
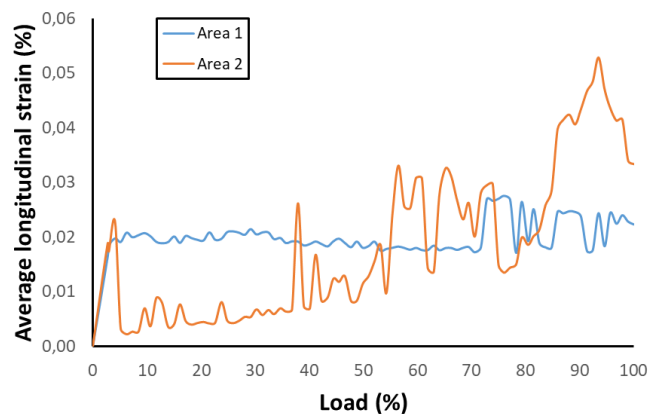
Fig. 7: Average longitudinal strain for the two areas analysed for the sample without finger (TT).
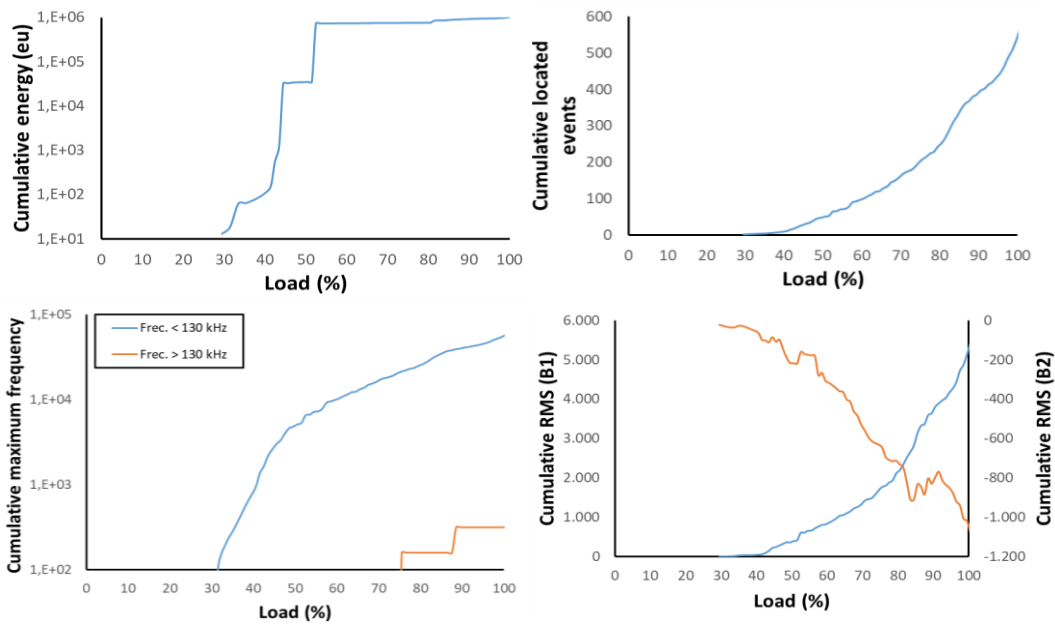
Fig. 8: Acoustic emission results for the sample without finger (TT). Top-left: cumulative energy for the located events. Top-right: cumulative located events. Bottom-left: cumulative maximum frequency. Bottom-right: cumulative RMS for band 1 and 2.

The longitudinal strain and acoustic emission results of the finger-joint (TF) specimen are presented in Fig. 9 and 10, respectively. In this case, the most representative finger-joint points are presented in Fig. 9. In general terms, AE signals start to be recorded from 40% of the maximum failure load, when the DIC images (Fig. 5-right) start to show a concentration of strain at the finger tips. At P14 in Fig. 9, a change of trend is observed from this value. Between 50% and 60% higher strain concentrations were observed in some tips, a fact that is observed at P4, with a small horizontal phase in this range. This fact is clearly observed in the cumulative AE energy. Similarly, from this percentage it is observed that signals whose maximum frequency is higher than 130 kHz start to increase, much earlier than in the specimen without finger. This may be an indicator that in the finger, the failure mechanisms, fibre breakage, are generated earlier than in the sample without finger-joint.

The next change in the strain pattern occurs at around 70% of the maximum failure load, which is observed both at points P3 and P12. This result can be observed in all the AE plots, with an increase in the cumulative energy: a change of the curve trend in the located events, a noticeable increase in the signals with a frequency higher than 130 kHz, and an increase in the cumulative RMS of the low-frequency band B1.

Finally, at around 90% of the failure, when the high strains extend to the whole central area of the specimen, a change in behaviour is observed again at points P3 and P12. As for the AE results, there is a notable increase for the cumulative energy as well as for the signals with a frequency greater than 130 kHz and a remarkable change in the cumulative RMS of the B1 band.
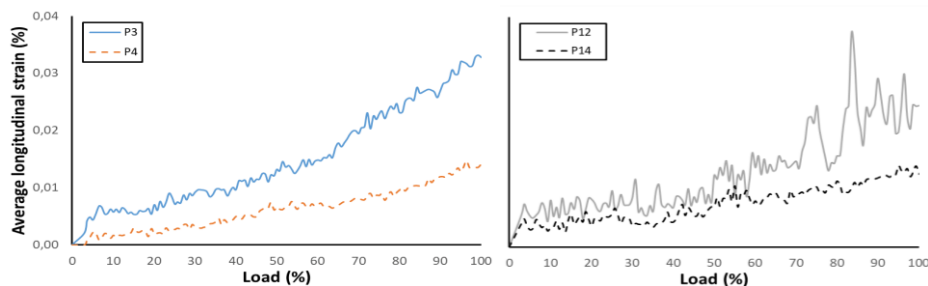
Fig. 9: Average longitudinal strain for the two areas analysed for the sample with finger (TF).
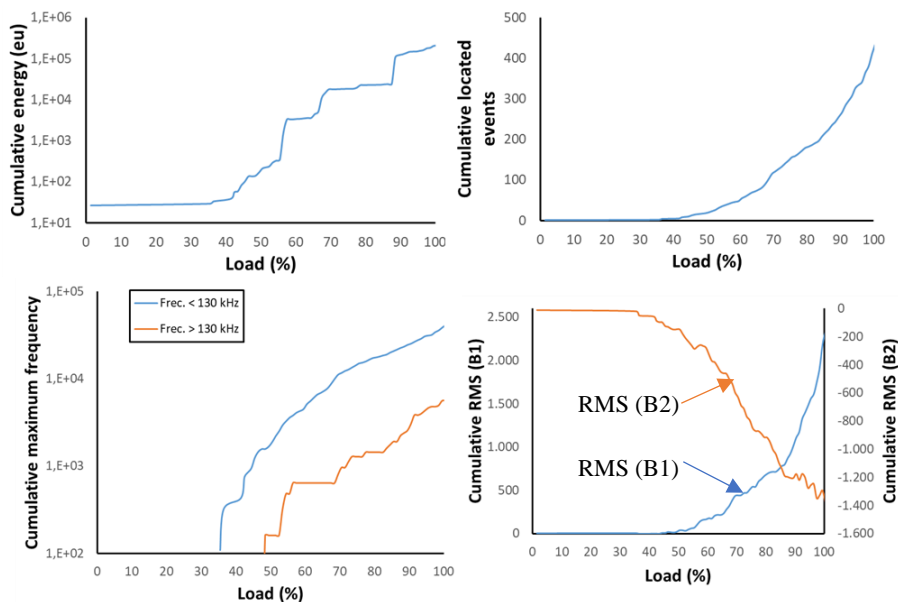
Fig. 10: Acoustic emission results for the sample with finger (TF). Top-left: cumulative energy for the located events. Top-right: cumulative located events. Bottom-left: cumulative maximum frequency. Bottom-right: cumulative RMS for band 1 and 2.

4. Conclusions

In this work, tensile tests have been carried out comparing specimens with and without finger, in order to evaluate their mechanical suitability as well as the quality of the fingers bonding. Two monitoring techniques have been used, digital image correlation and acoustic emission. It has been observed that the cumulative energy of the events located between the analysis sensors provides important information on the damage processes. It has also been observed that in the specimen with finger-joints, a high number of signals with a maximum frequency greater than 130 kHz are recorded. This may be due to the fact that in these finger-joints, a greater number of fiber breaks occur between the fingers.

5. References

[1]   Harte, A. (2016). Timber engineering: an introduction: Chapter 60. ICE manual of Construction Materials, p. 707-715.
[2]   UNE-EN 14080:2013 Timber structures. Glued laminated timber and glued solid timber. Requirements. European Committee for Standardization CEN.
[3]   Bustos, C., Hernández, R.E., Beauregard, R., Mohammad, M. (2011). Effects of end-pressure on the finger-joint quality of black spruce lumber: a microscopic analysis. Maderas Ciencia y Tecnología, vol. 13, p. 319-328, doi: 10.4067/S0718-221X2011000300007.
[4]   Lava, P., Cooreman, S., Coppieters, S. (2009). Assesment of measuring errors in DIC using deformation fields generated by plastic FEA. Optical Lasers Engineering, vol. 47, p. 747-753, doi: 10.1016/j.optlaseng.2009.03.007.
[5]   Ayarkwa, J., Hirashima, Y. (2001). Monitoring Acoustic Emissions from finger-joints from Tropical African hardwoods for predicting ultimate tenisle strength. Holzforschung, vol. 26, p. 1-13, doi: 10.1515/HF.2001.106.
[6]   Timbolmas, C., Rescalvo, F.J., Portela, M., Bravo, R. (2022). Analysis of poplar timber finger joints by means of Digital Image Correlation (DIC) and finite element simulation subjected to tension loading. European Journal of Wood and Wood Products, vol. 80, p. 555-567, doi: 10.1007/s00107-022-01806-6.

LONG TERM COUPLING OF AE SENSORS IN HIGH TEMPERATURE ENVIRONMENT

Anne Juengert[1,*], Maximilian Friedrich[1] and Andreas Klenk[1]

[1]Materials Testing Institute, University of Stuttgart, Germany
*Correspondence: anne.juengert@mpa.uni-stuttgart.de

ABSTRACT

Acoustic emission monitoring took place in a long-term test in a coal fired power plant in Germany for 4 years. The test object was a steel pipe with a ceramic matrix composite (CMC) jacket, which was installed in a bypass of a live steam line. The peak operating temperature was approx. 530 °C. The aim of the AE monitoring was to investigate damage evolution in the CMC jacket.

The test pipe was removed from the power plant in 2021. Due to several reasons, the jacket did not experience high loads during operation and therefore information about damage mechanisms in the AE data is rare. However, a lot could be learned from this project concerning long term stability of the equipment in rough environment, data storage and filtering and about sensor long term coupling of AE sensors at high temperatures.

The high temperature AE sensors were applied directly onto the surface of the steel pipe and the CMC jacket using a ceramic glue. Additionally, the sensors were held by stainless steel bands which were acoustically decoupled by mineral wool. The application of the sensors took place at a temperature of about 30 °C. It was not possible to check on the quality of the coupling during operation as the whole pipe was covered by insulation, including all sensors. Also, the sensors did not allow pulsing as test for the coupling quality. Effects like thermal expansion of sensors, CMC jacket and ceramic glue had to be considered. Additionally, the power plant adepts its electrical output to the demands by flexible operation. This leads to cyclic changes in temperature and a high amount of heating and cooling cycles, which affects the coupling condition of the AE sensors. During dismantling of the test pipe from the power plant, a visual inspection of the sensor coupling was possible. The condition of the sensor coupling was documented before and after the sensors were removed. Pencil lead breaks were performed to quantify the quality of coupling as well. It could be shown that long term coupling of AE sensors is possible even in high temperature environment combined with cyclic temperature changes.

Keywords: Acoustic emission, coupling, high temperature, ceramic matrix composite.

1. Introduction

Acoustic emission (AE) monitoring takes place to identify damages in components under load at an early stage to prevent catastrophic failure of safety relevant components. Early damages like micro cracks can be detected with AE sensors and activity and intensity of acoustic events may indicate damage progression. The technique is used since the 1970s and gains in importance as safety margins of components are reduced or components reach their end-of-life [1]. AE

monitoring is used for power plant components in fossil-fueled plants [2] and nuclear power plants [3]. In civil engineering AE monitoring is important for bridges and masonry structures [4, 5]. Momon et. al were able to classify AE data in fatigue tests at CMC at high temperatures and link them to damage mechanisms [6].

As the applications for AE monitoring increase in size, the challenge of long-term coupling of AE sensors also rises. There are guides to mount sensors for standard AE applications and in the laboratory [7, 8]. However, long-term coupling of sensors and coupling under difficult environmental conditions is still a field of research [9, 10].

This paper deals with AE monitoring of a material compound of a steel liner with a ceramic matrix composite (CMC) jacket for high temperature applications. Layered designs with fiber reinforced materials for pressure devices are used in aerospace since the 1940s. The aim of such material compounds it to combine the advantages of different materials and equalize their weaknesses.

The CMC-jacket in the material compound for high temperatures will reduce the creep strain compared to a full metal pipe. This offers the opportunity to use pipes with reduced wall thicknesses which are favorable for the nowadays more dynamic operation of fired power plants. Furthermore, the CMC could be used to reinforce existing pipes to increase their lifetime.

Fig. 1 shows the principal layout of the material compound used for the full-scale test. The steel liner guaranties tightness, deformability and corrosion resistance. The CMC-jacket supports the liner and offers creep resistance. The liner is coated with a ceramic coating, which protects against corrosion and improves the friction properties in the interface. The ceramic felt is used to compensate for different coefficients of thermal expansion of steel and CMC during manufacturing and operation and to allow a homogeneous load transfer. The materials and the overall project are described more in detail in [11] and [12].
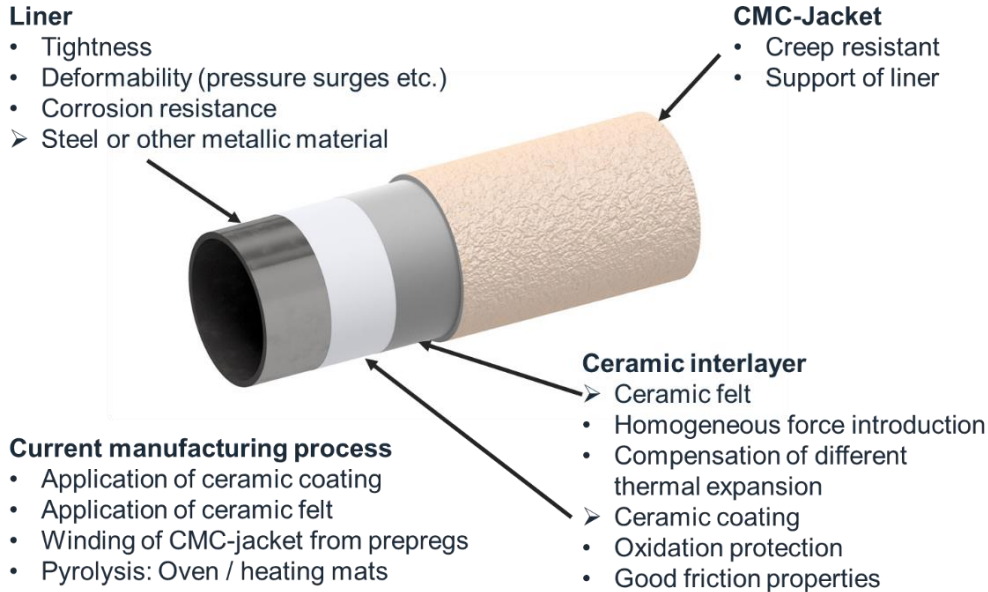
Fig. 1: Material compound used for a full-scale test in a coal-fired power plant

2. Full-scale test

Acoustic emission monitoring took place in a full-scale test of a CMC-jacketed pipe bend in a German coal fired power plant, the Grosskraftwerk Mannheim (GKM). The aim of the project was to show that the life time of components could be increased by jacketing a steel pipe with a ceramic matrix composite. For the full-scale test, a pipe bend (outer diameter 324 mm) with reduced wall

thickness was fabricated. After the manufacturing of this steel liner , a ceramic coating and a ceramic felt were applied before the CMC was wound around the liner from prepregs. Afterwards he CMC was pyrolyzed to gain full strength. The temperature of the pyrolysis was limited by the maximum annealing temperature for the steel liner and was set to 750°C.

After the pyrolysis the pipe bend was shipped to GKM and installed as bypass to a live steam pipe in the power plant. End of August 2018 the full-scale test went into operation. The full-scale test took place until September of 2021.

2.1. Installation and instrumentation

The pipe bend was installed in the power plant and different types of sensors were applied to monitor the liner and the jacket with regard to creep strain. Additionally, the temperature of the component was measured at different locations using thermocouples. Fig. 2 left shows the installed pipe bend in the GKM before insulation. The sensor positions are shown in Fig. 2 on the right.
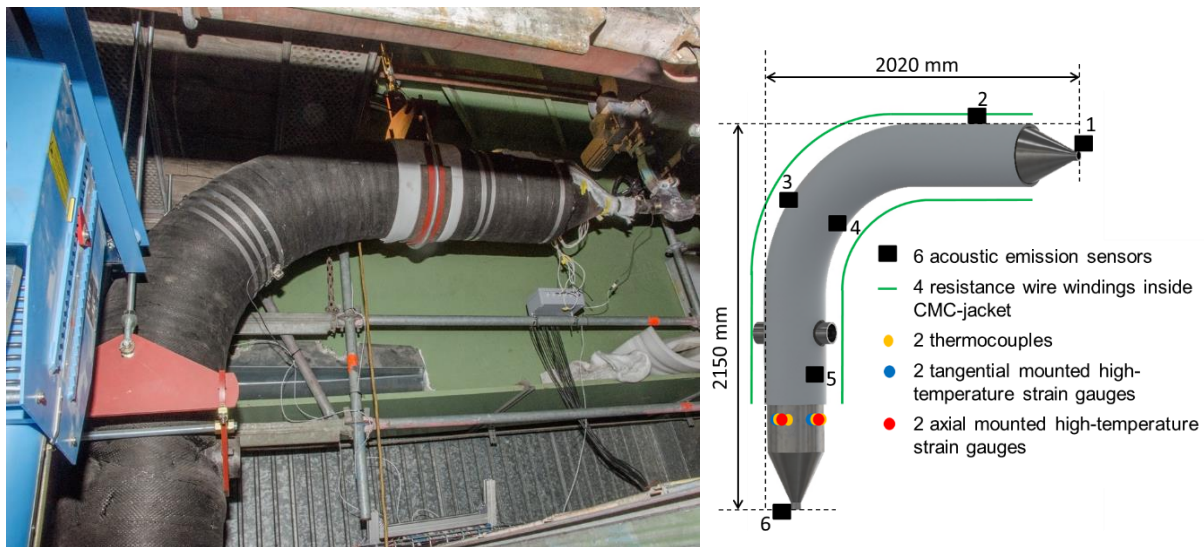
Fig. 2: left: pipe bend installed in GKM, right: scheme of instrumentation.

2.1.1. Strain monitoring of the liner and integrity monitoring of the jacket

The main damage mechanism for steel piping under temperature and pressure loading is creep. During creep the microstructure of the steel undergoes characteristic changes and the material experiences strain. To measure the creep strain of the liner, high temperature strain gauges are applied to the liner in tangential and axial direction (blue and red dots in Fig. 2 right) below the CMC jacket. To monitor the integrity of the the CMC jacket, small diameter high temperature resistant wires were wound in the jacket during the winding process. The change in the resistance of the wires is linked to the change in global strain state of the CMC jacket, whereby a failure of a resistance wire indicates a failure of the jacket. The entire jacket is monitored by resistance wire as marked in Fig. 2 with green lines.

2.1.2. AE monitoring

AE monitoring was used with the aim to detect fiber breakage and crack initiation and growth in the CMC jacket, which would cause acoustic emissions. Six AE sensors were placed on the pipe bend, four on the jacket and two on the liner as reference in Fig. 2 right. Common AE sensors work in temperature ranges up to about 200 °C. The operating temperature of the live steam line is about 530°C and only one type of AE sensors was suitable for this application. The sensor D9215 from Mistras is operating up to 540 °C and was used for the full-scale test. In general, high temperature AE measurements in power plants are done by applying wave guides to the surface. The waveguides usually are welded to the surface. This is not possible on CMC and the

waveguides could only be attached by glue. High temperature resistant glues are ceramic based and brittle and the connection will get lost in the presence of mechanical loading of the connection between waveguide an glue. At the same time, the waveguide itself is a great lever and is very likely to apply stresses on the connection. Thus, for the full-scale test the high temperature resistant AE sensors were applied directly to the surface. As can be seen in the following, this presented enough challenges.

The coupling of the sensors was a main issue and is discussed in the next section. According to the preliminary investigations a ceramic glue was used, which worked with water as binder. The CMC surface was oxidized with a heat gun in the spots, where the sensors would be placed. After that the glue was applied and the sensor was attached. To secure the sensors in case of vibrations or other external disturbances, a small housing from austenitic steel was put over the sensor and fixed with austenitic steel bands. Mineral wool that is used during insulation of the pipe bend, was used for the acoustic decoupling of sensor and housing. A photo of the setup is shown in Fig. 3 for the mounting on jacket (left) and liner (right). The sensor locations are shown in Fig. 2 right. The sensors on the liner were applied on the small diameter connection pipes to the live steam line . The mounting concept did not work on the conical parts of the pipe and the non-jacketed straight part of the big diameter pipe was needed for the other instrumentations.
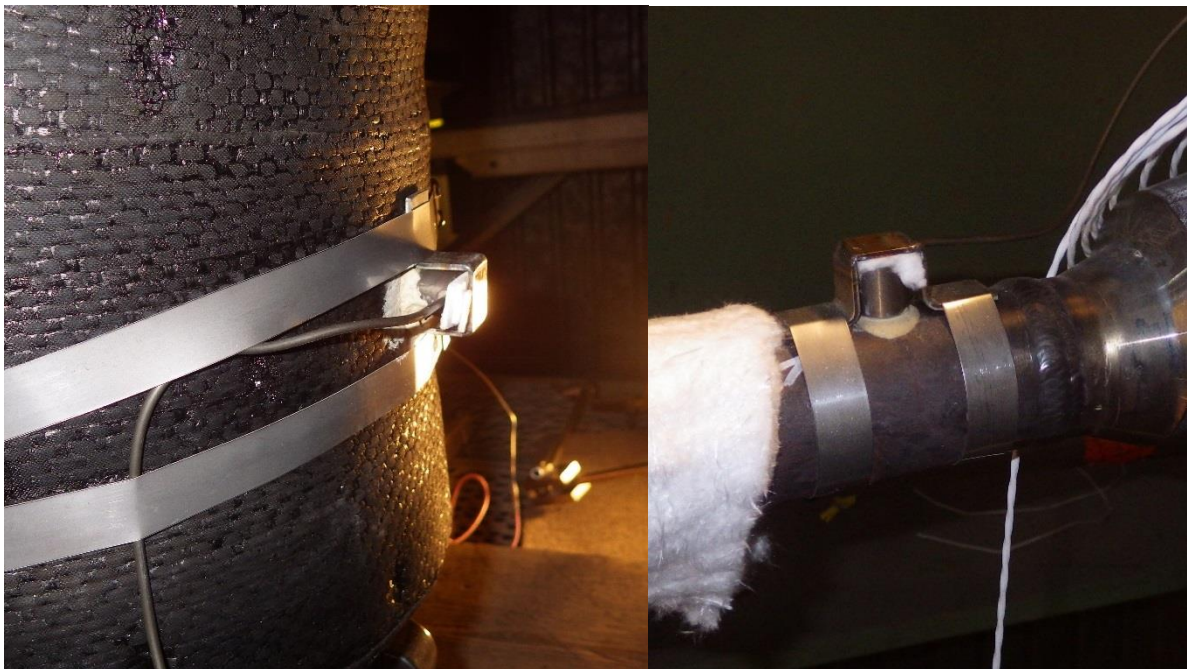
Fig. 3: AE sensors and housing mounted on jacket (left) and liner (right)

After installation pencil lead breaks were done at all sensor locations. The CMC does damp the acoustic energy very fast and a pencil lead break on the CMC in general is just recorded at the sensor nearby. Thus, a 2D- or 3D-localization of sound sources is not possible with the used sensor configuration. This would require a much higher sensor coverage of the material which is a matter of costs, as the high temperature resistant AE sensors are quite expensive.

After installation of the sensors, the pipe bend was insulated. Thus, the sensors are not accessible during the full-scale test before deinstallation.

In Fig. 4 the AE data from the first 30 days of operation are shown as example for the whole full-scale test. Additionally, the operating temperature and pressure are added in the plots, as both affect the AE activity. The sensors on the liner (top image in Fig. 4) act very sensitive to changes in both pressure and temperature. Furthermore, a higher activity is observed in times of complete cool down. The opening and closing of the valves between pipe bend and live steam line also generates characteristic signal patterns on the liner.

The AE activity of the jacket is high in the first two days of the full-scale test and then returns to a steady level. Changes in pressure and temperature also are visible in the AE data on the liner. Temperature changes in the live steam line lead to lateral movements of the whole piping system due to thermal expansion of all components. This leads to numerous possible acoustic sources. Plant operation also causes noise signals, e.g. operation of coal mills and turbines. However, progressive damage of the jacket would lead to significant increase of activity and intensity of AE signals. This could not be observed during the whole operation time of the full-scale test.
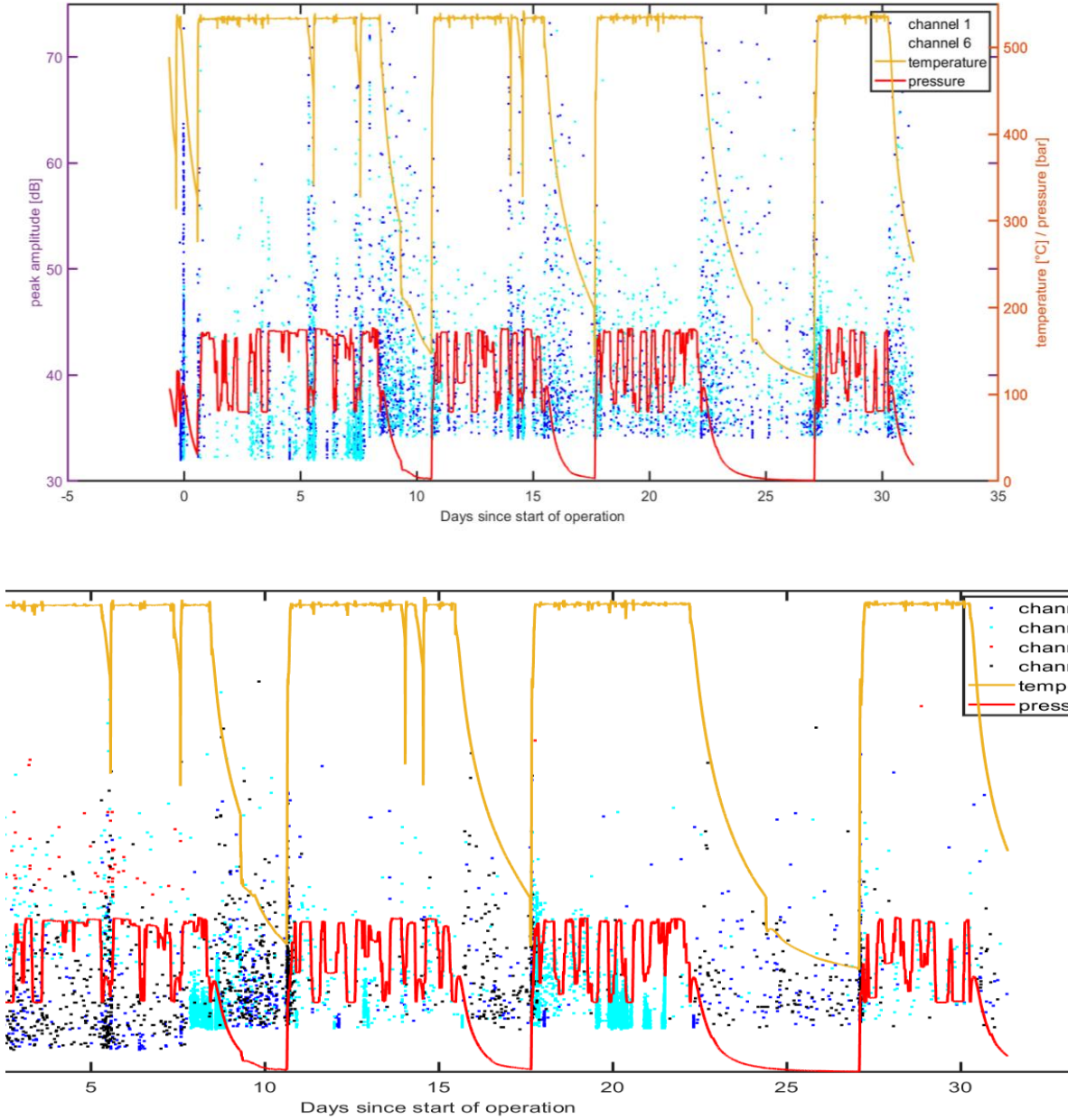
Fig. 4: AE signals recorded during the first 30 days of operation of the full-scale test. top: sensor 1 and sensor 6 on the liner, bottom: sensor 2 - sensor 5 on the jacket.

3. Application of AE Sensors

The coupling of the AE sensors was a big topic during the planning of the full-scale test. Several sensors should be placed on the CMC jacket. The coupling should be permanent for at least 3 years and durable during a high amount of cooling and heating cycles. The permanent cooling and heating cause additional stress in the bonding area, as the sensor, the glue and the CMC all have different thermal expansions.

3.1. Finding the right glue

The first step was to identify a sufficient glue for temperatures up to 530°C. All glues known to the authors that work in this temperature range are ceramic. However, ceramic is brittle and may break and lose connection during the start- and stop-cycles of the power plant. Different glues were tested in an oven. Therefore, metallic plates were glued onto the surface of a CMC-plate from the same material that later was used for the full-scale test. The metallic plates were from a alloy similar to the casing of the AE sensors to consider the different thermal expansion of CMC and metal. In Fig. 5 the plates are shown before and after 100 hours in the oven at 530°C. Unfortunately, only one metal plate was still attached after hardening of the glues but also loosened after 100 hours in the oven. Further investigations lead to the assumption, that the oxidation of the CMC, which takes place during the first heating and changes the CMC's color from black to white as excess carbon leaves the CMC, affects the bond. Thus, the surface should be oxidized before attaching the sensors.

Fig. 5: top: Photo of metal plates glued to CMC before test in the oven; bottom: photo of metal plates glued to the CMC after test in the oven

3.2. Oxidizing of CMC

In the tests in the oven, it turned out that the glues adhere to the oxidized surface better than to the not oxidized surface. The surface of the later test pipe for the full-scale test was not oxidized. Thus, the spots where the sensors were attached had to be oxidized before installation of sensors.
Different tests took place to investigate the necessary oxidation time with a common heat gun (see setup in Fig. 6). It turned out that a suitable oxidation is reached if a whitening of the surface is visible after about 10 minutes. In the same approach two different glues could be identified, that seemed suitable for the full-scale test.

Fig. 6: top: setup for oxidisation tests: heat gun, temperature and time measurement; bottom: applied sensors to spots with different stages of oxidisation before oven.

4. Coupling of AE sensors after test

During the full-scale test, there was no possibility to check the sensor coupling. The pipe bend was fully insulated and it was not possible to remove the insulation even partially as long as the full-scale test was running. The sensors under the insulation were not visible or accessible from the outside. The sensors could not be used to actively send ultrasonic pulses, thus, it was not possible to use one sensor and catch the signal with the other sensors to check the coupling. Additionally, the high sound attenuation of the CMC would have impeded this approach further.

Thus, the performance of the sensors during the full-scale test was the only indication of the coupling condition of each sensor. Sensor 4 and 5 only delivered few data after the first months of the full-scale test, thus it seems as if the coupling was reduced. However, the proof only could be made after deinstallation.

During deinstallation, first the insulation was removed. After that the sensors were inspected carefully to detect any possible damage. Here, no indications for failed coupling were visible. After the inspection, pencil lead breaks were performed at all sensor locations.

Table 1: Pencil lead breaks before and after long-term test.

	Sensor 1	Sensor 2	Sensor 3	Sensor 4	Sensor 5	Sensor 6
Amplitude before test (dB)	67.5	65.5	74.0	66.7	64.9	63.6
Standard deviation (dB)	4.6	3.3	0.0	3.2	5.2	4.0
Amplitude after test (dB)	61.1	66.2	67.3	64.3	49.6	52.8
Standard deviation (dB)	1.7	1.8	0.9	5.9	2.3	4.8
Difference (dB)	**6.4**	-0.7	**6.7**	2.5	**15.3**	**10.8**

The results of the pencil lead breaks before and after the tests are shown in Table 1. The mean amplitude from 4 pencil lead breaks and the standard deviation and the differences between both are listed. Four of the six sensors showed a significant drop in recorded amplitudes. The highest difference of 15.3 dB was recorded at sensor 5, which was located on the vertical part of the pipe on the jacket. Sensor 6, which was positioned on the vertical pipe on the steel liner, also lost about 10.8 dB in amplitude. Sensor 3 on the extrados delivered the highest amplitudes before the test, with all amplitude results in saturation (74 dB). The amplitudes still are highest, but a decrease of 6.7 dB is seen. Sensor 2 shows even an increase in amplitude after the test, but with regard to the standard deviation of the mean, the amplitudes before and after the test have to be considered equal.

Sensor 1: thin cracks visible in glue surface

Sensor 2: No visible cracks in glue surface

Sensor 3: No visible cracks in glue surface

Sensor 4: Some air inclusions in glue, cracks in glue

Sensor 5: Glue material missing, no visible cracks in glue surface

Sensor 6: glue material missing, cracks in glue
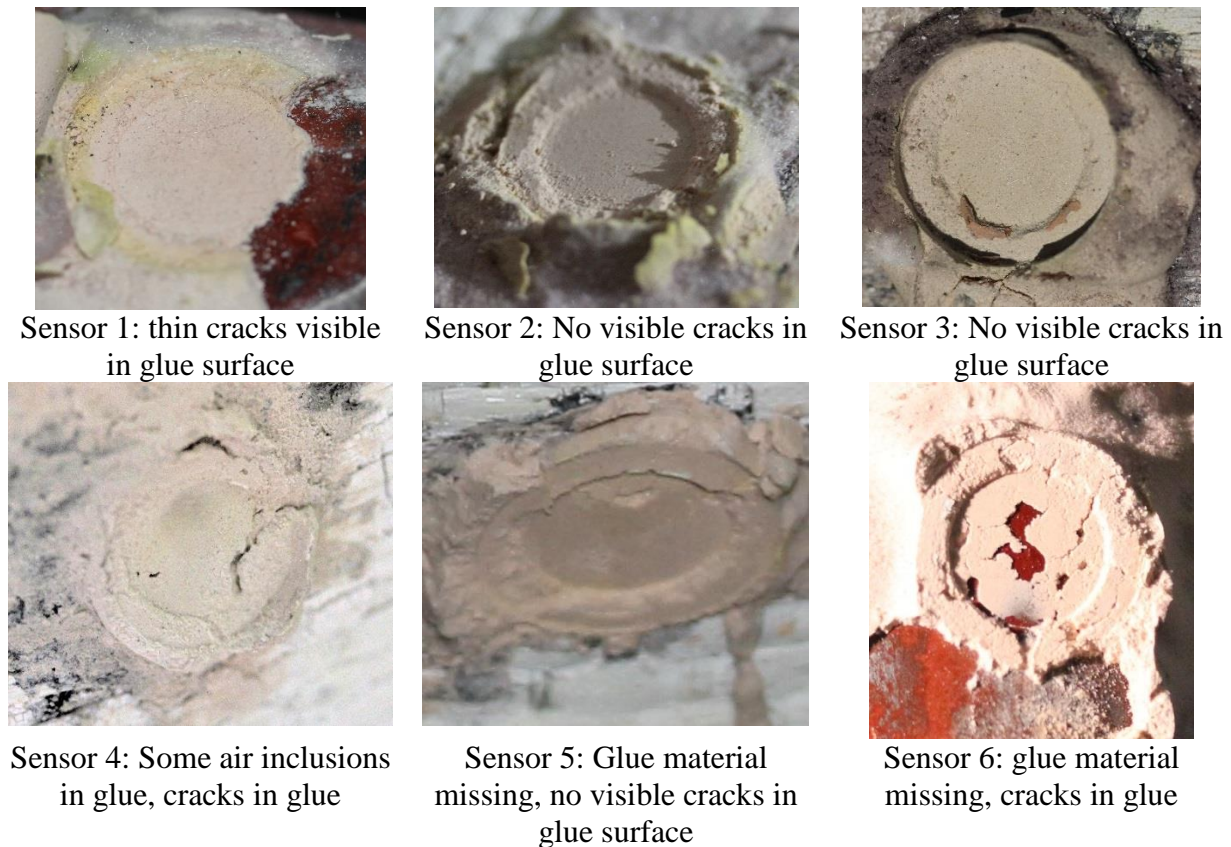
Fig. 7: Glue spots after deinstallation of sensors

The glue spots on the pipe were documented in photos during the deinstallation of the monitoring technique (Fig. 7). Some of the sensors went loose directly after the austenitic bands and houses were removed. It could not be estimated if the sensors loosened during the deinstallation or earlier during the test. Some of the sensors were still attached to the surface after removing of the housing. The glue surfaces of sensor 1 looked smooth, but shows thin cracks at a closer look. Sensor 2 and

3 did not develop cracks in the glue and the surface was smooth. Sensor 4 showes large cracks in the glue. At the positions of sensors 5 and 6, glue material stuck to the sensor face. Sensor 6 showed also big cracks in the glue. As can be seen, glue surface and pencil lead break amplitude do not correlate.

5. Conclusions

AE monitoring was applied during a full-scale test at a CMC-jacketed steel pipe in a coal fired power plant in Germany. High-temperature resistant AE sensors were used as the operating temperature of the pipe was about 530 °C.

Coupling of the sensors for three years of operation and no possibility to even check the coupling in between, demanded proper preparation of the test setup. Different glues were tested on the oxidized and non-oxidized surface of CMC and finally a ceramic glue was chosen. The glue required mixing a powder with water and could be handled well under the conditions in the power plant.

Additionally, test took place to investigate the necessary effort to oxidize the bonding areas before application of the sensors. It could be shown that a common heat gun can be used to oxidize the surface locally within a certain amount of time. This improves the bonding between sensor and material significantly.

A setup with small housings around the sensors, that were attached to the pipe with austenitic metal bands, was realized, to prevent the sensors from falling of in case of loss of adhesion. This proved sensitive for this application and worked quite well.

All AE sensors recorded signals continuously during the full-scale test despite permanent vibrations and high-temperature load. After removal of the insulation, the AE sensors were inspected and the bonding was visible good for all sensors. Pencil lead breaks before and after the tests revealed significant decrease in sensitivity at some locations, others were as good as before the test.

Thus, the sensor coupling was sufficient for the full-scale test and the extended investigations concerning coupling proved successful. It could be shown, that it is possible to apply AE sensors for longer times even in rough environments. The analysis of the big amount of data collected during the full-scale test is topic for other publications.

6. Acknowledgement

7. References

[1] Nakamura, Y. (1971) Acoustic Emission Monitoring System for Detection of Cracks in a Complex Structure. Materials Evaluation, vol. 29, No. 1, pp. 8-12.

[2] Morgan, B.C., Tilley, R. (1999). Inspection of power plant headers utilizing acoustic emission monitoring, NDT & E International, Volume 32, Issue 3, Pages 167-175, ISSN 0963-8695, https://doi.org/10.1016/S0963-8695(98)00068-1.

[3] Lee, J.-H., Lee, M.-R., Kim, J.-T., Luk, V., Jung, Y.-H. (2006). A study of the characteristics of the acoustic emission signals for condition monitoring of check valves in nuclear power plants, Nuclear Engineering and Design, Volume 236, Issue 13, Pages 1411-1421, ISSN 0029-5493, https://doi.org/10.1016/j.nucengdes.2006.01.007.

[4] Tonelli, D., Luchetta, M., Rossi, F., Migliorino, P., Zonta, D. (2020). Structural Health Monitoring Based on Acoustic Emissions: Validation on a Prestressed Concrete Bridge Tested to Failure. Sensors 20, no. 24: 7272. https://doi.org/10.3390/s20247272

[5] Verstrynge, E., Lacidogna, G., Accornero, F., Tomor, A. (2021). A review on acoustic emission monitoring for damage detection in masonry structures, Construction and Building Materials, Volume 268, 121089, ISSN 0950-0618, https://doi.org/10.1016/j.conbuildmat.2020.121089.

[6] Momon, S., Godin, N., Reynaud, P., R'Mili, M., Fantozzi, G. (2012). Unsupervised and supervised classification of AE data collected during fatigue test on CMC at high temperature. Composites Part A: Applied Science and Manufacturing, Volume 43, Issue 2, 2012, Pages 254-260, ISSN 1359-835X, https://doi.org/10.1016/j.compositesa.2011.10.016.

[7] ASTM E 650 (1997). Standard Guide for Mounting Piezoelectric Acoustic Emission Sensors.

[8] Bohse, J. (2014): Richtlinie SE 02 Verifizierung von Schallemissionssensoren und ihrer Ankoppelung im Labor, Fachausschuss Schallemissionsprüfverfahren, DGZfP.

[9] Ziegler, B., Dudzik, K. (2019). An Overview of different Possibilities to Master the Challenge of Coupling an AE-Sensor to an Object of Interest Partly using Examples of Previous Investigations. Journal of KONES Powertrain and Transport, vol. 26, No 1., pp. 207-214, ISSN: 1231-4005, DOI:102478/kones-2019-0025.

[10] Brunner, A. J. (2021). Structural Health and Condition Monitoring with Acoustic Emission and Guided Ultrasonic Waves: What about Long-Term Durability of Sensors, Sensor Coupling and Measurement Chain?. Applied Sciences 11, no. 24: 11648. https://doi.org/10.3390/app112411648

[11] Juengert, A., Friedrich, M., Huang, M., Klenk, A., Weihe, S. (2018). Monitoring of CMC-Jacketed Pipes for High-Temperature Applications. Proc. of ASME 2018 Pressure Vessels and Piping Conference PVP2018, July 17-20, Prague, Czech Republic, Paper No: PVP2018-85023.

[12] Friedrich, M., Huang, M., Juengert, A., Klenk, A., Weihe, S., Metzger, K. (2019). CMC-jacketed piping for high-temperature applications: Concept, laboratory tests and large-scale application test. Eds: Hausmann, J., M. 22nd Symposium on Composites. June 26-28. Kaiserslautern, Germany. Trans Tech Publications.

INDUSTRIAL APPLICATION OF ACOUSTIC EMISSION MONITORING – GENERAL CONCEPT AND SELECTED PRACTICAL EXAMPLE

Heribert Marihart[1,*], Mikhail Prokofyev[1] and Gerald Lackner[1]

[1]TÜV Austria; heribert.marihart@tuv.at, mikhail.prokofyev@tuv.at, gerald.lackner@tuv.at
*Correspondence: heribert.marihart@tuv.at

ABSTRACT

Acoustic emission monitoring (AEM) is a method for verifying the structural integrity of heavily stressed parts or key components while the plant is in operation. The condition of the monitored component can be determined by repeated short- or continuous long-term AEM. The selection of damage-relevant measurement data and the resulting evaluation serves to determine the actual condition of the test object.

Unlike for conventional acoustic emission testing, no shutdown of the plant is required for the measurements. The results can then be used as a quality assurance measure according to maintenance requirements of the owner/operator or as a supplement to the testing and inspection program. This contribution describes the general monitoring concept developed and established by the TÜV AUSTRIA Group as well as two selected industrial use cases.

Keywords: Acoustic emission, online monitoring, digitalization, industry 4.0.

1.   Introduction

A reliable monitoring system can be helpful in terms of safety and economic aspects, such as to operate the plant at operating conditions optimized for the service life or optimization of maintenance intervals. Built-in warnings and alarm criteria can be used to take appropriate actions to prevent plant damage and subsequent total plant failure. For this purpose, specially developed monitoring equipment and an automated data analysis processes are used to measure and to evaluate the actual condition of the monitoring object. For the condition evaluation a well-established procedure from the conventional acoustic emission testing, the cluster evaluation factor (CEF) developed by the TÜV AUSTRIA Group on basis of European standardisation, was extended to monitoring applications.

In order to meet the requirements of customers from oil and gas industry or from power generation industry, the hardware for monitoring on hot and cold surfaces as well as software for the transmission, storage and evaluation of the acoustic emission data were developed. In addition, intrinsically safe monitoring components were purchased and tested, enabling AEM in hazardous areas. Automated online data management allows the data to be processed in real time and to be visualized on a graphical web application (dashboard). In Fig. 1 an overview of the general measurement infrastructure of TÜV AUSTRIA Group is shown.
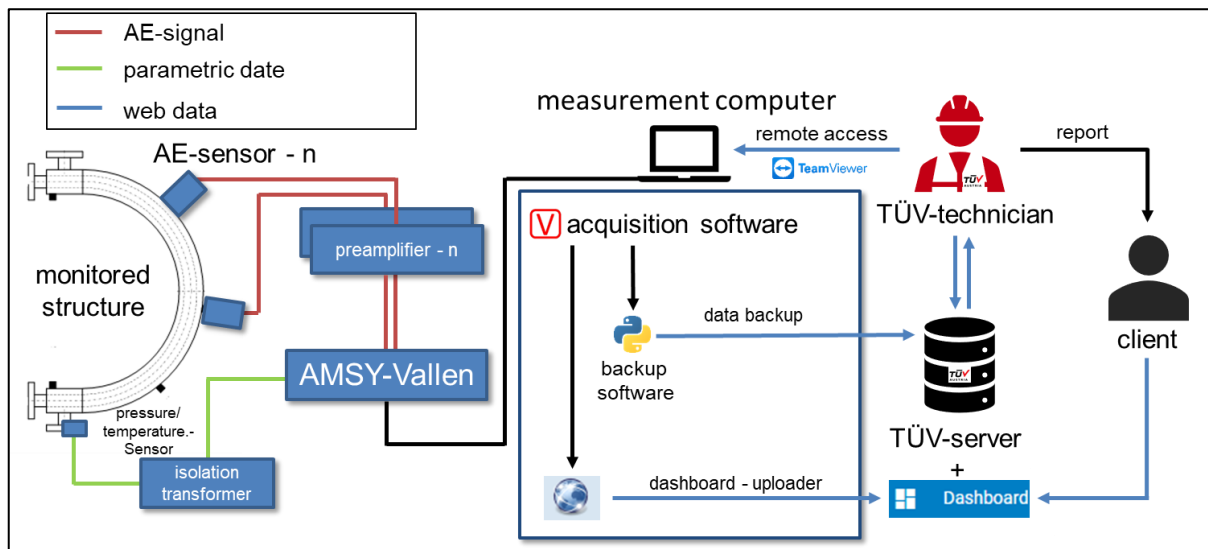
Fig. 1: Flow diagram of the general AE-monitoring concept of the TÜV AUSTRIA Group.

2. Operation

2.1 Monitoring Hardware

A wide range of pressure equipment is used in industry, with a variety of operating conditions. This can range from high temperatures, high pressures, large volume flows or even corrosive, explosive, or chemically reactive operating media.

Therefore, it is helpful to have a decision guideline which sensor could be used. The following matrix of operating temperature and operating zone has been created for all available sensors (see Fig. 2).

temperature / hazardous area	from -180 °C	up to 50 °C	up to 180 °C	up to 450°C
no	R15-LT	VS150-RIC VS160-NS VS150-BD	VS150-RIC + WG VS160-NS VS150-BD	VS150-RIC + WG VS160-NS + WG VS150-BD + WG
yes	-	VS150-BD	VS150-BD	VS150-BD + WG

Fig. 2: Application matrix: hazardous area/ temperature.

According to the required acoustic emission monitoring and the monitored object, the temperature range has to be determined, and the potential sensor type has to be selected depending on the operating zone.

Furthermore, a special magnetic sensor holder (see Fig. 3) with the option of a waveguide device was developed for application on hot surfaces. The construction is adaptable for different sensor sizes and can also be applied as a waveguide with the use of a special heat-resistant material, which allows temperatures up to 450°C. The inhouse build construction can also be applied for curved surfaces. For curved surfaces, the number of magnets can be varied from 4 to 2 and pressed directly onto the material with metal strips.
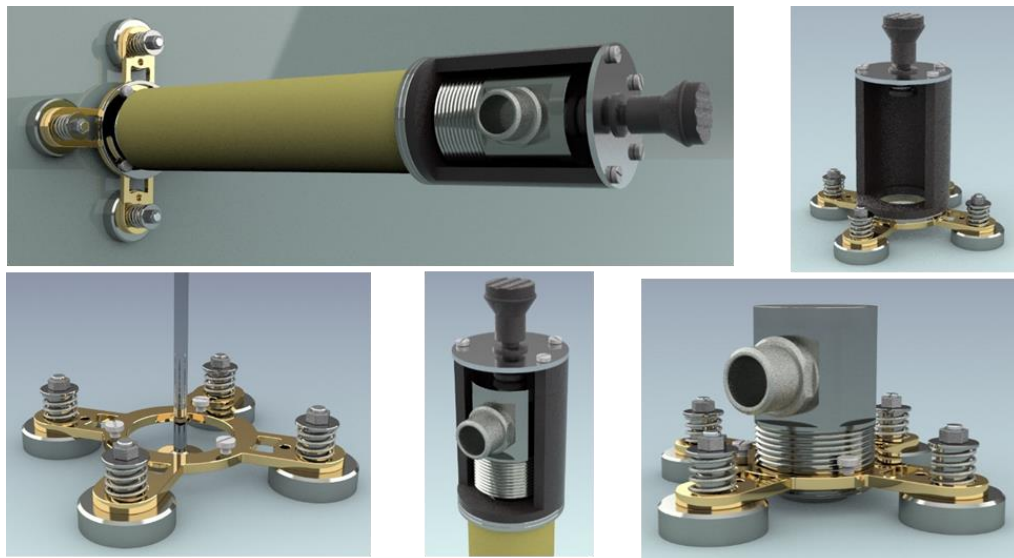
Fig. 3: Magnetic holder and waveguide device.

A graphite paste (PRO 533 GP graphite paste) is used as a coupling agent for high temperatures up to +450°C and a thermal conductive paste (Thermal Grizzly Hydronaut) for low temperatures. A number of laboratory tests with the Hsu-Nielsen source showed only 5 dB lower amplitude at the verification of the sensitivity of the waveguide device as the direct mounted sensor and also 20 dB higher amplitude as the older waveguide design.

Another important point is the supply of the operating parameters such as pressure and temperature. In our example of a digester, the input signal was mA and recorded as an output signal in V in the AMSY-6 by means of galvanic isolation. The recorded pressure and temperature are also used as condition monitoring. In the second example, the reactor, the input signal was intrinsically safe input (Ex-i) (mA) and again recorded in the AMSY-6 as output signal Ex i in mA by means of galvanic isolation.

The entire hardware for acoustic emission monitoring is situated in a so-called monitoring box (see Fig. 4). Two different sizes of those boxes have been designed for such purpose. The larger one is designed for long-term use and for hazardous areas. It is also equipped with a weather station. The smaller one is designed for shorter monitoring projects, is mobile and can also be transported in an airplane.

Fig. 4: Magnetic holder and waveguide device.

Both monitoring boxes are equipped with a rack system. An AMSY-6 as a 19" rack version from the company Vallen (MR19-V1) is installed.

A commercially available notebook serves as the measuring computer, which is used to record and handle the recorded data. It is also used to automatize the processes for data recording. But it can also be used for data transfer and remote maintenance.

A line filter was also integrated into the Monitoring Box, which is used to filter out disturbances from the power grid.

A unit supply power (USP) is able to back up the power supply for about 30 minutes and thus ensure a controlled shutdown of the measuring system.

The internet connection is established via a WLAN router with 2 SIM card slots and is connected to the PC with a network cable for security reasons.

2.2 Monitoring Software

The main function of the measurement computer and Vallens AMSY-6 on-site is to collect and to merge the AE-data with the operating parameter (pressure, temperature, volumetric flow rate…) in the measuring system. Subsequently with the Vallen VisualAE it is possible to carry out on-site calculations, like the CEF. The calculation of the CEF value is happening in real time via an Embedded Code Processor (ECP).

A new development of Vallen, which was established by us is the dashboard uploader. With this feature it is possible to extract selected data (amplitude, duration, risetime, CEF…) and send it to the Vallen dashboard. The dashboard is a graphic online application, which makes it possible to view the selected data from the dashboard uploader in real time. For the technician who is monitoring the structure it is easier to see the long-term changes in the parameters during the measurement period and also to react fast to sudden changes in the data. It is also possible to give the customer an access to dashboard, where he can view the data presented in the graphs designed by the technician with a view to the customer requirements.

To establish a high grade of measurement process automatization the "Automation Manager" from Vallen is used. For a better comparison 24h measurements are saved with previously configured data acquisition and visualisation files. With the "Auto Pulsing" function the measuring chain is checked at certain intervals. If a previously defined deviation of AE parameters occurs, an alarm should be sent as a result. Similarly, previously set limits of the acoustic emission results can trigger alarms.

During the monitoring period a large amount of data is accumulated. For an automated data management, a backup software in cooperation with TÜV AUSTRIA Data Analytics was developed. This program automates the backup of the data every 24h on a TÜV-server. Which makes is easier to be viewed and analyzed by the responsible technician.

For the maintenance, it is possible to access the measurement computer on-site with a secured connection remote over TeamViewer. Which is considerably reducing the on-site time for the technician.

3.   Examples of industrial applications

3.1 Pulp digester in the paper mill

The test object was a large pulp digester in a paper factory. The subject was the monitoring of a circumferential weld after repair welding of cracks. The aim was to monitor this area. The operating temperature was around +150°C and the pressure range was 4-10 bar.

For the monitoring, sensors VS160-NS with an extended temperature range of -50°C up to +180°C were mounted directly to the hot surface with magnetic holders by Vallen. The preamplifiers AEP3, also from Vallen, were clamped onto the insulation. Monitoring was carried out periodically for 3 days in 3 weeks cycles.

3.2 Tubular reactor in plastics industry

The test object was a more than 1000-meter-long tubular reactor from the plastics industry. The aim was to monitor possible cracks in individual pipe sections, such as pipe bends or straight pipe sections. The reactor itself is located in its own concrete shell and is in hazardous zone-II. The operating parameters are, working pressures of up to 3000 bar and surface temperatures of up to +180°C.

Long-term monitoring of over 1.5 years was chosen for this monitoring. The sensors used were the VS150-BD-V01 from Vallen, a hazardous version with an extended temperature range up to +180°C. The sensors were mounted with the magnetic holder developed in-house and a mounting device for curved surfaces. The AEP3N-BD-V01 served as preamplifier for this measuring chain. The preamplifiers were located outside of the hazardous zone. Connected to the sensor by a special AE-cable for a temperature range up to 200°C and lengths up to 80m.

4. Results and Reporting

During the measurement period large quantity of data is accumulated. The goal is to reduce the time needed for the evaluation of the monitoring data, or even to make a conclusion about the status of the monitored component in real time. For this we extended the cluster evaluation factor (CEF) developed by the TÜV AUSTRIA Group that is well-known tool in the classic acoustic emission testing [1,2]. Based on the numerous experiences from previous measurements during pressure testing, we are using the CEF to get a quick overview of the status of the monitored structure.

With the combination of the CEF and the parametric data it is possible to see the response of the monitored structure to the conditions of operation. The reports on the condition of the structure are made for every 24h (see Fig.5). The cluster evaluation factor is applied for on-line evaluation of located events. The calculation of the CEF in real time makes it possible to reduce the data of amplitude, energy, duration, and event rate to a single number. The evaluation range of CEF starts from 0 (no located events = 0 severity) up to 4 (very high severity).

Also, in regard of reporting, this system is very easy for the understanding of the customer of a complicated topic and a user-friendly color-coded system can be presented. The CEF can be viewed by the costumer in real time on the dashboard surface.
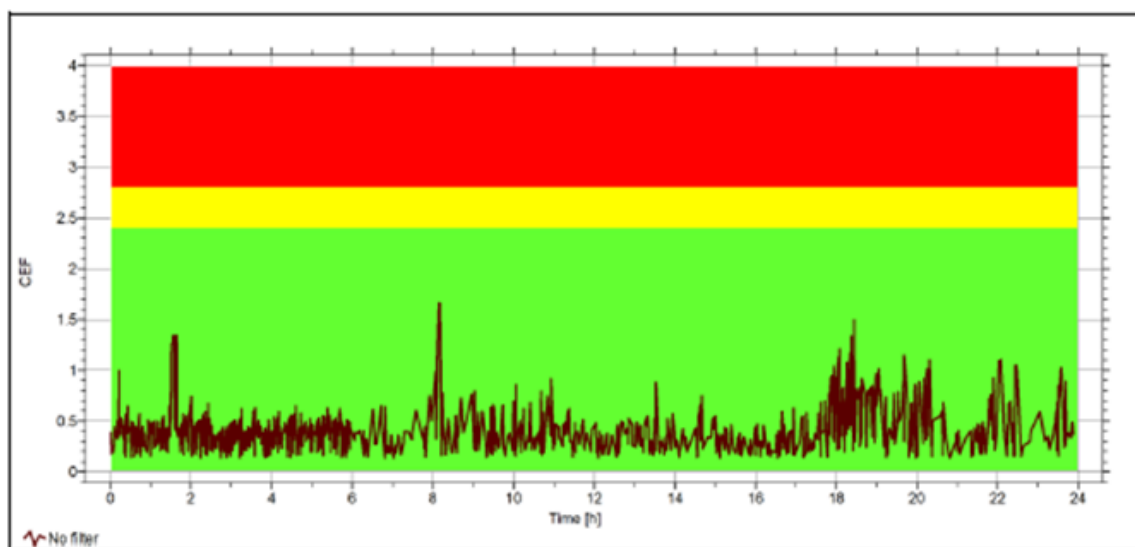
Fig. 5: Development of the Cluster Evaluation Factor (CEF) over the measurement period, reaction of the component to the operating conditions.

Beside the CEF, which is the overall response of the monitored structure during the monitoring period we are using the location of the AE-signals to show the local response of the component. The localisation of events in the period of 24h on the weld of a digester from the paper industry is shown in Fig. 6. The 24h period of measurement makes it possible to compare the accumulation of the events regarding their location and quantity. In the case of monitoring of the digester the positions of the cluster were also compared to the measurements from a PAUT Ultrasonic Testing. Besides the data which can be viewed by the customer in real time, reports are presented to the customer at regular intervals. Which summarize the results of the measurement for the monitoring period and an evaluation of the status of the monitored structure in the measurement period. Also, a recommendation how to proceed further with the monitoring is given, for example the frequency of measurements for short term AEM.
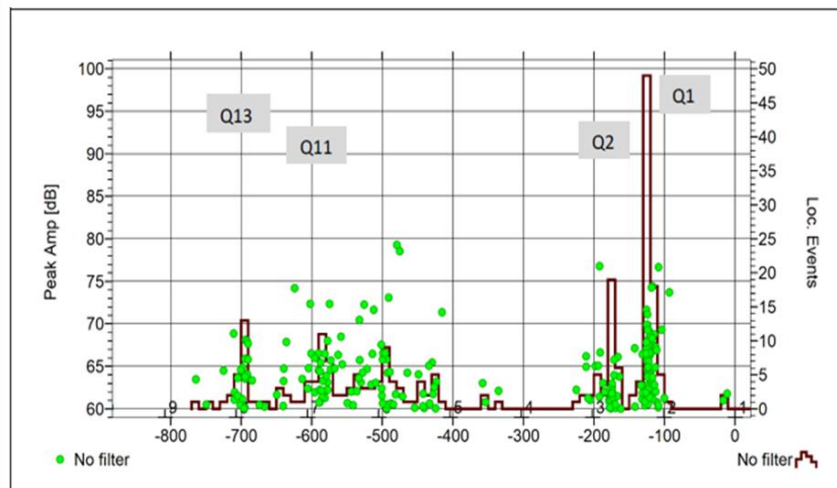
Fig. 6: Localization of the events during a 24h measurement period on the circumferential weld of a digester.

5. Conclusions

The concept developed by TÜV Austria Group was successfully used for several monitoring projects: short- or continuous long-term. Due to its flexibility, it offers a variety of options for adapting and using it on different objects and in different environments. A wide temperature range can be covered up to +450°C using an in house developed waveguide. The application in hazardous area (Ex), using the appropriate components, could also be carried out successfully. Due to the high degree of automation of the measurement and the data stream management, the system also offers significant savings in man-hours. By establishing the well-known concept of CEF for monitoring application, a real-time evaluation of the condition of the object could also be used successfully. An online presentation of the measurement data through the graphical interface of the dashboard provides the customer and the responsible technician with the possibility to view the data in real time.

6. References

[1]   Tscheliesnig, Peter; Schauritsch, Gert: Inspection of LPG vessels with AE examination. Journal of Acoustic Emission, Vol. 18, 2000, p. 138 – 143.
[2]   G. Schauritsch, "Schallemissionsprüfung an einem rissbehafteten Flüssiggaslagerbehälter – Ergebnisse zum Nachweis der Verfahrenseignung", Proceedings of 18. Kolloquium Schallemission, Vortrag #03, 2011.

FIBER OPTIC SENSING SYSTEMS

State-of-the-art sensing systems for unmatched performance in the most challenging environments

Our profile

OPTICS11 is an Amsterdam based high tech company that offers state-of-the-art fiber optic sensing systems for unmatched performance.

Optics11 has extensive experience with monitoring Acoustic Emission, Temperature (including cryogenic), Strain, Acceleration, and Pressure.

All Optics11 systems embrace innovative measurement techniques that allow to overcome most of the drawbacks and limitations of classic fiber-optic sensing systems such as limited bandwidth, limited sensitivity, and bulky sensor size.

Fiber optic sensing systems for

Monitoring in Cryogenic Environment

Structural Health Monitoring

Condition Monitoring

PIPE DENT EVALUATION BY ACOUSTIC EMISSION DURING HYDRAULIC PRESSURE TESTS

Václav Svoboda[1,*] and František Žemlička[1]

[1]Preditest Ltd., Pod Višňovkou 1662/23, 140 00 Praha 4, Czech Republic
*Correspondence: svoboda@preditest.cz

ABSTRACT

Buried pipelines transporting gas and oil are influenced by surrounding soil during long time service. In many cases they are locally deformed by soil movement, especially by hard stones. External local pressure makes limited deformation of original shape of pipe diameter in time. Those types of local deformations are known as a dents. At those areas, the insulation layer is usually damaged and small defects (like cracks) are created in dents. Colonies of small stress corrosion cracks are observed. In this contribution, the evaluation of typical dents is investigated by hydraulic pressure tests, including the fatigue tests. Acoustic emission was used to detect the behaviour of dent in pipe section until the limit state. AE monitoring during pressure tests gave very clear answer of defect activity vs. loading pressure. Parallel to this monitoring, another NDT method, MMM was used with promising results.

Keywords: Pipeline, pressure vessel, dent, NDT testing, pressure test.

1. Introduction

During the internal inspection (pigging) made on gas pipe DN1000, spirally welded, the dent was discovered and its position was localized. From this pipeline, the pipe section containing the dent was cut out for detailed investigation by hydraulic pressure test.

Acoustic emission method was used to monitor the behaviour of dent with stress corrosion cracks. In Fig. 1, there is a pipe section prepared for pressure test. On Fig. 2, schematic view of localized AE sensors around dent and another spiral weld of pipe can be seen. By this configuration of AE sensors it was possible to distinguish AE signals from dent and also from the rest of pipeline section. Strain and stress was controlled by application of group of strain gauges, located on outer surface of pipe and in area of the dent.
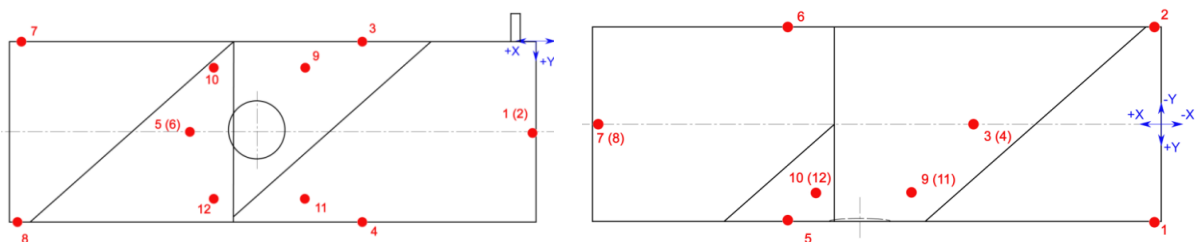
Fig. 1: Scheme of pipe section prepared for pressure test.
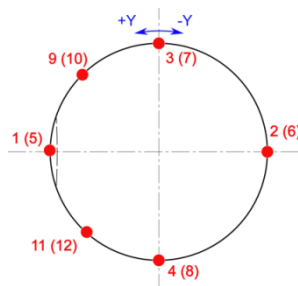
Fig. 2: Scheme of pipe section.

2. Methods

Pipe section was fixed in a laboratory equipped with a high pressure loop. With this loop, it was possible to provide a burst test on the pipe. Experimental set-up:
- multichannel AE system ACES IDT04 with special software was used,
- AE sensors, type PET04 with integrated pre-amplifier were fixed on the outer surface of pipe section,
- HP computer was used to collect AE data for the next evaluation.

Test procedure:
- calibration test to determine: sensor activity, attenuation curve, velocity of signal spreading in pipe material, verification of location accuracy. Results of calibration procedure are shown in Fig. 3,
- pressure tests, program of pressure tests was divided into 3 individual steps:
  - initial pressure test in scope of 0 – 7,4 MPa, repeated 3 times, as shown at Fig. 4,
  - fatigue pressure tests in 20 000 cycles in scope of 0 – 7,34 MPa,
  - burst test with increasing internal pressure till rupture, as shown in Fig. 5.
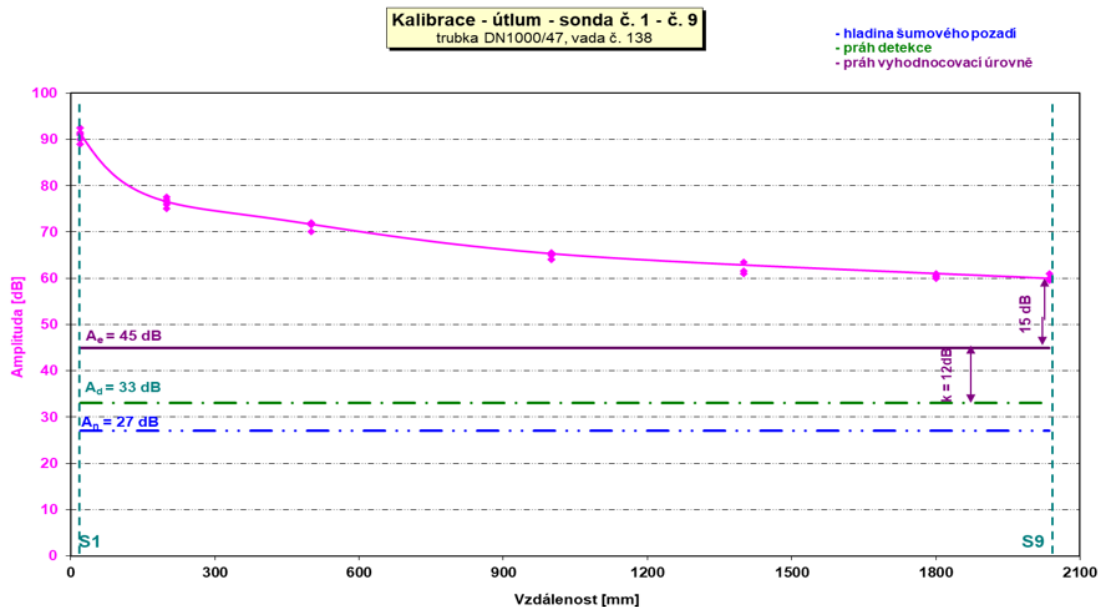
Fig. 3: Calibration curve.

Water was used as a pressurizing medium. All volume of pipe section, including area of dent, was monitored continuously by installed AE sensors configuration.
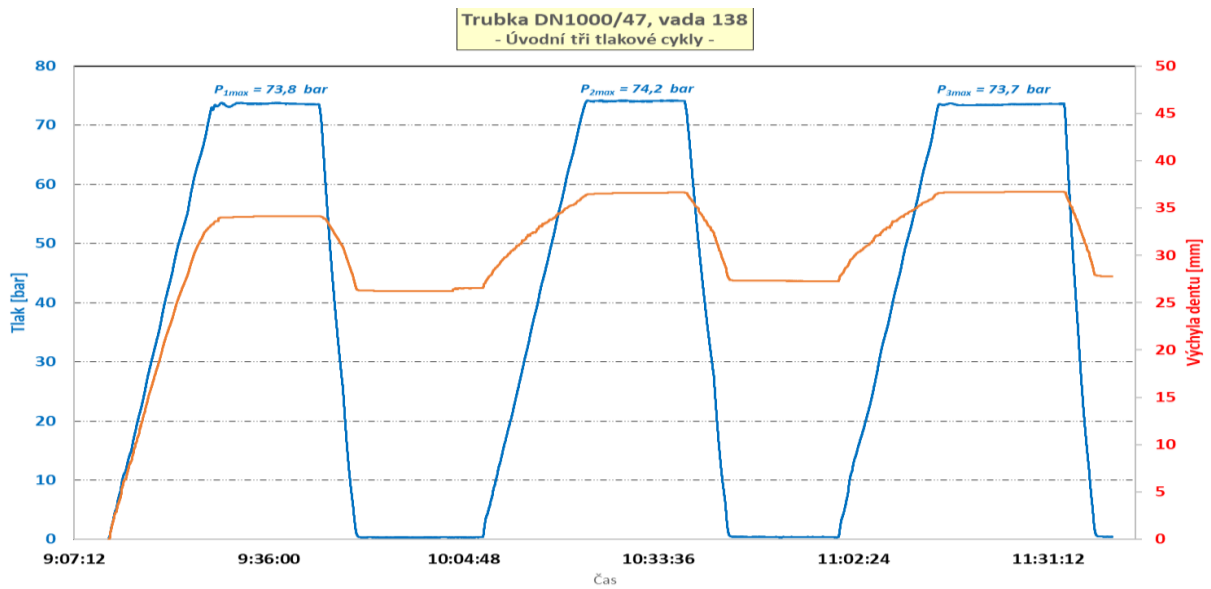
Fig. 4: Initial pressure test.
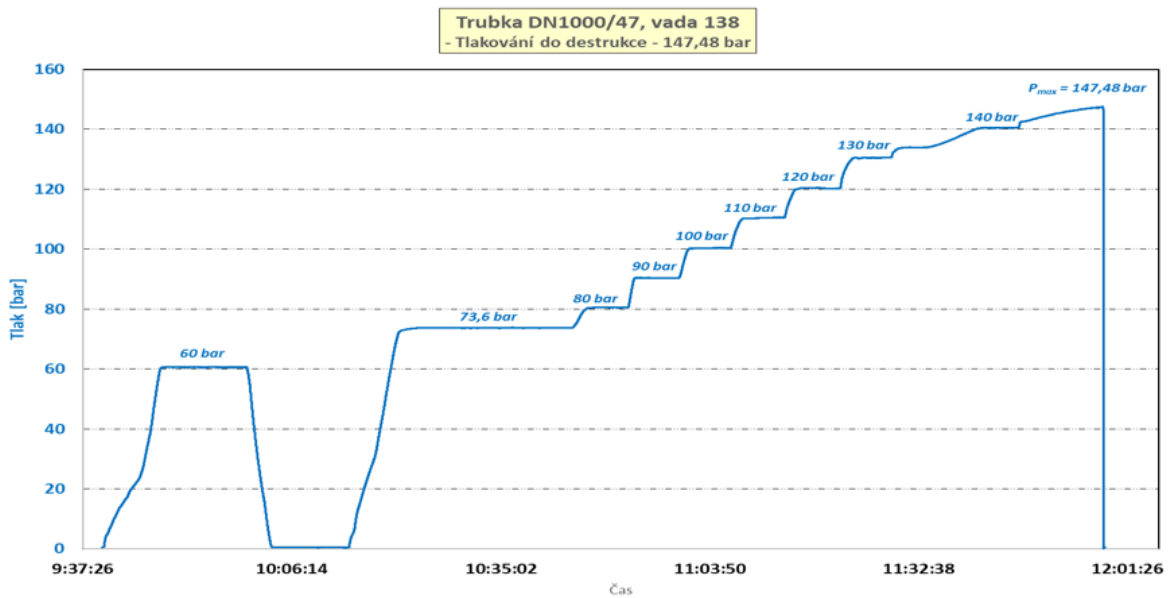
Fig. 5: Burst pressure test.

3.   Evaluation and results

During all three individual steps of pressurization large files of measured data were obtained. For the evaluation of measured data, special software for filtering was used and real AE events were localized on the pipe and also on the area of the dent.

3.1 Initial pressure test
Localized AE events after application of three cycles are shown in Fig. 6.
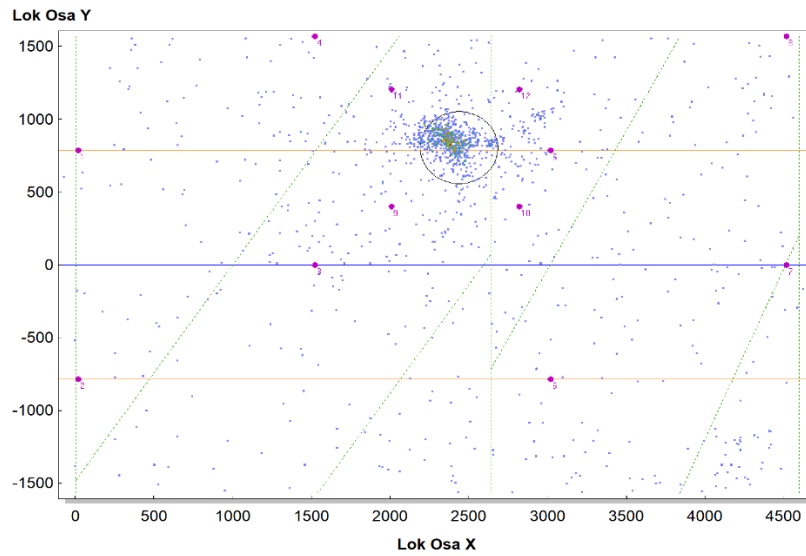
Fig. 6: Initial AE events localization.

It can be seen that at the dent area, most AE events are localized. This is due to the large plastic deformation inside the dent. See Fig. 4. In the first pressure cycle, the deformation in the dent reached nearly 33 mm. In the second cycle, the deformation was only 11 mm and in the third cycle deformation was 10 mm only. During cyclic loading the deformation in the dent bottom decreased to 7 mm. Registered and localized AE events from cycles 2 and 3 are shown on Fig. 7.
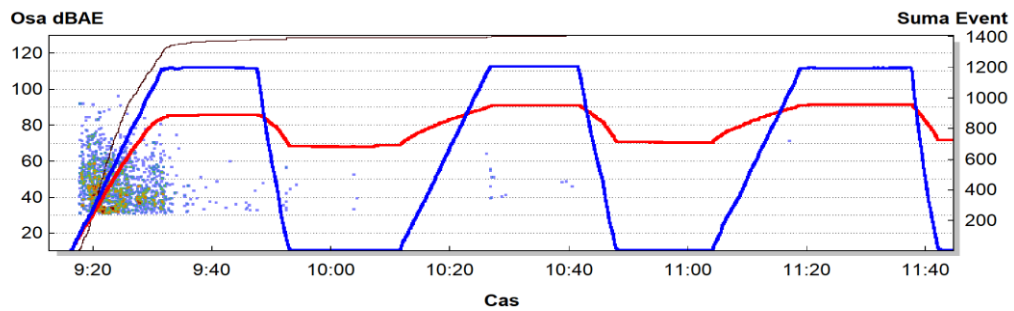
Fig. 7: AE events in all three cycles.
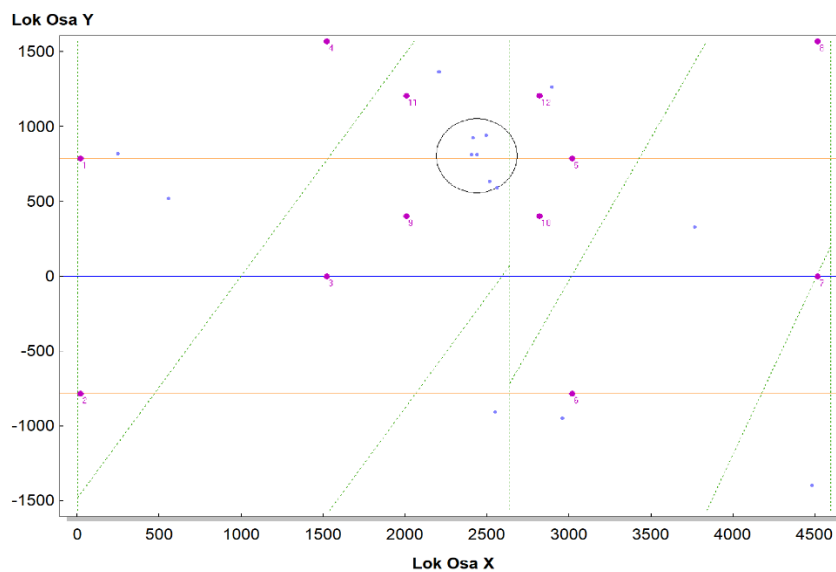
Fig. 8: Localized AE events from 2nd and 3rd cycle.

Due to large plastic deformation made in the 1st pressure cycle, only a small amount of AE events was localized in the area of dent. This is documented in Fig. 8.

3.2 *Fatigue tests by internal pressure*

Fatigue test was carried out with pressure cycling between 4 MPa to a maximum of 7,35 MPa. In Fig. 9, the localization map of registered AE events during 20 000 pressure cycles, can be observed.
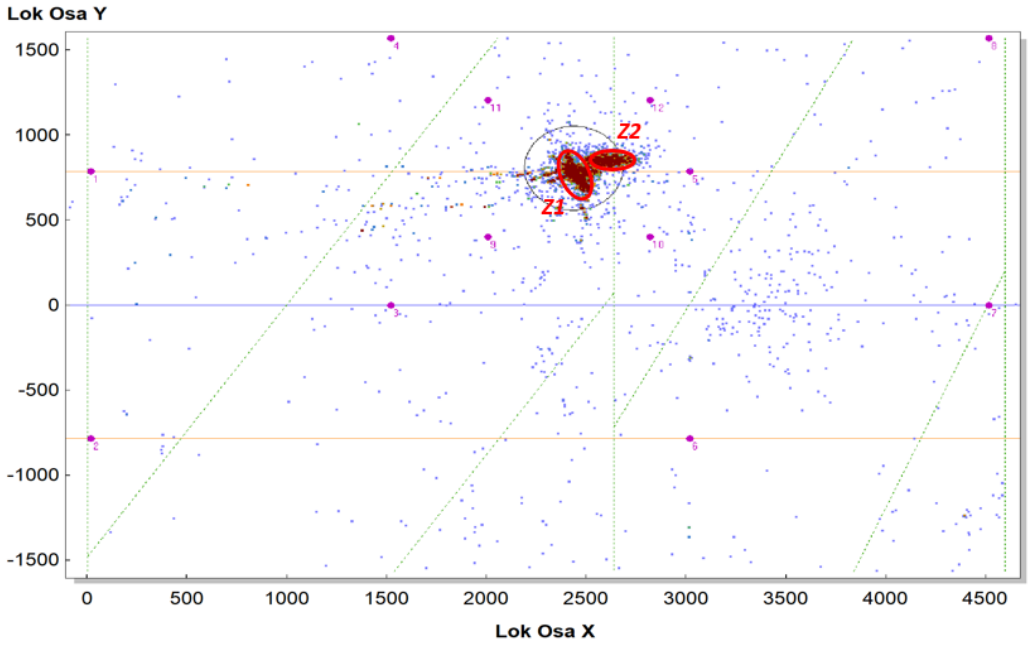
Fig. 9: Localized AE events after 20 000 pressure cycles.

Most of AE events were located in the area of the dent. In this area, two AE sources were localized, Z1 and Z2. AE source Z1 was localized directly in the bottom of the dent, where stress corrosion cracks were identified. Source Z2 was localized circumferential weld close to the dent. Time dependence of AE events during cyclic test is shown in Fig. 10.
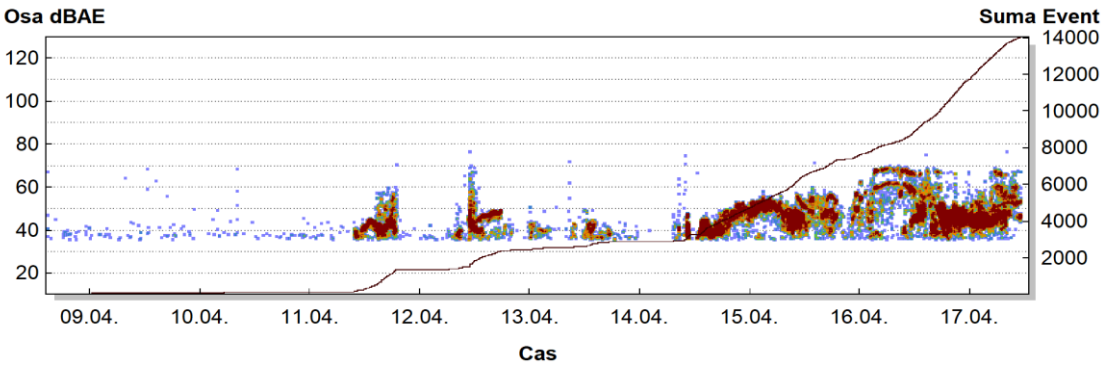
Fig. 10: AE activity during cycling.

From this graph it is clear, that AE activity started after reaching approx. 5300 pressure cycles. More intensive rate of AE event was registered after 10 400 cycles. Increased AE activity from AE source Z1 is in Fig. 11 and AE activity from source Z2 is in Fig. 12.
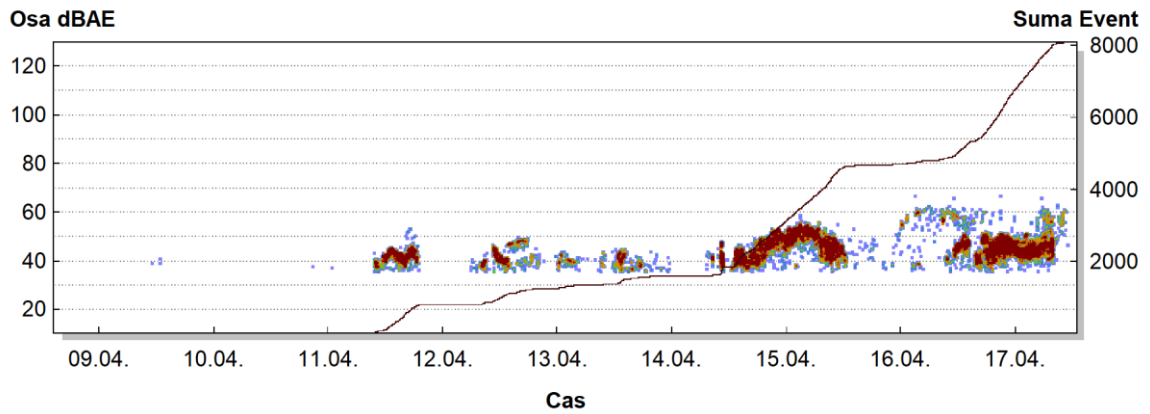
Fig. 11: AE source Z1.
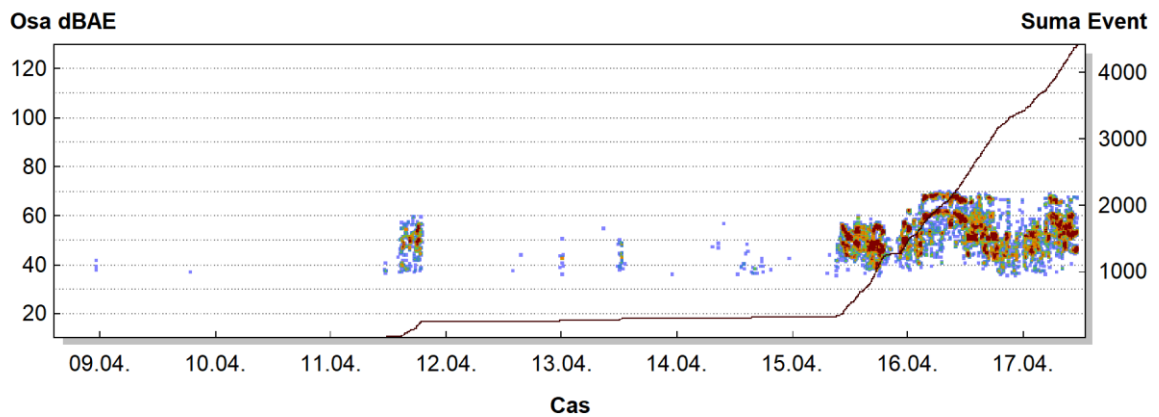
Fig. 12: AE source Z2.

Before the pressure test, few stress corrosion cracks were discovered in the dent, with a maximum depth of 4,2 mm. During the fatigue test, those cracks were propagating and after 20 000 cycles, they reached a depth of 6,3 mm.

3.3 Burst pressure test
Pressure and corresponding AE event activity during the burst test is presented in Fig. 13.
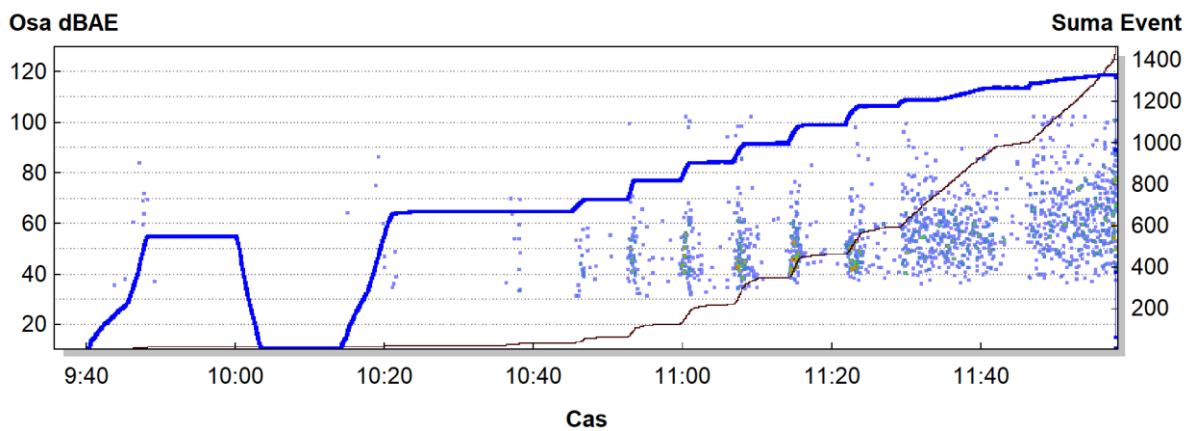
Fig. 13: AE activity during the burst test.

On the beginning of burst pressure cycle, one cycle was done up to 6 MPa, which corresponds to maximum working pressure in the pipeline. During this cycle, minimum AE events were observed.

The following pressurization was done continuously with a break after reaching prescribed level of pressure. Generally, increased AE activity was observed between pressures of 8 MPa to 9 MPa. When pressure crossed 13 MPa, a big deformation of the pipe was investigated by strain gauge measurements. Another increased AE activity was indicated when internal pressure crossed over 14 MPa. Final fracture of the pipe came when internal pressure reached 14,75 MPa.

Source of the final crack, propagating through the wall of the pipe, was located between the dent and the closed circumferential weld. Summary localization of AE sources after burst test is shown in Fig. 14.
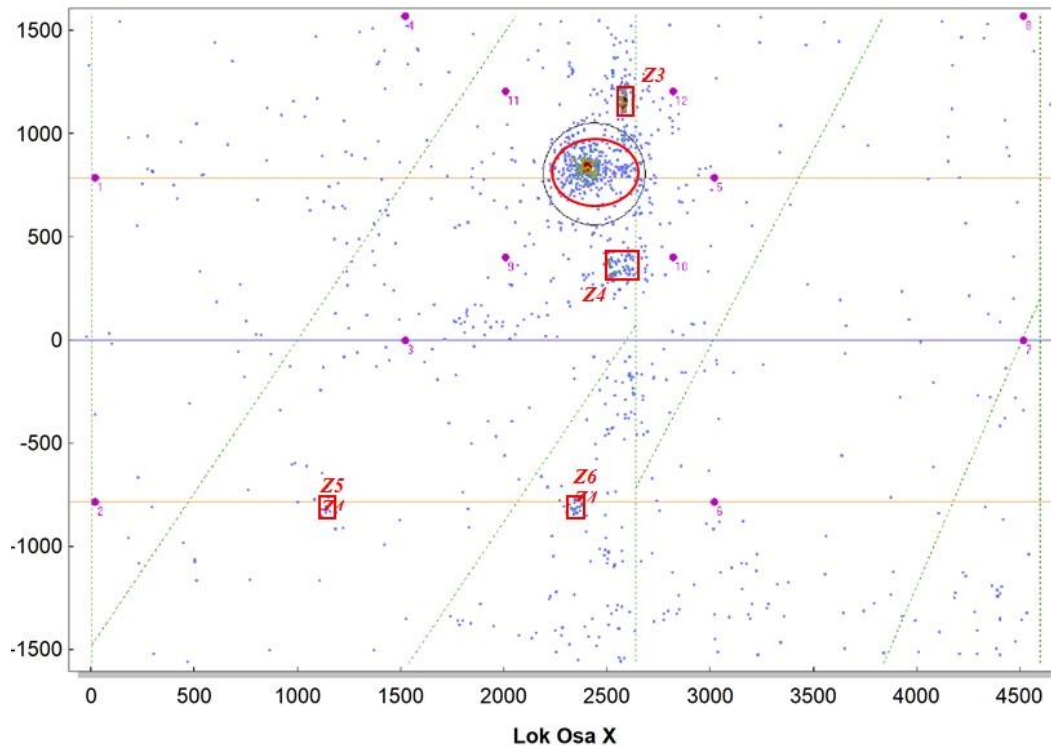
Fig. 14: AE activity sources during destruction.

4. Conclusions

On the base of experimental results it can be stated:
  ▪ acoustic emission method is a very useful tool for evaluation of defects in pipes loaded by internal pressure,
  ▪ a suitable arrangement of AE sensors on outer surface of the pipe specimen allowed us to distinguish AE events coming from the dent and from other parts of the pipe section,
  ▪ overloading of the pipe above the working pressure, up to 7,3 MPa, confirmed a positive effect to prevent propagation of existing natural stress corrosion cracks,
  ▪ during application of 20 000 pressure cycles, cracks started to propagate after reaching 5000 cycles and increased from initial depth of 4,2 mm to 6,3 mm,
  ▪ this type of a large dent in a pipe, containing an inside colony of small stress corrosion cracks, was not the source of pipe destruction during normal working pressure.

EFFECTIVE APPROACHES TO REMOTE ASSET MONITORING WITH ACOUSTIC EMISSION

Arturo Nunez[1] and Spilios Kattis[2]

[1]Mistras Group, Inc., Products & Systems Division, Pinceton Junction NJ, USA;
arturo.nunez@mistrasgroup.com
[2]Mistras Group Hellas, Athens, Greece; spilios.kattis@mistrasgroup.com

ABSTRACT

This paper presents the effectiveness of remote asset monitoring using acoustic emission. We will discuss different aspects of implementing an effective remote asset monitoring operation, such as considerations for the deployment of instrumentation in the field, instrumentation, communications, benefits of automatic data transfer from the monitoring system to a secure server, continuous automatic verification of hardware integrity, and automatic notification of potential damage or conditions affecting the asset integrity occurring.

We will provide an in-depth view of the cloud monitoring implementation processes, and the use of machine learning and other data analytics techniques to identify abnormal acoustic emission data patterns. The application of these tools to specific case studies in electric power transformers, power steam generators and civil infrastructure assets will be presented. Finally, we will illustrate how these capabilities help to provide timely, actionable information to the asset owner.

Keywords: Acoustic emission, remote monitoring, data analytics, cloud computing.

1. Introduction

The number of applications using acoustic emission for monitoring critical assets is increasing and has been adopted by different industries. This present different challenges from selection to the right instrumentation, number of sensors, type of sensors, location of the transducers, location algorithm to be used, amount of data to be collected, additional parameters to be monitored.

Once the monitoring solution has been selected the next step has to do with communications, how is the data going to transferred from the instrumentation to a secure location, is the data going to be transferred using a cell phone modem, a wifi or internet connection, is the connection secure, does the connection need to be built around a VPN tunnel or not, is the data encrypted?

Once the data transfer scheme has been defined, how is the data going to be displayed/presented to the end user? is it easy to understand? is the most critical information been presented? is it possible to automate some of the analysis process? what is the best way to create a data driven web application?

There are different approaches for effective monitoring, and we discuss some of the considerations that need to be taken when deploying a monitoring system for the remote condition assessment of critical assets.

2. Understanding the problem

The most important step at the beginning of a project is understanding the need for monitoring. Is the intent to monitor the asset as a predictive tool to try to detect defects during its normal operation, or does the asset owner knows about a manufacturing defect that has been detected in similar assets and wants to make sure this asset does not present the same defect, or a defect has been detected on the asset and the owner wants to monitor the area closely to determine if the defect is growing and under what operating conditions, or has the asset been repaired and the asset owner wants to make sure the repair was done correctly.

One of the more critical aspects is to make sure the defect for which the monitoring solution is been deployed is detectable by acoustic emission. This is the opportunity for the AE expert to set realistic expectations of what information can be provided by the monitoring solution, how often the information will be provided either on a data driven web application (if available) or via periodic reports. Once it has been determined that acoustic emission is an adequate method for monitoring, the next steps need to focus on some of the practical aspects of the solution.

3. Designing the monitoring solution

3.1 Number of sensors
This can be determined by performing a site visit to the asset to be monitored to perform a visual inspection as well as an attenuation study using different sensor types. This will allow the AE Expert to identify the sensor spacing as well as accessibility to mount the sensors.

3.2 Type of sensors
This is a crucial step to ensure the project success, it is recommended that during the site visit a background noise test is performed (mounting a wide band sensor on the asset to be monitored during normal operation) to determine the typical background noise and select the best frequency range for the application. This step can be skipped if the application is well known for the AE expert and a standard solution is available. The other aspects to consider are the asset temperature, presence of insulation, intrinsically safe area, exposed to the environment (the use of coated sensors might be required).

3.3 Mounting of sensors
After the site walk around visit and knowing the temperature of operation, it is possible to select the best approach to mount the sensors, this can be done by using magnetic holders or epoxy/glue. If the asset has insulation or is operating at high temperatures the use of waveguides can be needed.

3.4 Selection of monitoring system
This step requires a knowing the number of sensors and the distances between the sensors and the data acquisition unit as well as the requirements specific to the asset location (intrinsically safe, high EMI, high contamination, heavy rain, heavy wind, etc.). The environment will determine if the instrumentation will be installed outside of if it requires to be installed inside a climate-controlled room, the use of barriers might be needed if working on an IS zone. Other factors to consider include accessibility to the instrumentation in case maintenance is needed as well as communications to be used.

The type of data to be collected is an important consideration to select the data acquisition unit, sampling rate to be used, availability of filtering schemes (manual or automatic), waveform streaming and location algorithms capabilities, type of automatic notifications available (loss of power, channel issues, full hard drive, etc.). It is also useful to have tools to be able to test the system periodically and automatically for example by been able to perform weekly auto sensor tests.

Finally, the instrument's capability of adding other signals such as operating parameters or data from other monitoring systems/sensors is an important selection parameter. These signals can be added using external 4-20 mA modules or via Modbus.

3.5 *Data transmission*

The data that is been collected by the instrumentation and must be transmitted automatically (the practice of retrieving the data manually is not cost effective and defeats the main benefit of continuous monitoring: timely notifications). There are different options for the data transfer: cell phone modem, wifi, ethernet, satellite. The use of one or the other will depend on the amount of data been transferred, availability of cell phone providers, plant IT requirements, cost, bandwidth availability if using the plant's network. Regardless of the communication type used, the data must be secured, transmitted without affecting its integrity and automatically.

The data transmission is vital, this ought to be carefully planned and executed to make sure it is working from day one of monitoring. This requires working with the plant's IT group to make sure all their cyber security concerns are addressed, the use of special configurations (VPN tunnels, tokens, Virtual Machines, etc.).

In some instances, it is recommended to have the option to be able to connect to the instrumentation remotely to perform instrumentation checks, adjust instrument settings or perform software upgrades. This can be achieved using remote desktop connection or third-party programs like TeamViewer or LogMeIn. The use of these tools needs to be coordinated with the IT groups to ensure secure connections/compliance.

3.6 *Vizualization*

How the data is presented is of the utmost importance, a poor representation of the information can result on the misappreciation of the monitoring solution whereas a complex data driven web application can also been perceived as too complicated to use. Not all monitoring projects require a data driven web application, especially if the monitoring periods are short or if the application requires significant data processing/analysis before meaningful information is obtained.

If a data driven web application is needed/wanted, this can be developed in-house or using external service providers like AWS or Azure. The main advantages of using external service providers are uptime, built in security, tools available on their platform, etc., the main disadvantage is having a team of experts on those solutions and cost.

The data driven web applications need to be able to show the status of the monitoring system(s), location of events (planar,spherical,3D), see Fig. 1, alarms sent by the system and if desired automatic report generation with the condition of the asset. It might also have the option to allow the most advance users to plot data for pre-determined or customizable periods of time and/or have the capability of downloading data files directly from the web application.

Fig. 1: Different source location algorithms in data driven web applications, 2D, 3D, spherical.

3.7 Data analysis / reporting

For some applications the data analysis process can be automated (fully or partially), for others, there would be still a need for a manual data analysis. This requires the data to be transmitted periodically and available when the analysis will need to be performed. Once the data is analyzed a report can be sent to the asset owner, either via email and/or thru the web application. For long term monitoring projects, it is common to send a weekly report indicating the overall condition of the asset as well as a monthly/quarterly report with a more detailed analysis of the data.

Fig. 2 shows how the data flows between the instrumentation and the AE experts analyzing the data [1].
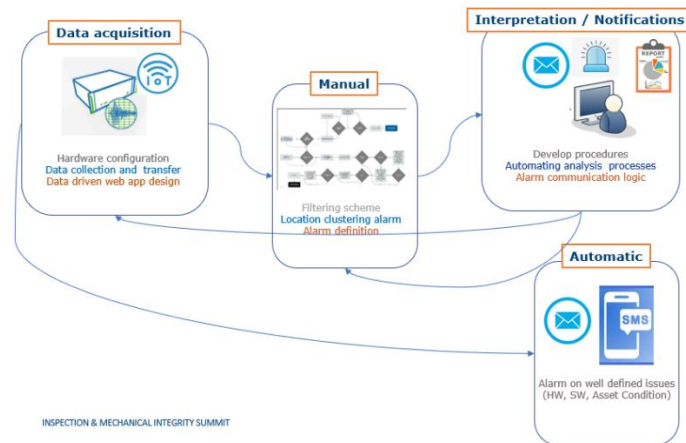
Fig. 2: Notifications from instrumentation and data availability for analysis.

3.8 Maintenance

An annual maintenance trip is a good practice, during these annual trips the instrumentation is checked to make sure is 100% functional. It is important that personnel involved on the monitoring of the asset communicates with the personnel performing the service trip. They can provide a list of issues to be checked on-site. Traveling with spare parts is also recommended to make sure sensors/cables are available to be replace if needed.

4. Case studies

4.1 Power transformer

A main power transformer on a wind farm [2] was generating gases indicating the presence of active fault, see tables 1 and 2. The type of gasses detected indicated a high intensity fault and if this unit failed the entire wind farm would be off-line.

Table 1: Nameplate information.

TYPE	TRANSFORMER
voltage	138 GrdY/79.67 – 34.5Y/19.92 – 13.69 kV
capacity	126.6 / 168.8 / 211 MVA
class	ONAN / ONAF / ONAF
core type	CORE
pumps	NO
ltc type	RMV-II-1500-72.5

Table 2: Gassing history.

DATE	H_2	CO	CO_2	CH_4	C_2H_6	C_2H_4	C_2H_2	TDCG	H_2O	OIL TEMP	O_2	N_2	IEEE DGA Status [2]
5/7/2021	23	259	599	8	2	10	4	299	6	37	1,220	10,500	3
4/29/2021	20	241	809	8	2	10	4	285	7	42	1,160	9,550	3
4/22/2021	24	247	778	8	1	10	4	294	1	46	1,090	10,100	3
4/17/2021	24	249	789	9	1	10	4	297	7	45	1,210	10,500	3
4/8/2021	23	234	780	12	4	9	4	286	9	45	58	9,420	3
4/2/2021	22	233	868	8	1	9	4	277	5		2,450	13,700	3
3/25/2021	21	213	727	8	1	9	4	256	4		3,050	16,300	3
3/18/2021	23	239	741	8	1	9	3	283	3		1,440	10,700	3
3/12/2021	23	223	728	7	1	9	3	267	7		1,500	10,800	3
2/27/2021	21	216	669	7	1	8	3	256	6		10,100	54,200	3
2/19/2021	21	203	708	7	1	8	2	241	6		5,730	32,000	3
2/6/2021	21	206	720	7	1	8	2	245	5		995	11,700	3
1/20/2021	22	198	703	6	1	7	2	237	3		708	9,440	3

An acoustic emission monitoring system was installed to try to detect and locate the gassing fault. After 1 month of monitoring, it was clearly observed that the fault was only active when the load tap changer operated in odd positions, see Fig. 3. When operating in odd positions, the preventive autotransformer is part of the electrical circuit which suggested a defect was located on this component [this correlation had not been observed by the asset owner before].
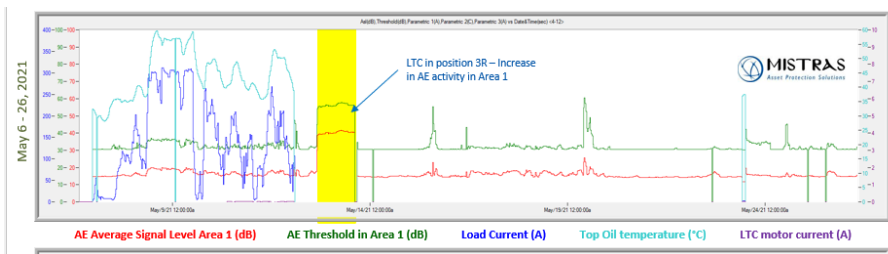
Fig. 3: Increase in acoustic activity when LTC operated on odd positions.

This information allowed the renewable energy company to lock the tap changer in an even position to prevent the fault from been active and this reducing any more damage and minimizing the risk of failure. The acoustic emission also provided information the fault location, see Fig. 4.
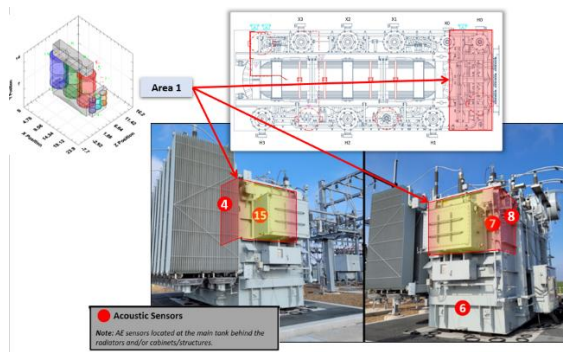
Fig. 4: Fault located on the area of the preventive autotransformer.

When the transformer owner was able to provide a spare unit, this transformer was sent to the transformer manufacturer's facility. An internal inspection was performed and damaged on the preventive autotransformer was seen most likely due to impact either during manufacturing or during transportation. The damage was observed on the winding as well as core laminations in the areas located during the monitoring.

The savings for the utility are significant since a catastrophic failure was avoided, there was no interruption of power generation by the wind site and the unit was eventually repaired and will continue to be used by this utility.

4.2 Boiler tube leak

An Acoustic Monitoring system (AMS) was installed at an Australian power station. In late 2021, the monitoring analyst first reported that there was a noticeable increase of acoustic energy particularly on the sensors installed on the west side of the boiler. As the energy and amplitude gradually climbed up higher, the acoustic data (trend and waveform) was reviewed and confirmed a suspected leak on the west side of the boiler. See Fig. 5.

Fig. 5: Boiler layout with normal acoustic profile on the left. Initial increase in activity on the right (red).

As the tube continued leaking and damage increased, the acoustic amplitudes/energy levels increased, triggering an alarm accompanied by an increase in 3.5x condensated water. This data confirmed a tube leak. As a precaution, the production and site manager were notified of the alarm. The sootblower system was shut down and local inspection took place.

The day after the leak was detected, sensors continued to detect increases in amplitude/energy. The unit was offline for 7 days as the unit was repaired, see Fig. 6 for the damaged found. Had acoustic technology not been monitoring the leak, the resulting damage could have been much more severe and costly. Based on power output and manpower, it is estimated that the power station saved over $500,000 USD.
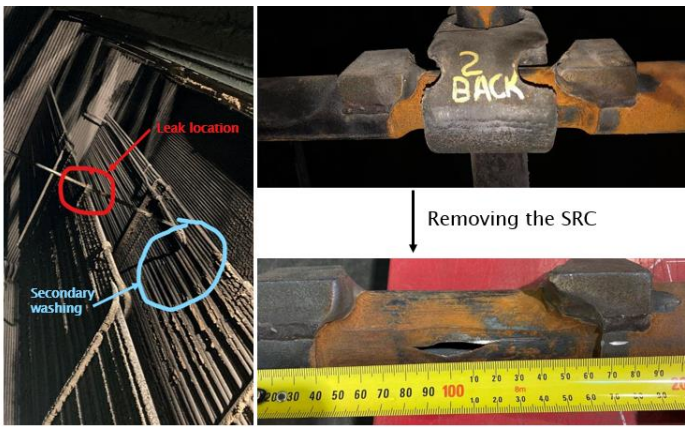
Fig. 6: Findings: fretting of tube 1.75"x0.375" under split ring casing (SRC). Tight crack 30mm long thin wall tube rupture with secondary washing over failure area.

5. Conclusions

The number of applications for acoustic emission monitoring has been increasing over the years and it is used on several industries. It is important that the proper steps are followed to ensure the information collected, processed, and analyzed provides useful information to the end user. The monitoring must be able to provide meaningful / actionable information that assist the asset owner in making decisions about the next steps (repair, inspection, additional testing, retirement, etc.)
As seen on the case studied presented, the savings can be significant if the monitoring is executed successfully and can allow the life extension of an asset and the reduction of risk in their operations.

6. References

[1]   Nunez, Arturo (2022). Get more from your AE Data – Inspection and Mechanical Integrity Summit – American Petroleum Institute.
[2]   Nunez, Arturo (2022). Continuous health monitoring of power transformers in wind farms ENERUM conference, San Antonio, Texas.
[3]   Nunez, Arturo; Kattis Spilios (2020). Webpage and Data Analytics implementation for Asset Monitoring using Acoustic Emission. Acoustic Emission Working Group 62, USA (Virtual).

ACOUSTIC EMISSION APPLIED TO MODE I FATIGUE DAMAGE MONITORING OF ADHESIVELY BONDED JOINTS

Rosemere de Araujo Alves Lima[1], Andrea Bernasconi[1] and Michele Carboni[1,*]

[1]Dept. Mechanical Engineering, Politecnico di Milano – Via la Masa 1, 20156 Milano, Italy;
rosemere.dearaujo@polimi.it, andrea.bernasconi@polimi.it
*Correspondence: michele.carboni@polimi.it

ABSTRACT

The use of adhesively bonded joints has increased considerably due to their lightweight, relevant strength-weight ratio and possibility to join multi-materials. Nevertheless, there are still some challenges in the application of this kind of joints in primary structures, such as guaranteeing their reliability during the components' useful life.

Structural health monitoring methods are suggested to ensure in-service safety and reliability of adhesive joints. The acoustic emission appears promising because it can detect the elastic waves produced within the material when it is under damage or straining.

This research focuses on mode I fatigue damage monitoring metallic double cantilever beam adhesively bonded joints using the acoustic emission method. Digital image correlation and visual evaluation were applied during fatigue interruptions to track the crack-tip position within the adhesive and correlate them with the acoustic emission outcomes.

The acoustic emission method is susceptible and different kinds of waves (background, friction and damage) can be easily assessed during the tests, producing an immense amount of data. So, unsupervised artificial neural networks for patterning recognition were proposed. Self-organising maps and k-means algorithms were used for data clustering and then classified regarding their sources. Finally, the acoustic emission results, digital image correlation and visual evaluations were compared.

Keywords: Acoustic emission, adhesive joints, mode I fatigue, pattern recognition, clustering.

1. Introduction

The use of adhesively bonded joints has increased in recent years due to the global interest in producing lighter structures with the implementation of advanced multi-materials and the necessity of high-performance joining solutions for different types of interfaces. The adhesively bonded joints present the main advantage of producing low impact in the adherends mechanical properties, reducing stress concentration compared to traditional fasteners [1].

Nonetheless, the single use of adhesively bonded joints is still challenging for the application in primary structures since it is difficult to ensure joint reliability during a components in-service life, under fatigue and critical environmental conditions. To overcome these drawbacks and ensure the joint's integrity and safety, some solutions can be implemented, such as the enhancement of the adhesives' mechanical properties, development of optimized finite elements analysis to better

predict the joint's mechanical behaviour in critical loading-bearing conditions, and the use of Non-Destructive Testing (NDT) [2] Structural Health Monitoring (SHM) methods [3].

Since SHM methods can assess the joints' integrity under in-service life, giving the possibility of their on-demand or real-time diagnosis and prognostic, implementing a condition-based maintenance system that saves time and maintenance costs of the structures, the interest of the scientific community in their application is increasing.

Among the different SHM methods, Acoustic Emission (AE) is a promising alternative due to its possibility of assessing the elastic waves produced within the monitored material when their strain energy is released during the deformation or damage initiation and propagation (even in small increments) [4]. The assessed elastic waves are then recorded and have their time-domain features (i.e., amplitude, duration, counts, energy and rise time) and waveform saved by the acquisition system as detailed in the flowchart of Figure 1.
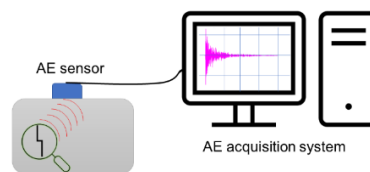
Figure 1: Flowchart of the acoustic emission system.

The AE method is susceptible also to background noise and elastic waves produced by friction within the material, recording a massive amount of data that requires a well-designed post-processing methodology for clustering and classifying the data related to damage sources from the ones related to noise. Time-domain or frequency-domain features filtering and, most recently, big-data algorithms such as supervised and unsupervised Artificial Neural Networks (ANN) are applied to clustering and AE sources classification.

The use of unsupervised ANN was applied in previous work to monitor the crack propagation within the bondline of metallic Double Cantilever Beam (DCB) specimens under quasi-static mode I crack propagation by using complementary algorithms (k-means and Self-Organised Maps) for the waveform's classification of the data related to the damage propagation from the background noise. In the same work, the AE results were compared with visual evaluation and Digital Image Correlation (DIC), where it was possible to localise the crack-tip position and the waveforms associated with the beginning of the onset of plasticisation ahead of the crack-tip (corresponding with the DIC outcomes). These interesting results can open new alternatives for using the AE method for monitoring adhesively bonded joints and help better understand the relationship between the AE signals and the damage mechanisms within the joints, possibly also under fatigue.

Only a few studies in the literature are dedicated to using the AE method for fatigue crack monitoring of adhesively bonded joints, particularly the relationship between the AE features and the damages mechanisms within the bondline [5]. J. A. Pascoe *et al*. 2018 [6], studied the use of acoustic emission to understand the fatigue crack growth within a single load cycle in adhesively bonded DCB joints. They focused on answering when damage occurs within single cycle fatigue tests, based on peak amplitude analyses of each signal. They could address the feasibility of this SHM method to monitor fatigue crack growth and its relationship with AE signals. However, still challenging to establish a well-defined link between the physical mechanisms correlated to the crack growth and the AE features and consequently do better filtering of the AE signals.

So, this work aims to study a clustering methodology based on unsupervised ANN using Self-Organised Maps (SOM) and k-means algorithms for classifying the AE signals assessed during mode I fatigue crack growth tests of metallic adhesively bonded DCB specimens. Principal Component Analysis (PCA) was also implemented to individuate the most significant time-domain, or frequency-domain AE features to be used during the clustering process. DIC and visual evaluation analysis were then performed to track the crack growth during the tests and compare them with the AE features.

2. Methodology

2.1 Materials and sample fabrication

DCB specimens were produced following the ASTM D3433, and dimensions are detailed in Figure 2 (a). The adherends were produced with a high-strength steel DIN 40CrMoMn7, and the 3M Scotch-Weld^{TM} 9323 B/A structural adhesive was used to join them, whose mechanical properties can be found in [7].

Before bonding, the adherends were sandblasted and cleaned with acetone to remove impurities and waxes. After that, a Teflon tape was applied at the beginning of the specimens to ensure a non-bonded region. Moreover, a razorblade was introduced to guarantee a sharp notch at the beginning of the specimens. Then, the adhesive was manually mixed and applied to the cleaned surface of the adherends from the razor blade until the free edge of the sample. A minimum adhesive thickness of 0.3 mm was ensured by adding a 2% weight of glass microspheres (250 – 300 μm of diameter) within the adhesive layer.

The specimens were cured in an oven for a total of 5.5 hours following three main steps: linear increase of the temperature until 65°C for 1.5h, followed by a hold at 65°C for two hours and, finally, a linear decrease of the temperature for two hours until the room temperature. For the present work, two specimens (S1 and S2) were tested with an initial crack length (a_0) equal to 65 mm.

(a)

(b)
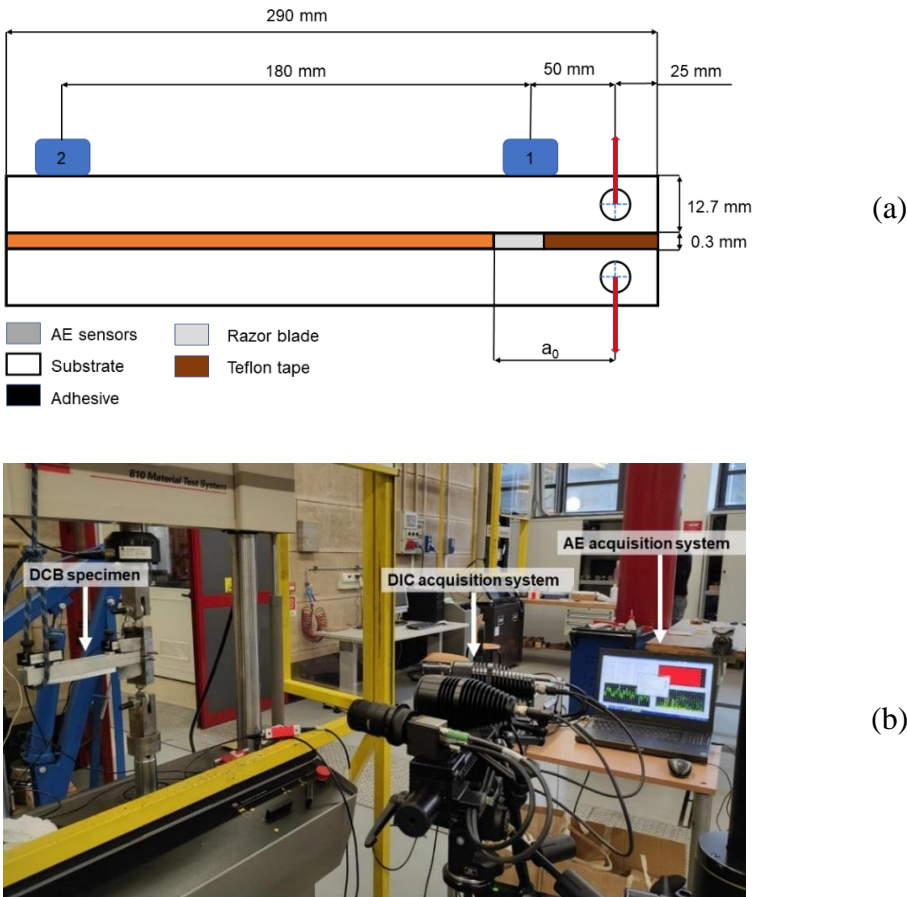
Figure 2: (a) DCB dimensions (drawings out of scale) and (b) testing setup.

For the crack growth measurement during the tests, both lateral surfaces of the specimens were previously whitely painted. The lateral surface used for the DIC analysis was furtherly painted using arbitrary black aerosol paint to create a fine speckle pattern.

2.2 Fatigue crack growth tests

A uni-axial MTS 810 servo-hydraulic testing machine with a load cell of 15 kN was used to perform mode I fatigue cracking growth tests. A constant amplitude load controlled test with a fatigue ratio (R = minimum load/maximum load) of 0.1. A testing frequency of 5 Hz and a maximum load equal to 850N was applied, as shown in Figure 2 (b).

The tests were interrupted every 5000 cycles to perform a monotonic loading ramp up to the maximum load applied during the fatigue cycles with a 0.5 mm/min speed rate. The maximum load was held for 10 seconds to allow crack length measurements by visual evaluation and DIC. After that, the machine unloads until the minimum load of the fatigue tests and the cycles then initiate again. The tests were performed until the specimen's complete failure.

A Dino-Lite digital microscope with a magnification of twenty times was used to take pictures of the white painted surface of the DCB specimens during the interruptions. The DIC analysis was made using the GOM – 3D Aramis adjustable system with an acquisition frequency of 3 Hz. The Aramis system's main characteristics are detailed in [8]. It is worth mentioning that the DIC acquisition system was synchronised with load and displacement input values from the testing machine.

The free post-processing software for image analysis FIJI – Image J (version 2020) and GOM Correlate (version 2020) were used for the visual evaluation and DIC pictures, respectively.

The acoustic emission analyses were performed during the cyclic and monotonic loading ramps using the Vallen ASMY-6 acquisition unit, two piezoelectric sensors units of type VS150-M (operating peak frequency in the range of 100 – 450 kHz) and a 34 dB Vallen AEP5 preamplifier, all connected by low-noise cables. Before the tests, a coupling silicon agent (OKS-110) was applied in the interface between samples and sensors to guarantee continuity during the AE signals transmission from the specimens to the acquisition system. The sensors were fixed on the specimen's surface by magnetic holders at a fixed distance of 180 mm between them, as shown in Figure 1 (a).

A sampling rate for acquiring the AE features and AE transient waveforms of 10MHz and 5MHz were set in the acquisition system, respectively. Moreover, an amplitude threshold (concerning a reference voltage amplitude of 1μV) of 45 dB and a minimum acquisition frequency equal to 25kHz were applied. It is worth mentioning that the amplitude threshold was selected based on a baseline ramp, where AE signals were detected in a condition where no damage started to propagate, assessing mainly signals related to background noise.

The Vallen AE-Suite Software and Vallen Control Panel (R2017.0504.1) were used to acquire and record the assessed AE data.

3. Acoustic emission post-processing analysis

The acoustic emission raw data of specimen S1 at the first 5000 cycles and the ninth bath of cycles (40000 – 45000) are shown in Figures 3 (a) and (b), respectively.

As shown in Figure 3 (a), the AE amplitude values are very spread during the whole group of cycles with a higher density of signals between 45 to 50 dB and an amount of AE signals around 78000 was recorded. Drawing attention to Figure 3 (b), other areas with a high density of AE signals can be observed. A wavy behaviour was observed in the region between 45 – 60 dB, and a signal's high-amplitude group was noticed at around 70 dB during this batch of cycles. Almost the same amount of AE hits was recorded in this group, about 70000.

No further conclusions can be taken from this raw data. At this point, it is hard to accurately understand if still there are AE signals related to background noise, friction or only hits corresponding to damage initiation and propagation. So, it is crucial to implement an efficient post-processing methodology.
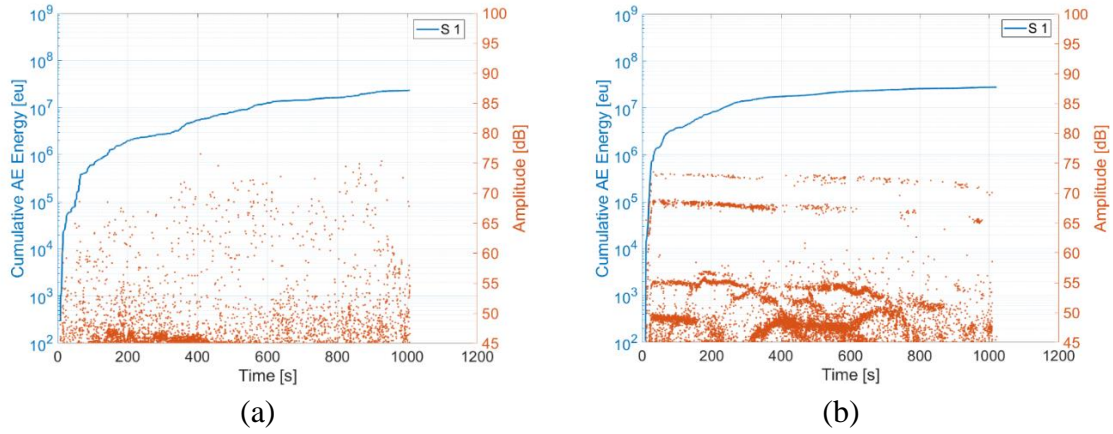
Figure 3: Specimen's S1 raw data at (a) 0 – 5000 cycles and (b) 40000 – 45000 cycles.

3.1 Classification and Clustering procedure

First, a selection of the most relevant AE features that can be used for the clustering procedure was done by applying the Principal Component Analysis (PCA). Time-domain (Amplitude, Duration, Energy, Rise Time and Counts) and Frequency-domain features (Peak frequency and Centroid frequency) of each recorded waveform were used as input for the PCA, whose calculation procedure is summarized in [9].

In general lines, the PCA is a multivariable data reduction method by creating new minimally correlated features called principal components and forming a symmetric covariant matrix. From the most significant principal component analysis and the variability of the related data, it is possible to determine the main features to increase the clustering procedure's efficiency, as seen in Figure 4. The PCA analysis made it possible to select the duration, energy and frequency as the primary input features for the unsupervised ANN clustering procedure based on creating a 2D topological map that classifies the data using neighbourhood functions (SOM algorithm), as described in [10].

Only by using the SOM it is not possible to divide the classified data into groups, so an additional k-means iterative algorithm was applied. The optimal number of clusters was determined by a combined evaluation of the performance of different indexing criteria such as Davies-Bouldin, Silhouette, and Calinski-Harabasz. An optimal number of 5 clusters was given after the analysis, as seen in the last graph of Figure 4.

Figure 5 shows the specimen S1 at the ninth block of cycles (40000 – 45000) after the clustering procedure. As can be observed, the wavy behaviour was well divided into two main clusters (3 and 4) that present different frequency signatures (cluster 3 – around 150 kHz and cluster 4 – about 100 kHz). The AE hits concentrated in the region of high amplitude values (approximately 70 dB) were grouped in a single cluster (number 5 – colour pink) and present frequency values around 100 kHz, and the highest values of cumulative energy highlighting the direct relationship between amplitude and energy values as stated in [6].
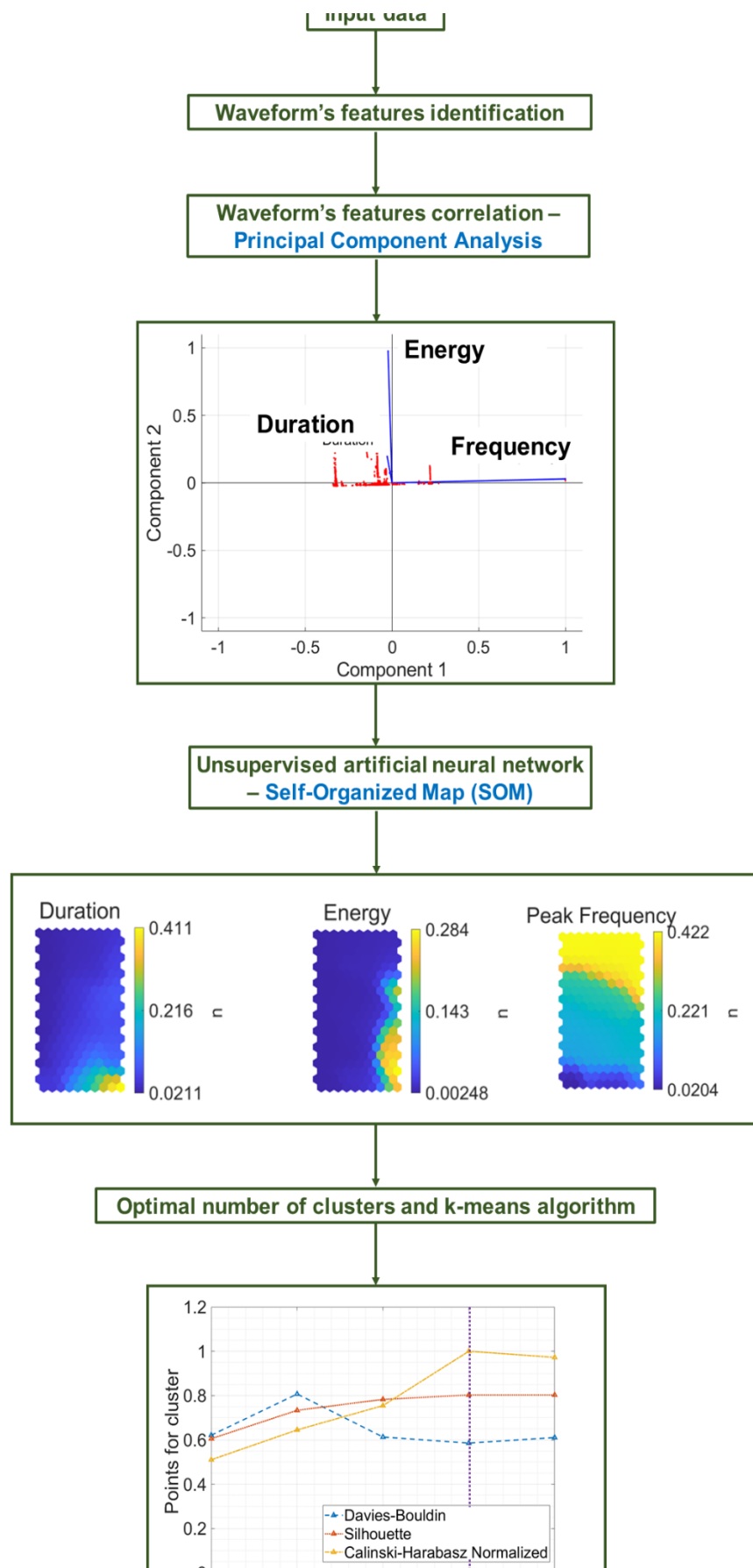
Fig. 4: AE clustering and classification procedure.
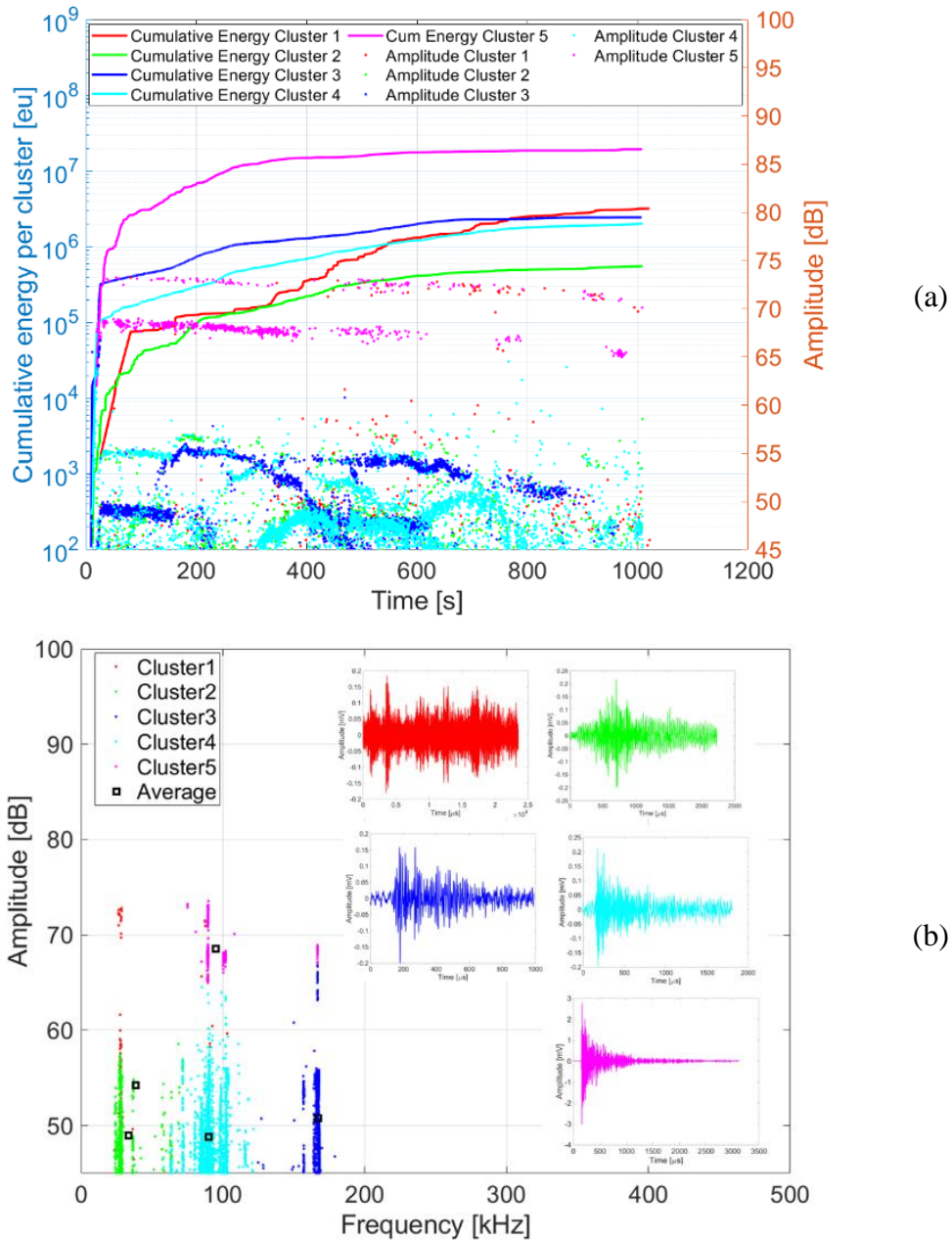
Fig. 5: Specimen S1 at 40000 – 45000 cycles after clustering procedure. (a) Cumulative energy and amplitude values of the clusterised AE data and (b) Frequency signature of each created cluster.

Clusters 1 and 2 instead are very scattered during the whole block of cycles and present the lowest frequency values around 50 kHz. Even if cluster 1 presents high amplitude values, it can be associated with noise or some friction during the tests due to its noisy representative shape shown in Figure 5 (b). So, the main representative clusters that can be used for further analysis are clusters 3, 4 and 5, with frequency signatures in the range from 80 to 150 kHz for the specific studied adhesive. Nonetheless, further research still has to be done to link better the possible damage mechanisms observed during the fatigue crack growth cycles and each classified cluster. It is worth mentioning that similar clustering results were found for specimen S2.

4. DIC, visual evaluation and AE final results

The visual evaluation and DIC crack length measurements obtained during the monotonic ramps for specimens S1, and S2 are shown in Figures 6 (a) and (b). Their results were also compared with the total cumulative energy obtained during the entire fatigue crack growth tests with a total of about 50000 and 100000 cycles for specimens S1 and S2, respectively. Figures 6 (c) and (d) show the total number of hits and the cumulative number of counts for the tests.
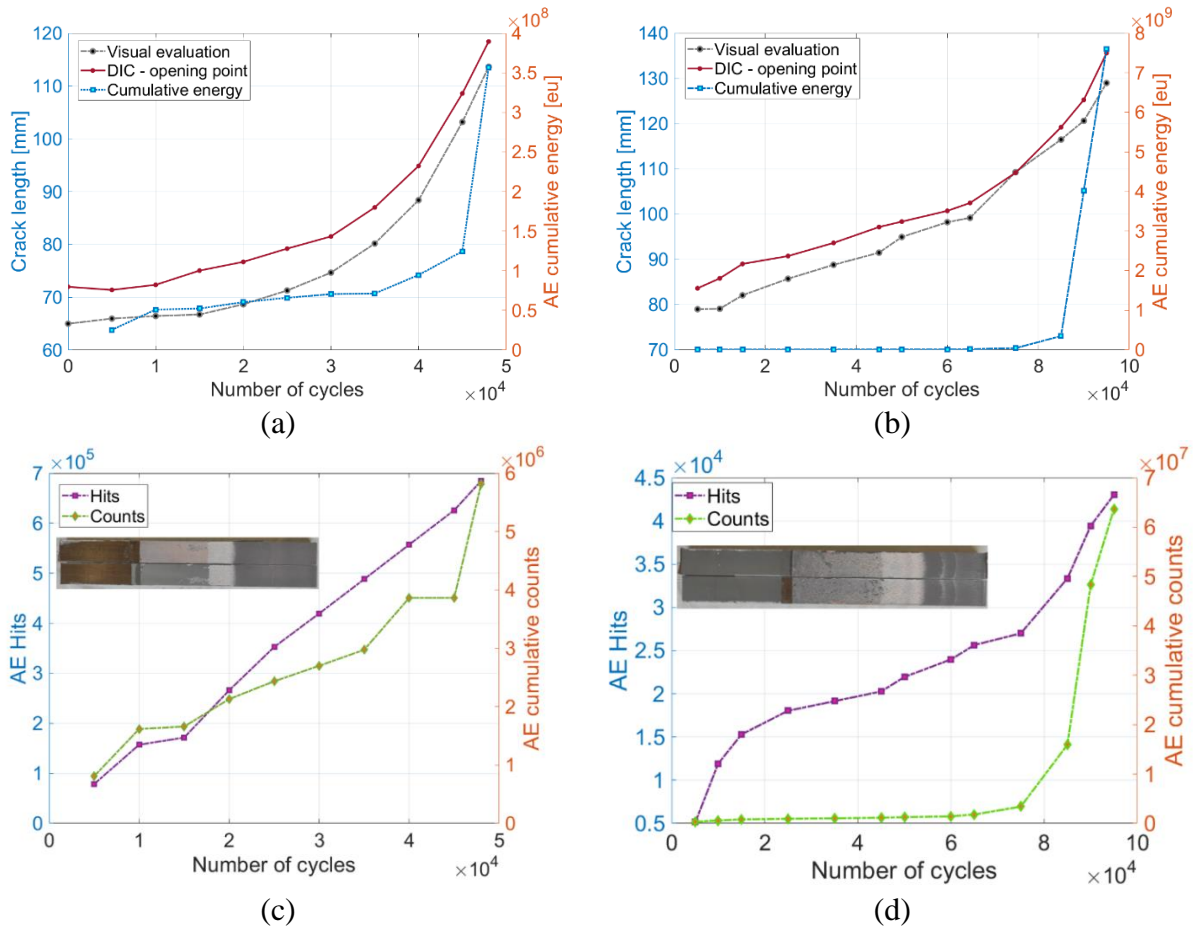
Figure 6: Comparison between DIC, visual evaluation crack length measurements and AE cumulative energy for specimens: (a) S1 and (b) S2, and cumulative hits and counts versus the number of cycles also for specimens: (c) S1 and (d) S2.

First, it is essential to mention that the main difference between the specimen's total number of cycles can be associated with the interfacial failure that occurred in specimen S1 compared to the cohesive failure observed in specimen S2. This can also explain the higher cumulative number of counts obtained for specimen S2, in which waveforms were observed with increased duration and, consequently, the number of counts (number of times that the waveform crosses the threshold) at the last blocks of cycles.

Another difference observed between both specimens is that the cumulative energy of specimen S2 is higher than specimen S1, as observed by S. T. de Freitas et al. 2018 [11]. They observed that the DCB adhesively bonded joints testes under quasi-static mode I that had obtained interfacial failure presented lower cumulative energy than those that underwent a cohesive failure.

As observed in Figures 6 (a) and (b), the crack length measured by the visual evaluation and DIC increase with the number of clusters. The DIC results represents the onset of the plasticisation within the adhesive layer, while the visual evaluation measured the crack-tip position. It was also observed that the cumulative energy of both specimens is almost constant for the whole test and

presents a huge increase next to the last stages of the tests when a high-speed crack propagation was observed. So, the cumulative acoustic emission energy can be useful to identify the fatigue ending the life of the specimens independently of the failure type.

5. Conclusions

This work aimed to study a methodology for acoustic emission clustering and classification of mode I fatigue crack growth within adhesively bonded joints. Moreover, a comparison between the crack growth measured by DIC, visual evaluation and AE features such as the cumulative energy. The main conclusions could be obtained:

- The proposed clustering procedure was able to classify the AE waveforms based on three main features: duration, energy and frequency. Suggesting that some groups can be associated with noise and/or friction. However, further studies should be pursued to understand better the damage mechanisms within the adhesive layer and the AE features;
- High cumulative energy was observed in the specimen that underwent a cohesive failure;
- A massive increase in the AE cumulative energy was observed at the final stages of the fatigue crack growth tests, a promising feature to identify high-speed crack propagation of the joints before its complete failure.

6. References

[1]   M. D. Banea, L. F. M. Da Silva, R. D. S. G. Campilho, and C. Sato, "Smart adhesive joints: An overview of recent developments," *J. Adhes.*, vol. 90, no. 1, pp. 16–40, 2014.

[2]   S. K. Dwivedi, M. Vishwakarma, and P. A. Soni, "Advances and Researches on Non Destructive Testing: A Review," *Mater. Today Proc.*, vol. 5, no. 2, pp. 3690–3698, 2018.

[3]   J. Weiland, M. Luber, R. Seewald, A. Schiebahn, R. Engelbrecht, and U. Reisgen, "Structural health monitoring of adhesively bonded joints: Proposing a new method by use of polymer optical fibers," *Procedia Struct. Integr.*, vol. 28, no. 2019, pp. 1249–1257, 2020.

[4]   G. Galanopoulos, D. Milanoski, A. Broer, D. Zarouchas, and T. Loutas, "Health Monitoring of Aerospace Structures Utilizing Novel Health Indicators Extracted from Complex Strain and Acoustic Emission Data," *Sensors*, vol. 21, no. 17, p. 5701, 2021.

[5]   M. Carboni and A. Bernasconi, *Acoustic Emission Based Monitoring of Fatigue Damage in CFRP-CFRP Adhesive Bonded Joints*, vol. 127. Springer International Publishing, 2021.

[6]   J. A. Pascoe, D. S. Zarouchas, R. C. Alderliesten, and R. Benedictus, "Using acoustic emission to understand fatigue crack growth within a single load cycle," *Eng. Fract. Mech.*, vol. 194, no. March, pp. 281–300, 2018.

[7]   A. Bernasconi, R. A. A. Lima, S. Cardamone, R. B. Campbell, A. H. Slocum, and M. Giglio, "Effect of temperature on cohesive modelling of 3M Scotch-Weld^{TM} 7260 B/A epoxy adhesive," *J. Adhes.*, vol. 96, no. 1–4, pp. 437–460, 2020.

[8]   R. A. A. A. A. Lima, R. Perrone, M. Carboni, and A. Bernasconi, "Experimental analysis of mode I crack propagation in adhesively bonded joints by optical backscatter reflectometry and comparison with digital image correlation," *Theor. Appl. Fract. Mech.*, vol. 116, no. July, p. 103117, Oct. 2021.

[9]   C. Barile, C. Casavola, G. Pappalettera, and P. K. Vimalathithan, "Multiparameter approach for damage propagation analysis in fiber-reinforced polymer composites," *Appl. Sci.*, vol. 11, no. 1, pp. 1–14, 2021.

[10]   R. A. A. Lima, M. Drobiazko, A. Bernasconi, and M. Carboni, "On crack tip localisation in quasi-statically loaded, adhesively bonded double cantilever beam specimens by acoustic emission," *Theor. Appl. Fract. Mech.*, vol. 118, no. February, p. 103286, 2022.

[11]   S. Teixeira de Freitas, D. Zarouchas, and J. A. Poulis, "The use of acoustic emission and composite peel tests to detect weak adhesion in composite structures," *J. Adhes.*, vol. 94, no. 9, pp. 743–766, 2018.

NDE4.0 A NATURAL STEP FOR ACOUSTIC EMISSION

Valery Godinez-Azcuaga[1], Obdulia Ley[1], Arturo Nunez[1], Ed Lowenhar[1] and Spilios Kattis[2]

[1]Mistras Group, Inc., Products & Systems Division, Princeton Junction NJ, USA
[2]Mistras Group Hellas, Athens, Greece
*Correspondence: valery.godinez@mistrasgroup.com; tel.: +1(609) 716-4055

ABSTRACT

This paper discusses an example of practical implementation of Acoustic Emission continuous monitoring in the context of the Fourth Industrial Revolution and the new NDE4.0 paradigm, on renewable electric power wind farms. This project incorporates new sensors, a remote-wireless smart AE instrument, cloud data analytics tailored for data fusion, automatic analysis, alarming, and a data-driven web application for the visualization of asset status in real- or close to real-time. This example clearly illustrates the roll of AE as a natural method for NDE4.0 realization at the beginning of the third decade of the 21st century.

Keywords: Acoustic emission, continuous monitoring, condition-base inspection, data analytics, edge and cloud computing, NDE4.0.

1. Introduction

The first decade of the 21st century saw a dramatic increase in computing power with a tremendous reduction in the size of electronic instrumentation. These two factors made possible the commercial deployment of powerful NDE instrumentation, including AE equipment, capable of producing high-resolution data from assets under inspection. This very granular data allows for better maintenance and repair of these assets. Nevertheless, even with these technological advances, the traditional paradigm of NDE inspections at regular intervals changed very little. However, due to financial pressure to maximize asset up-time, together with an increasing demand to maintain assets operating beyond their original life expectancy, the traditional fixed-schedule inspections philosophy is rapidly shifting to a condition-based inspection new paradigm. This new paradigm requires a continuous stream of data from permanently installed NDE sensors, and correlations with real time operational data, in order to know the asset condition in real time.

Recently, further electronics miniaturization, availability of high-density computer power, modern data analytics, relatively inexpensive data storage, and ubiquitous internet connectivity has created the conditions necessary for condition-based inspection, which are the same conditions necessary for moving NDE into the realm of the *Fourth Industrial Revolution* and what is called *NDE4.0*. Even with these advances, practical implementation of NDE4.0 remains a challenging proposition. However, in this context, Acoustic Emission (AE) as an NDE method is in a unique advantageous position to meet this challenge. By its physical nature AE produces large amounts of relevant data, which has been traditionally processed in real-time or with relative little delay, AE instrumentation has evolved to the point that it has built-in communications modulus for internet access via Wi-Fi

and cellular or LORA networks, which enables data accessibility to the customers via a Data-Driven Web Application (DDWA), and AE data integration with operational and weather data affecting the assets.

2. Industry4.0 and the need for NDE4.0

2.1 The fourth industrial revolution
The current trend of automation and data flow in manufacturing which leverages cyber-physical systems (Intelligent Sensors & Systems, Robotics, Digital Twins), the internet of things (IoT), advanced manufacturing (AM), cloud computing, and advanced data analysis using machine learning and artificial intelligence (ML & AI) is known as the fourth industrial revolution or Industry 4.0 and it is illustrated in Fig. 1. As pointed out by Singh and Vrana [1] the fourth industrial revolution "is a phase over which the suite of cyber-physical technologies is coming together to change the way humans work and live, produce and consume, learn and stay healthy and other things along the way; like NDE". This means that it is necessary that NDE technology evolves to satisfy the demands of Industry4.0.
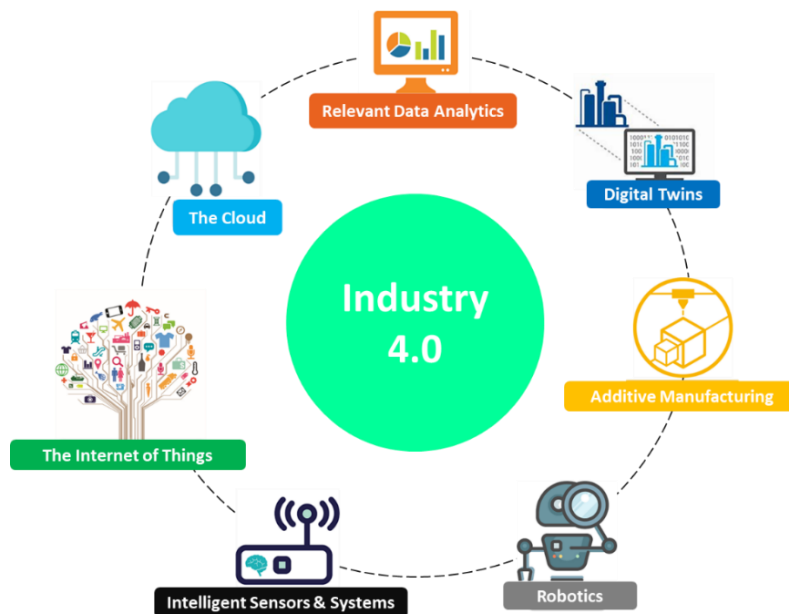
Fig. 1: The fourth industrial revolution or industry 4.0 refers to the marriage of physical assets and advance digital technologies.

2.2 Evolution towards NDE4.0
The evolution towards NDE4.0 is happening in different applications such as X-ray inspection during manufacturing [2], magnetic flux leakage and ultrasonic inspection in O&G assets [3], NDE sensors and augmented reality [4]. All these examples integrate one or more technical capabilities, depending in on its place along the evolution towards NDE4.0. Some of these capabilities include:
- on-board data processing,
- cloud connectivity,
- remote sotware and firmware updates,
- machine learning/artificial intellligence and digital twins,
- integration with virtual reality,
- cybersecurity.

As mentioned in the introduction, NDE applications using AE are in a unique position to move very quickly from the traditional NDE paradigm towards NDE4.0, specially in applications such

as continuous monitoring of civil infrastructure and other traditional power generating assets. More recently, the need for a better alternative to traditional NDE inspections, and to improve the Operation & Management (O&M) of renewable energy assets [5] has open the door for the commercial application of AE technology incorporating several aspects of NDE4.0.

3. NDE4.0 condition monitoring of renewable energy assets

In wind turbine generators (WTG), blade failures are one of the most common factors affecting continuous operation both onshore and offshore. Blade failures could result in not only blade loss, but also in damage to the turbine tower or surrounding turbines, in addition to a safety concern for nearby populations in the case of onshore installations. As mentioned in the previous section, AE-based continuous monitoring of renewable energy assets, specifically wind turbine blades, has emerged as a leading alternative to blade damage detection using drones or rope access personnel. Moreover, condition monitoring is the basis to establish condition-based maintenance programs to improve blade O&M programs. As discussed in section 2.2, this requires implementation of several NDE4.0 capabilities.

3.1 AE-NDE4.0 system

The system developed for wind turbine blades continuous monitoring consists of three Micro Electro-Mechanical System (MEMS) AE sensors, one per blade, a powerful specifically designed AE data acquisition system (AE-DAQs), and a cloud-based Data-Driven Web Application (DDWA).

The MEMS sensors, which integrate signal condition preamplifiers, are mounted inside the blades on the blade bulkhead and are connected to the AE-DAQs installed in the wind turbine hub. The AE-DAQs records, digitizes, pre-processes, and transmits the acoustic signals collected by the MEMS sensors to the cloud via a commercial cellular network. Fig. 2 shows a typical installation of the MEMS and AE-DAQs in a GE 1.6 wind turbine.
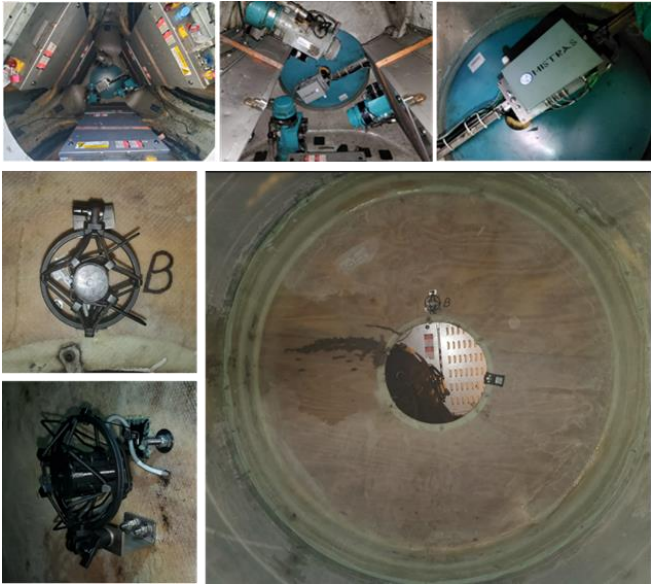
Fig. 2: Example of common data acquisition system (DAQ) and acoustic sensor installation on a GE 1.6 turbine. AE-DAQs is mounted on existing angle bracket (Top). MEMS Sensors are mounted on the wooden bulkhead inside of the blade using a special mounting bracket and affixed with bolts (Bottom). Cables are routed into the hub and connected to the AE-DAQs.

Cybersecurity, an important aspect of NDE4.0, is addressed by Open VPN client included, Encrypted Passwords, Encrypted OS & Programs, a Trusted Platform Module, Secure Remote update, and Remote Reboot.

3.2 Collection and analysis of AE data from wind turbine blades

The acoustic noise produced in the blade cavity is collected in three different ways: continuously recorded background noise, short-duration transient acoustic signals, and long-duration acoustic signals. Examples of each type of data is shown in Fig. 3.
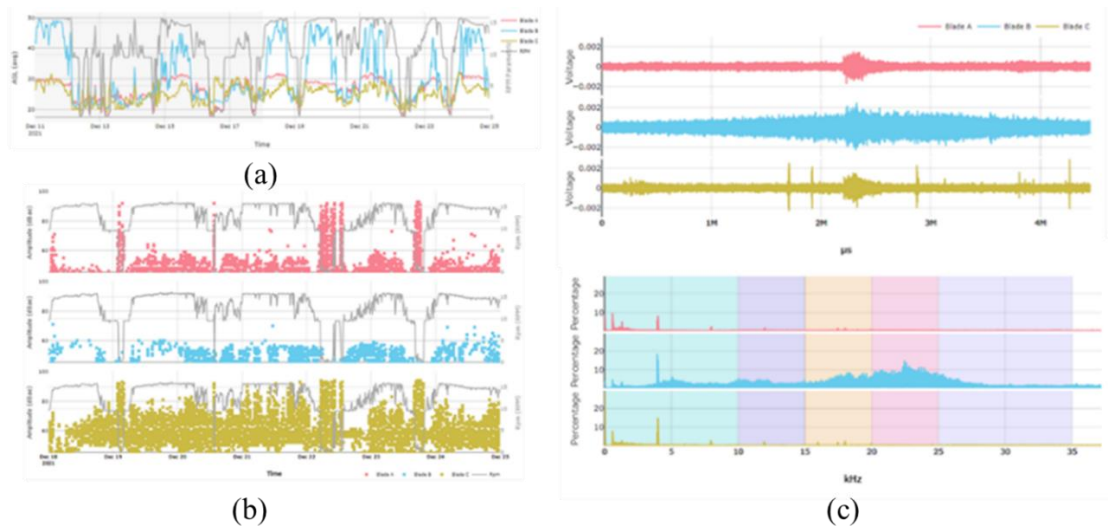
Fig. 3: Acoustic data collected during monitoring of wind turbine blades: (a) continuously recorded background noise, (b) short-duration transient acoustic signals, and (c) long-duration acoustic waveforms.

The background noise is collected every second on each blade and averaged over time. Generally, skin perforation damages are linked to very high background noise levels and specific frequency responses. These characteristics are continuously checked on the dataset and are used to generate alarms when the background noise level of a blade has increased with respect to verified normal values or with respect to the other blades in the turbine.

The short-duration transient acoustic signals are used to track the onset of damage like cracks and impacts that have a transient nature. The data is collected at high sampling rates, saved, and processed by the AE-DAQs to determine whether the activity passes or satisfies certain criteria associated to sources of noise, such as impacts, delaminations and cracking. Several acoustic parameters are collected and recorded for every signal breaking the predetermined threshold or sensitivity. The AE-DAQs can prescreen the AE signals collected and output alarms that are send to the DDWA for communication and further post processing.

Long-duration acoustic waveforms are recorded at pre-established time intervals, from all three blades, during a full rotor revolution. Frequency analysis of these signals is used to identify damage progression, and to find any changes in the background noise of each blade. These signals are used to automatically verify changes in the background noise before and after an alarm is activated. For instance, this logic is used to identify the occurrence of an impact or lighting strike strong enough to rupture the blade skin. Analysis procedures, which involve combination of data types, cross-referencing data trends, and changes among these are important for signature verification and to reduce the possibility of false alarms.

3.3 Post-processing in the data-driven web application

Once the acoustic data is in the cloud, processing is completed at the DDWA, where proprietary Structural Health Quantities (SHQ) for the blades are calculated. The SHQ are used to determine

the need to perform and prioritize inspections and follow-ups. Also, visualization, interpretation, blade acoustic activity ranking, alarm communication, reporting and archiving are performed in the DDWA. Fig. 4 shows the Farm view and single turbine summary dashboard that presents both the "Wind site view" along with the real time alarm (RTA) status and the single turbine summary "Dashboard" indicating both real time alarm and current status, and historical trends of the SHQ used to assess the acoustic response of a blade to current operational loads.

(a) (b)
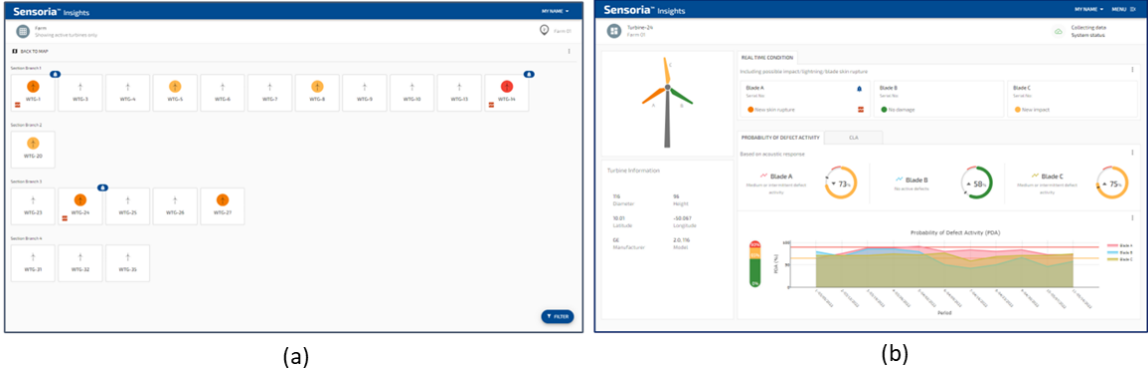
Fig. 4: Selected tabs from the DDWA showing: (a) Site view with active real time alarms and, (b) The single turbine dashboard with RTA and SHQ.

The DDWA runs post processing algorithms on the background that combine and correlate the different data sets collected per blade. It compares the responses of all 3 blades in a turbine among themselves, and with an "expected" response derived from tracking healthy blades under several months of operation. As an example, Fig. 5 shows the changes in background noise and power spectrum of signal from a blade running with a trailing edge crack before and after the blade was repaired.
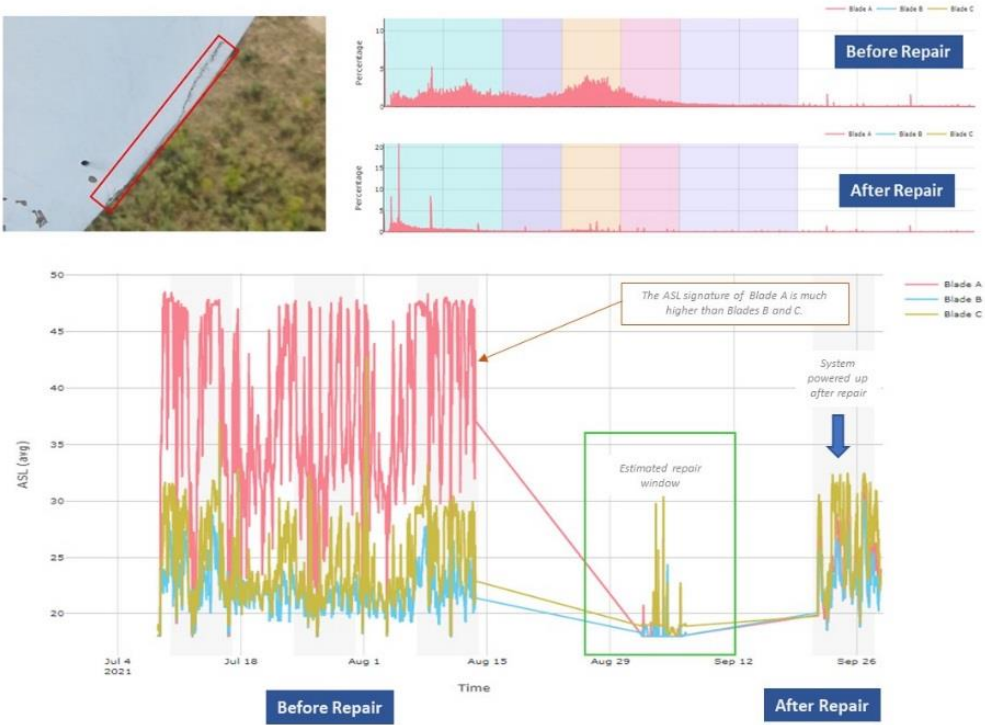
Fig. 5: Acoustic data before and after a trailing edge crack repair. Top left, picture of the damage. Top right, signals before and after repairing the damage. Bottom, background noise of all 3 blades in the turbine before and after the damage repair.

3.4 Real time alarms

One of the objectives of monitoring wind rotor blades is to use the data continuously collected by the system to generate real time alarms (RTA). These RTA identify when the acoustic behavior of a blade deviates from expected variations related to normal wind turbine operation. To date, 3 RTA alarms have been implemented:

- impact no rupture,
- skin rupture,
- impact & skin rupture.

Communication of alarms is done via email to a predefined group of personnel, including a highly trained team of analysts. The first type of alarm can be communicated within 1 hour of occurrence, as is resolved at the AE-DAQs level using the AE short transient signals. Communicating a possible blade skin rupture requires comparison of the current background noise response with the previous data point and the next data point. This past and future comparison is used to verify that the condition or change is sustained over time. This comparison is performed by contrasting the continuously recorded background noise and the frequency response of the long duration acoustic signals collected as a minimum 3 times a day. Finally, an alarm is produced when conditions are met within a small-time window, indicating that an energetic impact was linked to a blade skin rupture.

The DDWA provides a farm or site level view, where the user can graphically see any relevant active alarms or heightened status, and it requires the user to acknowledge the presence of an alarm. Fig. 6 shows turbine tiles in the site view indicating the existence of a previously detected blade skin rupture.

The occurrence of any alarm is saved into the turbine database and the history can be easily accessed by the user. Alarm icons remain active and displayed for a predetermined period of time with more drastic events remaining visible for longer time periods before the status is cleared.
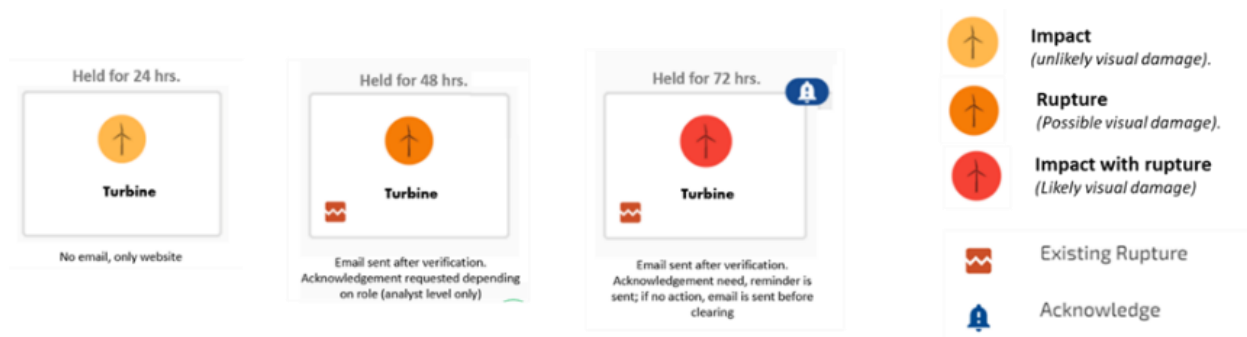
Fig. 6: Real time alarm (RTA) nomenclature and graphical representation as it appears on the DDWA "Farm view" screen.

3.5 Structural health quantities

Structural health or integrity of an asset, machine or structure refers to its ability to sustain the operation for which it was designed. The acoustic signatures of wind turbine blades are used to grade their structural health, prioritize asset inspection, and provide information between inspections to better manage asset operation.

Detection of damage onset and evolution is done by tracking transient and dynamic changes in acoustic signatures from the blades over time. In this way, a blade grading system that allows comparison among turbines and blades in the site or wind farm has been developed.

The grading system can ultimately be used to rank the blades depending on their acoustic signatures. Two important SHQ have been developed for this purpose:

- Crack-Like Activity (CLA). This SHQ is calculated based on a crack filter developed by tracking the acoustic characteristic of a group of blades with cracks confirmed by inspections over a period of several months. The filter is used to identify the level of signatures satisfying known signal behavior present in a dataset when cracks are present on a composite structure and growing.
- Probability of Defect Activity (PDA). The PDA of a blade is a percentage number that represents actively growing damage, and its magnitude is related to the detection of acoustic defect activity. The PDA calculation considers several acoustic features associated with specific defects activity, such as cracks, delaminations, and blade skin ruptures. High PDA values indicate the presence of abnormal spikes in acoustic activity, changes in acoustic trends, or deviations from normal behavior. PDA is calculated and displayed in the DDWA. PDA varies over time in response to turbine operation and weather, because these factors affect the mechanical load on the blade and therefore the acoustic activity collected by the sensors. Tracking PDA for every blade over time and comparing it with other blades in the same turbine or in the blade population on a wind farm allows to rank the blades from worst to best, and to identify which blades the inspection and repair resources should be focused on with higher priority.

Fig. 7 shows the SHQ for a turbine for over a year and in between inspection cycles. This turbine started showing high CLA activity on Blade A since early August 2021. Inspection in October 2021 showed the presence of a new crack, not seen during the previous inspection in September 2020. The CLA plot shows periods of activity and periods of inactivity when the crack is not growing. Such dynamic response is commonly seen acoustically in composite structures and materials. In addition, the PDA plot shows a trend increasing steadily, even in periods where the CLA is low, highlighting the need of follow up inspection.

Fig. 7: PDA (top) and CLA (bottom) of a wind turbine between inspection cycles. Blade A shows high values of CLA, and inspection corroborated the appearance of a chord crack on the blade around 40m from the root.

3.6 *Guiding inspections, maintenance, and improving reliability*

Knowing the moment that new damage on a wind turbine blade occurs, or when an existing damage is showing signs of activity, helps guiding the next steps and better prioritize and manage complex schedules. Knowing if a new damage on a blade occurs, or if the acoustic response of a blade with known critical defects dramatically changes between scheduled inspections, can be used to prioritize repair and inspection. Using SHQ derived from acoustic activity allows to plan and manage resources to improve uptime reliability. Combining, information for real time alarms, PDA and CLA a ranked list of blades that require more urgent inspection and follow up can be generated.

4. Conclusions

A system for remote continuous monitoring of wind turbine blades based on AE, which incorporates several aspects of NDE4.0 has been developed. This system provides early information about the onset and evolution of damage.

Knowing the condition of every blade when compared with the blade population of wind site allows to plan proactively for inspections and repairs, thus reducing repair cost and risk of unexpected blade failure.

As wind energy utilization continues to expand globally, the quantity of blades will increase worldwide, and blades already in operation will continue to age, making real-time condition monitoring a crucial aspect to operational efficiencies and maximization of uptime.

5. References

[1]   Ripi, S., Vrana, J. (2021). The World of NDE4.0 Let the Journey Begin.

[2]   Meynard, P., (2019). NDT 4.0: Robotics and defect recognition for automated quality control. The 11th International Symposium "NDT in Aerospace". November 13-15, Paris-Saclay, France.

[3]   Wassink, C., Greiner, M., Roy, O., Pearson, N., (2020). Deployment of Digital NDE solutions in the Oil and Gas Industry. Materials Evaluation, vol. 78, no.7, p.861-868, American Society for Nondestructive Testing.

[4]   Valeske, B., Osman, A., Römer, F., Tschuncky, R., (2020). Next Generation NDE Sensor Systems as IIoT Elements of Industry 4.0. Research in Nondestructive Evaluation, 31:5-6, 340-369, DOI: 10.1080/09349847.2020.1841862.

[5]   Godinez-Azcuaga, V. (2022). How to use remote blade condition monitoring to transform wind blade integrity management. Conference proceedings. Wind Europe 2022, 5-7 April, Bilbao, Spain.

IoT-AE Remote Unattended Long-term Monitoring System

Bearings wear

4G/5G NB-IoT

Wi-Fi

LoRa zigbee

Pipe/Valve leakage

Bridge Wire breaking

Wind Power Bearing /Blades Monitoring

Qingcheng IoT Cloud Platform or AWS or Customized Server

4G/5G Internet

4G/5G Internet

Bluetooth

PC Desktop

Smart-Phone

Products

SAEU3H AE Testing System

- Sample rate: 10MSPS, 16 bit
- 4, 20,or 48 channel
- Single USB rate: 300MB/s
- Frequency range: 1kHz 2.5MHz

RAEM1-6 Acoustic (AE) Remote Unattended Monitoring System

- 6 RAEM1 integrated
- IoT-AE system with Qingcheng IoT Cloud Platform
- Benchtop instrument: WiFi/cable to PC

RAEM1 Series (IoT-AE System)

- Single channel, triggered by signal or time
- Sensor, preamp and power internal or external
- Communications: 4G, NB-IoT, LoRa, Zigbee, WiFi or wired
- Onsite test: smartphones via Bluetooth
- Wireless time synchronization
- Remote online monitoring: IoT Cloud

Acoustic Emission Sensors

- various types, ultra-high temperature, tiny size, frequency bands, preamplifier integrated, etc.

RAEM2 Series (IoT-AE System)

- Single channel, triggered by time
- Sensor, preamp and power internal or external
- Communications: 4G, NB-IoT, LoRa, Zigbee, WiFi or wired
- Remote online monitoring: IoT Cloud platform
- Onsite test: smartphones via Bluetooth

QingCheng AE Institute

QingCheng AE Institute (QCAE) (previous name: Beijing SoundWel) has been a manufacturer of Acoustic Emission products from sensors to systems since 1998

+86-20-32290092

sales2@ae-ndt.com

www.en.ae-ndt.com

jessicajia

Room 601-9,Building 3, 232 Ke Zhu Road, Huang Pu District, Guang Zhou City, Guang Dong Province, China

IN SITU CONSIDERATION OF RESISTANCE OF BRIDGE GIRDER ACCORDING TO EC2 WITH AEM

Ana Brunčič[1,*], Andrej Štrukelj[2], Maja Kreslin[1], Andrej Anžlin[1] and Aljoša Šajna[1]

[1]Slovenian National Building and Civil Engineering Institute;
ana.bruncic@zag.si, maja.kreslin@zag.si, andrej.anzlin@zag.si, aljosa.sajna@zag.si
[2]University of Maribor, Faculty of Civil Engineering, Transportation Engineering and Architecture;
andrej.strukelj@um.si
*Correspondence: ana.bruncic@zag.si

ABSTRACT

The paper presents a case study of a considerably cracked and degraded bridge in Slovenia: with the implementation of in-situ measurements under bending and shear and the use of a non-destructive acoustic emission technique. Despite the existing crack system, the latter was able to detect microstructural changes. These were characterised by low values of average frequency (AF), as well as lower values of the rise time-amplitude ratio (RA), and energy. A correlation between shear capacity and acoustic activity was observed. This promises to expand the use of AE in the process of assessing of the load-bearing capacity of existing concrete structures.

Keywords: Shear resistance, shear crack, crack width, acoustic emission (AE) parameters, bridge girder, stiffness, elasticity, damage evaluation.

1. Introduction

The acoustic emission (AE) technique is provenly one of the non-destructive techniques (NDT) sensitive to damage initiation and progress in reinforced concrete (RC) structures. It can detect the onset of failure and identify its mode more accurately than any other NDT [1-3]. Shear deformations obtain AE events with longer waveforms and lower frequencies, while volumetric changes of material significant for tensile AE events are recognisable for their shorter duration and higher frequencies [1, 2], [4]. The first type of fracture in the material is known as mode II of cracking and the second one as mode I, since mode I is significant for the first stages of fracture during crack opening and mode II for the progression of fracture causing fretting or sliding [5]. Besides the number of counts and energy released, rise time (RT), defined as the delay between the onset and the highest waveform peak, and the RA value, giving the ratio of RT to maximum amplitude (A), appeared to be the most sensitive to the stress field changes in material [2, 3], [6-8]. Due to its passive nature, AE technique was already noticed as an application giving useful qualitative and quantitative insight into structural response when performing bridge health monitoring even under live load conditions [3, 4]. However, the vast majority of the tests were performed in the laboratory, mostly with cyclic loading and un-loading test protocols [5, 9].

Several effects were observed while tracking damage progression in material under loads, such as Kaiser effect or Felicity effect. The first one, naming phenomena when material emits acoustic waves only after a primary load level is exceeded, has been shown to exist at 70 to 85 % of ultimate strength in concrete material. The latter, describing the absence of the Kaiser effect, is more

significant for composite material [4]. Quantification of obtained AE data is mostly done with statistical analysis, preferably given through Historic and Severity indices [4] or b-value [8].

In the last decades, the structural safety of the existing infrastructure has become an important issue in Europe [10]. The reliability of the bridges is of special concern due to their indispensable role in transport connections, increase of the expected traffic load and degradation of a material due to environmental actions [10, 11]. Slovenian bridges built in the second half of the twentieth century are of particular concern due to their structural system, substandard shear reinforcement, negligible concrete cover and insufficient maintenance. Deterioration of concrete and corrosion of the reinforcement are the main damage mechanisms leading to the decrease of load-bearing capacity. This is hardly determinable by visual inspection despite evident deflections and cracks. Accurate evaluation of load bearing capacity, especially shear resistance, is thus rather difficult without drastic interventions in the structure of the bridge.

To obtain more information on the shear resistance of existing bridges with existing shear cracks case study of *in-situ* test was executed with a controlled loading condition on an approx. 60 years old two-span reinforced concrete (RC) bridge. It was assessed as unsafe for use and scheduled for replacement. The structural response of the bridge was monitored continuously through measurements of crack width, deflection, and collection of AE data. The structural performance of the bridge was analysed with the finite element method (FEM) based on the theory of elasticity and shear resistance evaluated by the criteria given in EN 1992-1-1 [12]. In this case study only edge girder of the bridge deck, with shear crack 0.9 mm wide was analysed.

2. Case study of a girder reinforced concrete bridge

2.1 Bridge structure and material properties

This two-span girder bridge was located in Slovene village, ensuring passage of local road over river. No data exist about the bridge design, construction, or maintenance. The superstructure of the bridge was comprised of two spans, each long 14.0 m, as shown in Fig. 1. Series of five girders assembling the deck of each span, as seen in Fig. 1, was bound together with transversal cross beams as shown in Fig. 3, and deck slab, giving significant rise of stiffness of the girder system. The railing of the bridge was removed before the test. Material properties were rather estimated than determined. Compressive strength f_c of concrete was assessed to be approx. 25 MPa – obtained indirectly through rebound number obtained with Proceq Original Schmidt hammer OS8000 without any core drilled and destructive compression tests performed. Modulus of elasticity of concrete E_c was assessed on several girders with ultrasonic pulse velocity tester Pundit 200. The average value of 23.6 GPa and Poissons number 0.30 were therefore assumed in FEM analysis. Other material properties of concrete were adapted by Eurocode 2 (EC2) [12]. Material properties of steel were attributed to tests performed on other similar bridges with embedded smooth steel reinforcement: yielding strength was assigned to be 250 MPa, strain at maximal stress ε_{su} 10 %, and modulus of elasticity E_s 190 GPa. All material properties are listed in Table 1, with the designation used in EC2. Distribution and size of steel reinforcement were determined using Proceq profoscope and verified with destructive testing: ending girders were assessed to have embedded 8 bars of 28 mm diameter placed in 2 rows as longitudinal reinforcement (Fig. 3) and stirrups of 10 mm diameter placed on average distance of 40 cm as shear reinforcement (Fig. 4). Condition state of the bridge is shown in Fig. 2.

According to estimated material and geometry properties bending capacity M_{ult} of edge girder was determined to be 1100.4 kNm with failure of concrete in compression ($\varepsilon_c/\varepsilon_s$ = 3.5 ‰/10.2 ‰), moment at which yielding of reinforcement occurs M_{rf} 1048 kNm, and cracking moment M_{cr} was calculated to be 148.6 kNm. Shear resistance was determined following Eurocode 2 [12], namely as shear resistance of concrete with included dowel action and aggregate interlock V_c 155.2 kN, shear resistance of concrete with stirrups by generalised stress field approach V_{sw} 97.7 kN with limiting the capacity of diagonal strut V_{max} 1446.2 kN.
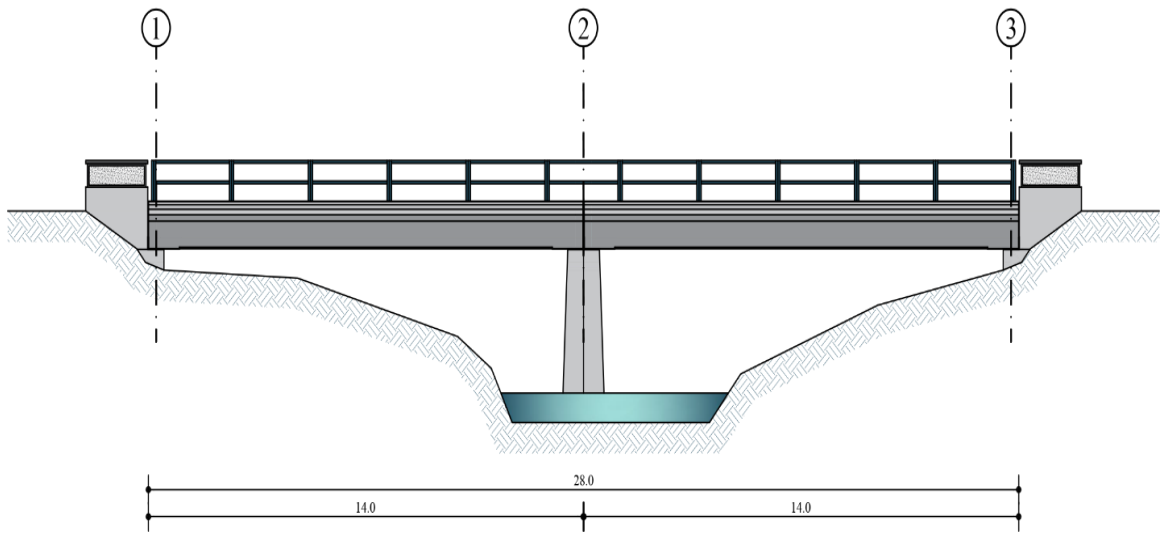
Fig. 1: Side view of a two-span girder bridge.

Fig. 2: Location of bridge (upper left), abutment with bearing of end girder (upper right), deterioration of concrete and steel corrosion (down left), shear cracks 0.9 m wide (down right).
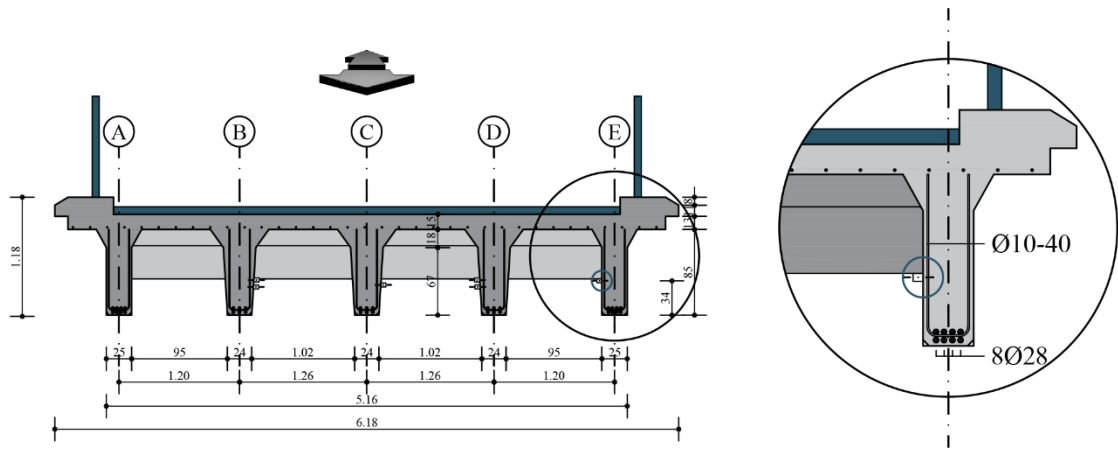
Fig. 3: Cross-section geometry of the two-span girder bridge.
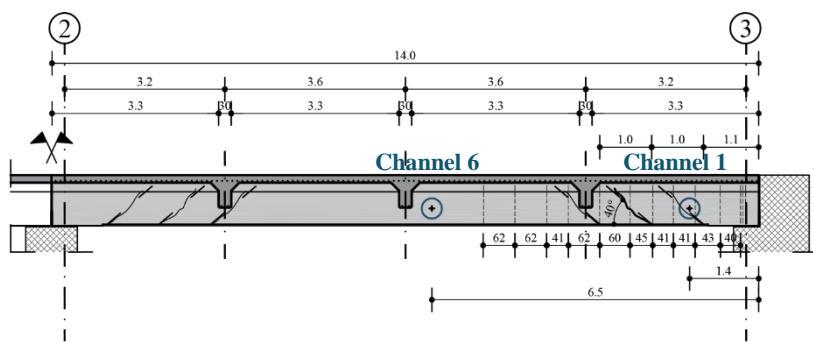
Fig. 4: Tested bridge span with indicated cross beams distributed over the length of girder system, positions of AE sensors (circles with dots), monitored shear crack (at a distance 2.1 m from the right end of girder) and indicated distribution of stirrups.

Table 1: Mechanical properties of concrete and steel.

CONCRETE		STEEL	
f_c (MPa)	25	f_y (MPa)	250
ε_{c3} (‰)	1.75	ε_y (‰)	2.0
ε_{cu3} (‰)	3.5	ε_u (%)	10.0
E_c (GPa)	23.6	E_s (GPa)	190

2.2 Test loading protocol

The loading was carried out with two types of concrete blocks, weighing approx. 2.5 t and 1.1 t. Each concrete block was weighed while being placed on the bridge deck by the crane. Two types of loading were performed successively: 1) a *three-point bending test* with the concentration of the concrete blocks in the mid-region of the span and 2) a combination of *shear and bending test* with the shift of half of the concrete blocks already placed at the midspan to the left of the most pronounced shear crack on egde girder. Both tests were performed successively: one after another without un-loading phase.

The loading history of both performed tests with the cumulative weight of concrete and the weight of each concrete block is shown in Fig. 5.
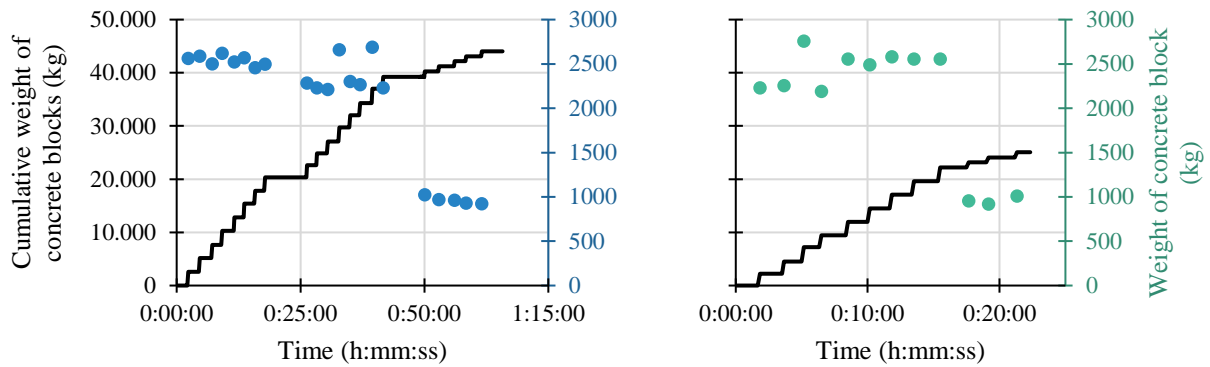
Fig. 5: Loading history of three-point bending test (left) and shear test (right).

2.3 Measured quantities and equipment setup

In order to assess the resistance of the structure and its behaviour, three types of data were acquired: 1) load weight, 2) deformations of structure (deflections and crack width) and 3) AE signals and their properties.

Load weight was measured with the weighting sensor RSCC3/5T-1 of capacity 5 t from Hottinger Baldwin Messtechnik (HBM). Measurements were performed on the crane arm during the lifting and placement of concrete blocks.

Mid-span displacement was measured on the upper side of both curbs and at the bottom of the middle girder with HBM's inductive displacement transducers (IDT) of type WA/100 mm. Crack width was measured on the inner side of the end girder on the downstream side with the self-made sensor. All measurements of deformations were computer controlled and processed with HBM's CATMAN-AP software.

The AE data acquisition was carried out with an outdoor DiSP-workstation unit. Real-time monitoring was enabled by the AEWin software and the acquisition system. Prior to acquiring any actual load test data, pencil lead break (PLB) tests were performed close to all sensors to check their sensitivity. Two sensors were placed on the end girder where crack width and displacement were measured, both approx. at the middle of web. First one was placed 1.4 m from end of the beam in the vicinity of the observed crack (Channel 1), and the second one 6.5 m from the end, near mid-span (Channel 6) as seen from Fig. 4. Threshold level was set to 45 kHz. All measurements and acquisitions were synchronised.

2.4 Structural analysis

To evaluate and compare the resistance of girder under observation, structural analysis with finite element method (FEM) was performed, based on obtained data. The system of longitudinal girders and transversal stringers was modelled with beam elements, with a T-shaped cross-section, and a deck slab with plate elements, as seen from Fig. 6. Maximal element size was 20 cm. Measured displacements indicated partial clamping at the middle and end support which was determined upon iteration during calibration of displacements. With the addition of bending stiffness at support 2 (Fig. 2) was 2×10^4 kNm/rad and 10^3 kNm/rad at support 3 roller supports was changed to partially clamped support. Loads were applied as surface load areas, contributed according to test loading protocol. Software SOFISTIK® was used for analysis.
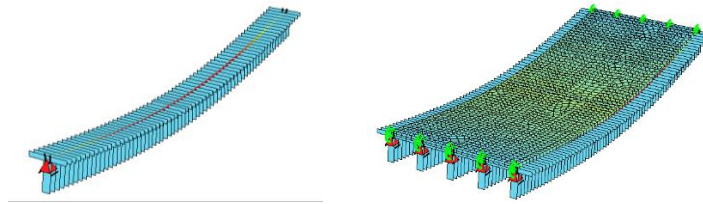
Fig. 6: Model for finite element analysis (girder modelled with beam elements and T cross section – left; deck modelled with plate elements, connected with beam elements in their centre of gravity).

3. Results

Obtained data from displacement measurements indicate linear elastic behaviour of structure during bending tests (Fig. 7) with ratio u_{el}/u 1.0. Soon after the beginning of the shear-bending test, elasticity theory could not be applied anymore since the ratio u_{el}/u dropped to approx. 0.5 with the apparent loss of initial stiffness, still it was used for determination of the load amount.
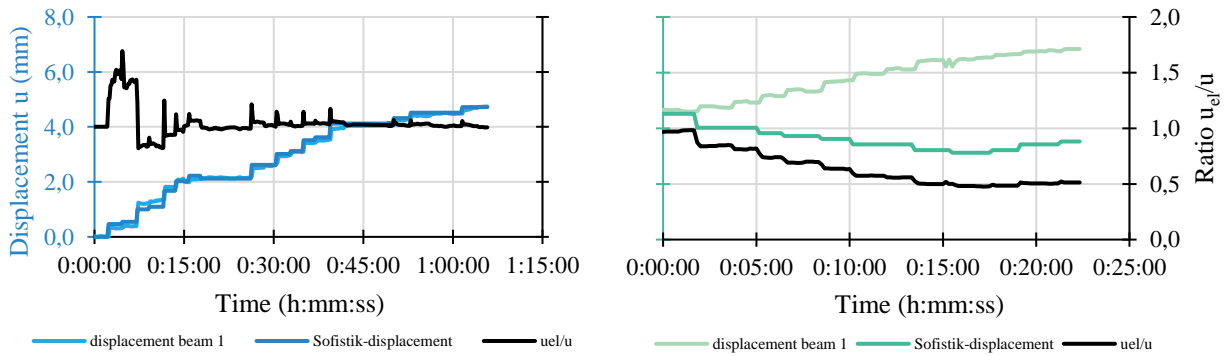
Fig. 7: Comparison of measured and calculated displacements: bending test (left) and shear test (right).

Correlation between crack width and displacement was retained throughout both tests with a notable difference in the behaviour of superstructure (Fig. 10): more pronounced increment of displacement of mid-span in bending test (blue) and crack width in shear test (green).
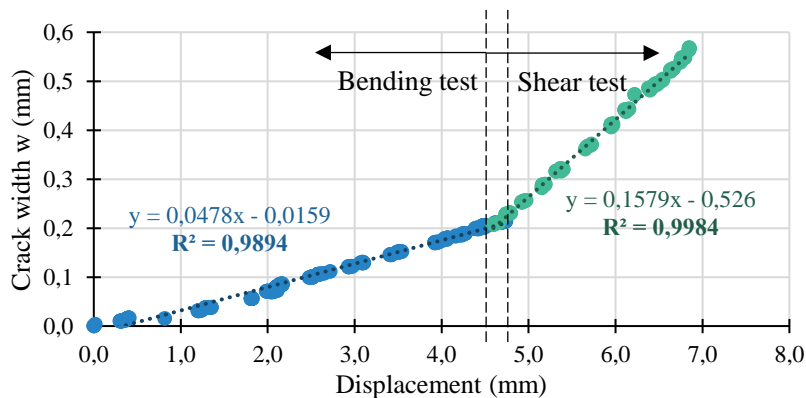
Fig. 8: Correlation between the measured displacement and crack width.

The time-dependent values of some typical AE parameters are depicted in Fig. 9 and 10. The line is the moving average of 20 counts.
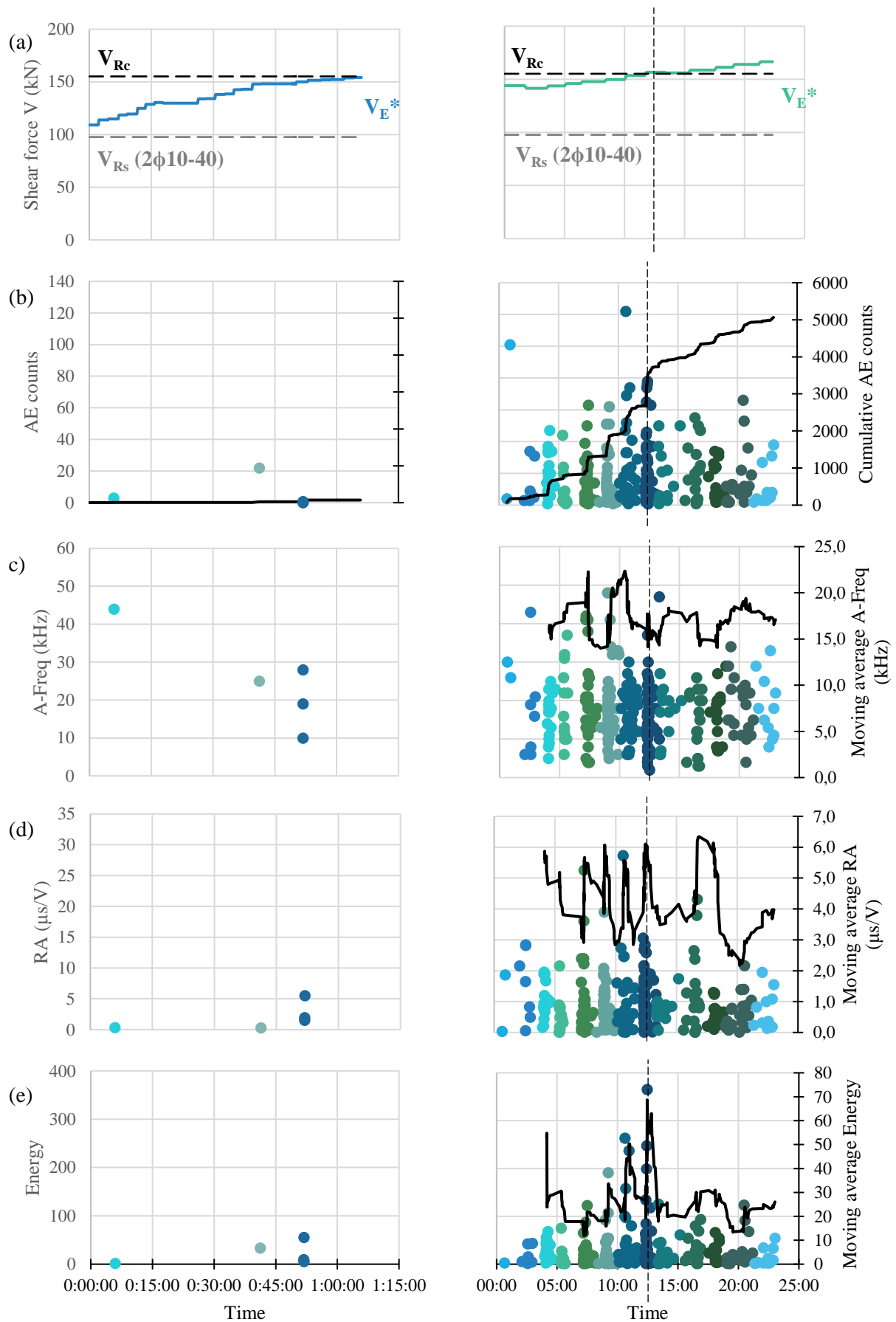
Fig. 9: Time history of (b) accumulated AE activity, (c) Average frequency, (d) RA, and (e) AE energy for the three-point bending test (left) and shear test (right) with shear force diagram (a) for Channel 1.
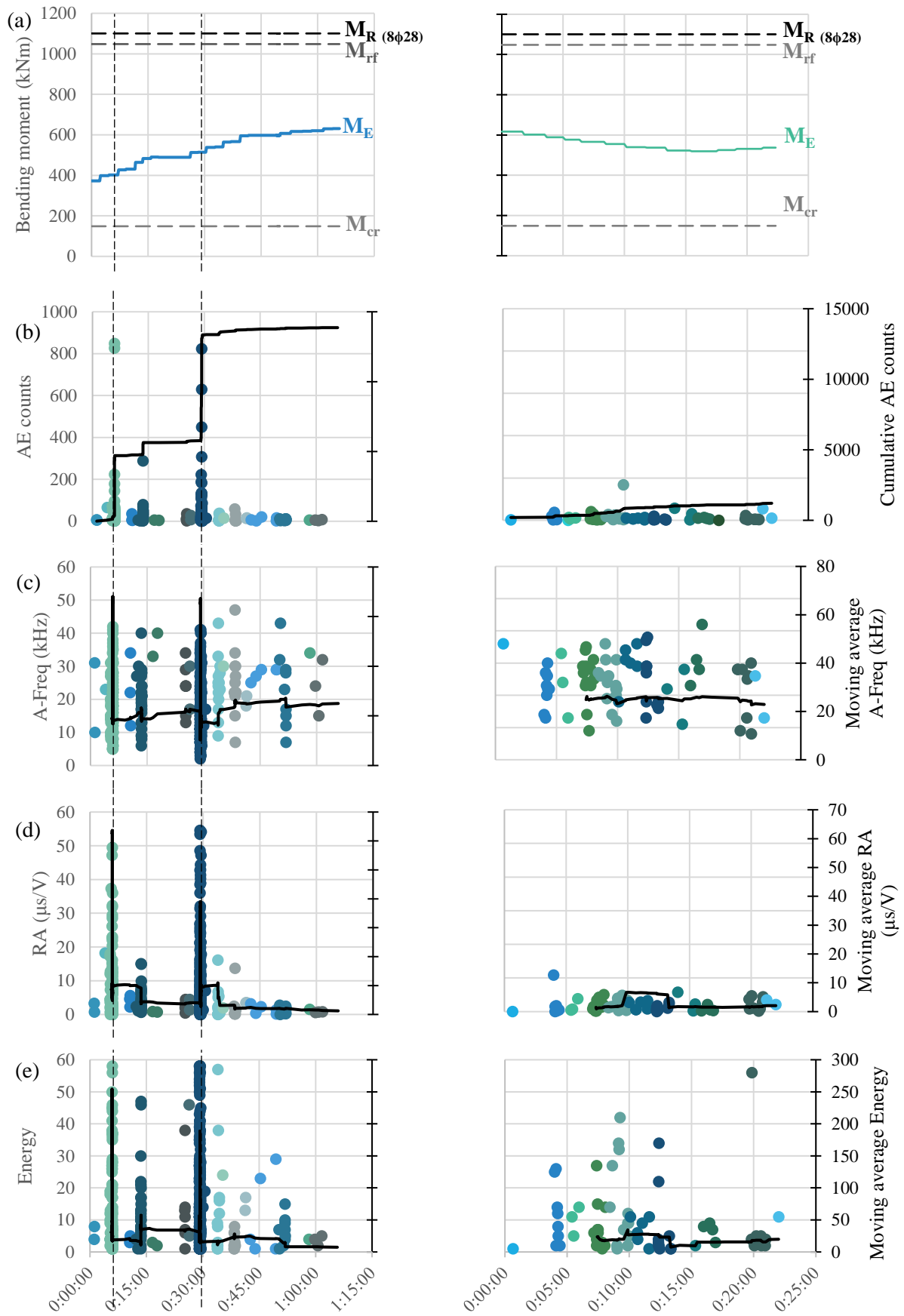
Fig. 10: Time history of (b) accumulated AE activity, (c) Average frequency, (d) RA, and (e) AE energy for the three-point bending test (left) and shear test (right) with shear force diagram (a) for Channel 6.
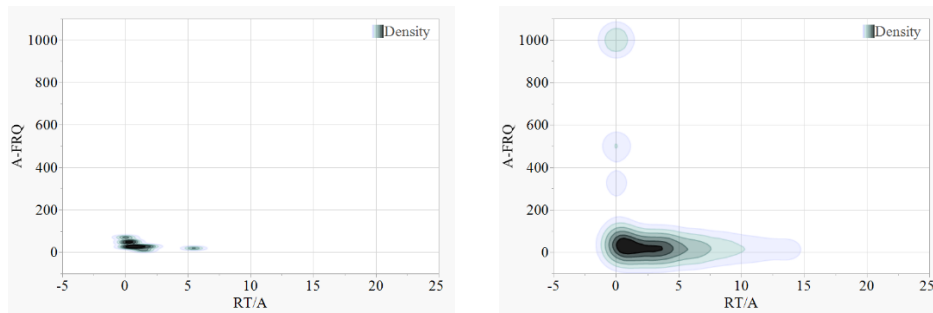
Fig. 11: Density scatter plot of AF/RA values of Channel 1 (left – three point bending test; right – shear test).
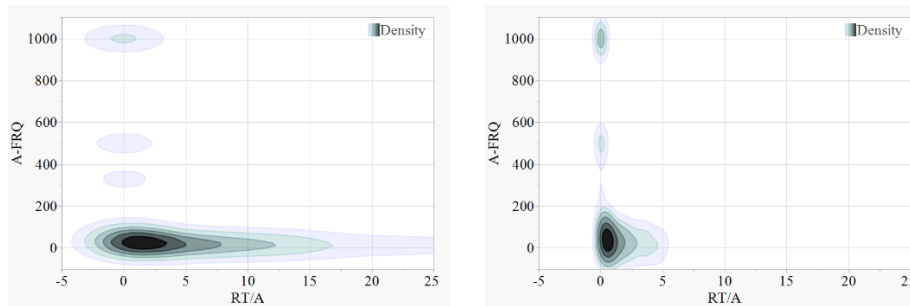
Fig. 12: Density scatter plot of AF/RA values of Channel 6 (left – three point bending test; right – shear test).

Slightly increased AE activity can be noticed in the mid-span of the girder during the bending test (Fig. 9 and 10): two peaks of AF, RA, and energy show weak intensification of micro cracking still, average values remain quite low and cannot be associated with the presence of any live and active cracks. As seen in Fig. 12 type of deformation was mostly intergranular and transgranular. Regarding bending resistance of girder, no major fracture mechanisms were expected, since load applied was not in range of yielding of longitudinal reinforcement or rupture of girder. General AE activity was lower in the shear test (Fig. 9 and 10), the number of recorded hits is almost three times smaller than the number of hits accumulated in the bending test. As in the bending test, average values of AF, RA and energy are low. However, they still demonstrate a connection with the resistance of the structure: in the eighth loading step, there is a noticeable increase in AE events, followed by a more quiescent phase with a noticeable drop of energy, AF, and RA values. As in the case of the bending test and seen from Fig. 11 type of deformation was mostly intergranular and transgranular, leading into obvious loss of stiffness and resistance. The coincidence of concrete shear capacity and acoustic activity is apparent, still, it must be noted that elasticity theory and the shear force determined by it cannot be directly applied in the case of performed shear test. Since, with any of the tests, the ultimate bearing capacity of the structure was not exceeded, the Kaiser and Felicity effects are not negligible in the interpretation of results. Given the clear pattern of the formed cracks, the question is how much energy can still be released when loading a structure with an unknown loading history.

4. Conclusions

AE is already recognised and established as a useful non-destructive technique for the assessment of microstructural changes in structures of the built environment. Yet examples of the use of AE in the characterisation of micro- and macrostructural changes and consequences leading to the specifics of the structural behaviour of existing structures are rare. From obtained and analysed data we can conclude:

- AE is a method that can give meaningful results even when determining the load capacity of existing structures.
- In the case of decaying structures with significant material degradation and an existing crack system, qualitative analysis can be made with AE, which provides an insight into the condition of the material(s) of the structure and the fracture behaviour of the structure.
- AE values acquired are markedly reduced in case of preexisting cracks, especially values of AF, RA, and energy. However, there are qualitative differences between the data, which enable the identification of additional fractures in the material structure.

The performed data analysis shows the potential of AE. Due to the corrosion of the reinforcement and the questionable adhesion with concrete, more comparative studies of this kind on real objects are needed.

5. Acknowledgments

6. References

[1]   D. G. Aggelis, "Classification of cracking mode in concrete by acoustic emission parameters," *Mech. Res. Commun.*, vol. 38, no. 3, pp. 153–157, 2011, doi: 10.1016/j.mechrescom.2011.03.007.

[2]   A. C. Mpalaskas, T. E. Matikas, D. G. Aggelis, and N. Alver, "Acoustic emission for evaluating the reinforcement effectiveness in steel fiber reinforced concrete," *Appl. Sci.*, vol. 11, no. 9, 2021, doi: 10.3390/app11093850.

[3]   S. Kashif Ur Rehman, Z. Ibrahim, S. A. Memon, and M. Jameel, "Nondestructive test methods for concrete bridges: A review," *Constr. Build. Mater.*, vol. 107, pp. 58–86, 2016, doi: 10.1016/j.conbuildmat.2015.12.011.

[4]   A. Nair and C. S. Cai, "Acoustic emission monitoring of bridges: Review and case studies," *Eng. Struct.*, vol. 32, no. 6, pp. 1704–1714, 2010, doi: 10.1016/j.engstruct.2010.02.020.

[5]   C. U. Grosse and M. Ohtsu, Eds., *Acoustic Emission Testing*. Springer-Verlag Berlin Heidelberg, 2008.

[6]   K. Du, X. Li, M. Tao, and S. Wang, "Experimental study on acoustic emission (AE) characteristics and crack classification during rock fracture in several basic lab tests," *Int. J. Rock Mech. Min. Sci.*, vol. 133, no. August 2019, p. 104411, 2020, doi: 10.1016/j.ijrmms.2020.104411.

[7]   V. N. Nerella, M. Nather, A. Iqbal, M. Butler, and V. Mechtcherine, "Inline quatification of extrudability of cementitious materials for digital construction," *Cem. Concr. Compos.*, no. 95, pp. 260–270, 2019.

[8]   D. D. Mandal *et al.*, "Acoustic Emission Monitoring of Progressive Damage of Reinforced Concrete T-Beams under Four-Point Bending," *Materials (Basel).*, vol. 15, no. 10, p. 3486, 2022, doi: 10.3390/ma15103486.

[9]   M. Ohtsu, "Acoustic Emission (AE) and Related Evaluation (NDE) Techniques in the Fracture Mechanics of Concrete," no. 2nd Edition, p. 330, 2020.

[10]   Y. Yang, D. A. Hordijk, and A. De Boer, "Acoustic emission study on 50 years old reinforced concrete beams under bending and shear tests," no. December, 2016.

[11]   E. J. Obrien, B. Heitner, G. Causse, and T. Yalamas, "Validation of bridge health monitoring system using temperature as a proxy for damage," no. August 2019, pp. 1–14, 2020, doi: 10.1002/stc.2588.

[12]   *EN 1992-1-1 Eurocode 2: Design of concrete structures - Part 1-1: General rules and rules for buildings*. 2004.

ACOUSTIC EMISSION ACTIVATION PROTOCOLS FOR ALKALI-SILICA REACTION DAMAGE ASSESSMENT IN CONCRETE

Charlotte Van Steen[1,*] and Els Verstrynge[2]

[1]Department of Civil Engineering, KU Leuven, Leuven, Belgium; charlotte.vansteen@kuleuven.be
[2] Department of Civil Engineering, KU Leuven, Leuven, Belgium; els.verstrynge@kuleuven.be
*Correspondence: charlotte.vansteen@kuleuven.be

ABSTRACT

As existing concrete structures age, several degradation phenomena can endanger their structural safety. A severe threat to the integrity of concrete is posed by the alkali-silica reaction, which starts internally by the formation and swelling of a hydrophilic gel and eventually leads to concrete cracking. The acoustic emission technique can be applied to monitor ongoing damage caused by degradation processes. However, due to the working principle of the technique, only active damage can be detected. This paper investigates damage activation protocols to assess already existing damage in a limited timeframe. Small concrete samples that were deteriorated up to a target damage level in an accelerated way are investigated. Several activation protocols such as changing the moisture content, applying temperature fluctuations, and heating the samples with a heat lamp are applied and analyzed. It is found that changing the moisture content is most promising in terms of AE activation, its ability to distinguish damaged and undamaged samples, and allow damage localization.

Keywords: Acoustic emission, reinforced concrete, alkali-silica reaction, damage assessment.

1. Introduction

Durability and serviceability of existing reinforced concrete (RC) structures has become an important concern. Besides reinforcement corrosion, one of the most harmful degradation processes is alkali-silica reaction (ASR). This damage process starts internally by the chemical reaction between reactive siliceous aggregates and a cement paste having a high alkali content. In order for the reaction to occur, the moisture content should be high enough. This leads to the formation of an expansive hydrophilic gel. Due to swelling of this gel, concrete cracking may be initiated which threatens the structural integrity.

In today's practice, deterioration due to ASR is determined by visual inspection of the typical cracking pattern and by petrographic examination performed on cores taken from the structure. Non-destructive techniques can be a valuable addition to assess the condition of RC structures from an early stage in the damage process. In this respect, the use of the acoustic emission (AE) technique has been investigated. Researchers have applied the AE technique in a laboratory environment to continuously monitor the damage progress [1-4]. It was found that the AE technique is able to detect ongoing crack formation due to ASR and that the AE activity is related

to the rate of ASR degradation [1]. AE intensity analysis showed a good correlation with the damage level when compared to petrographic analysis [1]. Farnam et al. [2] performed a signal-based analysis and found that the frequency of the AE events may be used to determine whether an aggregate or the concrete matrix is cracking.

Due to the working principle of the AE technique, only active damage can be detected, meaning that the damage needs to occur when the structure is monitored. In case of existing structures, it can be valuable to detect and locate the already existing damage. Therefore, damage needs to be activated in order to be measurable with the AE technique. A currently applied technique to activate damage in RC structures is proof loading using a static or moving load. An example on an ASR-affected bridge can be found in Yang et al. [5]. Damaged zones could be localized and the additional damage due to proof loading was found to be limited [5].

Proof loading can be applied on bridge decks in a straightforward manner. However, also several other structures such as RC wall panels, walls, columns, and tunnels can show deterioration due to ASR. For these applications, no damage activation method exists yet. Therefore, new damage activation protocols are needed to assess already existing damage and degradation progress in these types of structures.

This paper investigates protocols that activate degradation processes in concrete structures to allow AE-based damage assessment of slow degradation processes. Focus lies on an initial testing campaign on small concrete samples that were deteriorated in an accelerated way to a target ASR damage level. The aim is to develop a successful activation protocol that is able to: increase the AE event rate compared to a baseline level, distinguish undamaged and damaged samples, and locate damaged zones. The applied activation protocols will be evaluated as such.

2. Experimental program

2.1 Materials and specimen preparation

Two samples with dimensions 300x300x75 mm were made of which one was used as a reference sample (further denoted as 'ASR1') and one was deteriorated up to a target damage level (further denoted as 'ASR2'). ASR was accelerated by adapting the concrete composition and by placing the sample in an accelerated ASR setup.

In case of the composition, 50% of the aggregates was replaced by white glass as this is found to be very reactive (Fig. 1 a.) [6]. Ordinary Portland cement without fly ash (CEM I 52.5N) was used as it contains a higher alkali content compared to other cement types. To further increase the alkali content, 50% of the water was replaced by sodium hydroxide solution (1M NaOH). The final concrete composition is shown in Table 1. In each sample, a thermocouple was placed in the middle to measure internal temperature variations during the activation protocols (Fig. 1 b.). The samples did not contain any reinforcement.

Table 1: Concrete composition.

Materials	Aggregates 4/14	White glass 4/14	Cement CEM 52.5N	Sand 0/4	Water	1M NaOH
Amount (kg/m3)	635	635	350	620	82	82

In standardized accelerated tests (e.g. RILEM [7]), samples are stored at high humidity levels and at high temperatures. The higher the temperature, the faster the process [8]. Therefore, the sample that was subjected to accelerated ASR was stored in an oven having a temperature around 60°C while being immersed in water. The setup is shown in Fig. 1 c. The other sample was stored in a temperature-controlled room (±20°C).
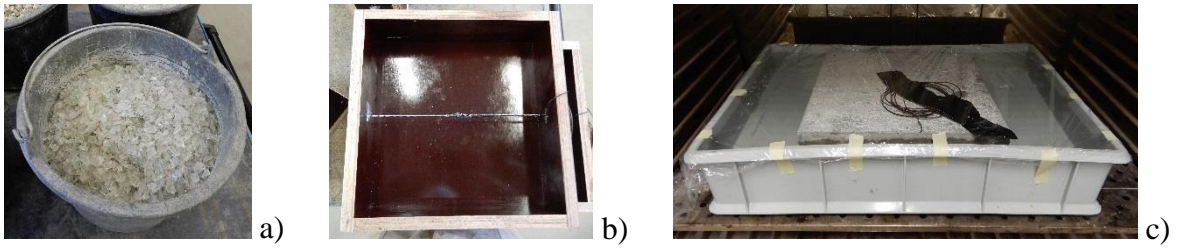
Fig. 1: a) White glass to replace 50% of the aggregates, b) mold with thermocouple in the middle, and c) accelerated ASR setup in oven.

On both samples, two DEMEC points were attached to all sides with a distance of 20 cm between each other to measure the elongation representing the evolution of ASR damage. The elongation was measured every two or three days during the accelerated ASR test for both samples and a visual inspection was carried out to follow-up crack formation. No AE monitoring was performed during the accelerated ASR test.

2.2 Activation protocols

The damaged sample was removed from the accelerated setup when an average linear expansion of 0.1% was reached and small cracks were visible. No expansion was measured for sample ASR1 meaning that ASR has not initiated. Next, the samples were stored for 6 weeks in a temperature-controlled room (20±1°C) in order that the degradation progress decreased to a very low rate. In week 7, the samples were placed in a climate chamber (20±1°C and 60±5% RH) and a baseline AE measurement was performed for 60 hours to have an idea about the AE activity. Hereafter, varying the moisture level and (ambient) temperature were investigated as possible activation protocols. Focus lies on activation protocols that do not include loading. The following conditions were varied during a first test series and shown in Fig. 2:

    (1) moisture level: spraying the samples with tap water every 15 minutes (6 times)
    (2) moisture level: wet-dry cycles by partly submerging in tap water (each condition had a duration of one hour, 2 cycles were performed)
    (3) ambient temperature (while being submerged in water): from 20 to 10°C in 7 hours
    (4) ambient temperature (while being submerged in water): from 10 to 30°C in 7 hours
    (5) ambient temperature (while being submerged in water): from 30 to 20°C in 7 hours
    (6) temperature: heat lamp (2x220W) in front of the samples (at a distance of 35 cm) for 1.5h
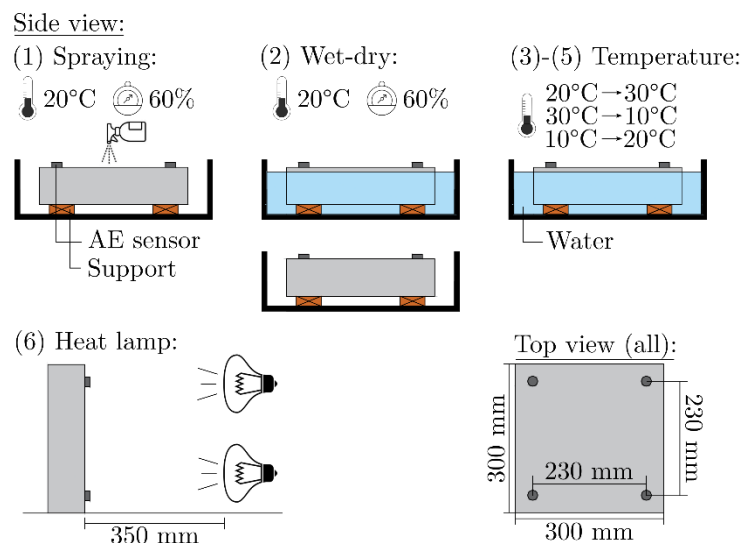
Fig. 2: Overview of the setups for the activation protocols.

In between each test protocol, the humidity level and temperature were kept constant at 20±1°C and 60±5% RH for a minimum of 15 hours. After the first test series, the protocols that seemed most promising were selected and repeated in a second test series to verify the results.

2.3 *Acoustic emission sensing*

A Vallen ASMY-6 acquisition system with eight channels was used during each activation protocol. Resonance sensors with a resonance frequency of 150 kHz (range 100-450 kHz) were attached on the specimen surface with vacuum grease. Four sensors were attached in a 2D setup on each sample. Fig. 2 shows the AE setup for each activation protocol. The amplitude threshold, pre-trigger time, duration discrimination time, and rearm time were set to 40 dB, 400 μs, 500 μs, and 500 μs respectively. The sampling rate was set to 5 MHz. With 8192 samples being stored, the length of the stored signal was 1638.4 μs. During acquisition, the digital frequency filter was set between 50 and 500 kHz.

3. Results and discussion

3.1 *Test series 1*

After 16 days in the accelerated ASR setup, an average linear expansion of 0.1% was measured on sample ASR2. When the sample was removed from the oven, stains and fine cracks (crack width <0.05 mm) in the typical ASR pattern could be observed indicating that ASR has initiated internally (Fig. 3 a). A larger crack was observed at the side with a maximum crack width of 0.1 mm (Fig. 3 b).
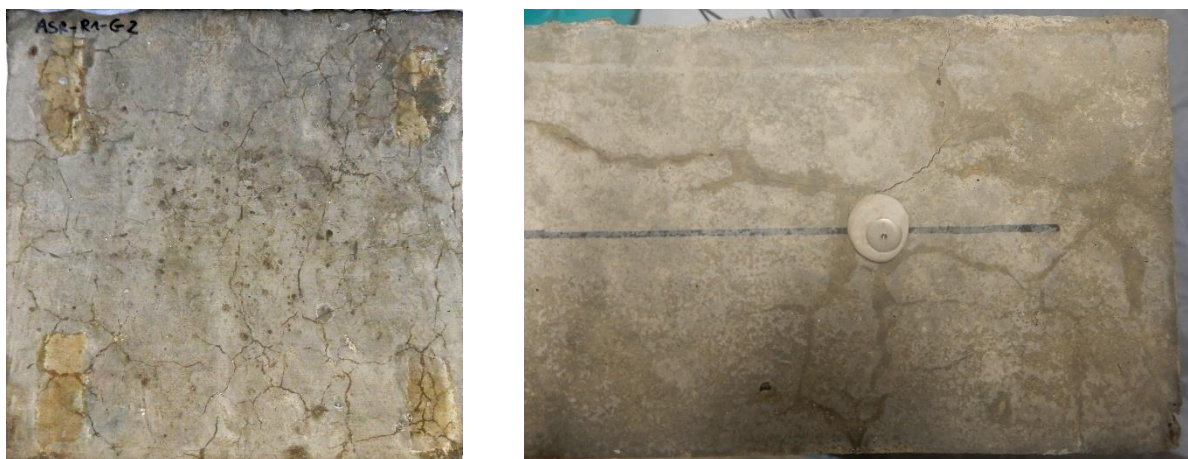
Fig. 3: a) Stains and cracks on the top surface of ASR2, and b) crack at one of the sides.

Fig. 4 gives an overview of the amount of AE events recorded per hour for the different activation protocols. It can be observed that wetting the samples by spraying or wet-dry cycles causes more AE events per hour to be detected compared to the baseline measurement. Also, upon wetting, more events are recorded for the damaged sample ASR2 than for the reference sample ASR1. This may be caused by the water being absorbed by the cracks resulting in an increase of the AE activity. In previous work on corrosion, it was found that daily fluctuations of the ambient temperature have an effect on the corrosion rate and therefore the AE activity [9]. In case of the ASR samples, varying the ambient temperature with a slow rate does not lead to an increase of the AE activity, nor in case of the reference sample, nor in case of the damaged sample. From the thermocouple measurements, it was noticed that the internal temperature change of the samples was around 6°C in case of activation protocols (3) and (5), and 13°C in case of activation protocol (4). For all slow temperature variations, AE activity levels are comparable with the baseline levels.

When a heat lamp is placed in front of the samples, which leads to a more rapid increase of the internal temperature of around 20°C in 1.5h, sample ASR1 recorded a substantial higher amount of AE events compared to its baseline level. Also ASR2 showed an increase in AE activity. In contrast to the activation protocols involving wetting of the samples, more events were recorded for the undamaged sample than for the damaged sample. It can be assumed that stress concentrations and new cracks arise in case of the reference sample due to temperature gradients and that existing cracks accommodate the thermal stresses and may therefore reduce further crack formation, yet friction in the existing cracks may occur and cause AE events. However, no clear differences could be noticed when analyzing the AE activity in the respective samples in terms of amplitude, energy, RA- and AF-values.
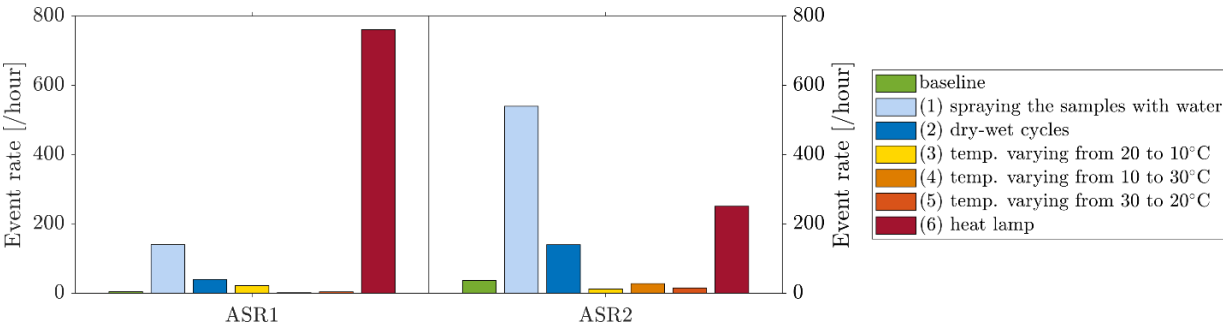
Fig. 4: AE event rate for each activation protocol for samples ASR1 and ASR2 for test series 1.

Fig. 5 shows the localization results of both the reference and damaged sample for the activation protocols during which most AE events were detected: spraying the samples with water (1), subjecting the samples to wet-dry cycles (2), and heating the samples with a heat lamp (6).
In case of wetting of the samples by spraying or wet-dry cycles, more events are localized in case of the damaged sample. Events are mainly localized in the vicinity of cracks. When the sample is suddenly heated, most events were localized in the reference sample. In case of the damaged sample, events are localized close to the largest cracks.

ASR1   ASR2

b)

ASR1   ASR2

c)
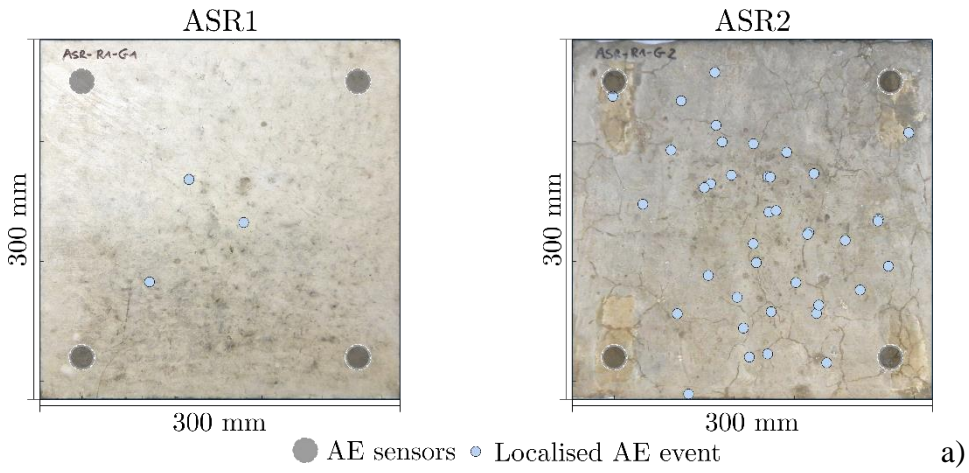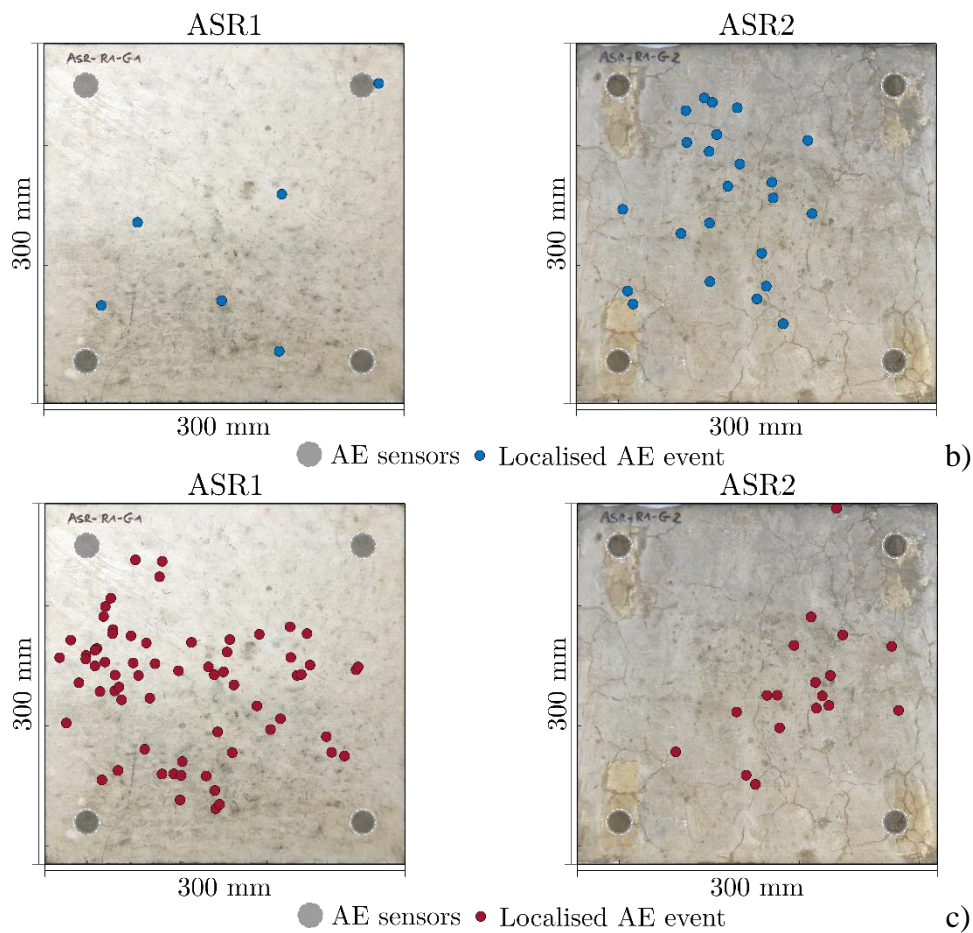
Fig. 5: Localization results of test series 1: a) spraying the samples with water, b) subjecting the samples to wet-dry cycles, and c) heating the samples with a heat lamp; The left figure shows the result of sample ASR1, the right figure shows the results of sample ASR2.

3.2 Test series 2

Three activation protocols were repeated on the same samples to investigate whether the obtained results are reproducible and the conclusions drawn from the AE data are consistent. In this test series, spraying of the samples (1), wet-dry cycles (2), and heating (6) were re-applied. The event rate (events/hour) for each sample and activation protocol is shown in Fig.6.
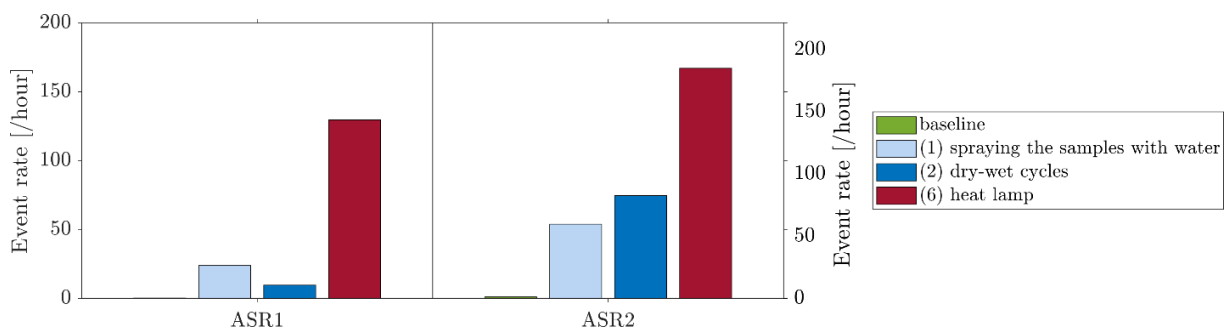
Fig. 6: AE event rate for each activation protocol for samples ASR1 and ASR2 for test series 2.

In case of wetting the samples by spraying or dry-wet cycles, again more AE events were detected for the damaged sample, which is similar to test series 1. In this test series, when heating the samples with heat lamps, more events were detected for the damaged sample, which does not agree with the previous findings. However, it should be noted that this time the samples were only heated until a temperature difference of 12°C was reached (compared to 20°C for test series 1) which took

around 1h. Hence, limited new cracking will have formed in ASR1, while friction in the existing cracks would still have occurred in ASR2.

The localization results are shown in Fig. 7. For each of the activation protocols, less events could be localized in general compared to test series 1. More events were localized for the damaged sample ASR2 compared to ASR1.
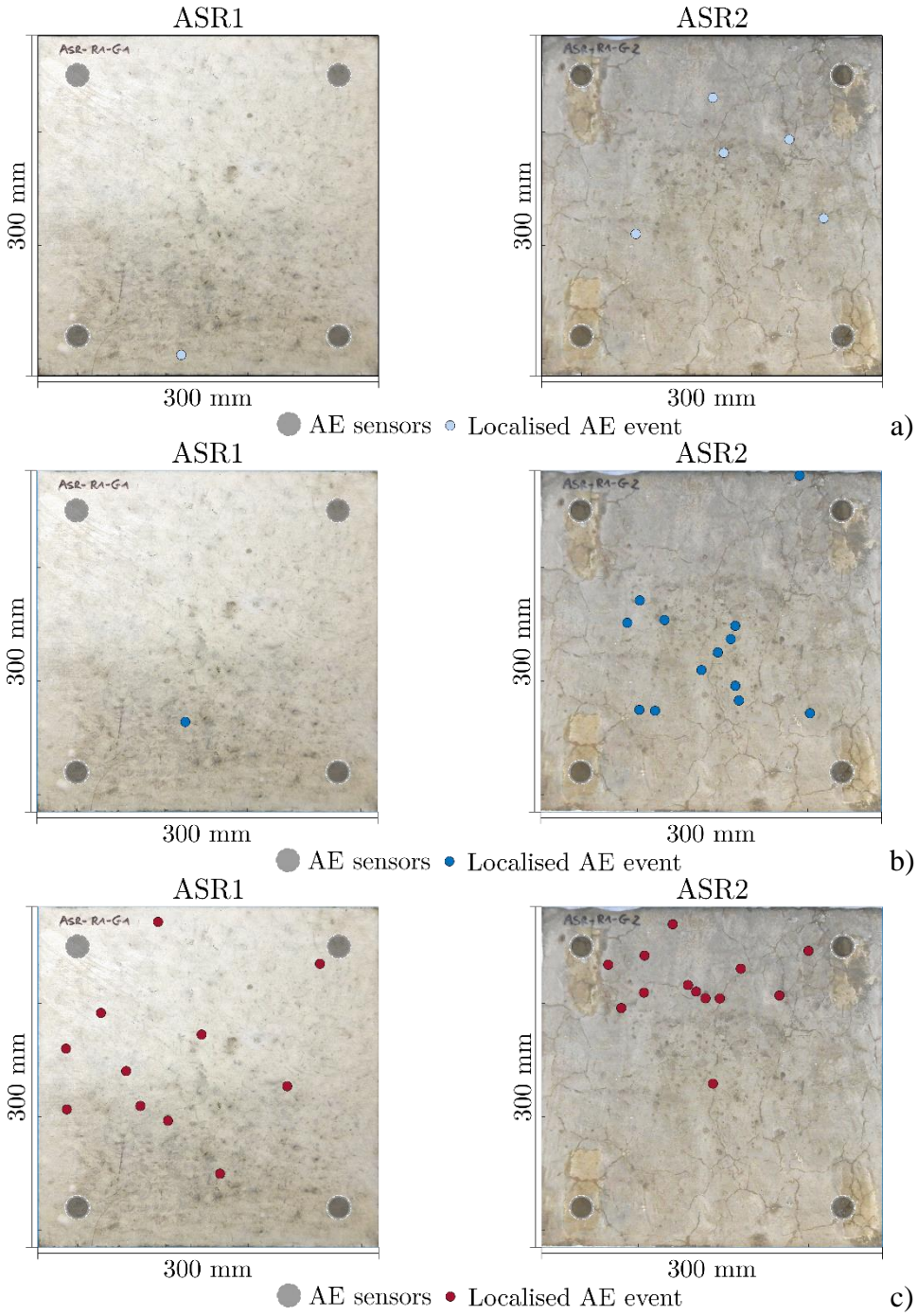
Fig. 7: Localization results of test series 2: a) spraying the samples with water, b) subjecting the samples to wet-dry cycles, and c) heating the samples with heat lamps; The left figure shows the result of sample ASR1, the right figure shows the results of sample ASR2.

3.2 Evaluation activation protocols

Table 2 gives an overview of the tested activation protocols and their potential to be used to assess existing damage due to ASR. In this table, the first row summarizes the tested activation protocols. The second, third, and fourth row indicate three requirements of a successful activation protocol,

respectively i) if the event rate is increased compared to the baseline measurement, ii) if the activation technique is able to distinguish between undamaged and damaged samples, and iii) if the activation protocol allows to localize damaged spots. Whether the statement is valid, partially valid, or not valid is indicated by +, + / - , and - respectively.

Table 2: Evaluation of the activation protocols with (+) indicating that the statement on the left is valid, (+-) indicating that it is partially valid, and (–) indicating that it is not valid.

Activation protocols	(1) Spraying	(2) Wet-dry cycles	(3)-(5) Temperature	(6) Heat lamp
Increase event rate?	+	+	-	+
Distinguish undamaged/damaged?	+	+	-	+-
Locate damaged spots?	+-	+-	-	+-

For all requirements, a positive mark (+) is preferred. For the first row on the increase of event rate, all activation protocols except increasing the ambient temperature lead to an increase of the AE activity. This increase in activity is required as a difference with the AE baseline level is preferred. Otherwise, the activation protocol does not have significant influence and would therefore be inefficient.

The second row concerns the ability to distinguish between damaged and undamaged samples. The eventual aim of applying an activation protocol is to have an insight in the different damage levels of a structure. Therefore, the protocol should be able to distinguish damaged from undamaged zones. Based on the AE activity, samples could be distinguished in case of the activation protocols that intervene with the moisture level of the sample. Increasing the ambient temperature did not allow to distinguish the damage level. In case of the heat lamp, an increase was noticed twice, but the results of the two test series were inconsistent.

The last row reflects on the ability to locate damaged spots. On a full-scale structure, localization of damage hot-spots would give the ability to pinpoint the zones that require more attention. It could allow more dedicated inspection. In test series 1, AE events were localized near the cracks in the damaged sample in case of spraying with water and wet-dry cycles. In test series 2, few AE events could be localized. Therefore, this was indicated as +-. It should be further investigated whether this protocol allows to localize damage correctly. In case of the heat lamp, events were localized around the most damaged zones in ASR2. However, the AE source locations were not consistent between both test series and also many events were localized for the undamaged sample making the protocol less reliable.

From this analysis, changing the moisture content seems the most promising activation protocol.

4. Conclusions

This paper investigated protocols for activating slow degradation processes in concrete to allow AE-based damage assessment. In an experimental testing campaign, a concrete sample was deteriorated in an accelerated way to a target ASR damage level. A non-damaged reference sample was used for comparison. Two test series were performed. In a first test series, several activation protocols were tested. After this first series, the protocols that seemed most promising were selected and performed again to verify the results in a second test series.

From the first test series, it was found that wetting the samples or heating the samples with a heat lamp gave best results in terms of AE activity and localization. Changing the ambient temperature

had no significant effect. In test series 2, wetting was found to give similar results compared to the first test series. In case of the heat lamps, findings were less in agreement, however, this might have been due to a change in heating time.

The activation protocols were evaluated based on three statements: (1) increase in AE activity, (2) differentiation of damaged and undamaged samples, and (3) localization of damaged zones. Changing the moisture content seems the most promising activation protocol.

Future work will focus on the application of these protocols on larger samples in which damaged and undamaged zones are present in the same sample. The protocols will also be applied on corroded RC samples to activate corrosion-induced damage.

5.   Acknowledgements

6.   References

[1]   Abdelrahman, M., ElBatanouny, M. K., Ziehl, P., Fasl, J., Larosche, C. J., Fraczek, J. (2015). Classification of alkali-silica reaction damage using acoustic emission: A proof-of-concept-study. Construction and Building Materials, 95, 406-413, doi: 10.1016/j.conbuildmat.2015.07.093.

[2]   Farnam, Y., Geiker, M. R., Bentz, D., Weiss, J. (2015). Acoustic emission waveform characterization of crack origin and mode in fractured and ASR damaged concrete. Cement and Concrete Composites, 60, 135-145, doi: 10.1016/j.cemconcomp.2015.04.008.

[3]   Soltangharaei, V., Anay, R., Hayes, N. W., Assi, L., Le Pape, Y., Ma, Z. J., Ziehl, P. (2018). Damage Mechanism Evaluation of Large-Scale Concrete Structures Affected by Alkali-Silica Reaction Using Acoustic Emission. Applied Sciences, 8, 2148, doi:10.3390/app8112148.

[4]   Tayfur, S., Yüksel, C., Alver, N., Akar, O., Andiç-Cakir, Ö. (2021). Evaluation of alkali-silica reaction damage in concrete by using acoustic emission signal features and damage rating index: damage monitoring on concrete prisms. Materials and Structures, 54, 146, doi: 10.1617/s11527-021-01749-z.

[5]   Yang, Y., Hordijk, D., de Boer, A. (2016). Acoustic emission study on 50 years old reinforced concrete beams under bending and shear tests. Conference proceedings, 8th International Conference on Acoustic Emission, 5-9 December 2016, Kyoto, Japan.

[6]   Topçu, I. B., Canbaz, M. (2004). Properties of concrete containing waste glass. Cement and Concrete Research, 34(2), 267-274, doi: 10.1016/j.cemconres.2003.07.003.

[7]   Nixon, P. J., Sims, N. (2016). RILEM Recommendations for the Prevention of Damage by Alkali-Aggregate Reactions in New Concrete Structures. Springer Dordrecht, doi: https://doi.org/10.1007/978-94-017-7252-5.

[8]   Saccani, A., Bonora, V., Monari, P. (2001). Laboratory short-term evaluation of ASR: A contribution. Cement and Concrete Research, 31(5), 739-742, doi: 10.1016/S0008-8846(01)00477-X.

[9]   Lyons, R., Ing, M., Austin, S. (2005). Influence of diurnal and seasonal temperature variations on the detection of corrosion in reinforced concrete by acoustic emission. Corrosion Science, 47, 413-433, doi:10.1016/j.corsci.2004.06.010.

ACOUSTIC EMISSION MONITORING OF THE TEXTILE REINFORCED CEMENT (TRC)-TO-MASONRY SHEAR BOND

Nadège Reboul[1,*], Mohamed Saidi[2] and Aron Gabor[1]

[1]Univ Lyon, Université Claude Bernard Lyon 1, LMC2 (Laboratoire des Matériaux Composites pour la Construction), 82 bd Niels Bohr, 69622 Villeurbanne, France;
nadege.reboul@univ-lyon1.fr, aron.gabor@univ-lyon1.fr
[2]Université Savoie Mont Blanc, LOCIE (Laboratoire Optimisation de la Conception et Ingénierie de l'Environnement), 60 rue du lac Léman, 73370 Le Bourget du Lac, France;
mohamed.saidi@univ-smb.fr
*Correspondence: nadege.reboul@univ-lyon1.fr

ABSTRACT

This study focuses on the potential of Textile Reinforced Cementitious (TRC) composites with alkali-resistant glass textile to reinforce masonry structures. In particular, a better identification of the debonding mechanisms is a crucial point for a more efficient use of these composites. Twelve single-lap shear bond tests are performed to investigate four strengthening configurations - two matrices and two reinforcement ratios. This paper discusses the applicability of acoustic emission to assess the damage state of TRC during adherence testing. The flexibility of the matrix used and the amount of reinforcement of the TRC affect the cumulative amplitude distributions. The accumulation of the partial frequency associated with high frequency (above 400 kHz) is a precursor of a strong contribution of the textile in the load transfer.

Keywords: Textile Reinforced Cement (TRC), TRC-to-masonry bond, Acoustic Emission, Univariate analysis.

1. Introduction

A strong need for reinforcement of existing masonry structures has emerged in recent years. In response, inorganic matrix composites are proving to be interesting and effective solutions to significantly increase the strength and/or ductility of these structures [1]. These composites are listed in literature as Textile Reinforced Mortar or Concrete (TRM or TRC), Fabric-Reinforced Cementitious Matrix (FRCM), Cementitious Matrix Grid (CMG). They consist of one or more layers of textile embedded in an inorganic matrix, and therefore offer good compatibility (chemical, physical and mechanical) with substrate when applied on masonry structural elements. In the context of structural strengthening by external bonding of composites, the tensile properties of the composites play a predominant role in the effectiveness of the strengthening. TRC-composites exhibit a non-linear tensile behavior, usually characterized by the following three phases [2]. The first phase is a linear elastic part until the matrix cracks. Then begins a multiple cracking phase, with the formation of transverse cracks whose number and location depend on the reinforcement ratio and on the fabric-to-matrix bond. At last, a crack-widening phase takes place

during which the openings of the existing cracks increase and the fabrics support the applied loads. TRC-composites usually failed either by textile failure when it reaches its tensile strength, or by slippage of the fabric from the inorganic matrix. When TRC-composites are externally bonded on masonry substrates, they usually failed prematurely due to debonding at the TRC-to-masonry interface, or at the textile-to-matrix interface in the TRC (interlaminar failure). In these cases, the textiles in composites, although relatively expensive, are not used to their full potential. It is thus appropriate to turn to a more detailed understanding of the TRC-to-masonry bond behavior, and the use of acoustic emission (AE) method may be of great interest in this context to provide information on the progressive damage in materials. The aim of this contribution is to characterize the behavior of two TRC-composites bonded to masonry by means of single-lap shear bond tests. AE sensors are installed on specimens for assessing damage mechanisms and their progression. A Distributed Fiber Optic Sensing (DFOS) and Digital Image Correlation are also mobilized to obtain a more detailed characterization of the behavior of the specimens.

2. Experimental study

Stack bonded clay brick prisms (Fig. 1 (a)) were prepared using five solid bricks of size $250 \times 120 \times 55$ mm^3, and a hybrid mortar, in volume proportions of 2 water: 1 cement: 2 lime: 4 sand. The TRC-composites, externally bonded to these masonry prisms, comprised one or two layers of an AR (Alcali Resistant)-glass textile and an inorganic matrix. Two different matrices were used, named M1 and M2. The M1 matrix was ettringitic, made of white cement, slag, gypsum, additives and water. The M2 matrix was composed of a Portland cement, silica sand, additives and water. These matrices have in common a high workability to avoid any damage to the optical fiber during casting. The mechanical properties of both substrate and TRC components are collected in Table 1. The bonded area between TRC and masonry was 250×50 mm^2 (length $\times$ width), and the fabric protrudes from the TRC by a length of 320 mm. Three specimens were tested for each combination, for a total of 12 tests. The four studied configurations are denoted by Mx-yL-z, with x, the type of matrix, y, the number of textile layers, and z, the specimen number. The single-lap shear tests were carried out using a Zwick testing machine, equipped with a 65 kN load cell. A steel system (Fig. 1 (b)) blocked the vertical movements of masonry. The end of the fabric was equipped with aluminum tabs, with a hole in which a pin was inserted and connected the specimen to the traction machine. The tests were performed under displacement control at 0.1 mm/min, until the specimen failed.

(a)   (b)   (c)   (d)
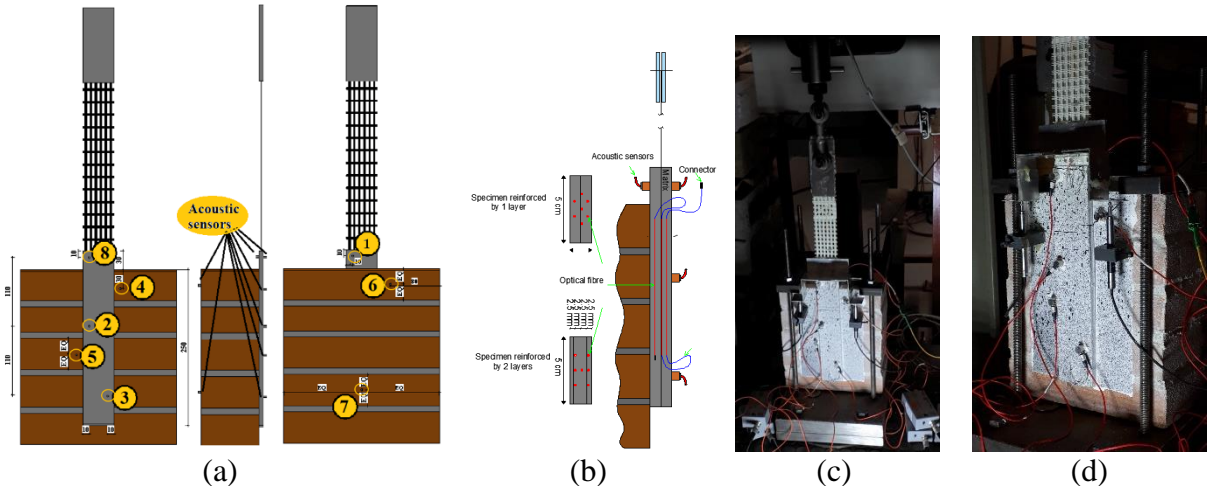
Fig. 1: Specimens geometry with locations of (a). AE sensors, and (b) optical fiber (c). Test setup, and (d) Failure mode for M2-2L-1.

Table 1: Properties of the constituent materials used.

MATERIALS	PROPERTIES
Masonry (characterized in [3], [4])	
Clay bricks	*Splitting strength*: 2.46 (MPa); *Compression strength*: 17.89 (MPa)
Mortar joints	*Flexural strength*: 6.58 (MPa); *Compression strength*: 26.63 (MPa)
Textile Reinforced Cement (TRC) composites (characterized in [5], [6])	
Matrix M1	*Tensile strength:* 3.5 (MPa); *Tensile modulus*: 10700 (MPa)
Matrix M2	*Tensile strength:* 4.5 (MPa); *Tensile modulus*: 14000 (MPa)
AR glass textile	*Cross-sectional area, and perimeter of a yarn*: 2.2 (mm^2), and 7 (mm) *Tensile strength:* 520 (MPa); *Tensile modulus*: 35000 (MPa)

A Mistras Express 8 AE system was used to measure the AE signals during testing. Eight wideband micro 80 sensors were placed on each specimen (see Fig. 1 (a)), preferentially positioned around the bonded area, where damage was expected. They were connected to 2/4/6 pre-amplifiers, with 40 dB gain. The AE timing parameters were chosen as 50 µs for Peak Definition Time, 100 µs for Hit Definition Time, and 200 µs for Hit Lockout Time. The threshold value was set to 40 dB, and the sampling rate was 2 MSPS. Two displacement transducers were bonded on either side of each specimen to measure the displacement.

Among the three identical specimens, for cost reasons, only one of them was equipped with an optical fiber sensor, linked with an ODiSI-6 LUNA device. As shown in Fig. 1 (b), the 2 m long fiber snaked through the TRC, hung in some lengths on the textile fibers, so that it allowed both textile and matrix strain measurements in the TRC-composite. The spatial resolution was 2.6 mm and the recording frequency was set to 1 Hz. The Digital Image Correlation technique was applied to measure the displacement field on the surface of both masonry prism and the TRC-composite.

3. Mechanical results

Different and mixed failure modes were observed in this study, and are listed in Table 2. The diagrams provided in this table allow to understand the coding by letters. Main failure modes were mode A, a cohesive failure at the TRC-to-masonry interface, mode C, a debonding at the textile-to-matrix interface, mode E, a crack propagation in the TRC, and mode F, a textile failure.

Table 2: Failure modes of specimens.
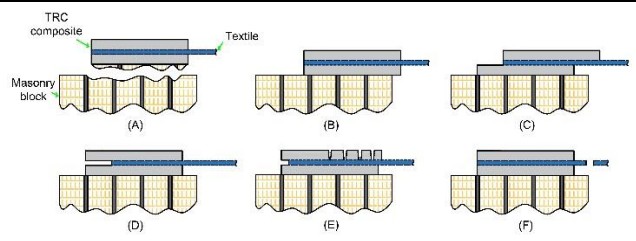
Specimen number	1	2	3	
M1-1L	A+C+E	A+C+E	A+C+E	
M1-2L	A+C+E	A+C+E	A+C+E	
M2-1L	F	A+E+F	E+F	
M2-2L	E+F*	F	A+C+E+F	*see Fig. 1(d)

Fig. 2 presents the response curves of the tested specimens, in terms of applied load in right axis, and textile axial stress in left axis. It can be noted that the softer the matrix is, the greater the deformability is. Moreover, higher reinforcement ratios result in higher failure loads, but do not have a significant influence on maximum textile axial stresses. For all specimens, the exploitation rates of textile (ratio between the maximum textile axial stress and the textile tensile strength) is on average 62%, with a standard deviation of 12%.

(a) 1 AR-glass layer   (b) 2 AR-glass layers
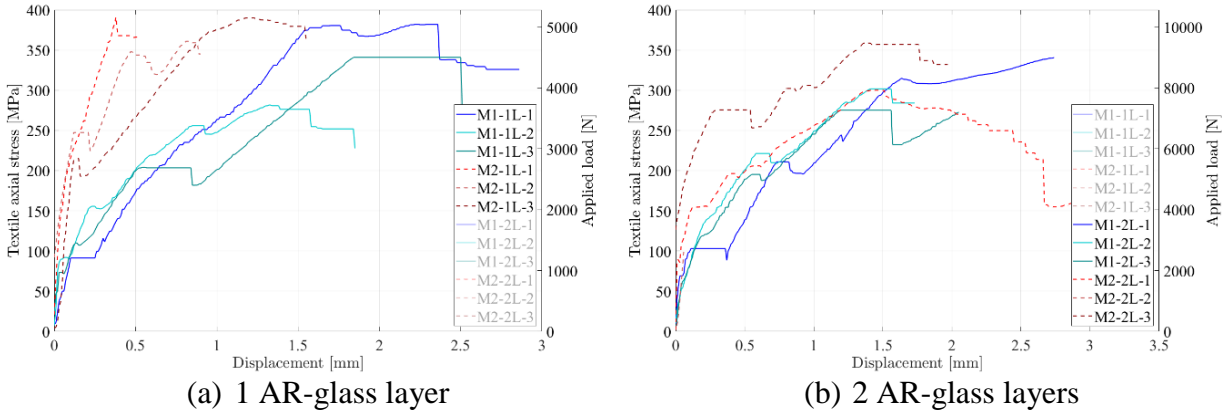
Fig. 2: Response curves of single-lap shear tests in terms of textile axial stress and applied load versus displacement for specimens with (a). one strengthening layer, and (b). two strengthening layers.

4. AE monitoring results

Univariate analysis was carried out by using features extrapolated from the recorded AE waveforms. The results presented here will focus on the evolution of the amplitude of the AE signals, and of the partial power, here named PP3, that measures the signals frequency contribution within 400-1000 kHz. Previous studies [7, 8] have shown that fiber failures lead to significant contributions at frequencies above 400 kHz. The monitoring of this feature is therefore important to know the contribution of the textile in the load transfer.

The DFOS technology measures the strains of the textile within the TRC and shows that, before cracking, the strain is maximal at the loaded end of the TRC, and decreases along the specimen, until reaching zero at a given distance, called stressed length, L_s (see Fig. 3).
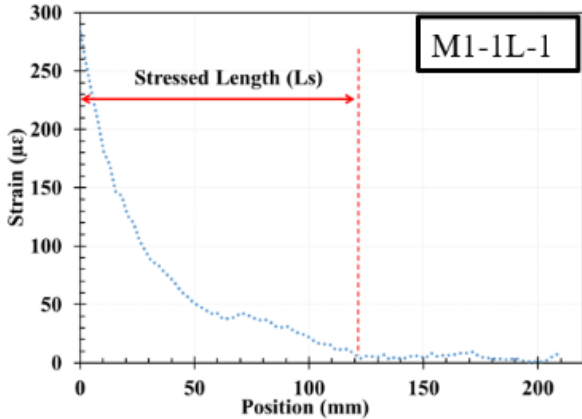
Fig. 3: Evolution of the textile strains of M1-1L-1 along the bonded length and definition of L_s.

Fig. 4 superimposes the evolution of L_s with the measured acoustic activity, and shows that as long as L_s was not almost stabilized, no acoustic activity was recorded.

(a) M1-1L-1

(b) M1-2L-1

(c) M2-1L-1

(d) M2-2L-1
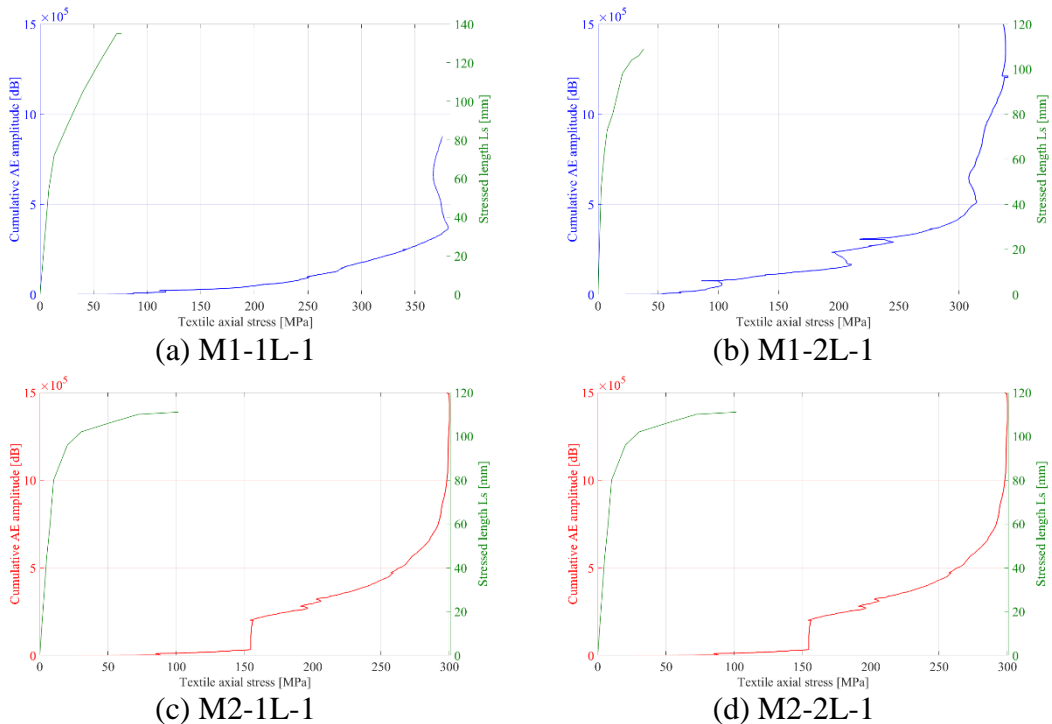
Fig. 4: Cumulative AE amplitudes and stressed lengths (DFOS) versus textile axial stress for the four specimens monitored with DFOS.

Fig. 5 shows a log-linear plot of the cumulative AE amplitude (by summing over all sensors) versus the textile axial stress for all the tested specimens. By setting aside M2-2L-2 which presents a singular behavior (failure mode, ultimate load), at low loads, the softer the matrix is, the higher the cumulative amplitude is. Gradually, the influence of the matrix is reduced and the cumulative amplitudes are relatively similar for all specimens at the failure. Moreover, with higher reinforcement ratios, the recorded cumulative amplitudes are higher, which can be related to the greater number of cracks developed in specimens with two strengthening layers.

(a) 1 AR-glass layer

(b) 2 AR-glass layers
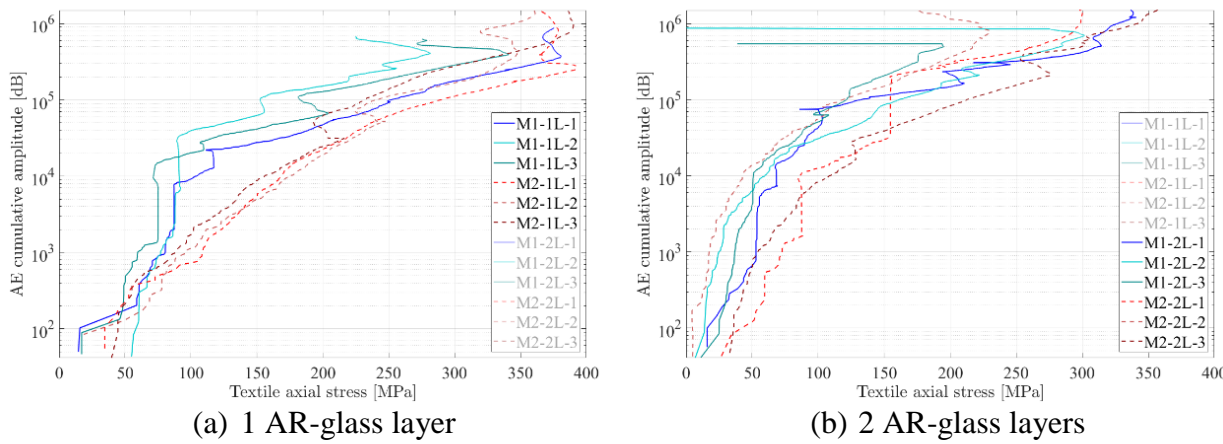
Fig. 5: Cumulative AE amplitudes (logarithmic scale) versus textile axial stress for specimens with (a) one strengthening layer, and (b). two strengthening layers.

Progressive accumulation of partial power PP3 versus the textile axial stress is shown in Fig. 6. Specimens whose cumulative PP3 increase most rapidly with loading are those with the lowest failure loads, and then with the lowest textile exploitation ratios.

(a) 1 AR-glass layer   (b) 2 AR-glass layers
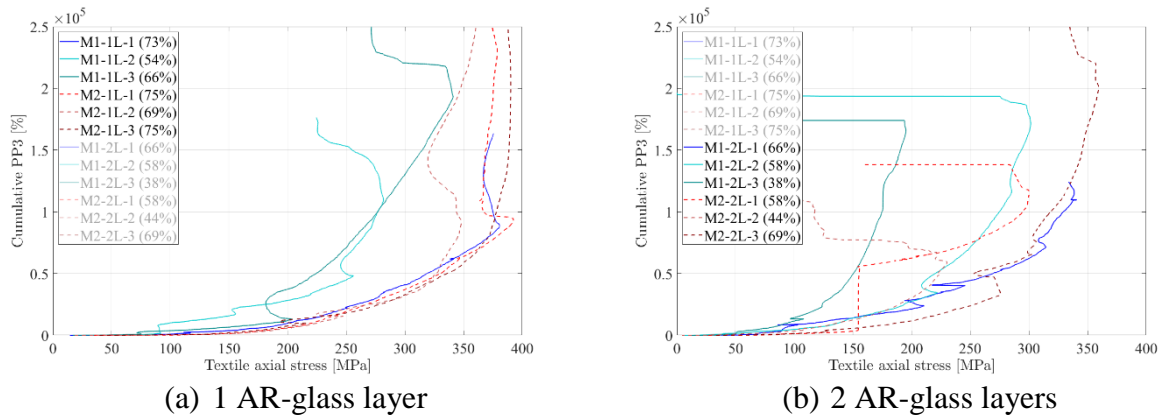
Fig. 6: Cumulative PP3 [400-1000 kHz] versus textile axial stress for specimens with (a) one, and (b). two strengthening layers. In the legends, in brackets, are indicated the exploitation rates of textiles.

To ascertain the link between PP3 and the contribution of textiles, it is interesting to look in more detail at the specimens that showed a type E failure mode, and equipped with DFOS and DIC, namely M1-1L-1, M1-2L-1, and M2-2L-1. For these specimens, Fig. 7 shows the evolution of cumulative PP3 over stress intervals of 25 MPa during loading. On the same figure is plotted the evolution of the total crack width (sum of all crack openings). At the time of cracking, the matrix no longer supports the applied load and the textile takes the full load. Strong increments of PP3 are then observed. Between two cracking instants, the opening progressively increases due to the progressive debonding at the textile-to-matrix interface. PP3-increments are then recorded, less important than during cracking, but present and relatively constant over all stress intervals between two cracks.

(a) M1-1L-1   (b) M1-2L-1   (c) M2-2L-1
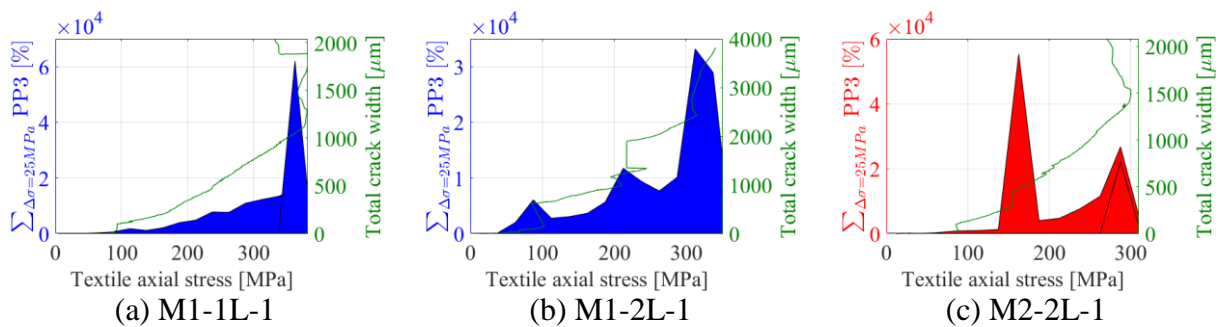
Fig. 7: PP3-increments per 25 MPa-stress intervals, in comparison with the total crack width (obtained by DIC), for specimens monitored by DFOS and DIC.

5.   Conclusions

This study focuses on the potential of acoustic emission to analyze the progression of debonding during shear bond tests on glass TRC to masonry substrate. The main results are as follows:
- The acoustic activity is initiated when the stressed length, over which the strains develop, is stabilized.

- The stiffness of the matrix has an influence on the acoustic emissions at low loads. Based on the two matrices used in this study, the softer the matrix, the higher the cumulative amplitudes.
- Specimens with two layers of textile record more intense acoustic activity than those with a single layer. This correlates with the opening of more cracks in the upper part of the cementitious matrix in these specimens.
- The higher the cumulative partial power PP3 (400-1000kHz), the more the failure occurs at a low textile exploitation ratio. Monitoring this indicator therefore provides information on a high rate of textile work at a given load.
- For specimens M1-1L-1, M1-2L-1, and M2-2L-1, equipped with DFOS and DIC, and failed by a type E failure mode, PP3 increments appear to be related to crack development in the specimens.

Further analysis needs to be developed, but this study shows that univariate analyses of the AE features already provide valuable insight into the levels of damage to the TRC during shear bond tests. It will be necessary to ensure that this method of analysis, on the scale of a structural element, remains viable on a larger scale.

6. References

[1] N. Reboul, Z. Mesticou, A. Si Larbi, et E. Ferrier, « Experimental study of the in-plane cyclic behaviour of masonry walls strengthened by composite materials », *Constr. Build. Mater.*, vol. 164, p. 70‑83, mars 2018, doi: 10.1016/j.conbuildmat.2017.12.215.

[2] G. de Felice *et al.*, « Mortar-based systems for externally bonded strengthening of masonry », *Mater. Struct.*, vol. 47, nº 12, p. 2021‑2037, déc. 2014, doi: 10.1617/s11527-014-0360-1.

[3] G. Ferrara, C. Caggegi, E. Martinelli, et A. Gabor, « Shear capacity of masonry walls externally strengthened using Flax-TRM composite systems: experimental tests and comparative assessment », *Constr. Build. Mater.*, vol. 261, p. 120490, 2020, doi: https://doi.org/10.1016/j.conbuildmat.2020.120490.

[4] G. de Felice *et al.*, « Experimental characterization of composite-to-brick masonry shear bond », *Mater. Struct.*, vol. 49, nº 7, p. 2581‑2596, juill. 2016, doi: 10.1617/s11527-015-0669-4.

[5] M. Saidi, M. Michel, et A. Gabor, « Analysis of early-age behaviour of textile-reinforced cementitious matrix composites (TRC) using different measurements techniques », *Measurement*, vol. 187, p. 110365, janv. 2022, doi: 10.1016/j.measurement.2021.110365.

[6] M. Saidi et A. Gabor, « Experimental analysis of the tensile behaviour of textile reinforced cementitious matrix composites using distributed fibre optic sensing (DFOS) technology », *Constr. Build. Mater.*, vol. 230, p. 117027, sept. 2019, doi: 10.1016/j.conbuildmat.2019.117027.

[7] M. Sause, « Identification of failure mechanisms in hybrid materials utilizing pattern recognition techniques applied to acoustic emission signals », 2010. doi: 10.13140/RG.2.1.4492.2088.

[8] N. Reboul, M. Saidi, et A. Gabor, « Using acoustic emission to assess the tensile behaviour of textile reinforced cementitious (TRC) matrix composites », *Constr. Build. Mater.*, vol. 310, p. 125216, déc. 2021, doi: 10.1016/j.conbuildmat.2021.125216.

WHEN AM (ADDITIVE MANUFACTURING) MEETS
AE (ACOUSTIC EMISSION) AND AI (ARTIFICIAL INTELLIGENCE)

Kilian Wasmer[1,*], Rita Drissi-Daoudi[2], Giulio Masinelli[1], Tri Quang-Le[1], Roland Loge[2] and
Sergey A. Shevchik[1]

[1]Empa - Swiss Federal Laboratories for Materials Science and Technology, Laboratory for Advanced
Materials Processing (LAMP), Thun, Switzerland;
kilian.wasmer@empa.ch, giulio.masinelli@empa.ch, quang.le@empa.ch, sergey.shevchik@empa.ch
[2]Ecole Polytechnique Fédérale de Lausanne (EPFL), Thermomechanical Metallurgy Laboratory – PX
Group Chair, Neuchâtel, Switzerland; rita.drissidaoudi@epfl.ch, roland.loge@epfl.ch
*Correspondence: kilian.wasmer@empa.ch; tel.: +41 58 765 62 71

ABSTRACT

Acoustic Emission (AE) is an effective method to monitor and control the quality in different technical processes and phenomena, including tribology and fracture mechanics. However, in highly dynamic processes such as Laser Additive Manufacturing (LAM) of metal, the processing of AE signals is very burdensome. At the same time, artificial intelligence (AI) has been considered as a new and powerful tool to overcome the complexity of the large data processing with a reasonable computational time. In this contribution, we have summarized our prior works. To start with, we demonstrated that the combination of AE with state-of-the-art signal processing including AI makes it possible to differentiate several process conditions, workpiece quality and materials. Then, we present some limitations when changing process parameters and materials. Finally, we also introduce alternative AI methods to reduce the amount of data needed to train the AI algorithms as well as transfer the knowledge from one material to another one. This will give the reader an overview of the advances of monitoring the LAM process combining AE with AI techniques to make a significant step forward in in situ and real-time process monitoring and quality control. In particular,

Keywords: Acoustic emission, additive manufacturing, artificial intelligence, machine learning, online monitoring.

1. Introduction

In the last decade, Additive Manufacturing (AM) has been considered by many industries and scientists as the next industrial revolution [1]. This is particularly the case for Laser Powder Bed Fusion (LPBF) technology, the most studied laser-based three-dimensional (3D) printing process. The reasons are threefold. First, it is considered as the most promising technology to alter the supply chain and logistics [2, 3]. Second, unlike conventional material removal methods, AM is based on additive material method. Consequently, the quantity of raw material employed is highly resource-efficient, creating essentially no waste and decreasing both tooling and material costs

extensively [4]. Lastly, it obliterates most geometrical constraints of the workpieces as compared to conventional subtractive manufacturing [5].

Although significant progress has been made by the machine manufacturers to increase the process efficiency and reliability, the latter is limited, thus, preventing this technology to be considered by industries where reliability and quality of the workpieces are of utmost importance such as medical and aerospace [1]. It is mainly due to the complexity of the underlying physics of the laser-powder material interaction generating short lifetimes events such as rapid material melting and solidification followed by cyclic heating and cooling; melt pool dynamics and defect formation (e.g. cracks and pores) [6]. Under such circumstances, the quality of the produced part is obviously highly dependent on the choice of process parameters such as laser characteristic (beam shape, size and quality), scan velocity and strategy, hatch distance, powder layer thickness, etc. In addition, these parameters are material and machine-dependent. Nevertheless, any slight deviations of these parameters or any minor changes in laser optics, mechanical and optical material properties, or particles configuration of the powder in the melt zone may result in porosity, cracking and/or residual stress inside the workpiece [7], resulting finally in poor mechanical properties [8]. One attractive solution to guarantee the reliability and quality of the produced parts are in the development of in situ and real-time monitoring systems [9].

Based on the different reviews on process monitoring and control in metal-based AM systems [7, 10-13], the most common monitoring method is in situ optical inspections of the process zone using photodiodes and high-speed cameras. Despite certain advantages, they are not industrialized yet as photodiodes are limited to the process zone's surface region whereas high-speed cameras involve high cost. In recent years, acoustic emission (AE) has attracted considerable attention as a promising alternative to optical and imaging sensors. AE are elastic stress waves generated by material transformation (e.g. in our case, laser-material interaction) and propagates within a medium (e.g. workpiece or air) [14]. Hence, it is one of the most effective monitoring methods for dynamical processes [15] and the reason are fourfold. First, AE have high sensitivity and great ability to quickly detect changes in processes. Second, AE sensors provide a high temporal resolution allowing localizing the events. Thirds, the hardware is relatively cheap. Last but not least, the data processing of AE signals is very fast since they are 1D signals as compared to imaging (2D data) or tomography (3D data). One of the first work was made by Wang *et al.* [16], who used a structure-borne AE sensor to monitor online crack initiation and propagation during the laser cladding process; a process close to AM. In 2017, Shevchik, Wasmer *et al.* started presenting and publishing their pioneer works on situ and real-time quality monitoring of the LPBF process by combining AE and artificial intelligence (AI) [17-20]. In these works, three qualities with pores concentration were produced by changing the process parameters. The AE signals were acquired airborne using a Fiber Bragg Grating (FBG). The AE signals were classified using various configuration of Convolutional Neural Network (CNN) and the accuracies ranged between 83 and 89%. Further improvements of the AI algorithms were published, in particular by using deep learning methods in conjunction with two time windows to enhance the defect localization [21] and reinforcement learning; a self-learn AI method [22]. Also in 2017, Gaja and Liou [23] fixed a structure borne sensors on the based plate during laser direct energy deposition (L-DED) process. Using an unsupervised pattern recognition analysis (*K*-means clustering) in conjunction with a principal component analysis (PCA), they successfully distinguish two main defects types (cracks and pores) and their signal characteristics. Similar work was performed by Koester *et al.* [24], who installed an AE structure-borne sensor below the based plate during L-DED of Ti-6Al-4V. The work studied correlations between AE and process noise with machine state variations and deposition parameters. Still, the data processing was straightforward and primarily qualitative. Finally, since 2020, the number of scientific contributions using AE for online monitoring of LPBF has increased significantly, each addressing a specific scientific question and bringing a small stone towards the development of a universal online monitoring system for laser AM processes [25-30].

In most, if not all, contributions found in the literature have in common that the method is developed for a single material with very narrow process parameters. Obviously, these limitations are very important hurdles in the perspective of its industrialization. This contribution is an extension of our previous works [9],[17-22] addressing those issues for LPBF processing using AE and AI. Thus, Section 2 presents the experimental setup, material and data acquisition system. Section 3 gives insight into the AE features analysis for various process regimes and materials. Section 4 investigates the origin of the AE features. Section 5 presents the main classifications results for various material combination. Section 6 presents an alternative method to reduce both computation time and dataset via deep transfer learning methods.

2. Experimental setup, material, data acquisition

The samples and data acquisition for these studies were performed on an in-house LPBF machine shown in Fig. 1 [taken from [31]]. This setup is made of an enclosed chamber hosting a base plate, a recoater, and an Ytterbium fiber laser operating in continuous mode (CW) with a 1070 ± 10 nm wavelength, a spot size of 82 μm ($1/e^2$), and a beam quality with an $M^2 < 1.1$. To avoid oxidation during the process, the chamber's atmosphere was monitored and had a maximum oxygen level of 200 ppm. The experiment was to produce a series of overlapping line tracks. The scanning strategy was one-directional and parallel, with a hatch distance of 0.1 mm. In addition, it was equipped with an AM4I Sensor, which is a rugged, low cost, and high-sensitivity airborne sensor. It has its peak sensitivity at around 40 kHz and was placed at 10 cm from the laser-material interaction zone. Based on our experience in laser processing and to satisfy the Nyquist Shannon theorem [32], the data acquisition rate was set to 1 MHz. To ensure that the laser-material interaction and the AE data obtained are synchronized, the recording of the signals was triggered by a photodiode using a beam splitter setup.

Fig. 1: Experimental setup with AE sensor. Taken from [31]; published by Elsevier under CC BY 4.0.

In order to address the questions relative to the transfer of knowledge between materials, three different alloys with distinct optical, mechanical and thermal properties were selected. They are *stainless steel* (316L), *bronze* ($CuSn_8$) and *Inconel* (Inconel 718), and all alloys had a powder particle size distribution ranging from 10 to 45 μm. The number of materials depended on the specific study. The material compositions and other details can be found in Drissi-Daoudi *et al.* [14].

Finally, this study focused on the main four process regimes that are considered in the AM community [9]. They are *balling*, *lack-of-fusion* (*LoF*), *conduction mode* (*CM*), and *keyhole pores* (*KP*). Typical microstructures and AE signals for the different process regimes are shown in Fig. 2. In Fig. 2(b), the acoustic signals are split in windows with sizes of 5 ms for further signal processing.

Fig. 2: (a) Typical cross-section of the different process regimes; (b) typical AE signals for the corresponding process regimes. Taken and modified from [31]; published by Elsevier under CC BY 4.0.

3.   Analysis of AE features during LPBF

Inspection of Fig. 2(b) indicates an increase in the amplitude of the AE signal when moving from *balling* to *keyhole pores* process regime. From a physical point of view, it could be considered that the amplitude values increases are directly proportional to the energy density imparted on the melt zone. However, when looking at many signals, a large variation is observed. Hence, in order to draw a definitive conclusion, further analysis is required. In this section, we present the results of feature analysis in the time, frequency and time-frequency domain as well as the *t*-Distributed Stochastic Neighbor Embedding (*t*-SNE) plots. The latter is a non-linear dimensionality reduction technique that is employed for identifying relevant patterns and visualization of high-dimensional feature space in lower dimensional space [33].

The analysis results of the AE features in the time, frequency and time-frequency domains are summarized in Fig. 3. The analysis in the time domain is plotted via the Root Mean Squares (AE_{RMS}) distributions in Fig. 3(a) for *balling*, *LoF*, *conduction mode*, and *keyhole pores* and Fig. 3(b) for the different materials and process regimes. From Fig. 3(a), similarities are observed between *balling* and *LoF*, whereas significant differences are visible between these two regimes and *conduction mode* and *keyhole pores*. Analyzing the AE_{RMS} further, significant discrepancies are perceived between materials and process regimes and evidence of this is in Fig. 3(b). The analysis in the frequency domain is shown in Fig. 3(c). It is observed that most frequencies for *balling* and *LoF* are found in the range 5-15 kHz whereas it is around 40 kHz for *CM* and *keyhole pores*. Finally, the analysis in the time-frequency domain is in Fig. 3(d) and the results are similar to the one in the time and frequency domains.
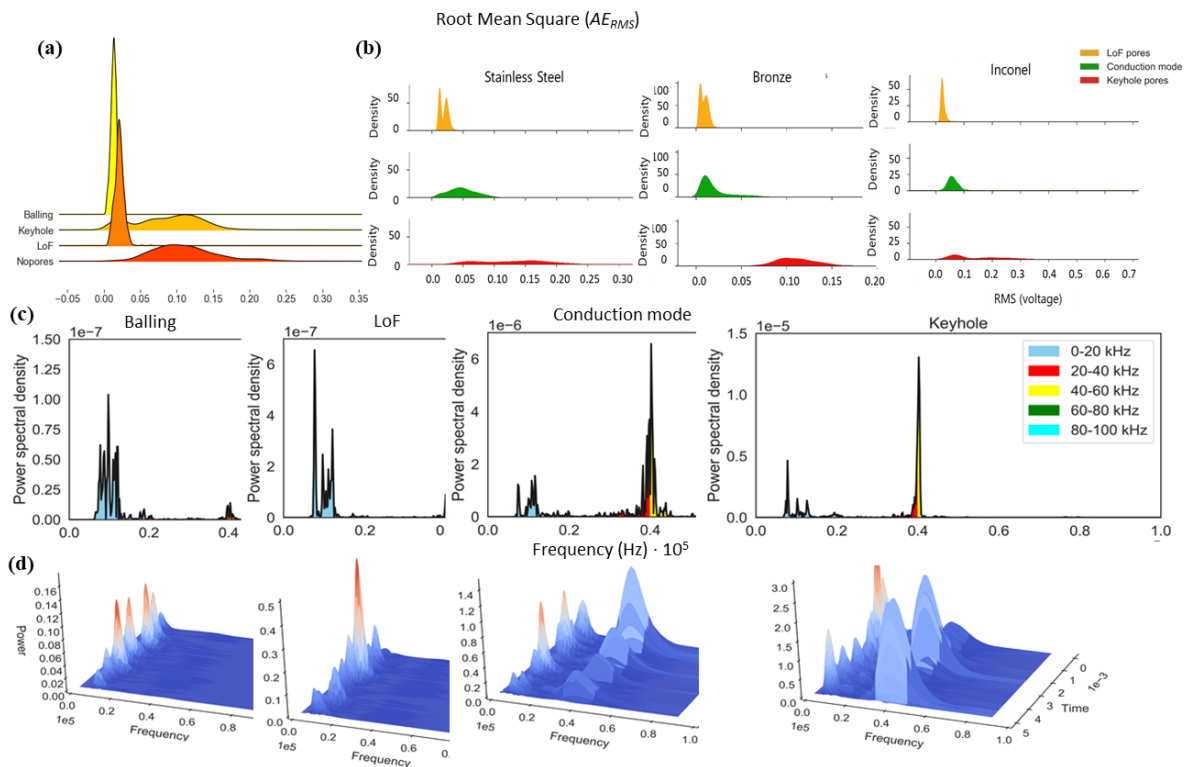
Fig. 3: (a) *Stainless steel* RMS distributions feature for process regimes; (b) RMS distributions for various materials and process regimes; (c) Fast Fourier Transform (FFT) plots for process regimes; (d) 3D wavelet representation of the acoustic signals for process regimes. (a), (c), and (d) taken and modified from [31]; published by Elsevier under CC BY 4.0. (b) taken and modified from [14]; published by Elsevier under CC BY 4.0.

The visualization of the plots corresponding to the investigated materials and process regimes in Fig. 3 was the motivation to extract statistical features as they can be used as inputs for ML models. To visualize the statistical features extracted, we opted for the *t*-SNE plots since they allow interpreting and visualizing a lower dimension representation to certify that the selected statistical features form distinctive clusters in the lower dimension space. For the *t*-SNE plots in Fig. 4, a value of 10 was chosen for the perplexity parameter after an exhaustive search. The perplexity is a hyper-parameter, which gives a ratio of preserving the data's local structure (number of neighbors) and global structure (overall shape). The *t*-SNE plot for the process regime of *stainless steel* is in Fig. 4(a) whereas Fig. 4(b)-(d) compare the *t*-SNE plots between materials but for the process regimes. Based on this figure, the results can be summarized as follows: the presence of clusters in the feature space demonstrates that the statistical features extracted from the four process regimes can be combined with ML algorithms to be classified. For alloys classification within a process regime, the classification task seems possible as well. Both types of classification will be challenging and would probably require a non-linear ML model.
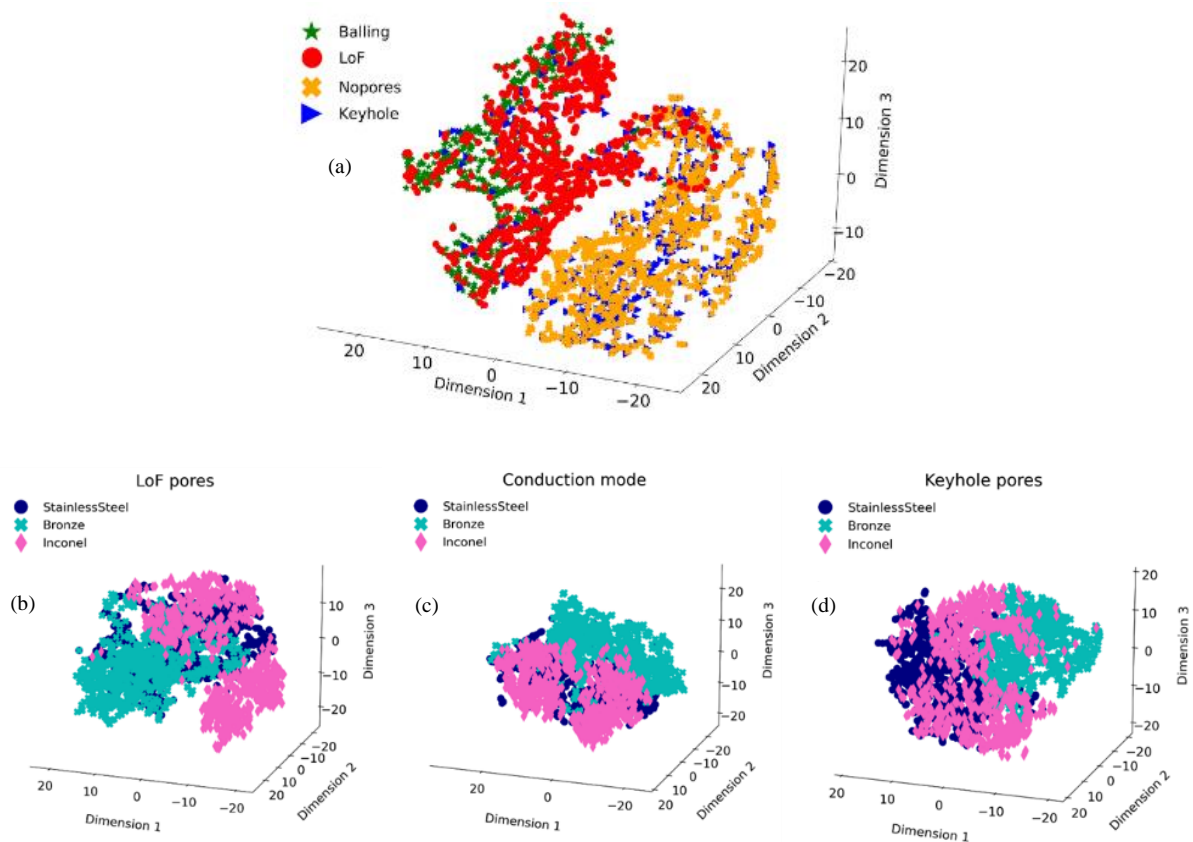
Fig. 4: Low dimension representation of the feature space using *t*-SNE with perplexity = 10 for (a) the process regimes (*balling*, *LoF*, *CM* and *keyhole pores*) and (b)-(d) the three alloys for the process regimes *LoF pores*, *CM* and *keyhole pores*. (a) taken from [31]; published by Elsevier under CC BY 4.0.

4. Analysis of the origin of the AE features

As mentioned in the introduction, AE system is one of the most effective monitoring methods for dynamical processes [15]. Due to its advantages, AE sensors have been used in AM, particularly L-PBF for online quality monitoring [16, 23-29] and combining AI [9, 14, 17-22, 30]. It is important to mention that these publications have in common the fact that experiments are

conducted for single material and single process parameter per regimes and/or category. Furthermore, it is well known that the major difficulty in using AE sensor is correlating the signals' with the real events. The main reason is the ability of the AE sensor to detect any acoustic wave reaching it, independently on its origin [34]. In the case of LPBF, the main AE sources are machine and environment noise, the various momentary events during the laser-material interaction as well as the process parameters themselves [14]. Consequently, to have a robust online monitoring system, it is of utmost importance to demonstrate that the AE feature selected for the classification task are only related to the laser-material interaction; which is responsible for the final workpiece quality. To achieve this goal, we selected the same process parameter for all three materials (*stainless steel*, *bronze* and *Inconel*) and two process regimes (*LoF* and *keyhole pores*). For *LoF*, the selected process parameters were a laser power of 50 W and scanning velocity of 350 mm/s. For *keyhole pores*, the process parameters were a laser power of 450 W with the same scanning velocity of 350 mm/s (See also Table 2). By selecting these process parameters and being able to accurately classify the correct material, it will prove that the AE features are solely correlated to the laser-material interaction and the process regime. The confusion matrix for classifying the three alloys and two process regimes using Random Forest (RF) as ML algorithms are presented in Table 1. The classification accuracy is visible in the diagonal (red cells) whereas the classification error are given on the same line. Based on this table, it can be concluded that the AE features selected for the classification task are not related to the undesired environmental or machine noise or the process parameters. This is confirmed by the fact that apart from *Inconel* for the *keyhole pores* category, all classification accuracies are higher than 97%. As already mentioned, this is a very important result for potential future industrialization of this approach.

Table 1: Confusion matrices of the RF models trained on *LoF* and *keyhole pores* across three alloys. All values are in %. Taken and adapted from [14]; published by Elsevier under CC BY 4.0.

Classif. accuracy [%] \ Ground truth	LoF pores			Keyhole pores		
	Stainless steel	*Bronze*	*Inconel*	*Stainless steel*	*Bronze*	*Inconel*
Stainless steel	100	0	0	97	0	3
Bronze	1	99	0	0	100	0
Inconel	1	1	98	11	1	88

5. Classification results for various materials and material combinations

In order to classify the different regimes, materials and their combination, additional experiments were performed and the experimental conditions are given in Table 2. In contrast to most contribution found in the literature [17-22, 25-26,34] and to extend the process phase space, two sets of process parameters were selected for each regime. The process parameters in red were the one selected to determine the origin of the AE features in Section 4.

Table 2: Two set of laser parameters for stainless steel, bronze and Inconel to induce the different process regimes; *LoF pores*, *conduction mode* and *keyhole pores*. In red, the first set of parameters for *LoF pores*, and *keyhole pores* is kept constant for the three alloys.

PROCESS REGIMES	Stainless Steel Laser		Bronze Laser		Inconel Laser	
	power [W]	velocity [mm/s]	power [W]	velocity [mm/s]	power [W]	velocity [mm/s]
LoF pores	50	350	50	350	50	350
	70	400	110	400	36	400
Conduction mode	180	350	300	350	100	350
	135	200	215	200	69	200
Keyhole pores	450	350	450	350	450	350
	250	150	396	150	127	150

The AE data acquired during the experiments given in Table 2 was analyzed following the procedure explained in Section 3. Based on this analysis, 304 features were selected from which 23 from the time domain, 18 from the frequency domain and 263 from the time-frequency domain. These features are the input of the ML algorithms; in this work Random Forest (RF) and all details can be found in Drissi-Daoudi *et al.* [14].

The first task is one on one alloy classification [14]. In other words, we want to classify the different regimes for each selected alloys separately and the results are given in Table 3. In this table, it is seen that most classification accuracies are higher than 93%. Based on these results and the fact that these alloys have very different optical, mechanical, and thermal properties, it can be concluded our methodology can be generalized to most metals.

Table 3: Confusion matrices of the RF models trained on *Stainless steel*, *Bronze* and *Inconel* across three regimes. All values are in %. Taken and adapted from [14]; published by Elsevier under CC BY 4.0.

		Stainless steel			Bronze			Inconel	
Classif. accuracy [%] / Ground truth		LoF pores	Conduction mode	Keyhole pores	LoF pores	Conduction mode	Keyhole pores	LoF pores	Conduction mode	Keyhole pores
LoF pores		93	1	6	98	0	2	98	0	2
Conduction mode		0	97	3	0	99	1	2	98	0
Keyhole pores		6	6	88	0	1	99	3	4	93

The second task is the one on all alloys classification [14]. In this case, we trained our AI model with all three alloys together and classify the regimes irrespective of the material. The results are given in Table 4. Based on the fact that the classification accuracy is above 92%, it can be concluded that it is possible to have a single AI algorithms that is material independent. This is important for future industrial application where multi-material or functional gradient material (FGM) will be produced.

The third task is the cross alloy classification- towards generalization [14]. In other words, the goal of this analysis is to verify whether the AE features are material dependent or not. To do so, we trained our AI algorithm with two materials and test on the third one. The confusion matrix for two cases are shown in Table 5. From this table, it is seen that when the model is trained with the data from *stainless steel* and *bronze* and then tested on *Inconel*, the overall accuracy is 80% with some difficulties for the regime *LoF pores*. In the opposite, when the model is trained with the data from *stainless steel* and *Inconel* and then tested on *bronze*, the overall accuracy drops as low as 35%. This indicates that the AE features are material dependent. Although this can be seen as an important limitation, it can also be seen as an opportunity and the reasons are twofold. First, we demonstrated that an AI model with the different materials can be build and so an alternative solution was given. Second, the fact that the AE features are material dependent give the possibility to use them for determining the processed material and so their respective process parameters.

The fourth task is a multi-label classification; materials and process regimes [14]. To address this task, a CNN was designed and optimized for classifying at once the different material and process regimes. All details on the CNN architecture can be found in Drissi-Daoudi *et al.* [14]. Table 6 presents the classification the results and it is seen that the overall accuracy for the process regimes are 93.3% whereas it is 94.0% for the materials. These results are of high industrial importance for two reasons. First, being able to distinguish between different materials gives the possibility to use our approach to determine the material during the first laser pulse and so select the process parameters from a table for the processed material. Second, it support the demonstration in Section 4 that the AE features are related only to the laser-material interaction and the associated process regime. If it was not the case, the classification accuracy for the *materials* in Table 6 would be much lower for the process regimes, *LoF pores* and *keyhole pores*. The reason is that one set of process parameters for these regimes were fixed and so it would have equal probability to be classified for each material; so reducing the classification accuracy [14].

Table 4: Confusion matrices of the RF models trained on the combined alloy dataset and tested for each alloy and process regimes. All values are in %. Taken and adapted from [14]; published by Elsevier under CC BY 4.0.

Classif. accuracy [%] \ Ground truth	LoF pores	Conduction mode	Keyhole pores
LoF pores	95	1	4
Conduction mode	0	97	3
Keyhole pores	3	5	92

Table 5: Confusion matrix of the RF model trained on two alloys and tested on a new alloy. All values are in %. Taken and adapted from [14]; published by Elsevier under CC BY 4.0.

Stainless steel + Bronze on Inconel Good case (80%)

	LoF pores	Conduction mode	Keyhole pores
LoF pores	61	0	39
Conduction mode	0	93	7
Keyhole pores	6	6	88

Stainless steel + Inconel on Bronze Bad case (35%)

	LoF pores	Conduction mode	Keyhole pores
LoF pores	100	0	0
Conduction mode	0	42	58
Keyhole pores	14	24	62

Table 6: Confusion matrices of the multi-label CNN model trained on two ground-truth labels. Left table: classification accuracy on the regimes. All values are in %. Taken and adapted from [14]; published by Elsevier under CC BY 4.0.

Ground truth / Classif. accuracy [%]	*Process regimes* (**93.3%**)			*Materials* (**94.0%**)		
	LoF pores	*Conduction mode*	*Keyhole pores*	*Stainless steel*	*Bronze*	*Inconel*
LoF pores	93.0	6.5	0.5	97.0	2.0	1.0
Conduction mode	6.0	91.0	3.0	2.0	91.0	7.0
Keyhole pores	0.5	3.5	96.0	0.5	5.5	94.0

6.   Transfer learning of process regimes across materials during LPBF

In Section 4, it was demonstrated that the AE features are material-dependent. Still, from an industrial point of view, developing an AI model for each material is time-consuming and costly. Hence, it is highly important to investigate how is it possible to transfer the know-how acquired on one material to another. The main goal is to reduce the amount of data needed for the next material as well as the computational efforts. In this section, we will just summarize one possible approach proposed by Pandiyan *et al.* [35], which is also known as deep transfer learning. Actually, transfer learning can be defined as an AI method where a model developed for a specific task is reused as the starting point for a new model on a second task. In Pandiyan *et al.* [35], the task can be referred to as two different materials; *stainless steel* (316L) and *bronze* (CuSn$_8$). Also the major four process regimes were selected: *balling*, *LoF pores*, *conduction mode* and *keyhole pores*. Finally, two sets of process parameters were also selected for each regime to extend the process phase space. All additional details such as experimental setup, data acquisition system, AI algorithms and architecture, results and discussion the experimental details can be found in Pandiyan *et al.* [35].

In this contribution, the general workflow of the proposed methodology for transferring the knowledge acquired for the different process regimes from *stainless steel* to *bronze* is shown in Fig. 5. In this figure, it is seen that two types of AI algorithms are considered for this task which are the VGG-16 and ResNet; two native Deep Learning (DL) networks. VGG16 is a type of CNN developed by Simonyan and Zisserman [36], from Oxford's renowned Visual Geometry Group, for object detection and image classification algorithm. Today, it is still one of the most popular algorithm for image classification and easy to use for transfer learning [35]. In 2015, He *et al.* [37] developed a newer type of CNN architecture to surmount the vanishing gradient problem (ResNet). In other words, ResNets are one of the most efficient Neural Network Architectures since they not only allow constructing networks with up to thousands of convolutional layers, but also help in maintaining a low error rate much deeper in the network [35].
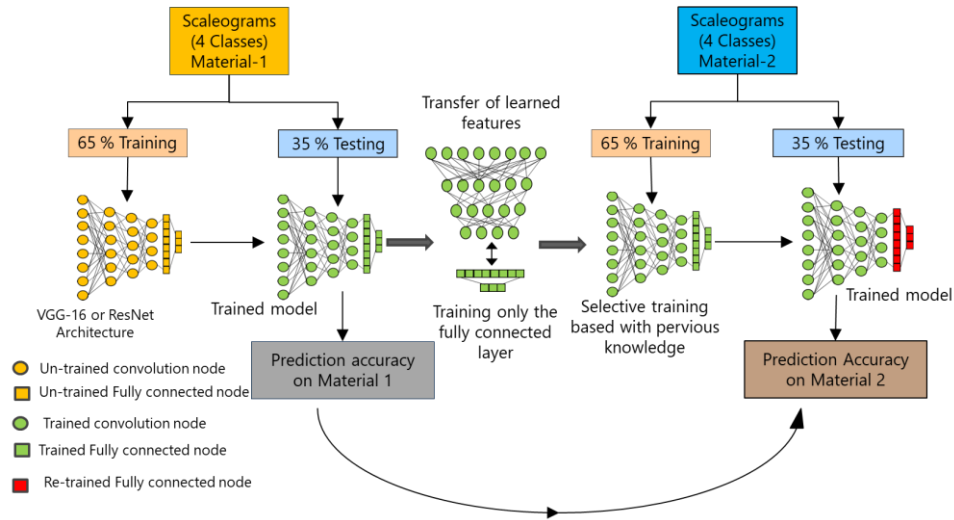
Fig. 5: General workflow of the deep transfer learning methodology using a CNN architecture. Taken and modified from [35]; published by Elsevier under CC BY 4.0.

The overall one-on-one alloy (prediction accuracy on Material 1 in Fig. 5) classification accuracies for *stainless steel* using the VGG-16 and ResNet-18 are given in Table 7. This table shows that the classification accuracies are as high as 96.1% (VGG-16) and 93.5% (ResNet-18). In this study, we also show that the process regimes *balling* and *LoF pores* are very well differentiable. This is a very interesting result as these two process regimes have in common an insufficient laser power to melt the powder fully and so very similar from a laser-material interaction point of view. These results again prove our approach's validity, at least for one on one material.

Finally, the confusion matrix for the VGG-16 and ResNet-18 models from the transfer learning on *bronze* using the full test dataset is given in Table 8 (prediction accuracy on Material 2 in Fig. 5). The overall classification accuracies for the VGG-16 and ResNet-18 are 85.0 and 81.6%, respectively. This decrease as compared to the one-on-one alloy was expected. It came as a surprise that for both models, the main misclassifications are between the process regimes *LoF pores* and *conduction mode*. Consequently, to understand these results, we also performed the classification task for one-to-one alloy for *bronze*. Actually, it was found (shown in Pandiyan *et al.* [35]) that there is also a significant misclassification (11-15%) between the same process regimes (*LoF pores* and *conduction mode*). This is certainly because one of the process parameters selected for these regimes may be in the transition regime between *LoF pores* and *conduction mode*, so there is a significant overlap of the features space between these two regimes. Based on Table 7 and Table 8, it is observed that the VGG-16 models performed better than the ResNet-18.

Table 7: Confusion matrix depicting the accuracy of trained VGG-16 network on *stainless steel* mechanisms in the test set. All values are in %. Taken and adapted from [35]; published by Elsevier under CC BY 4.0.

Classif. accuracy [%] / Ground truth	VGG-16 (96.1%)				ResNet-18 (93.5%)			
	Balling	*LoF pores*	*Conduction mode*	*Keyhole pores*	*Balling*	*LoF pores*	*Conduction mode*	*Keyhole pores*
Balling	97.8	0.0	1.7	0.5	93.8	4.3	1.7	0.2
LoF pores	3.0	95.0	1.5	0.5	3.5	93.3	2.2	1.0
Conduction mode	0.7	0.3	96.8	2.2	0.7	0.3	93.3	5.7
Keyhole pores	0.7	0.3	4.2	94.8	0.4	0.8	5.4	93.4

Table 8: Classification matrix of the models via transfer leaning for mechanisms occurring during the LPBF process of bronze using the full dataset. All values are in %. Taken and adapted from [35]; published by Elsevier under CC BY 4.0.

Classif. accuracy [%] / Ground truth	VGG-16 (85.0%)				ResNet-18 (81.6%)			
	Balling	LoF pores	Conduction mode	Keyhole pores	Balling	LoF pores	Conduction mode	Keyhole pores
Balling	94.0	3.5	2.5	0.0	89.0	5.5	5.3	0.2
LoF pores	2.0	76.5	21,0	0.5	3.0	74.5	20.7	1.8
Conduction mode	3.0	17.2	75.8	4.0	2.5	21.2	72.0	4.3
Keyhole pores	0.0	1.5	5.0	93.5	0.0	1.8	7.2	91.0

7. Conclusions

In this contribution, we summarized prior works in demonstrating that when AM (Additive Manufacturing) meets AE (Acoustic Emission) and AI (Artificial Intelligence), it leads to a very promising solution for in situ and real-time monitoring.

To start with, we presented the experimental setup: an in-house LPBF machine made of a controlled atmospheric chamber hosting a base plate and equipped with a Ytterbium fiber laser (1070 nm; spot Ø 82 μm), a rugged, low cost, and high sensitivity airborne AE sensor. The data acquisition rate was 1 MHz to satisfy the Nyquist Shannon theorem [32]. The materials investigated were *stainless steel* (316L), a *bronze* ($CuSn_8$) and an *Inconel* (Inconel 718). In terms of process regime, we focused on the main four process regimes considered in the AM community [9]; *balling*, *lack-of-fusion* (*LoF*), *conduction mode* (*CM*), and *keyhole pores* (*KP*).

Three main conclusions could be drawn based on the analysis of the AE signals in the time, frequency and time-frequency domains [31]. First, all four process regimes are functions of the energy density imparted into the melt zone. Second, it was found that these four regimes exhibit discrete energy levels and that the frequency bands between 1 kHz and 60 kHz carried most of the energy. Third, *t*-SNE feature reduction technique suggested that these regimes are clustered in the feature space so that they must be differentiable using state-of-the art AI algorithms.

Based on the classification results for one on one alloy, one of all alloys and cross alloy classification- towards generalization; three conclusions could be drawn [14]. First, it was proven that the classification task for one on one alloy has very high accuracy (> 93%). Considering the significant variation in the optical, mechanical, and thermal properties of the materials investigated, it can be concluded that the proposed approach is valid at least for most metals. Second, the one on all alloys AI model reached also high classification accuracies (>92%). This ascertains that the proposed method can also be used for processing multi-materials or FGM. Third, it was found that cross alloy classification- towards generalization does not always work. This indicates that the AE features are material dependent. However, we were able to overturn this limitation in a positive manner. We used this information to make a multi-label classification task (process regime and material). In other words, we developed a new method that is able not only to detect the process regimes but also the material being processed. This may give the possibility to use the first laser pulse to determine the material and so the corresponding process parameters.

To address the AE features material dependences, we proposed an alternative based on deep transfer learning method [35]. We tested two neural network architectures known as VGG-16 [36] and ResNet-18 [37]. It was found that the classification accuracy of the transfer models were 85.0 and 81.6% for VGG-16 and ResNet-18, respectively. The reason of this slight lower classification

accuracy is due to an overlap of the AE features between the regimes *LoF pores* and *conduction mode*. The origin of this overlap was certainly caused by having one of the process parameters selected in a transition regime and not fully in the *LoF pores* or *conduction mode* regime.

Finally, based on all the results mentioned above, it can be concluded that combining AE and AI is a very promising solution for in situ and real-time monitoring of AM processes.

8. References

[1] Sreerag, C., Gajjela, R., Manupati, V., Machado, J. (2021). Chapter 1 - Additive manufacturing: a thrive for industries, Additive Manufacturing - A Tool for Industrial Revolution 4.0, Woodhead Publishing Reviews: Mechanical Engineering Series, p. 1-16, doi: 10.1016/B978-0-12-822056-6.00011-4.

[2] Khajavi, S.H., Partanen, J., Holmström, J. (2014). Additive manufacturing in the spare parts supply chain, Computers in Industry vol. 65, p. 50–63, doi: 10.1016/j.compind.2013.07.008.

[3] Attaran, M. (2017). Additive manufacturing: the most promising technology to alter the supply chain and logistics, vol. 10, no 3, p. 189-205, doi: 10.4236/jssm.2017.103017.

[4] Frazier, W.E. (2014). Metal additive manufacturing: a review, Journal of Materials Engineering and Performance, vol. 23, p. 1917–1928, doi: 10.1007/s11665-014-0958-z.

[5] Zhai, Y.W., Lados, D.A., Lagoy, J.L. (2014). Additive manufacturing: making imagination the major limitation. JOM vol. 66, p. 808–816, doi: 10.1007/s11837-014-0886-2.

[6] Zhang, L.C., Attar, H. (2016). Selective laser melting of titanium alloys and titanium matrix composites for miomedical applications: a review, Advanced Engineering Materials, vol. 18(4), p. 463–475, doi: 10.1002/adem.201500419.

[7] Everton, S.K., Hirsch, M., Stravroulakis, P., Leach, R.K., Clare, A.T. (2016). Review of in-situ process monitoring and in-situ metrology for metal additive manufacturing, Materials and Design, vol. 95, p. 431-445, doi: 10.1016/j.matdes.2016.01.099.

[8] Lewandowski, J.J., Seifi, M. (2016). Metal additive manufacturing: a review of mechanical properties, Annual Review of Materials Research, vol. 46, p. 151-186, doi: 10.1146/annurev-matsci-070115-032024.

[9] Shevchik, S.A., Kenel, C., Leinenbach, C., Wasmer, K., (2018). Acoustic emission for in situ quality monitoring in additive manufacturing using spectral convolutional neural networks, Additive Manufacturing, vol. 21, p. 598-604, doi: 10.1016/j.addma.2017.11.012.

[10] Tapia, G., Elwany. A., (2014). A review on process monitoring and control in metal-based additive manufacturing. Journal of Manufacturing Science and Engineering, vol. 136, no. 6, paper ID 060801, p. 1-10, doi: https://doi.org/10.1115/1.4028540.

[11] Grasso, M, Demir, A.G., Previtali, B., Colosimo, B.M. (2018). In situ monitoring of selective laser melting of zinc powder via infrared imaging of the process plume. Robotics and Computer-Integrated Manufacturing vol. 49, p. 229-239, doi: 10.1016/j.rcim.2017.07.001.

[12] Yan, Z., Liu, W., Tang, Z., Liu, X., Zhang, N., Li, M., Zhang, H. (2018). Review on thermal analysis in laser-based additive manufacturing. Optics and Laser Technology vol. 106, p. 427-441, doi: 10.1016/j.optlastec.2018.04.034.

[13] Lee, J., Park, H.J., Chai, S., Kim, G.R., Yong, H., Bae, S.J., Kwon, D. (2021). Review on quality control methods in metal additive manufacturing. Applied Sciences, vol. 11, paper ID 1966, doi: 10.3390/app11041966.

[14] Drissi-Daoudi, R., Pandiyan, V., Logé, R., Shevchik, S.A., Masinelli, G., Ghasemi-Tabasi, H., Parrilli, A., Wasmer, K. (2022). Differentiation of materials and laser powder bed fusion processing regimes from airborne acoustic emission combined with machine learning, Virtual and Physical Prototyping, vol. 17, no. 2, p. 181-204, doi: 10.1080/17452759.2022.2028380.

[15] Grosse, C., Ohtsu, M., Aggelis, D.G., Shiotani, T. (2022). Acoustic emission testing basics for research - applications in civil engineering, 2nd ed., Springer, Berlin, Heidelberg, doi: 10.1007/978-3-030-67936-1

[16] Wang, F., Mao, H., Zhang, D., Zhao, X., Shen, Y. (2008). Online study of cracks during laser cladding process based on acoustic emission technique and finite element analysis, Applied Surface Science, vol. 255, no. 5, p. 3267–3275, doi: 10.1016/j.apsusc.2008.09.039.

[17] Wasmer, K., Kenel. C., Leinenbach. C., Shevchik. S.A. (2017). In situ and real-time monitoring of powder-bed AM by combining acoustic emission and artificial intelligence, Conference proceedings, Additive Manufacturing in Products and Applications - AMPA2017 – Industrializing Additive Manufacturing, M. Meboldt and C. Klahn (eds.), Zürich, Switzerland, p. 200-209, Springer International Publishing, doi: 10.1007/978-3-319-66866-6_20.

[18] Wasmer, K., Kenel, C., Leinenbach, C., Shevchik, S.A (2017). In situ and real-time monitoring of powder-bed AM by combining acoustic emission and machine learning, Conference proceedings, Laser in Manufacturing (LiM2017), Munich, Germany, 26 – 29 June 2017.

[19] Wasmer, K., Kenel, C., Leinenbach, C., Shevchik, S.A (2017). In situ quality monitoring in AM using acoustic emission: A machine learning approach, Conference proceedings, Material Science & Technology Conference 2017 (MS&T17), Pittsburgh, USA, p. 386 – 388, 8 – 12 October, 2017, 10.7449/2017/MST_2017_386_388.

[20] Shevchik, S.A., Kenel, C., Leinenbach, C., Wasmer, K. (2018). Acoustic emission for in situ quality monitoring in additive manufacturing using spectral convolutional neural networks, Additive Manufacturing, vol. 21(May 2018), p. 598-604, doi: 10.1016/j.addma.2017.11.012.

[21] Shevchik, S.A., Masinelli, G., Kenel, C., Leinenbach, C., Wasmer, K. (2019). Deep learning for in situ and real-time quality monitoring in additive manufacturing using acoustic emission, IEEE Transactions on Industrial Informatics, vol. 19, no. 9, p. 5194-5203, doi: 10.1109/TII.2019.2910524.

[22] Wasmer, K., Le-Quang, T., Meylan, B., Shevchik, S.A. (2019). In situ quality monitoring in AM using acoustic emission: A reinforcement learning approach, Journal of Materials Engineering and Performance, vol. 28, no. 2, p. 666–672, doi: 10.1007/s11665-018-3690-2.

[23] Gaja, H., Liou, F. (2017). Defects monitoring of laser metal deposition using acoustic emission sensor, The International Journal of Advanced Manufacturing Technology, vol. 90, p. 561–574, doi: https://doi.org/10.1007/s00170-016-9366-x.

[24] Koester, L.W., Taheri, H., Bigelow, T.A., Bond, L.J., Faierson, E.J. (2018). In-situ acoustic signature monitoring in additive manufacturing processes, AIP Conference Proceedings 1949, paper ID: 020006, doi: 10.1063/1.5031503

[25] Kouprianoff, D. (2020). Investigation of acoustic emission signal during laser powder bed fusion at different operating modes, The South African Journal of Industrial Engineering, vol. 32, no. 3, p. 279-283, doi: 10.7166/32-3-2663.

[26] Kouprianoff, D., Yadroitsava, I., du Plessis, A., Luwes, N., Yadroitsev, I. (2021). Monitoring of laser powder bed fusion by acoustic emission: investigation of single tracks and layers, Frontiers in Mechanical Engineering, vol. 21(June 2021), p. 1-17, doi: 10.3389/fmech.2021.678076.

[27] Mohammadi, M.G., Mahmoud, D., Elbestawi, M. (2021). On the application of machine learning for defect detection in L-PBF additive manufacturing, Optics & Laser Technology, vol. 143(November 2021), paper ID: 107338, doi: 10.1016/j.optlastec.2021.107338.

[28] Gutknecht, K., Cloots, M., Sommerhuber, R., Wegener, K. (2021). Mutual comparison of acoustic, pyrometric and thermographic laser powder bed fusion monitoring, Material and Design, vol. 210(Novembre 2021), paper ID: 110036, doi: 10.1016/j.matdes.2021.110036.

[29] Petrich, J., Snow, Z., Corbin, D., Reutzel, E.W. (2021), Multi-modal sensor fusion with machine learning for data-driven process monitoring for additive manufacturing, Additive

Manufacturing, vol. 48(B, December 2021), paper ID: 102364, doi: 10.1016/j.addma.2021.102364.

[30] Pandiyan, V., Drissi-Daoudi, R., Shevchik, S.A., Masinelli, G., Quang-Le, T., Logé, R., Wasmer, K. (2021) Semi-Supervised Monitoring of Laser Powder Bed Fusion Process Based on Acoustic Emissions, Virtual and Physical Prototyping, vol. 16, no. 4, p. 481-497, doi: 10.1080/17452759.2021.1966166.

[31] Pandiyan, V., Drissi-Daoudi, R., Shevchik,, S.A., Masinelli, G., Logé, R., Wasmer, K., Analysis of time, frequency and time-frequency domain features from acoustic emissions during laser powder-bed fusion process. Procedia CIRP, vol. 94(2020), p. 392–397, 2020, https://doi.org/10.1016/j.procir.2020.09.152.

[32] Jerri, A.J. (1977) The Shannon sampling theorem - Its various extensions and applications: A tutorial review. Proceedings of the IEEE, vol. 65, no. 11, p. 1565-1596, doi: 10.1109/PROC.1977.10771.

[33] van der Maaten, L., Hinton, G. (2008) Visualizing Data using *t*-SNE. Journal of Machine Learning Research, vol. 9, no. 86, p. 2579-2605.

[34] Le-Quang, T., Shevchik, S.A., Meylan, B., Vakili-Farahani, F., Olbinado, M.P., Rack, A., Wasmer, K., (2018) Why is in situ quality control of laser keyhole welding a real challenge? Procedia CIRP, vol. 74, p. 649–653, doi: 10.1016/j.procir.2018.08.055.

[35] Pandiyan, V., Drissi-Daoudi, R., Shevchik, S., Masinelli, G., Le-Quang, T., Logé, R., Wasmer, K. (2022). Deep transfer learning of additive manufacturing mechanisms across materials in metal-based laser powder bed fusion process, Journal of Materials Processing Technology, vol. 303(May 2022), paper ID: 117531, doi: 10.1016/j.jmatprotec.2022.117531.

[36] Simonyan, K., Zisserman, A., (2014). Very deep convolutional networks for large-scale image recognition. Published as a conference paper at ICLR 2015, arXiv preprint arXiv:1409.1556, doi: 10.48550/arXiv.1409.1556

[37] He, K., Zhang, X., Ren, S., Sun, J., (2015). Deep residual learning for image recognition. arXiv preprint arXiv:1512.03385, doi: 10.48550/arXiv.1512.03385.

Measurement Equipment and Customized Solutions for Acoustic Emission Testing

We develop and produce innovative technology that makes a true difference for the safety of humans, the environment and the preservation of infrastructure. This commitment differentiates us from other suppliers and defines who we are: Vallen Systeme – The Acoustic Emission Company

AMSY-6 System

The AMSY-6 System is a fully featured, multi-channel Acoustic Emission measurement system. It forms a flexible basis that can be customized, extended and configured to the needs of an application.

The field of applications ranges from various inspection tasks such as pressure vessel testing, leakage testing to research and structural health monitoring of large objects

spotWave Device

The spotWave device is a portable single channel AE-measurement unit that can be controlled by a Laptop, Tablet PC, Smartphone or IoT device. It is a fully featured AE measurement device. The software supports the Vallen pridb and tradb data file format.

Typical applications are leakage detection, hot spot monitoring, AE research, etc.

Acoustic Emission Sensors

A wide range of sensors is offered covering any AE testing application.

Sensors are available for standard environments, explosion hazardous areas, for underwater applications, high temperature surfaces and harsh environments.

Sensors supporting the SmarLine™ protocol register themselves with an AMSY-6 system and minimize the configuration effort.

Vallen AE Suite Software

Unmatched flexibility and transparency at all times makes the Vallen AE Suite Software the preferred tool of choice for all acoustic emission applications.

Its modular architecture can be configured and extended to match any requirement of an application.

It offers everything from simple data visualization over complex analysis and pattern recognition to automation and web-based dashboards.

Measurement data is written to a database structure that complies with SQLite3 standard. It can be accessed from any application supporting SQLite3 which includes Matlab, Python and many more fast development environments.

ONLINE MONITORING OF MANUFACTURING PROCESSES BY ACOUSTIC EMISSION

Abdelkrim Saidoun[1], Quang Ahn Vu[1] and Fan Zhang[1]

[1]CETIM, 52 avenue Félix Louat, France;
abdelkrim.saidoun@cetim.fr, quanganh.vu@cetim.fr, fan.zhang@cetim.fr

ABSTRACT

For many years, Cetim has been working on on-line control methodologies for manufacturing processes in order to reduce or even eliminate controls on finished parts. After the first works by conducted by the Acoustic Emission technique (AE) on the monitoring of sheet metal stamping process [1], the monitoring of new manufacturing processes such as metal cutting, wire drawing, spot welding, forging and especially are under study. In the present paper, the results of acoustic emission monitoring carried out on additive manufacturing production and also wire drawing are presented. For both processes on-line control during manufacturing is particularly important. Due to the geometric complexity of the parts produced by additive manufacturing, suitable non-destructive testing (NDT) means are limited. In addition, these are generally small series or even single parts with a long manufacturing time. For their part, wire drawing manufacturers currently have only visual inspection, unable to detect fine scratches on the wire at the output of production.

Keywords: On-line control, acoustic emission, crack detection, shaping of metals, spot welding, additive manufacturing.

1. Introduction

In a globalized world where the competition is more and more intense, the optimization of processes and the quality of production are principal preoccupations for manufacturers. Metal additive manufacturing (AM) has evolved considerably in recent years in industries such as aerospace, medical, automotive, and other high-tech areas. Laser powder bed fusion (L-PBF) is one of the most widely used AM techniques with many commercial systems available [2]. The L-PBF process involves many variables and a non-optimal setting (or variation) of these variables can result in reduced part quality or even damages, which are note usually easily detected.
Regarding the drawing process, its purpose is to reduce the section of a wire by passing it through a die, under the action of continuous traction. This wire is used mainly for the manufacture of fasteners obtained by stamping (screws, nuts, mechanical safety components, etc.). The quality of the finished product is sometimes threatened by defects (scratches, shocks) which are attributed to different causes (wear of the tool, lubrication, chemical or mechanical treatment, etc.).
After the first demonstrator "MOST" dedicated to the monitoring of processes under press, particularly sheet metal stamping [1], the objective of this study is to test the feasibility of monitoring by AE of new manufacturing processes in order to set up a monitoring system complementary to "MOST".

2. Online monitoring of additive manufacturing based on acoustic emission

2.1 Experimental procedure

The production was carried out on a ProX machine of 3D Systems using a IN625 powder. It contains 3 parts in Fig. 1:

- part A: superimposed combs C1 & C2 (each comb h= 8 mm). In this part, crack events were predicted at different heights in the interfacial zones between supports and horizontal parts,
- part B: reference part with standard process parameters (Ø 20mm, h=16mm). In principle, any crack event should not occur,
- part C: Comb C3 in order to compare with the case of C2 (validation of AE location on the platform and on height) (h= 16 mm),
- ghost parts (GP): without lasing in order to create a temporal separation between the main parts.
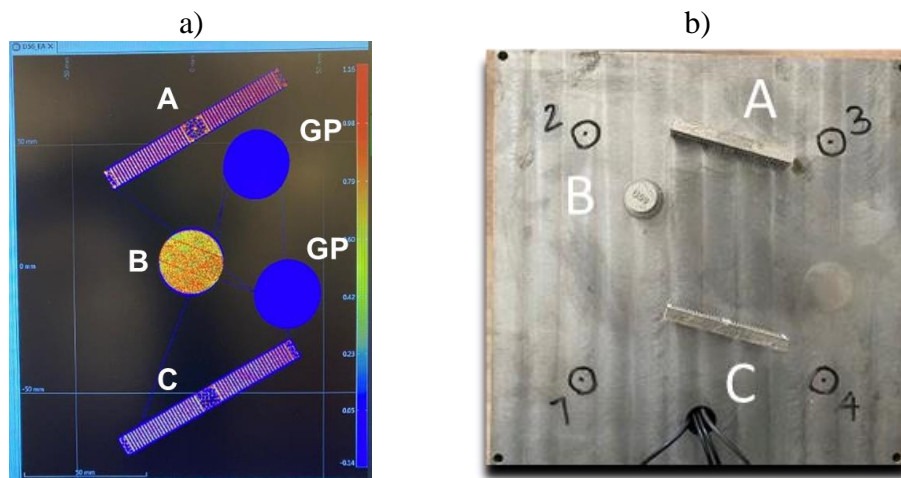
Fig. 1: a) Manufacturing plan of the 3 parts, b) finished parts.

Fig. 2 shows the finished parts with indication of the positions of the possible break points. In view of the rupture zones provided on the combs, the objective of the AE monitoring is to be able to detect them and locate/distinguish them in time and space.
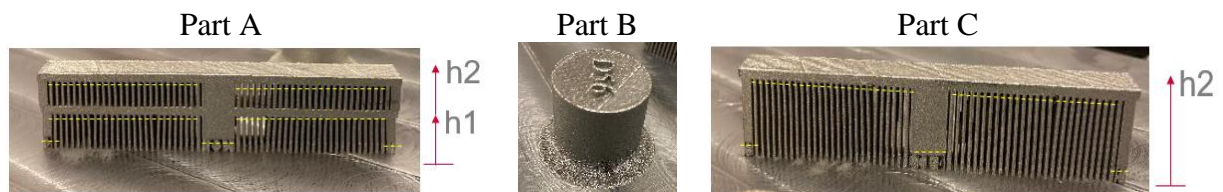
Fig. 2: Three finalized pieces with indications of fragile points (yellow dotted line).

2.2 AE instrumentation/equipment

Nature and characteristics of the instrumentation used to achieve the AE monitoring are as follows:

- sensors:
    - brand: Vallen,
    - type: Resonant piezoelectric,
    - frequency: 150 kHz,
    - sensibility: ≥ 60 dB ref. $V.m^{-1}.s^{-1}$,
    - intrinsic background noise: ≤ 5 μV (RMS),
    - number: 4,

- preamplifiers:
  - brand: Vallen,
  - type: AEP4H,
  - gain: 34 dB,
  - filtering: 20 kHz (high pass),
  - number: Equal to the number of sensors.

Connection between preamplifier and sensor is ensured by a cable not exceeding 1.0 meters length:
- acquisition system:
  - description: multichannel system for characterization and localization of acoustic emission sources with signal filtering within the frequency range 95-850 kHz,
  - brand: Vallen,
  - type: AMSY6,
  - number: 1,
  - acquisition threshold: 40 dB_{AE} (fixed value),
  - acquisition filtering: none.

A specific support adapted to the ProX machine has been designed in order to install the PZT sensors. Indeed, the support has an empty space in the lower part, in which the AE PZT sensors are installed in contact with the bottom surface of the build plate in Fig. 3. The sensor-plate coupling is ensured by a silicone grease and magnetic support.
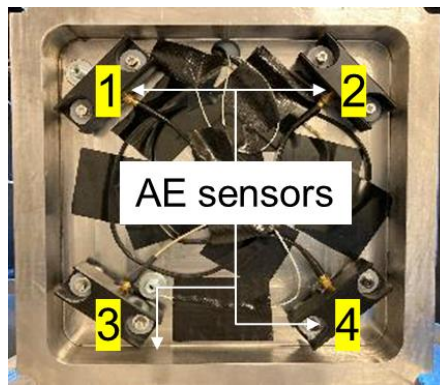
Fig. 3: ProX machine instrumentation by AE sensors, photodiode, and thermocouples.

2.3 Results & analysis

Fig. 4 shows the temporal evolution of the signal amplitude measured by the PZT sensor n°1 during the entire period of manufacture including 1h of cooling (results are similar for the other sensors).

Zoom of a period with high amplitude events (red) Part A   Zoom of first layers periode (yellow) Part A
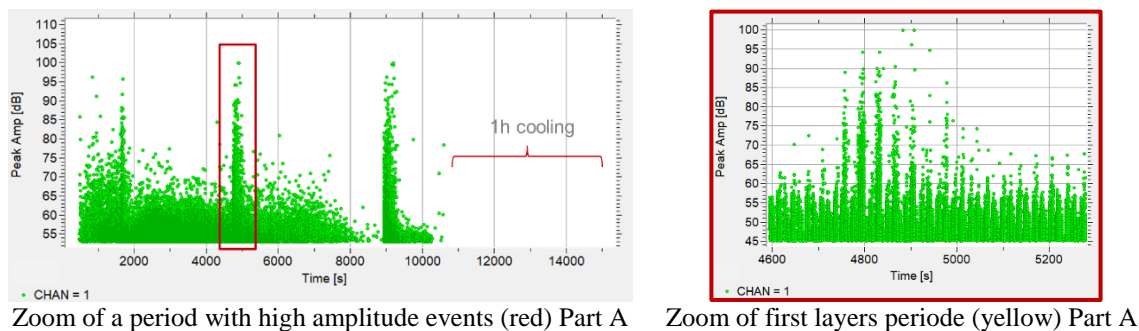
Fig. 4: Time-based AE data from the PZT n°1 during the entire period of manufacturing.

Fig. 5 presents the localization results for high amplitude AE signals (surrounded in red Fig. 4). It is important to note that the location was calculated following a 2D approach which considers the AE sources on the plane of the PZT sensors. Such a location therefore presents an uncertainty of the order of centimetres, as the real position of the sources is on the parts. Despite this point, the localization results show good consistency, high amplitude corresponds to the combs (parts A and C) and note the reference part B.

In addition, by correlating with the manufacturing time, the layers during which the breaks occur correspond well to the first horizontal layers of the supports-part boundary zones (indicated by the yellow lines in Fig. 2).
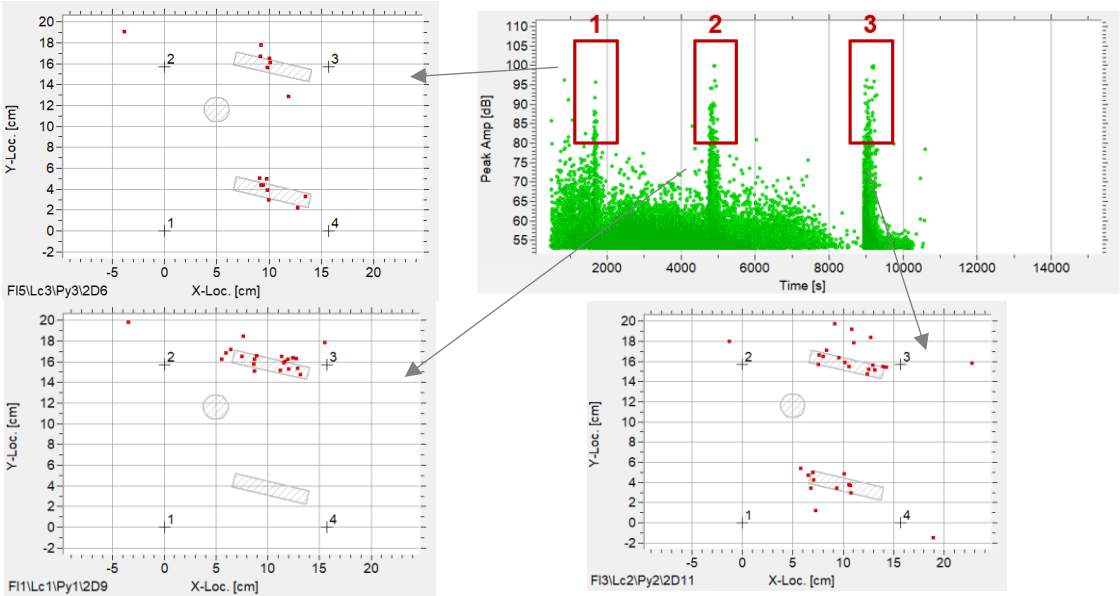
Fig. 5: Localization results of the high amplitude of AE signals during the entire period of manufacturing.

Fig. 6 presents the images of the finished parts with the indications of the anomalies observed. concerning the combs, at the interfaces between the toothed supports and the parts, it can be observed that certain teeth have deviated from their theoretical position 'circled in yellow'. Between the two deformed teeth, the surface is irregular and looks like a scar from a repaired break.

The combs were also controlled by X-ray computed tomography. The images obtained showed a good consistency with the observations above on finished parts (Fig. 7).

Part A   Part C
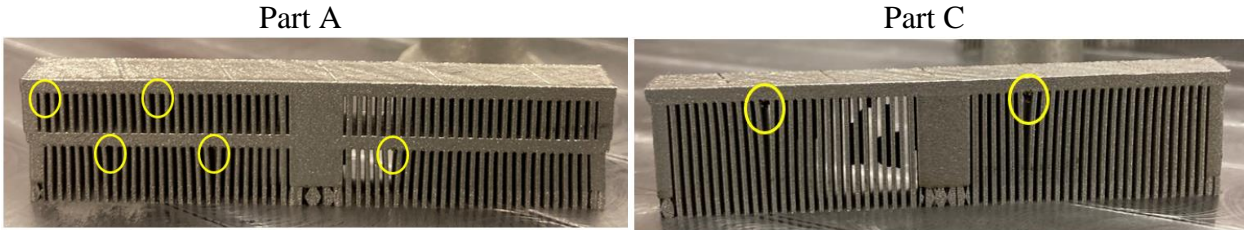
Fig. 6: Visual observation on finished parts that are still attached on the board.

Part A - comb 1	Part A - comb 2	Part C
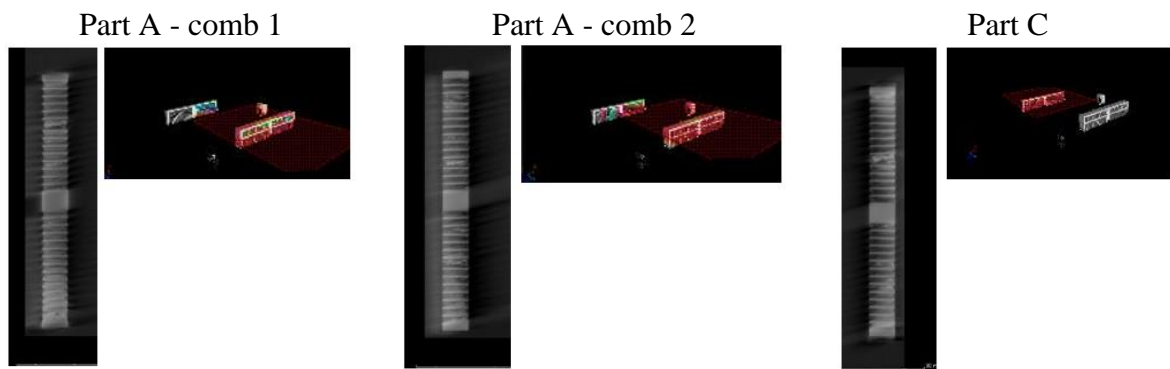
Fig. 7: The results of X-ray computed tomography on finished parts.

2.4 Conclusions

The experimental strategy implemented on the ProX machine enables to:

- detect high amplitude of AE signals (>80 dB$_{AE}$) and correlate them in real time with the manufacturing position thanks in order to detect defects,
- 2D location of the high amplitude of AE signals related to defects.

3. On-line monitoring of the wire drawing process based on acoustic emission

3.1 Experimental procedure

Nature and characteristics of the instrumentation used to achieve the AE monitoring are the same as in AE instrumentation/equipment section (the number of sensors is 01). Fig. 8 presents the drawing tool (die) instrumentation plan. Indeed, due to high temperature during the drawing process, it was necessary to deport the location of the acoustic emission sensor via a waveguide. The latter is screwed into the drawing tool.
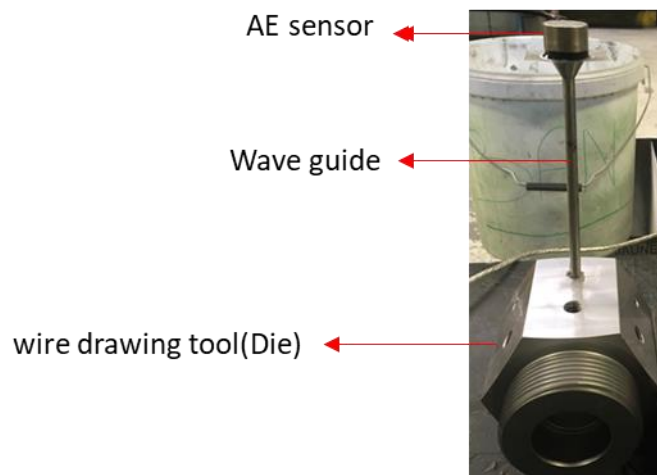
Fig. 8: Instrumentation of the wire drawing tool by AE sensor.

In the present study, two damage situations were analyzed:

- scratches caused by the wear of the wire drawing machine (die): in this case a specific tool has been designed to voluntarily generate scratches. It consist of a screw placed at the level of the tool holder in order to simulate scratches caused by wear or breakage of the die (Fig. 9),
- scratches caused by a lack of surface treatment (lubrication): in this case, a variation in the state of surface lubrication has been made (Fig. 9).
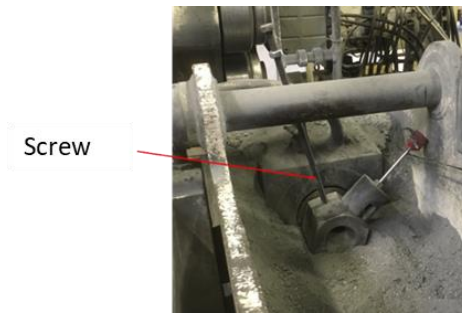
Fig. 9: Tools for generating scratches during drawing (1) at the level of the drawing tool (2) upstream of the tool.

Zones without lubrification
Zones with lubrification
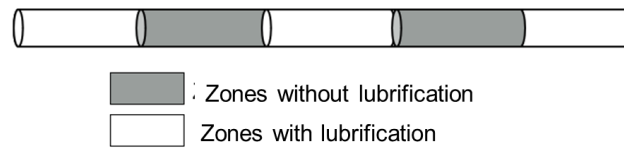
Fig. 10: Scheme of the procedure for a cable with and without surface treatment.

Specific steel screws (to prevent wear caused by friction between the wire and the screw allowing scratching) have been manufactured. This is intended to associate a default form with an AE signature in Fig. 11.

screw

Extremity form

Wire
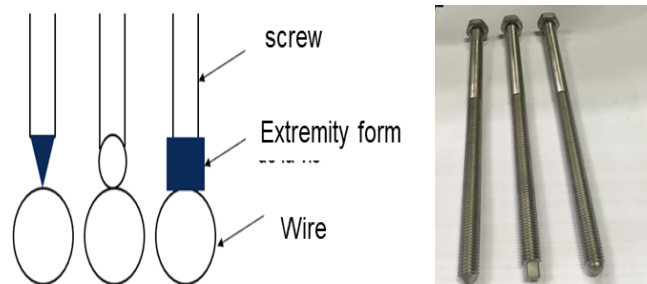
Fig. 11: The different screws used in the feasibility tests.

3.2 Results & analysis – reference phase

Tests were carried out on 4 different steel grades as well as different speeds and section reductions in Table 1.

Table 1: Parameter of the series produced (material references, drawing speed, section reduction).

	MATERIAL REFERENCES	PARAMETERS
01	C10CD1740Y01	RS : 18 --> 17,35-40 mm / V = 2 m.s-1
02	23MB4D1717M55	RS : 17,9 --> 17,17 mm / V = 1,80 m.s-1
03	23MB4D1717M55	RS : 17,8 --> 17,17 mm / V = 1,80 m.s-1
04	23MB4D1789G55	RS : 19,05 --> 17,8 mm/ V = 2,25 m.s-1

Fig. 12 shows the evolution of the RMS value as function of time during the drawing of the four cables.
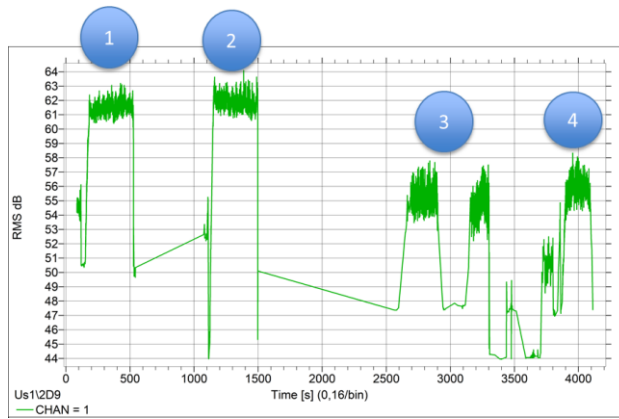
Fig. 12: Learning phase - evolution of the RMS value as a function of time.

We observe that the RMS reference level mainly depends on:
- type of material,
- wire drawing speed,
- section reduction level achieved.

3.3 Results & analysis – scratch generation phase

Table 2 summarizes the scratch generation steps with the different tools.

Table 2: Summary of the tests carried out.

MATERIAL REFERENCES	EXTREMITY FORM
23MB4D1717M55	triangular
23MB4D1717M55	triangular
C10C1650Y05	triangular => square => circular

Fig. 13 shows the evolution of the RMS value as function of time:
- the scratches generated with the different tools show a clear increase in RMS compared to the reference value (reference value varies depending on the material in particular),
- the dimensions of the scratches generated have an impact on the AE response,
- the largest scratches (square screw) have the highest RMS levels, then the scratches generated by a round screw and finally those generated by a triangular screw.
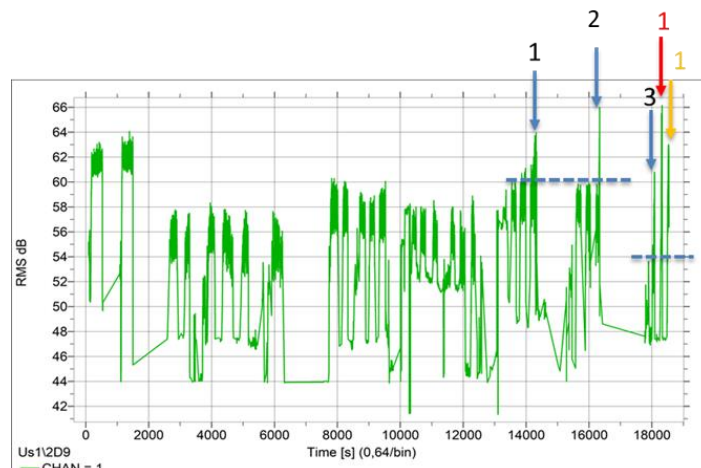
Fig. 13: Scratch phase - evolution of the RMS value as a function of time.

3.4 Results & analysis – variation of the surface treatment phase

In this phase, the impact of the surface treatment condition on the AE data is analyzed. Fig. 14 presents the evolution of the RMS as a function of time for the cable cases with/without polymer. The lack of polymer causes a significant increase in the RMS value (about 6 dB compared to the reference threshold).
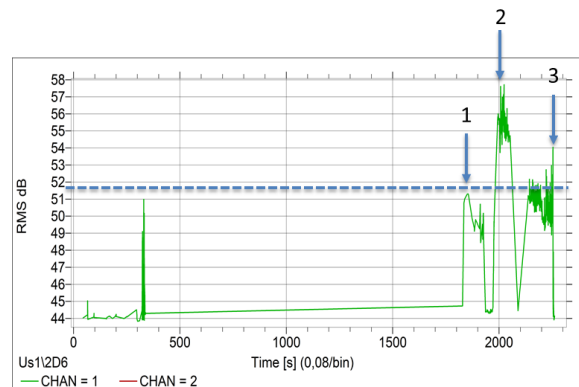
Fig. 14: Evolution of the RMS as a function of time for the cases of a cable with polymer (1 and 3) and without polymer (2).

3.5 Conclusions

In this first part of this document, the feasibility of monitoring the wire drawing process by AE in real time has been studied:

- the experimental plan developed enable both to respond to the difficulties of instrumentation and also to the needs of monitoring the wire drawing process,
- the AE method has shown its potential to detect scratches at the wire drawing tool,
- the EA method has also shown its sensitivity in detecting the lack of surface treatment,
- RMS value tracking is well suited for wire drawing process monitoring,
- the reference threshold may vary depending in particular on the material of the cable.

4. General conclusions

In this paper, on-line monitoring of two manufacturing process (additive manufacturing and wire drawing) based on acoustic emission are presented. In the case of additive manufacturing, the problem of cracks that occur in particular during laser impacts on thin layers and without support has been studied. The AE results obtained show the possibility of detecting this type of damage with a temporal monitoring of the intensity of the signal generated but also by a 2D localization on the plane of the location of the sensors. Concerning wire drawing, the problem of scratches on the finished cable was first considered by considering the wear of the die but also the lack of surface treatment (lubrication). The AE results obtained and in particular the monitoring of the RMS value show the sensitivity of AE to this type of damage.

In view of this study, other AE monitoring feasibility of new manufacturing processes (ex: clipping the clamps, …) are in progress. the final objective is to develop a new AE demonstrator complementary to MOST meeting the needs of these applications.

5. References

[1] A. Saidoun et H.Catherine, «Monitoring of Stamping By Acoustic Emission (AE), »Jornal of Acoustic Emission, pp. S20-S30, 2018.

[2] D. Kouprianoff, I. Yadroitsava, A. d. Plessis, N. Luwes et I. Yadroitsev, «Monitoring of Laser Powder Bed Fusion by Acoustic Emission : Investigation of Single Tracks ans Layers,» Frontiers in Mechanical Engineering, vol. 7, 2021.

ACOUSTIC EMISSION MONITORING OF IMMERSION QUENCHING BATH ATTRIBUTES

Bor Mojškerc[1,*], Janez Grum[1], Tomaž Kek[1] and Roman Šturm[1]

[1]Faculty of Mechanical Engineering, University of Ljubljana
*Correspondence: bor.mojskerc@fs.uni-lj.si

ABSTRACT

This paper describes the use of acoustic emission (AE) testing for monitoring immersion quenching bath attributes. Immersion quenching is a heat treatment process used to change the mechanical properties of metallic workpieces. The quenching bath cooling attributes degrade with prolonged use, thus affecting the workpiece mechanical properties. A non-destructive monitoring method of the quenching bath is required. An AE measurement system is proposed for this purpose. Steel specimens are quenched in tap water, deionized water, 5 % NaCl-water solution and 5 % detergent-water solution. AE is measured with four piezoelectric sensors. The influence of quenching bath attributes on specimen cooling is described together with the measured AE signals. AE signal peak amplitude diagrams are evaluated. A reference AE peak amplitude signal is presented with the measurements. The quenching bath attribute assessment method is established by monitoring the amount of outlying AE signals in regard to the reference AE signal. The results confirm that AE monitoring provides a decent way of assessing quenching bath attributes and thus also the quenched specimen mechanical properties.

Keywords: Acoustic emission, non-destructive testing, immersion quenching, heat treatment.

1. Introduction

The process of heat treatment is often used to change mechanical properties of metallic materials. Appropriately heat treated workpieces exhibit a longer working period and a higher monetary value. Properly heat treated steel is an integral part of different industries. The immersion quenching of steel improves hardness and strength via a martensitic transformation. Material mechanical properties are influenced by quenching bath attributes, such as quenchant type, temperature, agitation and concentration [1, 2].

In order to achieve a desirable quality of heat treated workpieces, the quenching process should be monitored using non-destructive testing. Acoustic emission (AE) testing can be used in monitoring a variety of objects, structures and manufacturing processes. Recent research shows an interest in monitoring quenching via measuring an acoustic signature in regard to the workpiece mechanical properties. The acoustic signature can be used to evaluate the quenching process deviations.

Kudo et al. [3] used pattern recognition to detect boiling on a steel heater. Kichigin et al. [4] researched boiling during quenching of steel specimens in various quenching baths. Specimen temperature was correlated to frequency and amplitude properties of boiling. Okumiya et al. [5, 6] investigated quenching heat transfer stages. The acoustic signal frequencies were examined for

film boiling, nucleate boiling and convection. Narazaki et al. [7] quenched Ag specimens and presented the relation between sound pressure, workpiece temperature and heat transfer phases. Establishing a correlation of acoustic characteristics with workpiece mechanical properties was proposed. Kobasko et al. [8, 9] proposed an acoustic method of monitoring quenching quality in regard to heat transfer phases. Grum and Ravnik [10, 11] presented the frequency and amplitude attributes of acoustic signals during quenching of various steel specimens in water or in water-polymer solutions. The signals were measured with a hydrophone. Prezelj and Čudina [12] used a hydrophone to investigate steel quenching in water-polymer solutions with various concentrations. Erich et al. [13] examined the relation between acoustic signals during quenching of steel and properties after quenching. Nikhare et al. [14] evaluated the relation of the acoustic signal and specimen size or temperature for quenching of tool steel. Mojškerc et al. [15, 16] presented a method of monitoring steel quenching with non-destructive AE measurements.

This paper provides an AE method of monitoring quenching bath cooling conditions in order to establish improved control of liquid quenching baths. This is achieved with a comparison of the amount of outlying AE signals when quenching in various baths.

2. Experimental methods

A steel for quenching and tempering 25CrMo4 was used in the experiments. The steel type is used in the aviation, automotive and machine industry. Circular steel bars were cut and machined to dimensions of ϕ24x100 mm. Twelve specimens were produced for quenching in four different quenching baths.

Specimens were heated in an Ar inert gas furnace to reduce oxidation and its impact on generated AE signals. The austenitization temperature and time were set to 880 °C and 30 min. Following heating, each specimen was quenched in a designated bath with a temperature of 25 °C:

- Tap water
- Deionized water
- 5 % salt-water solution
- 5 % detergent-water solution

Deionized water is used for quenching due to its stability in comparison with tap water. Tap water contains gases, salt particles and other substances which affect the quenching process. Quenching bath salt contamination leads to a higher cooling rate. A salt-water solution was used to demonstrate this effect. Specimen cleaning agents can have an effect on cooling attributes. A detergent-water solution was used to investigate the bath contamination with a cleaning agent.

During quenching, events such as film boiling and nucleate boiling can be observed. These events lead to sound pressure variations and the generation of AE. The generated AE can be measured using piezoelectric sensors positioned on the quenching bath. The used experimental system is presented in Fig. 1. Four piezoelectric AE sensors VS150-M (Vallen Systeme) were used. The mounted sensors were connected with preamplifiers to the AMSY-5 AE measuring device.
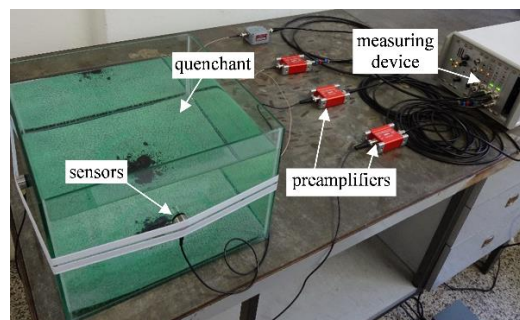
Fig. 1: Experimental system for immersion quenching of steel and AE measurements.

3.   Results and discussion

AE peak amplitude for specimen quenching in various baths is presented in Fig. 2 (a)-(d) for four AE channels. Heat transfer phases such as film boiling, transition, nucleate boiling and convection can be observed for tap water quenching. Film boiling has a short duration and high AE peak amplitude. The AE peak amplitude decreases with nucleate boiling transition. The number and size of vapour bubbles also decrease. Only a few vapour bubbles can be observed in the convection stage.

Quenching in deionized water exhibits a longer AE signal duration in comparison with quenching in tap water. During nucleate boiling, individual larger bubbles with higher AE peak amplitude can be observed. This occurs due to the mineral ion absence promoting the formation of smaller bubbles.

In comparison with quenching in tap water or deionized water, a similar AE signal can be seen when quenching in 5 % salt-water solution. Film boiling shows a shorter duration due to the addition of salt. Concentrated surface boiling can be observed at the end of the AE signal, causing a temporary increase in AE peak amplitude.

In comparison with other quenchants, a significant difference in cooling attributes and AE signals is observed for quenching in 5 % detergent-water solution. After specimen submersion, formation of a detergent film occurs, causing a relatively low cooling rate with constant AE peak amplitude. After a time period of 20 s, smaller bubbles combine to form a thin vapour film with explosive nucleate boiling on the bottom side of the specimen. During explosive boiling, the AE peak amplitude increases significantly. The bubble formation intensity and the AE peak amplitude decrease with further specimen cooling. A longer AE signal duration occurs in comparison with previous quenchants.
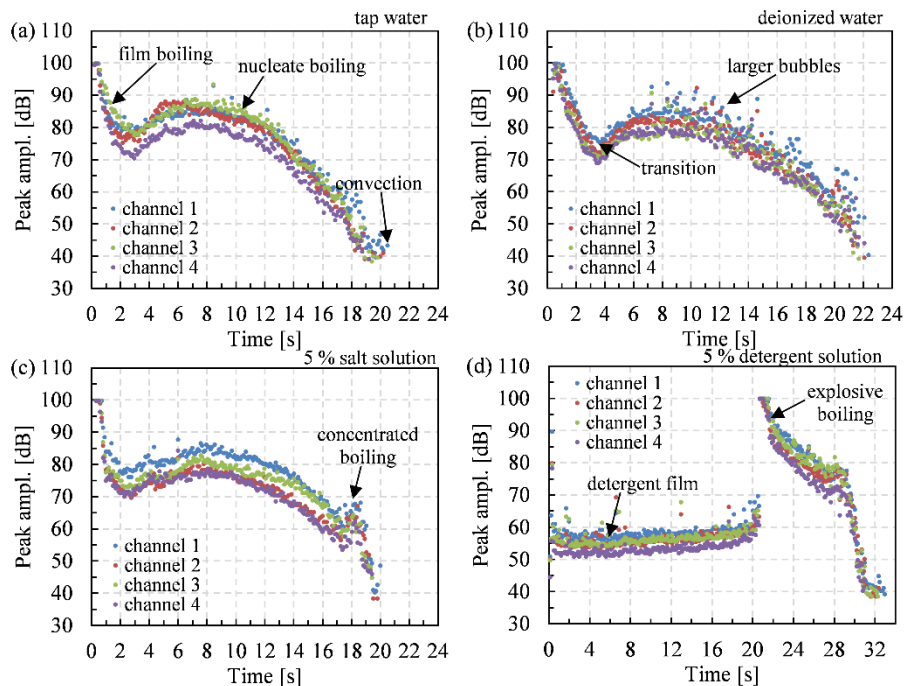
Fig. 2: AE peak amplitude for quenching in (a) tap water, (b) deionized water, (c) 5 % salt-water solution and (d) 5 % detergent-water solution.

AE peak amplitude for three specimen quenchings with four channel measurements is presented in Fig. 3 (a)-(d) for various quenching baths. When quenching in tap water, AE signal scatter can be observed at the end of nucleate boiling. This occurs due to deviation of AE signal duration caused by the generation of individual, smaller bubbles on the specimen surface.

Quenching in deionized water exhibits larger bubbles in the nucleate boiling stage, which lead to a slight AE signal scatter. The appearance of isolated bubbles with low AE peak amplitude can be observed at the end of nucleate boiling, similar to quenching in water.

Short duration film boiling, relatively constant nucleate boiling and concentrated boiling with an increase of AE peak amplitude occur when quenching in 5 % salt-water solution.

Quenching the specimens in 5 % detergent-water solution leads to high AE peak amplitude variations for the three quenching tests. The deviations of explosive boiling start time and AE signal duration imply process instability.
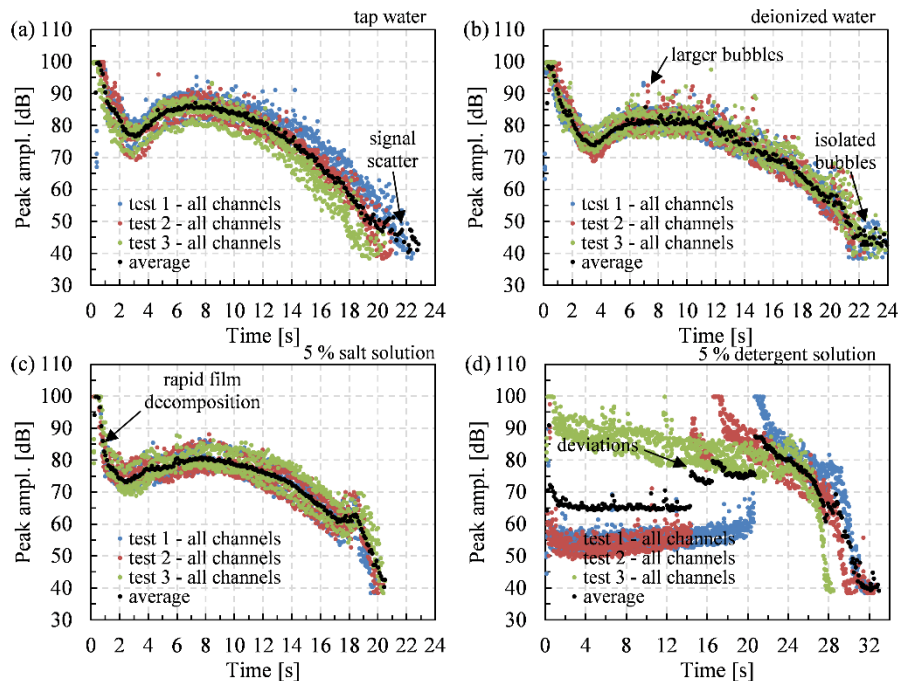
Fig. 3: Test and channel average of AE peak amplitude for quenching in (a) tap water, (b) deionized water, (c) 5 % salt-water solution and (d) 5 % detergent-water solution.

AE peak amplitude for quenching in tap water was chosen as the reference AE signal for monitoring changes in the quenching bath cooling attributes. The AE peak amplitude was divided into time periods of 0.5 s and standard deviation for four measuring channels and three quenching tests was calculated. Quenching bath adequacy was determined with the number of outlying AE signals. Comparison results are presented in Fig. 4 (a)-(d). The average AE peak amplitude for quenching in tap water is located within the reference zone.

For quenching in deionized water, outlying AE signals can be detected at the start and towards the end of nucleate boiling. In comparison with tap water quenching, the AE and cooling characteristics during deionized water quenching have changed.

For quenching in 5 % salt-water solution, the outlying AE signals are measured during film boiling and nucleate boiling. AE peak amplitude of concentrated boiling is located within the reference zone. A shorter AE signal duration can be observed in comparison with the reference zone.

In comparison with the reference AE interval, high deviations occur for quenching in 5 % detergent-water solution. Nearly all of the AE signal packets are outside of the prescribed zone.
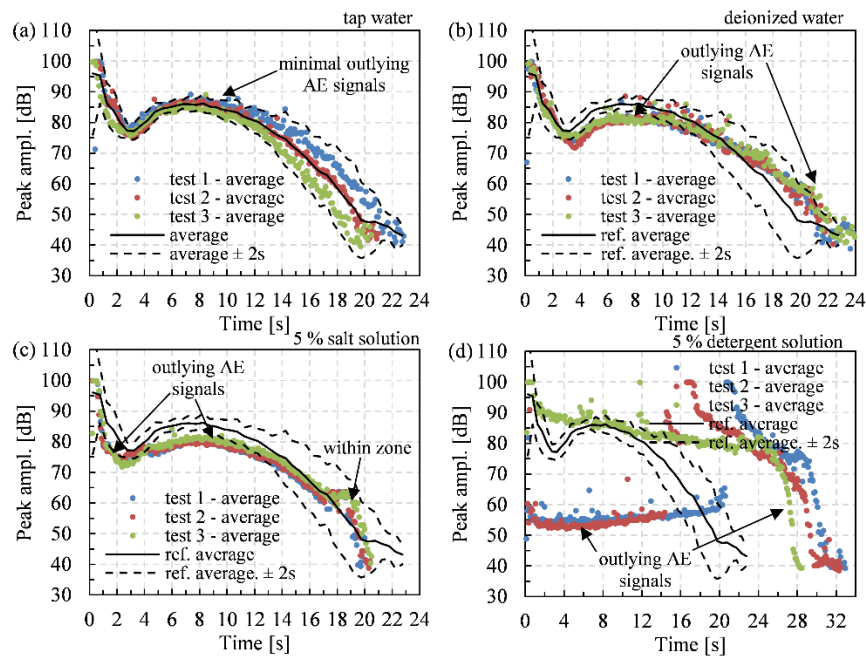
Fig. 4: Reference zone of AE peak amplitude for quenching in (a) tap water, (b) deionized water, (c) 5 % salt-water solution and (d) 5 % detergent-water solution.

A comparison of the number of outlying AE signals is presented in Fig. 5. Quenchants with outlying AE signals above 10 % were deemed unsuitable for additional quenching. The amount of outlying AE signals is within the acceptable zone for quenching in tap water. For quenching in deionized water, a high amount of outlying AE signals can be seen. For quenching in 5 % salt-water solution, the amount of outlying AE signals is further increased. For quenching in 5 % detergent-water solution, over 70 % of the detected AE signals exceed the acceptable zone.
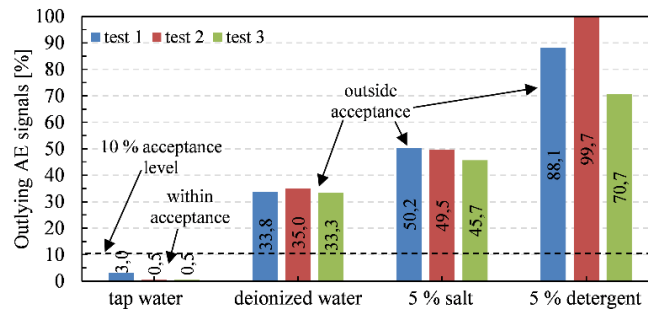
Fig. 5: Comparison of the amount of outlying AE signals for various quenching baths.

4. Conclusions

This paper investigated AE signals during immersion quenching of steel specimens. Experiments were performed for quenching in tap water, deionized water, 5 % salt-water solution and 5 % detergent-water solution. The AE signals generated during the process were measured. The variations of quenching bath cooling attributes were investigated with AE signal peak amplitude. A reference zone for acceptable AE signals was established and a comparison between quenchants was made using the amount of outlying AE signals during quenching. The quenching bath maintenance and cleaning operation period can last from a week up to months. The research results imply that the presented AE method could be used for improving the timing of quenching bath maintenance, while also providing non-destructive quality monitoring of workpieces.

161

5. References

[1] Liščić B., Tensi H.M., Canale L.C.F., Totten G.E. (2010). Quenching Theory and Technology, 2nd edition. CRC Press.
[2] Sinha A.K. (2003). Physical Metallurgy Handbook, 1st edition. McGraw-Hill.
[3] Kudo K., Ohta M., Ohsawa T. (1985). Boiling detection experiments by acoustic analysis applying linear discriminant function. Progress in Nuclear Energy, vol. 15, p. 763-769.
[4] Kichigin A.M., Povsten S.G. and Tyltin A.A. (1997). Acoustic control over the cooling process in the course of quenching. Heat Transfer Research, vol. 28, p. 64-68.
[5] Okumiya M., Tsunekawa Y., Doi K., Ikuta H., Tanaka Y., Tomita Y., Nagai T. (2007). Apply the sound of boiling to discrimination of cooling process. Conference proceedings, Proceedings of the 16th International Federation for Heat Treatment and Surface Engineering Congress, Brisbane, Australia.
[6] Okumiya M., Tsunekawa Y., Doi K., Ikuta H., Tanaka Y., Tomita Y., Nagai T. (2008). Acoustic technique to discriminate boiling state during quenching. International Heat Treatment and Surface Engineering, vol. 2, p. 131-134.
[7] Narazaki M., Takatsudo I., Fuchizawa S. (1988). Boiling noise in the water quenching of hot metals. Netsu Shori - Journal of the Japan Society for Heat Treatment, vol. 28, p. 93-99.
[8] Kobasko N.I., Moskalenko A.A., Deyneko L.N., Dobryvechir V. (2009). Electrical and noise control systems for analyzing film and nucleate boiling processes. Conference proceedings, Proceedings of the 7th IASME/WSEAS International Conference on Heat Transfer, Thermal Engineering and Environment, Moscow, Russia.
[9] Kobasko N.I., Moskalenko A.A., Deyneko L.N. (2014). Investigations of nucleate boiling processes during quenching based on possibilites of noise control system. Materials Performance and Characterization, vol. 3, p. 86-96.
[10] Ravnik F., Grum J. (2009). Sound emitted at boundary layer during steel quenching. Strojniški vestnik - Journal of Mechanical Engineering, vol. 55, p. 199-209.
[11] Grum J., Ravnik F. (2006). Investigation of sound phenomena during quenching process. International Journal of Materials and Product Technology, vol. 27, p. 266-288.
[12] Prezelj J., Čudina M. (2011). A sound pressure field during the quenching of a steel specimen in different water solutions. Metalurgija, vol. 50, p. 37-40.
[13] Erich N.J., Nikhare C., Conklin C., Loker D.R. (2015). Study of acoustic signals and mechanical properties dependence during cold drawn A36 steel quenching. Conference proceedings, Proceedings of the International Deep Drawing Research Group, Shanghai, China.
[14] Nikhare C.P., Ragai I., Loker D., Sweeney S., Conklin C., Roth J.T. (2015). Investigation of acoustic signals during W1 tool steel quenching. Conference proceedings, Proceedings of the ASME International Manufacturing Science and Engineering Conference. Charlotte, North Carolina, United States of America.
[15] Mojškerc B., Kek T., Grum J. (2018). Feasibility study of monitoring the steel quenching process using acoustic emission technology. Applied Acoustics, vol. 129, p. 335-345.
[16] Mojškerc B., Grum J., Kek T. (2018). Acoustic emission characterisation of specimen surface-area-to-volume ratio during immersion quenching. Insight, vol. 61, p. 257-263.

USE OF ACOUSTIC EMISSION TO MONITOR ADIPIC ACID CRYSTALLIZATION

Roger de Souza Lima[1,*], Ana Cameirão[1] and Eric Serris[1]

[1]Mines Saint-Etienne, Univ Lyon, CNRS, UMR 5307, Centre SPIN, F – 42023 Saint-Etienne, France
*Correspondence: roger.de-souza-lima@emse.fr

ABSTRACT

Crystallization is regarded as an important unit operation for separation and purification. However, it is still difficult to control or to optimize the crystallization process due to the complexity of the coupled phenomena taking place simultaneously in the liquid and solid phases. In order to overcome such drawbacks, different analytical technologies have been implemented in the literature for monitoring the key crystallization parameters. In our work, a multi-probe monitoring system composed of acoustic emission, spectroscopic and imaging probes was applied to the crystallization of a model system (an aqueous solution of adipic acid). The crystallization was carried out under vacuum or atmospheric pressures. The goal was to demonstrate the usefulness of the multi-probe system for monitoring the crystallization process, with special attention to the information given by the acoustic emission, in terms of absolute energy, and the spectroscopic probes. Firstly, the influence of the crystal load on the absolute energy is demonstrated. Then, it is shown how the absolute energy can capture the modifications in the crystallization dynamics due to the different experimental conditions. Such dynamics can also be observed from other acoustic emission descriptors.

Keywords: Multi-probe monitoring system, adipic acid, semi-batch crystallization, absolute energy.

1. Introduction

Crystallization is a common process for purification and formulation of crystalline materials in the industrial scale. Applications can be found in various fields, such as pharmaceutical, chemicals, food chemicals, etc [1]. Furthermore, different compounds, either organic or inorganic, can thus be crystallized at different production rates (depending on the size of the crystallizer and the application). As a result, crystallization is a very versatile operation. Regarding the formation of crystals, the onset of crystallization is possible once a certain supersaturation is achieved (the solute solubility threshold is exceeded and the system is in a thermodynamically unstable state). The formation of a crystal is composed of two main steps: nucleation, which is the birth of a new crystal, and growth, where the volume of the crystal increases over time. Other phenomena, such as agglomeration or breakage of the generated crystals, have an influence on the product final size distribution [1].

The control or the optimization of the crystallization process are complex, due to the influence of the following parameters during the formation of the solid phase: the local supersaturation and

hydrodynamic conditions, the crystallizer design, the crystallization kinetics, the potential formation of polymorphic phases, etc. In this way, the control of this operation requires a good experimental knowledge of the physicochemical properties of the product and the impact of the operating conditions on the kinetics of nucleation, growth, agglomeration as well as on the shape and size of the crystal. In order to better control the crystallization process, different analytical technologies have been developed in the literature for *in situ* monitoring the properties of the liquid and solid phases.

The acoustic emission method appears to be an interesting *in situ* method for real-time monitoring of industrial processes [2]. It is based on the measurement of the mechanical energy (in the form of a wave) produced within a material. Thanks to its non-intrusive and non-destructive character, the acoustic emission method has been used more frequently in the field of materials (aeronautics, automotive, building) [3], but applications in granulation in fluidized bed, powder compaction, heterogeneous reaction, drying and mixing powders [2, 3] have been developed. For the crystallization process, few papers have been published regarding the use of the acoustic emission method [2–7].

The present work deals with the application of acoustic emission, along with other analytical methods, to study the semi-batch crystallization of a model molecule under different operating conditions. After the introduction of the developed experimental set-up, the results are shown mainly in relation to the measured absolute energy (an acoustic parameter). The amplitude and number of counts are also presented as a function of the different crystallization trials.

2. Materials and methods

2.1 Investigated system

Adipic acid (Merck, Germany) was used as a model solute. Such compound is mainly employed as a precursor for the nylon production. Adipic acid was used in previous acoustic emission experiments in our group [8]. Deionized water was used for the preparation of the solutions.

2.2 Experimental set-up

The experimental set-up is presented in Fig. 1. Two jacketed glass vessels were employed in the crystallization experiments: a smaller vessel (with approximately 1 L of solution), which was used for feeding solution to the crystallization vessel (with initially 2.2 L of solution). The latter was equipped with a Rushton turbine. A variety of probes were added to the crystallizer for the acquisition of different process data. Apart from the usual temperature and pressure probes, the analytical methods consisted of an ATR-FTIR (attenuated total reflection combined with a Fourier transform infrared spectrometer) spectroscopy (Bruker, France), a camera immersed in the liquid phase (*EZProbe*, LAGEPP, France) and acoustic emission probes (MISTRAS, France).
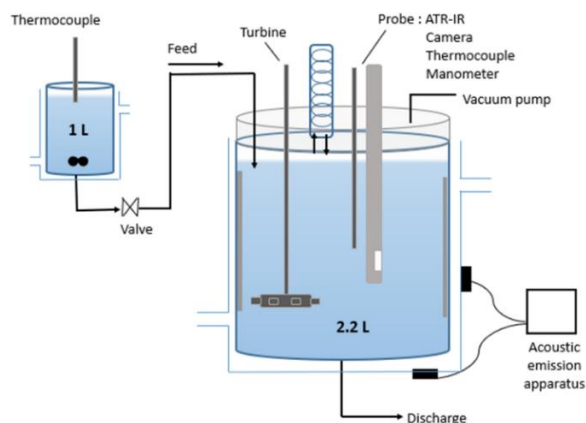
Fig. 1: Semi-batch crystallization set-up.

The ATR-FTIR was employed for the measurement of the dissolved solute mass fraction in the liquid phase, after conversion of the measured infrared spectra to mass fraction values with the help of a calibration curve. The spectra were acquired with a spectral resolution of 4 cm^{-1} every 10 seconds. The immersed camera was used for the acquisition of data related to the crystal size through time, with an observation zone of 1 x 1.2 mm and pixel size of 2 x 2 μm. Apart from a few representative crystal images, the results from the image processing will not be presented here. The acoustic emission probe was used for monitoring the dynamics of the crystallization process during the experiments. The acoustic emission parameters are given in Section 2.4.

2.3 Experimental procedure

The experimental conditions are presented in Table 1. The solution in the feeding vessel is undersaturated (solute concentration inferior to the saturation, or equilibrium, concentration) and at atmospheric pressure for all experiments. The crystallization vessel, on the other hand, is at saturated conditions and can be either at atmospheric pressure or under vacuum. All trials were carried out in *triplicate*.

Table 1: Experimental conditions related to the feeding vessel and the crystallizer.

PARAMETER	FEEDING VESSEL	CRYSTALLIZATION VESSEL
Temperature	60 °C	20 °C
Dissolved solute initial mass fraction	9,0 % w/w	1.8 % w/w
Pressure	1 bar	1 bar or 200 mbar
Agitation speed	-	400 rpm

In the beginning of each experiment, the hot solution in the feeding vessel was transferred to the crystallizer. As a result, the volume of the liquid in the latter was gradually increased. Once all the solution from the feeding vessel was transferred, the experiment was carried with only the crystallization vessel. At this point, the volume of the solution in the crystallizer remained constant.

2.4 Acoustic emission parameters

Two R15 acoustic emission sensors added to the set-up were positioned on the external lateral wall and on the bottom of the crystallization vessel. Coupling grease was used between the glass wall and the sensor for improving the transmitting efficiency of acoustic signals. The collected signals were amplified, filtered and processed with the help of the chart of digitalization PCI II (Mistras, France). As a result, different acoustic emission descriptors were obtained, such as the number of counts, the signal amplitude, frequency and absolute energy (defined from the integration of the acoustic signal).

A threshold level of 25 dB was applied for the measurements, in order to reduce the influence of the set-up noise (agitation, thermostatic bath operation, etc.). The sampling rate was 1 000 kHz, the sensors were connected to a pre-amplifier of 40 dB and an analog filter set between 100 and 3 000 kHz. The peak definition time (PDT), the hit definition time (HDT) and the hit lockout time (HLT) were set at 100, 200 and 400 μs, respectively. The PDT parameter specifies the time allowed for the determination of the signal maximum, or amplitude. The HDT parameter specifies the end of an acoustic event, which means that the event is ended if the threshold is not exceeded for a certain time. The HLT parameter defines the time from which a new acoustic event can take place [9].

3. Results and discussion

3.1 System dynamics from the temperature profiles of the liquid phase

In order to help understanding the dynamics in the crystallization vessel during a semi-batch trial, the temperature profiles of the liquid phase over time are plotted in Fig. 2. The orange curves correspond to the trials carried out with the crystallization vessel under vacuum, while the blue curves represent the trials at atmospheric pressure.

As the crystallization vessel was fed with the hot solution from the feeding vessel, starting at the point (I) in Fig. 2, the temperature of the liquid phase was gradually increased. This temperature rose until the end of the feeding period, marked by the point (II) in Fig. 2, then the temperature of the liquid phase was cooled down by the jacket towards the initial setpoint. For the trials carried out under vacuum, the temperature increase is greater and faster than for the trials at atmospheric pressure. Indeed, the temperature rises at a rate of 2.8 °C/min for the trials under vacuum, against 0.5 °C/min for the trials at atmospheric pressure. Such difference is related to the feed flow rate used in these two pressure conditions. For the vacuum conditions, the feed flow rate was 7.8 g/s, which is approximately six times greater than the flow rate at atmospheric pressure (1.4 g/s).
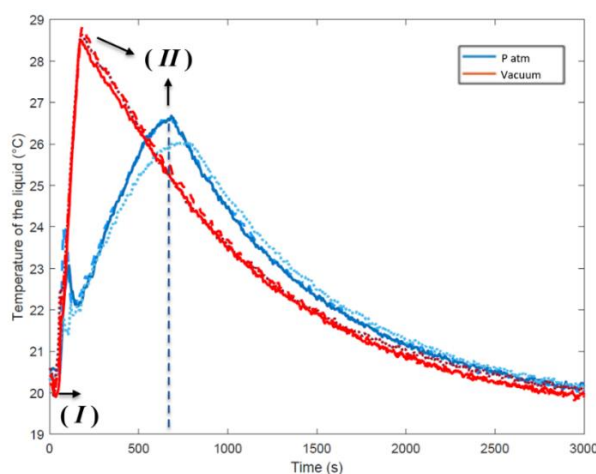
Fig. 2: Temperature profiles of the liquid phase in the crystallization vessel during a semi-batch trial. The blue curves correspond to the trials at atmospheric pressure, while the red curves correspond to the trials under vacuum. Additionally, the points (I) and (II) refer to the beginning and the end of the feeding period.

3.2 Representative images of the adipic acid crystals

The adipic acid crystals generated during the trials at atmospheric pressure and under vacuum are presented in Fig. 3, in the top row and lower row, respectively. Regarding the trial at atmospheric pressure, the crystals were firstly detected around 300 s with a minimum size at approximately 50 μm. As the time progressed, at 480 and 600 s in Fig. 3, the crystal number and size increased. A single adipic acid crystal, mostly transparent in the images, had a hexagonal shape, but crystal agglomerates with diverse geometrical forms and opaque were also observed in the images. Regarding the images observed during the trial under vacuum, during the feeding period, the majority of the objects detected in the images were bubbles (at 60 s in Fig. 3). As the solution cooled down (after 200 s), the crystals could be neatly observed in the images. No modification on the crystal shape was observed from the modification of the crystallization pressure conditions. Despite the trial duration of 3 000 s, no image could be obtained after 1 000 s due to the blockage of the camera observation window by an accumulation of crystals.
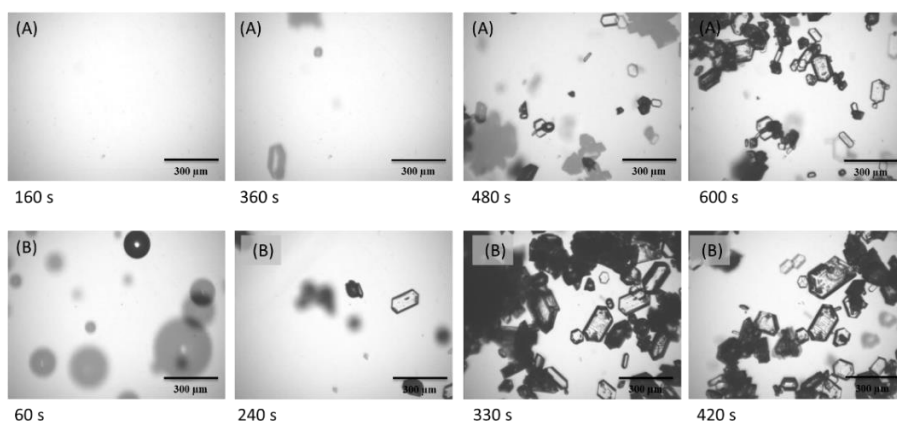
Fig. 3: Representative images of the adipic acid crystals at different time instants during the trials at atmospheric pressure (top row images – A) and under vacuum (lower row images – B).

3.3 Absolute energy as a descriptor for monitoring the crystallization process

From the acoustic emission signals, a variety of descriptors can be extracted (number of counts, signal frequency and amplitude, etc.). Consequently, it is important to find, among such rich information, the most effective acoustic descriptor to first describe a given phenomenon. The choice of such descriptor is based upon its sensibility to the modifications happening during the studied phenomenon and the ease at which such descriptor can be interpreted. For the present work, the absolute energy was used as an indicator of the dynamics during the crystallization of adipic acid.

In Fig. 4, the absolute energy is plotted through time for the trials at atmospheric pressure (blue curve) and under vacuum (orange curve). The absolute energy was calculated every 100 ms and was given in attoJoule (1 aJ = 10^{-18} J). The lower figure represents the absolute energy measured during the first 1 000 s of the trial. Starting with the trial at atmospheric pressure (blue line), most of the measured data were inferior to 0.5×10^4 aJ until approximately 300 s and then increased gradually towards 2.5×10^5 aJ at the end of the trial. For the trial under vacuum (orange line), an increase in the absolute energy was measured at around 50 s and once more after 200 s. At the end of the trial under vacuum, the absolute energy was approximately 1×10^5 aJ.

Regarding the crystallization process, for both trials, the feeding period started at 50 s. The appearance of the first crystals could be detected visually at approximately 300 s for the trial at atmospheric pressure (blue line) and as soon as the feeding period started for the trial under vacuum (orange line). Consequently, for the trial at atmospheric pressure, between 50 s and 300 s, no crystals were formed – at least not in enough quantity to provide any significant modification in the measured absolute energy. Most of the data obtained during this period were most likely to correspond to the bubbles created by the feed rate over the liquid surface in the crystallizer. After 300 s, at atmospheric pressure, the absolute energy was measured as a consequence of the crystallization dynamics taking place. As a matter of fact, the formation of crystals, their growth, agglomeration and breakage gave rise to a certain number of crystals in suspension with a certain particle size distribution. The collision between these particles and their environment generated the measured absolute energy.

Regarding the trial under vacuum (orange line), as soon as the feeding period started, the adipic acid crystals were formed. Additionally, such crystals were mostly concentrated on the surface of the liquid in the crystallizer and remained mostly "locked" in place despite the agitation in the vessel. After the end of the feeding period (around 200 s), the solution started to be cooled down and new crystals were formed, which correspond to the increase in the absolute energy after the indicated time. As the crystallization progressed and the crystal population varied in size distribution and number, the absolute energy values increased. It should be noted that the disturbance observed at 400 s in the orange line corresponds to an operator manipulation over the set-up.
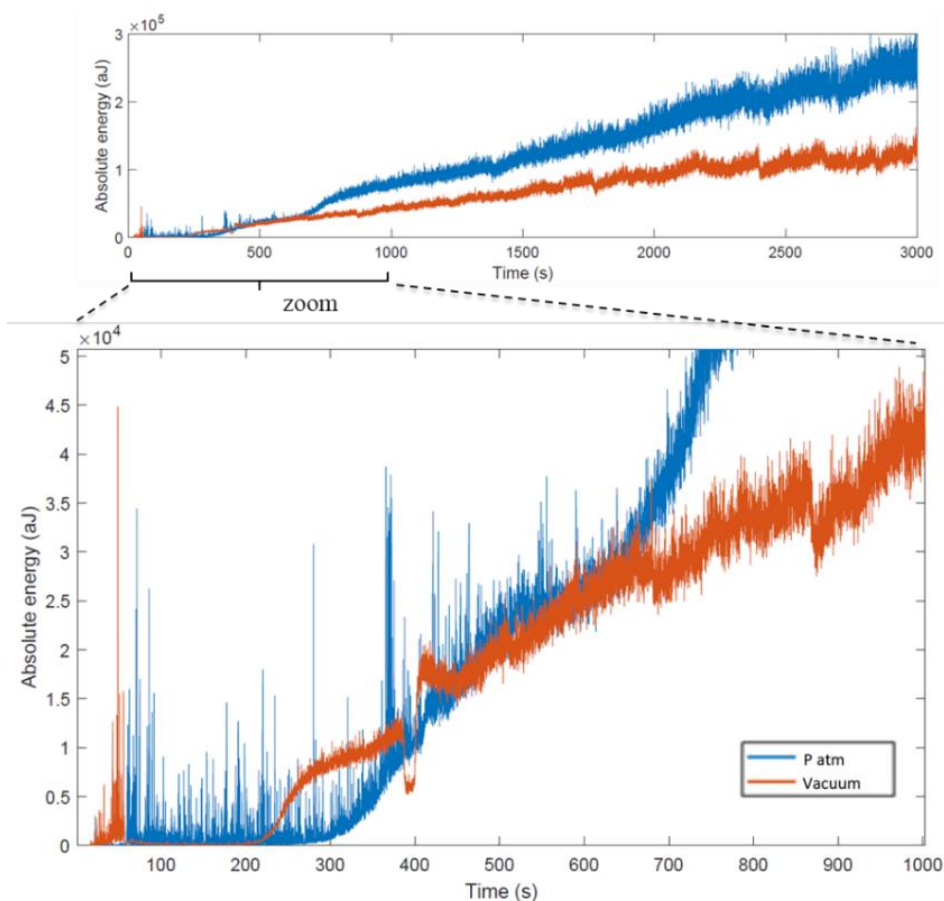
Fig. 4: Absolute energy acquired throughout the crystallization trial. The trials carried out at atmospheric pressure or under vacuum are represented by the blue and orange plots, respectively. The lower figure corresponds to the first 1000 s of the trial.

Regarding the difference in the absolute energy at the each of each trial (blue and orange plots), it is most likely a consequence of a difference in the mass of crystals in suspensions (which contribute to the generation of acoustic energy). As a matter of fact, in the trial under vacuum, a part of the formed crystals was concentrated at the liquid surface, while for the trial at atmospheric pressure, the crystals were mostly dispersed throughout the liquid phase. Thus, the crystals present at the liquid surface in the trial under vacuum did not contribute as much to the generation of acoustic energy, hence the absolute energy difference between the trials.

In order to demonstrate that the absolute energy was indeed correlated to the quantity of crystals in the liquid phase, the results from the ATR-FTIR spectroscopy were used. As a matter of fact, the measured spectra in the liquid phase were converted to dissolved adipic acid mass fraction with the help of a calibration curve. With the adipic acid mass fraction over time and the known total adipic acid mass in the system (constant), the mass of crystals could be calculated at each time instant from a mass balance. The calculated mass of crystals was then divided by the total mass of adipic acid in the system, which gave as a result the crystal load. The crystal load is plotted in Fig. 5 as a function of time (black line, right side of the plot), along the absolute energy (blue line, left side of the plot) for the trial at atmospheric pressure. Both absolute energy and crystal load showed the formation of crystals, with an increase in their respective values, after approximately the same time, 300 s and 400 s, respectively. Additionally, the relation between these two variables can be expressed as shown in Fig. 6. From this figure, the absolute energy varies the most once the crystal load is superior to 0.25. When the crystal load is inferior to 0.25, the absolute energy varies from zero to approximately 0.25×10^5 aJ. Once the crystal load increases from 0.25 to 0.47, the absolute energy rises from 0.25×10^5 aJ to 2.5×10^5 aJ.
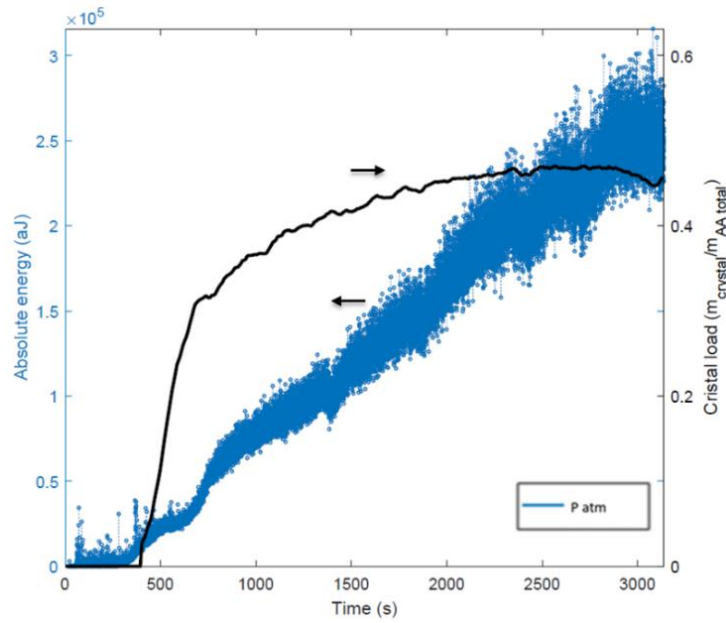
Fig. 5: Crystal load (black line, right side of the plot) and absolute energy (blue line, left side of the plot) as a function of time. The crystal load corresponds to the mass of crystals over the total mass of adipic acid in the system.
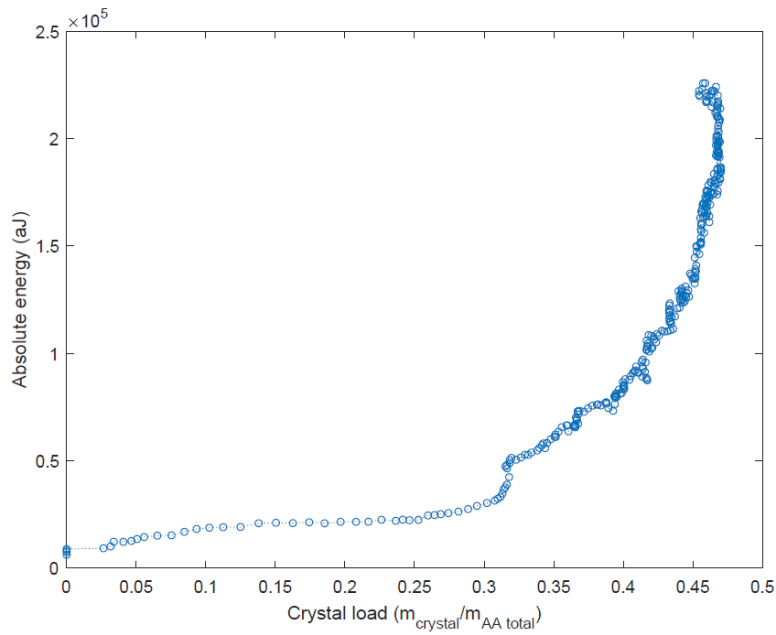
Fig. 6: Absolute energy as a function of the crystal load for the trial at atmospheric pressure.

3.4 Other acoustic emission descriptors

As mentioned previously, different acoustic descriptors are obtained from the acoustic signals. Apart from the absolute energy showed in the previous sections, the number of counts and the signal amplitude for the crystallization trials are shown in Fig. 7. The blue and red points correspond to the trials at atmospheric pressure and under vacuum. The data is presented for the first 1 000 s of each trial (from a total of 3 000 s), since the process dynamics change the most within this time period. The number of counts represents the number of times the acoustic signal threshold is crossed. The signal amplitude and frequency are characteristics of the wave form and are calculated through time.

Regarding the number of counts in the top plot in Fig. 7, three slopes can be identified for the trial at atmospheric pressure (blue points). A first increase in the number of counts from the beginning of the trial until a point around 250 s (number of counts inferior to 2.5×10^6), a second slope where the number of counts increases rapidly (number of counts inferior to 5×10^6) and a third slope that remains approximately the same until de end of the trial. The first slope corresponds to the noise detected during the feeding period until the formation of the first crystals. The second slope was most likely to belong to the birth of the new crystals and the third slope correspond to the other processes during crystallization: growth, agglomeration and breakage and eventually the formation of new crystals. For the trial under vacuum (red points), the following steps could be observed: a first increase in the number of counts, followed by a plateau, a second rapid increment in the measurement and a final steady increase in the number of counts.

Regarding the signal amplitude, there were clearly two patterns during the crystallization trial: for the first one, the signal amplitude varied from 25 dB up to 65 dB until 250 s or 300 s for the trials at atmospheric pressure and under vacuum (blue and red points), respectively. In the second phase, the signal amplitude remained between 50 and 60 dB for both trials. For the trial at atmospheric pressure (blue points), such transition corresponded to the formation of crystals in the liquid phase. For the trial under vacuum, this transition corresponded to the second mass production of crystals in the liquid phase (the first one corresponding to the beginning of the feeding period).
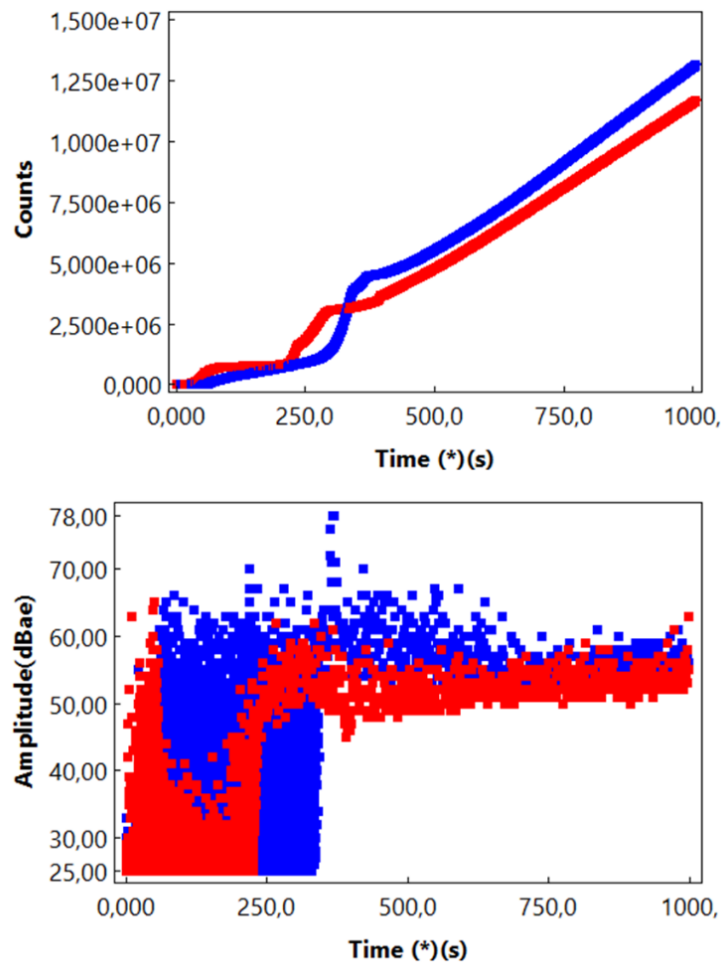
Fig. 7: For the trials of adipic acid crystallization, from top to bottom: number of counts, signal amplitude and signal frequency. The blue and red points correspond to the trials at atmospheric pressure and under vacuum, respectively.

4. Conclusions

A multi-probe system was employed for monitoring the semi-batch crystallization of an aqueous solution of adipic acid. After the presentation of the dynamics in the crystallizer from the temperature profiles, the acoustic emission data was presented in terms of absolute energy. Such parameter was found to be the most straightforward acoustic parameter to track the dynamics occurring during the formation of the crystals. As a matter of fact, the absolute energy could be used to track the onset of particle formation and increase of the crystal load, as a result of the correlation of the absolute energy with the data from the ATR-FTIR spectroscopy. Other acoustic descriptors, such as the number of counts and the signal amplitude could be used to complement the observations from the absolute energy measurements. The acoustic emission was found as an important tool to monitor modifications in the crystallizer, consequently the next steps of our studies will be the application of such technique to monitor the crystallization operation at the industrial scale. As a result, the next trials are expected to show the applicability of such analytical technique and its capacity for providing insightful information of an industrial crystallizer.

5. References

[1] Myerson, A., Ginde, R. (2002). Handbook of industrial crystallization: Chapter 2. Crystals, crystals growth and nucleation. Woburn: Butterworth-Heinemann, p. 33-65

[2] Gherras, N., Serris, E., Fevotte, G. (2012). Monitoring industrial pharmaceutical crystallization processes using acoustic emission in pure and impure media. International Journal of Pharmaceutics, vol. 439, no 1-2, p. 109-119

[3] Wang, X., Huang, Y., Michelitsch, T. (2019). Acoustic emission detection of crystallization in two forms: monohydrate and anhydrous citric acid. Pharmaceutical Development and Technology, vol. 24, p. 416-426

[4] Fevotte, G., Wang, X., Ouabbas, Y. (2014). Acoustic emission, a new sensor for monitoring industrial crystallization processes. IFAC Proceedings Volumes, vol. 47, p. 2727-2733

[5] Wang, X., Lu, J., Ching, C. (2007). Application of direct crystallization for racemic compound propranolol hydrochloride. Journal of Pharmaceutical Sciences, vol. 96, p. 2735-2745

[6] Lube, E., Slatkin, A. (1989). In-process monitoring of crystal perfection during melt growth. Journal of Crystal Growth, vol. 98, p. 817-826

[7] Wade, A (1990). Acoustic emission: Is industry listening? Chemometrics and Intelligent Laboratory Systems, vol. 8, p. 305-310

[8] Serris, E., Cameirao, A., Gruy, F. (2016). Monitoring industrial crystallization using acoustic emission. Conference proceedings, The 32nd European Conference on Acoustic Emission Testing (EWGAE 2016), Czech Society for NDT, European Working Group on Acoustic Emission, Sep 2016, Prague, Czech Republic. p. 451-460. Hal-014110018

[9] Unnthorsson, R. (2013). Acoustic emission – Research and Applications. Chapter 1: Hit Detection and Determination in AE Bursts. Intech, p. 1-19

ON TRAILING WAVES RATHER THAN LAMB WAVES BEING GENERATED BY BURIED IN-PLANE DIPOLES IN THICK PLATES

Marvin Hamstad[1] and Markus Sause[2]

[1]University of Denver, Denver, CO, USA; mhamstad@du.edu
[2]University of Augsburg, Institute of Materials Resource Management, Augsburg, Germany;
markus.sause@mrm.uni-augsburg.de

ABSTRACT

The potential for trailing waves (TWs) rather than Lamb waves to be observed in the out-of-plane displacement signals from acoustic emission (AE) sources in thick plates was examined. Finite element modeling (FEM) was done for buried in-plane dipole (IPD) sources in steel plates with thicknesses up to 125 mm and propagation distances from 250 mm to 1500 mm. The domain was large enough so that significant reflections were not observed during the primary signal arrivals. The run times extended to 1 ms. "Ring-type" sources were used so that axisymmetric modeling could be done. The rise time of the IPDs was typically 1 µs with a cosine-bell time dependence, and the two 1 N forces were spaced by 200 µm. The IPDs were located at several depths from very near the top surface of the plates to the midplane. The displacements as a function of time were obtained on both the top and bottom surfaces. The analysis primarily considered a bandpass of 80 kHz to 500 kHz. In addition, fast Fourier transform results and time/frequency analysis were used. The typical character of TWs consisted of a train of short wave-packets (each 10 to 25 microseconds). The significant-amplitude TW packets arrived after an arrival time corresponding to the Rayleigh wave velocity. The number of packets in the train increased with increasing propagation distance. The likelihood of the signals exhibiting TWs increased with increases in plate thickness, increases in the distance of the IPD below the surface of interest. The presence of the TWs complicates the determination of fixed velocity arrival times necessary for source location determination. Also, since TWs rather than Rayleigh waves appear for IPD depths at some distance below the surface used to sense AE signals, there are potential issues when the AE approach depends on a Rayleigh wave being present.

Keywords: In-plane dipoles, trailing waves, thick plates, modeled dipole sources.

1. Introduction

Some fairly recent references in the field of ultrasonics have been published relating to the concept of trailing waves (TWs) [1-3]. Both experiments and modeling were done for thicker plates, when they were excited by pulses from an ultrasonic transducer on either a plate transverse surface or an end of the plate. TWs were observed in a plate thickness regime between bulk waves and Lamb waves. The experiments and modeling showed the presence of a train of TWs when the product of the frequency of the pulse and the plate thickness was greater than 15 MHz mm for steel plates [1, 2]. Since acoustic emission (AE) sources (in contrast to the situations of the above references) are

typically buried self-equilibrating point sources with a broad frequency content, the question arises as to whether such trains of TWs can appear in the waves generated by such AE sources in thicker plates. Also, since in AE field applications the frequencies in the signals are typically less than 0.5 MHz, the potential for observation of TWs may depend on testing of thicker plates. The use of AE on thicker steel plates was published many years ago [4,5] for thicknesses 80 mm and 152 mm respectively. These works were directed towards nuclear reactor components. Based on the above discussion, the goal of this work is to use finite element modeling (FEM) to examine conditions of occurrence and characteristics of TWs in the out-of-plane surface displacement signals generated by buried in-plane dipole (IPD) sources in thicker steel plates.

2. Modeling conditions and geometry

All numerical computations are carried out within the software program Comsol Multiphysics 5.4 using the "Structural Mechanics Module". The software program uses an implicit formulation to solve transient coupled partial differential equations. The settings follow the validated approach established in [6,7]. The geometry considered is shown in Fig. 1. To lower the numerical intensity of the model, a 2D-axisymmetric approach was chosen instead of a full 3D approach. The cross-section studied including the typical dimensions of thickness (75mm) and disc radius (2000mm) are included. The IPD is located 100 μm distance to the axis of symmetry, oriented in parallel to the x-axis. As test source function, a force is applied in the x-direction using a cosine-bell shape function reaching a maximum F_m=1 N within a rise-time t_s=1.0 μs. Depth position of the IPD is varied along the z-axis to range from half the thickness of the plate (0%) to the top surface (100%). To terminate unwanted reflections, a low-reflecting boundary condition is implemented on the far right of the modeled cross-section following [6,7]. A mapped mesh with a maximum edge length of 0.5 mm together with a time step of 50 ns is chosen for the computation, fulfilling convergency criteria as outlined in [7]. Evaluation is made for the out-of-plane displacements (z-displacement) at distinct intervals along the x-axis.
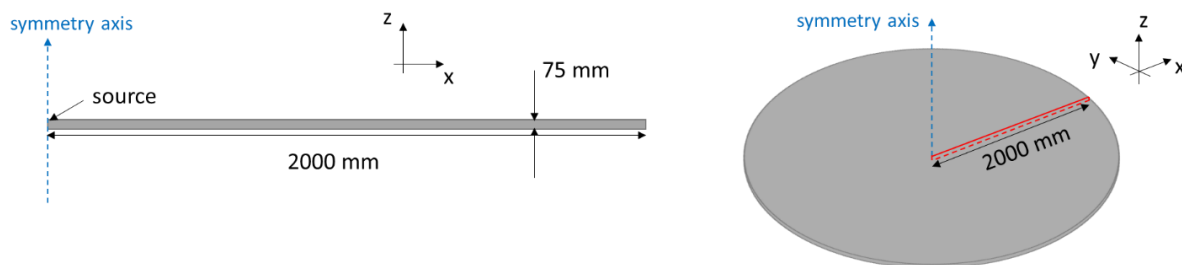
Fig. 1: 2D-axisymmetric geometry studied and corresponding view on 3D equivalent with cross-section marked in red. Nominal dimensions of length and thickness for one case study only.

3. Results for 75 mm thick plate; broadband from 80 kHz to 500 kHz

It is appropriate to discuss a key observation relative to the formation and propagation of the IPD-based TWs. Since the case on a mid-plane dipole (0%) provides the clearest situation to point out the observation, the focus is on that case for a 75 mm thick plate. In order to view "snapshots" of the wavefield in certain regions along the plate at specific times, without significant overlapping rigid body movement, the out-of-plane velocity wavefield (z-direction) was used for visualization instead of the out-of-plane displacement. Fig. 2 shows two snapshots at 260 μs (top) and 292 μs (bottom). The colors correspond to the signs of the out-of-plane velocity (crests) in the waves that travel from one surface to the opposite one. Expanded views (to scale) of these snapshots were

used to find the initial and final horizontal positions of "start" and "end" representing wave propagation of one wave package from one surface to the opposite one. When the waves reach a surface, they create the TWs as a part of their reflections. Using the red or blue wave crests "V's" (shown in the figure), where a crest of one color reaches and reflects right at the surface, to consistently track single colors from "start" on one surface across to finish ("end") on opposite surfaces to find the difference in absolute position along the x-axis between the two images. For the example shown in Fig. 2 the reflection "start" on the top surface was estimated to be at 529.6 mm, and the estimated reflection "end" on the bottom surface was estimated at 600.5 mm. Then, the horizontal position difference was used with the plate thickness of 75 mm to calculate the angled distance (103 mm) from one surface to the other. Division by the time difference of the two snapshots (32 μs) resulted in a propagation velocity "across" thickness for the waves. This velocity, 3.23 mm/μs, was 3 % greater than the calculated shear velocity of 3.13 mm/μs. This result provided evidence that the wave propagation from one surface to the next was at the shear velocity.
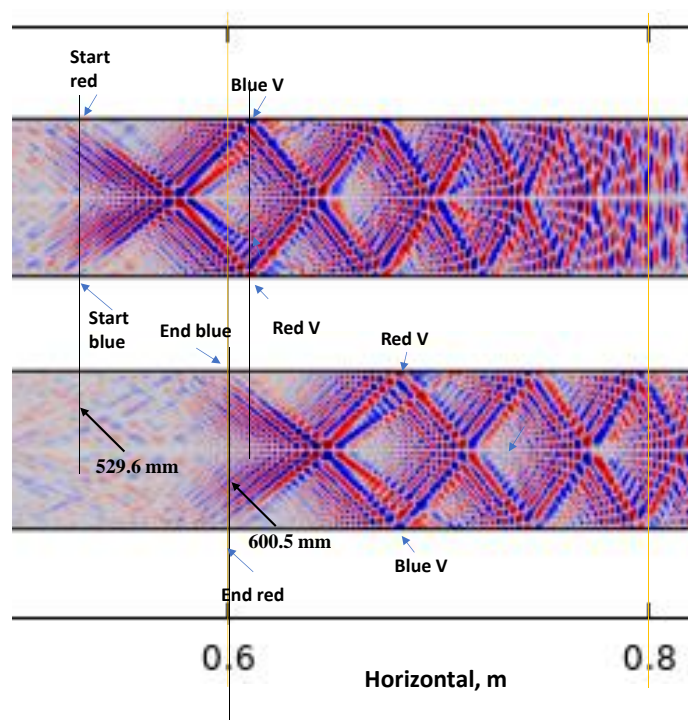
Fig. 2: "Snapshots" of the out-of-plane velocity (z-direction) at two times (top at 260 μs and bottom at 292 μs) for a 0% IPD in a 75 mm thick plate.

Fig. 3 demonstrates the out-of-plane displacement signals on both the top surface (a) and bottom surface (b) at a series of six propagation distances (250 mm to 1500 mm) for a dipole level at 66% (i.e., 12.75 mm below the top surface, based on half the thickness with 0% at the mid-plane). Clearly part (b) shows a train of short-duration wave packets, TWs, in the bottom surface signal at each propagation distance. The length or duration of the full signal increases as the propagation distance increases due to the spawning of new trailing waves (shown later) at the end of the signal. Thus, the number of TWs increases with propagation distance. At a propagation distance of 250 mm, the total signal duration is about 90 μs, and this duration increases to about 440 μs at 1500 mm. The peak amplitude of the signals at each propagation distance is found at latter TW or the last arriving TW. It can be verified that the dominant amplitudes of the TWs occur after the calculated arrival time of the Rayleigh velocity, as the TWs before this time have smaller peak amplitudes. On the contrary, part (a) shows the top surface signal amplitude peaks are from a Rayleigh wave at all the propagation distances. TWs with small peak amplitudes can be observed after the arrival of the Rayleigh waves. The total signal durations change over a similar range as

for the bottom surface signals. For both the top and bottom surface signals, the durations in this case of the individual TWs are typically about 10 to 25 µs depending on the selected (by eye) start and end of each wave packet.
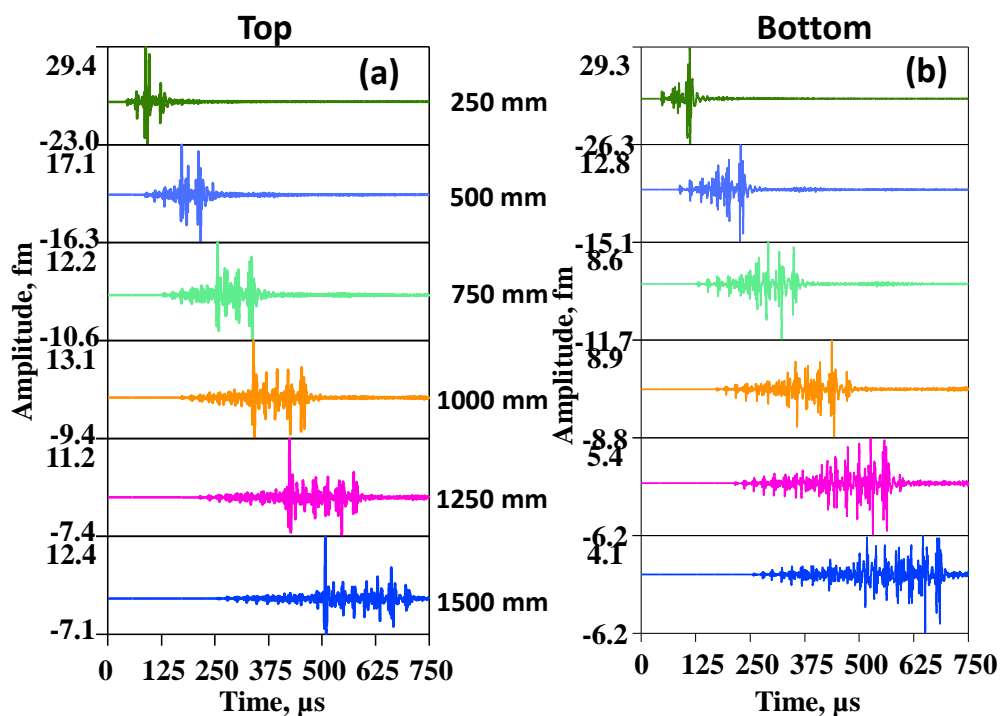
Fig. 3: Out-of-plane displacement for an IPD at 66%, as a function of propagation distance for both top (a) and bottom (b) surfaces.
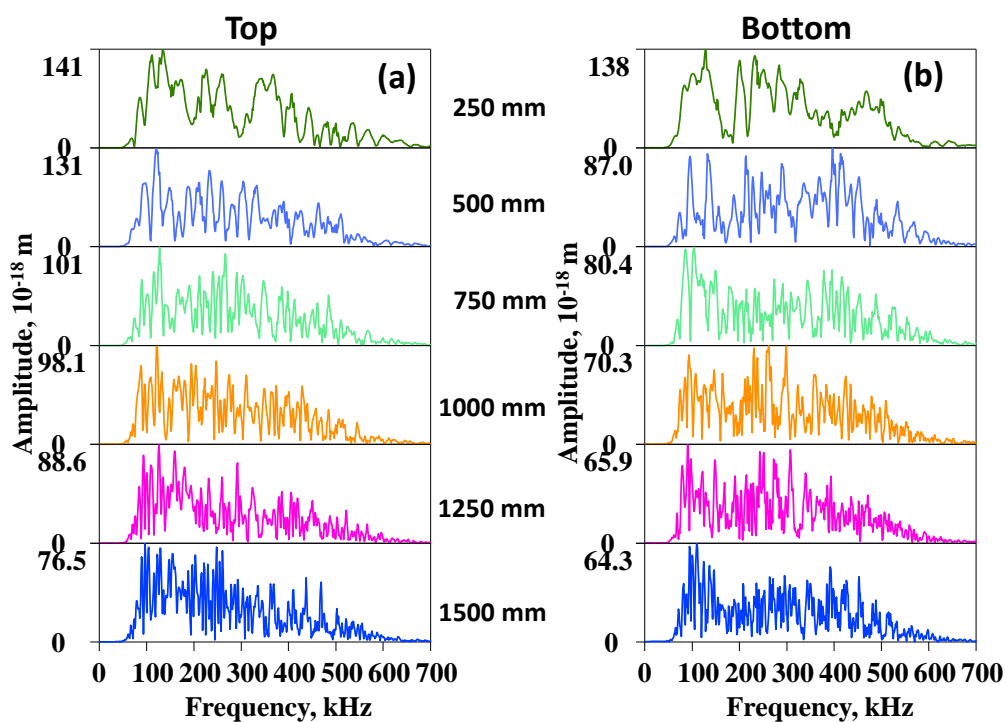
Fig. 4: FFT for the signals in Fig. 3 at 1500 mm propagation distance.

Using the signals at 1500 mm, shortened from 250 µs to 750 µs (the region of the main signal), the fast Fourier transforms (FFT) were calculated. Fig. 4 shows that the signals from both surfaces are broadband from the 80 kHz high pass frequency out to about 600 kHz, which is beyond the filter low-pass frequency. Similar FFT results are apparent (not shown) for the shorter propagation distances. Some further frequency aspects of the TW packets can be illustrated using time/frequency analysis by the Choi Williams Distribution (CWD) [8]. Fig. 5, left column, shows the signals and CWD results for both surfaces at 1500 mm for the primary signal to beyond the end of the last TW (250 µs to 750 µs). These results show the broad frequency range of each TW that is consistent with the FFT results. They also show the dominance of the Rayleigh wave (arrives at about 517 µs) in the top surface results. The results also clearly emphasize the spacing of the wave packets and the fact that the spacing shows a slight increasing trend as the time increases. Fig. 5, right column, focuses the CWD results for the time period after the Rayleigh wave arrival time. This permits a clearer view of the time offset of the arrivals of the TW packets between the two surfaces that is due to the offset from the mid-plane of the IPD.
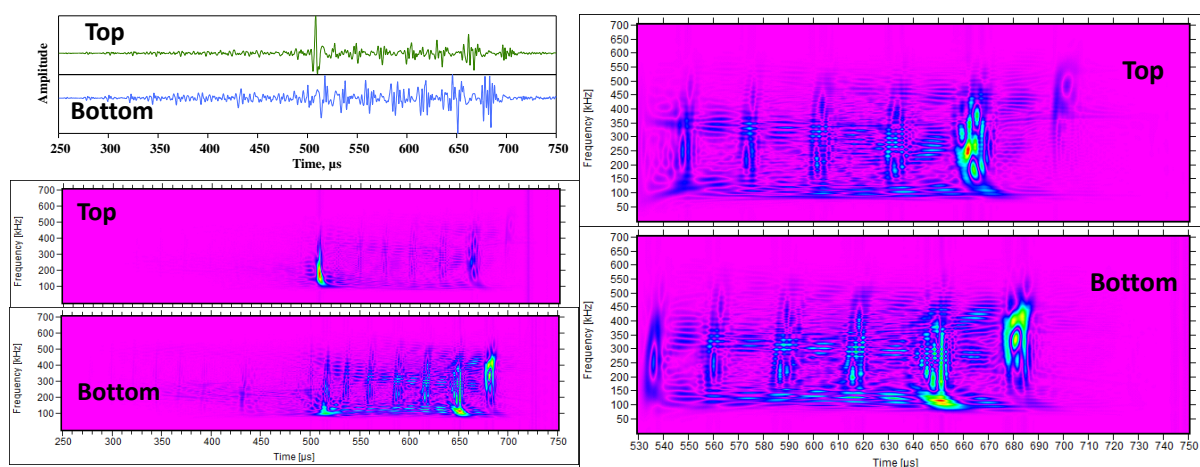
Fig. 5: Signals and CWD results for the signals in fig. 3 at 1500 mm propagation distance, for both top and bottom (left), and shorter time period both surfaces (right).

3.1 Change of level of IPD

When the level of the IPD in the plate thickness was altered several aspects changed. Fig. 6 (left two columns) compares the out-of-plane displacement of the signals at 1500 mm for both surfaces for five different depths (98%, 80%, 66%, 33% and 0%). The top surface signals show that the Rayleigh wave is no longer present for the 33% and 0% IPD positions. Instead, at these source depths, the TWs dominant with much later arrivals of the peak amplitudes compared to the Rayleigh wave arrival time. As the dipole depth moves further down from the top surface, Rayleigh peak amplitude decreases, and relative to the Rayleigh wave amplitude, the TWs show a gradual increase in amplitude. The bottom surfaces have no Rayleigh waves and the TWs dominate. Only in the 98% case, a small time period of low frequency A_0 Lamb wave is present (see red arrow). Using the shown signal time period, FFT results were calculated for this 1500 mm propagation distance. The results in Fig. 6 (right two columns) for the top surface signals again demonstrate broadband signals. For the bottom surface, the 98% dipole position has a lower frequency peak at about 93 kHz with a rapid falloff as the frequency increases (see red arrow, for A_0 contribution). For the other levels, the broadband behavior is dominant.
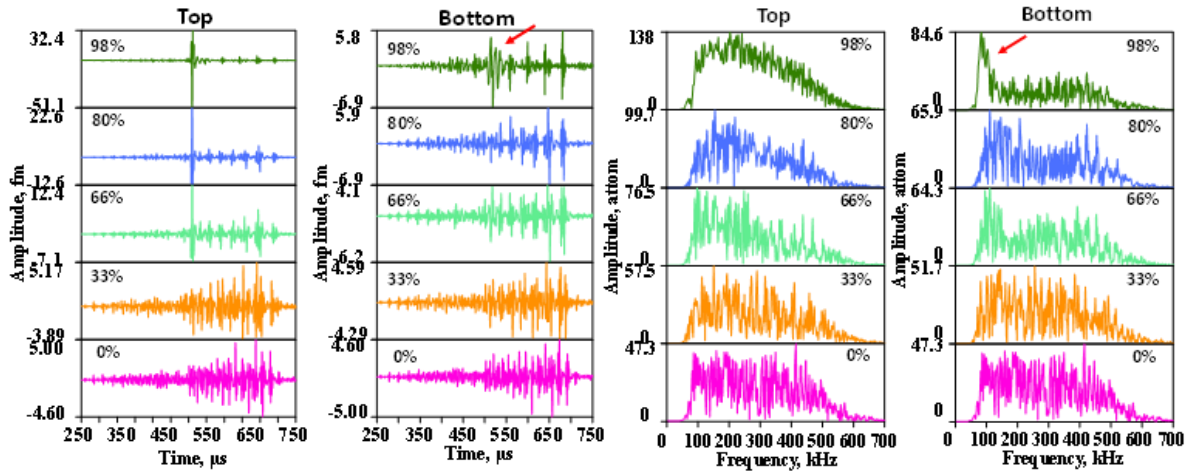
Fig. 6: Signals left two columns and corresponding FFT results right two columns at 1500 mm propagation distance as depth of IPD increases.

3.2 For 0% case, examine velocity of TWs along a plate

Using the 0% case in a 75 mm thick plate cases some interesting observations can be made. Fig. 7 compares, for the 0% dipole at 1500 mm, the signals and CWD results for both the top and bottom surfaces for a time region of 550 µs to 750 µs, which is after the arrival time of the Rayleigh velocity. There the TWs packets arrive at the same time at both surfaces with opposite signs.

The velocity of the TWs along the bottom surface was examined for this 0% case (75 mm thick) using the signals at closely spaced distances (1000 mm to 1275 mm at 25 mm intervals). By tracing the individual TWs, the propagation velocity for seven selected TWs was estimated. Fig. 8 shows the data as well as the estimated velocities. The "oldest" traced TW had a lower velocity (4.21 mm/µs), and the most recently formed one had a higher velocity (5.8 mm/µs). The figure also shows the formation of new trailing waves (D, E, F and G) as the propagation distance increased, as well as, the growth in amplitude of these newly formed TWs.
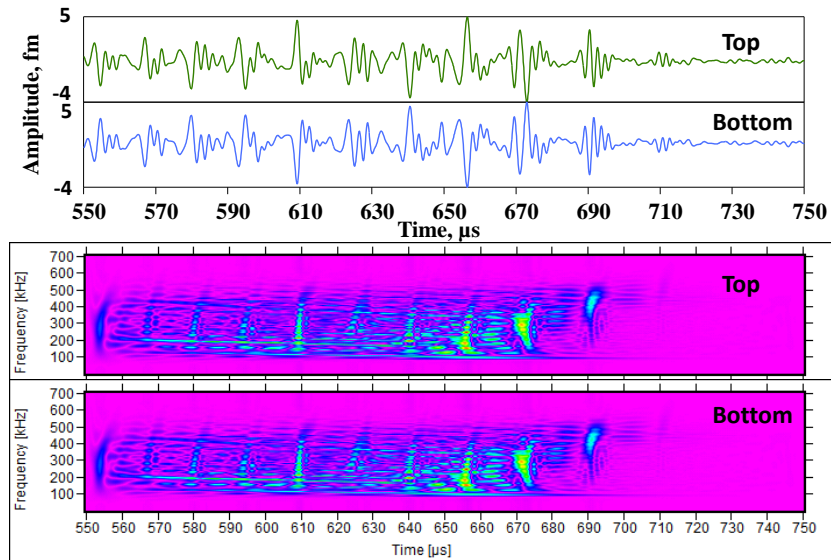
Fig. 7: Signals and CWD at 1500 mm for time period after Raleigh arrival; 0% IPD.

TW ID	Velocity, mm/μs
A	4.21
B	4.26
C	4.55
D (new)	4.92
E (new)	5.16
F (new)	5.59
G (new)	5.8
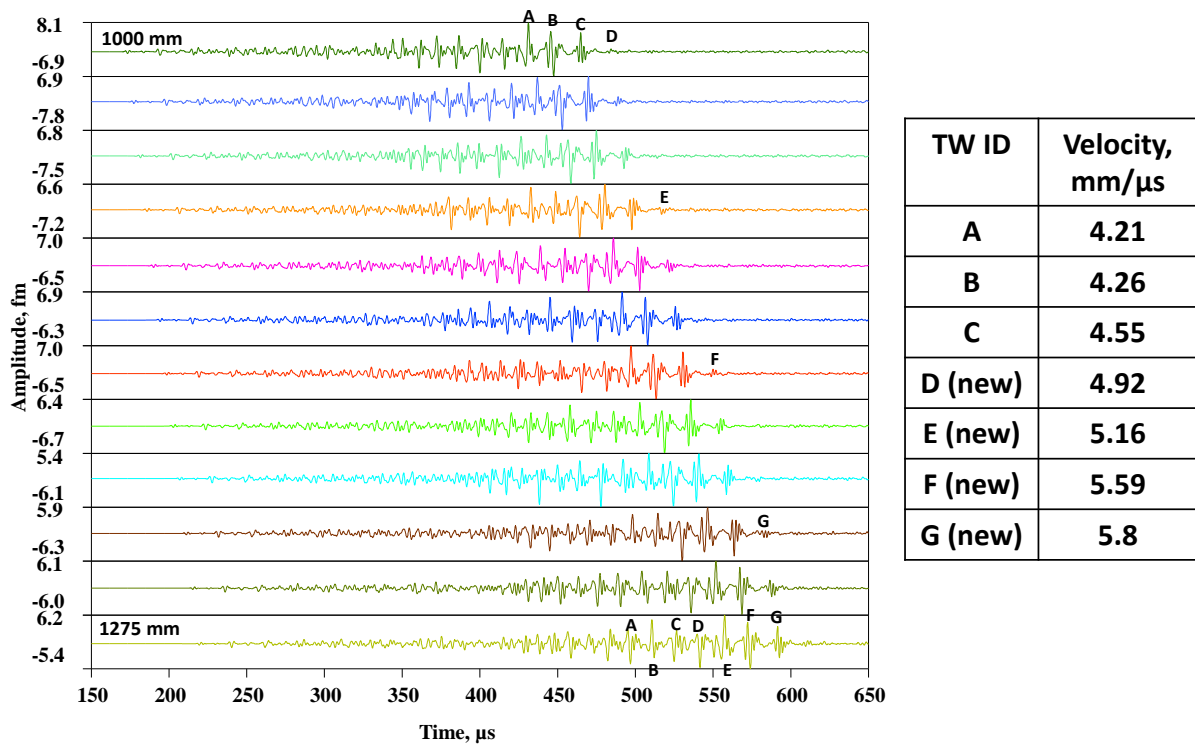
Fig. 8: Signals for 0% IPD at closely spaced propagation distances. Table of estimated propagation velocities of "traced" TWs.

4. Dipoles at 66% as a function of changes in the plate thickness for 1500 mm propagation

For an 80 kHz to 500 kHz bandpass, Fig. 9 illustrates, for both surfaces, the large differences in the signals as the plate thickness increases from 6.25 mm to 125 mm. The bottom surface signals for a propagation distance of 1500 mm clearly show that at 6.25- and 12.5-mm Lamb waves are dominating in particular the fundamental flexural mode (verified by use of CWD with superimposed group velocities, not shown). For the thicknesses of 50, 75, 100 and 125 mm, the TWs dominate the bottom surface. For the top surface, and thicknesses of 6.25 mm and 12.5 mm, Lamb modes dominate (verified by use of CWD with superimposed group velocities, not shown). At thicknesses of 50, 75 and 100 mm a Rayleigh wave dominates. For these three relatively thick plates lower amplitude TWs are present and grow relative to the Rayleigh wave amplitude as the thickness increases. Finally, at a thickness of 125 mm, the TWs dominate. Also, it is clear in these TW cases, as shown in Fig. 10, the time spacing between the TWs increases and there are fewer TWs in a fixed time period as the thickness increases at a fixed propagation distance. This is consistent with the longer path between the surfaces. There is a question as to what mode(s) is dominating for the 25 mm thickness on both surfaces? Fig. 11 illustrates for both surfaces, using the CWD along with superimposed group velocity curves [8] that multiple Lamb modes, rather than TWs, are present including S_0 thru S_1 and A_0 thru A_2. Also, higher frequencies of some of these modes are present due to the bandpass extending to 500 kHz, and for the top surface there is evidence of the Rayleigh wave at the highest frequencies. Thus, the transition between Lamb wave dominance and TW dominance for this frequency band occurs between 25 mm and 50 mm plate thicknesses.
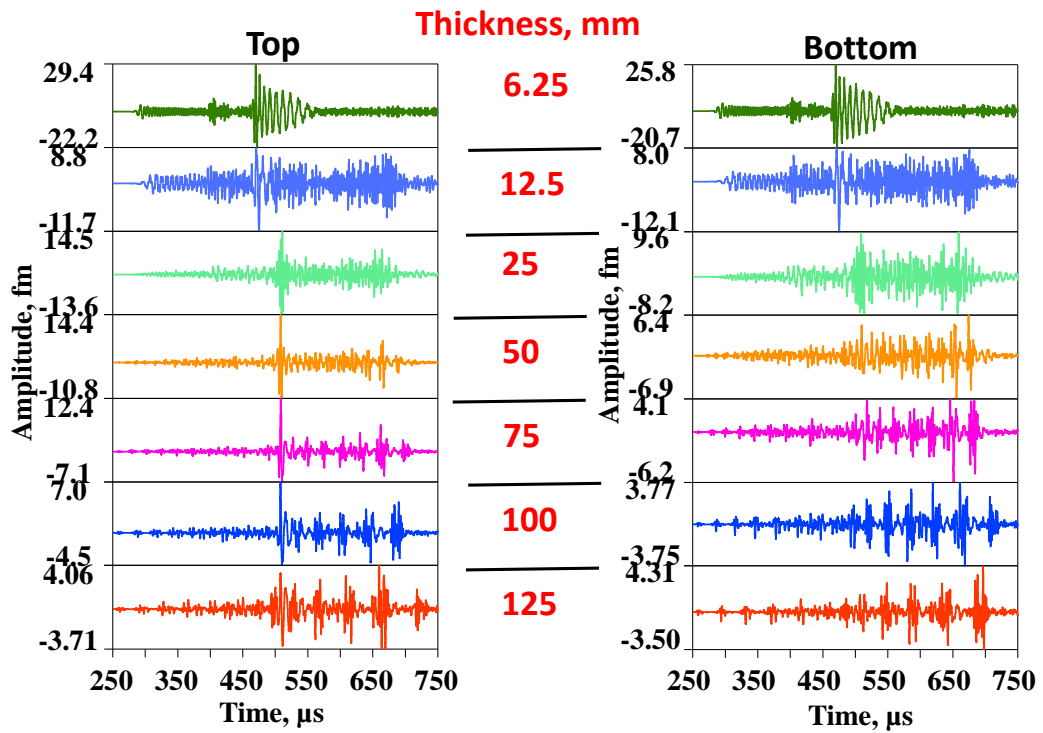
Fig. 9: Signals for 66% IPD at 1500 mm versus plate thickness.
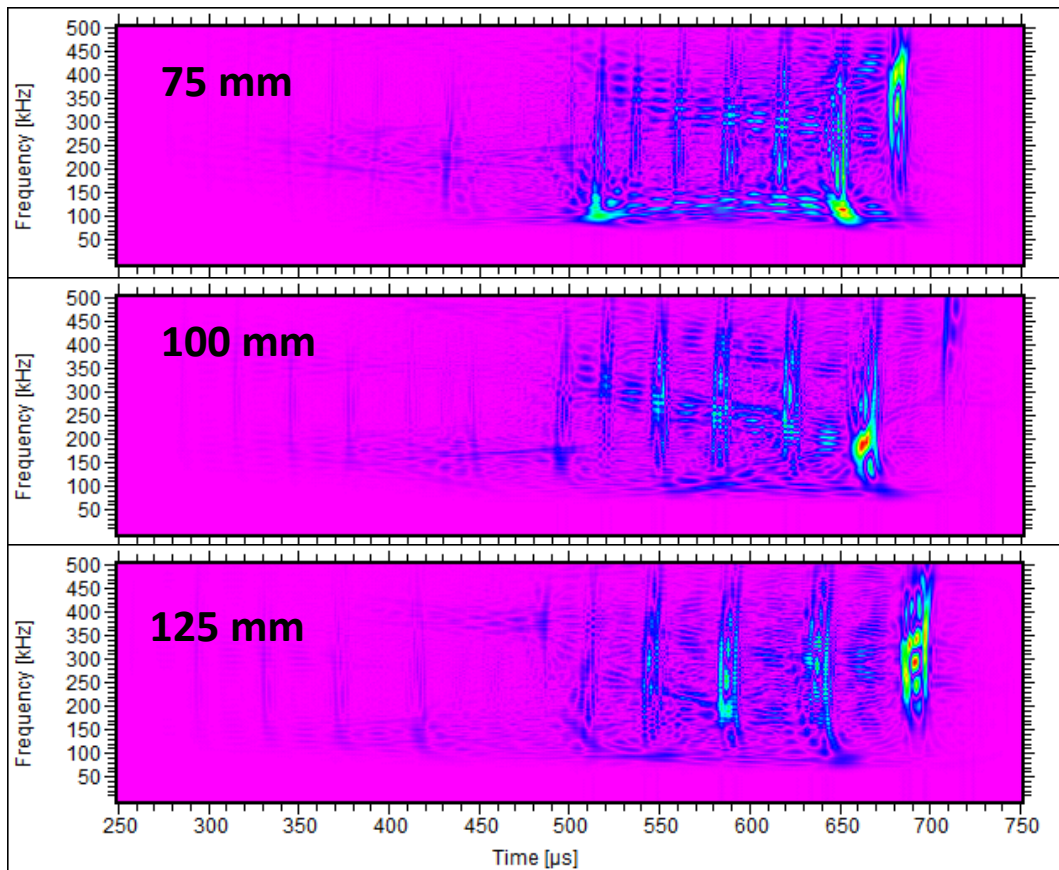
Fig. 10: CWD from bottom surface signals for 66% IPD for thicknesses of 75 mm, 100 mm and 125 mm at 1500 mm propagation distance.
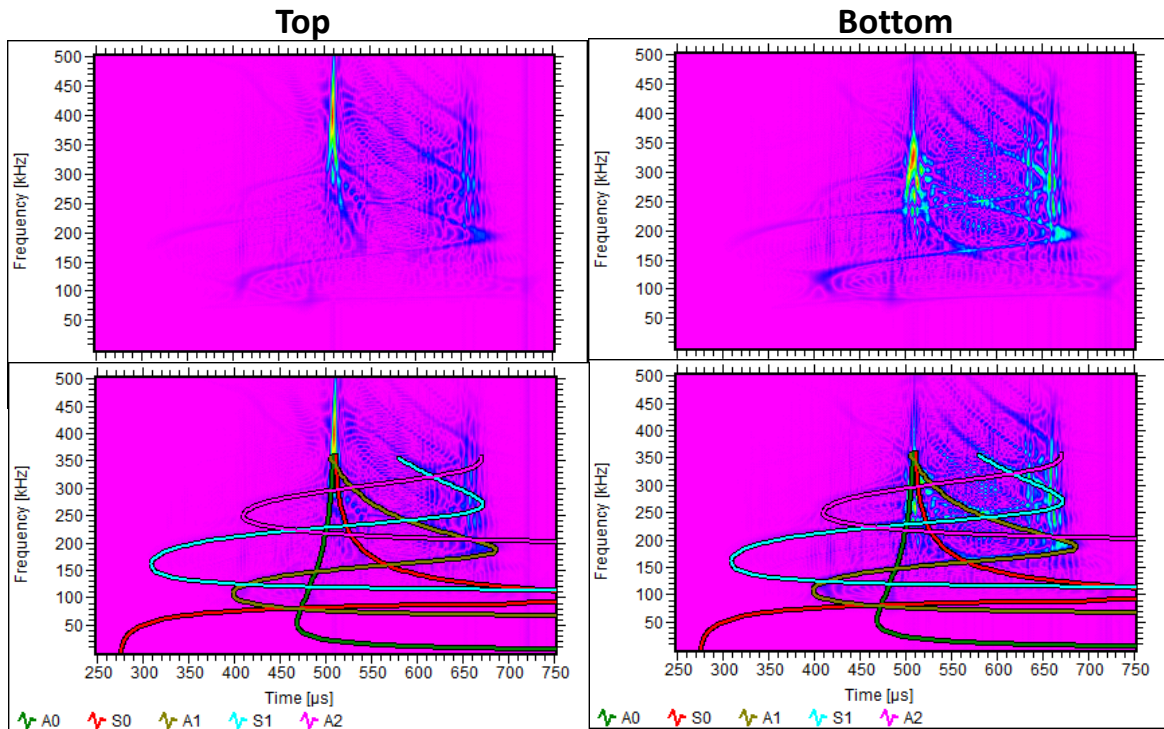
Fig. 11: CWD for 66% IPD for plate thicknesses of 25 mm, showing Lamb modes on both surfaces at 1500 mm propagation distance.

5. Discussion of results relative to source location, source identification and pencil lead breaks

5.1 Source location

In order to gain some insight into the potential issues with the determination of arrival times for source location calculations in the presence of TWs, two cases (80 kHz to 500 kHz filter) were compared as illustrated in Fig. 12 at two different propagation distances (750 mm and 1500 mm). First, an IPD at 66% in a 75 mm plate, and second, an IPD at 66% in a 12.5mm plate. In the latter case, typical Lamb waves are present on both surfaces, and this situation is the common case in AE work where standard techniques have been applied. It should be pointed out that in this 12.5 mm case, the durations are longer than for the 75 mm case. As shown in the figure there are large differences in the signal on the two surfaces in the 75 mm case. Rayleigh waves are dominant on the top surface, while TWs are dominant on the bottom surface with their maximum amplitude near the end of the TWs. Further, on the bottom the number of TWs increases with propagation distance. Also, as shown earlier at certain IPD levels there may not be a Rayleigh wave on either surface. When Rayleigh waves are present on the monitored surface, standard AE techniques for source location can be applied using sensors with higher frequency sensitivity. Threshold-determined arrival times coupled with the Rayleigh velocity would be expected to result in AE locations. When the monitored surface in thicker plates is dominated by TWs, the ability to carry out source location may be compromised without special considerations. This situation is likely to occur when the sources are on or near the opposite surface (e.g., the inside of a thick-wall pressure vessel) from the sensor locations. Since the number of trailing waves increases with increased propagation distance, and the peak amplitudes are near the end of the sequence of TWs, it is unlikely that a threshold-based approach would yield arrival times at a known propagation velocity. Also, the very first arrivals are unlikely to be detected, due to their relatively small amplitudes compared to the peak amplitude. Consistent with the initial nature of this study, further possible approaches to source location were not considered.
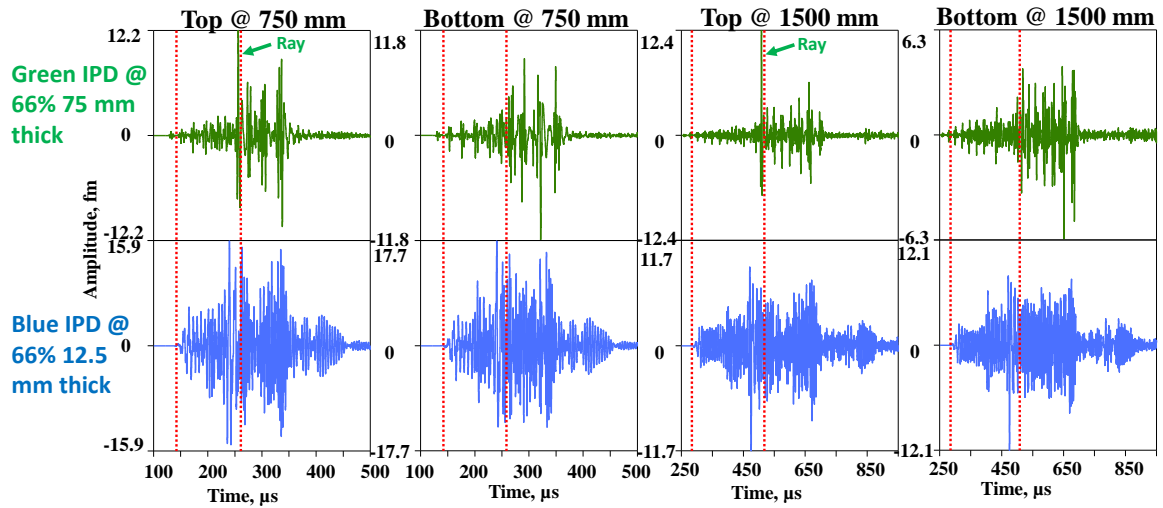
Fig. 12: Comparison of signals on both surfaces at two propagation distances for 66% IPD in 75 mm (top row) and 12.5 mm (bottom row) thick plates. Vertical cursors at calculated arrival times of extensional mode and Rayleigh wave.

5.2 Source identification

Since frequency content can be an important part of source identification, this aspect was examined in the 75 mm thick plate by FEM runs for different rise times. Four different values, 1 µs, 2.5 µs, 5 µs and 10 µs, were used for the IPD source (located at 66%). The signals and FFT results for both surfaces at a propagation distance of 1500 mm are shown in Fig. 13 for the 80 to 500 kHz bandpass. The top surface results show a dominate Rayleigh wave as the rise time increased up to a 5 µs rise time, while the bottom surface signals show dominant TWs up to a 2.5 us rise time (verified using the CWD, not shown). Since the FFT results show a progressive loss of higher frequencies as the rise time increases, the source rise time may be indicated in the thick plates by FFT results even in the presence of TWs. Again, consistent with the initial nature of this study, further possible approaches to source identification were not considered.
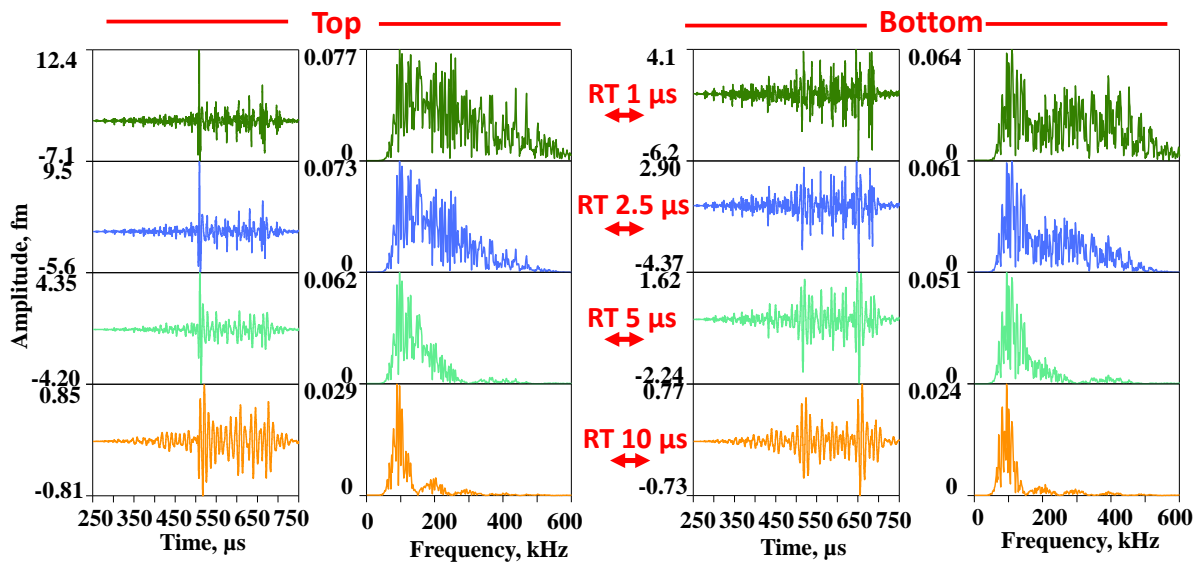
Fig. 13: Signals and FFT results on both surfaces for 66% IPD in 75 mm plate as a function of source rise time.

181

5.3   Pencil lead breaks (PLBs)

In Fig. 14, the broadband, 80 kHz to 500 kHz, signals and CWDs on both surfaces are compared for a top surface out-of-plane monopole, 98% IPD and 66% IPD (all 1 μs rise time) for a 75 mm plate at 1500 mm propagation distance. Since PLBs are often used in field testing, the question is whether the signals generated by PLBs provide guidance as to the characteristics of the signals that will be present from real buried sources. The top surface signals, with Rayleigh wave domination, are similar for all three source cases. Some traces of TWs appear for the 66% dipole, but the Rayleigh wave still is dominate. In the bottom surface results, the monopole signal is dominated by a lower frequency portion of the A_0 mode (shown earlier). The 98% dipole has both TWs, as well, as this low frequency portion of the A_0 mode. In contrast, the 66% signals are dominated by multiple TWs. For both surfaces, the monopole (applied to the top surface) signals are of *much* higher amplitude (up to 40 dB) than the IPD signals. These differences would be important in the case of field testing when the PLB is on the top surface (monitored surface) and the IPDs positions are near the "bottom" surface such as in the case of a large pressure vessel with a flawed inner surface.
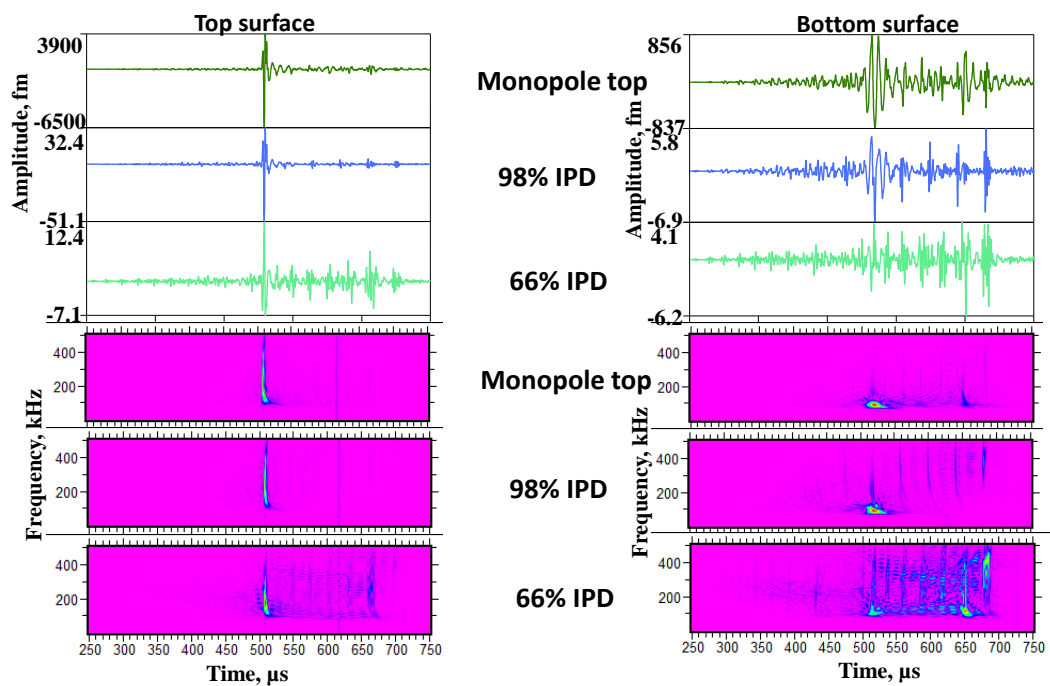
Fig. 14: Signals and CWD for both surfaces at 1500 mm propagation distance for out-of-plane top surface monopole, IPD at 98% and IPD at 66%, filtered 80 kHz to 500 kHz.

6.   Conclusions

6.1   Characteristics of TWs in thick steel plates:
- Formed by successive reflections of shear waves travelling between opposing plate surfaces.
- Clearest view in frequency vs. time; where each TW is visible as broadband signal.
- Dominant TW amplitudes are those post the calculated Rayleigh wave arrival time; when no dominant Rayleigh wave is present.
- As plate thickness increases, number of TWs, in a fixed time period, decreases and spacing between them increases at a fixed propagation distance.

- Transition from Lamb waves to TWs for thickness > 25 mm; for 1 µs rise time source under current modeling conditions.
- For IPD near a surface, Rayleigh wave amplitude dominates, still see lower amplitude TWs in signals.
- New TWs form, grow in amplitude and increase in number at the signal ends as the propagation distance increases; resulting in longer signal durations.
- These TWs propagate along the bottom plate surface with velocity of about 5.8 mm/µs for newly formed ones to 4.2 mm/µs and less for the earlier formed ones. From closely spaced propagation distances, IPD at 0%, 75 mm.

6.2 Key implications for AE in thick plates:
- For broadband sensors, the current filtering of 80 kHz to 500 kHz implies will observe TWs in signals for thicker plates, in this study at greater than 25 mm. For 25 mm and less thickness, Lamb waves (including higher modes) were dominant.
- Signal arrival time approaches (for source location purposes) used for Lamb waves will likely need to be altered when TWs dominate due to their different characteristics.
- Comparing a top surface monopole (like PLB) to an IPD at 98% in a 75 mm plate, demonstrated the much higher amplitude, up to 40 dB, of the monopole signals on both surfaces.

7. References

[1] Greve, D.W., Zheng, P., Oppenheim, I.J. (2008). The transition from Lamb waves to longitudinal waves in plates. Smart Mater. Struct. 17, 035029 (6pp); doi:10.1088/0964-1726/17/3/035029.

[2] Greve, David W., Oppenheim, Irving J., Zheng, Peng (2008). Lamb waves and nearly-longitudinal waves in thick plates. Proc. SPIE 6932, Sensors and Smart Structures Technologies for Civil, Mechanical, and Aerospace Systems, 69321I (8 April 2008); doi:10.1117/12.775919.

[3] Shao, Yongsheng, Zeng, Lian, Lin, Jing, Wu, Wentao, Zhang, Hui (2019). Trailing pulses self-focusing for ultrasonic-based damage detection in thick plates," Mechanical Systems and Signal Processing 119, p. 420–431.

[4] Votava, E. and Jax, P. (1979). Inspection of nuclear reactors by means of acoustic emission during hydrostatic test. *Acoustic Emission Monitoring of Pressurized Systems*, ASTM STP 697, W. F. Hartman and J. W. McElroy, Eds., American Society for Testing and Materials, p. 149-164.

[5] Naus, D. J. (1979). Acoustic emission monitoring of intermediate pressure vessels tested under the ORNL heavy section steel technology program," *Ibid*, p. 91-105.

[6] Sause, M.G.R., Hamstad, M.A., Horn, S. (2012). Finite element modeling of conical acoustic emission sensors and corresponding experiments. Sensors Actuators A Phys., vol. 184, p. 64–71.

[7] Sause, Markus G.R., Hamstad, Marvin A. (2018). Numerical modeling of existing acoustic emission sensor absolute calibration approaches. *Sensors and Actuators A: Physical* 269, p. 294-307. doi:10.1016/j.sna.2017.11.057.

[8] "AGU-Vallen Wavelet version R2010.0202 and "Vallen Dispersion version R2010.0202," Vallen Systeme GmbH, Germany.
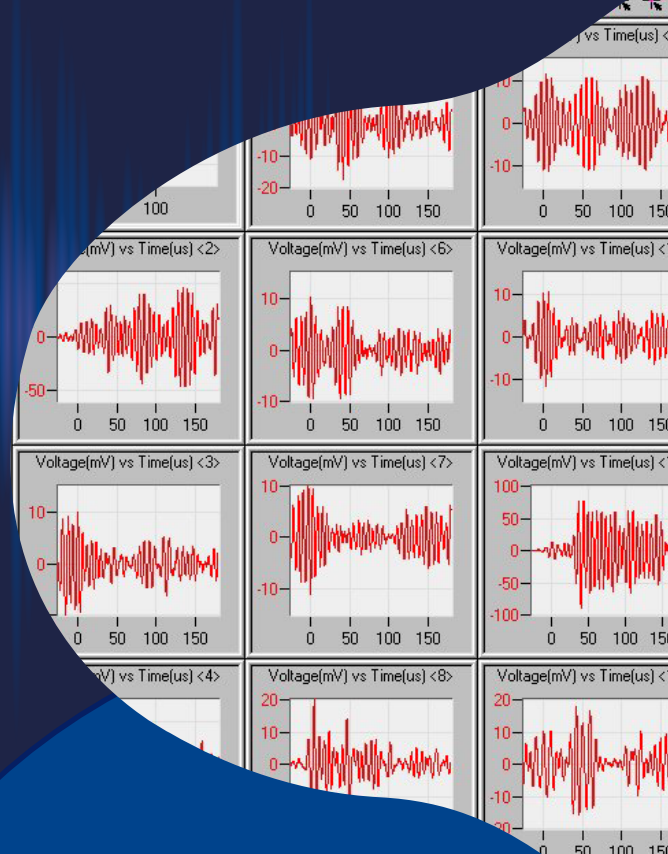
IMPACT SOURCE IDENTIFICATION ON PIPES USING ACOUSTIC EMISSION ENERGY

Chika Judith Abolle-Okoyeagu[1], Javier Palacio Torralba[2], Yuhang Chen[2] and Robert Reuben[2]

[1]Robert Gordon University, Aberdeen, UK; j.abolle-okoyeagu@rgu.ac.uk
[2]Heriot Watt University Edinburgh, UK; jp27@hw.ac.uk, r.reuben@hw.ac.uk
*Correspondence: j.abolle-okoyeagu@rgu.ac.uk

ABSTRACT

Impact is a common source of damage in pipes and pipeline systems and detecting the location and nature of damage is vital for reliability and safety of these systems. The main difficulty in the use of AE technology for such applications is being able to investigate the extent to which the temporal structure of such a non-impulsive event can be reconstructed using sensors located on the external surface of a pipe at some distance from the source. There is currently no reliable way of relating the temporal structure of the generating event to the temporal structure of an AE source. This work uses a set of matching AE experiments and finite element simulations to study the relationship between the generating AE event (dropped ball on a steel surface) and the resulting stress-time history recorded at a given point on the surface of the pipe.
Two test objects were used; a solid cylindrical steel block of diameter 307mm and length 166mm and a 2m pipe length of diameter 100mm and wall thickness 10mm. The AE resulting from the surface impacts was recorded over a period of 2 seconds for both experiments and simulations. The work builds on an earlier study with the same test objects using impulsive sources.
The results confirmed that a mechanical disturbance which is extended in time can be identified from its energy-time imprint carried on the stress wave.

Keywords: Acoustic emission, finite element analysis, AE energy, solid cylinder, steel pipe.

1. Introduction

Pipelines play a significant role in the transport of both gases and liquids, particularly in the oil and gas industry. There is a constant interest in improved levels of monitoring of these structures, as pipeline accidents are quite often disastrous both to people and the environment [1]. A good number of studies have recommended Acoustic Emission Monitoring (AEM) for the continuous surveillance of structures, machines and processes [2-5] and this paper tackles how a quantitative approach can be applied to pipeline integrity assessment.

AE is a term used to describe high-frequency (0.1 to 1MHz) elastic stress waves generated by the rapid release of mechanical energy often associated with structural degradation [6,7]. In pipelines, the main known sources are leaks, fatigue, and impact from external forces, although, in some applications, flow noise and abrasion may generate significant AE. Over the years, AET has become an accepted Non-Destructive Testing (NDT) technique with potential applications to pipelines [8] and this is due to its ability to provide information on the structural health of a pipeline

by using relatively few monitoring points and relying on propagation characteristics to locate faults such as leaks.

Just as in any other NDT testing technique, AET has limitations, the most significant being its inability to effectively determine as many characteristics of an AE source as one might expect for its very high temporal resolution. Much of this is because a number of processes produce AE, and not all of these give rise to signal that is of interest. There are, therefore, still research challenges in determining the nature, severity and location of multiple and/or prolonged sources, using signals acquired at one or more sensors mounted on the pipe surface [9].

Although the use of Finite element analysis (FEA) to simulate acoustic emission wave propagation has been a subject of research for over two decades [10-12], much of the work applying FEA has been focussed on a description of propagation [13,14].

2. Overall approach

This approach follows from an earlier study with the same test objects using impulsive sources [15]. Two different test objects were used; a solid cylinder and a 2m steel (ASTM A106/99) pipe. The solid cylinder was 307mm diameter and 166mm long and was used standing on one of the circular faces, with the opposite circular face being used as the test surface (Fig. 1).

The pipe was of length 2m, external diameter 0.08 m and internal diameter 0.1m. The external cylindrical surface was used as the test surface with both source and sensors being mounted on it (Fig. 2). A guide tube was used to guide the ball bearing on to the centre of the surface of the cylinder. The configuration was chosen to be close to the actual technological application.

For the experiments on both the pipe and the solid cylinder, a ball bearing drop was used to simulate sources with an extended temporal structure. The preamplifiers were set at a gain of 40dB and a sampling rate of 5Msamples/s with a pre-trigger of 1000 points was used. The system also acquired 50,000 points from the second sensor interlaced with the trigger. Three different sized balls (17g, 3g and 0.3g) were dropped from the same height (0.3m) onto the surface of both the solid cylinder and the pipe. Unlike the ball bearing drop on the solid cylinder, the ball bearings were dropped onto a flat steel plate placed on the pipe, for practical reasons.

Abaqus 6.10 was used for the simulations to model a steel cylinder and pipe fixed at both ends and subject to loading 0.2m from one end. The cylinder, pipe and ball models were both simulated as three dimensional, elastically deformable steel solids. Both the steel ball and pipe sections were modelled as 3D homogenous linear elastic continua, and an 8-node linear brick elements (C3D8) were used to discretize the model. Linear elements being used on the assumption that the stresses/displacements caused by the deformation and the propagating wave were within the elastic range. An element of size 0.01mm and time step of 1×10^{-9} second were used for the simulations. Stress time-histories were recorded at a distance of 0.5m from the location of impact for a total time of 2s.

Just as with the experiments three different sized balls (17g, 3g and 0.3g) were simulated to drop from the same height (0.3m) onto the surface of both the solid cylinder and the pipe.

The analysis was carried out at two different timescales; short (initial interactions free of reflections) and long (involving several bounces).
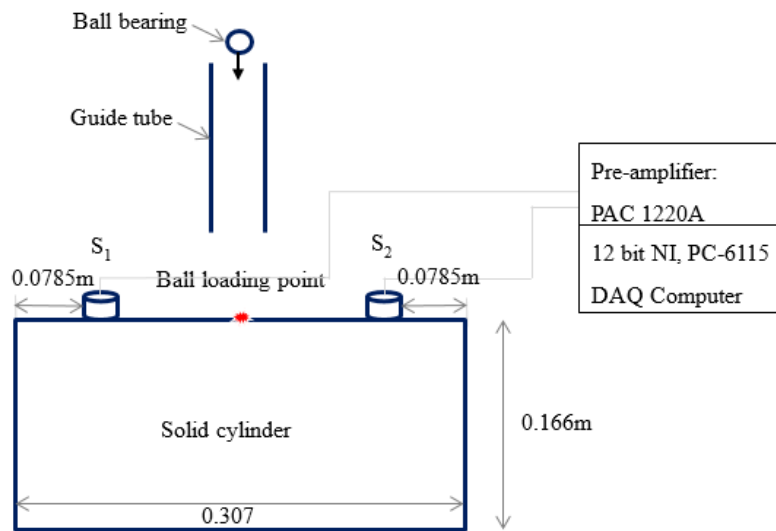
Fig. 1: Schematic representation of ball bearing drop on solid cylinder.
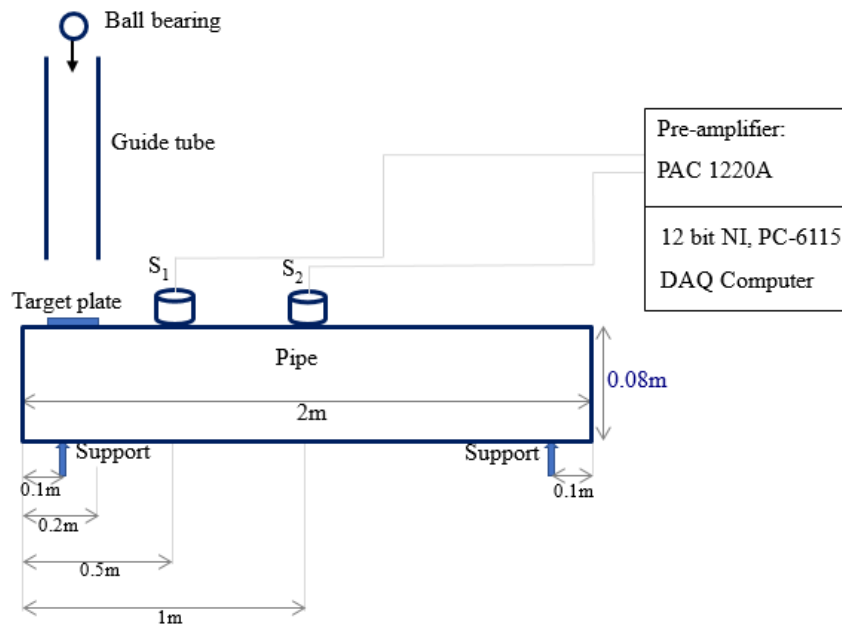
Fig. 2: Schematic representation of ball bearing drop on pipe.

3. Experimental result and analysis

3.1 Solid cylinder

Fig. 3 shows typical raw AE signals for the three potential energies and ball sizes. As can be seen, the ball bounces several times over a period of around 1second, each bounce being characterised by a burst of AE lasting about 0.1second with an increase in energy as the ball mass is increased.
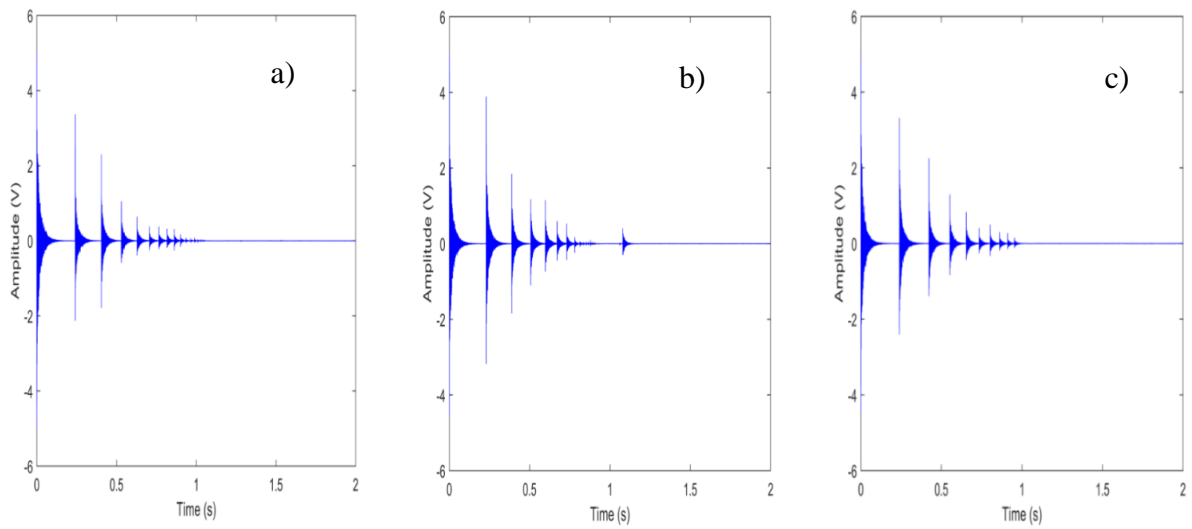
Fig. 3: Typical long-timescale AE signal balls dropped from 30cm height. a)17g b) 3g c) 0.3g on the solid cylinder.

Fig. 4 shows 140μs around first wave arrival for the three ball sizes. It can be seen that, irrespective of the ball bearing size, each first arrival is characterized by a low amplitude component of duration about 1μs, followed by a high amplitude component, which contains the peak amplitude.
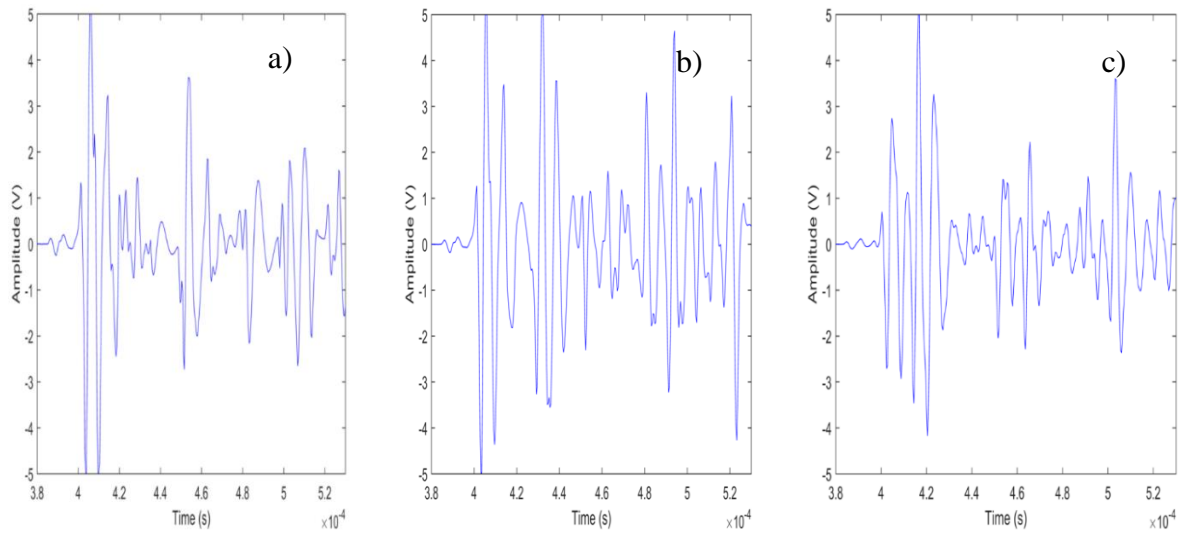
Fig. 4: Short-timescale AE signal dropped from 0.3m unto the solid cylinder. a)17g b) 3g c) 0.3g.

The measured (AE) energy was then calculated for each of the first four impacts for each of the ball bearing masses by integrating over the entire length of the burst.

Fig. 5 shows a plot of the measured energy against the incident energy in the first four bounces for each of the masses. As can be seen, the relationship between incident energy and measured energy, whilst not linear, is at least continuous for each of the ball sizes. However, there is clearly also an effect of ball radius, since the curves for each of the ball sizes are not continuous. The plots are shown at two scales on the ordinate so that the trends at low incident energy can be more clearly seen.
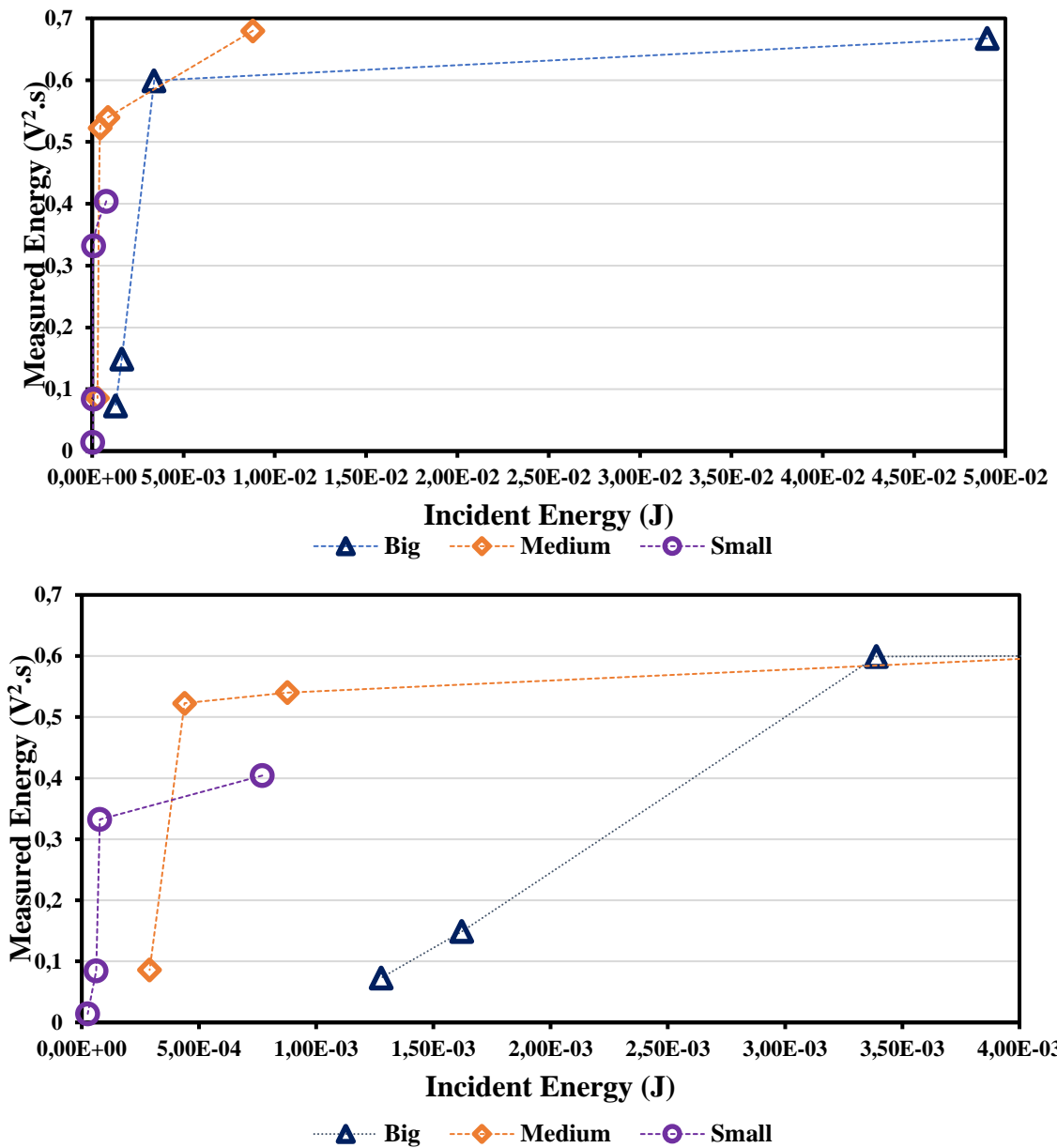
Fig. 5: Plot of measured energy vs incident energy in the first four bounces for all ball sizes dropped on the solid cylinder from 30cm.

3.2 Pipe

Fig. 6 show typical records of the first 2 seconds of AE signal for balls dropped from 30cm height. As can be seen, just as with the solid cylinder, the ball bounces are characterised by a burst signal of duration of about 0.1s, the peak of the burst reducing with successive bounces.
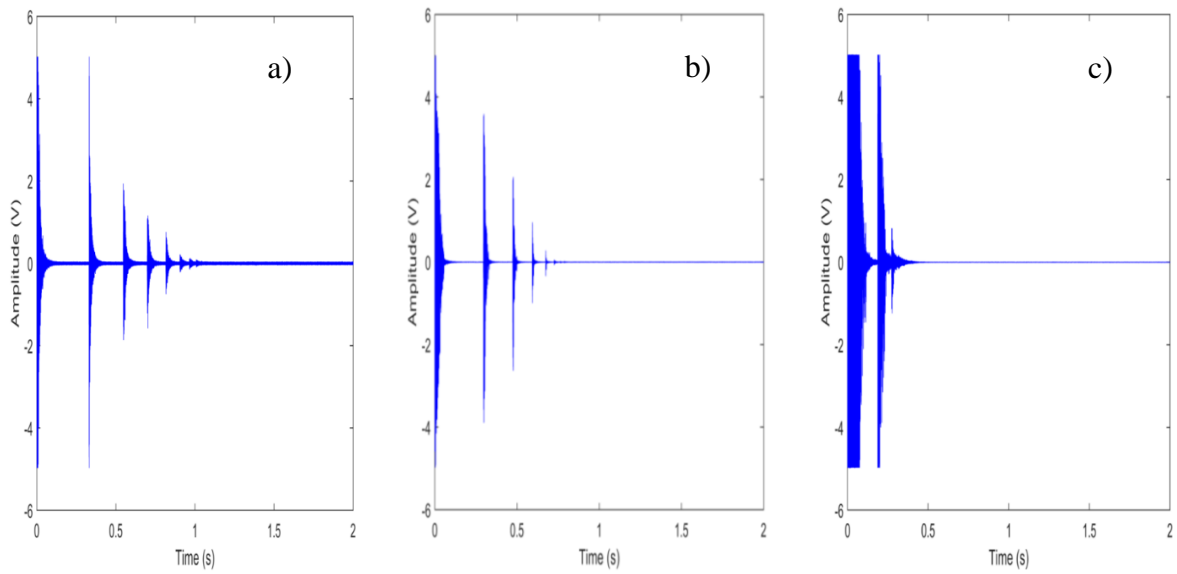
Fig. 6: Typical long-timescale AE signal for balls dropped from 30cm height a) 0.3g b) 3g c) 17g for sensor at 0.5m on the 2m pipe.

A comparison of Fig. 6 with the cylinder equivalent (Fig. 3) shows that the amplitude is a little higher for the pipe, although there are fewer bounces, somewhat further apart. It might be noted that the heaviest ball (Fig. 6c) has saturated the preamplifier and that the actual signal will be somewhat higher than depicted. The saturation seen in Fig. 6c was expected as is usually the case in applications with strong AE-sources.

Fig. 7 shows the first 100 μs around first wave arrival at the first sensor for typical raw AE time series recorded at S1, on the pipe (first wave arrival) for three ball sizes dropped from 30cm height. Comparison with the equivalent signals for the solid cylinder (Fig. 7 with Fig. 4) shows the records for the pipe to be more complex, also, it can be seen that each first arrival is again characterized by a low amplitude component followed by a high amplitude component, which contains the peak amplitude.
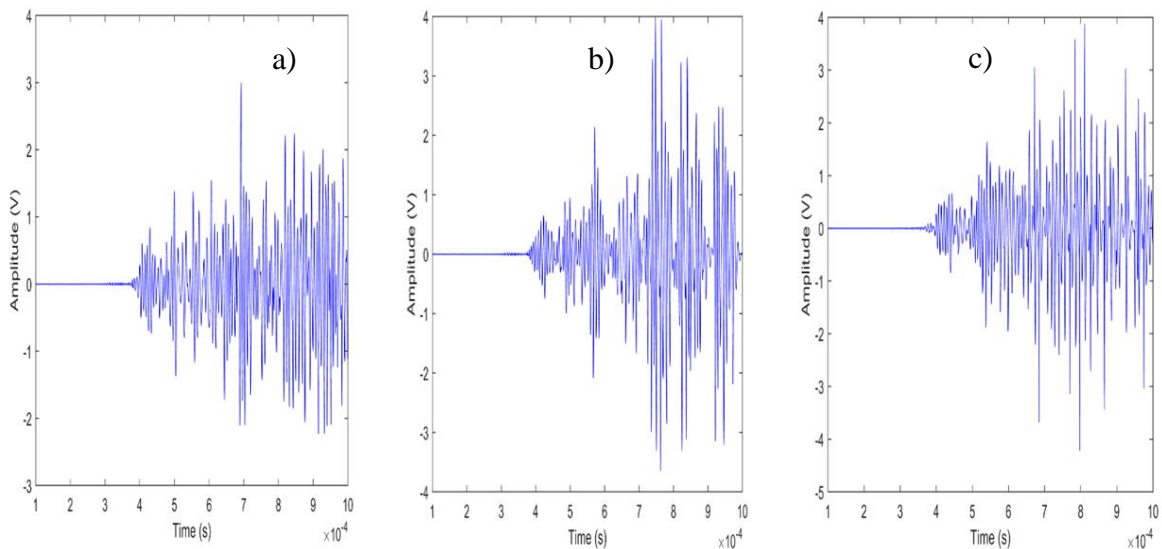
Fig. 7: Typical raw AE time series recorded at S_1, on the pipe (first wave arrival) for three ball sizes dropped from 30cm height (a – 0.3g, b – 3g, c –17g.

Figs. 8 and 9 show plots of measured energy vs. incident energy for the first four bounces for balls dropped onto the reference object and onto the pipe.
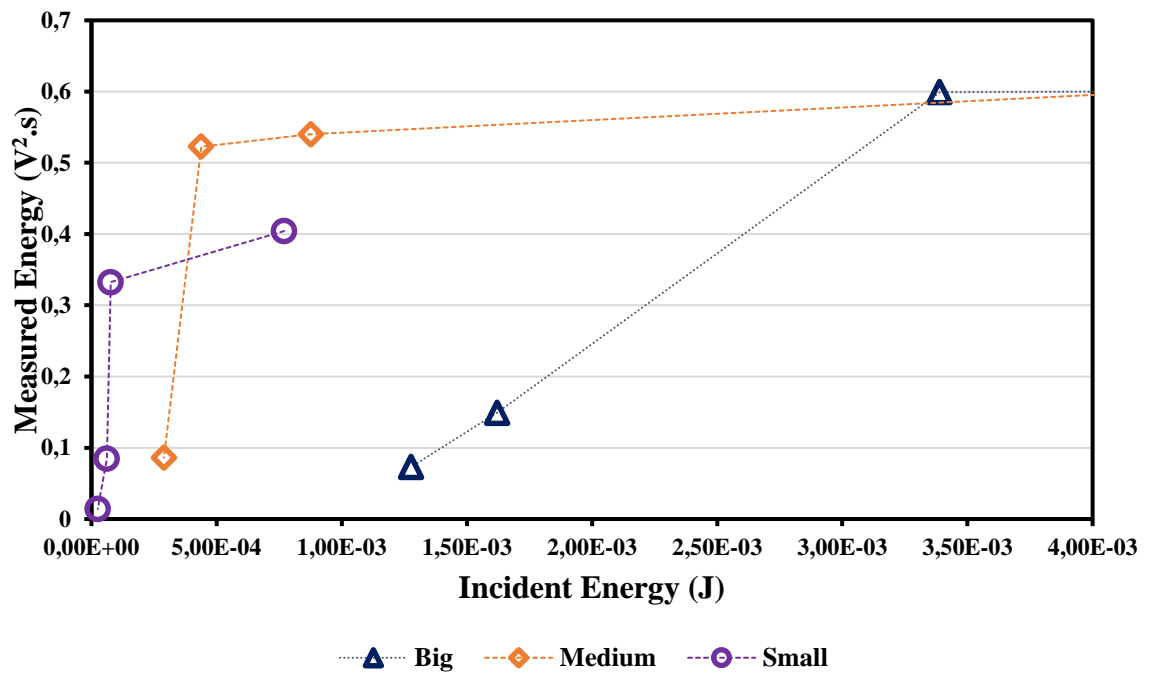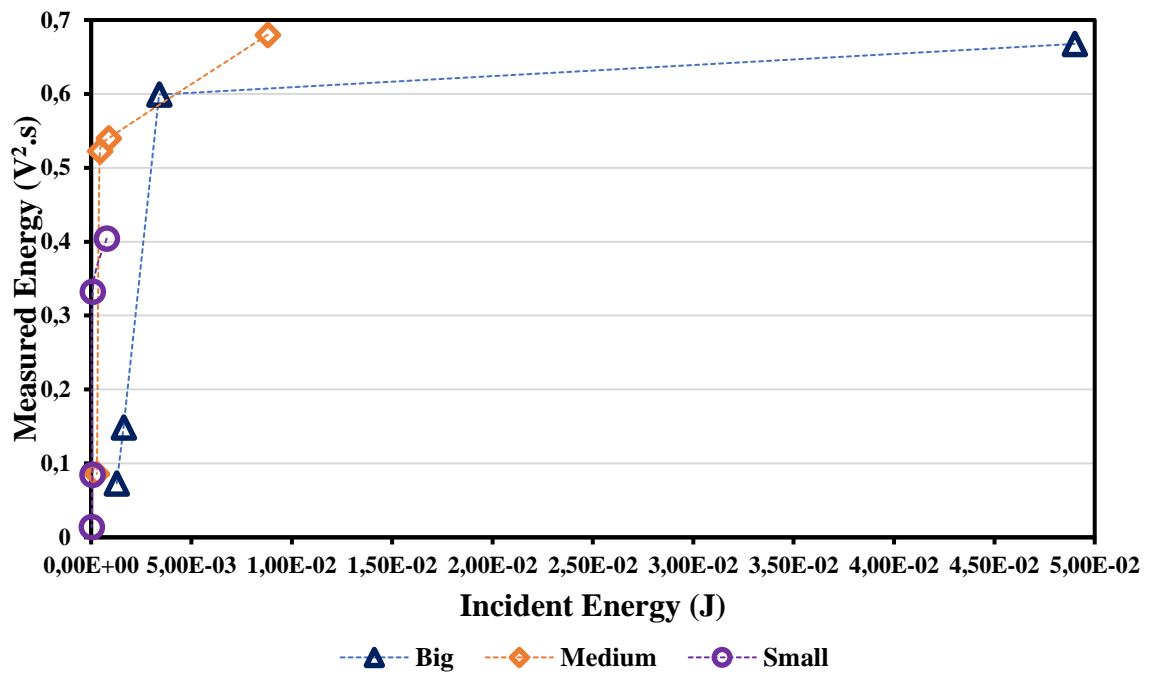
Fig. 8: Plot of measured energy vs incident energy in the first four bounces for the three ball sizes dropped from 30cm height onto the cylinder.
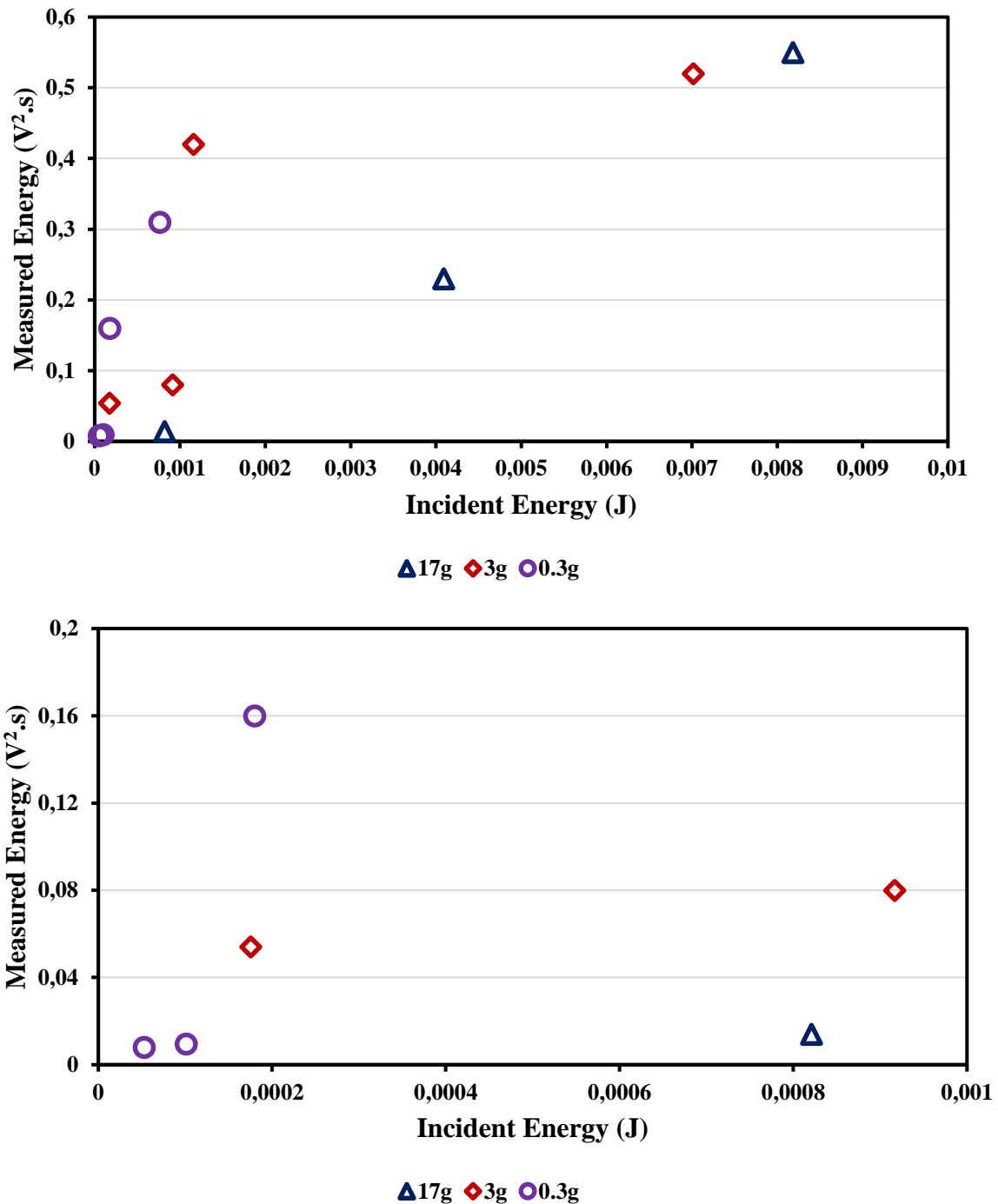
Fig. 9: Plot of measured energy vs incident energy in the first four bounces for the three ball sizes dropped from 30cm height onto the pipe.

From Figs. 8 and 9, it is clear that the pipe experiments show similar general behaviour to those on the solid cylinder, i.e. that the measured energy increases with incident energy, but that the rate of increase is lower for the heavier masses (and radii). This is most likely to be due to the fact that the heaviest masses are have enough momentum to displace the plate if they do not land directly above the contact line between plate and pipe.

Figs. 10 and 11 show plots of measured energy vs incident energy for the first bounce for each of the ball sizes for both the reference object and the pipe. As already observed, the mass (or perhaps the radius) of the ball does not lead to the expected linear increase in measured AE energy and this effect is even more marked for the pipe than it was for the solid cylinder.
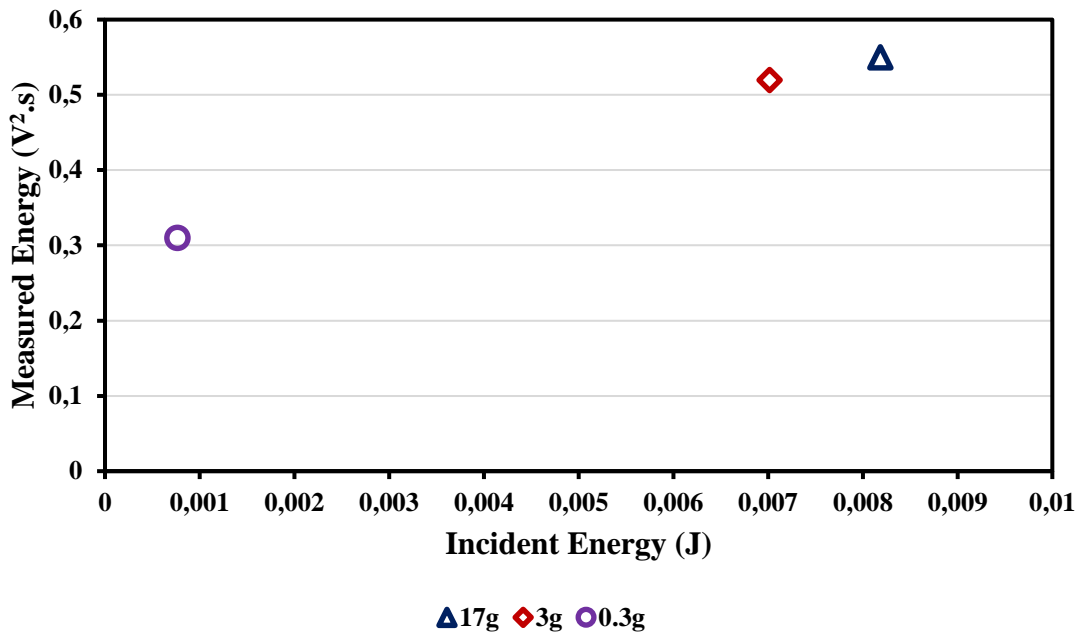
Fig. 10: Plot of measured energy vs incident energy in the first bounce for the three ball sizes dropped from 30cm height onto the cylinder.
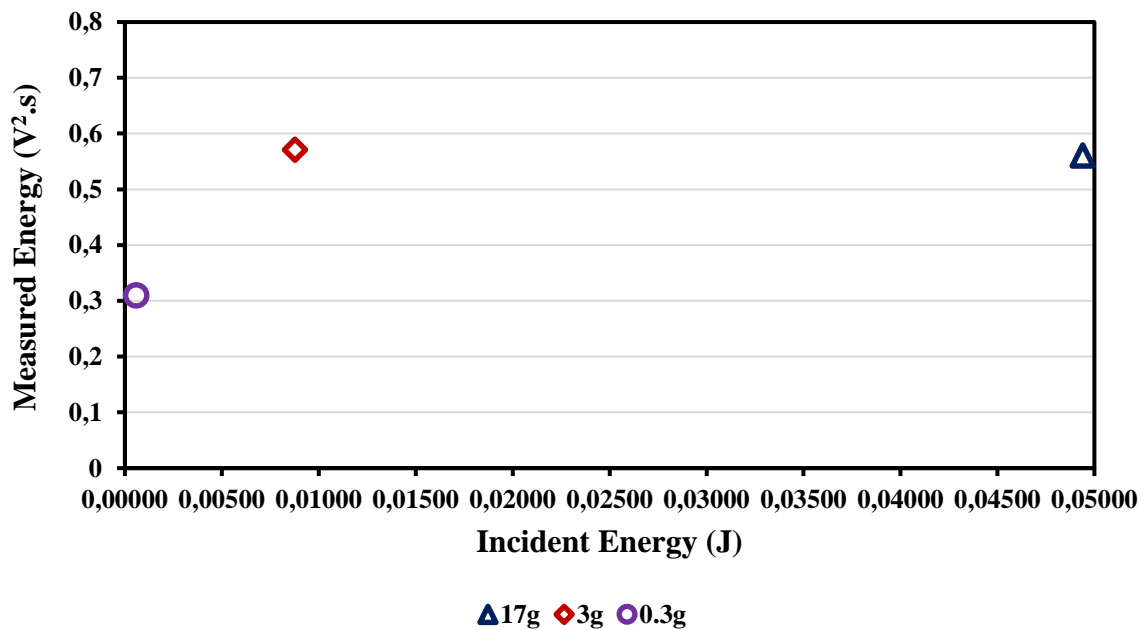
Fig. 11: Plot of measured energy vs incident energy in the first bounce for the three ball sizes dropped from 30cm height onto the pipe.

4. Simulation result and analysis

Just as with the corresponding experiments, the simulated results were recorded as time series, which start when the source is activated. The stress time signals obtained from the simulations at S_1 for 0.3g, 3 and 17g balls dropped from 0.3m heights is shown in Fig. 12 for the first 2 seconds. Comparing these with the corresponding experiments (Fig. 6) shows that the duration of the individual bounces is far longer in the simulations, most noticeably for the lightest ball. This can be attributed to the undamped reverberation of the AE wave in the simulations.
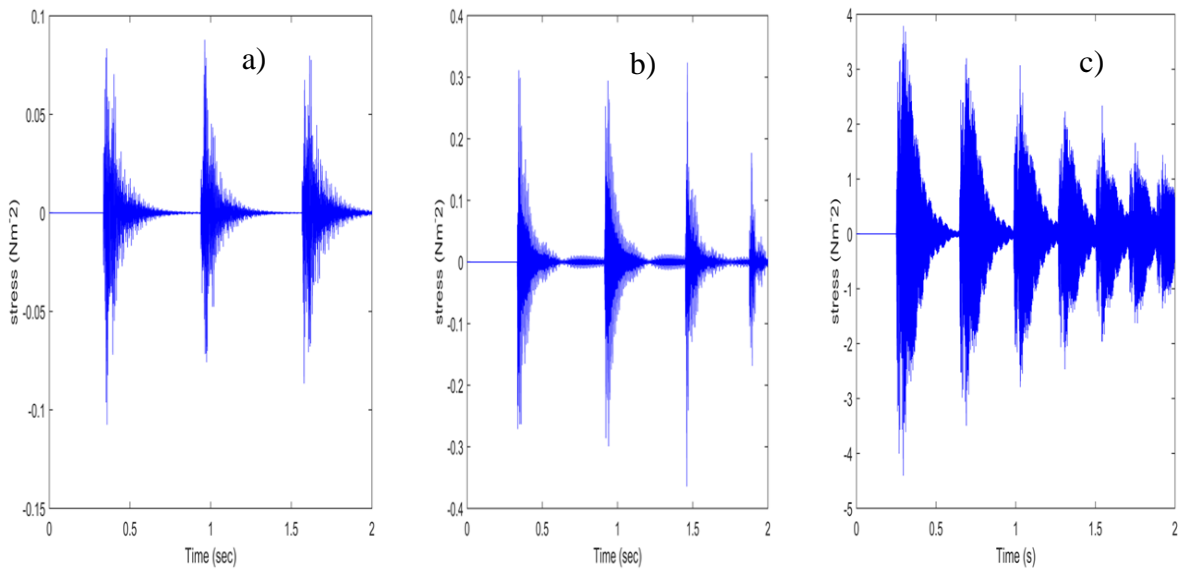
Fig. 12: Time series of Cauchy stress for virtual sensors at 0.5m from the simulated source on a pipe for balls dropped from 30cm height a) 0.3g b) 3g c) 17g.

Fig. 13 show the stress time signals for the first bounce for the plots shown in Fig. 12, it can be seen that the general amplitude increases with ball mass. Also, in contrast with the measurements, the increase in measured energy with incident energy is continuous across all simulations.
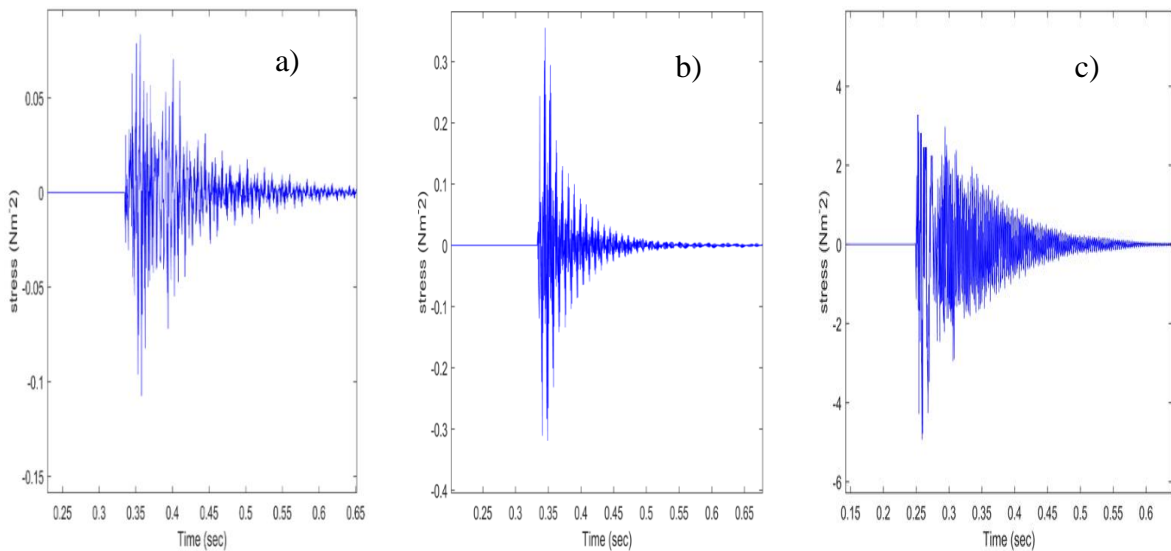
Fig. 13: Raw medium time series of Cauchy stress for virtual sensors at 0.5m from the simulated source on a pipe for balls dropped from 30cm height a) 0.3g b) 3g c) 17g.

Fig. 14 shows a plot of the simulated energy vs incident energy in the first four bounces dropped from 30cm height for the three ball sizes. It can be seen that in contrast with the measurements, there is very little difference in calculated incident energy between bounces, which is not surprising, since the coefficient of restitution for the simulations is unity.
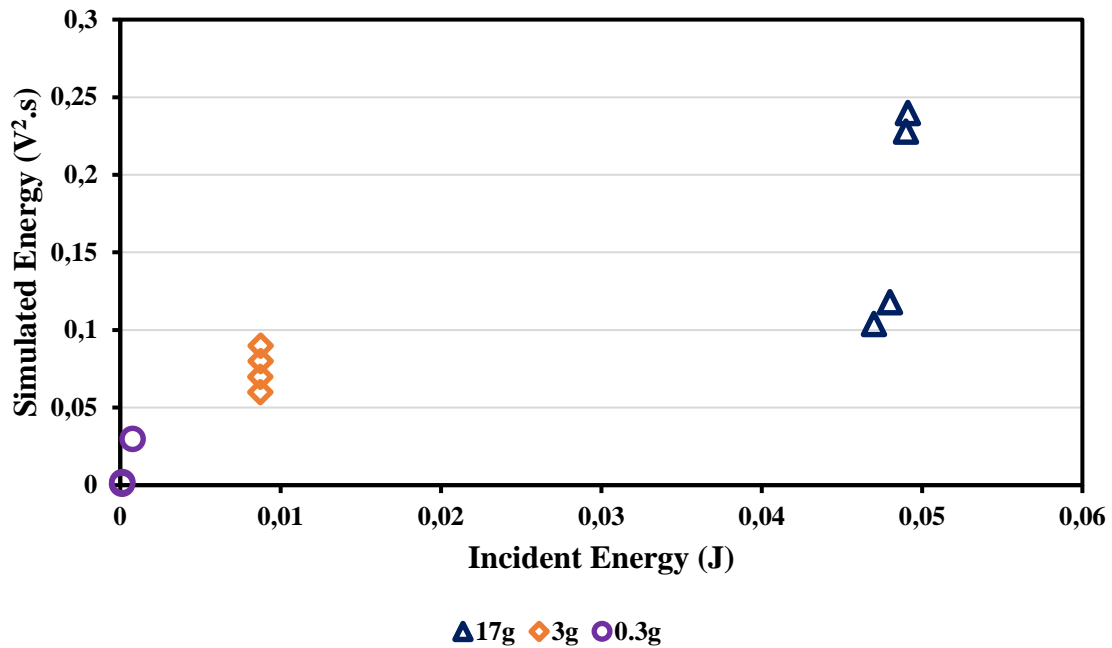
Fig. 14: Plot of simulated energy vs incident energy in the first four bounces dropped from 30cm height for the three ball sizes.

5. Conclusions

The ball drops onto the solid cylinder produced signals in which the first arrival and several rebounds could be discerned over a period of around 1 second. Each impact produced a burst of duration around 0.1 second, sufficient time for multiple reflections from the bottom face and edge of the cylinder. Despite this, there were clear relationships between the incident energy of the dropped object and the measured AE energy, confirming that these would be suitable sources to give a model for practical mechanical disturbances on the pipe.

The experimental and simulation results show that the relationship between measured or simulated energy and estimated incident energy increased continuously, and the differences could be attributed to the practical aspects of the experiments, including changes in coefficient of restitution associated with plastic deformation.

The experiments and simulations exhibited the expected behaviour with a burst of AE signalling the first landing and several subsequent bursts corresponding to the ball bouncing upwards and returning to the surface. In comparison with the equivalent experiments on the flat cylindrical surface, the ball drops on the pipe exhibited a longer burst with each bounce and somewhat more erratic behaviour with subsequent bounces.

Finally, although there was some suggestion that the heavier ball impacts might have involved plastic deformation, such events would be of little interest to a pipeline operator. Mechanical interactions which are of industrial interest are likely to involve such sources as excavators, drills or fishing gear and there would need to be a way of determining the severity of the event in terms of damage to the pipe.

6. References

[1] Haastrup, P. and Brockhoff, L.H., 1991. Reliability of accident case histories concerning hazardous chemicals: an analysis of uncertainty and quality aspects. *Journal of hazardous materials*, *27*(3), pp.339-350.

[2] Shehadeh, M., Steel, J.A. and Reuben, R.L., 2006. Acoustic emission source location for steel pipe and pipeline applications: the role of arrival time estimation. *Proceedings of the Institution of Mechanical Engineers, Part E: Journal of Process Mechanical Engineering*, *220*(2), pp.121-133.

[3] Vidya Sagar, R., Raghu Prasad, B.K. and Sharma, R., 2012. Evaluation of damage in reinforced concrete bridge beams using acoustic emission technique. *Nondestructive Testing and Evaluation*, *27*(2), pp.95-108.

[4] Nivesrangsan, P., 2004. *Multi-source, multi-sensor approaches to diesel engine monitoring using acoustic emission* (Doctoral dissertation, Heriot-Watt University).

[5] Webster, J., Marinescu, I., Bennett, R. and Lindsay, R., 1994. Acoustic emission for process control and monitoring of surface integrity during grinding. *CIRP annals*, *43*(1), pp.299-304.

[6] Roberts, T. and Talebzadeh, M., 2003. Acoustic emission monitoring of fatigue crack propagation. *Journal of constructional steel research*, *59*(6), pp.695-712.

[7] Berkovits, A. and Fang, D., 1995. Study of fatigue crack characteristics by acoustic emission. *Engineering Fracture Mechanics*, *51*(3), pp.401-416.

[8] Shehadeh, M.F., 2006. *Monitoring of long steel pipes using acoustic emission* (Doctoral dissertation, Heriot-Watt University).

[9] Ding, Y., Reuben, R.L. and Steel, J.A., 2004. A new method for waveform analysis for estimating AE wave arrival times using wavelet decomposition. *NDT & E International*, *37*(4), pp.279-290.

[10] Zelenyak, A.M., Hamstad, M.A. and Sause, M.G., 2015. Modeling of acoustic emission signal propagation in waveguides. *Sensors*, *15*(5), pp.11805-11822.

[11] Sause, M.G. and Richler, S., 2015. Finite element modelling of cracks as acoustic emission sources. *Journal of nondestructive evaluation*, *34*(1), pp.1-13.

[12] Sause, M.G., Hamstad, M.A. and Horn, S., 2012. Finite element modeling of conical acoustic emission sensors and corresponding experiments. *Sensors and Actuators A: Physical*, *184*, pp.64-71.

[13] Abolle-Okoyeagu, C.J., 2019. *Acoustic emission monitoring of pipes: combining finite element simulation and experiment for advanced source location and identification* (Doctoral dissertation, Heriot-Watt University).

[14] Prosser, W.H., Hamstad, M.A., Gary, J. and OGallagher, A., 1999. Reflections of AE waves in finite plates: finite element modeling and experimental measurements. *Journal of Acoustic Emission*, *17*(1-2).

[15] Okoyeagu, J.A., Torralba, J.P., Chen, Y. and Reuben, R., 2014. Acoustic emission source identification in pipes using finite element analysis. In *Proc. of 31 Conf. on European Working Group on Acoustic Emission* (pp. 3-5).

IDENTIFICATION OF DAMAGES INTO A POLYMER STRUCTURE BY AE - TRANSITION FROM TENSILE SPECIMEN TO STRUCTURE

Eric Lainé[1,*], Jean-Claude Grandidier[1], Anne-Laure Gorge[1], Maxime Cruz[1] and Eric Maziers[2]

[1]Institut Pprime, CNRS, ISAE-ENSMA, Université de Poitiers, F-86962 Futuroscope, France;
eric.laine@ensma.fr, grandidier@ensma.fr, anne-laure.gorge@ensma.fr
[2]TotalEnergies One Tech Belgium, Zone Industrielle Feluy, B-7181 Seneffe, Belgique;
eric.maziers@totalenergies.com
*Correspondence: eric.laine@ensma.fr

ABSTRACT

This paper aims to study the damage mechanisms with acoustic emission technique (AE) in a polymer sandwich structure that contains three layers: two polyethylene skins and the polyethylene foam core (skin-foam-skin). First, a classical tensile test was carried out to correlate the acoustic signals with plasticity initiation and damage of a polyethylene sample. The results obtained are similar to those observed in other studies. Moreover, it is possible to separate the signal due to cavitation from the signal due to necking propagation. In a second step, the technique is used to detect the rupture of a polymer skin on a rotomolded skin-foam-skin structure (bottle). Tests were performed on this bottle by applying internal water pressure. Two tests are conducted with interruptions more or less early to determine the first damages and understand their evolution. Finally, different parameters (average frequency, RA value, etc.) are measured to understand and quantify the perceived damage. A structural damage scenario is proposed based on the AE/RX correlation and the mechanical behavior.

Keywords: Polymer, multilayer, acoustic emission, damage, tensile test, structure test.

1. Introduction

In the literature, many works are devoted to determining the damage of composite, metallic and structured materials using the acoustic emission (AE) technique. However, there are very few papers on AE for thermoplastic polymers [1-7] and none to our knowledge for sandwich polymer structures. One reason may be that polymers strongly attenuate ultrasonic waves and are less energetic.

The challenge is to verify that this technique can apprehend damages in a polymer sandwich material. The objective is to characterize the failure scenarios of a multilayer polymer structure by combining RX and AE. A new sandwich material consists of a foamed polyethylene (PE) layer between two polyolefin skins, inner and outer layers. The structure (7 liters bottle) is produced in a rotational molding process [8-10], a polymer conversion technology mainly designed to produce hollow plastic parts. This sandwich material (skin-foam-skin) considerably increases the bending stiffness for the same weight. Therefore, it is easy to imagine its interest, particularly in the automotive [11], aeronautical, storage and transport industries.

If some materials can capture acoustic signals during mechanical stress by their components (fibers) or their morphology, it is not the same for semi-crystalline polymer materials. The latter are increasingly used in various applications (automotive, aerospace, transportation...). On the other hand, as these materials are increasingly used under extreme conditions, new methodologies are necessary to precisely follow the degradation of their properties to predict their lifetime. The mechanisms of plastic deformation, damage, and fracture have been extensively studied [12-18]. Despite all this work, the characterization of PE damage remains a real challenge.

However, one of the challenges is verifying whether this AE technique can apprehend damage in a complex polymer structure (skin-foam-skin). Specifically, the representative structure used in this research is a three-layer rotomolded bottle. The question to be answered is whether AE associated with tomography can obtain information on the damage in a multilayer. The difficulties are the complexity of the multilayer structure (skin-foam-skin), two different materials (PE foam, PE skins), different density materials, the internal environment (water), the 'decimetric' dimensions of the bottle, and the interface between skin and foam which present a gradient of density.

In order to identify the mechanisms with AE tools, it is essential to develop a specific protocol. The first phase consists of determining the first acoustic signal linked to the first apparition of the damage. Therefore, an analysis of the acoustic activity during a tensile test can be performed on polymer samples that constitute one of the skins of the sandwich material and are recognized as a reference. Different loading - unloading internal pressures should be applied at the structure level on a multilayer rotomolded bottle instrumented with height sensors. A second challenge is locating the first damage area in a complex multilayer structure. The bottles in the initial state are tomographed in order to be compared with the scans taken after each test interruption to correlate these signals to damage.

The material and structure are introduced in the following paragraph, and then the experimental systems and the associated acoustic emission technique are detailed in the experimental procedure paragraph [19]. Finally, the paragraph on results and discussion presents the results of the tensile and bottle tests before concluding.

2. Material and structure

2.1 Material
The material is polyethylene (PE) which is a new generation metallocene medium density polyethylene (mMDPE) with hexene as comonomer. This polymer has a density of 0.940 g/cm^3. The sandwich material is manufactured by rotational molding, a polymer conversion technology specifically designed to produce polyethylene foam with a density of 0.200 g/cm^3.
The polyethylene tensile specimens tested in this work are cut from monolayer rotomolded bottles with the polyethylene material.

2.2 Structure
The bottles tested (Fig. 1a) are sandwich structures (Fig. 1b) composed of a layer of expanded polyethylene foam between two layers of polyethylene, called skins. The dimensions of multilayer rotomolded bottle are: height 330mm, width 200mm and depth 140mm (Fig. 1c, Fig 1.d). The bottle has a rectangular section, the bottom of the bottle is slightly curved, and the edges have outer and inner radii of curvature of 15mm and 5mm, respectively. The skins and foam are 2mm and 10mm thick, respectively. The bottle is produced with a threaded cap. It is cut by machining at this point to install the clamps that hold and seal the bottle during pressure testing [19].
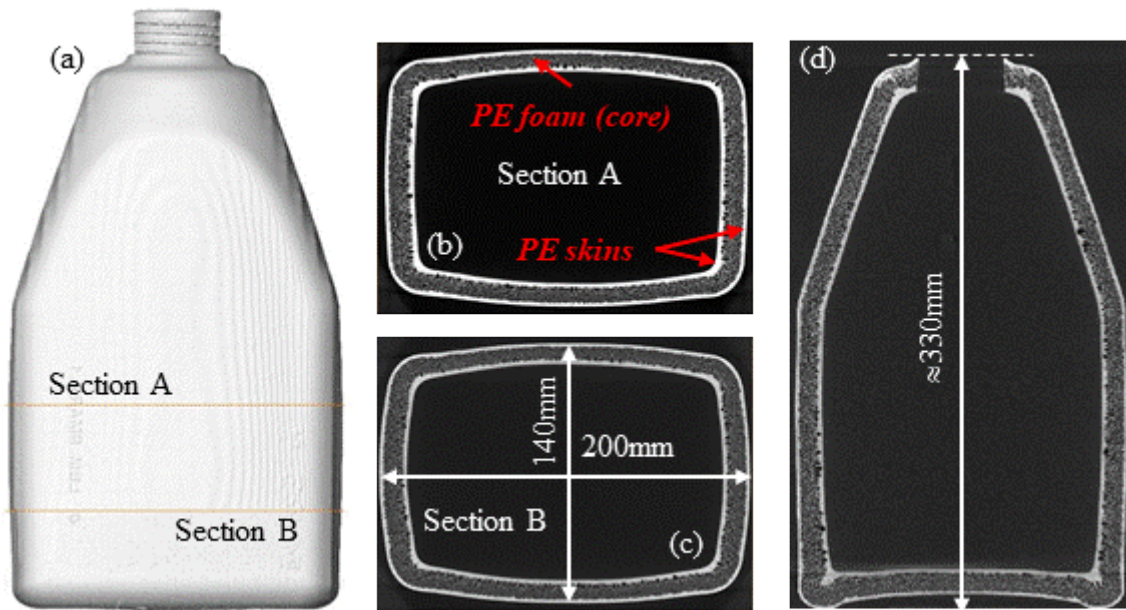
Fig. 1: (a) Bottle tomography – (b) and (c) Tomographic images of two cross sections – (d) Tomography of a longitudinal section of the bottle (bottle axis) [19].

3.   Experimental procedure

3.1 Tensile tests and acoustic emission

The uni-axial tensile tests were conducted in an Instron 1195 testing machine (500N load cell)..
These tests are performed at one constant strain rate $1.75 \ 10^{-3} \ s^{-1}$ with the Videotraction® system [20] and performed at ambient temperature (±1∘C). Strains are calculated from the displacement of four marks applied to the surface of the specimen (Fig. 2a, Fig. 2b). During tests, the four marks are monitored in real time by a CCD camera. The logarithmic (or true) longitudinal (ε_l) and transverse (ε_t) strains are calculated with the current and initial distances between longitudinal and transverse (in width direction) marks, and the increments of these values [19-20]. The Cauchy stress in the loading direction (or True stress) is determined from the current axial load, the initial cross-section area of the specimen and the true transverse strain, in isochoric framework and assuming isotropy of true transverse strains (in width and thickness) [19-20].

To capture the AE signals during the tensile tests (Fig. 2a), a two-channel PCI-2 from Mistras Group is employed. The test is therefore performed with two Micro-80 piezoelectric acoustic sensors (100 kHz - 1 MHz bandwidth and 10 mm diameter) with a PAC 1220A preamplifier (40 dB gain), which are positioned on the tensile specimen (Fig. 2b). When recording the AE signals, the operator defines a detection threshold (35 dB) below which no signal is registered. The acquisition system is configured before each test using the mine-breaking procedure [21-22]. The characteristics of a signal are well known, such as duration, rise time, and amplitude. In addition, only signals with sufficient intensity to reach both sensors can be located and situated along the specimen. For these tests, the signals are therefore divided into two categories: non-localized signals (called "AE hits") and localized signals (called "AE events").

3.2 Structure experimental (ENDOMAT) and acoustic emission

The experimental test bench "Endomat" [19,23] is a tri-axial mechanical test machine allowing the following stresses: tension-compression (1200kN), torsion (55kN), and internal pressure (1200bar). In addition, this bench makes it possible to impose mechanical compression and internal pressure on a structure simultaneously. The practical dimensions of the test machine are 700x700x1800mm, which allows the fastening of large structures. In this work, only the pressure

load is used. The tension-compression axis is locked during all the tests to position and hold the bottle. A specific assembly has been designed to link the structure to the test bench, allowing positioning, holding, and sealing during the internal pressure tests. This system allows the bottle to be subjected to mechanical compression and internal pressure in different modes: monotonic, charge-discharge, creep, fatigue (cyclic).

An 8-channel express system from the Mistras group is used for recording AE signals during bottle testing. In addition, damage monitoring is carried out by acoustic emission measurement. During all the tests, the bottles are instrumented with eight piezoelectric acoustic sensors with a PAC 1220A preamplifier (gain of 40dB) presented in the previous paragraph. They are placed on the bottle with silicone grease and held in place with adhesive tape (Fig. 2c).The position of the sensors is in "square" (Fig. 2d) on the two main sides. When recording AE signals, the operator determines a detection level (32dB) below which no signal is registered. Similarly, the propagation is evaluated by the mine breakage procedure [21-22]. In addition, the acquisition system calculates the time-dependent parameters (amplitude, number of counts, rise time, duration, energy) in real-time. These characteristics are directly related to the waveforms' shape, mainly exploited for the analysis of acoustic signals.
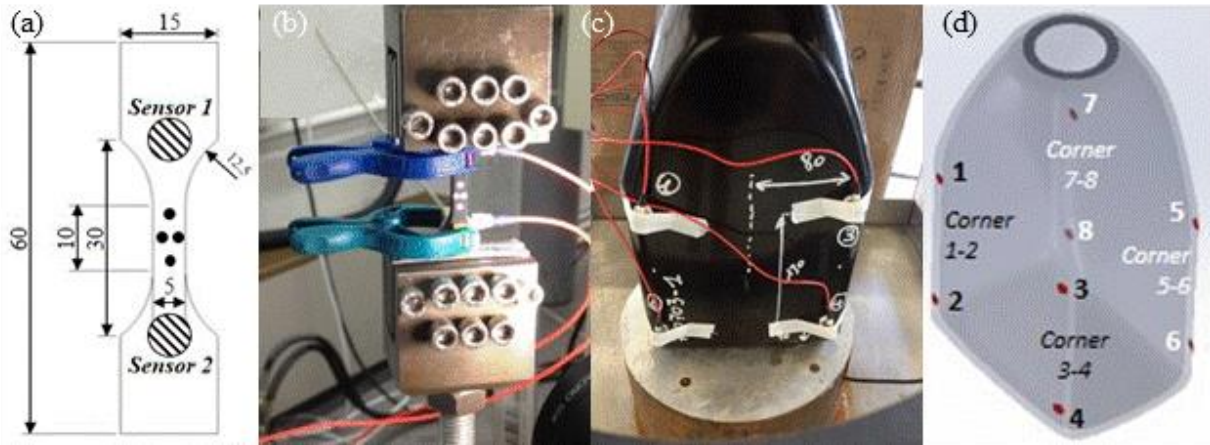
Fig. 2: (a) Location of the four markers and two AE sensors on a tensile test specimen (dimension in millimeters) - (b) Tensile test on PE specimen -(c) and (d) Positioning of AE sensors on bottle.

3.3 AE parameter analysis [19]

During a test with the acoustic emission technique, the first analysis that can be done is to represent all the recorded signals in the form of amplitude - number of counts. This mapping should be signal-free in the lower right and upper left corners to validate the system acquisition parameters. Signals with small amplitude and large count number correspond to mechanical noise, and those with large amplitude and small count number correspond to electromagnetic noise [24].

On the other hand, the method based on the classification of cracks based on the code JCMS-III B5706 [25] is also applied. This method has been used for concrete, from four-point bending tests and its direct shear tests on specimens [26]. To categorize active damage, AE parameters of the maximum amplitude A_{mv} (Volts) and the rise time noted τ_r (ms) are used to calculate RA value (ms/V). The average frequency noted $A\text{-}FRQ$ (kHz) is calculated from AE count AE_C and the duration time τ_d (ms) as:

$$RA = \tau_r / A_{mv} \qquad\qquad (1)$$

$$A\text{-}FRQ = AE_C / \tau_d. \qquad\qquad (2)$$

From these two parameters, the mechanisms occurring in different families of materials can be classified. For example, cracks are easily categorized into tensile and shear cracks for concrete [26]. These parameters will be discussed for the different protocols. However, a criterion defined on the ratio of the RA value and the average frequency for crack classification has not been proven [26]. Finally, the maximum amplitude A_{mdB} in decibels of an AE signal in time domain is given by the following formula:

$$A_{mdB} \text{ [dB]} = (20 \log A_{mv}10^6[\mu volt]) - G \tag{3}$$

where the voltage in $\mu volt$ is A_{mv} and G is the preamplifier gain. Finally two other parameters can be analyzed: the AE signal count (N) and amplitude (A_{mv}). In general, These two parameters are associated by the following relationship [27,29]:

$$N = \alpha \, A_{mv}^{-m} \tag{4}$$

where α and m are constants [28]. In the equation (4), the m parameter is negative, which indicates that large amplitude AE signals are seen less often than small amplitude ones. For fatigue crack growth of a steel material, Yuyama et al. [29] determined that $m \approx 2$. In contrast, Yamabe et al. [28] identified that $m = 1.8$ for rubber from the static growth test. Thus, they complete that since the value m obtained from the static growth of rubber is coherent with that determined from the growth of fatigue cracks in steel. This value is accepted as related to failure behavior, i.e., crack growth [27]. In the specific case of polymers, the damage modes are limited, and the mechanisms that can generate acoustic waves are visco-plasticity (high speed), cavitation - coalescence - tearing. At the scale of a complex structure, damping increases the difficulty and does not permit analysis counts and events. In order to develop in this study a first classification for damage in a polymer sandwich structure, the classical AE descriptors are analyzed as the RA value and the A-FRQ and the parameters of the equation (4).

4. Results and discussions

4.1 Evaluation from the tensile test on PE sample

During the tensile test on the polyethylene specimen, 24 AE events and 357 AE counts located between the two sensors are transmitted and discriminated during the acoustic activity recording. Fig. 3a illustrates the number of counts as a function of amplitude. This distribution confirms that the measurements are reliable and therefore not due to mechanical and/or electromagnetic noise. Fig. 3b shows the temporal evolution of the load and the true stress during the whole duration of the tensile test and the superimposed amplitude of the received acoustic signals. About the load curve, three zones can be distinguished:
  - the first one from the beginning of the test to the maximum load represents the first damage (cavitation) and the initiation of the neck,
  - the second zone which corresponds to the decreasing load (neck localization),
  - the third one where the load plateau corresponding to the neck propagation is observed.

The acoustic signal amplitude varies between 35 and 60dB. A decrease in the average amplitude is observable during the test. The maximum is achieved in the first zone, well before the initiation of the neck. As the mechanical load increases, acoustic emissions are primarily developed between the first bend of the load curve and the maximum load point. This corresponds to the formation of cavitation in the useful area. During the evolution of the necking phase, the AE activity decreases sharply, and the signals have lower amplitudes (35 to 40dB). The signal parameters are correlated with each other by tracing the amplitude versus the number of counts, this distribution is comparable to [7]: as the amplitude increases, the number of counts increases.

In order to better correlate the number of cumulative acoustic signals and tensile properties, the true stress-true strain curve (Fig. 4a and Fig. 4b) is plotted on the same graph by converting time to strain. Fig. 4a is a zoom (the first 5% of the strain) of Fig. 4b. Thus, for the true stress-true strain curve, the initial slope represents the elastic mechanical parameter of the material, i.e., the modulus. The first acoustic signals appear at about ≈0.6% true longitudinal strain and true stress of ≈5.5MPa. Five AE events are detected at the beginning of the true stress - true strain curve (Fig. 4a), with almost the highest amplitudes and the rest after shrinkage with lower amplitudes. From about 25% strain, which corresponds to zone 2, where the load decreases (neck location), and the number of AE signals decreases sharply. This can be seen in Fig. 4b, where the curves representing the cumulative number of AE hits and AE events respectively tend towards a plateau.
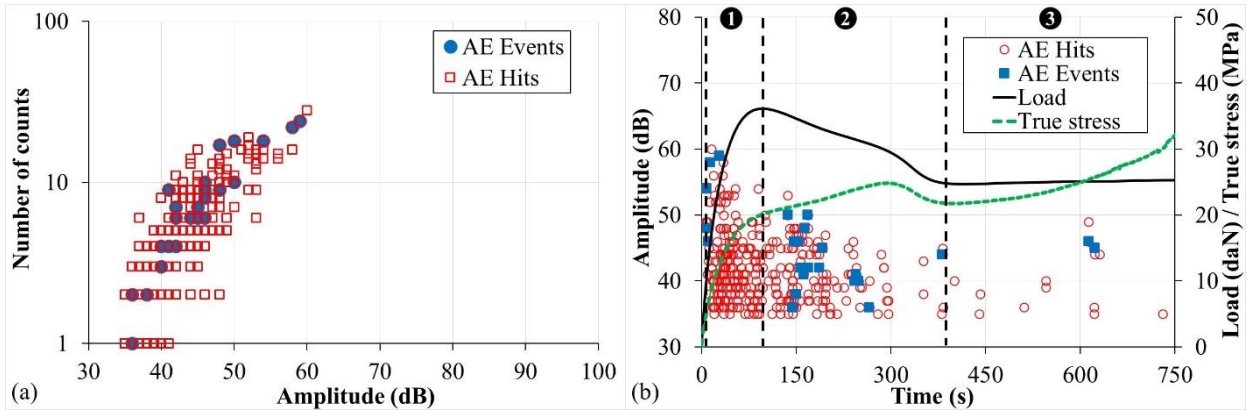
Fig. 3: (a) Number of counts vs Amplitude on a tensile test specimen - (b) Amplitude, Load and true stress vs Time [19].
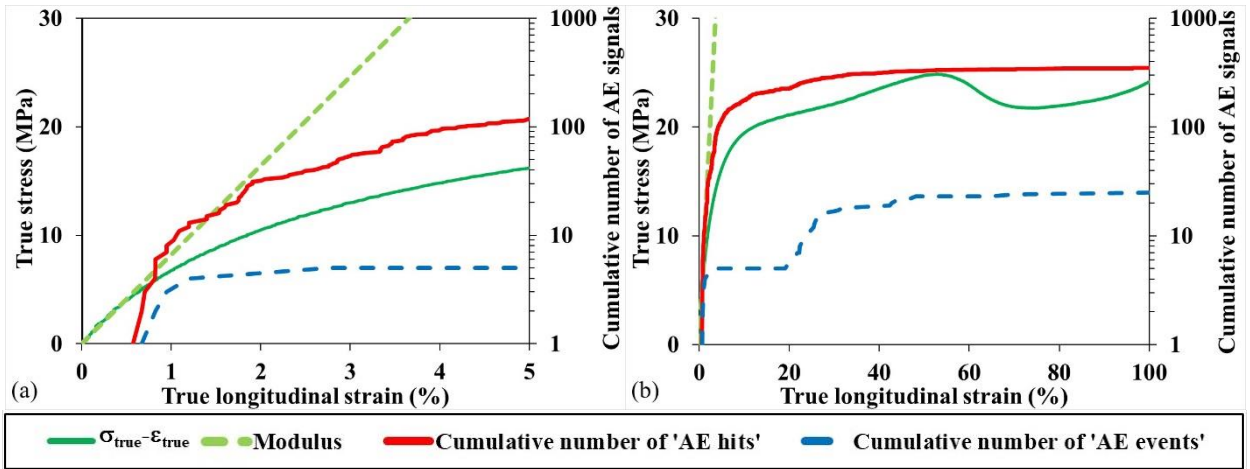
Fig. 4: True stress, Cumulative AE events and AE hits vs True longitudinal strain (a) up to 5% strain and (b) up to 100% strain [19].

4.2 Identification of first damage on a sandwich structure

This first structural test aims to determine the relationship between the first acoustic signs and the local damage in the multilayer bottle subjected to increasing internal pressure. To identify this relationship, the test is stopped as soon as the first acoustic signals are perceived. At each stop, the bottle is removed from the test bench, emptied, and scanned to localize the first damage, then reinstalled on the test bench to pursue the testing. One of the significant difficulties of this procedure is to perfectly reposition the bottle on the bench between each test, significantly repositioning the acoustic sensors on the bottle.

During the first three interrupted tests (at 2, 3, and 5 bar), acoustic signals (only AE hits) are received on sensors 1,2,5, and 7. The tomographic evaluation does not provide any information to link the first AE signals to local degradation of the inner skin. These first pulses are due either to a very local degradation or the noise generated by the machine. Nevertheless, the characteristics of the signals are very similar to those seen at the time of the linearity loss of the traction curve. Of course, it is impossible to exclude machine noise completely, but comparing the first events under is convincing enough to link these signs to the initiation of the first damage in the same way as the tensile test. In this situation, the tomography is not sufficiently accurate to localize and observe the consequences of these mechanisms, which should be cavitation mechanisms.

For the fourth load, it is decided to increase the pressure directly to 5 bar, then to increase by 1 bar steps depending on the level of detection of the acoustic signals. During the test, an acoustic activity appears already between 4 and 5 bar on sensor 1, then on sensor 3 between 5 and 6 bar. The test continues with a constant level of 6 bar. In parallel to sensor 1, acoustic signals are detected by sensor 3. The test is then interrupted after these 10-11 hits to scan the bottle. At the end of the unloading, 2 new hits are visible on sensor 1 with a slightly higher amplitude. In contrast, the other sensors (2,4,5,6,7,8) did not detect acoustic signals during this test. This first experiment suggests that the first hits are either a sign of the initiation of the first damage or parasitic events of the machine and the assembly that is recorded with the required filtering. The first hits at 40dB are well in line with wall failure mechanisms, which are the first mechanisms that emerge during the pressure rise. Finally, the distribution of hits is similar to that measured under tensile stress.

4.3 Localization of failure of a skin (bottle)

An analysis of the acoustic signals suggests that they are located between sensor pairs 1-2 and 3-4 and close to sensors 1 and 3. Tomographic images of this area indicate that the inner skin of the bottle is starting to be damaged (Fig. 5a, Fig. 5b). A small crack developed in an area of thin skin at the initial cavities at the skin/foam interface (Fig. 5a). It is also imperative to note that not all thinner areas are affected by this magnitude of load damage. The first damage occurred near the bottom bend, an area of stress more complex than the walls of the bottle.
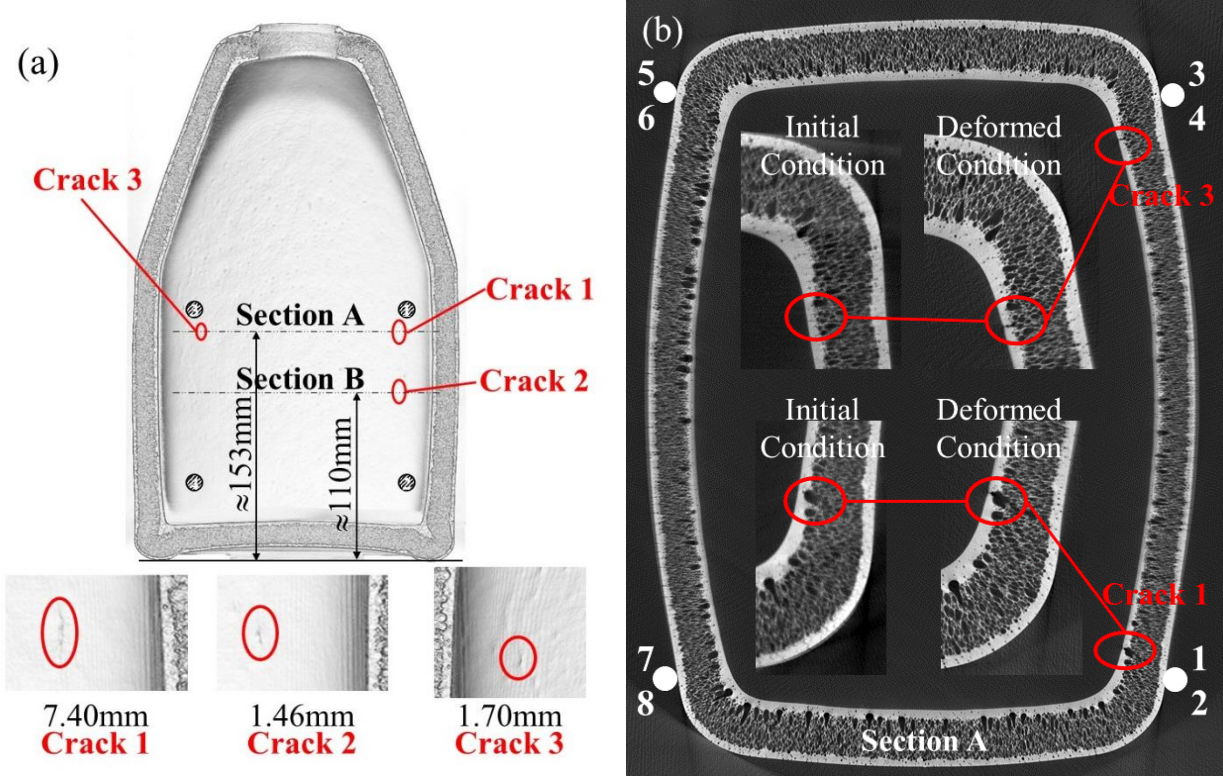
Fig. 5: (a) Location of rupture zone on the bottle (test 1) - (b) Section A of Fig. 5a [19].

No local breakage is detected on the opposite side (sensors 5 to 8). The 20 hits recorded during the test are split between the two sensors 1 and 3, respectively 16 and 4 hits. The cracks measured locally are 7.4 mm for crack 1 and 1.7 mm for crack 3. Likely, crack 2 between sensors 1 and 3 is not detected. If a link can be established between the number of occurrences and the length of a crack, then we can observe that here the ratios are very similar; thus, this ratio is 0.463 for crack 1 and 0.425 for crack 3.

4.4 *A-FRQ* and *RA values*

Fig. 6a plots *A-FRQ* versus *RA* value for all acoustic signals for zones 1, 2, and 3 as defined in Fig. 3b. These figures indicate that most AE signals have a high *A-FRQ* value and a low *RA* value for a tensile test. To our knowledge, unlike concrete, no study has attempted to use these parameters to categorize damage. Obviously, a single test is not sufficient, especially a tensile test. However, two sets can be distinguished: AE signals with high amplitude and high *A-FRQ* (low *RA* value) and those with low amplitude and high *A-FRQ*.

For other materials (such as concrete) tested under various loads, the literature has shown that two damage modes can be differentiated by a line that separates high *A-FRQ* and low *RA* value and low *A-FRQ* and high *RA* value. This one is naturally material-dependent. However, no study to date has given any indication of the slope of this line for a polymer. Therefore, we arbitrarily choose the case where the proportion of the *RA* value and the average frequency is set to 1:20. Most of the signals are above this line, and the few signals below correspond to events at the end of loading when the necking unfolds with high values of true longitudinal strains. By superimposing the evolution of the *RA* and *A-FRQ* values with the loading as a function of time, a dependence of these values according to the three damage evolution zones appears [19].

Fig. 6b plots *A-FRQ* versus the *RA* value of each acoustic signal received from sensors 1 and 3 during the bottle test (test 1). The *A-FRQ* and *RA* characteristics correspond to the damage initiation distribution in the tensile tests. Therefore, it appears reasonable to link these hits to damage initiation and the first small crack in the inner skin. The second test on a multilayer bottle leads to the same results and conclusions [19].
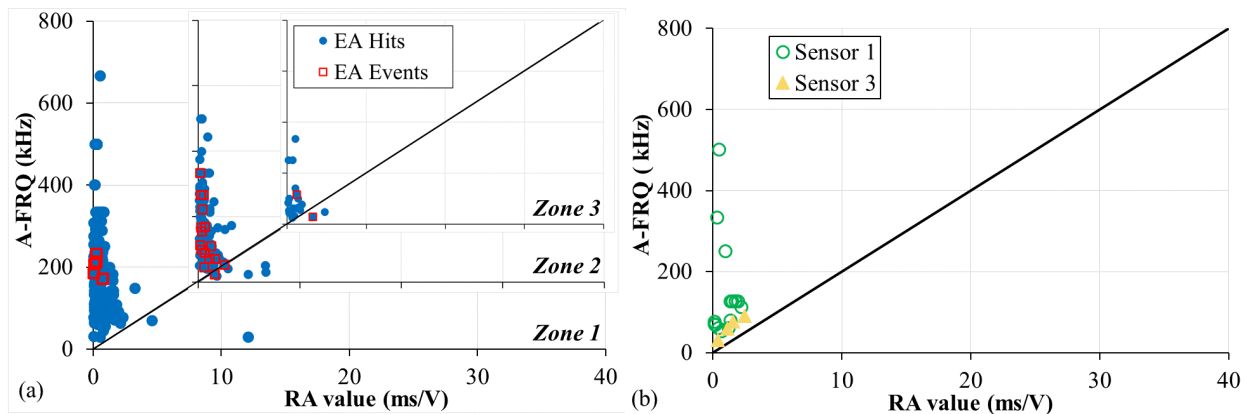
Fig. 6: Relationship between *A-FRQ* and *RA* value (a) tensile test - (b) bottle test (test 1).

4.5 *AE event count (*N*) and amplitude (*A_{mv}*)*

Fig. 7 presents the number of AE events (*N*) versus amplitude (*A_{mv}*) acquired from the bottle during the static internal pressure and tensile tests. The data at N≥1 was plotted because a few AE signals were created due to the swelling process. Using equation 4, the coefficient m can be directly determined from the dots in Fig. 7. The value of m identified for the tensile test is 1.90 for amplitudes larger than 42dB (12.6V). For bottle tests 1 and 2, where the acoustic activity was enough to exploit these parameters, the value of m is very close to 1.90. The fracture behavior is correlated to this slope. Thus, the value found for this polymer, which is representative of the crack growth energy, is between the values for steel [29] and rubber [28].
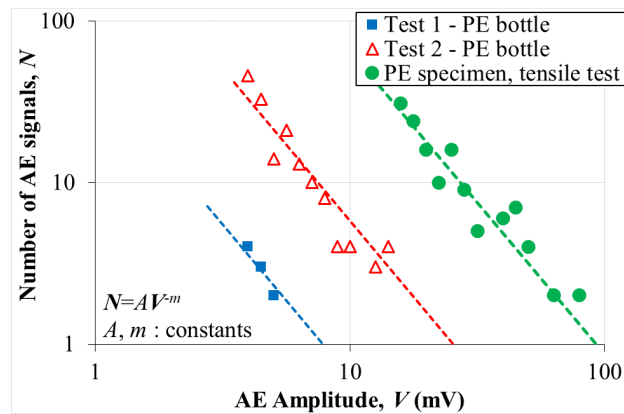
Fig. 7: Relationship between the number of AE signals and the AE amplitude obtained from tensile test and bottle tests [19].

5. Conclusions

Finally, the comparison of the acoustic recordings of the structure tests with the tensile test is significant. The failure scenario of the inner skin of the sandwich structure subjected to internal water pressure is proposed based on a cross-referencing of AE measurements and tomographic observations. Two tests on two distinct multilayer bottles with polymeric skins such as PE demonstrate that the use of AE permits the capture of damage and/or structural failure. Thus, the transition from a tensile sample to an industrial sandwich structure (rotomolded bottle) is validated. Furthermore, in a complex environment (pressurized water) with a PE sandwich structure, it is possible to detect by acoustic emission the first stages of damage at 6 bars and the propagation of cracks up to the stage of high rupture of the inner skin. Additional results are reported in [19]. This work initiates a new approach which will have to be confirmed in the future by complementary tests (shear, cracks growth) to complete the understanding of the damage evolution.

6. Acknowledgments

7. References

[1]   Betteridge, D., Connors, P.A., Lilley, T., Shoko, NR, Cudby, M.E.A., Wood, D.G.M. (1983). Analysis of acoustic emissions from polymers, Polymer, vol. 24, no. 9, p. 1206-1212.
[2]   Ronkay, F., Czigany, T. (2006). Cavity formation and stress-oscillation during the tensile test of injection molded specimens made of PET, Poly Bull, vol. 57, no. 6, p. 989-998.
[3]   Bohse, J. (2000). Acoustic emission characteristics of micro-failure processes in polymer blends and composites, Compos Sci Technol, vol. 60, p.1213-1226.
[4]   Qian, R., Wang, T., Shen, J. (1983). Acoustic emission during stretching of polymers, Polymer Communications, vol. 2, p.168-175.
[5]   Galeski, A., Piorkowska, E., Koenczoel, L., Baer, E. (1990). Acoustic emission during polymer crystallization, J Polym Sci part B: Poly Phys, vol. 28, no. 7, p. 1171-1186.
[6]   Teofilo, E.T., Rabello, M.S. (2005). The use of acoustic emission technique in the failure analysis of PET, Polymer Testing, vol. 45, p. 68-75.

[7] Casiez, N., Deschanel, S., Monnier, T., Lame, O. (2014). Acoustic emission from the initiation of plastic deformation of Polyethylenes during tensile tests, Polymer, vol. 55, p. 6561-6568.

[8] Emami, M., Takacs, E., Vlachopoulos, J. (2010). Study of Foaming Mechanisms in Rotational Molding, ANTEC 2010.

[9] Emami, M., Thompson, M.R., Takacs, E., Vlachopoulos, J. (2011). Rheological Effects on Foam Processing in Rotational Molding, ANTEC 2011.

[10] Emami, M., Thompson, M.R., Takacs, E., Vlachopoulos, J., Maziers, E. (2013). Visual Studies of Model Foam Development for Rotational Molding Processes, Advances in Polymer Technology, vol. 32, p. 809-821.

[11] Maziers, E. (2013). Skin-foam-skin TP-Seal® rotomolded structures: a new concept for the production of car bodies for urban mobility, Plastics Engin, vol. 69, no.9, p. 40-42.

[12] G'sell, C., Jonas, J.J. (1981). Yield and transient effects during the plastic deformation of solid polymers, J Mater Sci, vol. 16, p. 1956-1974.

[13] Galeski, A. (2003). Strength and toughness of crystalline polymer systems, Prog Polym Sci, vol. 28, p. 1643-1699.

[14] Pawlak, A, Galeski, A. Rozanski, A. (2014). C,avitation during deformation of semi-crystalline polymers, Prog Poly Sci, vol. 39, p. 921-958.

[15] G'sell, C., Dahoun, A. (1994). Evolution of microstructure in semi-crystalline polymers under large plastic deformation, Mater Sci Eng, vol. 175, p.183-199.

[16] Lin, L., Argon, A.S. (1994). Structure and plastic deformation of polyethylene, J Mater Sci, vol. 29, no. 2, p. 294-323.

[17] Plummer, C.J.G., Goldberg, A., Ghanem, A. (2001). Micromechanisms of slow crack growth in polyethylene under constant loading, Polymer, vol. 42, no. 23, p. 9551-9564.

[18] Hamouda, H.B.H., Simoes-Betbeder, M., Grillon, F., Blouet, P., Billon, N. (2001) Creep damage mechanisms in polyethylene gas pipes, Polymer, vol. 42, no. 12, p. 5425-5437.

[19] Lainé, E., Grandidier, J.-C., Cruz, M., et al.. (2020). Acoustic emission description from a damage and failure scenario of rotomoulded polyolefin sandwich structure subjected to internal pressure for storage applications, Mechanics & Industry, vol. 21, p. 614-619.

[20] G'Sell, C., Hiver, J.M., Dahoun, A., et al. (1992). Video-controlled tensile testing of polymers and metals beyond the necking point, J. Mater. Sci. vol. 27, no. 18, p. 5031–5039.

[21] Nielsen, A. (1980). Acoustic Emission Source based on Pencil Lead Breaking, The Danish Welding Institute Publication, vol. 80, p. 15-20.

[22] Jemielniak, K. (2001). Some aspects of acoustic emission signal pre-processing, J Mat Proc Tech, vol. 109, p. 242-247.

[23] Lainé, E., Dupré, J.C., Grandidier, J.-C., Cruz, M. (2021). Instrumented tests on composite pressure vessels (type IV) under internal water pressure, International Journal of Hydrogen Energy, vol. 46, no. 1, p. 1334-1346.

[24] Malpot, A. (2017). Etude du comportement en fatigue d'un composite à matrice polyamide renforcé d'un tissue de fibres de verre pour application automobile, Thèse, ISAE-ENSMA.

[25] JC MS-III B5706 (2003). Monitoring method for active cracks in concrete by acoustic emission, Japan: Federation of Construction Materials Industries.

[26] Ohno, K., Ohtsu, M. (2010). Crack classification in concrete based on acousyic emission, Const. and Bulding Mat., vol. 24, p. 2339-2346.

[27] Ohtsu, M. (1996). The history and development of acoustic emission in concrete engineering, Mag Concr Res, vol. 48, p. 321–330.

[28] Yamabe, J., Matsumoto, T., Nishimura, S. (2011). Application of acoustic emission method to detection of internal fracture of sealing rubber material by high-pressure hydrogen decompression, Polymer Testing, vol. 30, p. 76-85.

[29] Yuyama, S., Kishi, T., Hisamatsu, Y. (1984). Effect of environmental, mechanical conditions, and materials characteristic on AE behavior during corrosion fatigue processes of an austenitic stainless steel, Nucl Eng Des, vol. 81, no. 2, p. 345-355.

SIDCOF - INSPECTION AND SURVEILLANCE OF PENSTOCKS

Johann Catty[1], Olivier Duverger[1], Abdelkrim Saidoun[1] and Fan Zhang[1]

[1]CETIM, 52 avenue Félix Louat, France; johann.catty@cetim.fr, olivier.duverger@cetim.fr, abdelkrim.saidoun@cetim.fr, fan.zhang@cetim.fr

ABSTRACT

The SIDCOF (Innovative Forced Pipe Diagnostic System) project, carried out within the framework of FUI 22, aims to develop innovative NDT methods and tools in three batches allowing:

- *In situ monitoring of penstocks*
- *A robotic inspection of the inside of the pipes to avoid human intervention in a complex environment*
- *A software platform to process data and help the operator to make decisions*

This paper will focus on the 1st batch. The work has enabled the development of sensor networks permanently installed directly on the pipe for monitoring installations and monitoring in real time the damage caused by rockfall, landslides and water leaks. Two dedicated systems have been developed and validated under real operating conditions.

The first is based on a network of connected autonomous extensometers, each module of which operates wirelessly and is energy independent. It is able to follow the deformations of pipes in risk areas following landslides. This tool greatly simplifies the implementation of sensors and automatically routes the data produced by these sensors to the cloud. A totally IIOT product.

The second uses a network of acoustic emission sensors to detect and locate (with an accuracy of the order of a few meters) in real time falling rocks, and the appearance of leaks on the pipe. The tool developed is a dedicated multi-channel system for on-board electronics and processing. The data processed is transferred automatically to the client cloud via the 4G network.

The SIDCOF project is led by SETEC with CETIM, SOREA, ETE and Sub C Marine as partners, funded by BPI France, TENERRDIS, INDURA, Région Occitanie, Région Auvergne Rhône Alpes.

Keywords: Monitoring, penstock, acoustic emission, extensometer, leak detection.

1. Introduction

Maintaining critical structures such as forced pipes (hydroelectric power plants) in operational conditions often becomes complex when these structures are inaccessible and likely to be damaged by landslides or rock falls. Sending staff to perform periodic measurement campaigns, apart from the time required for these inspections, can be dangerous, if not impossible, in poor weather conditions. On the other hand, the delay between an incident and its consideration by the operator can be problematic and cause additional damages. All these arguments therefore argue for permanent real-time monitoring of the health state status.

The SIDCOF project, led by Setec engineering company, Cetim (research center), SubC Marine (robotic integrator) and the hydroelectric park operator Soréa (CNR), has led to the development of several innovative pipe monitoring systems, including a system based on acoustic emission technique (EA) and the measurement of deformations.

2. Acoustic emission

2.1 Definition of the technique

AE testing is a Non-Destructive Testing method (NDT), widely used in the industry to evaluate the health state of structures such as:

- pressure vessels (storage tanks, reactors, …),
- pipelines,
- mechanical structure, such as crane,
- bridges,
- aircraft structures (wings), etc.

This technique necessitates to solicit the structure, and then, earing the AE waves emitted by this structure. The diagnosis is based on the quantification of all the signals recorded during the test. By using calculation based on the Delta-t (difference of arrival time of the signals on each sensor), it is possible to calculate the origin of the AE waves.
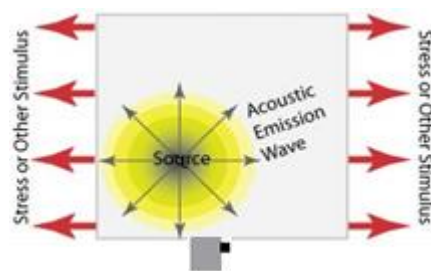
Fig. 1: AE technique basic principle.

2.2 Specificities of penstock monitoring

A penstock, as studied in the frame of this project has a small diameter (<1m) and corresponds to the most common middle power hydroelectric installation. Then, comparing to the length, we can consider that this penstock is a 1-dimension structure (Length >>> diameter). This has an impact on the way the AE system can localize events such as rock falls.

It is also important to consider the fact that these structures are localized in mountains, far from any broadband and fast network. Then, transmission of information to the data center has to be well studied and optimized as much as possible.

2.3 AE preliminary study

This project has been focused on the Penstock that delivers water to 'Les Moulins' hydroelectric power plant, situated in the Maurienne Valley, in the heart of the French Alps.

The length of the penstock is about 2 km, with a denivelation of 600 m between the water inlet and the powerplant. Built in the 60's, it has been partially replaced, but some old parts remain and needs to be carefully monitored. Based on the risk study performed by the owner, it has been decided to install a monitoring system on a critical section of 300 m length, due to frequent rock falls and some landslides. It is also important to note that this area is very close to an active seismic area (swarm), that could provoke sudden landslides/rock fall also.

Fig. 2: Les Moulins penstock.

Fig. 3: An AE sensor and its preamplifier installed inside a protection box in a tunnel section.

In order to optimize our AE monitoring system, we have studied in a 1st stage all the parameters that could impact on the performances of detection. Then, many types of sensors have been tested, with different frequencies, different conceptions, more or less adapted to this hard environment (differences of temperature, snow, ice, etc.). For each type of sensor, we have also evaluated the capacity to detect what was initially defined:

- strong impact such as rock falls,
- leak that could be provoked by a rock fall, a landslide or due to the corrosion.

Based on these results, we have chosen a type of sensors and installed a network of 12 sensors able to monitor the 300 m section of the penstock. As the penstock is not straight, it is important to adapt the location of the sensors to the geometry of the penstock.

2.4   1st on-line monitoring stage

For 16 months (from July 2018 to November 2019) the data coming from the 12 sensors have been recorded by a classical and high-performance AE data acquisition system (Valle AMSY-6). A very detailed study of these data has led to the following conclusions:

- meteorological conditions such as rain and storms strongly impact raw data. It generates a huge number of events and can provoke sudden but temporary increase of Rms values of each sensor. Then, it is challenging to distinguish an event representing an expected rockfall or leak inside these raw data. A basic analysis of AE is not relevant because it includes a majority of non-significant data, not useful to assess the health state of the structure. Therefore, it is crucial to restrain the analysis to events that are well identified and that can be discriminated from 'background noise',
- these 16 months monitoring has given very interesting information on some areas that are more prone to rockfalls (Fig. 4: area at X = 110 m, between sensors n°9 & n°10). It can help the end-user to preventively protect some parts of the penstock, and get more information on the critical periods (November/December in this case),

- our AE sensors and the installation procedure (gluing the sensor, protection, …) has been efficient and have shown a very good stability to cross more than one year, and one winter.
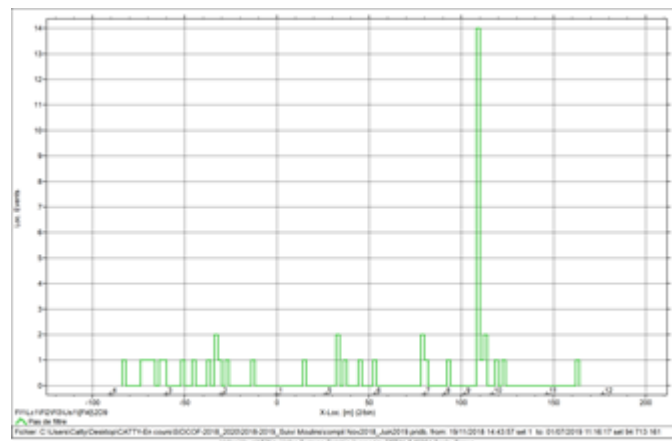
Fig. 4: AE sensors location and AE events located along the penstock.

2.5 Development of a specific AE system

Based on this 16-months monitoring period, it was possible to define the specifications of a new innovative AE monitoring system. Why? Traditional systems could be utilized. But our objectives were to develop a system fitted to the need, not just for fun and for the pleasure of research, but to obtain a competitive and dedicated system. Our motivation is also to be eco-responsible and to use as few resources as possible: less performances as possible, less amount of data as possible. A small-data concept.

2.6 Results

The AE monitoring system demonstrator has been developed in stages, starting at the end of 2018. The final version (demonstrator) has been installed on site in September 2020.

The sensors permanently placed on the pipe, are set in the case of 'Les Moulins penstock' every 30 to 50 meters. The data acquisition system is based on C-Rio modules (National Instruments) that allow 12 synchronous channels (expandable to 128 channels). A software has been developed on LabVIEW language, integrating some original concepts of data acquisition that give the advantage of being less affected by unwanted signals provoked by background noise without losing any capacity of events location.

The computer sends information through the 3G/4G network to a supervisory system (developed by Setec) that can instantly alert hydroelectric plant staff by email, sms, etc. Moreover, it is possible to fully control this system remotely. It is for example possible to change data acquisition parameters, alarm criteria, etc., from any computer or smartphone.

Some tests have been done to demonstrate its capability in detecting leaks and rockfalls:
- leaks: with our monitoring system, a leak such as what can be observed in Fig. 5 can be easy detected at a distance greater than 50 m, up to 80 m. As a leak generates a continuous acoustic activity, Rms indicator is the most interesting parameter, as shown in Fig. 6,
- rockfalls: we have provoked high energy sources that can be compared to the energy of a rockfall. In Fig. 7, we have generated such a source every 2 meters approximately, from the position 0 m to the position 24 meters. We clearly observe a strong correlation between the theoretical position and the position that has been calculated from AE signals recorded by our monitoring system.

Fig. 5: Simulation of a leak.
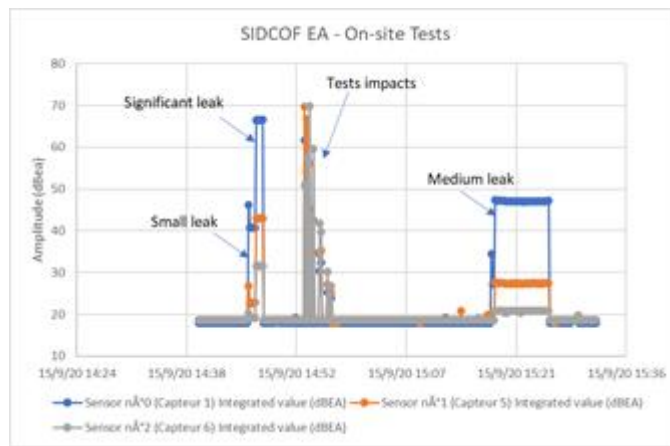
Fig. 6: Effect of some leaks on rms values.
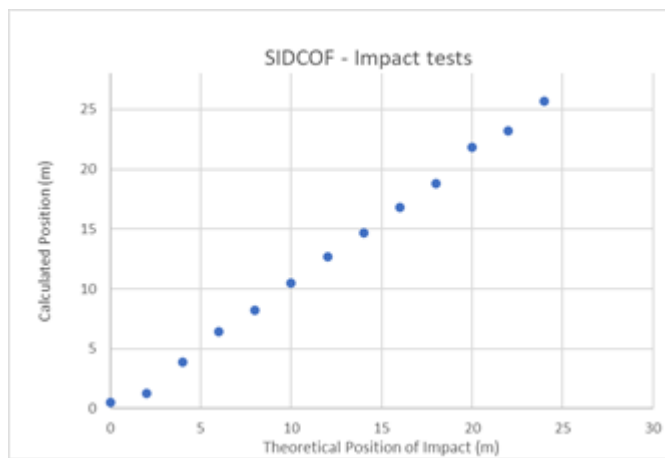
Fig. 7: Impact tests.

2.7 Conclusions

This acoustic emission system developed in the frame of this project shows unique characteristics and architecture that allow for high-cost savings compared to standard acoustic emission systems and make it compatible with the target market. This development has led to a 1st demonstrator that is still operational since September 2020.

We want to highlight the fact that this system has been designed to be economical, from all points of view: performance, volume of data, and therefore power consumption because we aim to make it self-sufficient in energy. But we have also proven that this system has sufficient performance to answer the problem, no less than a commercial system costing 10 times more.

For example, a classical system would generate around 5 GO/year of data, when this prototype only generates 450 à 500 MO/year. This is again a saving of data, but in cascade a saving of energy, and post-treatment.

Today, this original development deserves to be more widely disseminated to other sectors of the industry that may have similar problems: detection of leaks in any type of equipment under pressure (pipe, pipeline, forced pipe, storage, reactor, etc.), impact detection (mainly for pipes, forced pipes, etc.).

3. Extensometry

3.1 Definition and benefits of the technique

Extensometry technology has been developed to measure changes in length of an object. The objective of this 2nd monitoring system is to complement the information given by AE monitoring: AE can detect sudden and local events but is not able to detect long term and slow changes; At the contrary, Extensometry is designed to measure very small deformations that can lead by accumulation to the breakage of the penstock. The 2 tools are very complementary and allow an optimal monitoring of such structure.

3.2 Specificities of penstock monitoring

The most feared event for a penstock is the mechanical failure. For each penstock, many parameters need to be taken into account to assess the risk of breakage. Then, a deep knowledge of the structure, its environment and history is required. For example:
- the risk is a characteristic specific to each hydroelectric installation,
- it is geographically distributed along the penstock,
- the risk evolves over time, it may increase and require the implementation of new risk reduction measures, or, conversely, decrease following maintenance work on the installation, and make unnecessary existing prevention measures.

The rupture of a penstock is generally the consequence of a chain of facts and multiple causes. Because the final cause of failure is the uncontrolled accumulation of stresses in the penstock producing plastic deformation of the material and thus reducing its breaking strength margin. When ground movements are present and considered critical for the installation, it is essential to monitor them in geographical areas exposed to these phenomena.

3.3 Preliminary study

A first measurement campaign has been performed in October 2018 in a risky area (based on previous observations). The goal is to measure longitudinal strains. Each instrumented straight section of the penstock has four measuring points equally distributed over the diameter. At each measuring point, two quantities are determined:
- the longitudinal deformation of the wall,
- the surface temperature of the wall,

- data are recorded every second and sent to the cloud via LORA network. Measurements have been analyzed between October 2018 and August 2019. It has shown that:
  - the variations in the longitudinal deformations observed are between -135 μm/m and +100 μm/m,
  - mean temperature is around 4°C, varying from -1°C to 21°C,
  - a strong correlation is observed between the strain and the temperature: 92% of the variability of the longitudinal strain observed over the period from March to May 2019 is explained by the temperature variation.

3.4 Development of a specific extensometer autonomous system - SENSCOF

Based on previous study, an autonomous and communicative extensometer, based on the "thick layer" sensor technology has been developed by the Annecy Mechatronic Center, called SENSCOF.

Fig. 8: SENSCOF sensible element installed on the penstock.
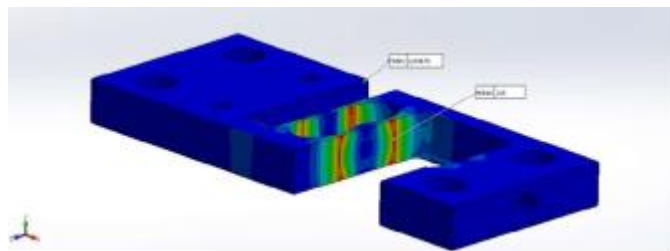
Fig. 9: Von Mises stresses calculated in the extensometer.

These sensors have been tested on a mechanical bench. The linearity deviation observed is less than 1% of the maximum applied load (800μm/m).
A specific electronic module has been designed for this sensor, powered by a battery, and including a wireless transfer of the data through LORA network. Several SENSCOF modules have been installed on the 'Les Moulins' penstock in December 2019.
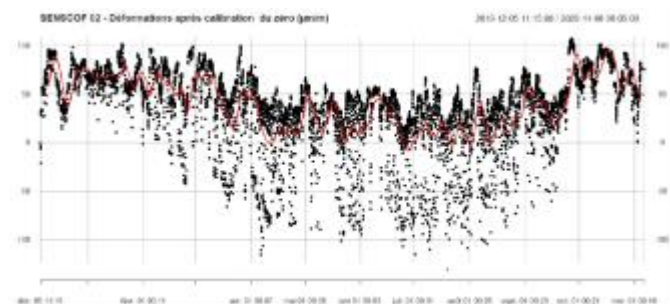
Fig. 10: Strain trend recorded by SENSCOF n°2 from Dec. 2019 to Nov. 2020.

By using the temperature trends measured by each SENSCOF module, it is possible to extract the strain due to the temperature variations and the strain from mechanical reason. The Fig. 11 gives the mechanical strain trend for the same period (Dec. 2019 to Nov. 2020).
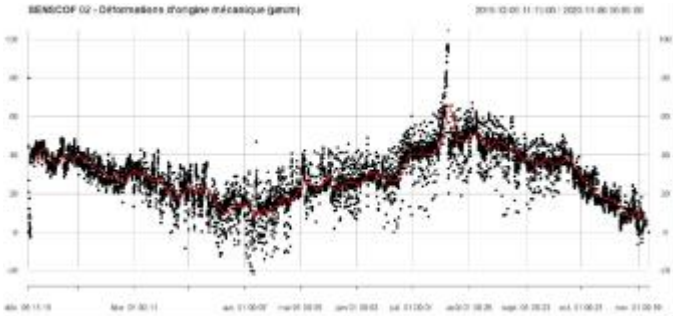
Fig. 11: Mechanical strain trend recorded by SENSCOF n°2 from Dec. 2019 to Nov. 2020.

4. Fusion of data

From these 2 developments (AE and extensometry), we can deliver very accurate information on the health state of the Penstock. But from the End-user point of view, it is not very easy to extract immediate information from these data. A software platform called 'Proxymae' has been designed by SETEC to help the end-user by:
- performing the archiving of the data,
- allowing custom extraction and periodic report,
- sending alarms,
- performing more deep analysis of the data.
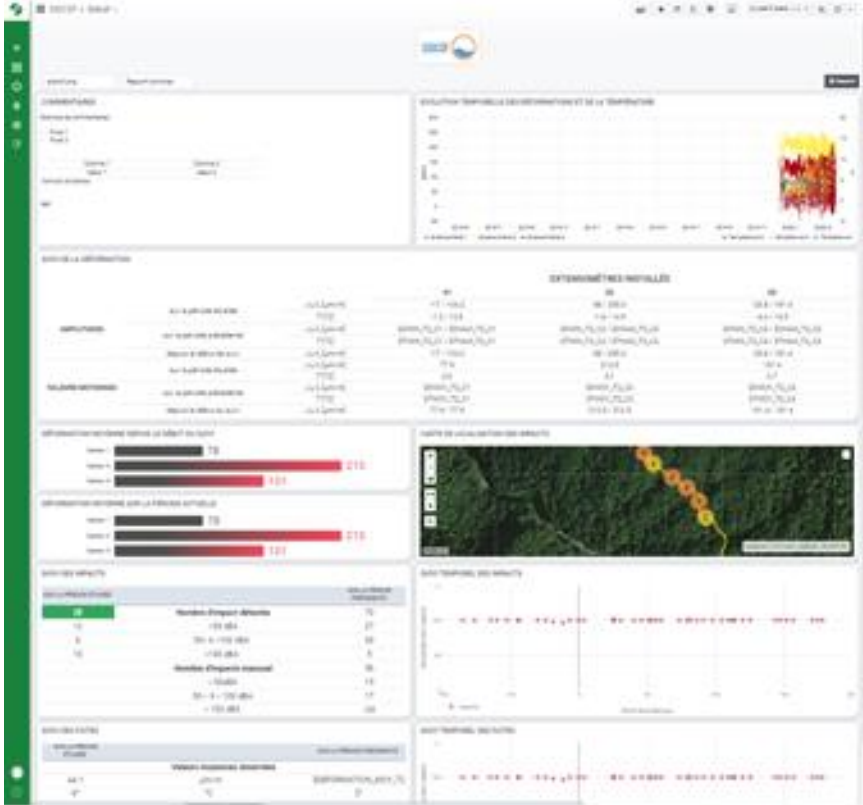
Fig. 12: View of Proxymae web page.

5. Conclusions

The SIDCOF (Innovative Forced Pipe Diagnostic System) project has been successfully carried out resulting in the development of several original monitoring tools:

- an AE monitoring system that has been developed in order to fit the market, including original concepts that make our system economical and eco-responsible by optimizing its performances and amount of data,
- an extensometer module based on the "thick layer" sensor technology which is autonomous and connected to the cloud.

These 2 tools are also designed to work in harsh environment and in areas where data communication is limited. A dedicated software platform aggregates these data and gives a synthetic view of the behavior of the penstock. Using these 2 monitoring systems, the structure is under control. Any landslide, rockfall or water leak will be instantaneously detected and people in charge of the powerplant will be automatically alerted. What remains to be done?

- further optimize the sensors: integrated amplification, increasing the energy autonomy,
- enrich the software platform: more agility, enhancement of specific data, documentary consultation or generalization of information, etc.,
- continue development: assembly in progress with industrial partners to switch from TRL7 to TRL9.

6. Acknowledgements

7. References

[1]   O. Duverger., SIDCOF - Surveillance des effets de mouvements de terrains sur des conduites forcées à partir de mesures de déformations et de températures, CETIM Report, 2020.
[2]   J. CATTY, SIDCOF - Lot 4_Monitoring EA de Conduites Forcées-Rapport Final, CETIM Report, 2020.

A NEW APPROACH TO ULTRASONIC CHARACTERIZATION OF FLUID EMBEDDED IN TWO VISCOELASTIC LAYERS USING THE TRANSFER MATRIX METHOD

Tafkirte Mounir[1,*], Hamine Adil[1] and Mesbah Hicham[1]

[1]Laboratory of Metrology and Information Processing (LMIP), Faculty of Science, Ibn Zohr University, B.P. 8106, 80000 Agadir, Morocco

*Correspondence: mounir.tafkirte@edu.uiz.ac.ma

ABSTRACT

In the present work, our objective is to characterize fluids by the ultrasonic pulse echo method. Nowadays, the characterization of these fluids has received a great scientific and practical importance, it requires the development of a more efficient control technique in order to meet the desired quality and safety rules. Indeed, a matrix transfer approach has been introduced to model the signal propagation in a multilayer medium immersed in a fluid. This approach is mainly based on the calculation of the scattered signal in the time domain of a multilayer immersed in water in order to verify the ability to calculate the ultrasonic parameters, and possibly the velocity and attenuation. We then deduce the acoustic properties of fluids and compare with literature data (experimental). This approach has also been suggested as a new alternative to exploit for fluid characterization.

Keywords*:* Ultrasonic testing, backscattered signal, multilayered, transfer matrix method, ultrasonic parameters.

1. Introduction

The Ultrasonic Non-Destructive Testing (UDT) technique offers a good combination of quality control and ease of use. It enables the examination of composite parts without damaging them, without modification of the material properties, and remains safe for the user. The principle of the ultrasonic technique consists of exciting the elastic plate immersed in water by an incident plane wave, the scattering acoustic phenomena are observed and then the backscattering waves are detected. The fluid bonded between two plates has been used mainly in quality control or reinforcement of plates as an adhesive material and has also proved to be useful in the evolution of materials [1-3].

The accurate simulation of acoustic wave propagation in complex structures are widely used for the characterization of the medium, and the detection of defects. In this context, the propagation of an ultrasonic wave through a complex structure is considered a process to produce long-duration acoustic signals [4-8]. Furthermore, the simulations can be quite time-consuming. The objective of this research is to predict the acoustic signal generated by the propagation of waves transmitted through a multilayer structure immersed in water at normal incidence, from a quadrupole formalism associated with a method based on the transfer matrix (TMM) [9,10]. The backscattered signal in the time domain of a multilayer immersed in water are calculated and plotted. The elastic

property (Ultrasonic parameters) of the fluid layer is estimated based on the time representation by which the relation between phase velocity (attenuation) and frequency is obtained. the acoustic properties of fluids are compared with literature data (experimental) at the central frequency of 5 MHz. The comparison confirms the validity of the TMM to model the ultrasonic signals.

The rest of the paper is structured as follows. The principle of ultrasonic wave propagation through a multilayer is described in section 2. Section 3 is devoted to the results and discussion. Finally, section 4 presents the conclusion.

2. Ultrasonic waves models

2.1 The transfer matrix method (TMM)

The acoustic wave is considered as a plane wave perpendicular to an excitation surface and transmitted along the positive x axis. In theory, the plane wave is simulated by a sinusoidal function multiplied by the Hanning window at a center frequency of 5 MHz.
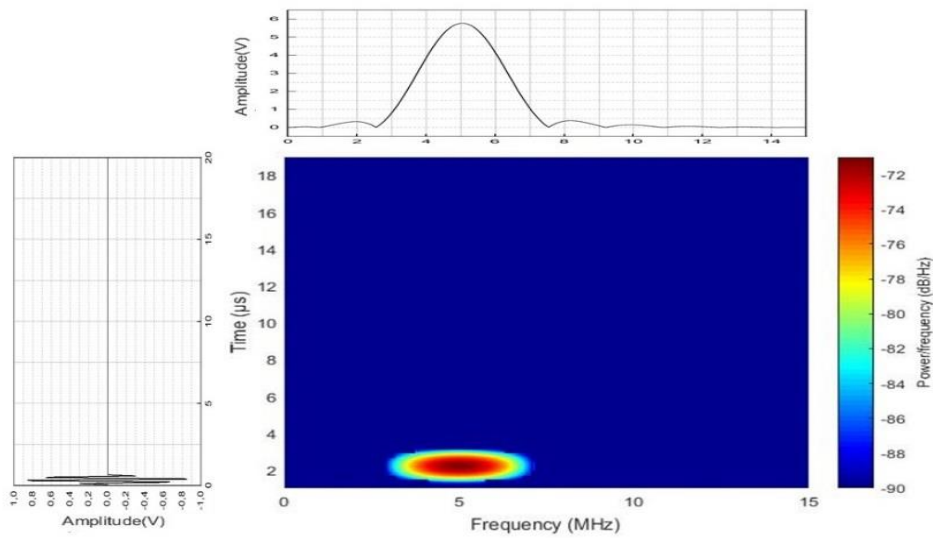
Fig. 1: Signal spectrum, time signal, time-frequency image for plane wave.

The multilayer structure consists of three layers: two solid layers separated by a fluid layer. The solid layers are labeled with indices 1 and 2, with density $\rho 1,2$ and sound speed $C1,2$. The fluid is labeled with index 1 and it is described, by parameters $\rho 1$ and $C1$.

In the presented model, the layer can be represented by a quadrupole. By adopting the quadrupole formalism and knowing M and N, we can deduce ve and $-Te$ as a function of vs and $-Ts$ as state variables. The expression of stress and velocity [9]:

$$v(x,t) = \frac{\partial u}{\partial t} \tag{1}$$

$$T(x,t) = c_l \frac{\partial u}{\partial x} \tag{2}$$

where c_l is the longitudinal velocity in the layer. At the interfaces between the fluid and the solid layer, the displacement field, stress and velocity at the interface must be continuous.
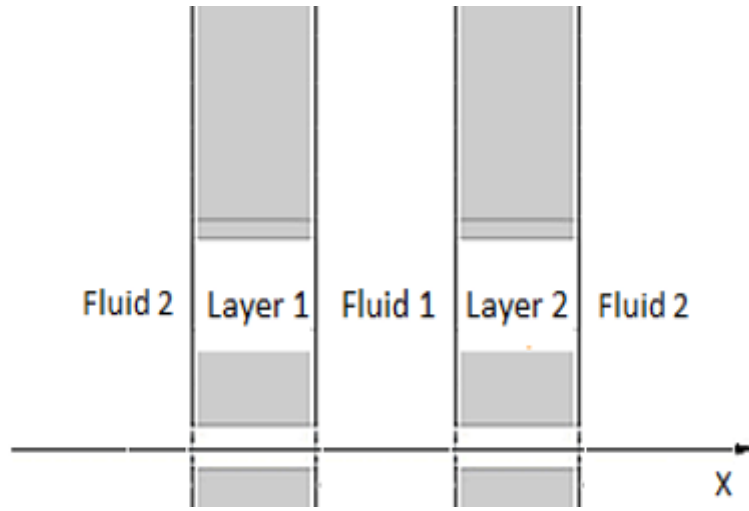
Fig. 2: The schematic of the transfer matrix model.

The relationship between the state variables on the input and output side of the multilayer can be written in the matrix form [9]:

$$\begin{bmatrix} v_e \\ -T_e \end{bmatrix} = \begin{bmatrix} a_{11} & a_{12} \\ a_{21} & a_{22} \end{bmatrix} \begin{bmatrix} v_s \\ -T_s \end{bmatrix} = [T] \cdot \begin{bmatrix} v_s \\ T_s \end{bmatrix} \tag{3}$$

The coefficients a_{ij} are parameters depending on the thickness and the elastic characteristic of each layer. The backscattered wave e through a multilayer structure immersed in a fluid is established using the expression of the reflection coefficient [9]:

$$R(f) = \frac{Z_2 . a_{11} + Z_2 . Z_2 . a_{12} - a_{21} - Z_2 . a_{22}}{Z_2 . a_{11} + Z_2 . Z_2 . a_{12} + a_{21} + Z_2 . a_{22}} \tag{4}$$

where Z_2 is the acoustic impedance of the fluid. These calculations are made using long signals, which give all possible echoes.

3. Results and discussion

The signal in Fig. 3, shows the superposition of two components: the first corresponds to echoes backscattered by the plexiglass layer (1), and the second to those backscattered by the glass layer (2). In the first component, we see groups separated in time, while in the second part, the groups are difficult to isolate. This can be explained by the fact that glass has a strong reflective power which strongly conserves the energy of the signals compared to plexiglass. More precisely, the difference in impedance between the water layer (1), and the solid layer (glass or plexiglass) causes energy losses due to transmissions and reflections at interfaces.
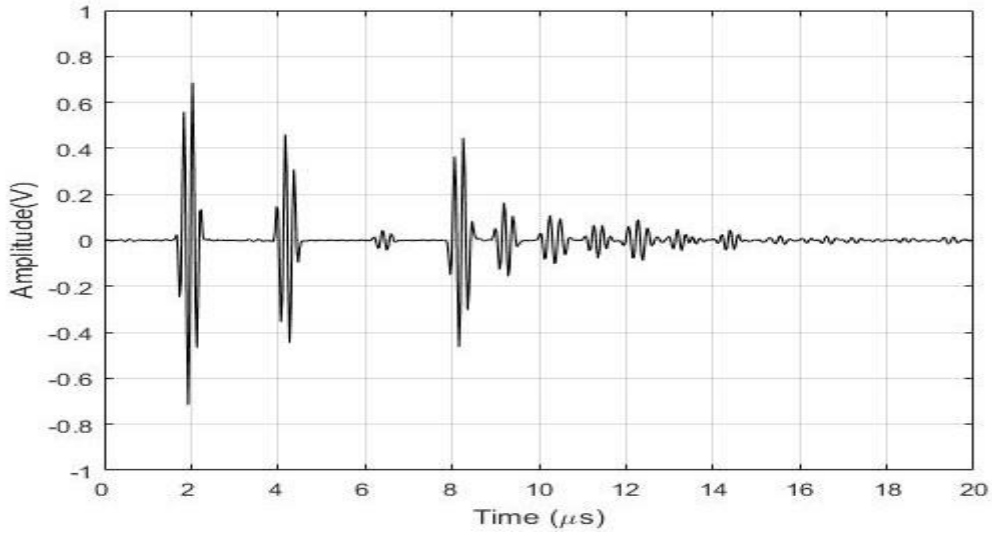
Fig. 3: The time signal backscattered obtained by the presented model for the multilayer structure plexiglass(3mm)/water(3mm)/glass(3mm).

We designate φ_2 and φ_4 the phases of A_2 and A_4, respectively. The phase difference between φ_2 and φ_2 can be written according spectral method and unwinding of phase method [11] as:

$$\Delta\varphi(f) = \varphi_4 - \varphi_2 = -\frac{2\omega D}{v_p(f)} + \pi \qquad (5)$$

The phase velocity is expressed by:

$$v_p(f) = \frac{2\omega D}{\pi - \Delta\varphi(f)} \qquad (6)$$

The attenuation is related to the amplitude spectra ratio $A_4(f)/A_2(f)$:

$$\alpha_{water} = \frac{1}{2D}\ln\left(\frac{A_4(f)}{A_2(f)}\varepsilon_{ref}\right) \qquad (7)$$

where D is the thickness of layer. Fig. 4 shows the phase velocity and attenuation of water. The phase velocity found at 5 MHz is 1490 m/s, which is close to the literature value 1480 [5,12]. In contrast to the attenuation of the longitudinal wave at 5 MHz is 0.6371 Np/m, which agrees well with the published values [5,12]. The comparison between the literature values shows that the maximum absolute relative error is 0.6% and 0.727%, respectively. This ratio is also less than 1%.
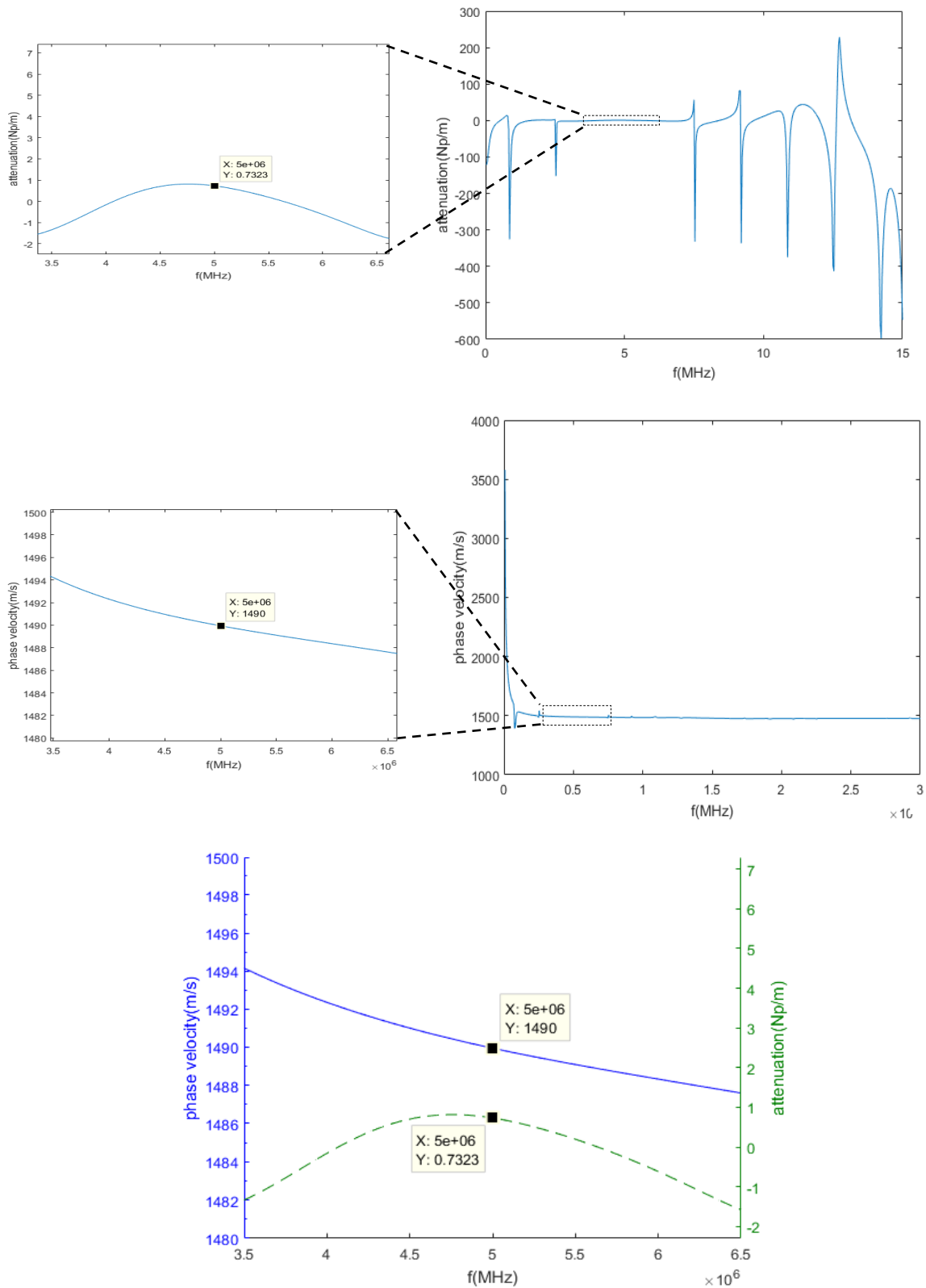
Fig. 4: The attenuation and phase velocity of the water obtained by presented model, at center frequency f = 5 MHz.

4. Conclusions

In this article, we presented the transfer matrix method to calculate the ultrasonic backscattered through to a multilayer structure immersed in a fluid at normal incidence. The ultrasonic parameters of water calculated by the proposed model are compared and show a good agreement with the data available in the literature (Experimental). the model can be suggested as a new alternative to exploit for the characterization of the fluid embedded in two viscoelastic layers.

5. References

[1] P. K.Singh, S. Bhatt, Investigation of Acoustical Parameters of Polyvinyl Acetate, Appl. Phys. Res. 2 (1). doi:10.5539/apr.v2n1p35.

[2] C. E. Teeter, Absorption of Supersonic Waves in Liquids, J. Acoust. Soc. Am. 18 (2). doi:10.1121/1.1916391.

[3] C. J. Burton, A Study of Ultrasonic Velocity and Absorption in Liquid Mixtures, J. Acoust. Soc. Am. 20 (2) (1948) 186{199. doi:10.1121/1.1906362.

[4] N. P. Rao, K. C. Reddy, Ultrasonic absorption in binary liquid mixtures, Pramana 8 (3) (1977) 245{254. doi:10.1007/BF02847417.

[5] C. Randall, Ultrasonic measurements of the compressibility of solutions and of solid particles in suspension, Bur. Stand. J. Res. 8 (1) (1932) 79. doi:10.6028/jres.008. 009.

[6] N. Santhi, P. L. Sabarathinam, M. Emayavaramban, C. Gopi, C. Manivannan, Molecular interaction studies in binary liquid mixtures from ultrasonic data, E-Journal Chem. 395 7 (2) (2010) 648{654. doi:10.1155/2010/487874.

[7] N. Ghodhbani, P. Marechal, H. Duo, Ultrasonic broadband characterization of a viscous liquid: Methods and perturbation factors, Ultrasonics 56 (2015) 308{317. doi:10.1016/j.ultras.2014.08.013.

[8] J. R. Pellam, J. K. Galt, Ultrasonic propagation in liquids: I. Application of pulse technique to velocity and absorption measurements at 15 megacycles, J. Chem. Phys. 14 (10) (1946) 608{614. doi:10.1063/1.1724072.

[9] M. Tafkirte, A. Hamine, A transfer matrix model and application spectral and time-frequency to study an ultrasonic waves backscattered by different plates immersed in water, Mater. Today Proc.doi:10.1016/j.matpr.2020.05.206.

[10] 420 [14] B. Hosten, M. Castaings, Transfer matrix of multilayered absorbing and anisotropic media. Measurements and simulations of ultrasonic wave propagation through composite materials, J. Acoust. Soc. Am. 94 (3). doi:10.1121/1.408152.

[11] D. J. McClements, P. Fairley, Ultrasonic pulse echo reflectometer, Ultrasonics 29 (1) (1991) 58{62. doi:10.1016/0041-624X (91)90174-7.

[12] J. M. Pinkerton, The absorption of ultrasonic waves in liquids and its relation to molecular constitution, Proc. Phys. Soc. Sect. B 62 (2) (1949) 129{141. doi:10.1088/405 0370-1301/62/2/307.

FIBER OPTIC SENSING SYSTEMS

State-of-the-art sensing systems for unmatched performance in the most challenging environments

Our profile

OPTICS11 is an Amsterdam based high tech company that offers state-of-the-art fiber optic sensing systems for unmatched performance.

Optics11 has extensive experience with monitoring Acoustic Emission, Temperature (including cryogenic), Strain, Acceleration, and Pressure.

All Optics11 systems embrace innovative measurement techniques that allow to overcome most of the drawbacks and limitations of classic fiber-optic sensing systems such as limited bandwidth, limited sensitivity, and bulky sensor size.

Fiber optic sensing systems for

Monitoring in Cryogenic Environment

Structural Health Monitoring

Condition Monitoring

ACOUSTIC EMISSION ANALYSIS OF THE CORROSION PROGRESS ON COATED ALUMINUM ALLOY AA2024-T3 DURING EXCO TESTS

Chihab Abarkane[1], Ane M. Florez-Tapia[2], Yanis M. Benane[3], Maria Lekka[1],
Eva García-Lecina[1] and Jesús M. Vega[1]

[1]CIDETEC, Basque Research and Technology Alliance (BRTA), Paseo Miramón 196, 20014 Donostia-San Sebastián, Spain; cabarkane@cidetec.es, mlekka@cidetec.es, egarcia@cidetec.es, jvega@cidetec.es
[2]VICOMTECH, Basque Research and Technology Alliance (BRTA), Mikeletegi Pasealekua, 57, 20009 Donostia-San Sebastián, Spain; amflorez@vicomtech.org
[3]MISTRAS Group SA, 27 rue Magellan 94370 Sucy-en-Brie, FRANCE;
yanis.benane@mistrasgroup.com
*Correspondence: cabarkane@cidetec.es

ABSTRACT

Localized corrosion is one of the most dangerous damages that can occur on metals, affecting the structure/component integrity. The early detection of such corrosion type is challenging for field applications, especially if a coted metal is used (e.g. coated aluminum alloys used in the aeronautical industry). In the present study the use of the Acoustic Emission technique (AE) is proposed to monitor the evolution of the localized corrosion, from the initial pitting that evolves to intergranular corrosion (IGC) prior to the material exfoliation (EFC). Coated (anaphoretic e-coating) aluminum alloy 2024-T3 coupons were exposed to the EXCO solution (ASTM G34) for different time spans, and characterized by optical microscopy to evaluate the degradation. The most relevant parameters that characterize the AE signals were identified, allowing to classify practically all intervals of activity (≈80-90%) into 4 well-differentiated classes. The time distribution of such classes is in good agreement with the different stages (mechanisms) of the corrosion process as identified by the microstructural characterization. The AE data analysis has revealed the promising potential of this technique to distinguish between the different steps of the corrosion process, and pave the way to the detection of localized corrosion on coated aluminum alloys.

Keywords: Acoustic emission, corrosion, aluminum alloy, exfoliation, early detection.

1. Introduction

The aluminum alloys are still playing a significant role in the design of lightweight aircrafts, and consequently, the control of the corrosion process is a matter of importance for the aerospace industry in terms of structure integrity as well as financial savings regarding the maintenance and repair operations costs. In particular, the aluminum alloys are prone to undergo localized corrosion, which is one of the most dangerous damages as it can develop and affect the material in depth. Thereby, different corrosion mechanisms are expected to occur depending on factors such as the microstructure, mechanical stresses on the material, the aggressive environment, etc. As reported

in literature, the localized corrosion could be explained in three main steps [1,2]: i) the localized corrosion initiates as small pits, and then extends under the surface at grain boundaries; ii) the IGC attack reaches the main direction of the material leading to the undermining of the surface grains (interphase); iii) the main directional attack lifts the surface grains producing a layered appearance (exfoliation, EFC).

The EFC, as an advanced form of IGC, is expected to promote several damages in the bulk. This form of corrosion spreads along a multitude of planes parallel to the direction of rolling or extrusion, which is usually favored in areas where water can concentrate in riveted or similar joints. Moreover, at the latest stages implies the physical detachment of the material at sub-surface level. This latter feature can facilitate the detection of these phenomena using non-destructive techniques (NDT) rather than other type of corrosion sensors.

Some authors have reported findings regarding the mechanisms of localized corrosion on aluminum alloys, as for example by investigating the pitting corrosion and the transition to the IGC [3]. Other authors [2,4], meanwhile, have investigated the advanced stage of the localized corrosion on aluminum alloys, i.e. EFC, using EXCO test (ASTM G34) [5], which is widely applied on alloys 2xxx and 7xxx for the assessment of the EFC resistance.

Concerning the monitoring of dynamic processes, the acoustic emission (AE) has been largely proved to be a powerful technique for early detection of the damage undergoing in different materials and structures, long before reaching critical state [6-8]. However, the application of such technique to detect localized corrosion has been scarcely investigated, and mostly related with the detection of the hydrogen evolution bubble's during pitting corrosion [9,10] or IGC [11] on bare aluminum alloy.

The present work is dealing with the application of the AE technique for localized corrosion monitoring. The material used consisted of aluminum alloy AA2024-T3, typically used in aerospace industry, and coated with an anaphoretic e-coating primer, which includes an artificial defect that exposes locally the bare metal, simulating the access of the aggressive agent through in-service defects.

2. Experimental description

2.1 Materials

The experimental testing was conducted on coated aluminum alloy AA2024-T3 (typically used in aircraft's manufacturing). The microstructure of the substrate was revealed chemically and then examined with the optical microscope along and perpendicular to the rolling direction, as depicted in Fig. 1. It can be observed that the grains are stretched parallel to the upper surface, although without creating a layered microstructure. Table 1 lists the chemical composition of the aluminum alloy AA2024 used in this study.

Sheets of 1 mm thickness were pretreated as follows: i) 3min of alkaline degreasing on a commercial product (Bonderite C-AK 18, Henkel) followed by ii) immersion in nitric acid (30% v/v) for 2 min (pickling). Then, samples of 75x100 mm2 were immersed on a Cr-free E-coat tank system (anaphoretic) and coated with nano silica-based colloidal polyurethane as a primer.

Table 1: Chemical composition of AA2024 aluminum alloy.

	Si (%)	Fe (%)	Cu (%)	Mn (%)	Mg (%)	Cr (%)	Zn (%)	Ti (%)	Al (%)
Al 2024	0.082 ±0.008	0.078 ±0.015	4.31 ±0.19	0.48 ±0.02	1.49 ±0.05	0.026 ±0.003	0.13 ±0.02	0.027 ±0.006	Balance
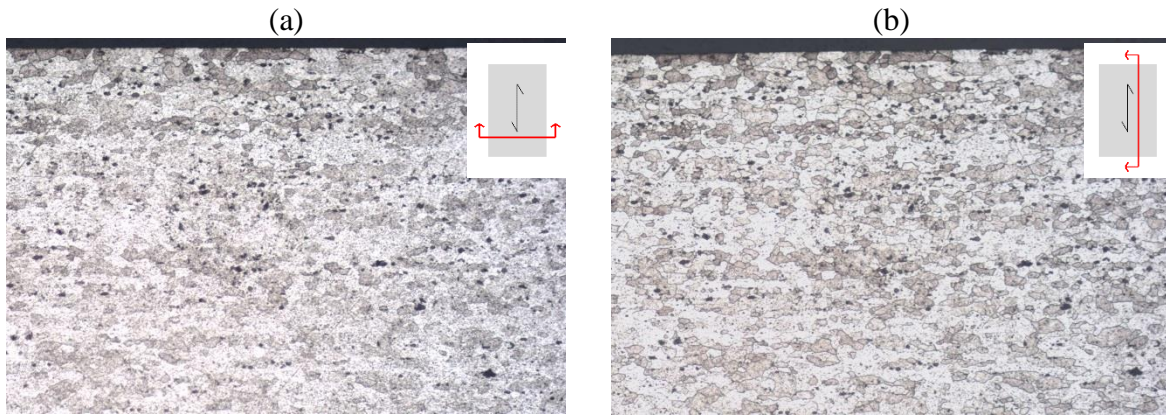
Fig. 1: Optical micrograph of the aluminium alloy AA2024-T3: a) perpendicular to the rolling direction, b) along the rolling direction.

2.2 Potentiodynamic polarization

Experiments were conducted at room temperature, using a standard three-electrode cell. 1 cm^2 of area was exposed for the working electrode, a Saturated Calomel Electrode (SCE, V_{SCE} = + 0.244 V vs SHE) was used as reference electrode and a Pt mesh as counter electrode. The solution of 1M NaCl was deareated with Ar 24h before the anodic polarization experiment on the bare aluminum AA2024-T3. Prior to the polarization, the specimen was exposed to the solution for 30 min under open circuit potential conditions (OCP≈0.75 V), and then polarized from -0.8 V to 0.0 V, at a scan rate of 0.167 mV/s using a Biologic SP-200 potentiostat.

2.3 EXCO test

The EXCO test, which is a standardized immersion test, was used with the aim of triggering the exfoliation corrosion (EFC). As stated on the standard G 34-01 ASTM, the electrolyte consisted of a reagent mixing sodium chloride NaCl 4.0M, potassium nitrate KNO3 0.5M, and nitric acid HNO3 0.1M. The EXCO solution was applied by immersion to the coated specimens through a tubular cell (Fig. 2a).

In order to provide a direct and effective way for the electrolyte to reach the substrate, an artificial pore-like defect of around 150 μm diameter was created by laser across the E-coating (Fig. 2b). This way, the most affected area by the corrosion process was known beforehand, which enabled the subsequent characterization.
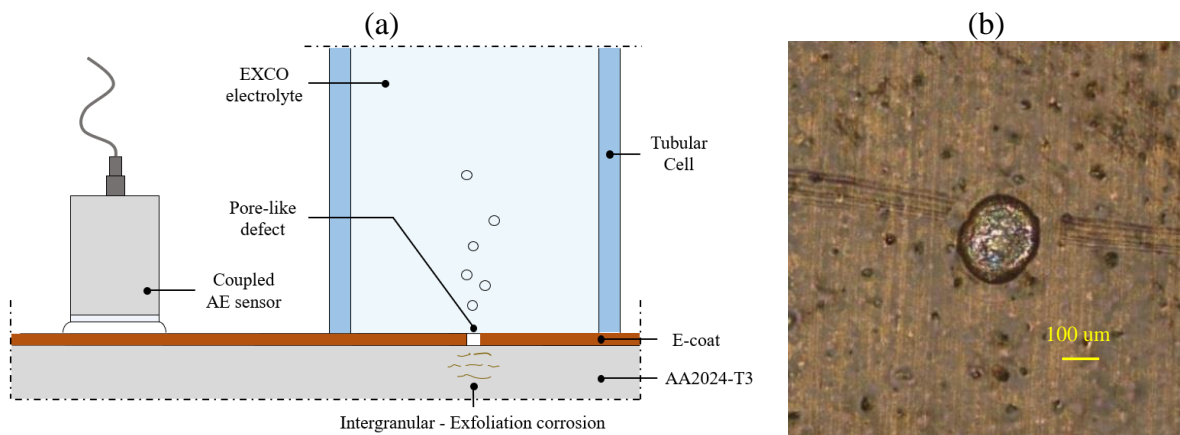
Fig. 2: a) Experimental set-up of EXCO test along with AE monitoring. b) Confocal image of the pore-like defect.

Electrochemical measurements, as the potential, were recorded during each test with the help of a potentiostat SP200 (BioLogic), under open circuit potential (OCP) conditions using a three electrodes system, on which the reference electrode was Ag/AgCl electrode.

2.4 AE acquisition

The acquisition system Micro-SHM (Physical Acoustic Corporation -PAC-) recorded the AE signal during each experiment. The AE data was processed in real time and visualized by means the software AEwin. The sensor PKBBI (Physical Acoustic Corporation -PAC-), equipped with an integrated preamplifier (Gain = 26 dB), was of high and flat response in the range of 20-600 kHz, as shown by the sensitivity curve illustrated in Fig. 3. The threshold for the data acquisition was of 25 dB_{AE} based on background noise measurements, with a sample rate of 2 MHz.
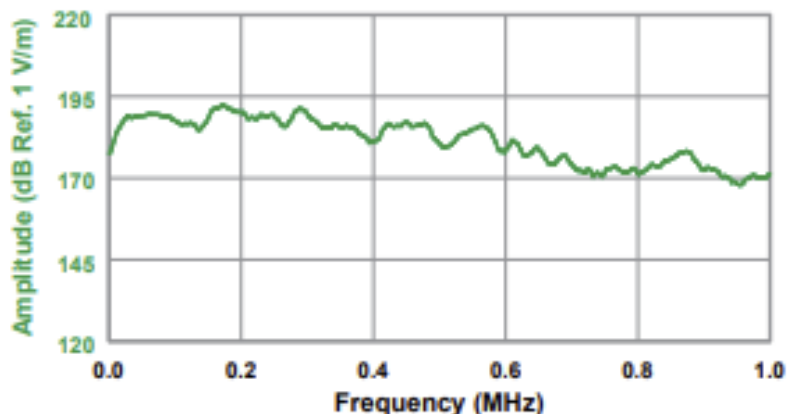
Fig. 3: Sensitivity curve of wide-band sensor PKBBI.

Fig. 2a shows the experimental set-up, consisting of a tubular cell clamped to the upper surface of the specimen and filled with EXCO electrolyte, jointly with the AE sensor coupled to the same surface with the help of a clamp and using silicon grease.

3.   Corrosion characterization

In order to get information of the different corrosion mechanisms (e.g., pitting, IGC) involved in EFC with time (initiation, early-stage corrosion and corrosion propagation), OCP has been monitored with time. Fig. 4a shows the OCP of different tests using EXCO solution, where an OCP around -0.58/-0.62 V is obtained from the beginning of the test. These values of the relative potential indicates a continuous corrosion of the AA, hindering the formation of any protective layer. According to the breakdown potential value obtained in the potentiodynamic polarization from Fig. 4b, it can be assumed that the OCP potential could be associated also to the dissolution of intermetallic particles (IMP) of Al_2CuMg [12].

On the other hand, the steady trend indicates that no significant changes were observed along EXCO test. This fact is probably suggesting that the aggressiveness of this electrolyte (pH=3.6-3.8) is too high, and is hindering the variation of the OCP with time. Thus, OCP cannot be an useful tool to distinguish different stages of the corrosion process.
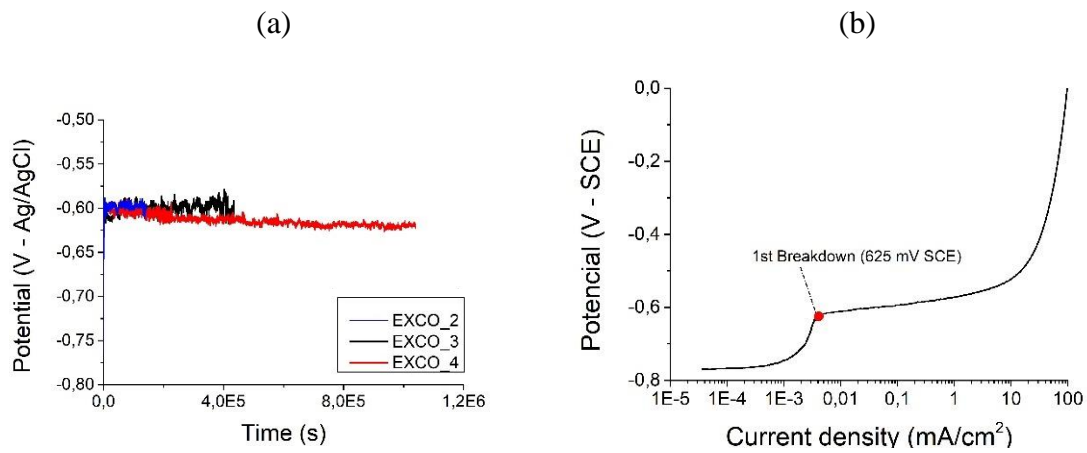
Fig. 4: a) Evolution of relative potential during tests EXCO_2-4. b) Potentiodynamic polarization curve of AA2024-T3 in Ar-deaerated 1.0M NaCl.

Besides, after each test the specimen was characterized by examining micrographs using an optical microscope. This characterization post-mortem, consisted of a cross-section of the most damaged area, i.e. across the pore-like artificial defect. Fig. 5 is revealing the impact of the corrosion throughout the material during the test. At this point, it should be noted that the experiment has been conceived intentionally with different duration for each test in order to get information from the characterization post-mortem at different times, that is, from initiation (i.e., pitting corrosion) to trigger EFC. Table 2 summarizes the duration of the five tests.

Table 2: Duration of each EXCO test.

TEST	DURATION (h)
EXCO_1	15
EXCO_2	39
EXCO_3	120
EXCO_4	288
EXCO_5	800

It must be pointed out that the localized corrosion is a stochastic phenomenon, due to several uncontrolled elements as for example: the location of the IMP on surface, the porosity of the E-coat (acting as pathways for the electrolyte to reach the substrate), the grains size and orientation, etc. However, even though the low reproducibility of the tests, micrographs show different corrosion damages during the whole process (Fig. 5). In this way, after 15h of test (EXCO_1) the pitting corrosion has already started, and later (EXCO_2, 39h) some intergranular corrosion (IGC) can be distinguished. After 120h (EXCO_3), the pitting corrosion has grown in depth in a bulk form, while the IGC has grown following a main direction. In a further stage (EXCO_4, 288h) the pitting corrosion has probably led to some detachments of the Al matrix, while an interphase was completely formed parallel to the exposed surface. In a very advanced stage (EXCO_5, 800h), the interphase evolved from IGC is extending over a wider area, although the typical layered appearance of the EFC was not observed. This fact could be explained by three facts: i) the EXCO electrolyte is lixiviating the corrosion products inside the interphase, which were supposed to mechanically lift-up the surface layers, ii) the microstructure of the AA2024-T3 (see Fig. 1) lacks EFC-prone laminar grains, iii) the stiffness of the E-coat is limiting the lift-up of the surface grains.
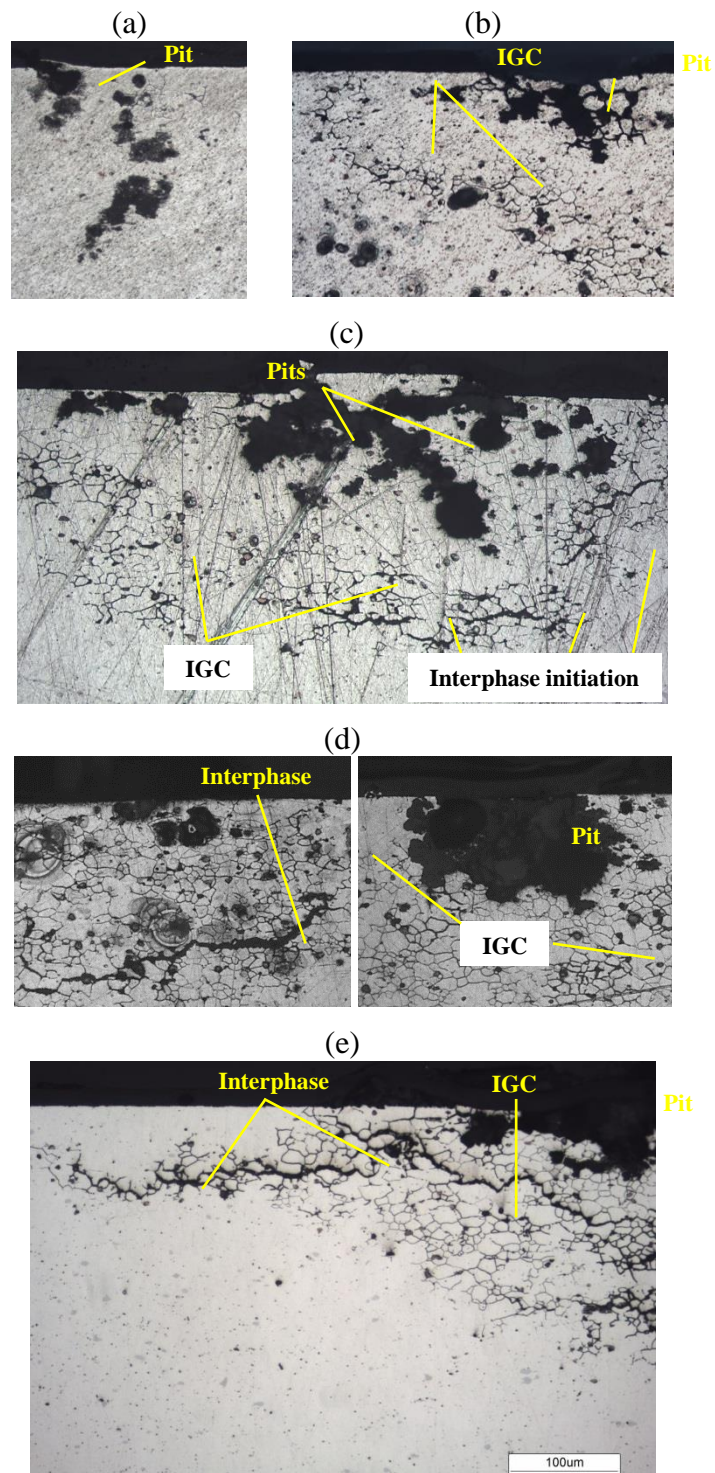
Fig. 5: Micrographs of cross section from optical microscope after EXCO test: a) EXCO_1 (15h), b) EXCO_2 (39h), c) EXCO_3 (120h), d) EXCO_4 (288h), e) EXCO_5 (800h).

4. AE data

The acoustic emission (AE) data was processed according to the acquisition setting. Consequently, AE signals and their corresponding parameters were obtained and analyzed aiming to extract reliable information able to determine the corrosion process.

Firstly, the most relevant AE parameters were selected using the Principal Component Analysis (PCA). Then, some of those parameters were excluded from the analysis due to high correlations:

e.g., Signal Strength or Energy (correlation >0.9 with Absolute Energy). Therefore, the analysis focused on Amplitude, Rise Time, Absolute Energy and Frequency Centroid.

Once defined the most significant AE parameters, the AE signals were examined through the original parameters as well as by dimensionality reduction techniques as PCA or t-distributed stochastic neighbor embedding (t-SNE). As result, the data structure was found to be a single compact group of signals as shown by t-SNE chart of Fig. 6a. By calculating the Silhouette coefficient, the optimum number of clusters was found to be two. However, it can be seen in the PCA chart (Fig. 6b), with the 3 principal projections, that the clustering doesn't provide a real separation of the data.

(a)   (b)
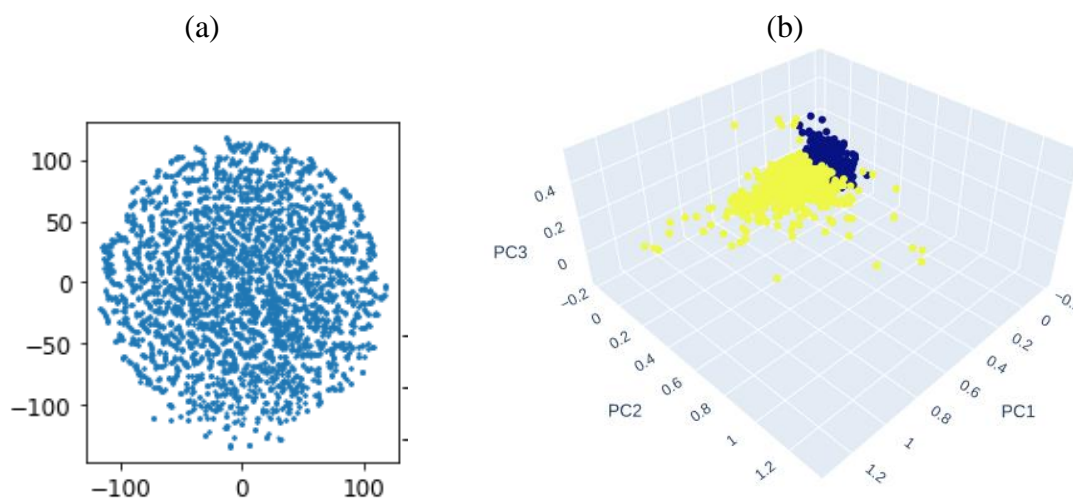
Fig. 6: Data structure of AE signals from the test EXCO_3: a) t-SNE chart with perplexity=5, and b) PCA chart with 3 principal projections.

Alternatively, the AE analysis was performed by grouping signals in intervals of 30 min and data was processed according to the following process:

1) The mean values of the AE parameters (Amplitude, Rise Time, Absolute Energy and Frequency Centroid) allowed to identify four classes (*i-iv*) of intervals. Then, ranges of values were defined tentatively for each AE parameter and class.
2) All intervals above certain activity (>100 hits) were placed in one of the four classes according to the preliminary ranges of AE parameter's values.
3) Statistics as the mean ($\bar{x}$) and quartiles (Q1, Q2 and Q3) were extracted from all the intervals included in each class. This way, the range of values of AE parameters was statistically defined for each class, as listed in Table 3.

Table 3: Range of values of AE parameters for each class.

	Class i	*Class ii*	*Class iii*	*Class iv*
Amplitude (dB$_{AE}$)	26-27	<28	26-30	>28
Rise Time (μs)	<35	>35	>35	>35
Ab. Energy (aJ)	0-2.0	<2.5	2.5-10	>5.0
Fr. Centroid (kHz)	>255	>250	>230	<235

The AE data recorded during the EXCO tests (1-5) was processed and up to 80-90% of all intervals fitted into the ranges that have been defined statistically for each class and AE parameter. This fact is of significant relevance and agrees with the post-mortem characterization (micrographs in Fig.

5): even though that the EXCO test are not completely replicable due to the stochastic process of localized corrosion, similar mechanisms and intervals were found in different tests. Table 4 summarizes the mechanisms and the predominant classes for each test.

Table 4: Corrosion mechanisms underwent during EXCO tests and predominant classes extracted from the AE data.

	CORROSION MECHANISMS	*PREDOMINANT CLASSES*
EXCO_1	Pitting	ii* (*very few signals)
EXCO_2	Pitting + IGC	ii
EXCO_3	Pitting + IGC + Initial interphase	i, ii, iii
EXCO_4	Pitting + IGC + Interphase	i, ii, iii, iv
EXCO_5	Pitting + IGC + Interphase	ii, iii, iv

Clearly, the AE data is evolving from intervals of class *i/ii* toward class *iii* and lastly class *iv*. Similarly, the localized corrosion process, as widely reported in literature, progresses during EXCO tests from pitting toward IGC, and even undermining the boundary of grains in a main direction (interphase). The agreement between the evolution of the AE data and the progression of the localized corrosion is more than evident, although groups of singular AE signals cannot be distinguished in this experiment to identify each mechanism. However, taking into account the range of values of AE parameters (see Table 3) for each class, the following trend can be clearly observed: i) the Amplitude and the Absolute Energy increase gradually from 26 to more than 28 dB_{AE} with the progress of corrosion, and from 0 to more than 5.0 aJ, respectively, ii) the Frequency Centroid decreases from more than 255 kHz to less than 235 kHz. This finding suggests that the selected AE parameters are sensitive to the evolution of the localized corrosion, and therefore to the mechanism behind each stage.

5. Conclusions

The standardized EXCO test was applied to coated (anaphoretic e-coating) aluminum AA2024-T3. The aim was to trigger localized corrosion in a well-controlled way through different mechanisms: from initiation by pitting to EFC. Two conclusions can be drawn from this experiment:
- The AE technique was able to detect consistently the evolution in time of the localized corrosion through different mechanisms for all EXCO tests, overcoming limitations using conventional electrochemical measurements due to the aggressiveness of the electrolyte. Nevertheless, further investigations must be addressed in future to characterize the AE signatures of such mechanisms and enable the AE technique for localized corrosion monitoring.
- The methodology consisting of applying EXCO solution to a defected e-coating, despite the stochastic nature of the corrosion process, was consistent for different tests given that similar sequence of mechanisms was observed.

6. Acknowledgments

7. References

[1] Ketcham, S. J., & Shaffer, I. S. (1972). Localized Corrosion—Cause of Metal Failure. Philadelphia, PA, American Society for Testing and Materials. STP-516, 3-16.

[2] Karayan, A. I., Jata, K., Velez, M., & Castaneda, H. (2016). On exfoliation corrosion of alloy 2060 T8E30 in an aggressive acid environment. Journal of Alloys and Compounds, 657, 546-558.

[3] Zhang, W., & Frankel, G. S. (2003). Transitions between pitting and intergranular corrosion in AA2024. Electrochimica Acta, 48(9), 1193-1210.

[4] Marlaud, T., Malki, B., Deschamps, A., & Baroux, B. (2011). Electrochemical aspects of exfoliation corrosion of aluminium alloys: The effects of heat treatment. Corrosion Science, 53(4), 1394-1400.

[5] ASTM, G. G 34–90. Annual book of ASTM Standards, section, 3, 129.

[6] Ono, K. (2008). Structural integrity evaluation by means of acoustic emission. In Acoustic Emission and Critical Phenomena (pp. 23-38). CRC Press.

[7] Aggelis, D. G., Barkoula, N. M., Matikas, T. E., & Paipetis, A. S. (2012). Acoustic structural health monitoring of composite materials: Damage identification and evaluation in cross ply laminates using acoustic emission and ultrasonics. Composites Science and Technology, 72(10), 1127-1133.

[8] Carpinteri, A., Lacidogna, G., & Pugno, N. (2007). Structural damage diagnosis and life-time assessment by acoustic emission monitoring. Engineering Fracture Mechanics, 74(1-2), 273-289.

[9] Mazille, H., & Rothea, R. (1994). The use of acoustic emission for the study and monitoring of localized corrosion phenomena. In Modelling aqueous corrosion (pp. 103-127). Springer, Dordrecht.

[10] Idrissi, H., Derenne, J., & Mazille, H. (2000). Detection of pitting corrosion of aluminium alloys by acoustic emission technique. J. Acoust. Emiss, 18, 409-416.

[11] Bellenger, F., Mazille, H., & Idrissi, H. (2002). Use of acoustic emission technique for the early detection of aluminum alloys exfoliation corrosion. Ndt & E International, 35(6), 385-392.

[12] Guillaumin, V., & Mankowski, G. (1998). Localized corrosion of 2024 T351 aluminium alloy in chloride media. Corrosion Science, 41(3), 421-438.

ACOUSTIC EMISSION MONITORING OF ABRASION AND CORROSION IN DOUBLE-WALLED PIPELINES

Kilian Tschöke[1,*], Alexander Pietzsch[1], Thomas Kippert[2] and Lars Schubert[1]

[1]Fraunhofer IKTS, Maria-Reiche Straße 2, 01109 Dresden, Germany;
kilian.tschoeke@ikts.fraunhofer.de, alexander.pietzsch@ikts.fraunhofer.de,
lars.schubert@ikts.fraunhofer.de
[2]KRONOS TITAN GmbH, Peschstr. 5, 51373 Leverkusen;
thomas.kippert@kronosww.com
*Correspondence: kilian.tschoeke@ikts.fraunhofer.de

ABSTRACT

At KRONOS TITAN, double-walled pipelines are used in production of Titandioxid. An abrasive medium is transported in the inner pipe at high temperatures. In the outer pipe, cooling water ensures that the process is cooled down. During the process, it is important that no abrasion leads to complete wall erosion and thus to leakage between the inner and outer pipe. During a test campaign lasting several months, a section of such a pipe was instrumented with acoustic emission measurement system on the outer pipe and the abrasion process in the inner pipe was monitored with AE until the removal of the pipe section. Different AE-signal parameters (Events, Hits, Energy and Frequency) were investigated regarding their suitability and are discussed in this contribution. The results of the acoustic emission measurements with regard to the location and progress of damages were then compared and verified with classic NDT test results.

Keywords: Acoustic emission, monitoring, corrosion, double-walled pipelines, corrosion rate.

1. Introduction

At KRONOS TITAN, double-walled piping is used in the production of Titandioxid. The pipe is part of a cooling system to cool down the product after combustion. The abrasive medium is transported inside the inner pipe, while the outer pipe is used to cool the inner medium. In the process, it is important and desirable to detect corrosion and abrasion of the inner pipeline. In this way, wall penetration and mixing of the two media can be avoided. Non-destructive testing of the wall thickness of the inner pipe is currently only possible to a limited extent in the dismantled state of the pipeline section. For this purpose, the pipeline section is removed at regular intervals and checked at the accessible points.

During this feasibility study different acoustic methods were investigated for monitoring of wall abrasion. Both methods are based on evaluation of guided elastic waves with difference in excitation and evaluation of acoustic signal. The passive method (AE) uses acoustic signals generated by process and affected by ongoing abrasion and the active method (AU) excites guided waves and evaluates travel times of guides waves between adjacent sensors. Acoustic emission testing in particular has been used for many years in various industrial areas to monitor damage

processes at critical installations [1]-[5]. The implementation and evaluation of active method is not part of this proceeding and just mentioned for the sake of completeness.

Challenge of this measurement is the indirect measurement of the AE induced by the abrasion effects. AE has to be transferred from the inner tube through the cooling water to the outer tube wall where the sensors are located. The following Fig. 1 gives an overview.

2.   Description of work

2.1   Measurement setup

The acoustic emission measurements were carried out on a 3 m long pipe section during operation over 3 measurement campaigns in the period from 09.09.2021 - 10.01.2022. The measurements were carried out with a multi-channel acoustic system (MAS2[1] [6]), preamplifiers of type PreAmp MCE 6.3 with 40 dB and the acoustic emission sensors of type KAR601S (IKTS):

MAS2 Parameters:
- Bulk Sampling Frequency 12.50E+06 Hz
- Sampling rate/channel 0.32E-06 s
- Pretrigger 1024 samples
- Posttrigger 16260 samples

KAR601S Parameter:
- AE sensor bandwidth 10-500 kHz
- AE sensor capacitance 150 pF

A total of 7 sensor belts with 2 AE sensors each are used. The sensors are alternately rotated by 90° to each other and fixed on the pipe segment. Four different localisation planes (P1-P4) are used for localization of AE-Events as shown in Fig. 1 (lowest figure):
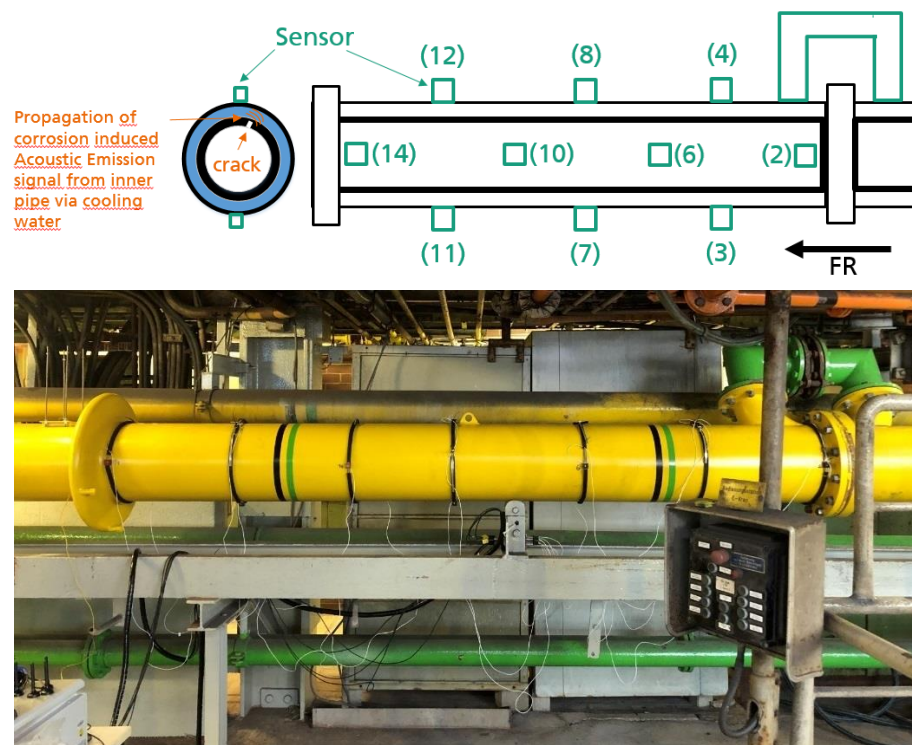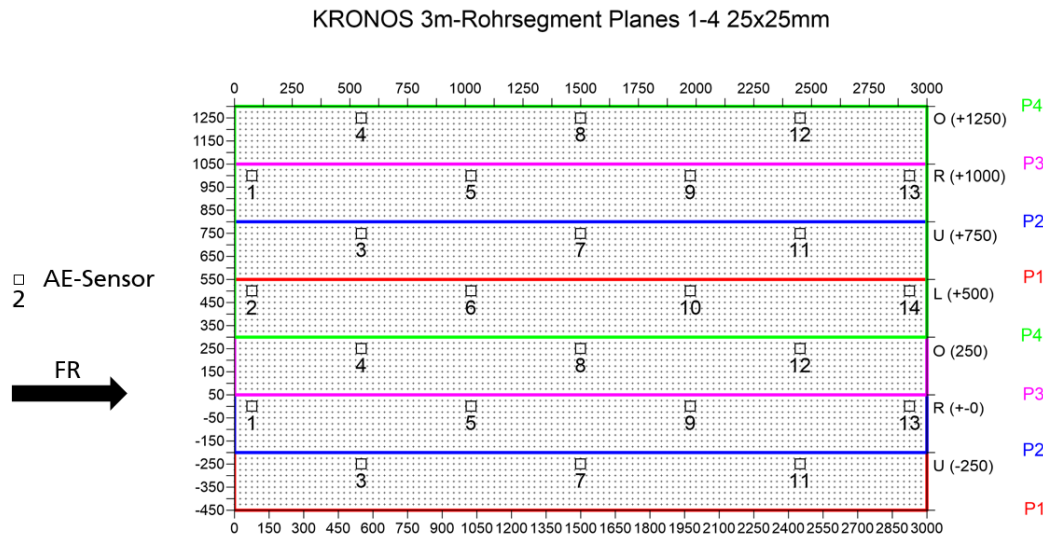
Fig. 1: Overview about sensor installation; schematic (top), instrumented pipe segment (middle) and localization planes (bottom) with indication of flow direction (FR).

2.2 Evaluation

The 2D location plot contains the 4 location planes (P1-P4) used for evaluation, whereby the 4 planes for planar location result from the unwinding of the pipe surface.

The data acquisition is performed by 14 AE sensors, which are applied in pairs via 7 sensor rings on the pipe. A sound event is assigned to the plane in which the triggering AE sensor is located as centrally as possible.

In order to be able to locate as precisely as possible, the high-frequency symmetrical wave modes were suppressed by a dynamic bandpass filter and the low-frequency, but high amplitude asymmetrical wave mode A0 was used. As sound velocity c for the localization 3000 m/s were applied. The evaluation like localization and parameter calculation are based on the recorded time signals after the measurements. The following parameters were calculated and displayed in Fig. 2:

- Hits and cumulative hit history
- Events
- Energy (related to the source location)
- Cumulative energy of the sound emission events

The measurement system is configured to allow the recording of operational and environmental parameters in time synchronization with the acoustic channels. During these accompanying measurements, the temperature was also recorded as an analog signal and included in the evaluation. Measurements were carried out from 09.09.2021 to 10.01.2022 in 3 measurement campaigns of 6 weeks duration each.

Fig. 2: Presentation of AE measurement results from measurement campaign 1-3 for the period 09.09.2021 - 10.01.2022.

Fig. 2 shows the temperature curve (blue curve) of the pipe section. The change between ambient temperature and process temperature (~150°C) indicates process interruptions and a ramp-up and ramp-down of the plant.

The black curve represents the cumulative hit history, while the red curve shows the localized events. The magenta curve shows the cumulative progression of the energy of the events calculated back to the source location. The slope of this energy curve follows the course of the hit or event curve. The green bars are assigned to the individual energies of > 0.6 pJ of the events.

It can be observed that high individual energies are mainly seen in the shutdown and start-up processes of the plant as well as at increased operating temperatures of the plant (T>165°C). This suggests that events with high energies indicate higher abrasion or wearing in the pipe.

Subsequently, it was investigated to what extent the AE data can be used to localize the acoustic emission events (and thus the locations of potential wall abrasion) in the longitudinal and transverse directions of the pipe. For this purpose, all events in the circumferential direction were averaged and plotted in Fig. 3.

AE_210909_180421-220110_000000_AIC_KD_LIM_EVT_X0_[mm]-Timediff_[s]-Event-Density_DENS
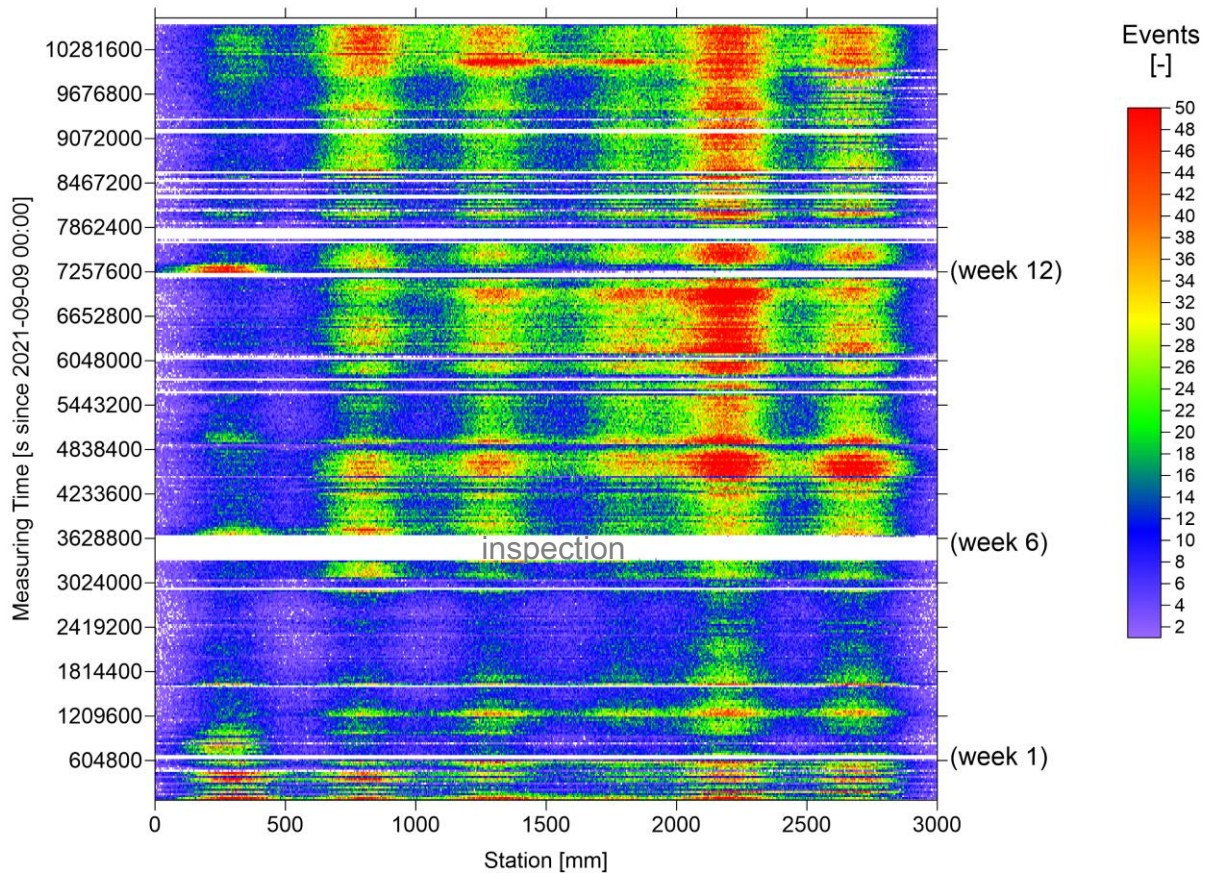
Fig. 3: Plot of averaged AE data over the period 09.09.2021-09.01.2022 in the parameter range, X-coordinate: station [mm] (pipe length), Y-coordinate: measurement time [s] since 09.09.2021 00:00, color-coded: Number of located events.

A particularly large number of events can be observed in the range X=2300 mm, which are already visible during the first weeks. In general, an increase in AE events can be observed after the first inspection after 6 weeks, which suggests changed operating parameters in the plant management. Fig. 4 presents the cumulative energies back calculated to the source location. Particularly obvious are the high energies at the inflow (0<X<500 mm), which already occur during the first days of the test and are prominent during the entire duration of the measurement campaign. Shortly before the first inspection at week 6, increasingly high energies are also visible up to X=1000 mm. As the duration of the test continues, these increase and also become noticeable at the end of the test in the rear area of the instrumented pipe section (up to X=2500 mm).

In the following it was examined whether it is possible to localize at which point in circumferential direction of the pipe the events with the highest energies occur. For this purpose, the X-coordinate in Fig. 5 was averaged. The energy of the acoustic signals from sections of 500 mm length each were added up and plotted over their circumferential coordinate. The left plot in Fig. 5 shows the result for the subsection of the X coordinate 2000 mm to 2500 mm, while the right plot shows the subsection 2500 mm to 3000 mm respectively. It can be seen that each plot represents different locations in the pipeline as "acoustically active". The amount of actual wall erosion at these locations could not be investigated in the project, as these areas (in contrast to the inflow area) are not accessible for NDT measurements.
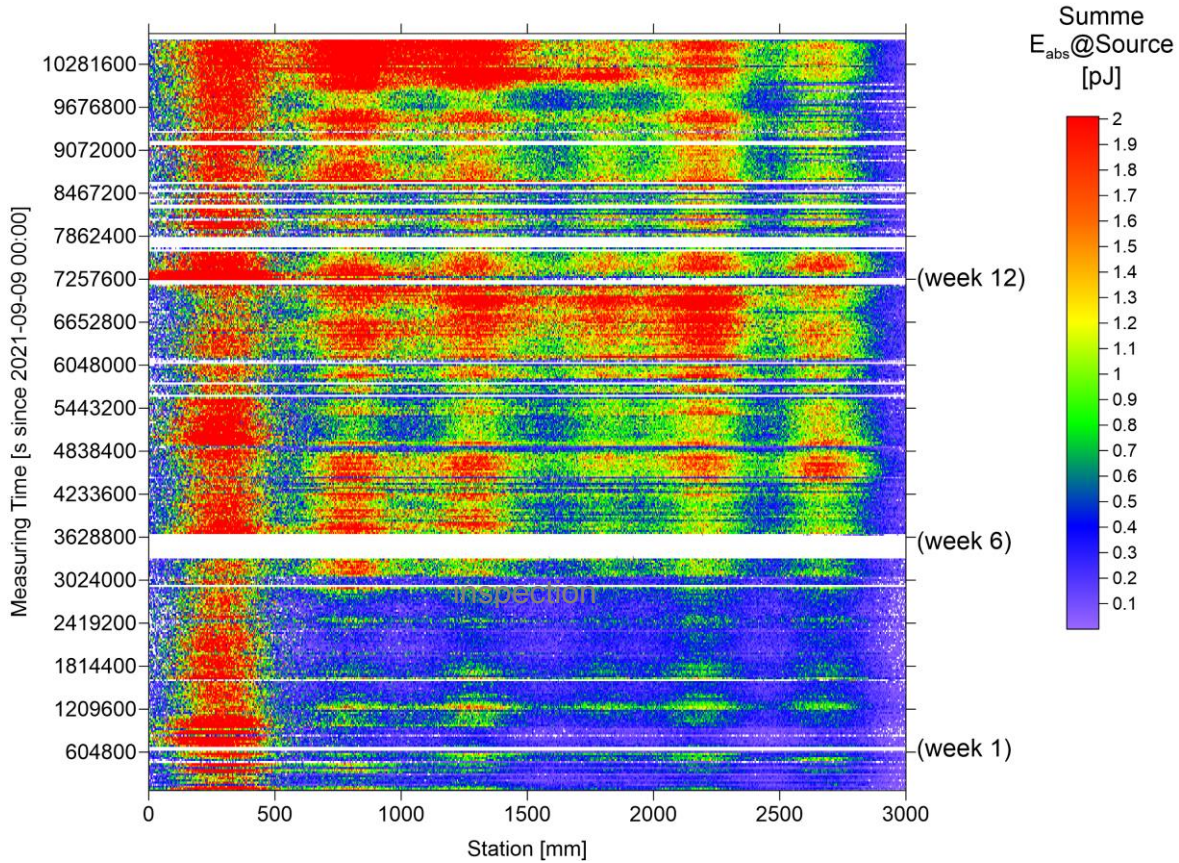
Fig. 4: Plot of averaged AE data over the period 09.09.2021-09.01.2022 in parameter range, X-coordinate: station [mm] (pipe length), Y-coordinate: measurement time [s] since 09.09.2021 00:00, Color-coded: sum of energy of burst signals related to source location [pJ].
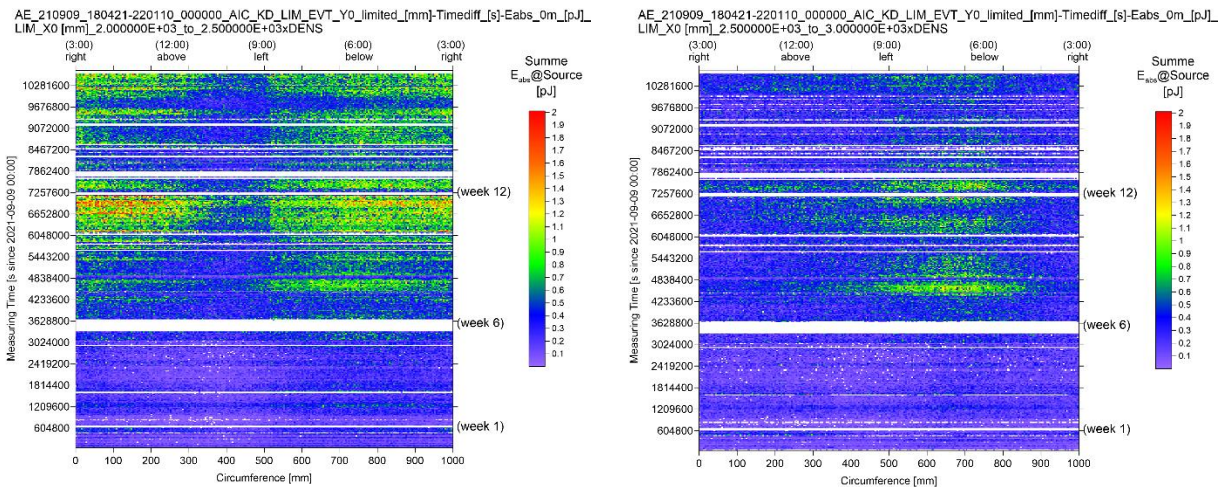
Fig.5: Plot of averaged AE data over the period 09.09.2021-09.01.2022 in the parameter range, X-coordinate: circumference of pipe section [mm], Y-coordinate measurement: time [s] since 09.09.2021 00:00, for station X0 [mm]: 2000 to 2500 mm (left plot) and station X0 [mm]: 2500 to 3000 mm (right plot); color-coded: sum of energy of burst signals related to source location [pJ] (cell size x=4mm y=8h).

3. Discussion

The above given plots show an increase in event density over the measurement period. In the longitudinal direction, the X coordinate between 2200 mm < X < 2400 mm is particularly significant, showing strong AE indications over the entire duration of the measurement campaign. The energy of the burst signals is highest at the inlet of the tube. This can be explained by the inflowing medium and possibly also by a (design-related) offset of the pipe sections. In the progress of the measurement campaign, the energy of the burst signals increases from the inlet in the longitudinal direction up to approx. X= 1800 mm. The sum of the energies also increases in the longitudinal direction of the pipe in the course of the measurement campaign.

In the evaluation in circumferential direction an increase in the energy of the burst signals or the summed energy between "12 o'clock" and "3 o'clock" can be seen in the circumferential direction. Especially after week 12 of the experiment this becomes obvious, indicating changes in the process or in the plant.

It can be observed that high individual energies are mainly seen in the shutdown and start-up processes of the plant as well as at increased operating temperatures of the plant (T>165°C). This suggests that events with high energies indicate higher abrasion or wearing in the tube.

Table 1: Results of thickness measurements at Row 1-8 for NDT inspections on 15.10.2021 and 01.12.2021, respectively.

	Wall thickness [mm] 15.10.2021								Wall thickness [mm] 01.12.2021							
	R1	R2	R3	R4	R5	R6	R7	R8	R1	R2	R3	R4	R5	R6	R7	R8
P1	5,2	5,9	6,0	5,9	5,9	5,8	5,8	5,8	3,9	5,3	5,8	5,7	5,7	5,6	5,5	5,4
P2	5,6	5,9	5,9	5,8	5,8	5,7	5,7	5,7	5,1	5,6	5,6	5,4	5,3	5,3	5,2	5,2
P3	4,7	5,1	5,7	5,7	5,7	5,7	5,7	5,6	4,3	4,7	5,4	5,4	5,3	5,3	5,3	5,3
P4	4,7	4,9	5,9	5,9	5,9	5,9	5,9	5,9	3,9	4,1	5,1	5,8	5,8	5,8	5,8	5,8
P5			4,5			5,7	5,8									
P6			4,1			5,6	5,9									
Ø in mm	5,05	5,45	5,35	5,825	5,825	5,73	5,8	5,75	4,3	4,925	5,475	5,575	5,525	5,5	5,45	5,425

The wall thickness of the pipeline was 6 mm at all points at the beginning of the test. After 6, 12 and 18 weeks, ultrasonic thickness measurements were carried out on the accessible area of the inflow as part of the routine inspection during turnaround. In the process, the wall thickness was repeatedly measured at different positions P1-P6 on different rows R1-R6. Table 1 and Table 2 summarizes the measured values on 15.10.2021, 01.12.2021 as well as on 09.01.2022. The distance between adjacent rings R was 30 mm starting 30 mm away from the edge of the pipe section (see Fig. 6). In relation to the inflow side in the direction of flow as seen in Fig. 6, position P1 was at 9 o'clock, P2 at 6 o'clock, P3 at 3 o'clock and P4 at 12 o'clock, respectively. Positions P5 and P6 were only measured on 15.10.2021 and were located between P3 and P4, i.e. at approx. 1 o'clock and 2 o'clock.

	Wall thickness [mm] 09.01.2022							
	R1	R2	R3	R4	R5	R6	R7	R8
P1	2,9	4,7	5,6	5,5	5,5	5,4	5,2	5,2
P2	4,5	5,3	5,3	5,0	4,8	4,9	4,8	4,7
P3	3,7	4,3	5,1	5,1	5,0	4,9	5,0	5,0
P4	3,2	3,4	4,3	5,6	5,7	5,6	5,7	5,7
Ø in mm	3,575	4,425	5,075	5,3	5,25	5,2	5,175	5,15

Table 2: Results of thickness measurements at Row 1-8 for NDT inspections on 09.01.2022.
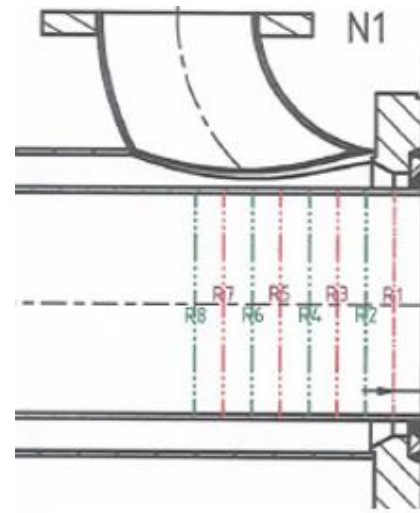
Fig. 6: Location of positions of ultrasonic thickness measurements R1-R8.

Already after 6 weeks, average wall reduction at Ring R1 to 5,05 mm was measured. At the second turnaround after 12 weeks, this was already 4.3 mm at R1. After 18 weeks, the average wall thickness at R1 was 3,575 mm and the minimum wall thickness at single point fell below the critical dimension with 2,9 mm at R1-P1 and the pipeline was replaced.
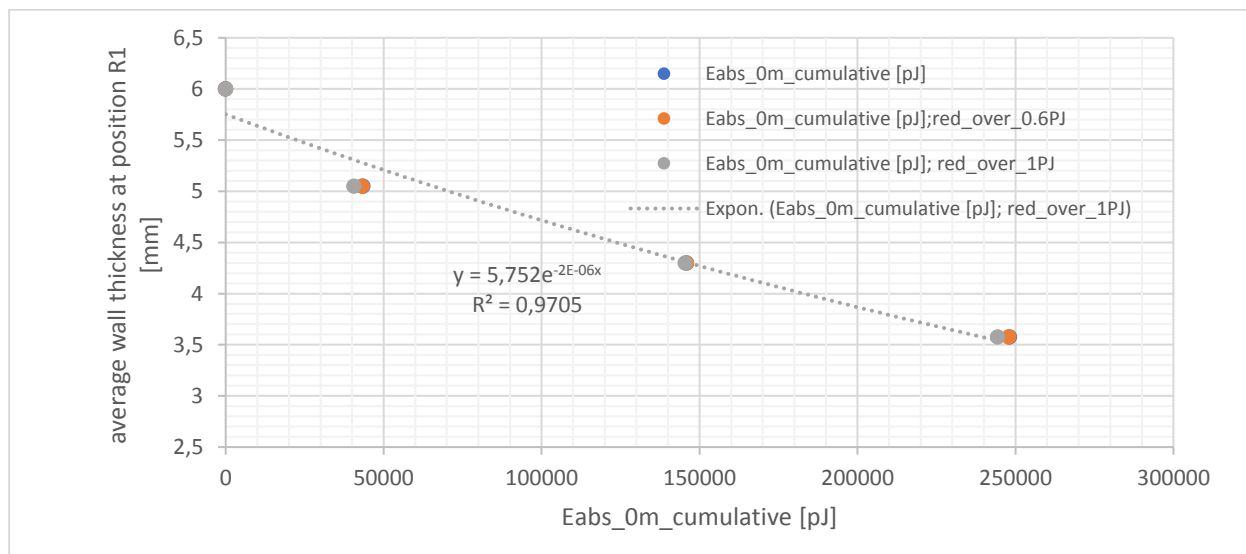
Fig. 7: Correlation of average wall thickness at position R1 in mm and sum of cumulative energy of all acoustical events located so far for different energy thresholds of 0 pJ (blue), 0.6 pJ (orange) and 1 pJ (grey).

It can be observed that, as expected, the greatest wall erosion occurs directly at the beginning of the pipe at the inflow and decreases with increasing X-coordinate. Fig. 7 compares the averaged residual wall thickness at ring R1 with the acoustic summed energies. AE signals of different energy levels were included in the calculation of the acoustic energies. The blue measurement points show all summed up individual energies, for the orange and gray ones only individual energies above 0.6 pJ and 1 pJ were allowed. All curves show an exponential trend, even if just high energy values above 1pJ are considered.

An evaluation of the increase of the 1 pJ curve results in an energy increase of 80.000 pJ to 90.000pJ per mm wall ablation. At this point it should be mentioned that this value depends on the used measuring system (especially the capacity of the transducer) and the specific measuring and data evaluation settings and cannot be easily transferred to other acoustic emission measuring systems.

4.   Conclusions

In this feasibility study, a double-walled pipe section was instrumented with acoustic emission measurement technology and the wall thickness removal was monitored with acoustic emission. In parallel, the actual wall thickness removal was determined by ultrasound at certain points in time during rotational inspections. Despite the indirect measurement of the sound on the upper side of the outer pipe, the application of the AE technique is possible and reasonable. A large number of AE events were recorded during the measurement period. Increasing AE indications and energies throughout the pipe indicate wall thickness degradation, which could be confirmed via conventional wall thickness measurements. Likewise, direct changes in the operation of the plant or process can be read indirectly from the AE data.

Increasing wall erosion could be determined by evaluating the energy levels of the acoustic emission signals. In the present case, the cumulative acoustic emission energy increased by 80.000 pJ − 90.000 pJ per millimeter of wall erosion. Further work should investigate the transfer to other pipeline sections or pipelines, data reduction as well as include correlation of acoustic emission parameters with plant process data.

5.   References

[1]   Frankenstein, B.; Fischer, D.; Weihnacht, B. & Rieske, R.: *Lightning safe rotor blade monitoring using an optical power supply for ultrasonic techniques*; 6th European Workshop on Structural Health Monitoring, 2012.

[2]   Weihnacht, B.; Klesse, T.; Neubeck, R. & Schubert, L.: *Monitoring of hot Pipes at the power plant Neurath using guided waves*; Sensors and Smart Structures Technologies for Civil, Mechanical, and Aerospace Systems, 2013.

[3]   Weihnacht, B.; Schulze, E. & Frankenstein, B.: *Acoustic Emission Analysis in the Dynamic Fatigue Testing of Fiber Composite Components*; 31st Conference of the European Working Group on Acoustic Emission, 2014.

[4]   Tschöke, K.; Weihnacht, B.; Gaul, T.; Schulze, E.; Schubert, L. & Neubeck, R.: D*etermination of Defect Sizes with the help of Structural-Health-Monitoring Methods based on Guided Waves*; 7th European-American Workshop on Reliability of NDE, 2017.

[5]   Tschöke, K.; Gaul, T.; Pietzsch, A.; Schulze, E. & Schubert, L.: *On the Application of Actively and Passively Excited Guided Elastic Waves for the Monitoring of Fiber-Reinforced Plastics*; MDPI aerospace, 2020, 7, 1-12.

[6]   Sause, M.; Schmitt, S.; Trattnig, H.; Altmann, D.; Pietzsch, Alexander; Stephan, Mareike; Schubert, Lars: *Vergleich von Messsystemen zur Schallemissionsprüfung von Faserverbundwerkstoffen*, 22. Kolloquium Schallemission und 3. Anwenderseminar Zustandsüberwachung mit geführten Wellen Karlsruhe, 27. – 28. März 2019.

INVESTIGATION OF DELTA-T MAPPING SOURCE LOCATION TECHNIQUE BASED ON THE ARRIVAL OF A_0 MODES

Han Yang[1,2,*], Bin Wang[2], Dandan Liu[1,2] and Stephen Grigg[1]

[1]TWI Ltd, Granta Park, Great Abington, Cambridge, CB21 6AL, UK;
dandan.liu@brunel.ac.uk; stephen.grigg@twi.co.uk
[2]Department of Mechanical and Aerospace Engineering, Brunel University London, Uxbridge UB8 3PH, UK; bin.wang@brunel.ac.uk
*Correspondence: han.yang9407@gmail.com

ABSTRACT

The main assumptions made for traditional Time of Arrival (TOA) source location techniques are constant wave speed and straight wave path between the acoustic emission (AE) source and the sensors. However, because of material inhomogeneity and structural complexity, wave velocities may vary in different directions and a direct wave path may be very difficult to be achieved. Therefore, to solve these problems, researchers developed delta-T mapping source location technique, which has been shown to have good accuracy for source location in aerospace structure because complex geometric features are considered when training the mapping data and accurate wave speed data are not required. However, this technique relies on identifying the arrival time of S_0 (extensional) Lamb mode, which may not be distinguished from background noise due to low-amplitude AE sources such as corrosion or large source-to-sensor distance. As shown in Figure 1, source location accuracy in a corrosion test on a simple plate was greatly improved after the velocity of A_0 (flexural) Lamb mode was used in the source location algorithm. Therefore, identifying the arrival time of A_0 modes and hence building delta-T maps are more feasible to solve the problem. Experiments have been carried out with an artificial AE source on a thin complex steel plate. A threshold crossing method based on wavelet coefficient was used to estimate the arrival time of A_0 modes. The average error (3.9 mm) of the source locations predicted by delta-T mapping based on A_0 arrival was larger than that (1.8 mm) of S_0 arrival, which can be explained by the difficulties in accurately identifying the arrival of A_0 modes.

Keywords: Acoustic emission, delta-T mapping, flexural Lamb mode, complex plate, source location.

1. Introduction

Corrosion damage is one of the most important and costly problems worldwide. According to a recent study conducted by Koch et al. [1], the estimated global cost of corrosion is 2.5 trillion dollars, or 3.4% of the global GDP in 2013. In addition to the huge economic loss, structural failures caused by corrosion damages can lead to serious individual safety and environmental consequences. For example, in April 1992, 215 people were killed and another 1500 people were injured due to the sewer explosion in Guadalajara, Mexico. The huge economic loss was estimated

at 75 million dollars. The accident was due to the leakage of corroded gasoline into a nearby sewage main [2]. The sinking of the Erika (a tanker) on 12th of December, 1999 was another accident caused by corrosion. Some spilled 19,000 tons of heavy oil resulted in devastating pollution to the maritime environment. In this disaster, big loss in revenue from tourism and fishing industries had been felt by the local people [2].

In order to prevent detrimental events resulting from corrosion, it is of great importance to monitor corrosion in suite and identify the onset of corrosion before structural integrity is compromised. Structural Health Monitoring (SHM), which is defined as the process of continually monitoring engineering structures for the identification of damage, is gaining widespread interest for increased industrial applications. To infuse continued confidence in the structural integrity, NDE inspections are performed periodically, which forms the basis of SHM system. NDE techniques such as ultrasonic and X-ray methods have been proven to be very effective for detecting a considerable number of defects in materials and have been widely in industries [3]. Despite its merits, there appear to be some possible negative consequences of periodic NDE-based inspections. In order to perform NDE, many components need to be removed from testing equipment and refitted thereafter, thus requiring a long period of time. Moreover, areas of difficult access and complex geometry is particularly difficult to examine by the NDE techniques. Thus a revision of the traditional SHM system is desirable, with a transition from lengthy periodic NDE inspection to an autonomous SHM system in which the structural integrity of the target equipment is continuously, autonomously in-service monitored. The phenomenon of acoustic emission (AE), which is one type of NDE methods, lends itself well to such a system. AE is defined as the transient elastic energy released by a material when it experiences a change of deformation in its structure [4].

Unlike other conventional NDT techniques, AE stands out as an integral and passive NDT method since it detects transit elastic waves radiated by deformation of a structure. AE offers a number of advantages for the development an autonomous SHM system; it is a desirable technique which has the capability to globally monitor large scale structures using a suitable array of sensors. Damages in areas inaccessible for physical inspection with current NDE methods can be detected. Moreover, it provides the ability of continuously testing and in situ monitoring structures without requiring a total stoppage or shutdown of structures. Furthermore, the locations of AE sources can be determined with an appropriate sensor array.

In the calculation of AE source location, difficulties in applying traditional source location method, Time of Arrival (TOA) technique, in complex structures was reported by Baxter et al. [5]. To overcome these difficulties, Delta-T mapping technique was developed by Baxter et al. [5] and an improvement in AE source location accuracy in complex structures has been shown. Hence, Delta-T mapping is regarded to be a suitable method for AE source location of corrosion damages in complicated geometric structures. The current Delta-T mapping technique relies on identifying the arrival time of S_0 Lamb mode. However, according to the corrosion test results on simple plate, it was very likely that the first arrival of signals recorded by AE sensors was A_0 mode. Therefore, a method for determining the arrival of A_0 mode is proposed in this study. Using this method, Delta-T mapping technique based on the arrival of A_0 mode is developed and tested using artificial AE sources.

2. Corrosion test on simple plate

A commercial sheet of grade S275 mild steel (Lakeland Steel Ltd., Cumbria, UK) was used for the investigation. The specimen (500 mm × 300 mm × 3 mm) was washed in de-ionised water and then rinsed with acetone solution. After rinsing, the specimen was dried under a stream of cold air. The investigations were carried out in 3.5 % sodium chloride solution (pH= 5.7). The solution was placed in a cylindrical thin-walled plastic vessel (Outer Diameter= 80 mm, height= 80 mm and thickness= 2 mm). There is a small hole (diameter =8 mm) on the bottom to allow for the specimen to be in contact with the solution, that is, providing an exposed surface area of 16π mm^2. A

waterproof silicone sealant (Everbuild Building Products Ltd., Leeds, UK) was applied around the hole to attach the cylindrical vessel to the specimen and prevent the leaking of the test solution.

The uniform corrosion process was controlled in typical three-electrode electrochemical cell at room temperature. The specimen was served as the working electrode and a coiled platinum wire was used as a counter electrode. The measurement of the potential was made against a reference saturated Ag/AgCl/NaCl electrode. The electrochemical corrosion process at the static corrosive potential was controlled using a potentiostat/galvanostat system Gill AC (ACM Instruments, Cumbria, UK).

In addition to the potentiostatic measurements carried out by application of electrochemical, digital measurement system, measurements of uniform corrosion by AE method were carried out simultaneously. As shown in Fig. 1, three Nano 30 sensors (Mistras Group Inc.,New Jersey, United States) were mounted on the surface of the specimen. The centre of the circular surface area exposed to sodium chloride solution coincided with the centre point of the top surface of the specimen.

The Nano-30 sensor were coupled with the specimen by way of Loctite 595 Transparent Sealant (Henkel Loctite Corporation, Helsinki, Finland) and amplified with AEP4H (Vallen Systeme GmbH, Germany) at 34 dB gain. Outputs of all the sensors were linked to a Vallen 16-channel AMSY-6 AE System (Vallen Systeme GmbH, Germany).
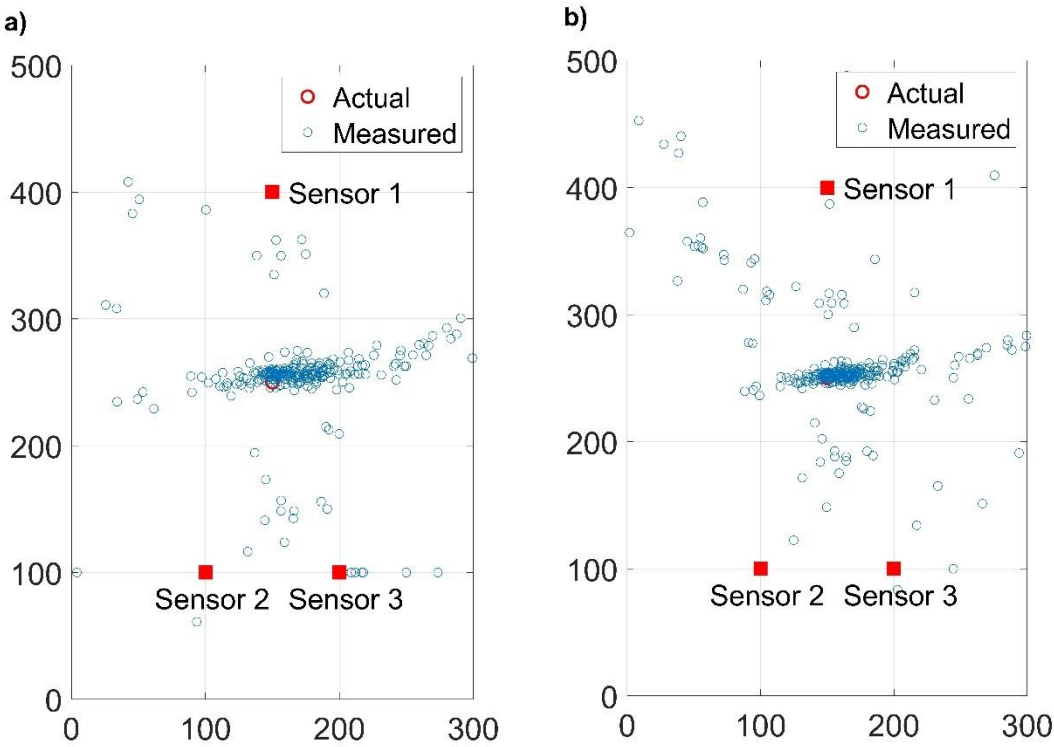
Fig. 1: Source location results in a corrosion test; a) velocity of S_0 modes was used. b) velocity of A_0 modes was used.

As seen in Fig. 1, compared to the source location results using the velocity of S_0 mode, source location accuracy was greatly improved after the velocity of A_0 mode was used in the source location algorithm. Hence, it was very likely that the first arrival of signals recorded by AE sensors was A_0 mode.

3. Delta-T source location technique based on A_0 arrival

A method for determining the arrival of A_0 mode is proposed in this section. Using this method, Delta-T mapping technique based on the arrival of A_0 mode is developed and tested using artificial AE sources.

3.1 Method for determination of A_0 modes

An automatic arrival time determination technique, two-step AIC picker, was proposed by Sedlak et al. [6] to determine the arrival time of S_0 mode. In this technique, AIC picker, which is regarded as a reliable tool for automatic onset detection, is applied twice on the transient signals to eliminate the influence of ambient noise.

The frequency contents and dispersion characteristics of S_0 modes are significantly different from those of A_0 modes, thus resulting in the difference between the entropy of S_0 modes and that of A_0 modes. Since the AIC function is based on the measurement of similarity in entropies, it might provide reliable outcomes when identify the arrival of A_0 modes and present two clearly distinct regions, e.g., an entropy portion where S_0 modes dominates, and an entropy segment where A_0 modes dominates. Therefore the two-step AIC picker was modified to identify the arrival time of A_0 mode. The visual description of each step of modified two-step AIC picker algorithm is presented in Fig. 2.
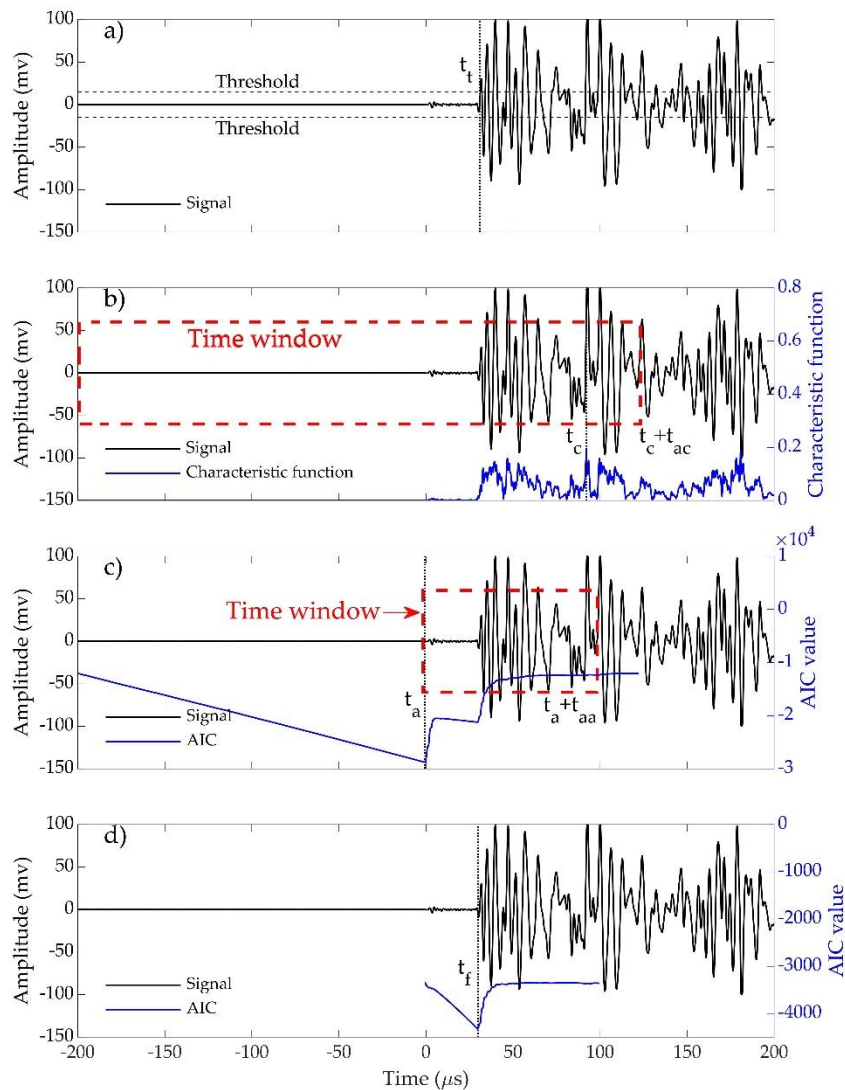
Fig. 2: Visual description of each stage of modified two-step AIC picker algorithm.

The 4 steps associated with modified two-step AIC picker are detailed below.

a) The first step of this technique is the determination of the time of the first threshold crossing. The threshold is determined to be 15 mV in the study by trial and error. If the time of the first threshold crossing t_t exceeds 6 μs, then the computation will continue and the following steps will be performed. Otherwise, the computation will terminate and t_t is considered to be the arrival time of A_0 modes.

b) A characteristic function $CF(i)$ as shown in Equation 1 of the signal $x(i)$, which was proposed by Sedlak et al. [6], was calculated. R is a constant and determined to be 4 according to ... The time window is set to start in the beginning of original signal and ending on time $t_c + t_{ac}$, where t_c is the time when the characteristic function reaches its global maximum value and t_{ac} is a time delay specified through trial and error. t_{ac} is determined to be 30 μs in this study.

$$CF(i) = |x(i)| + R|x(i) - x(i-1)| \qquad (1)$$

c) AIC function is applied on the shortened time window in step b). Time t_a which attains the minima of the AIC value indicates the estimated point of signal onset. The time window is updated and starts at time t_a and ends on $t_a + t_{aa}$, where t_{aa} is a time delay specified through trial and error and equals to 100 μs.

d) The AIC function is recalculated and applied on an updated time interval at Step c). The arrival of A_0 modes is now represented by the global minimum the recalculated AIC function.

3.2 Experimental Delta-T Mapping Training on a Complex Plate

To collect the data for delta-T mapping technique, artificial AE events were generated on complex geometry mild steel plate with four holes based on standards of Hsu-Neilsen source (H-N) sources. The locations of the AE sensors and holes relative to the origin placed on the bottom left corner of the plate were given in Fig. 3. The method in Section 3.1 was used to identify the arrival of A_0 modes and delta-T maps were constructed according to the steps detailed in Baxter et al. [5]. In order to test the performance of delta-T maps, six extra H-N sources were generated at six off-grid locations in the experiment.

	X coordinate	Y coordinate	Radius
A	80	300	40
B	60	170	20
C	240	270	30
D	220	150	30
Sensor 1	35	465	-
Sensor 2	265	465	-
Sensor 3	35	35	-
Sensor 4	265	35	-
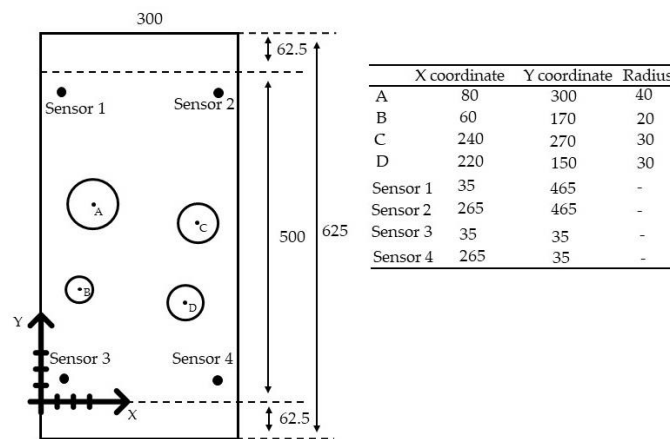
Fig. 3: Schematic layout of the sensors on a complex geometry plate (unit: mm).

The source location results and the associated Euclidian distance errors are documented in Table 1. As seen, compared with that of the TOA, the accuracy is significantly improved after the delta-T mapping technique was applied. The average errors of H-N source locations calculated by delta-T based on S_0 arrival and A_0 arrival are 1.8 mm and 3.9 mm respectively. Other than H-N source 2, delta-T based on S_0 arrival shows a higher degree of accuracy over delta-T based on A_0 arrival, which can be explained by the difficulties in accurately identifying the arrival of A_0 modes.

Table 1: Actual locations of H-N sources and results calculated by TOA, delta-T (S_0) and delta-T (A_0) (units: mm).

	H-N source 1			H-N source 2			H-N source 3			H-N source 4		
	X	Y	Error	X	Y	Error	X	Y	Error	X	Y	Error
Actual	70	210	-	130	210	-	170	390	-	230	230	-
TOA	83.0	207.2	13.3	134.5	79.4	11.5	169.0	197.5	7.6	213.6	223.9	17.5
Delta-T (S_0)	67.4	210.1	2.6	132.9	90.0	2.9	169.9	390.3	0.4	231.1	230.5	1.2
Delta-T (A_0)	73.1	213.1	4.3	129.6	89.8	0.5	172.7	391.0	2.8	222.2	228.8	7.9

4. Conclusions

In this study, the corrosion test on simple plate was performed and results indicated that it was very likely that the first arrival of signals recorded by AE sensors was A_0 mode. Therefore, Delta-T mapping technique based on the arrival of A_0 mode was proposed to locate corrosion damage on a complex plate. Delta-T mapping technique based on the A_0 arrival was tested using artificial AE sources. The average errors of H-N source locations calculated by delta-T based on S_0 arrival and A_0 arrival are 1.8 mm and 3.9 mm respectively. Though delta-T based on A_0 arrival shows a lower degree of accuracy over delta-T based on S_0 arrival, it should be noted that delta-T based on A_0 arrival is very promising on monitoring some low amplitude AE sources such as corrosion. In the future, corrosion tests will be performed on a complex plate. Delta-T mapping technique based on the A_0 arrival will be used to locate corrosion damages on complex plate.

5. References

[1] G. Koch, J. Varney, N. Thompson, O. Moghissi, M. Gould, and J. Payer, "International measures of prevention, application, and economics of corrosion technologies study," *NACE Int.*, p. 216, 2016.
[2] P. R. Roberge, *Corrosion inspection and monitoring*, vol. 2. John Wiley & Sons, 2007.
[3] Q. Y. Lu and C. H. Wong, "Applications of non-destructive testing techniques for post-process control of additively manufactured parts," *Virtual Phys. Prototyp.*, vol. 12, no. 4, pp. 301–321, 2017.
[4] R. K. Miller, E. v. K. Hill, and P. O. Moore, "Nondestructive Testing Handbook, vol.5, Acoustic Emission Testing," *American Society for Nondestructive Testing, Inc.* Columbus: American Society for Nondestructive Testing, p. 541, 2005.
[5] M. G. Baxter, R. Pullin, K. M. Holford, and S. L. Evans, "Delta T source location for acoustic emission," *Mech. Syst. Signal Process.*, vol. 21, no. 3, pp. 1512–1520, 2007.
[6] P. Sedlak, Y. Hirose, S. A. Khan, M. Enoki, and J. Sikula, "New automatic localization technique of acoustic emission signals in thin metal plates," *Ultrasonics*, vol. 49, no. 2, pp. 254–262, 2009.

FAILURE FORECAST METHOD APPLIED ON BURST TEST DATA TO VALUATE ITS PRACTICABILITY FOR ACOUSTIC EMISSION TESTING AND MONITORING PURPOSES

Gerald Lackner[1,*], Heribert Marihart[1] and Mikhail Prokofyev[1]

[1]TÜV AUSTRIA SERVICES GMBH, Vienna, Austria
*Correspondence: gerald.lackner@tuv.at

ABSTRACT

This paper describes the performance of a laboratory burst test on a test object with a severe real-world crack, the interpretation and evaluation of the acoustic emission (AE) data in general and in particular the results of further AE data trend analysis utilising the failure forecast method at different sections in testing time. The objective of this exercise is to gain experience in application of this method and to check whether or not it could be employed for testing and/or monitoring purposes. The burst pressure prediction as well as the ratio between the actual test pressure and the burst pressure prediction, the failure convergence, are consistent with the usual AE data evaluation throughout the test. Test sequences with a strong progressive increase of activity trend in AE data are highlighted by a gradually increasing failure convergence. This method has the potential to complement state-of-the-art evaluation techniques for testing applications, in particular with activity trend analysis. Due to the good results obtained already with a rather simple approach, remaining useful life prediction for on-line monitoring applications seems to be within reach.

Keywords: Structural integrity, predictive maintenance, metallic pressure equipment, failure prediction, remaining useful life.

1. Introduction

The failure forecast method, originally developed to predict volcanic eruptions, has been presented at several occasions in recent years to be well suited for remaining useful life predictions in structural health monitoring. The general principle of this method is to exploit *near-continuous* measuring data taken from a *self-accelerating* degradation process like crack growth under fatigue load [1]. Modern acoustic emission (AE) instruments have the ability to handle several thousands of AE data sets with all relevant AE signal parameters per second. This allows to track the ongoing crack growth process with sufficient temporal resolution.

Acoustic emission testing (AT) on metallic pressure equipment for assessing the structural integrity requires to evaluate the severity of the found indications for a certain degradation process, e.g. crack growth. This is generally done by a combination of selected AE intensity parameters and the AE activity. The total activity can be presented in a graph showing the cumulative sum of detected hits or events associated to crack growth with time, so that the derivate represents the (incremental) activity as hits or events per unit time. In case of a critically severe indication, the

shape of the total activity graph is often referred to as *progressive increase* of activity. Encountering this activity behaviour in the course of a pressure test shall trigger a decision to decrease the rate of pressurisation or to hold the pressure constant or even to depressurise immediately the equipment in order to prevent failure [2]. If a pressure hold phase is initiated and continued activity is experienced, an immediate depressurisation shall be done. Since progressive increase can be interpreted as another expression for self-accelerating, the failure forecast method seems to be applicable to estimate the burst pressure when applied on data representing the ongoing degradation of a pressure equipment under time dependent load during a pressure test. This would complement the severity assessment with results from AE data trend analysis. Finally, the results of the severity assessment of the detected indications determine qualitatively the actual condition of the test object. Typically this involves a grading system composed of different severity classes together with recommendations for further maintenance actions assigned to each class.

Interpretation and evaluation of AE data from on-line monitoring applications are based on the same principles compared to testing, which allows then to extend the established methods and techniques towards monitoring applications. There even might be an advantage for the latter. For testing applications it has to be taken into account that the operational conditions causing potentially degradation are preplaced by a test set-up for a controlled stimulation of service related degradation effects. In contrast, on-line monitoring applications do not have such limitations, they even require that the component is under the operational conditions which may cause the degradation process(es) under consideration. Extending the monitoring report with a prediction for the remaining useful life as an illustrative indicator for the expected rate of further degradation will increase greatly the benefit for the owner/operator of the component.

2. Failure forecast method and time of failure estimation

As stated in [1], Voight, when following the work of Fukuzono on landslides to investigate the process of slope failure, found a rather general behaviour of rate-based failure mechanisms to predict volcanic eruptions and proposed an empirical formula

$$\frac{\mathrm{d}^2 \Omega}{\mathrm{d}t^2} = A \left(\frac{d\Omega}{dt}\right)^{\alpha} \tag{1}$$

where Ω is a quantity describing the degradation in time t and A as well as α are constants depending on the particular degradation process. The degradation rate is then represented by the derivate of Ω. Integration of Equation (1) with $\alpha > 1$ and the bounds t as well as t_f, the time of failure, leads approximately to

$$\left(1 / \frac{\mathrm{d}\Omega}{\mathrm{d}t}\right)^{\alpha-1} \approx (\alpha - 1) A \left(t_f - t\right) \tag{2}$$

were the reciprocal of the degradation rate at t_f is assumed to be next to zero. Additionally, taking advantage of the frequent finding that α is about 2, Equation (2) can be further developed to

$$1/\dot{\Omega} \approx A \left(t_f - t\right) \tag{3}$$

which allows finally the estimation of t_f by linear regression analysis with sufficient pairs of variates consisting of the reciprocal of the degradation rate $\dot{\Omega}$ and the time t of observation as indicated in Fig. 1. Near-continuous data are required to allow good approximations for the degradation rates, which are calculated as the quotient of the measured increase of degradation and the time period between two consecutive, discrete measurements. With reference to Equation (3), the line of best fit is given by

$$1/\dot{\Omega} = k\,t + d \qquad (4)$$

where the slope k is the negative value of A and the intercept d is the product of A and t_f. The calculations for k and d are implemented in almost every spreadsheet software and are easily applicable once the measurement data for the pairs of variates are available.
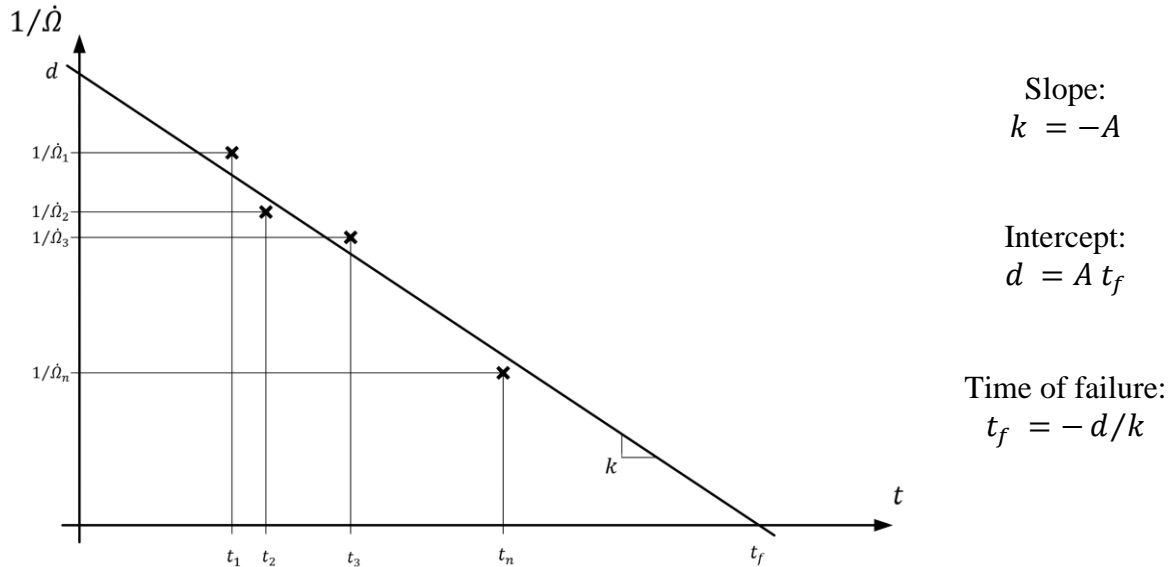
Fig. 1: Estimation of the time of failure t_f with linear regression analysis on pairs of variates consisting of the reciprocal of the degradation rate $\dot{\Omega}$ and the time t of observation for the frequent case where α is about 2, A and α are process dependent constants, t_f is calculated using the slope k and the intercept d from the obtained line of best fit.

3.   Identification of potential defects with acoustic emission testing

Usually the added value of combining a pressure test (hydraulic or pneumatic or combined) with acoustic emission testing (AT) is twofold: On the one hand, when on-line and in real-time, AT allows to pressurise the equipment till to the maximum test pressure in a safe way and on the other hand, due to its off-line capabilities, the found indications may be correlated with areas of the test object's load-bearing shell to obtain the positions of potential defects. While pressurising the equipment, the main focus lies in evaluating the data against the real-time criteria for safe pressurisation, whereas after completion of the test, preferably when the equipment has been depressurised already, the emphasis is on narrowing down suspicious areas in order to perform follow-up at reasonable efforts.

Knowledge as well as experience are necessary to assess in real-time with certainty the severity of the current situation. Critical sources meeting the fail criteria of the test have to be identified in time and in any case. One major qualitative criterion to assess the source severity is the occurrence of a certain trend in AE data, the so-called progressive increase of activity and/or intensity. Intensity related burst signal parameters are the maximum amplitude, the energy and to some extent also the ring down counts [3]. In this regard, a descriptive example for the progressive increase of the cumulative sum of ring down counts versus load for a cracked pressure vessel steel sample is taken from [4] and shown in Fig. 2, left. For comparison with the case at hand, the same way of data presentation for a heat-resistant steel with a real-world crack is shown in Fig. 2, right. According to [2], the test operator shall analyse in real-time if such a trend is given or not on any channel. Although the quantities of the AE parameters are measured with high accuracy, the required real-time trend analysis can be performed just roughly in a rather vague manner. The

exemplary solution in [2] focuses on the signal energy as an intensity parameter. A threshold value is set and in case it has been reached or exceeded the test operator needs to check, if in two consecutive load intervals of 5 % of the maximum test pressure the energy has doubled on any channel. Other criterions for real-time analysis using the results of event location calculation are defined and require for their correct application a high level of training and practical experience. Nevertheless, no definition for a criterion to identify the progressive increase in activity is defined in [2].
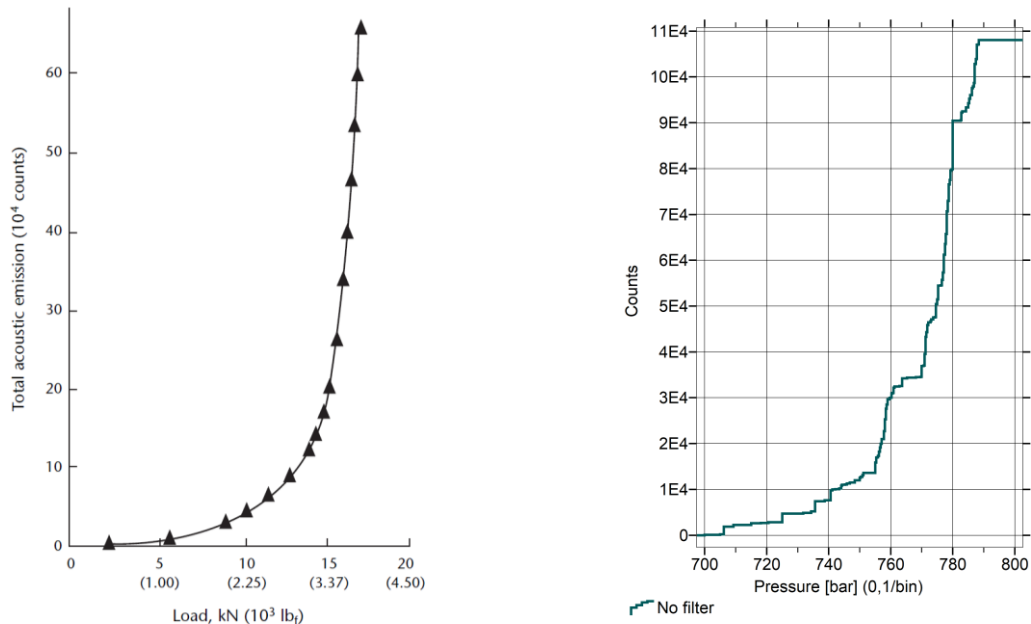
Fig. 2: Cumulative sum of ring down counts vs. load; pressure vessel steel in the presence of a crack (left), symbols represent experimental data, solid line represents results obtained with a theoretical model, published in [4] as Fig. 21 on page 65; heat-resistant steel for thermal power plant applications with a real-world crack (right) due to hydrogen induced stress corrosion cracking as described in chapter 4.

In order to support test operators in performing their job safely, an effective tool has been developed to aid source severity assessment on-line and in real-time [5]. The cluster evaluation factor (CEF) developed by TÜV AUSTRIA allows to quantify the severity of each and every located event within any location cluster by using the characteristics of degradation indicating burst signals as protypes for the assessment. However, the CEF technique tends to focus on the intensity parameters whereas in comparison the activity parameters are somewhat underrepresented. The trend analysis within CEF is possible to a limited extent for both, AE intensity and AE activity.

4. Burst test on a test object with a severe crack

4.1 Background

A coal-fired power plant was built around 2010 where a new material was used for the membrane walls of the boiler to raise the temperature to 600 °C and the pressure to 280 bar at the entrance of the steam turbine. The proof test was passed but during the test operation of the boiler hundreds of leaks were found at certain areas of the membrane walls. The damage analysis revealed that hydrogen induced stress corrosion cracking at welds including their heat affected zones was the root cause of the problem. In order to go ahead, all of the leaking areas of the membrane walls had to be cut out and replaced by repair parts. Furthermore, extensive non-destructive testing (NDT),

mainly radiographic testing, was performed and hundreds of further cracks were found and had to be repaired as well.

One question among many others was, if undetected cracks could be identified when using AT simultaneously to the hydraulic proof test after completion of the repair and/or using AE on-line monitoring during the test operation as well as during the normal service of the boiler. To answer this question, a burst test on a quite specific test object inside a work shop was conducted. The following subchapter gives more details to the test object, the test performance and the data evaluation. However, the main findings of the burst test were such that the idea of using AE was scrapped. Not because the results were poor, but because it was demonstrated very clear that under the proof test conditions with water at ambient temperature (cold water) the crack growth will be stimulated only when loaded far beyond the admissible maximum test pressure of the boiler system. This is a consequence of the temperature dependence of the material's yield strength, which may decrease nearly by half from ambient temperature (cold water) to operational temperature (600 °C). And the monitoring approach was not realised because the problem with the leaking boiler could not be solved by replacing defective areas. The membrane walls were leaking again during the test operation subsequent to the first repair. Finally, the owner decided to replace the complete boiler by a new one made from a well proven material that has stood the test of time already and in this way the power-plant could be taken into operation with a few years of delay.

4.2 Performance and data evaluation

The test object shown in Fig. 3, right was pressurised with water at ambient temperature inside a work shop till to failure. Several defective parts taken from different areas of the membrane walls were cut out and joined by welding to obtain a pipe-like test object, which was put then under a hydraulic burst test accompanied by AT.
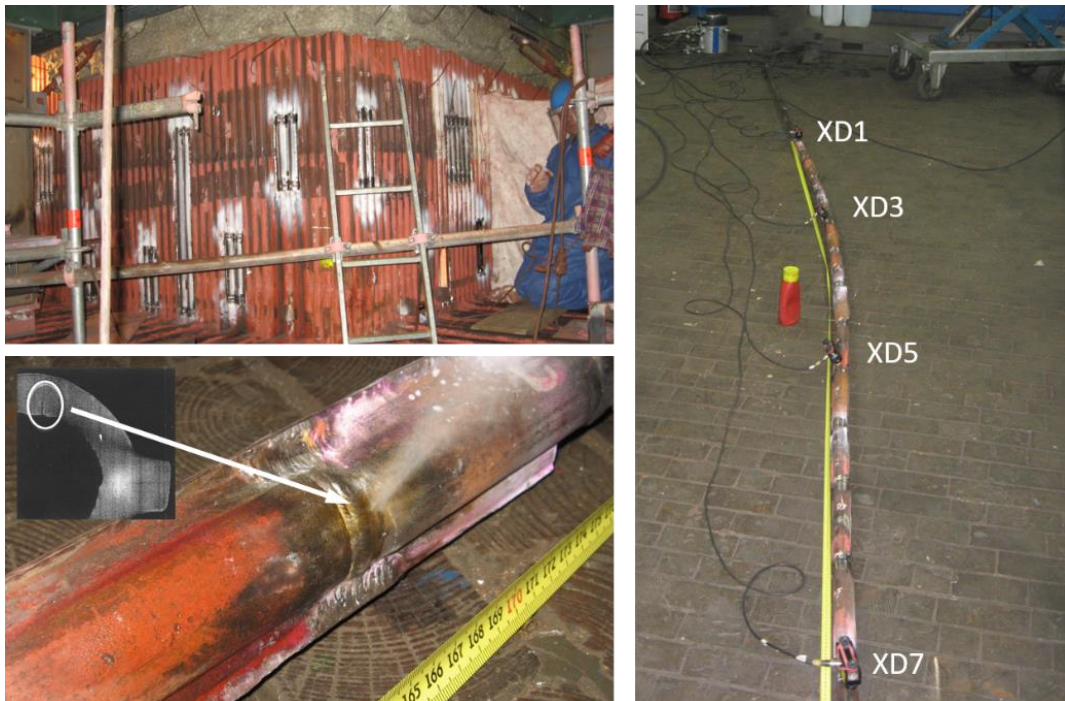
Fig. 3: A section of the boiler (top left) with welded repair parts in replacement for cut-outs in the membrane walls; the test object (right) on the floor of the work shop consisting of several cracked parts joined by welding and equipped with four sensors VS150-RIC labelled as XD1, XD3, XD5 and XD7; close-up of test object (bottom left) after failure at 788 bar in leak-before-break mode around 169 cm away from the origin of the x-axis (near to XD1).

Four VS150-RIC sensors from Vallen Systeme, Germany were mounted with magnetic holders to allow linear location calculation. Exemplary, a certain section of the boiler is depicted in Fig. 3, top left to give an impression of the situation during the repair activities at the membrane walls. The photo in Fig. 3, bottom left has been taken right after the test object became leaky at 788 bar by leak-before-break fracture at around 169 cm away from the x-axis origin (near to sensor XD1). The image of the X-ray tomography from the crack as it was found before the pressurisation is inserted in that picture. The leak is indicated by spray mist exiting from the orifice.

The pressurisation was performed using a hand pump. The objective was to demonstrate that severe cracks can be found with AE in the course of the proof test and/or later on while the boiler is in operation. The pressurisation profile was adjusted to the actual AE response of the material to the applied load so that at least a few load-unload sequences could be realised till to failure. Those sequences are usually part of a proof test and were intended to aid the assessment of the applicability of this NDT method for this particular purpose. Fig. 4, top holds a graph with the cumulative sum of located events and the pressurisation profile, both versus time of testing. As the test object approaches failure, the progressive increase of AE activity trend becomes more and more evident. Fig. 4, bottom shows the corresponding linear location plot with an accumulation of located events near to 170 cm and detected maximum amplitudes of up to more than 80 dB$_{AE}$ without distance correction. The test object failed finally at 788 bar at this position.
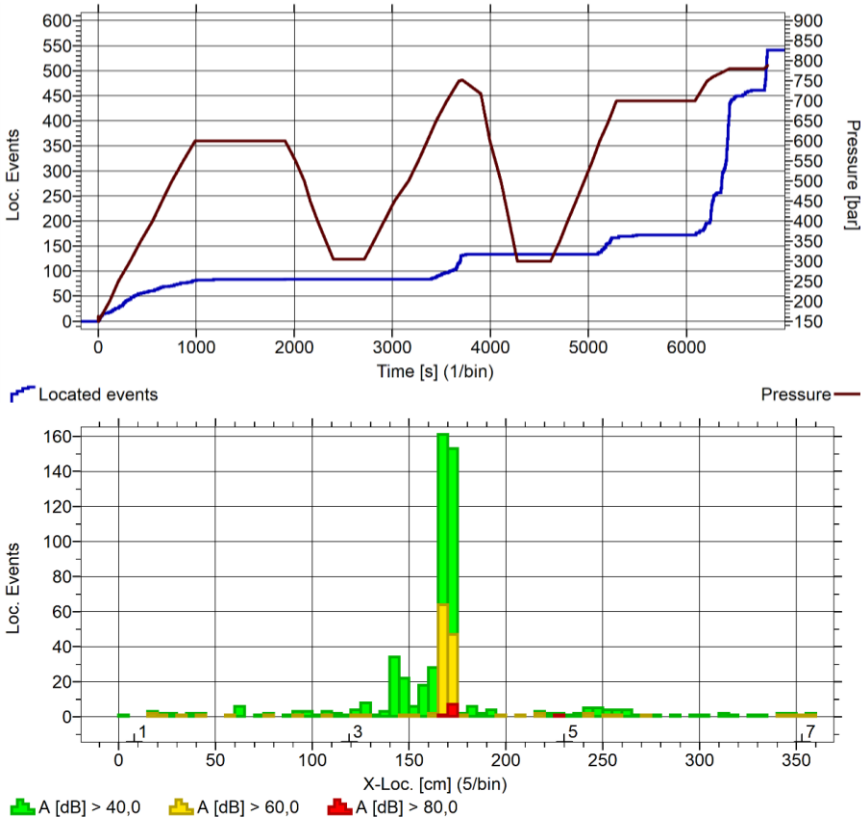
Fig. 4: Visualisation of AE data taken from a burst test on a test object consisting of several cut-out parts from affected areas of the membrane walls; cumulated sum of located events and corresponding pressure versus time (top); location plot (bottom) with positions of sensors XD1, XD3, XD5 as well as XD7 and accumulated located events near to 170 cm correlating with the position of the final failure of the most severe crack in leak-before-break fracture.

There were also other positions with X-ray indications for cracks like near to 140 cm or close to 225 cm. At the latter position a repair weld along the axis and across the original horizontal weld of the membrane wall panel was apparent. This suggested that the test object had been burst tested already. But no definite statement to clarify the situation could be given by the owner/operator.

Evaluating the data with TÜV AUSTRIA's CEF technique shows very well, that in case of a regular test the fracture of the test object could have been prevented. This can be taken from Fig. 5 where the value of CEF is given in testing time (top) as well as along the x-axis (bottom) and from the usual CEF boundaries for structural integrity assessment:

- class A (structural integrity sufficient) when $0 \leq CEF \leq 2{,}4$;
- class B (structural integrity questionable) when $2{,}4 < CEF \leq 2{,}8$; and
- class C (structural integrity insufficient) when $2{,}8 < CEF$.

If it had not been a test till to failure on purpose, the pressure had to be held constant at about 5200 s (640 bar) for to decide either to continue or to abort the test (CEF = 2,73, class B). One very strong argument for aborting the test at that point in time would have been, that AE was detected even below the previous maximum load. However, the final decision to abort the testing activity and to depressurise the equipment had to be done at about 6300 s (758 bar) at the latest (CEF = 3,24, class C), still with some safety margin against fracture. Failure was forced then to happen on purpose at 788 bar.
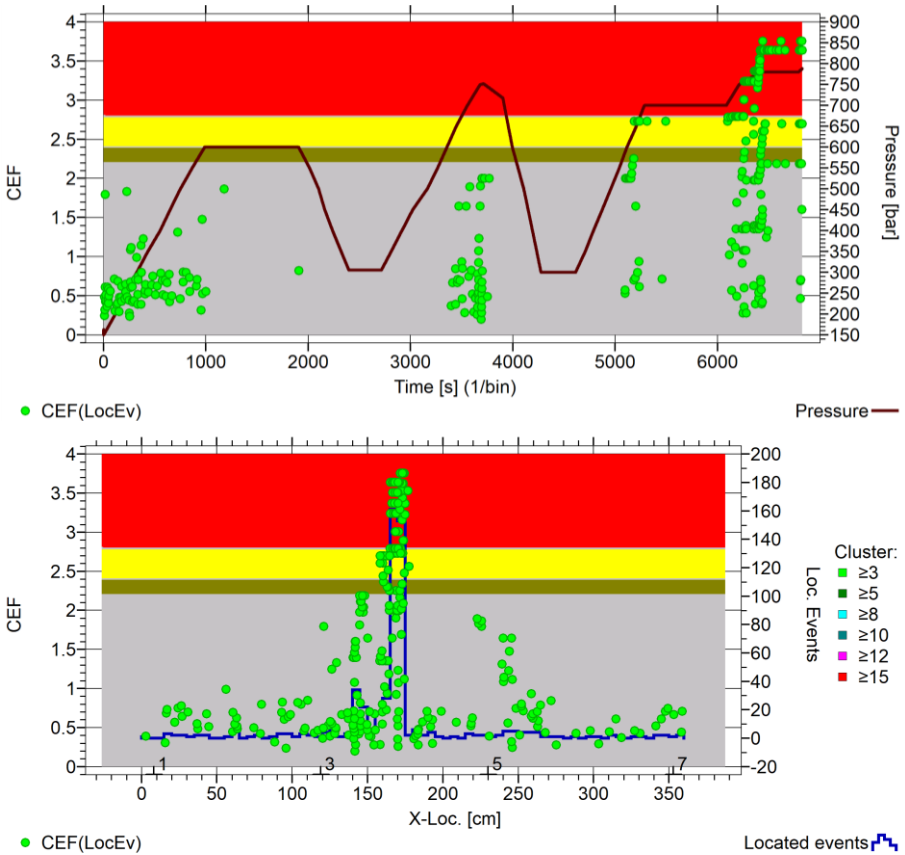
Fig. 5: Cluster evaluation factor (CEF) in time (top) and along the x-axis (bottom) for the test object with a crack at about 170 cm, which evolved in the course of a burst test inside the work shop till to failure in leak-before-break mode on purpose.

4.3 Failure forecast method and burst pressure prediction

The application of the failure forecast method on the estimation of the burst pressure is rather complementary to the proposals listed in [1] like crack growth under fatigue load or creep crack growth. However, the attempt seemed to be well justified due to similarity of the degradation behaviour in time. The expectation was that this new technique proves to have the potential for becoming a valuable tool for AE data interpretation and evaluation, in particular for enhanced

trend analysis of AE data. The comparability with the proven technique based on CEF is possible and allows to verify if the results gained with this new technique are consistent with the results obtained by the proven technique when applied on the same AE data.

One of the basic requirements to employ the failure forecast method is to make sure that the considered degradation process is self-accelerating. It other words, the observed process needs to be a positive feedback process where the rate of degradation does increase with the ongoing degradation [1]. Applied to AE activity it follows that if the hit rate is rather constant or even decreasing then a self-accelerating process must not be assumed and thus, the failure forecast method is inapplicable. Another limitation of the described application is that the constant α introduced in chapter 2 is not known but assumed to be around a value of 2. Altogether results in a rather moderate accuracy for the obtained values of the burst pressure. Nevertheless, in the world of AE there is sufficient room for qualitative considerations and the personal learning curve covers the experience that at times exceptions proof the rule. It might well be that the major benefits of the failure forecast method in AE will be a better valuation of the severity of the observed degradation process and its further evolution in time. As there is no criterion to characterise the trend of progressive increase in AE activity - except for the usual qualitative description - at the time being, the failure forecast method has the potential to complete in one way or another the set of AE data evaluation tools already available [5], [6].

Thus, to provide AE activity trend analysis, the cumulated sum of AE hits N_{hit} had been selected as the quantity to represent the degradation of the test object. Consequently, the reciprocal hit rate $1/\dot{N}_{hit}$ together with the corresponding time t of acquisition were used to compile the pairs of variates. The reference point in time for the linear regression analysis was the same as for the AT performance and evaluation - the start time of the test at 150 bar. The AE data acquired on channel 3 with XD3 according to Fig. 3, bottom was used as input since the leak appeared nearest to XD3 compared to the position of the other sensors. A number of 20 consecutive pairs of variates were employed to calculate the slope, the intercept as well as the time of failure. This procedure was applied to all AE data sets beginning from next to the start of the test at 150 bar (20 hits off-set) till to fracture at 788 bar. The linear regression results as well as the results of subsequent, correlated calculations were assigned then always to the latter of the 20 hits. The time till to failure was calculated by subtracting the time of acquisition from the time of failure. The prediction for the burst pressure was obtained simply by extrapolation and using the local approximate of the pressurisation rate estimated from the pressure and corresponding time values assigned to the former as well as to the latter of the 20 hits. It has to be noted that only those hits were used to calculate the burst pressure prediction, where the slope was negative and the numerically obtained approximation for the derivate of the hit rate was positive. This approach was intended to ensure that the condition for positive feedback was satisfied.

The three graphs shown in Fig. 6 illustrate the performed calculations. The diagram on the bottom shows the pressurisation profile and the cumulated sum of located events, both with time. Located events were chosen instead of hits from channel 3 due to their direct link to physical events within the material. This might be helpful in the further discussion regarding the obtained findings. The diagram in the middle shows the results of the burst pressure estimations with time and the diagram on top is a graph with the ratio between the actual test pressure and the predicted burst pressure, again with time. The ratio is termed failure convergence and quantifies how close to failure the test object is at the time of test with reference to the burst pressure prediction. Three stages of the burst test are noticeable, marked by yellow arrows and labelled I, II as well as III in Fig. 6, bottom:

I) Sudden change in event rate indicates that the defect became more severe at around 725 bar. With respect to the intensity of the AE signals, there seems to be no need to react. However, from the AE activity point of view this is something to consider. At that time, the pressurisation was stopped and the test object depressurised down to 300 bar. The burst pressure prediction results in values near to the actual burst pressure experienced later on. The failure convergence gives results of 0,9 and more.

II) Incipient AE activity already below the previous maximum load (at about 570 bar) indicates that the defect is going to become critical. The values of the burst pressure prediction underline this finding regarding criticality since they are lower at this stage compared to stage I. The failure convergence results again in values of more than 0,9. The value of CEF approaches the bound to class C (see Fig. 5, top) so that everything has to be ready for immediate depressurisation of the test object in case of a regular test. As this was a burst test, another pressure hold phase was initiated.

III) The AE activity raises very quickly after the hold phase (at about 700 bar) and increases as the pressure increases. The CEF exceeded the value of 2,8 (see Fig. 5, top) and thus, the criteria for class C (ultimate stop criterion) was met. However, the test object was taken till to fracture on purpose and in deviation to the regular test procedure. Predictions for the burst pressure and the failure convergence approximate the final actual burst pressure and values of 1, respectively.
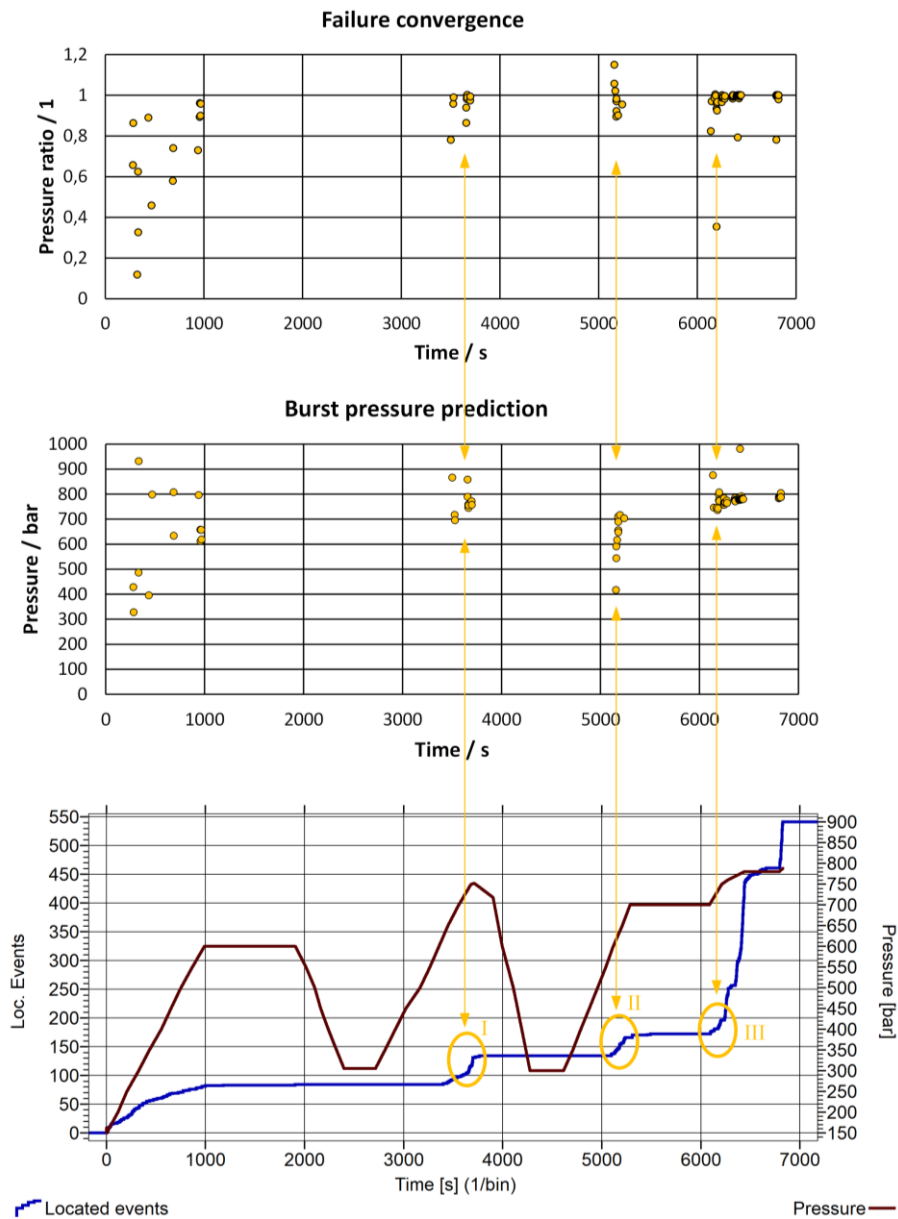
Fig. 6: Results of data analysis on basis of the failure forecast method with time; pressurisation profile and cumulated sum of events (bottom); burst pressure prediction (middle); failure convergence as ratio between the pressure at the time of test and the burst pressure estimation (top).

5. Conclusions and outlook

The application of the failure forecast method on burst test data to predict the burst test pressure and to provide a criticality indicator for assessing the given situation in the course of the test was successful and a first step to develop a complementary tool for the interpretation and evaluation of testing as well as monitoring data. Activity trend analysis is an advantageous enhancement to the general view on the degradation process under consideration. The results are in line with those obtained from currently used techniques, e.g. the severity grading with the cluster evaluation factor. Intensity trend analysis is possible as well, in case AE parameters like energy or ring down counts are selected to represent the ongoing degradation process.

Optimisation of the data quality prior to the application of the numerical methods, in particular for the regression analysis, might increase the accuracy of the predictions. Integration of the prediction process and subsequent calculations into the data visualisation software will raise the ease of use and thus support the utilisation to further develop the technique. Criterions for activity trend analysis may be implemented in testing procedures/instructions to support test operators in real-time decision taking. Assessment of monitoring data regarding remaining useful life seems to be within reach.

6. References

[1] Corcoran, J. (2017). Rate-based structural health monitoring using permanently installed sensors, Proc. R. Soc. A, vol. 473, http://dx.doi.org/10.1098/rspa.2017.0270.

[2] EN 14584:2013. Non-destructive testing - Acoustic emission testing - Examination of metallic pressure equipment during proof testing - Planar location of AE sources, p. 11.

[3] EN 1330-9:2017. Non-destructive testing - Terminology - Part 9: Terms used in acoustic emission testing

[4] Bassim, M.N. (2005). Macroscopic origins of acoustic emission: Chapter 2, Part 5. Miller, R.K., Hill, E.v.K., Moore, P.O. (Eds.), Nondestructive Testing Handbook, 3rd ed., vol. 6 Acoustic Emission Testing, ASNT, p. 61-68.

[5] Tscheliesnig, P., Schauritsch, G. (2000). Inspection of LPG vessels with AE examination, Journal of AE, vol. 18, p. 138-143.

[6] Ono, K. (2007). Structural integrity evaluation using acoustic emission, Journal of AE, vol. 25, p. 1-20.

IoT-AE Remote Unattended Long-term Monitoring System

Bearings wear

4G/5G
NB-IoT

Pipe/Valve leakage

Wi-Fi

Bridge Wire breaking

LoRa

zigbee

Wind Power
Bearing /Blades
Monitoring

Qingcheng IoT
Cloud Platform
or AWS or
Customized Server

4G/5G
Internet

4G/5G
Internet

Bluetooth

PC Desktop

Smart-Phone

Products

SAEU3H AE Testing System
- Sample rate: 10MSPS, 16 bit
- 4, 20, or 48   channel
- Single USB rate: 300MB/s
- Frequency range: 1kHz 2.5MHz

RAEM1-6 Acoustic (AE) Remote Unattended Monitoring System
- 6 RAEM1 integrated
- IoT-AE system with Qingcheng IoT Cloud Platform
- Benchtop instrument: WiFi/cable to PC

RAEM1 Series (IoT-AE System)
- Single channel, triggered by signal or time
- Sensor, preamp and power internal or external
- Communications: 4G, NB IoT, LoRa, Zigbee, WiFi or wired
- Onsite test: smartphones via Bluetooth
- Wireless time synchronization
- Remote online monitoring: IoT Cloud

Acoustic Emission Sensors
- various types, ultra-high temperature, tiny size, frequency bands, preamplifier integrated, etc.

RAEM2 Series (IoT-AE System)
- Single channel, triggered by time
- Sensor, preamp and power internal or external
- Communications: 4G, NB IoT, LoRa, Zigbee, WiFi or wired
- Remote online monitoring: IoT Cloud platform
- Onsite test: smartphones via Bluetooth

QingCheng AE Institute

QingCheng AE Institute (QCAE) (previous name: Beijing SoundWel) has been a manufacturer of Acoustic Emission products from sensors to systems since 1998

+86-20-32290092

sales2@ae ndt.com

www.en.ae-ndt.com

Room 601-9,Building 3, 232 Ke Zhu Road, Huang Pu District, Guang Zhou City, Guang Dong Province, China

jessicajia

DEVELOPMENT OF AN ACOUSTIC EMISSION TECHNOLOGY PACKAGE FOR COPVS INSPECTION AND RECERTIFICATION

Obdulia Ley[1] and Valery Godinez-Azcuaga[1]

[1]Mistras Group, Inc., Products & Systems Division, Princeton Junction NJ, USA;
obdulia.ley@mistrasgroup.com, valery.godinez@mistrasgroup.com
*Correspondence: obdulia.ley@mistrasgroup.com; tel.: (+1 609 716 40421)

ABSTRACT

Composite overwrapped pressure vessels (COPVs) are used in many applications from 10,000 ft below sea levels to outer space. COPVs are designed to sustain high pressure, carry a large volume of a pressurized gas, and offer excellent weight reduction. These vessels can be subjected to complex modes of failure, some of which are dominated by fiber-bundle breakage (FBB). Due to the safety implications of COPV failure, they are subjected to stringent certification requirements by DOT, ASME and ISO. In this document, we present results of a test campaign designed to collect and characterize acoustic signatures of fiber bundle breakage (FBB), as well as deriving experimentally the "single energy event criteria" (SEEC) required by relevant testing codes and procedures.

Testing was performed on type 4 carbon fiber COPVs. Three vessels were tested, aged by pressure cycling to simulate refilling operations for 10 years, and were damaged by high velocity impacts. Hydrostatic tests following DOT requalification test procedures were performed at different stages of the ageing process, and the vessels were loaded to failure. The data set provided signals of FBB on damaged vessels.

Keywords: Modal acoustic emission, requalification, broad band sensor, composite overwrapped pressure vessels, virtual gas pipelines, hydrogen storage.

1. Introduction: COPV's and safety regulations

Composite overwrapped vessels or COPV's are critical containers that offer high strength and low weight. COPV's are mostly used for storage of propellants, as well as elements required for life support. There are several types of COPV's (classified as type 1 through type 5) and the classification depends on construction materials and construction procedure, as well as the maximum vessel operational pressure. In general, COPV's consist of a liner, a filament wound layer and an epoxy resin. COPV's were developed by NASA in the early 1970's with the intent of reducing the weight of firefighter's breathing apparatus, achieving about 50% reduction.

COPV's are used for transportation of gaseous products by stacking dozens of them on large trucks, in what are called "virtual pipelines". COPV's in this virtual pipelines can be severely damaged internally by high-energy impacts on the road without leaving any external indication. Also, they experience fatigue as they undergo filling/emptying operations. Common failure mechanisms of COPV's are:

- low energy matrix cracking and splitting,
- delamination between layers,
- fiber to matrix debonding,
- fiber pull out,
- fiber breakage,
- fiber bundle breakage or FBB.

Failure of a COPV offers a safety risk, so ensuring the vessel is able to sustain operational loads is of paramount importance to the different industries employing COPVs. For that reason, the design of COPV's is subjected to construction codes, manufacturing is verified via hydrostatic tests, and requalification testing every 5 years is commonly required in different industrial sectors, including transportation. In the United States, codes for vessels construction and requalification have been published by regulatory bodies such as:
- the American Society of Mechanical Engineers (ASME) particularly the Boiler and Pressure Vessel Code (B&PVC),
- the International Organization for Standardization (ISO),
- the American Society of Testing Materials (ASTM),
- the Department of Transportation (DOT),
- the National Board of Boiler and Pressure Vessel Inspectors (NBBI).

In this paper, we discuss research performed as part of the development of a technology package to test COPV's type 3, 4 and 5 under both: ASME X section 8 and DOT modal AE testing criteria. This technology package consists of a specialized broad band sensor, a data acquisition AE board, as well as the acquisition and postprocessing software used to analyze and filter the waves collected from COPV's during testing.

For the technology package development, several COPV's were impacted, pressure cycled, and pressurized monotonically to failure. The burst pressure measured was used to identify if the impact and ageing cycling were successful, and if the requalification test performed successfully identified a vessel that was compromised and should have failed the requalification test.

2. Acoustic emission testing of COPV's

During the AE testing of the COPV, the vessel is stressed by hydrostatic or pneumatic loading, and the test pressurization sequence used follows the specifications of the code under use. Fig. 1 shows the loading scheduled used by the ASME Section X, Appendix 8 code on the lefts hand-side, and DOT requalification test loading schedule is shown in the right hand-side.
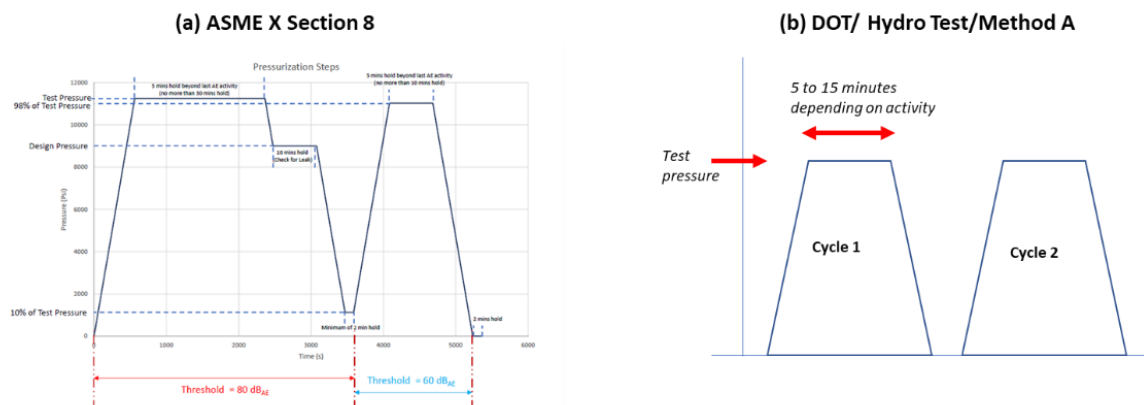
Fig. 1: Example of loading schedule commonly used in ASME X section 8 MAE code and in DOT MAE code.

The AE test method is designed to detect structurally significant defects and damage in the composite fiber wrap. As signal analysis capabilities have improved over time due to availability of computing power and postprocessing, the complexity and type of analysis performed on the waves collected by the acoustic emission sensors have evolved. Depending on the level of complexity in data collection and analysis, the acoustic emission technique can be divided into 'feature based AE' and 'modal AE'.

Table 1: Listing of published codes for testing and requalification of COPVs.

NAME OF CODE/STANDARD	YEAR ISSUED	TECHNICAL EMPHASIS
1st DOT Exemption (Tube Trailer Cylinders)	1983	FAE/Event clusters
ASTM E 1419-91 (Seamless Cylinders)	1991	FAE/Event clusters
ASME B&PVC V Art. 11 (FRP Tanks & Vessels)	1983	FAE
ASME B&PVC X RT-6 (Class II FRP Vessels)	1988	FAE
ASME/ANSI RTP-1 (FRP vessels < 15 psi)	1989	FAE
ASME SE-1419 (Seamless Cylinders)	1991	FAE/Event clusters
ASME B&PVC VIII Code Case 2390-1 (CRPV)	2003-2008	FAE with MAE appendix
ISO-/DIS 16148 (Periodic AT +UT) (Metal)	2006	FAE
ASME BPVC-VIII Code Case 2579-1 (CRPV)	2007	FAE
ASME BPVC-X App. 8 (Class III H_2 storage)	2011	MAE
National Board B 10-601 (Cylinder Requalification)	2014	MAE
ISO-19016 (Gas Cylinders / Composite Construction)	214	MAE

Since the 1980's, the regulatory bodies, such as ASME (B&PVC), NBBI and others, have published testing and requalification criteria using the acoustic emission technology, and the procedures for data analysis and collection have changed over time. Table 1 shows a timeline of the use of AE technology in the testing and requalification codes, and the introduction of the modal AE technique to extend the analysis of the acoustic activity.

2.1 Feature based acoustic emission (FAE)
The featured based AE (FAE) focuses on the calculation of wave features at the moment of detection and the use of correlations between such features for classification. In FAE, waveform analysis is not the primary methodology, and interpretation is based upon the following principles:
- genuine AE increases as the load increases,
- strong increase before failure gives effective warning,
- continuing AE during load holds reveals high stress,
- existing damage gives frictional AE, indicated by Felicity effect and AE during unloading.

FAE was started to be used in the 1970's and it is still widely used today, it provides a low cost/effort technique to identify the response of a COVP under the stress of the test, and its main limitation is the accuracy for source identification and location.

2.2 Modal acoustic emission (MAE)

Modal acoustic emission (MAE) focuses on the collection and detailed analysis of the waveforms, particularly on the identification of the Lamb waves and dispersion curves in the composite material used to form the COPV under study. MAE requires:
- the use of a broad band sensor,
- waveform recording,
- calculation of spectrograms,
- calculation of dispersion curves.

These requirements, increase the cost of deployment, as well as the level of experience and needed for data analysis of signatures.

Given the increased complexity of MAE test compared with FAE test, the development of friendly software programs that allow pre-processing and classification of the waves collected during the test is an important aspect necessary to extend the utilization of the technology. In response to this, Mistras developed MAE technology package with a specialized software created to calculate the energy normalization and energy released in specific energy frequency bands, as well as the identification of the waves passing fiber bundle breakage (FBB) criteria, as required by testing and requalification codes requiting MAE analysis, as shown in Table 1.

3. Signal interpretation: MAE rejection criteria

MAE codes focus on the analysis and the identification of signals from FBB because it is the most severe kind of event as far as pressure vessel strength is concerned. AE waveforms produced by fiber-bundle breakage can be distinguished in practical testing by the presence of the highest frequencies available in AE signals, and by analyzing the relative energies of various spectral ranges within the frequency spectrum. Fiber breakage is associated to a broader spectrum. Fiber breaks may be present alone or they may occur during matrix fracture, in which case the waveforms will be superimposed on each other during testing and requalification. Analysis for fiber bundle breakage is performed only during a pressure hold. To determine if FBB has occurred, the frequency spectra of the direct E and F waves are examined and the fraction of energy released in various frequency ranges or U_i for $i=0, 1, 2$; defined as the partial energy released in the *i-th* frequency band defined as follows:
- U_0 energy on the frequency band from 50 to 400kHz (that corresponds to the full frequency range considered),
- U_1 energy on the frequency band from 100 to 200kHz, which contributes to FBB,
- U_2 energy on the frequency band from 250 to 400kHz, which contributes to FBB.

Other relevant scaling energies are computed, such as:
- fiber breakage U_{FB}^{AE} and fiber bundle breakage (FBB) U_{FBB}^{AE},
- quiescent energy U_{QE},
- background oscillation energy U_{BEO}.

The U_i and the scaling energies U_{FB}^{AE} and U_{FBB}^{AE} are used to identify relevant signatures produced by sources of interest such as fiber breakage and fiber bundle breakage. By comparing frequency response and energy release in different frequency bands of a collected waveform, one can identify the presence of signatures associated to the inability of the vessel to sustain load. In general, activity with most energy released in the 50kHz is linked to frictional events, and activity with energy release between 50 and 100 kHz is linked to low energy matrix cracking. Finally, broken fiber vibration or oscillation that can show up at just about any point in the pressurization after fiber (bundle) breaks have occurred arising as frictional events on pressurization and

depressurization The waveform and spectrum of a fiber-bundle vibration is a high frequency signal in the range of 200 to 250lHz

Once the partial energy release of the wave at each frequency band of interest (U_i for $i=0, 1, 2$) has been calculated, the values are compared with the scaling energy parameters according to the MAE code rejection criteria. For the DOT requalification code, the rejection criteria are summarized in Fig. 2. This diagram shows the 3 different test the collected waves are compared against to identify FBB. This comparative analysis is performed after appropriate filtering (i.e. removal of signals resulting from flow noise, mechanical events and EMI). The comparative analysis requires to identify/set the value of 3 main constants: F_2, M_1, and M_2, which is commonly done by using tabulated values offered within the code.

The scaling energy parameters (F_2, M_1 and M_2) listed above are dependent of vessel type and construction and the current codes do not provide a clear procedure to determine them. However, as part of this study, an experimental procedure to determine the single energy event criteria SEEC has been developed.
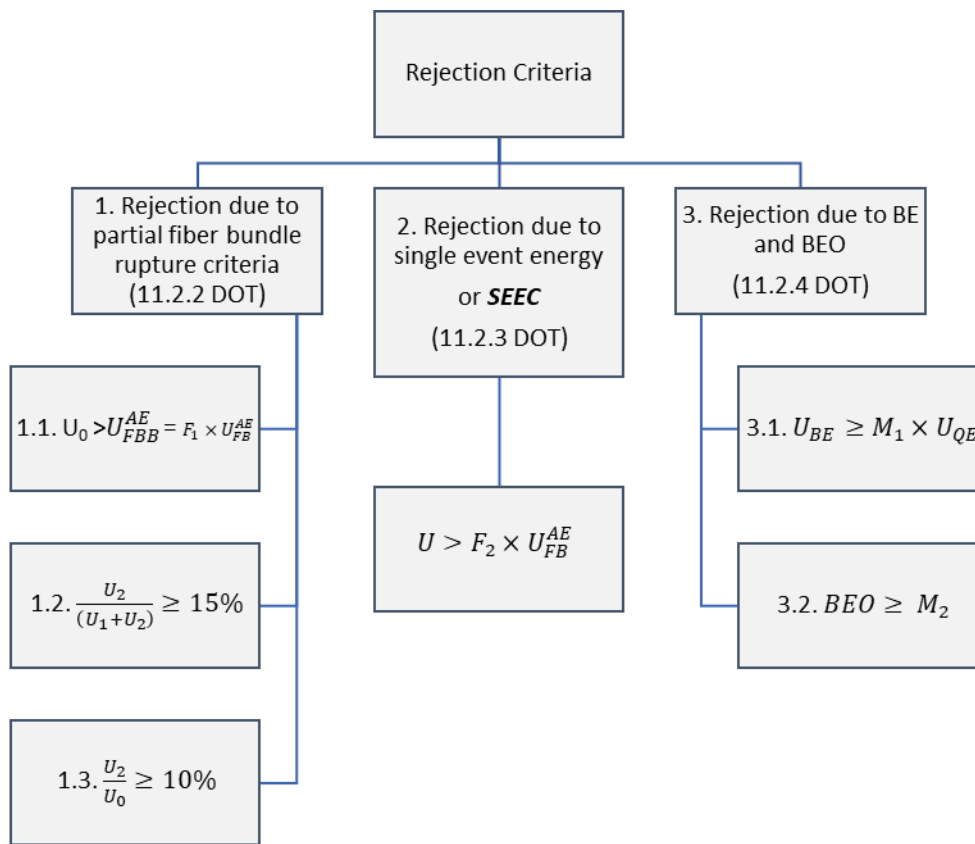
Fig. 2: Summary of rejection criteria for DOT MAE procedure for requalification of COPV's types 3, 4, 5. (From tables offered in the DOT code $F_2 = 10\,000$, M_1 commonly ranges between 2 and 4 for high strength carbon fiber, and M_2 commonly ranges between 2 and 4 for high strength carbon fiber).

4.   Summary of tests performed

Hydrostatic tests following DOT Method were performed on three different type 4 COPV's. Vessel #1 has undergone a few impacts performed at different locations along the vessel using similar procedures to those outlined in ISO 11515. Each impact performed had different intensity and increased in strength progressively, as shown in the test summary table below (Table 2 and Fig. 3). Vessel #2 was subjected to minimal ageing by cycling the vessel from 300psi to a pressure

of 3600 psi (or operational pressure) for 2000 cycles; and vessel #3 was impacted one time with an energy of 5,000 J, was subsequently cycled from 360 psi to two thirds of the design pressure which corresponded to the vessel's working pressure or 3,600 psi that is equivalent to the working pressure. All vessels were tested using Method A and pressurized to failure after that.

Vessel #1 and vessel #2 were instrumented with AE sensors during the pressurization to burst allowing data collection. Vessel #3 was not instrumented with sensors during the burst test. The pressurization to burst of vessels #1 and #2 included two holds at 6,000 psi and 7,000 psi. The pressure holds were added with the intent to gather damage signals without any possible flow noise and be able to apply the FBB filtering criteria. The pressurization to failure of vessel #3 was monotonic.

The objective of these tests was to verify that the data analysis procedure implemented by Mistras following the DOT MAE guidelines is being correctly applied, and that a vessel failing requalification test failed is effectively linked to the presence of known damage and earlier rupture in a burst test. For vessel #1 and vessel #2, the pressure at which the vessel failed was close to the expected burst pressure (see Table 2); but for vessel #3 it was reduced about 30% of the expected burst value due to the 5,000J impact.

The number of pressurizations performed per test and other general information is presented in the diagram shown in Fig. 3. Table 2 shows a summary of the waves collected during each test after the different filtering strategies applied during the analysis (after filtering that removes flow noise, EMI, mechanical friction, and the FBB criteria shown in Table 2). The waves or signals passing the FBB are then verified by direct observation of the waveform, FFT and spectrogram. The data collected from both pristine and damaged vessels have been used to verify the expected energy associated to FBB.
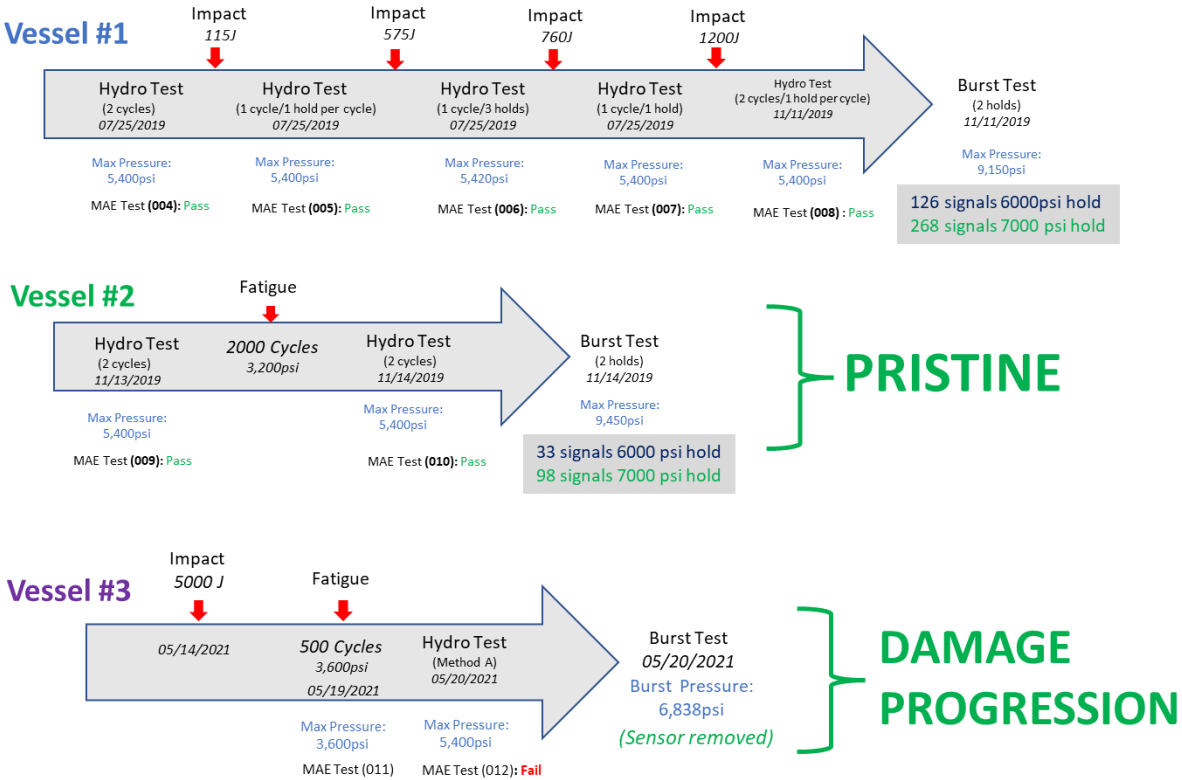
Fig. 3: Summary of COPV tests performed during this validation and verification project.

As observed in Table 2, the number of signals passing the FBB criteria significantly increased during the pressure hold at 7,000 psi performed as part of the burst tests (test# 008 during burst on vessel #1 and test# 010 during burst on vessel #2) and for vessel #3 method A test, as compared with the other tests performed on pristine vessels with and without fatigue cycles (test# 004, test#

005, test# 006, test# 007, test# 008 and test# 010). Table 2 shows the number of FBB signals verified by visual observation (# FBB VERIFIED) for every test, these waves have U_{FB}^{AE} equal or larger than 50×10^3 aJ and amplitude greater than 80dB, consequently these values were used as a way to identify rapidly signals passing the appropriate FBB conditions and when available the vessel was likely compromised and should fail the requalification test. The requalification failure was verified when the vessel burst at a pressure lower than expected. For instance, the requalification test # 012 on vessel #2 performed after impact and cycling had signals passing FBB and when taken to failure, the vessel burst at less than 7,000 psi which is less than the expected burst pressure.

Table 2: Summary of data collected during test performed. Test nomenclature shown in Fig. 3. For this analysis the SEEC energy considered was 6.79×10^9 aJ and the U_{FB}^{AE} was 50×10^3 aJ.

TEST NUMBER/ VESSEL	DAMAGE STATUS	TEST RESULT	# WAVES (HOLD)	# FBB (VERIFIED)	BURST PRESSURE
SUMMARY OF HYDROSTATIC TESTS					
004 Vessel #1	Pristine	Pass	0	0	9,150 psi
005 Vessel #1	Impact 115J	Pass	3	0	
006 Vessel #1	Impact 575J	Pass	540	0	
007 Vessel #1	Impact 760J	Pass	133	0	
008 Vessel #1	Impact 1200J	Pass	464	0	
009 Vessel #2	Pristine	Pass	10	0	9,450 psi
010 Vessel #2	After 200 cycles 3,200 psi	Pass	5	0	
012 Vessel #3	Impact 5000J and after 500 cycles 3,600 psi	Fail	155	10	6,838 psi
SUMMARY OF FATIGUE TESTS					
011 Vessel # 3	After impact 5000J	Cycled from 360 to 3600 psi	No hold	8	6,838 psi
SUMMARY OF BURSTS TESTS					
008-Burst vessel #1	Four impacts through the vessel	6000 psi hold	1548	6	9,150 psi
		7000 psi hold	2626	16	
010-Burst vessel #2	Two hydro tests and 2000 cycles to 3600 psi	6000 psi hold	301	0	9,450 psi
		7000 psi hold	804	3	

The burst test performed on vessel #1 (test# 08-burst) shows higher activity and energy, as well as a reduced burst pressure compared with the burst test performed in the pristine/fatigued vessel #2 (test# 010-burst). The increased activity and intensity observed in the burst tests and the pressurizations following impacts is explained by the Kaiser and Felicity effect. Finally, vessel #3 (test# 012) due to the impact and cycling shows clear FBB signals that fail the vessel under the MAE DOT document.

As an example, Fig. 4 shows the data that passed the FBB filters in test# 012 after impact testing and fatigue. The plots in this figure show horizontal and vertical lines used to separate those signals that have absolute energies larger or equal than $U_{FB}^{AE} = 50\text{x}10^3$aJ and amplitude larger than 80dB. In addition, Fig. 5 shows examples of some of the waveform spectrograms of some of the signals passing filtering and visual verification.
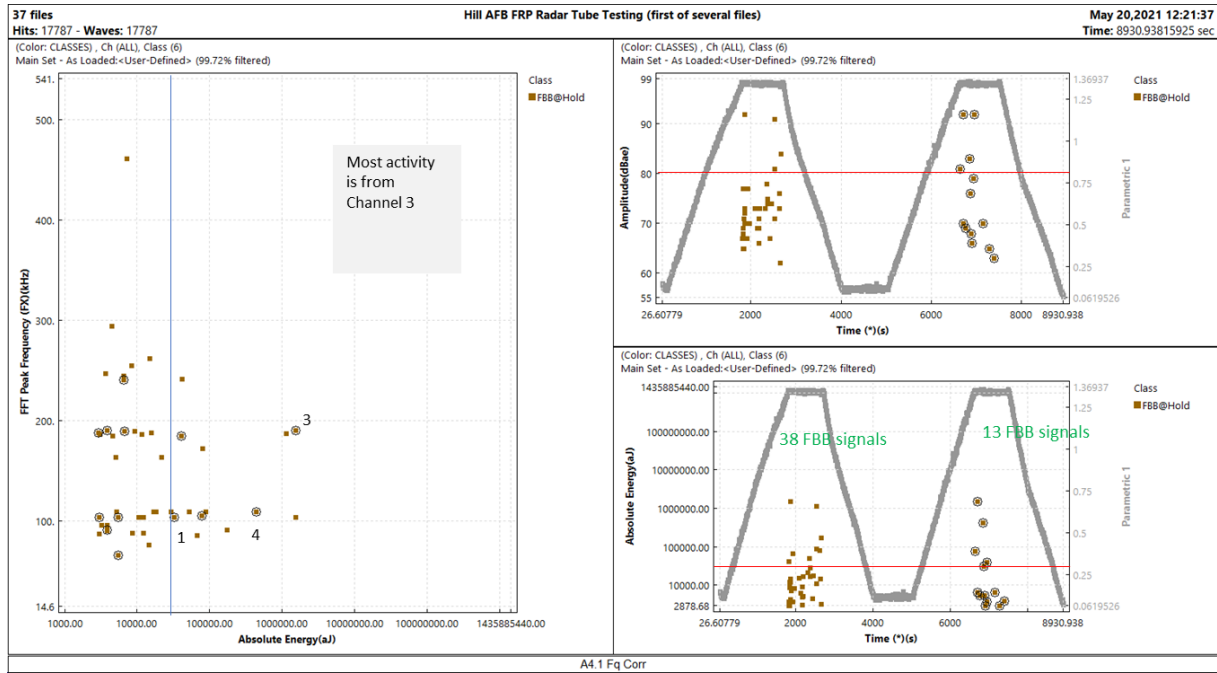
Fig. 4: Summary of activity collected in test 012 on vessel #3 after a 5000J impact and 500 fatigue cycles to 3600psi. Data in brown shows to activity satisfying FBB criteria (SEEC energy considered was $6.79\text{x}10^9$aJ and the $U_{FB}^{AE} = 50\text{x}10^3$aJ. Top right plot shows the amplitude collected over the duration of the test (grey trace shows a voltage signal proportional to the vessel pressure). Bottom right plot shows the absolute energy of the waves passing the filtering and the left hand side plot shows the correlation between peak frequency and absolute energy.
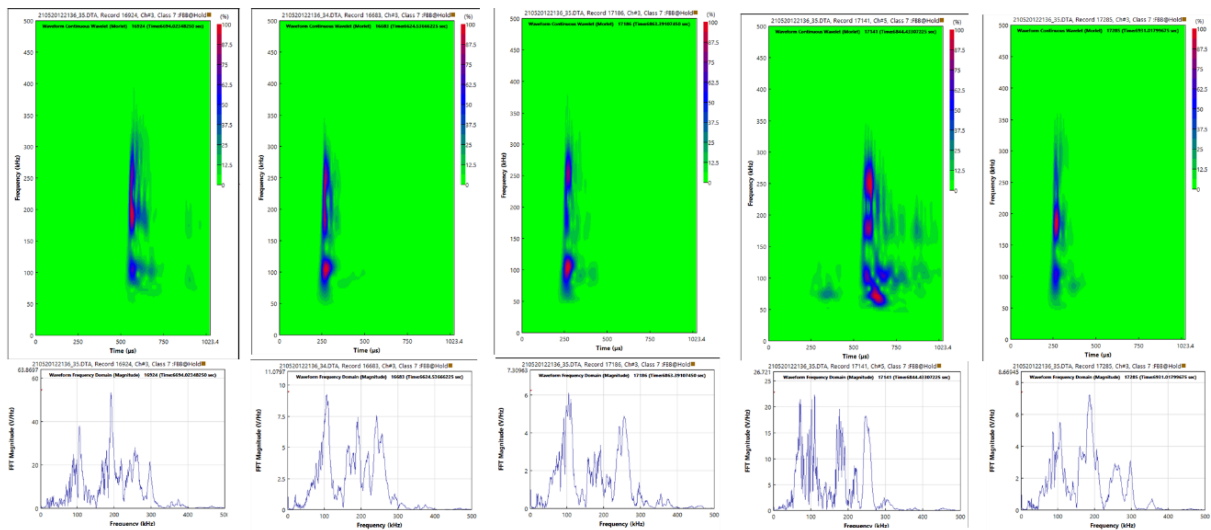
Fig. 5: Examples of selected spectrograms of signals collected in test 012-MA of vessel #3. These signals passed the high energy level FBB criterion by setting the U_{FB}^{AE} energy to $50\text{x}10^3$aJ. The spectrograms shown correspond to signals that pass the visual verification.

4.1 Experimental determination of the single energy event criteria (SEEC)

In the tests to failure performed in this project, the burst pressure experienced corresponded to 9,150 psi and 9,450 psi for the impacted vessel (vessel #1) and the cycled vessel (vessel #2), respectively. These values are higher than the expected rupture value of 8,600 psi, due to the slow loading and the presence of holds throughout the test.

During the last stage of the burst test, i.e. the monotonic load increase after 7,000psi hold, both vessels presented audible pings that were linked to an observable jump in the cumulative absolute energy plot of the tests. In test# 008 for vessel #1 (impacted vessel) these pings started to take place at 7,768 psi and continued as shown in Fig. 6. The activity shown corresponds to raw data without any type of filtering. The energy jumps seem to have taken place before the 8,600psi expected burst pressure. The energy jumps seen while testing vessel #2 (cycled vessel) are shown as well; it is observed that the jumps took place at a higher pressure during the last phase of the monotonic increase after the 7,000psi hold (Fig. 6).
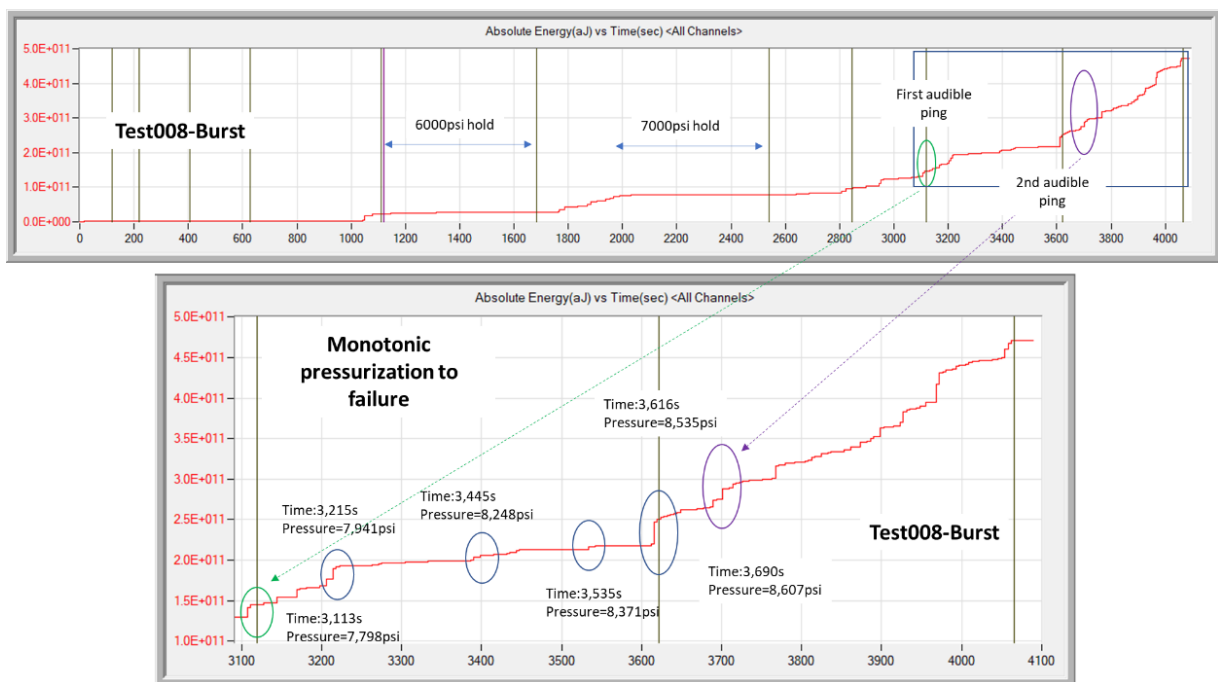
Fig. 6: Cumulative absolute energy of released of all activity collected during the burst test performed on vessel #1 (test 008-burst) after a series of impacts were performed. The bottom plot shows the early part of the last monotonic increase to burst pressure (9,150psi) and the energy jumps experienced, as well as the pressure at which there were experienced. All these jumps took place before the expected burst pressure of 8,600psi. Data shown corresponds to raw activity collected during the test without any filtering.

A very important result from these two tests was the identification of the SECC energy during the last stage of the monotonic pressurization to failure. During this stage, the vessels presented two strong audible pings. The vessel manufacturer indicated such activity takes place as the vessel approaches failure. The times at which the pings were identified were marked, and further analysis identified clear events that passed all filtering. Waveforms are shown in Fig. 7. These waveforms show energies ranging between 1.67×10^9aJ and 3.67×10^9aJ, indicating that the SEEC should be set in that range. The waves in Fig. 6 also show the expected two wave modes.
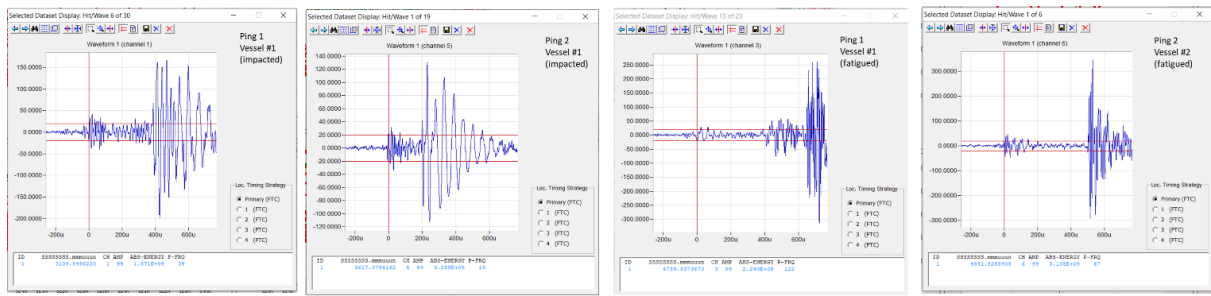
Fig. 7: Experimental determination of SEEC by identifying signals associated to response seen in burst tests as vessel approaches to failure.

5.   Conclusions

The main objective of this project was to develop a technology package for deploying modal AE testing of COPV's based on ASME 10 Section 8, ISO and DOT. The appropriate sensor, data acquisition board and software necessary to collect the signals based on the codes requirements were developed, tested and verified.

As part of the work performed for the validation and verification process, three vessels were tested using hydrostatic method A test based on the DOT TR20180502 MAE test criteria. Vessel #2 was pristine and cycled, vessel #1 was impacted multiple times in different locations and vessel #3 was impacted with high energy and cycled to allow the damage to propagate. The vessels were loaded to failure and FBB signals were recorded. As expected, vessels with increased damage level produced more AE signals and more FBB signals as well.

During the burst test, an audible ping was linked to occurrence of signals passing FBB filters, and to events with the highest energy collected during the test. These events were used to experimentally define SEEC to 6.79×10^9aJ. Comparing data from the tests, the signals passing the FBB criteria, and the SEEC, the U_{FB}^{AE} was defined as 50×10^3aJ for the vessel construction tested.

6.   References

[1]   Pat B. McLaughlan, P.E. Scott C. Forth, Lorie R. Grimes-Ledesma, "Composite Overwrapped Pressure Vessels, A Primer" Technical Review: NASA/SP–2011–573, March 2011.
[2]   DOT-Pipeline and Hazardous, Materials Safety Administration, "Modal acoustic emission (MAE) Examination Specification for Requalification of Composite Overwrapped Pressure Vessels (Cylinders and tubes)", July 2021.

EVALUATION OF EXPERIENCE FROM LONG-TERM AE MONITORING

Andreas J. Brunner[1] and Horst Trattnig[2]

[1]Retired from Empa, Swiss Federal Laboratories for Materials Science and Technology, Dübendorf, Switzerland; andreas.brunner@empa.ch
[2]Vallen Systeme GmbH, Wolfratshausen, Germany; horst.trattnig@vallen.de
*Correspondence: andreas.brunner@empa.ch

ABSTRACT

A working group within the Committee on Acoustic Emission Testing of the German Society for Nondestructive Testing (FA-SEP of DGZfP) has collected published data on the long-term behavior of the AE or the Guided Ultrasonic Wave (GUW) measurement chain (sensor, sensor coupling and mounting, signal transmission, data acquisition and storage). Since only scant data is publicly available, the working group drafted a questionnaire for collecting respective information from the committee members. The returned questionnaires indicate that data acquisition and storage likely pose problems more frequently than other parts of the measurement chain. The only exception noted was for one case of integrity monitoring at elevated temperatures. In this case, sensor sensitivity was observed to decrease compared to the performance at room temperature, requiring the mounting of additional sensors for achieving AE source location with the same resolution. Based on the empirical information, recommendations for long-term monitoring with AE and GUW are discussed. These comprise, e.g., periodic checks of sensors and measurement chain, periodic data back-up, and planning of maintenance and repair.

Keywords: Acoustic emission (AE), guided ultrasonic waves (GUW), structural integrity monitoring, process monitoring, long-term equipment durability, measurement chain failures.

1. Introduction

Recently, AE and Guided Ultrasonic Waves (GUW) are finding new applications in long-term structural health or integrity monitoring [1] as well as in process monitoring or control [2-3]. In established, often standardized AE and GUW testing, e.g., proof testing or periodic inspection of pressure vessels or storage tanks [4-5], the test durations are typically limited between a few hours up to a few days. The test duration hence is the main difference between these and the structural health or process monitoring. For structural integrity and process monitoring, in some cases, there may be special environmental conditions, e.g., radiation in nuclear power plants [6-8], elevated or strongly varying temperature in conventional power plants [9] and in industrial production lines [10], or mechanical vibration spectra in road or rail transportation and aircraft operation [11,12]. Therefore, for long-term stability and performance of the AE or GUW measurement chain the question is how the operating conditions and environment will affect that. As discussed in [1], there is scant quantitative data on the long-term behavior of sensors, sensor coupling and

mounting, signal transmission device and data acquisition as well as data storage equipment available in scientific or technical publications. Manufacturers' data sheets often define operating temperature ranges for sensors and data acquisition equipment [13-14], but whether these suffice for long-term applications of several decades is not documented. AE service providers may have experience on how long sensors and other components of the measurement chain may last under various environmental conditions, but such information is typically not published.

A questionnaire distributed among the members of the Committee on Acoustic Emission Testing of the German Society for NDT (DGZfP), therefore, aimed at collecting information on the performance of the measurement chain (sensor, coupling and mounting, signal transmission, data acquisition, data storage and data analysis equipment) in long-term monitoring applications. "Long-term" in this context was defined as continuous or intermittent monitoring over durations of one year or more. Of course, expected service lives of several decades for structures in transportation industry (for aircraft and railway cars thirty years or more), or in civil engineering (for bridges fifty years or more) may constitute quite a challenge for AE or GUW measurements. The experience from the questionnaires can be summarized as follows: (1) sensor service life can vary between one or a few tests up to thirty or more years, depending on the usage and the ambient environment. Sensor failure mainly seems to occur due to external actions, e.g., mechanical impact of foreign objects or improper manual handling resulting in torn-off sensor cables or loose sensor mounting. However, there are also indications that use at elevated temperatures or in temperature cycles (up to near the Curie-temperature of the PZT sensor material) may affect the sensitivity of the sensors and through ageing possibly limit their service life. This will be discussed in detail later. (2) Adhesive bonding of sensors with thermoset adhesives seems to be the method of choice for reliable long-term sensor coupling, but there is no long-term experience publicly documented. (3) Measurement hardware (data acquisition and data storage) may also fail, e.g., in severe service environment such as temperature cycling and vibrations, or exposed to dust or humidity, or combinations of these. Considering the required reliability and availability as well as repairability in the equipment design and the choice of the electronic components is recommended [1]. (4) Software for data acquisition and analysis, in principle, can be operated in the long-term, except where public domain or general programs or code are used for which support will cease, or if the original software will not be compatible with such programs anymore, if they are needed, e.g., for signal transmission. (5) An essential part of any long-term AE or GUW monitoring has to include planning of periodic performance checks and of maintenance or repair actions. Availability of spare or replacement parts may become increasingly important with longer monitoring operation. In the following, the focus will be on temperature effects on the sensitivity and performance of the PZT-transducers, the main type used in AE and GUW monitoring setups.

2. Thermal effects on piezo-ceramic AE transducers

2.1 Temperature variation in ambient environments

Even in comparatively short duration AE or GUW measurements, the ambient temperature and relative humidity may vary to some extent. For example, the ISO standard for test climate for plastics [15] defines temperature and relative humidity values suitable for conditioning and testing of polymers. "23/50" and "27/65", i.e., 23°C and 50% relative humidity or 27°C and 65% relative humidity are standard climates for non-tropical and tropical countries, respectively. "23/50" is the climate required for data used in plastics data sheets and material properties data banks. Both standard climates come in two classes, the first (class 1) with variation limits of ±1°C for temperature and ±5% for relative humidity, and the second (class 2) with ±2°C and ±10% relative humidity limits, respectively. These limits are defined for polymers, a class of material with properties that are quite sensitive to variation in both, temperature and humidity. For other materials classes, e.g., metals and metal alloys or ceramics, the temperature and humidity dependence of properties is less pronounced.

Nevertheless, the potential temperature dependence of transducer performance may require consideration. Fig. 1 illustrates the effect of short-term temperature cycling on sensor sensitivity. Repeated variation of temperature between -40°C and +110°C for a sensor type VS75-V with a specified operating temperature range between -5°C and +85°C [13] shows changing sensitivity. For the same test signal input, peak amplitudes are lower at lower temperatures and slightly higher at +110°C, both after sufficient hold time for temperature equilibration. The initial sensitivity recovers, once the temperature stabilizes at room temperature (+25°C). Within several cycles (only partly shown in Fig. 1), no trend for a permanent change in sensitivity with an increasing number of cycles can be observed within the amplitude measurement resolution of 16 bit.
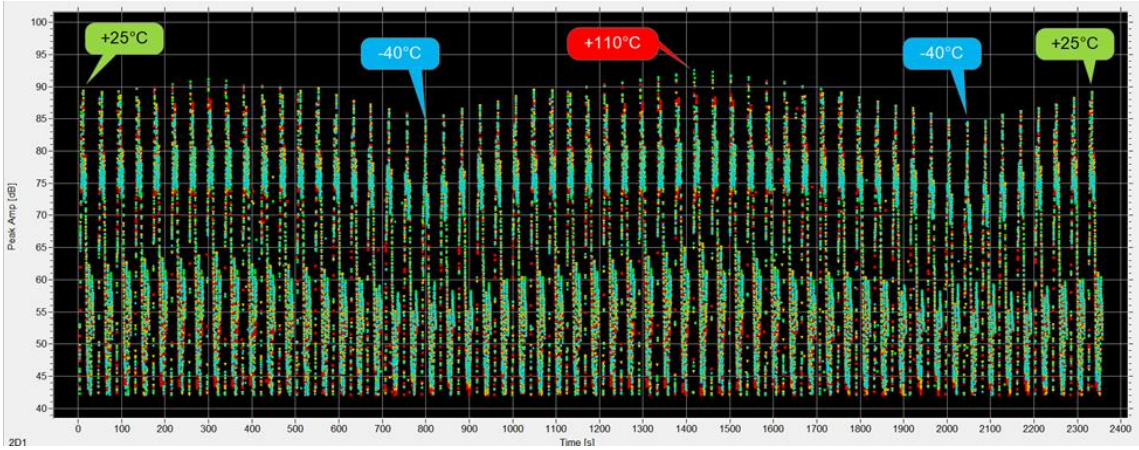
Fig. 1: Sensitivity test performed on an AE transducer VS75-V for repeated temperature cycling between -40°C and +110°C.

Fig. 2 and Fig. 3 show results of periodic sensor tests for AE sensors, one type VS75-V and one type VS75-RIC performed over a service duration of 18 and 15 years, respectively with the same setup for sensor verification. Fig. 2 shows a comparison of sensor sensitivity after 18 years of regular outdoor usage by a service provider in Europe. There seems to be a trend for the recent measurement in 2021 (blue curve) to be slightly lower than that of 2003 (red curve). In the specified frequency range (30–100 kHz), the sensitivity differs by 1 dB or less. This might be due, at least in part, to differences in coupling the sensor, but, in any case is no cause for concern. The small differences below 30 kHz are outside the specified frequency range and are not significant.
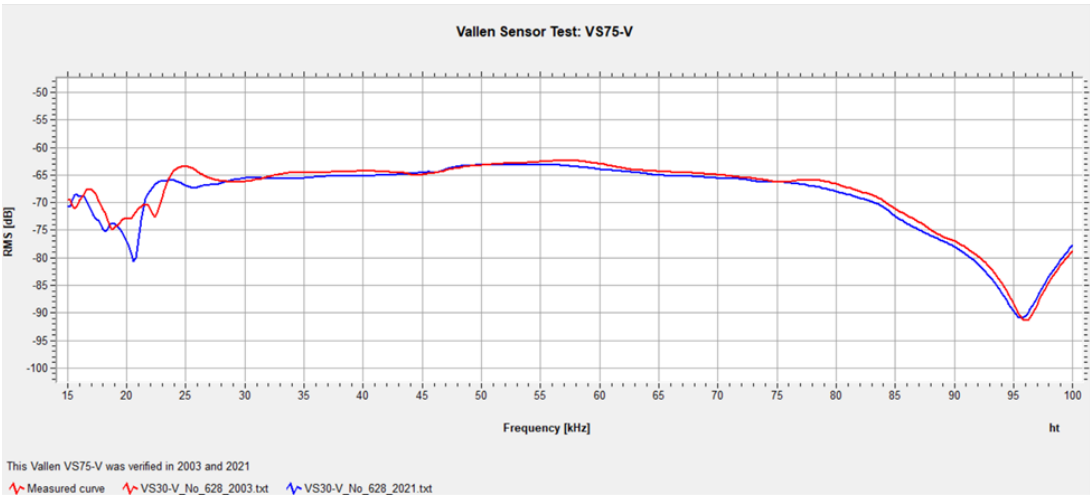
Fig. 2: Selected results of periodic sensor tests for one AE sensor (type Vallen VS75-V) performed over a service duration of 18 years, with the same setup and transducer for sensor verification.
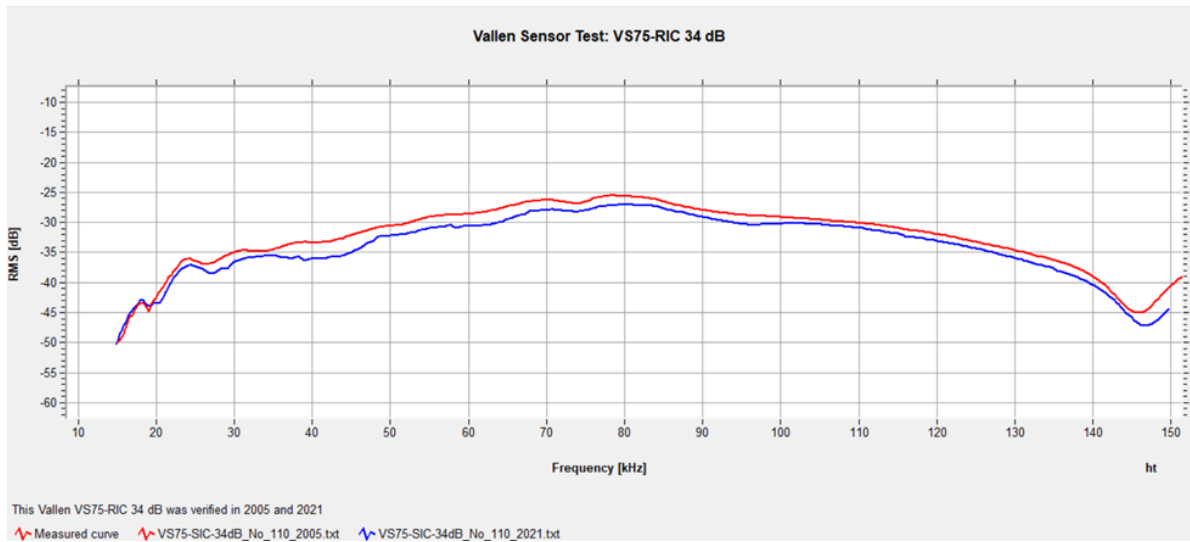
Fig. 3: Selected results of periodic sensor tests for one AE sensor with integrated preamplifier (type Vallen VS75-RIC 34 dB) performed over a service duration of 15 years, with the same setup and transducer for sensor verification.

Fig. 3 shows two sensitivity measurements on a sensor type VS75-RIC, taken 15 years apart. The recent measurement in 2021 (blue curve) is consistently below that of 2006 (red curve) with a difference of about 2-3 dB in the specified frequency range. The use of the sensor was similar to that shown in Fig. 2. Beside slight differences in coupling (as for the measurements in Fig. 2), ageing of the integrated analogue amplifier electronics likely may contribute to the observed difference. The relative contributions from these potential causes, however, are not quantifiable.

2.2 Temperature exposure or temperature cycles

Table 1 shows average signal amplitudes (Av. Amplitude) from five lead pencil breaks each, at several distances from a sensor (type ISR15CA-HT). This sensor mounted on a chemical reactor vessel (24CrMo10 steel), is checked at room temperature (around +20°C) and at elevated surface temperature (between +100°C and +110°C). The amplitudes show a clear decrease in sensor sensitivity observed at elevated temperatures. This required adapting the sensor array with shorter sensor-to-sensor distances for maintaining the required source location accuracy. Even though it is unknown whether the observed decrease of sensitivity at elevated temperature (within the specified operating temperature of +150°C maximum) induced a permanent degradation of sensor performance or not, the observation is important for planning long-term AE monitoring at elevated temperature. It can further be noted that the magnet holders for mounting the sensors also yielded reduced holding forces at surface temperatures between +100°C and +110°C.

Table 1: Lead pencil breaks for sensor check at room temperature and around +120°C.

PARAMETER	*VALUE*	*VALUE*	*VALUE*	*VALUE*	*VALUE*	*VALUE*	*VALUE*
Distance [mm]	50	300	500	800	1200	1600	2100
Av. Amplitude [dB$_{AE}$] +20°C	83	78	76	72	73	72	71
Av. Amplitude [dB$_{AE}$] +110°C	77	72	70	66	67	66	63

Most of the commercially available AE or GUW transducers use piezo-ceramic lead-zirconate-titanate (PZT). The Curie temperature T_C of PZT limits the operating temperature of such transducers. Depending on the type of PZT, there is a fairly large range of T_C starting at about +225°C and going up to about +350°C [16,17]. For temperatures close to or above T_C, therefore, other types of piezo-materials or other types of sensing methodology have to be used. Even though piezo-materials with higher T_C do exist, their efficiency for sensing structural waves is often less than that of PZT. These issues are discussed, e.g., by [18,19]. A viable alternative to PZT sensors for AE monitoring, also at higher temperatures above +350°C, are fiber optics based transducers, see, e.g., [20-23] for more details, To put the service life-time requirements for AE transducers operated at elevated temperatures in perspective, e.g., [18] notes an expectation of sensor operation for aircraft turbine components over service durations of up to 100'000 hours, roughly equivalent to 11 years, and that at temperatures between +500°C and +1000°C. In automotive applications, PZT stack actuators are e.g., used for injector devices. Electric cycle tests with fields of 3.0 kV/mm at +22°C and +50°C yielded clearly higher reductions in piezoelectric and dielectric coefficients for the latter (48% and 28%, respectively) after 10^8 cycles [24].

Fig. 4 shows effects of thermally induced degradation in properties of two types of PZT presented in [25]. Even short exposures to elevated temperatures of 10 minutes lead to measureable changes in the piezoelectric constant d_{33}. Dimensionless aging rates and relaxation times (in hours) calculated from fitting the measured data show a clear increase and decrease, respectively, with increasing temperatures. Temperatures in this case were varied between 30% and 80% of the respective T_C for one type of soft (Nb-doped, PZT-5A type [16], with T_C = +360°C) and one type of hard PZT (Fe-doped, PZT-4 type [16], with T_C = +325°C). The dimensionless ageing rates are calculated from the measured d_{33} piezoelectric coefficient (initially amounting to 375 and 315 pC/N for soft and hard PZT, respectively) after the heat treatments at different temperatures according to equation (1).

$$(dimensionless)\ ageing\ rate = \frac{1}{\log(t_2) - \log(t_1)} \left(\frac{d_{33t2} - d_{33t1}}{d_{33t1}} \right) \tag{1}$$

where t_1 and t_2 are the number of hours just after heat treatment (192 hours) and after ageing (1344 hours), respectively, and d_{33t1} and d_{33t2} are the piezoelectric property measured at t_1 and t_2, respectively. Similarly, relaxation times after the heat treatments are calculated according to equation (2) from fitting an exponential function to the measured data.

$$d_{33} = d_{33c} + d_{33t}\ exp\left[-\left(\frac{t}{\tau} \right)^{\mu} \right] \tag{2}$$

where d_{33c} and d_{33t} are the time-independent and time-dependent property, respectively, and t and τ are the ageing and the relaxation time, respectively, and μ a stretching factor.
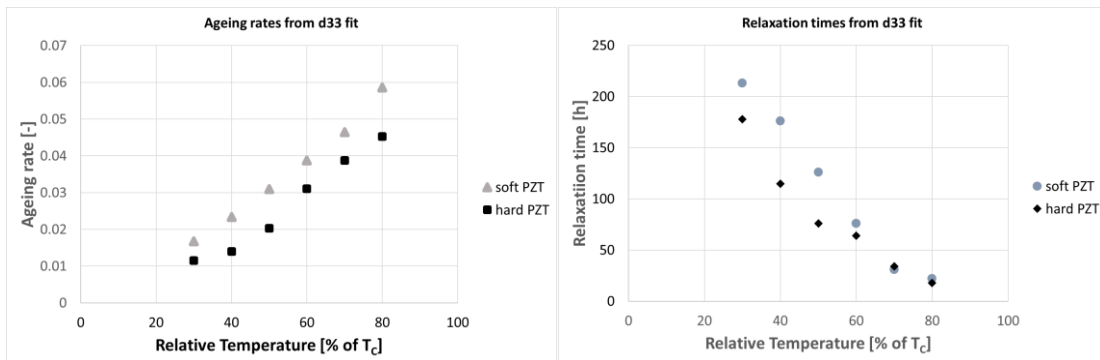
Fig. 4: Dimensionless ageing rates and relaxation times τ for one type of soft (Nb-doped, PZT-5A type, T_C 360°C) and hard PZT (Fe-doped, PZT-4 type, T_C 325°C), data plotted from Tables 2 and 3, respectively from [25] each after exposure to elevated temperatures between 30% and 80% of the respective T_C for 10 minutes.

Fig. 4 shows that ageing rates and relaxation times are higher for soft than for hard PZT, and both are changing with the applied annealing temperature. The ageing rates increase and the relaxation times decrease for both types of PZT. These changes occur already after short annealing durations of 10 minutes. A slight decreasing trend during the measurement period before annealing (around 168 hours) continued similarly after the drop due to annealing for at least 1128 hours. There are hence no indications of recovery of the property value after annealing over at least 1100 hours, independent of the annealing temperature. Whether this behavior of selected PZT-materials might also occur in PZT-based sensors is not clear at this point.

3. Discussion

Since AE and GUW are also implemented for process monitoring and may find more and more use for process control, the operating conditions, in some cases, may be more severe than for infrastructure monitoring, e.g., on bridges in moderate or tropical climate zones, with the typical daily and annual temperature and humidity variations. Even comparatively high ambient temperatures up to +50°C are expected to still be moderate for low T_C (+225°C) and even less detrimental for high T_C PZT materials (+360°C). In process monitoring, the transducers may experience larger temperature variation or changes of ambient environment occurring faster, or both. Mechanical loads such as, e.g., machine vibrations may also have to be considered in planning and set-up of process monitoring beside the temperature changes.

Operating sensors at elevated temperature or under cyclic temperature conditions may reduce their sensitivity as indicated by the data in Table 1. For further investigation of such effects, it is essential to have sensor sensitivity curves as a function of frequency (as in Fig. 2 and 3) acquired before and after the tests, and, if possible, at selected intervals in-between. Only these will indicate whether the observed performance reductions are temporary or at least partly, permanent.

Considering the data from materials characterization with respect to thermal annealing at elevated temperatures (Fig. 4) and the limited documented performance of sensors during monitoring (estimated to currently amount to 4-5 years [26]) it cannot be excluded that changes may occur over much longer monitoring periods. Whether this may also occur due to daily or annual variations in ambient temperatures in long-term applications, or in process monitoring under more severe conditions over several decades is simply unknown. Periodic sensor checks at sufficiently short time intervals are a minimum requirement for ensuring successful monitoring with AE sensors made from PZT.

4. Summary and outlook

There is scant published experience on the long-term behavior of AE or GUW based monitoring systems for assessing structural integrity or identifying occurrence of damage, and basically none, if the service-life of structures spans several decades [1]. Even equipment manufacturers and service providers do not have such long-term experience. Published data so far cover monitoring over periods of about one to two years, but often intermittent, with the data acquisition equipment removed in between. However, there are examples of infrastructure monitoring, e.g., a bridge in Ulm [26] for about four years now with PZT-transducers permanently mounted that did not show any significant sensitivity changes so far.

Assuring long-term monitoring for several decades, however, poses a challenge for the development and operation of such monitoring systems. A recent review [1] had collected experience from literature and from a questionnaire sent to AE practitioners in Germany, Austria and Switzerland. With respect to service life of PZT-transducers, a conclusion was that mechanical damage, e.g., mechanical impact or applying other stresses on sensor mounts or cables is a potential source of failure. Therefore, periodic checks of sensor performance are necessary, e.g.,

by pencil lead breaks at defined positions of the test object or by exciting the transducers to emit propagating elastic waves. Observed changes, of course, can be due to sensitivity loss in the sensor itself or in the mounting and coupling of the transducers, but may also contain contributions from changes in the object that is monitored. The data sets of these GUW may hence also be analyzed for indications of defect initiation or growth in the monitored structure, complementing the AE monitoring. For this, acquisition of full waveforms rather than AE signal parameter sets is recommended, offering direct information on changes in frequency content of the signals. With respect to the performance of other parts of the measurement chain not discussed here, e.g., data acquisition or data storage hardware and software for data acquisition and analysis, the review [1] also provides some information. For hardware, designing equipment with a certain amount of redundancy as well as planning of maintenance and repair, and the procurement of spare parts are essential aspects for achieving sufficient reliability and technical availability.

5. References

[1]   Brunner, A.J. (2021). Structural Health and Condition Monitoring with Acoustic Emission and Guided Ultrasonic Waves: What about Long-term Durability of Sensors, Sensor Coupling and Measurement Chain? Applied Sciences, vol. 11, no. 24, 11648, p. 1-20, doi: /10.3390/app112411648

[2]   Shevchik, S., Masinelli, G., Kenel, C., Leinenbach, C., Wasmer, K. (2019). Deep Learning for In Situ and Real-Time Quality Monitoring in Additive Manufacturing Using Acoustic Emission. IEEE Transactions on Industrial Informatics, vol. 15, p. 5194–5203, doi: 10.1109/TII.2019.2910524

[3]   Pandiyan, V., Shevchik, S., Wasmer, K., Castagne, S., Tjahjowidodod, T. (2020). Modelling and monitoring of abrasive finishing processes using artificial intelligence techniques: A review. Journal of Manufacturing Processes, vol. 57, p. 114–135, doi: 10.1016/j.jmapro.2020.06.013

[4]   ASTM E1067/E1067M Standard Practice for Acoustic Emission Examination of Fiberglass Reinforced Plastic Resin (FRP) Tanks/Vessels, p. 1-16, doi: 10.1520/E1067-18

[5]   EN 12819 (2019). LPG equipment and accessories - Inspection and requalification of LPG pressure vessels greater than 13 m³, p. 1-35.

[6]   Jones, R.H., Hutton, P.H., Friese, M.A., Wolf, S.M. (1984). Observation and Identification of Crack Growth Modes in Reactor Steels Using Acoustic Emission. Proceedings Workshop, PNL-SA-12656, University of Denver, March 14-15, 1984.

[7]   Runow, P. (1985). The Use of Acoustic Emission Methods as Aids to the Structural Integrity Assessment of Nuclear Power Plants, International Journal of Pressure Vessels & Piping, vol. 21, p. 157-207.

[8]   Ayo-Imoru, R.M.; Cilliers, A.C. (2018). A survey of the state of condition-based maintenance (CBM) in the nuclear power industry. Annals of Nuclear Energy, vol. 112, p. 177–188, doi: 10.1016/j.anucene.2017.10.010

[9]   Jüngert, A., Dugan, S., Udoh, A. (2016). Acoustic Emission Testing under Difficult Conditions. 32nd European Conference on Acoustic Emission, European Working Group on Acoustic Emission, September 7-9, 2016 Prague, Czech Republic, p. 239-246.

[10]   Koester, L.W., Taheri, H., Bigelow, T.A., Bond, L.J., Faierson, L.J. (2018). In-situ acoustic signature monitoring in additive manufacturing processes, 44th Annual Review of Progress in Quantitative Nondestructive Evaluation, Volume 37, AIP Conference Proceedings 1949, p. 020006-1 – 020006-8, doi: 10.1063/1.5031503

[11]   Wang, J.F., Liu, X.-Z., Ni, Y.-Q. (2018). A Bayesian Probabilistic Approach for Acoustic Emission-Based Rail Condition Assessment. Computer-Aided Civil and Infrastructure Engineering, vol. 33, p. 21–34, doi: 10.1111/mice.12316.

[12] Mendoza, E., Prohaska, J., Kempen, C., Esterkin, Y., Sun, S.J. (2013). In-flight fiber optic acoustic emission sensor (FAESense) system for the real time detection, localization, and classification of damage in composite aircraft structures, Proceedings SPIE 8720, Photonic Applications for Aerospace, Commercial, and Harsh Environments IV, p. 87200K-1 – 87200K-9, doi: 10.1117/12.2018155

[13] Vallen GmbH (2017). Acoustic Emission Sensors, Specification. p. 1-50 https://www.vallen.de/wp-content/uploads/2019/03/sov.pdf (accessed June 7, 2022).

[14] Physical Acoustics. Sensors. https://www.physicalacoustics.com/sensors/ (accessed June 7, 2022).

[15] ISO 291 (2008). Plastics — Standard atmospheres for conditioning and testing, p. 1-12.

[16] MIL-STD-1376B (SH) (1995) Piezoelectric ceramic material and measurements guidelines for sonar transducers. p. 1-32.

[17] Promsawat, N., Promsawat, M., Janphuang, P., Marungsri, B., Luo, Z.H., Pojprapai, S. (2017). Investigation of the effect of temperature on aging behavior of Fe-doped lead zirconate titanate. Functional Materials Letters, vol. 10, no. 3, 1750026, p. 1-4, doi: 10.1142/S1793604717500266

[18] Jiang, X.N., Kim, K.G., Zhang, S.J., Johnson, J., Salazar, G. (2014). High-Temperature Piezoelectric Sensing. Sensors 2014, vol. 14, p. 144-169, doi:10.3390/s140100144

[19] Stevenson, T., Martin, D.G., Cowin, P.I., Blumfield, A., Bell, A.J., Comyn, T.P., Weaver, P.M. (2015). Piezoelectric materials for high temperature transducers and actuators. Journal of Materials Science: Materials in Electronics. vol. 26, p. 9256–9267, doi: 10.1007/s10854-015-3629-4

[20] Xiong, W.; Cai, C.S. (2012). Development of Fiber Optic Acoustic Emission Sensors for Applications in Civil Infrastructures. Advanced Structural Engineering, vol. 15, p. 1471–1486.

[21] Willberry, J.O.; Papaelias, M.; Franklyn Fernando, G. (2020). Structural Health Monitoring Using Fibre Optic Acoustic Emission Sensors. Sensors, vol. 20, 6369, p. 1-31, doi: 10.3390/s20216369

[22] Zhang, L.; Tang, Y.; Tong, L. (2020). Micro-/Nanofiber Optics: Merging Photonics and Material Science on Nanoscale for Advanced Sensing Technology. iScience, vol. 23, 100810, p. 1-23, doi: 10.1016/j.isci.2019.100810

[23] Matsuo, T., Cho, H., Takemoto, M. (2006). Optical fiber acoustic emission system for monitoring molten salt attack. Science and Technology of Advanced Materials, vol. 7(1), p. 104-110, doi: 10.1016/j.stam.2005.11.010

[24] Wang, H., Lee, S.-M., Lin, H.-T., Stafford, R. (2016). Performance of PZT stacks under high-field electric cycling at various temperatures in heavy-duty diesel engine fuel injectors. Proc. SPIE 9806, Smart Materials and Nondestructive Evaluation for Energy Systems 2016, 98060Q (1 April 2016), doi: 10.1117/12.2219414

[25] Promsawat, M., Phuetthonglang, A., Marungsri, B., Promsawat, N., Janphuang, P., Luo. Z.H., Pojprapai, S. (2017). Effects of temperature on aging degradation of soft and hard lead zirconate titanate ceramics. Ceramics International, vol. 43, no. 13, p. 9709-9714, doi: 10.1016/j.ceramint.2017.04.145

[26] Niederleithinger, E., Sodeikat, Ch., Epple, N., Liao, C.-M., Hindersmann, I. (2021) Acoustic emission and ultrasonic monitoring of a prestressed concrete bridge in its final years. Proceedings 1st Conference of the European Association on Quality Control of Bridges and Structures (Eurostruct), Padua, Italy, August 29 – September 1, 2021, p. 1-10.

A NEW ISO STANDARD FOR AE SENSOR SENSITIVITY DETERMINATION USES THE FACE-TO-FACE STIMULATION METHOD

Hartmut Vallen[1]

[1]Vallen Systeme GmbH; hartmut@vallen.de

ABSTRACT

This paper summarizes a Final Draft International Standard (FDIS) developed by ISO TC 135 SC 9 WG 9. Since the draft comprises 60 pages, only an overview can be presented in this compressed format.

Keywords: Sensor sensitivity verification, sensor calibration, laser vibrometry, calibration standards, verification standards.

1. Introduction

Many standards for acoustic emission (AE) testing of safety critical structures specify a required sensitivity of the acoustic emission sensors to be used. This means, each AE sensor manufacturer and each AE service provider shall ensure that the sensors sold and used meet such requirements. But this turns out to be rather difficult:

All presently existing ISO and ASTM standards for AE sensor sensitivity determination, ISO 12713 and ISO 12714, ASTM E1106 and E1781, require a heavy, immobile transfer block which makes the setup for most of the users of acoustic emission systems impractical and too expensive. Only very few laboratories in the world are equipped with such a setup. A widely accepted standard using an economic, easy-to-use setup is urgently needed. A new ISO standard in development is intended to help solving this need. The full name of that standard will read: ISO 24543 Non-destructive testing — Acoustic emission testing — Verification of the receiving sensitivity spectra of piezoelectric acoustic emission sensors.

The ISO 24543 project has been initiated in summer 2019 by the German standardization body DIN. The Final Draft International Standard ISO/FDIS 24543 has been prepared in June 2022 for the final vote. Publication of ISO 24543 is scheduled for end of 2022. This paper presents essentials about this standard. It is an update of [1], presented on Nov. 5, 2019, at the World Conference on Acoustic Emission (WCAE) in Guangzhou, China. Purpose of this paper is to inform the AE society about the status of this work and about an overview over the structure and the contents of the new ISO document.

2. Clause 1 of ISO/FDIS 24543: Scope

ISO/FDIS 24543 specifies a method for the determination of the receiving sensitivity spectra of a piezo-electric acoustic emission sensor, in absolute units of volts output per motion input, whereby the motion can be particle displacement (e.g. in nanometres) or particle velocity (e.g. in millimetres per second) over a frequency range used for acoustic emission testing, … whereby the sensor is stimulated by a motion pulse in normal direction to the sensor's face from a directly coupled piezoelectric transmitter.

ISO/FDIS 24543 also specifies a method for the determination of the transmitting sensitivity spectrum of a piezoelectric transmitter in absolute units, e. g. in nanometres output per volt input, by measuring both the particle displacement pulse over the transmitter's active face and the transmitter's input voltage spectrum, using a scanning laser vibrometer.

ISO/FDIS 24543 does not include the known cancellation effects on a sensor's response, when the angle of incidence differs from normal (90°) or when the length of the wave passing across the sensor's sensitive face is shorter than about 10 times the dimension of the sensor's sensitive face. ISO/FDIS 24543 does not specify a method to measure the influence of different materials on a sensor's sensitivity, but this effect is addressed in Annex F.

3. Clauses 2 to 9 of ISO/FDIS 24543

Three mandatory clauses (Clauses 2 to 4) concern normative references, terms and definitions, symbols and abbreviated terms.

Clause 5 provides an overview over the face-to-face setup, which is used to determine the receiving sensitivity of the sensor under test (SUT), and over the laser vibrometer setup, which is used to determine the transmitter's transmitting sensitivity.

Clause 6 defines the requirements on the hardware described in Clause 5.

Clauses 7 and 8 explain details and present procedures for the determination of the receiving sensitivity spectra using the face-to-face setup (see chapter 5), and the transmitting sensitivity spectra using the laser vibrometer (LVM) setup (see chapter 6).

4. Annexes A to F of ISO/FDIS 24543

All Annexes are of type "informative". Annex A provides templates for a transmitter list and for a list of sensor types.

Annex B provides examples of commercially available products which can be used to perform the procedures of the standard: A function generator model, a transmitter model, a transient recorder model, a type of mirror foil, and a scanning laser vibrometer model.

Annex C provides general and historic information about sensor verification methods, some fundamental problems encountered with primary sensor calibration and how ISO/FDIS 24543 relates to such problems, and a summary about advantages and disadvantages of the face-to-face method.

Annex D and E provide additional information concerning receiving and transmitting sensitivity determination.

Annex F shows how – in theory - the sensitivity spectra obtained from face-to-face setup can be adapted to the acoustic impedance of the test object material.

5. Basic elements of the face-to-face stimulation setup

Fig. 1 shows the block diagram for the face-to-face stimulation setup. Purpose of this setup is to measure the response of a piezoelectric AE sensor on a known particle displacement stimulation by a piezoelectric transmitter for the calculation of the sensor sensitivity R_D, a relevant property of an AE sensor.

Meanings of the blocks and symbols in Fig. 1 from left to right:

FG: function generator, U_F: electrical stimulation pulse signal to TM,
TM: piezoelectric transmitter,   SUT: sensor under test,
U_S: sensor output signal   TRA: transient recorder with inputs A, B, and T
PC: personal computer   D: graphical display

The FG generates the stimulation pulse U_F. The TM converts U_F into a particle displacement pulse. The SUT converts that pulse into the electrical output U_S. U_S and U_F are captured by channels A and B of the TRA, triggered by the FG and transferred to the PC for data processing and data visualization at D.
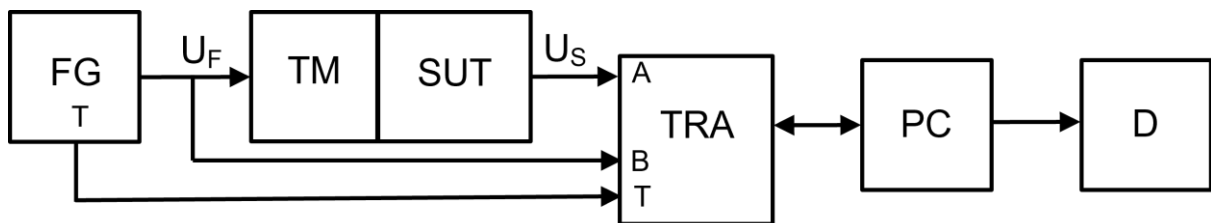
Fig. 1: Basic elements of the face-to-face stimulation setup and relevant signals.

Fig. 2 shows examples of the signals U_F and U_S. U_F is a 1 MHz sine wave starting at 90°, the standby voltage from FG is +10V but is shown in Fig. 1a as 0 V, due to an offset compensation. U_F reaches a minimum of -18V at (90+180)° and returns to 0 V at (90+360)°.

a: Signal U_F from FG   b: Short sensor response U_S c: Long sensor response U_S
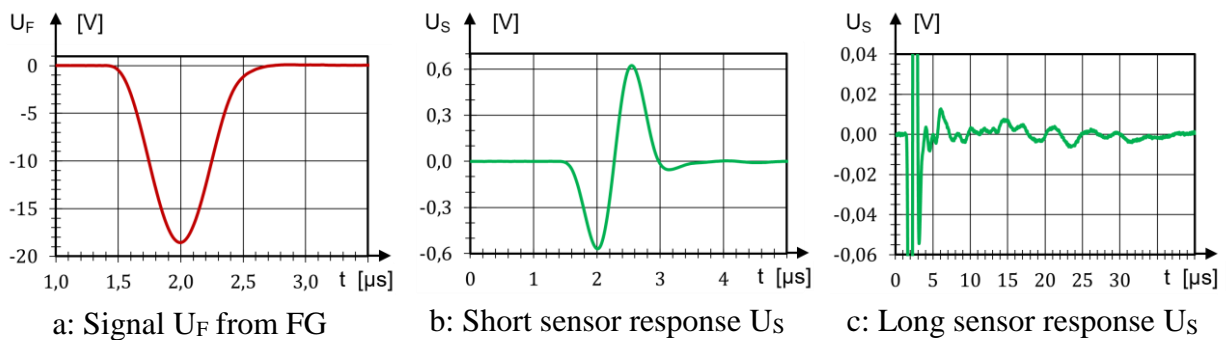
Fig. 2: Examples of relevant signals of the face-to-face setup in the time domain.

Fig. 2b shows a short part of U_S, the response of a wide-band SUT. Fig. 2c shows the same signal over an extended time scale and a zoomed amplitude scale. In the time range of about 10 to 30 µs reverberation peaks of about 5 to 10 mV peak-to-peak (pp) can be seen. Even though this is only 0,4 to 0,8% of the 1,2Vpp main response in Fig. 2b, such low amplitude reverberations have influence on the resulting sensitivity spectra and need to be considered.

6. Basic elements of the laser vibrometer setup
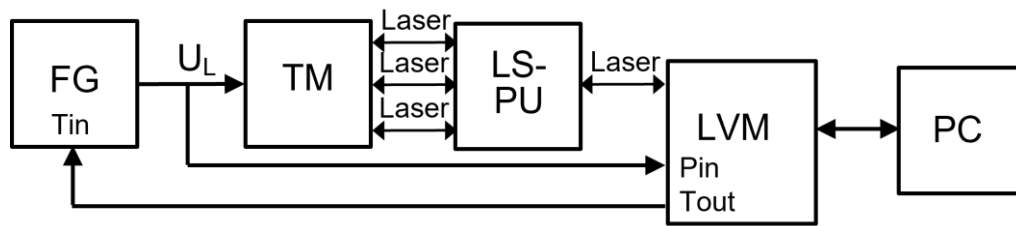
Fig. 3: Block diagram of the laser vibrometer setup.

Fig. 3 shows the block diagram of the laser vibrometer (LVM) setup. Purpose of this setup is to measure D in picometer. D is the displacement pulse at the free active surface of the piezoelectric transmitter, in the time domain. From the spectrum of D and U_L, the transmitting displacement sensitivity spectrum T_D is calculated. T_D is a relevant property of the piezoelectric transmitter.
The LVM measures over the laser channel the motion pulse, generated by the transmitter (TM) in response to the stimulation voltage (U_L), which is captured by the LVM's parametric channel (Pin). U_L is generated by the function generator (FG), like U_F in face-to-face setup, but triggered by the LVM (Tout).
The LVM exchanges data and commands with a personal computer (PC).

7. Displacement measurement over different areas of a transmitter face

It has been described in [2] and [3] that measuring only the motion at the centre point of a transmitter is not sufficiently representative for a larger area on the face since the motion distribution over the transmitter's face is not perfectly uniform. In order to measure the displacement output over a representative area a laser scan positioning unit (LS-PU in Fig. 3), an integral part of the LVM, is used to direct the laser beam of the LVM sequentially to one of 21 measurement positions.
The 21 positions are distributed over five concentric rings over the transmitter's active face. The average displacements over five different center distances are measured and converted to five different transmitting sensitivity results, for SUT's of five different diameters of sensitive faces.
Table 1 of ISO/FDIS 24543 specifies for five ranges of SUT diameters the proper transmitting sensitivity result to be used. For example, for a SUT with less than 5,1 mm diameter of the sensitive face, only the displacement sensitivities from the centre point and from the 4 positions of ring 1 are considered.

8. Relations between relevant spectra

Formula (6) of ISO/FDIS 24543 defines the receiving displacement sensitivity spectrum (R_D) of an AE sensor to: "$R_D = R_{SS} - T_D$" whereby R_{SS} is the signal to stimulation ratio, obtained from the face-to-face setup, and T_D is the transmitting displacement sensitivity, obtained from LVM setup. R_{SS} equals the spectrum of the sensor output U_S, subtracted by the spectrum of the stimulation voltage U_F. T_D equals the spectrum of the measured displacement D, subtracted by the spectrum of the stimulation voltage U_L.
The symbols of the spectra of U_F and U_S are designated $F(U_F)$ and $F(U_S)$, with 0 dB referring to 1 mV. The spectrum of D is designated $F(D)$ with 0 dB referring to 1 pm.
0 dB of R_D refers to 1 mV/pm, what means the sensor delivers 1 millivolt output per picometre input. 1 mV/pm is equal to 1 V/nm.

0 dB of T_D refers to 1 pm/mV, what means the transmitter delivers 1 picometre displacement output per mV input. 1 pm/mV is equal to 1 nm/V.

In addition to the receiving displacement sensitivity R_D, ISO/FDIS 24543 supports also the determination of the receiving velocity sensitivity R_V in dB, with 0 dB referring to 1 Vs/mm, using the formula $R_V = R_D - (20 \times lg(2\pi f) - 120)$, where f is the frequency in kHz.

9. Examples of sensitivity spectrum results

Legend
M   magnitude in dB
f   frequency in kHz
————— receiving displacement sensitivity R_D in dB, with 0 dB referring to 1 V/nm
————— receiving velocity sensitivity R_V in dB, with 0 dB referring to 1 Vs/mm
————— deviation of R_D, if transmitter TMA is used instead of TMC
————— deviation of R_D, if 100 µs widow length is used instead of 50 µs
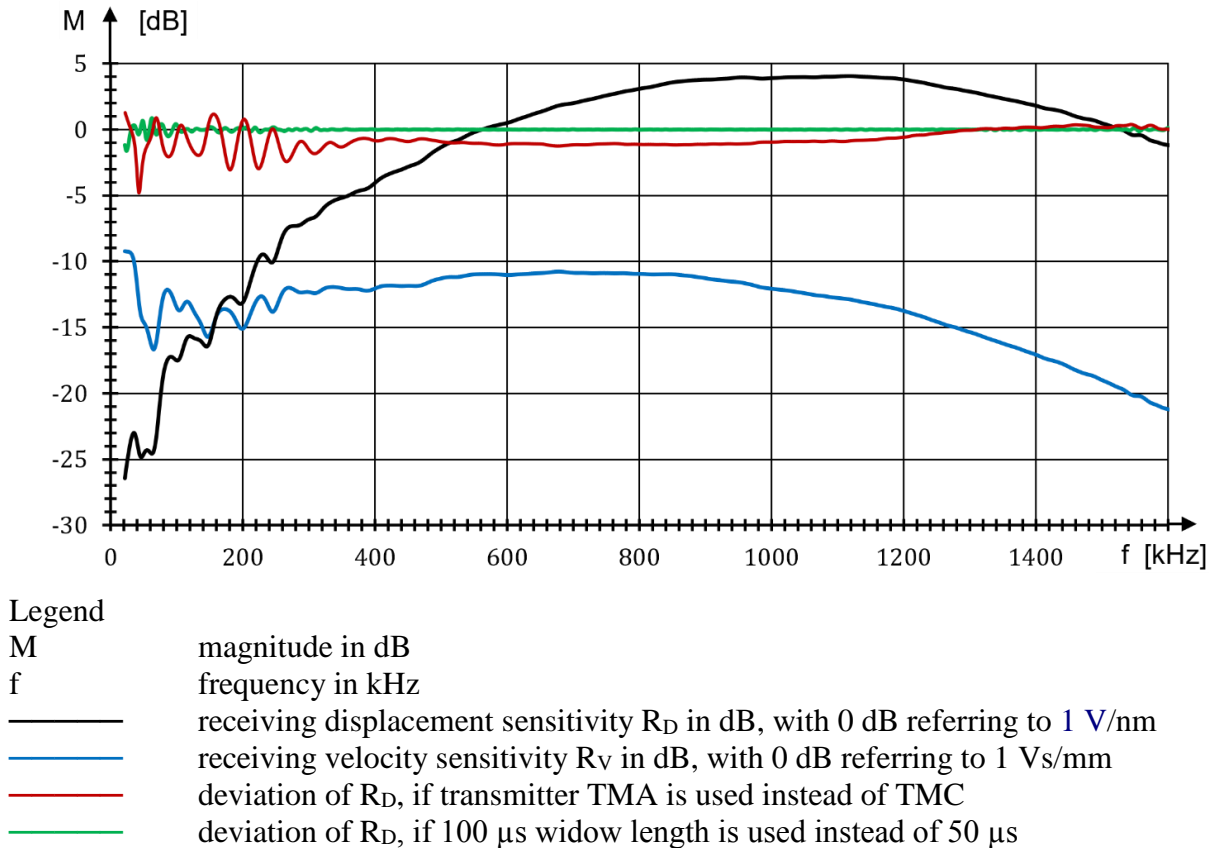
Fig. 4: Sensitivity spectrum results for a wide-band SUT (SUT01).

Fig. 4 shows in black and blue the results of the displacement (R_D) and velocity (R_V) receiving sensitivity spectra of a wide-band sensor (model V103, Olympics), using TMC and the 50 µs long FFT window W7. Since the diameter of the sensitive face of this sensor model is 12.6 mm (0,5 inch), the transmitting sensitivity, that considers the average displacement at the centre point and at rings 1 to 3 (12 positions) on transmitter TMC are used, according to Table 1 of ISO/FDIS 24543. In this paper, only results of using two transmitter units, TMA and TMC, are shown.

The red and green curves in Fig. 4 show additional information. The curve in red shows the deviation of black and blue, if transmitter TMA instead of TMC is used. The curve in green shows the deviation of black and blue, if the 100 µs long FFT window W8 is used instead of the 50 µs long window W7. ISO/FDIS 24543 deals with such variations in detail.

Fig. 5 shows the receiving displacement sensitivities of a SUT01 (wide-band) and a SUT03 (150 kHz narrow-band) sensor. One can easily see that above 100 kHz and below 440 kHz, the sensitivity of the narrow-band sensor lies 10 to 25 dB above that of the wide-band sensor.

Fig. 6 shows sensitivities of three SUT-types in a lower, 20 to 210 kHz range. Black and blue correspond to Fig. 5. The red curve shows the sensitivity of a SUT04 sensor, a 30 kHz low-frequency sensor. In range 20 to 60 kHz, the red curve lies about 15 dB above SUT03 (150 kHz narrow-band).

Legend

M   magnitude of receiving sensitivity R_D in dB, with 0dB referring to 1 V/nm
f   frequency in kHz
                   SUT01 receiving displacement sensitivity R_D
                   SUT03 receiving displacement sensitivity R_D
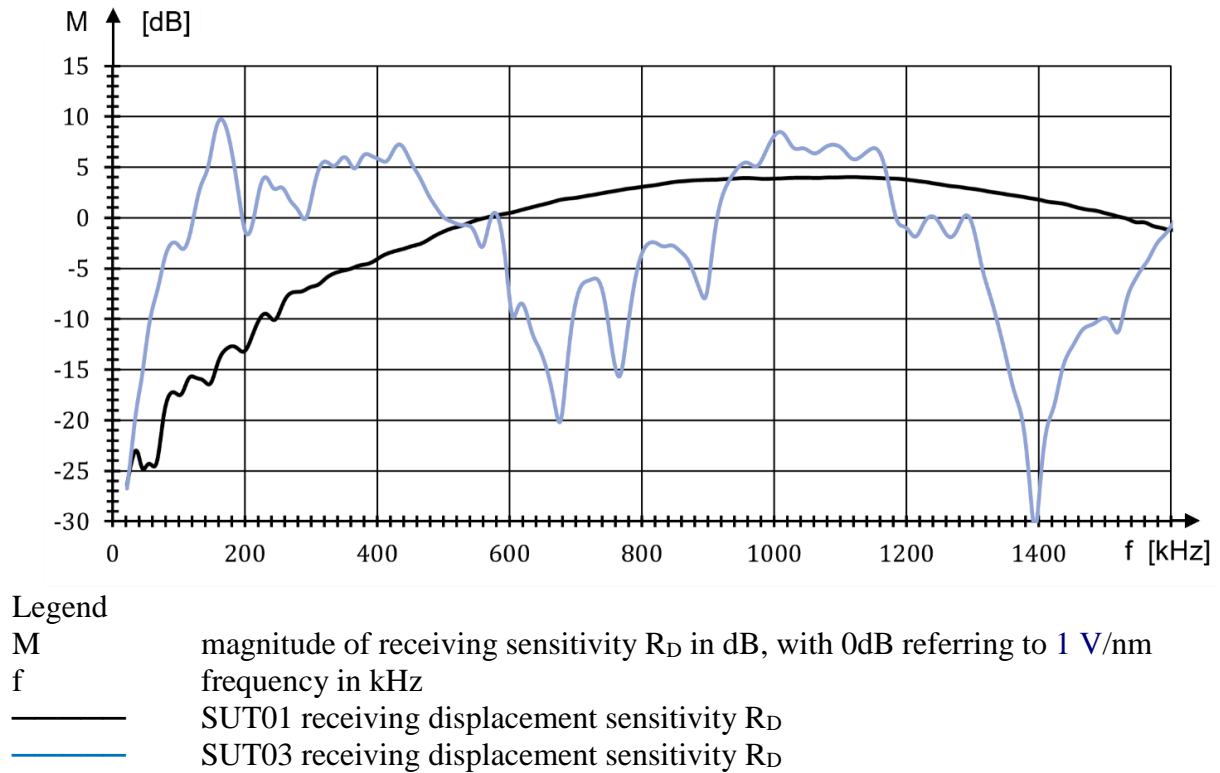
Fig. 5: Sensitivity result for SUT01 (wide-band) and SUT03 (150 kHz narrow-band).

Legend

M   magnitude of receiving sensitivity R_D in dB, with 0dB referring to 1 V/nm
f   frequency in kHz
                   SUT01 receiving displacement sensitivity R_D
                   SUT03 receiving displacement sensitivity R_D
                   SUT04 receiving displacement sensitivity R_D
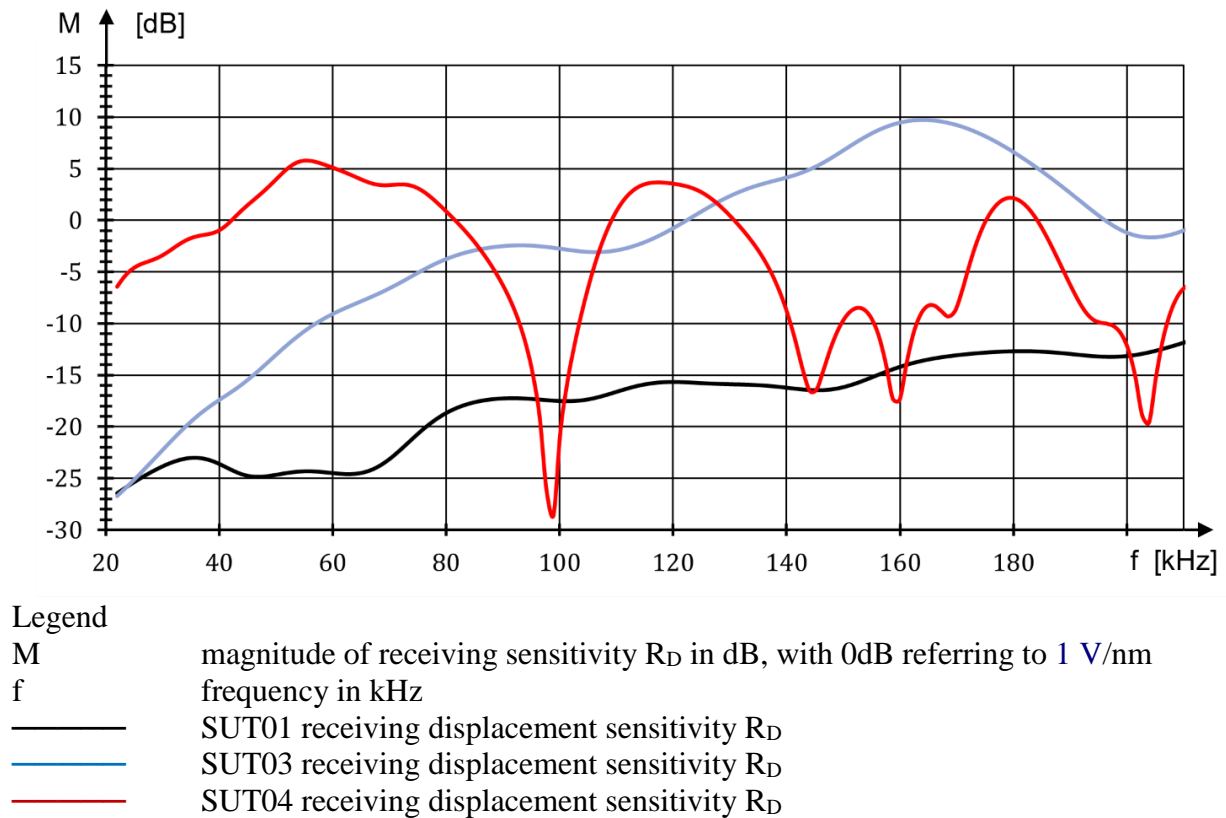
Fig. 6: Low-frequency results for SUT01 (wide-band) SUT03 (150 kHz narrow-band) and SUT04 (30 kHz low-frequency).

10. Omissions

This paper summarizes on 8 pages some essential items of the new ISO standard 24543 in FDIS status (final draft international standard), which comprises 60 pages.

Due to space and time constrains, several items treated by the standard are here not addressed, some of the omitted items are:

- a fixing tool for holding SUT and TM in place and the coupling agent used to ensure good reproducible and stable acoustic coupling quality,
- sensitivity determination of sensors with integral preamplifiers,
- testing electrical crosstalk from transmitter to SUT,
- influence of sensor cable capacity and cable length,
- understanding FFT results, scaling effects and more,
- the role of the FFT time window,
- the minimum FFT time window length for low-frequency analysis,
- minimizing the influence of a step in time domain on the FFT result,
- criteria to sort out unsuitable transmitter units,
- calibration of the laser vibrometer,
- improving the signal-to-noise ratio of the LVM displacement output by averaging then thousand signals and applying a Savitzky-Golay filter,
- detection of a drift of a transmitter's sensitivity,
- and more.

11. References

[1] Vallen H. (2019). About an initial draft of a standard concerning sensitivity verification of acoustic emission sensors. Springer Proceedings in Physics, vol. 259, p. 33-40, doi: 10.1007/978-981-15-9837-1.

[2] Ono K., Cho H., Vallen H., M'Closkey R.T. (2021). Transmission sensitivities of contact ultrasonic transducers and their applications. Sensors 2021, 21, 4396. doi:10.3390/s21134396.

[3] Burks B., Hamstad M.A. (2015). An Experimental-numerical Investigation of the face-to-face Sensor Characterization Technique. ME (Materials Evaluation) vol. 73, No.3, p. 414-423.

INTERNET OF THINGS ACOUSTIC EMISSION FOR UNATTENDED QUANTITATIVE LEAKAGE MONITORING

Jiehui Xie[1], Zhipeng Xie[1] and Yating Liu[1]

[1]Qingcheng AE Institute (Guangzhou) Co., Ltd; xjh@ae-ndt.com, xzp@ae-ndt.com, lyt@ae-ndt.com
*Correspondence: xjh@ae-ndt.com

ABSTRACT

This paper analyzes the theoretical basis of acoustic emission monitoring of leakage in principle. Based on the actual field leakage experiments, the following quantitative relationships are obtained: the quantitative relationship between the amount of leakage and the acoustic emission parameters under the same pressure; the quantitative relationship between different pressures, acoustic emission parameters and leakage rate under the condition of the same valve opening; the characteristic relationship between different leakage openings and acoustic emission parameters under the same pressure difference (tank wall plug). An online experimental demonstration system of leakage rate of water pipes is established. The acoustic emission collector automatically detects the leakage and leakage rates, and transmits the data to the cloud server. After the alarm conditions are set, the alarms will be pushed to the mobile phone if the alarm conditions are met. The cloud server is open for readers to view the results.

Keywords: Acoustic emission, leakage, quantitative, Internet of Things, unattended, alarm.

1. Introduction

Valves and pipelines are widely used in all walks of life, ranging from aerospace industry, marine industry, petrochemical industry to domestic water supply and gas supply. However, in the long-term effects of erosion and corrosion in valves and pipelines, it leads to the untight seals in valves and the reduced wall thickness, which often occurs leakage accidents. Although conventional detection methods (such as direct observation method, flow balance method, negative pressure wave method, operating pressure method, etc.) have been widely used, their deficiency is that they rely on professionals to go for the site inspection, and need to scan point by point or even need to dig and check the buried pipeline, which involves high labor intensity and low work efficiency.

As one of the important branches of the applications of acoustic emission (AE) technology, acoustic emission leakage detection technology has been widely recognized in recent years due to its advantages of dynamic, high sensitivity and wide coverage. However, the current technology and equipment still rely on acoustic emission technical experts to analyze acoustic emission data in order to determine whether and how much leakage there is. Thus it limits the wide range of industrial applications of this technology. This paper analyzes the theoretical basis of acoustic emission monitoring of leakage in principle. Based on the actual field leakage experiments, the following quantitative relationships are obtained: the quantitative relationship between the amount of leakage and the acoustic emission parameters under the same pressure; the quantitative

relationship between different pressures, acoustic emission parameters and leakage rate under the condition of the same valve opening; the characteristic relationship between different leakage openings and acoustic emission parameters under the same pressure difference (tank wall plug). An online experimental demonstration system of leakage rate of water pipes is established. The acoustic emission collector automatically detects the leakage and leakage rates, and transmits the data to the cloud server. After the alarm conditions are set, the alarms will be pushed to the mobile phone if the alarm conditions are met. The cloud server is open for readers to view the results.

2.   Acoustic emission principles and theoretical basis of leakage monitoring

The principle of acoustic emission signals produced by leakage is that when the medium is ejected from the gap due to pressure difference to form turbulent flow, the medium in the turbulent flow has impact and friction with the sealing surface of the medium, which stimulates the elastic stress waves. The signal strength and frequency range of the elastic stress waves are closely related to the turbulent velocity of the medium, which is pressure difference, the leakage rate, the valve medium and the structures. The generated leakage signals propagate along the pipe walls and in the medium. When the acoustic emission sensor is coupled on a reasonable position on the surface of the pipe, the signal can be received. The piezoelectric effect of the sensor is used to convert the elastic wave signals into voltage signals, which are then amplified, analyzed and displayed by the acquisition AE equipment.
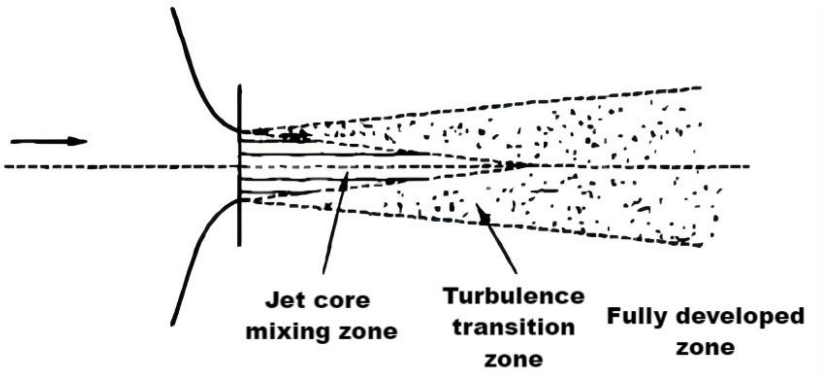
Fig. 1: Pipe jet leakage model.

Typical leakage signals have continuous and random non-stationary characteristics and their frequency distribution has an obvious steep peak, so that it has a certain anti-interference ability. It can be seen from the jet leakage model that the leakage signals are mainly generated in the turbulent mixing zone and the transition zone. The high frequency frictional impact signals are mainly generated near the leakage outlet while the low frequency oscillation signals are mainly generated in the position far from the leakage outlet. Generally speaking, the larger the leakage amount, the greater the energy density of the acoustic emission signals generated from the leakage. When the pressure difference increases, the impact sound caused by the leakage blockage will be generated, which is much higher than the turbulence signals, and these signals can be used as meaningful signals for detection.

When the gas or liquid leaks from the leak hole under a certain pressure, continuous mechanical waves are stimulated at the leak hole. When the acoustic emission waveform stimulated by the leak is observed by the oscilloscope, its shape is continuous waves with small amplitude fluctuation without following any patterns. The frequency band distribution of leakage acoustic emission wave varies from several Hz to several hundred kHz depending on the size of the leak hole, the leakage speed and the leakage medium. The suitable acoustic emission sensors are chosen to receive the acoustic emission waves from leaking location, then the mechanical waves are

transformed into electrical signals followed by amplification and then are transmitted to the acoustic emission host equipment. After signal processing and analysis, the amount of leakage information is obtained. After the appropriate threshold is set, when the AE signal reaches the threshold, it outputs an alarm. Through the Internet of Things (IoT) communication, the amount of leakage and the alarming AE parameters are transmitted to the Internet cloud platform, following by pushing the messages to the administrator user terminals, to achieve the purpose of intelligent alarming for unattended quantitative leakage monitoring.

3. Quantitative experiments of acoustic emission leakage

3.1 Experiment background introduction

The experiment was carried out at a submersible manufacturing company in Shenzhen. The submersible, the external valve and the flow meter used in the experiment are shown in Fig. 2 and Fig. 3. There is enough volume inside the submersible to pump air at a certain pressure, so that the pressure can be stabilized in a small range for the subsequent leakage tests. The valve inspected is a ball valve, whose nominal diameter is 15 mm. There is no leakage when the valve is completely shut. A gas flow meter is connected to the rear end of the valve to quantify the leakage rate.

The SAEU3H-4 digital acoustic emission detector from Qingcheng AE Institute (Guangzhou) was used in the experiment, with the compatible acoustic emission sensors, coaxial cables, acquisition AE cards and the analysis software to form the whole acoustic emission detection system. The acoustic emission sensor was the SR40M resonant sensor (the center frequency was 40 kHz and the frequency range was 15 kHz-70 kHz), and the external preamplifier had 40 dB gain. Details were shown in the figures below. The pencil lead breaking sensitivity test was 99 dB.
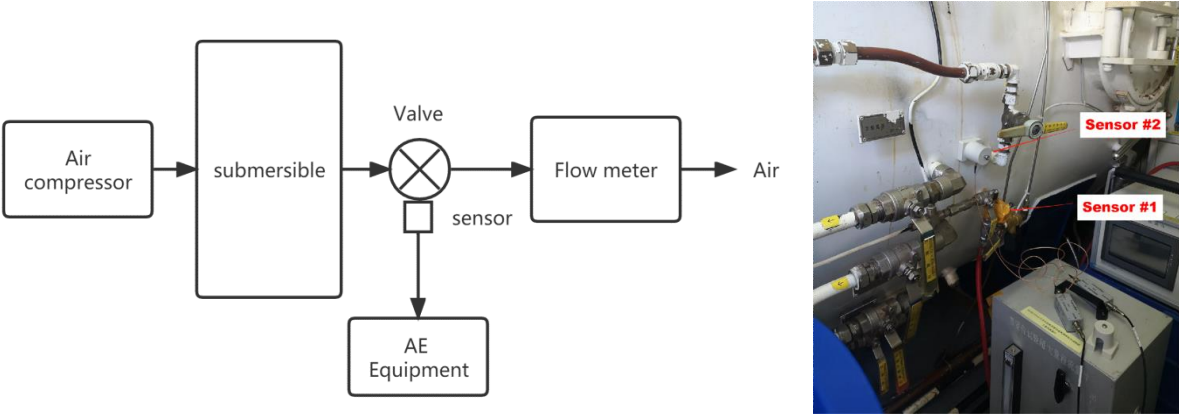
Fig. 2: Experiment connection and the field picture.

Table 1: Acquisition settings.

Sampling rate 1000kHz	EET: 30ms	Filter 20kHz~400kHz
HDT: 300us	HLT: 1000us	Threshold 23dB

3.2 Quantitative relationship between different leakage amounts and acoustic emission parameters under the same pressure difference

Tank gauge pressure: 0.1 MPa. Kept the acoustic emission equipment sampling the signals continuously. Different valve openings were obtained by manually turning the ball valve, and the leakage rate was measured by the flow meter. The flow meter remained stable in the following stages: 0 L/h - 42 L/h - 64 L/h - 310 L/h - 540 L/h - replacing with a large range flow meter - 650 L/h - 430 L/h - 230 L/h - 110 L/h - 38-6 L/h - 1.7 L/h - 0 L/h.

The leakage rate ranged from 0 to 650000 mL/h in a continuous process, and the relationships between the leakage and acoustic emission were shown in the figures below:
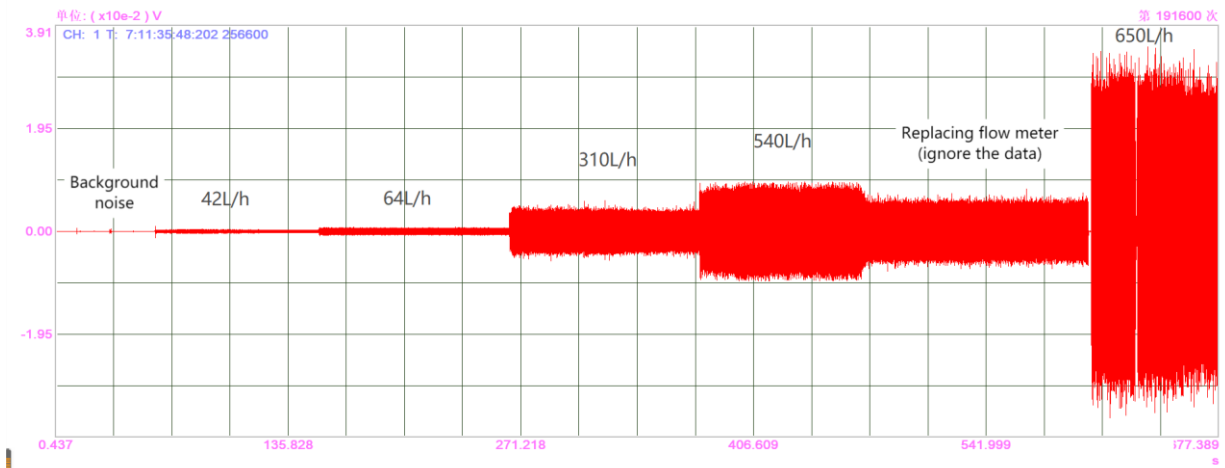
Fig. 3: Continuous waveform in time domain (different leakage rates at the same pressure).
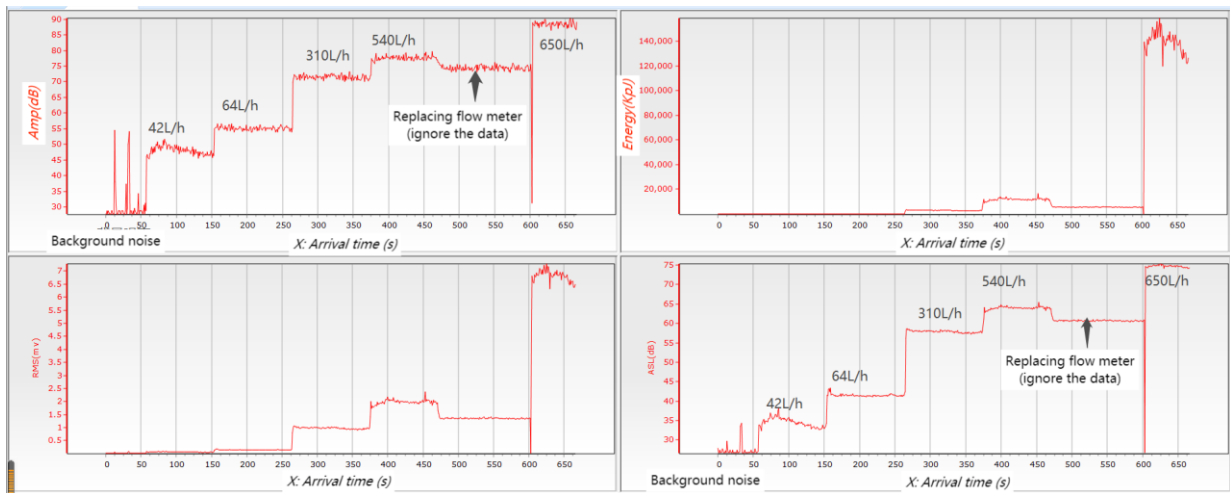
Fig. 4: Different AE feature parameters in time domain under different leakage rates.
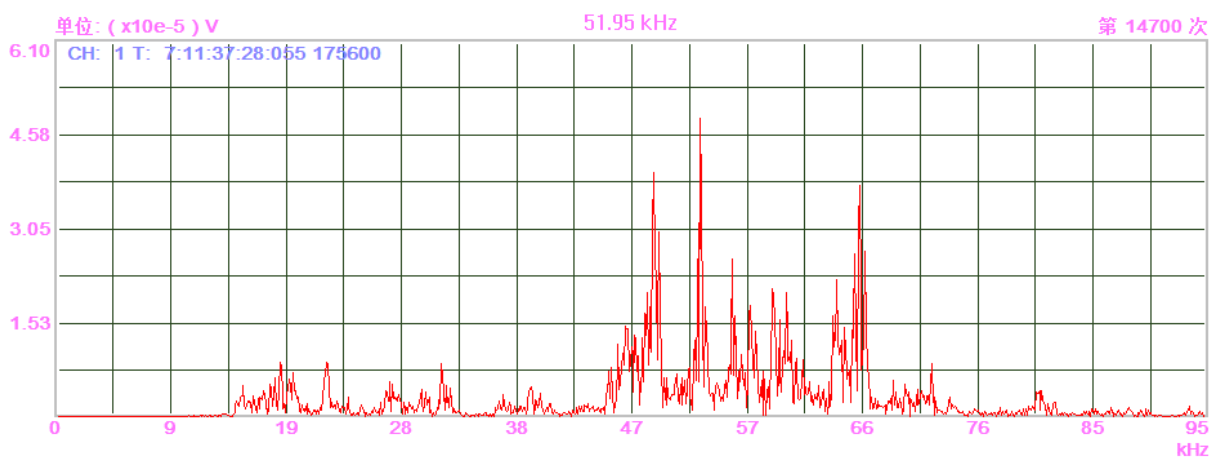
Fig. 5: Typical frequency domain view of leakage.

Statistical AE characteristic parameters at each stage are shown in the following table:

Table 2: Different leakage rates and AE characteristic parameters.

No.	Leak rate (mL/h)	Wave Amp. (mV)	Amp. (dB)	Counts	Energy (KpJ)	RMS (mV)	ASL (dB)	Freq. Range (kHz)
1	0	±2 (burr)	26.6-30	1-80	0-1	0.007-0.023	14-25	40-60
2	42000	±26	46-51	1530-1680	9-22	0.055-0.085	33-37	40-60
3	64000	±54	54-56	1600-1700	65-75	0.14-0.16	41-43	40-60
4	310000	±420	68-72	1700-1800	2500-3200	0.95-1.05	57-58	40-60
5	540000	±900	76-79	1750-1850	11000-13000	1.9-2.1	64-65	40-60
6	650000	±3000	85-90	1300-1450	120000-140000	6.5-7.5	74-76	40-60
7	430000	±820	72-76	1750-1850	8000-10000	1.7-1.85	62-63.7	40-60
8	230000	±600	70-74.5	1560-1724	4680-6480	1.25-1.46	60-61.1	40-60
9	110000	±300	63-70	1733-1800	1440-1980	0.7-0.8	54.9-56.3	40-60
10	38000	±102	56-60.7	1656-1756	138-185	0.21-0.25	44.6-46	40-60
11	6000	±6.1	38-45	1390-1560	3.3-8.8	0.035-0.045	29.2-30.7	40-60
12	1700	±4.2 (burr)	26.6-44	1-1529	0-8.3	0.006-0.2	11-32	40-60
13	0	±2 (burr)	26.6-30	1-80	0-1	0.007-0.023	14-27.4	40-60

The above data were drawn as follows: X axis (leakage rate) - Y axis (acoustic emission parameters) coordinate scatter diagrams:

Fig. 6: Correlation graphs of different leak rates and AE characteristic parameters.

Note that since the leakage rate from 540 L/h to 650 L/h was replaced with a large-range flow meter and there was some deviations between the flow meters, the 0-650 curve could not be completely consistent with the 650-0 curve. With the leakage pressure differences, the trending (slopes) was basically the same.

3.3 Quantitative relationship between different leakage amounts and acoustic emission parameters under the valve openings but different pressure differences

The valve opening was kept consistent throughout the process. The leakage rate was measured by the flow meter. The pressure in the tank increased to different pressures, and it was gradually reduced from high to low through other exhaust ports to maintain at several stable pressure stages: 0.42MPa, 0.31MPa, 0.21MPa, 0.1MPa, 0.05MPa, 0.02MPa, 0.02MPa (the valve was closed). The continuous process diagrams were (arrows showing the decompression process, and the value was not for reference):
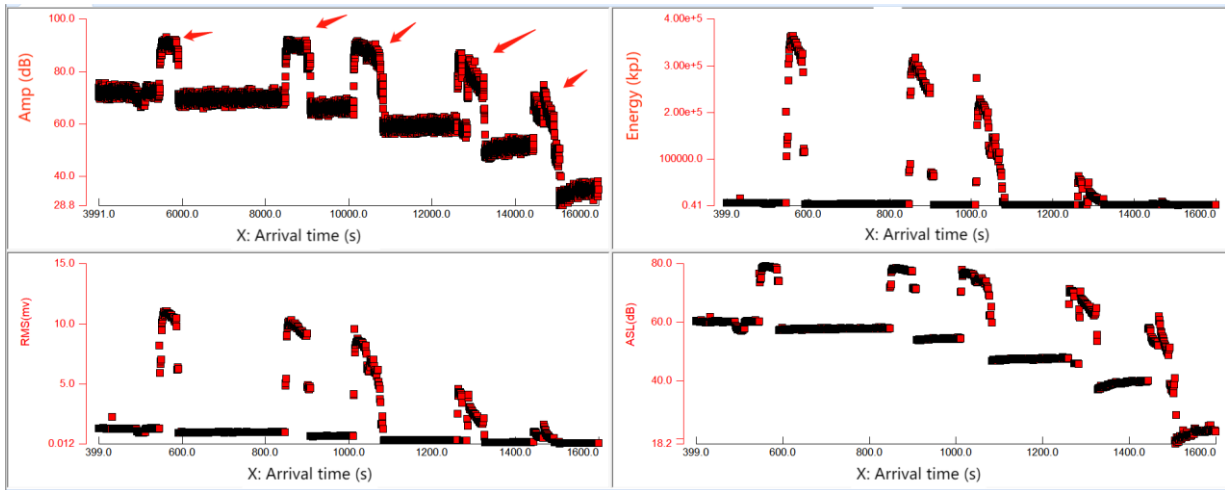
Fig. 7: Continuous waveform in time domain (same valve openings but different pressures).

After filtering processes, the following graphs were obtained:
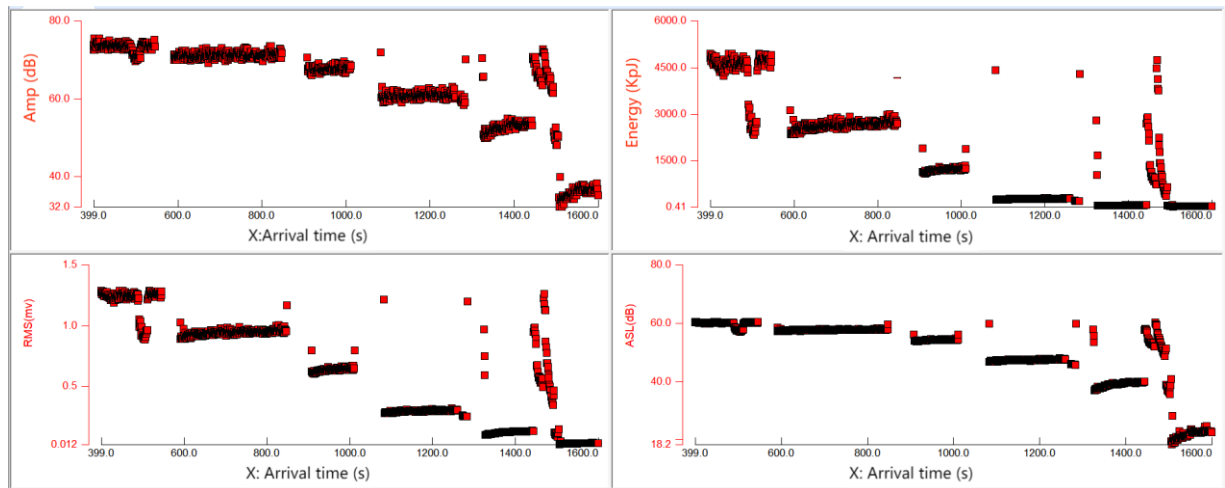
Fig. 8: Continuous waveform in time domain (same valve openings but different pressures) after filtering.

The tank pressure, leakage rate and acoustic emission parameters at each stage are shown in the following table:

Table 3: Different leakage rates and AE characteristic parameters under same valve openings but different pressure.

No.	Tank pressure (MPa)	Leakage rate (L/h)	Amplitude (dB)	Energy(KpJ)	RMS(mV)	ASL(dB）
1	0.42	286	72-75	4300-4800	1.2-1.3	60-61
2	0.31	227	69-72	2300-2700	0.85-0.95	56-58
3	0.21	168	65-68	900-1100	0.58-0.62	53-54
4	0.1	110	58-63	0.3-250	0.28-0.33	46-47
5	0.05	71	50-55	0.01-40	0.09-0.12	37-40
6	0.02	38	33-38	0.001-1	0.01-0.05	19-25
7	0.02	0	28-30	0-1	0.007-0.023	14-25

The above data were drawn as follows: X axis (leakage rate) - Y axis (acoustic emission parameters) coordinate scatter diagram:
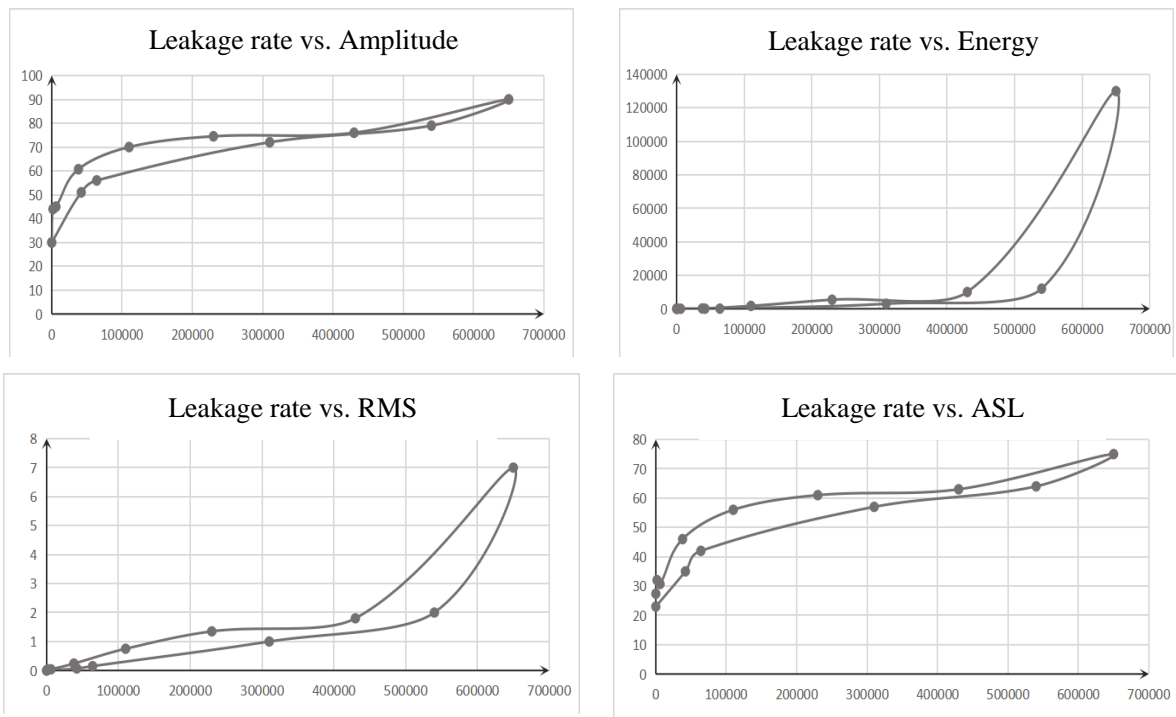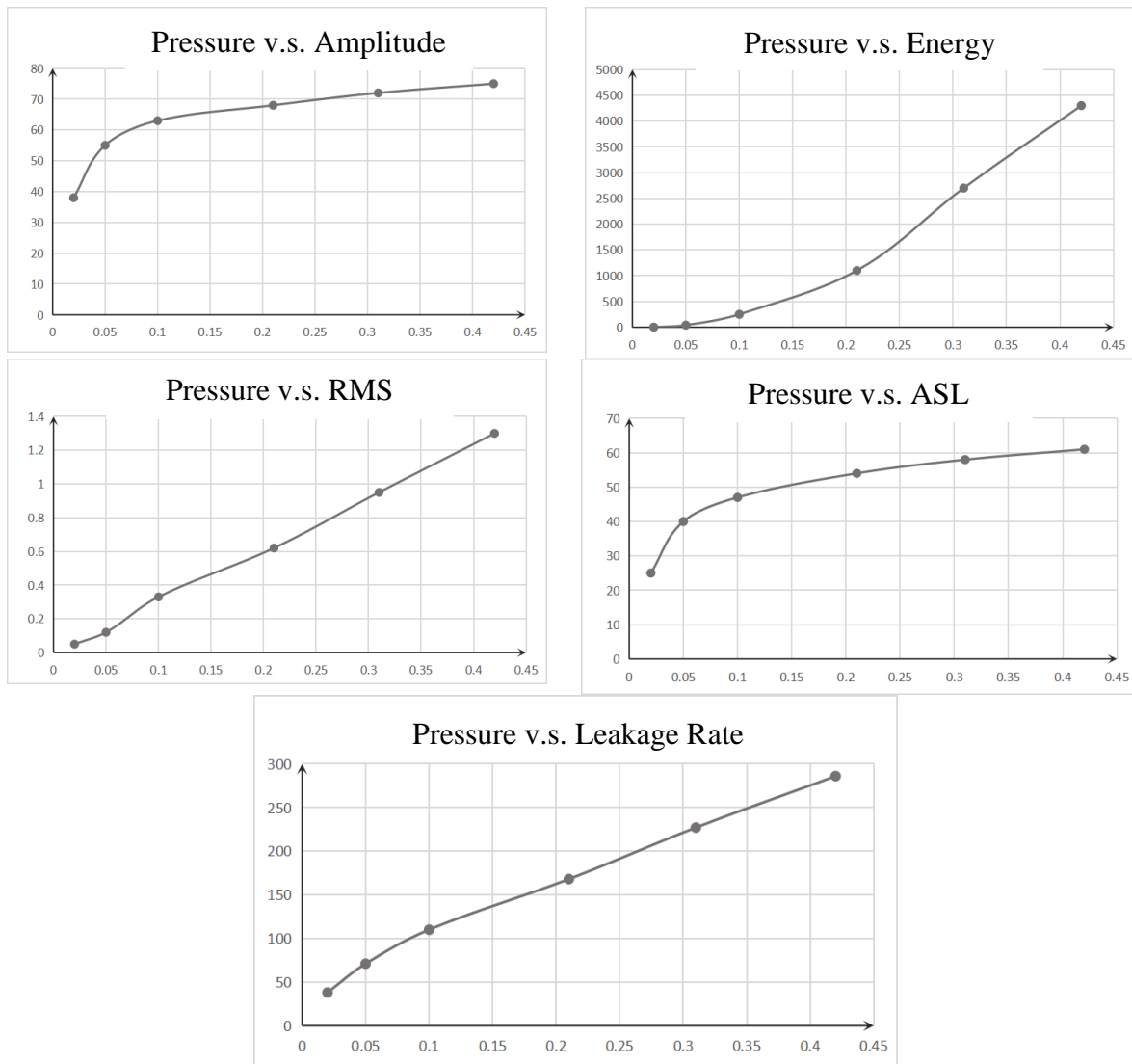

Fig. 9: Correlation graphs of different pressures and AE characteristic parameters.

3.4 Tank wall plug: The relationship between different leakage openings and acoustic emission parameters under the same pressure difference

The tank was filled with 0.1 MPa air pressure. The test object was the plug on the outer wall of the container. By rotating the plug at different angles, the gas was seeped from the plug gap. The approximate leakage situation could be known through air bubbles (when collecting signals, the bubbles on the plug would be wiped dry to eliminate the interference signals generated by bubble rupture). The sensor was positioned at 1 meter away from the plug. This experiment was a qualitative experiment of leakage. Rotating the plug at a small angle made the gas leak slightly, or a little larger amount. They would be compared with when there was no leakage, as shown in the figures below.

Fig. 10: Plug and when it leaked slightly.
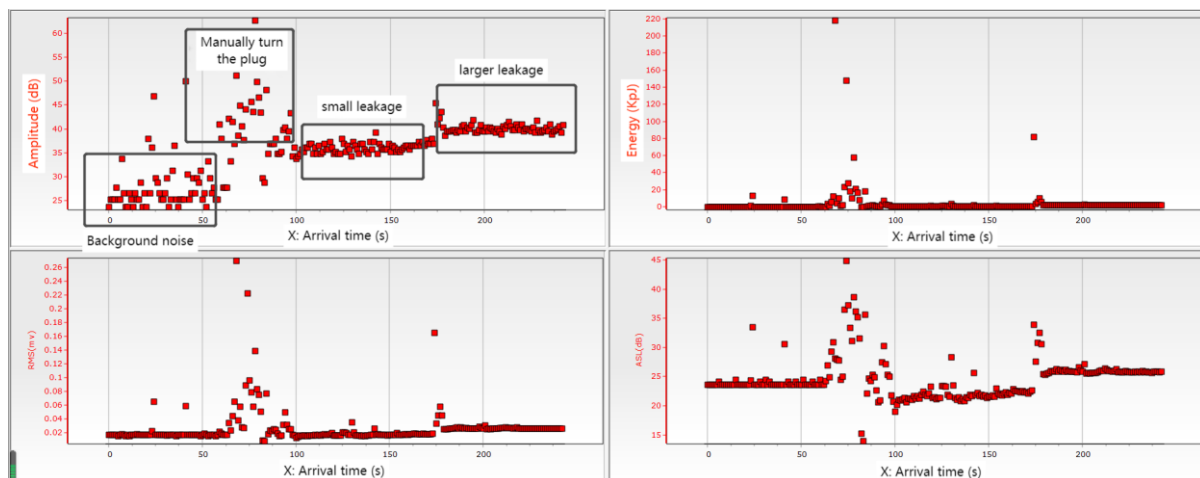
Fig. 11: Plug leakage experiment whole process correlation graphs.

3.5 Summary of the experiment

- The leakage was located near the valve spool. The closer the sensor was to the spool, the stronger the leakage signal was. So the best installation position of the sensor was near the spool.
- Low frequency sensors (15-70khz) could be used for gas leakage signals.
- Under the same pressure, the larger the leakage rate was, the larger the acoustic emission parameters (amplitude, energy, RMS, ASL) were. The amplitude and ASL increased rapidly in the front segment and slowly in the back segment, while the energy and RMS increased slowly in the front segment and quickly in the back segment.
- Under the same leakage aperture: pressure was basically proportional to the leakage rate; Pressure was basically proportional to RMS. The relationship between pressure and

amplitude: with the increase of pressure, the amplitude increased rapidly at first, then became slowly; The relationship between pressure and energy: with the increase of pressure, energy rose slowly at first, then rapidly; The relationship between pressure and ASL: with the increase of pressure, the amplitude increased rapidly at first, then slowly.

- Energy, RMS and ASL could all be used as the criterion of leakage quantification, and ASL was the best.
- Plug (pipeline leakage) qualitative judgment of leakage acoustic emission characteristics were obvious. Even 1 meter away from the leak source, it could still distinguish a very small leakage signal (the foam bubbles determined that the leakage was very small. The foam bubbles needed to be wiped dry during measurement).
- Medium, pressure difference, leakage aperture size, sensor installation position and other factors directly affected the acoustic emission characteristics of valves and pipelines, which need to be calibrated on site. Once calibrated, they will be used for life.

4. Online water pipe quantitative leakage demonstration experimental system

4.1 System introduction

As shown in the figure below, the faucet and water pipe were used to generate leaks, and the sensor was installed next to the faucet. The RAEM1 acoustic emission remote system from Qingcheng AE Institute was applied. The collector body was a small aluminum alloy shell cylinder. It was an intelligent IoT AE system integrating AE signal acquisition, analysis, storage with communications networking. It adopted the Linux system which was a long-term stable operation including watch-dog function and it was suitable for unattended monitoring for a long time. The collector collected signals and automatically determined whether there was leakage and the amount of leakage, and then transmitted them to the cloud server through 4G. Users could log in to the cloud server to view real-time and historical parameters, or set alarm push to mobile phones. The collector was set: sampling frequency: 1000kHz; the EET: 30ms; HDT 300us; HLT 1000us; threshold 30dB; Sensor resonant frequency 35kHz and frequency range 15khz-70khz. The schematic diagram and equipment layout were shown below:
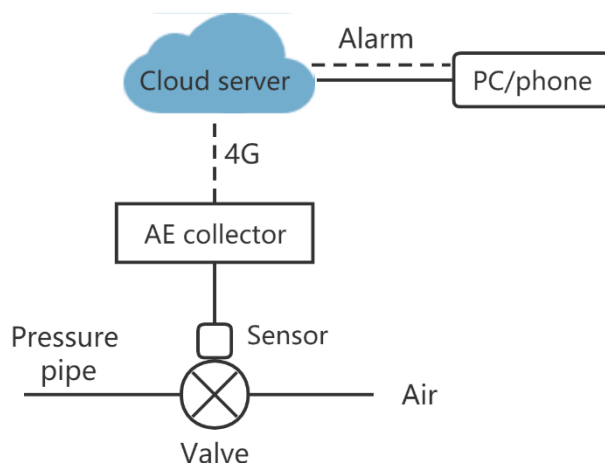
Fig. 12: Online water pipe quantitative leakage experiment system.

4.2 Experiment calibration

Opened the faucet at different angles and connected the leaked fluid with a measuring cup. The relationship between the leakage rate and ASL was shown in the following table:

Table 4: Faucet leakage rate calibration.

No.	Leakage rate (L/H)	ASL (dB)
1	0	32
2	8.5	38
3	18	47.8
4	29.5	53.2

Plot the scatter diagram as shown below:
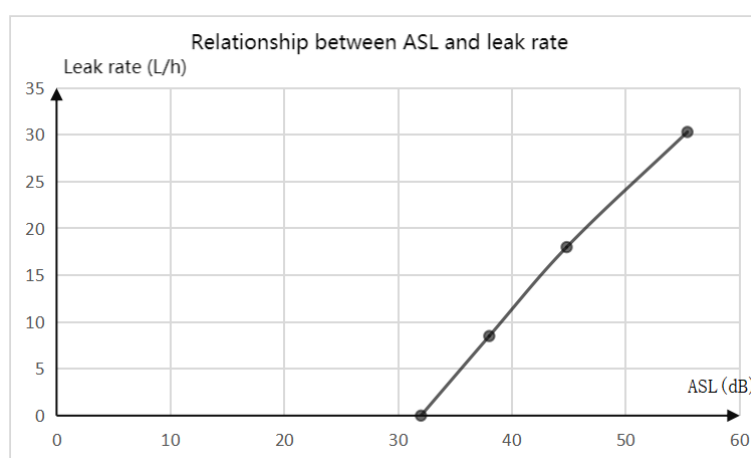
Fig. 13: Correlation graph of faucet leakage rate and ASL.

According to the figure above, ASL and leakage amount basically have a straight slope. Let the leakage amount be:

$$L = k \times ASL + b \tag{1}$$

No. 2 and No. 3 data were k =1.4 and b = -44.7. Therefore, the relationship between leakage amount and ASL is:

$$L = 1.4 \times ASL - 44.7 \tag{2}$$

When the above formula was set to the collector, the collector could calculate the leakage amount and transmitted the leakage parameters to the cloud platform through 4G to achieve quantitative online leakage monitoring.

4.3 On-line quantitative leak monitoring

Logged in to the cloud server to view real-time data. Below was the open cloud server for long-term online monitoring where the readers could access to view data at any time. (url: https://signin.aliyun.com/login.htm#/main; Account: qc@1269046717299274.onaliyun.com; Password: qc123456). As shown in the figure below, it could be clearly seen the time when the leakage occurred and the corresponding leakage rate.
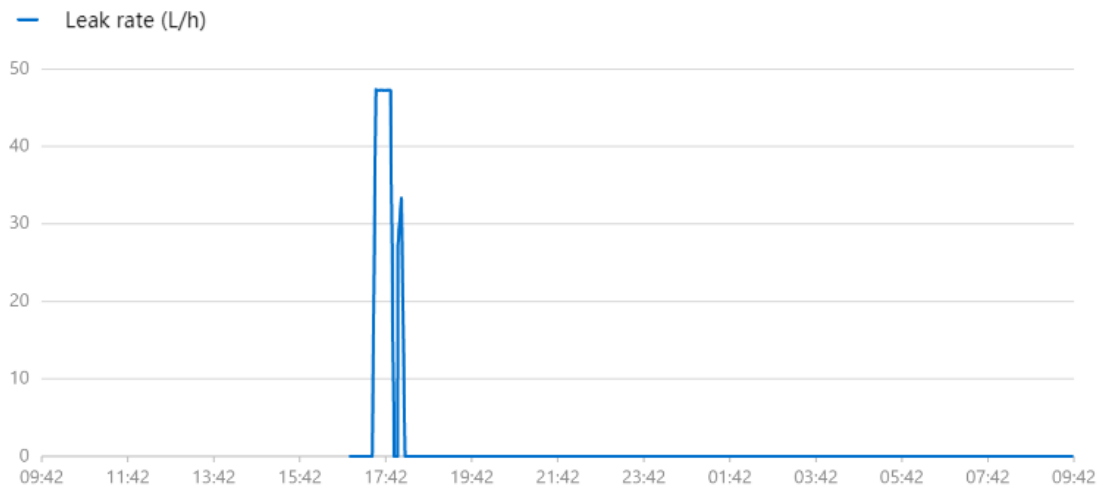
Fig. 14: Cloud server historic leakage amount.

The appropriate alarms were set. The setting rules of this demonstration were as follows: 1L/H≤ leakage ≤10L/H output level 2 alarm; 10L/H≤ leakage ≤20L/H output level 3 alarm; 20L/H≤ leakage ≤30L/H output level 4 alarm; 30L/H≤ leakage ≤10L/H output level 5 alarm. For example, the setting of level 3 was as shown below.

Fig. 15: Set proper alarm.

When the alarm condition was reached, the system pushed the alarm information to the mobile phone. You could also log in the server through the mobile phone/computer to view and process the historical alarm information, as shown in the picture below.
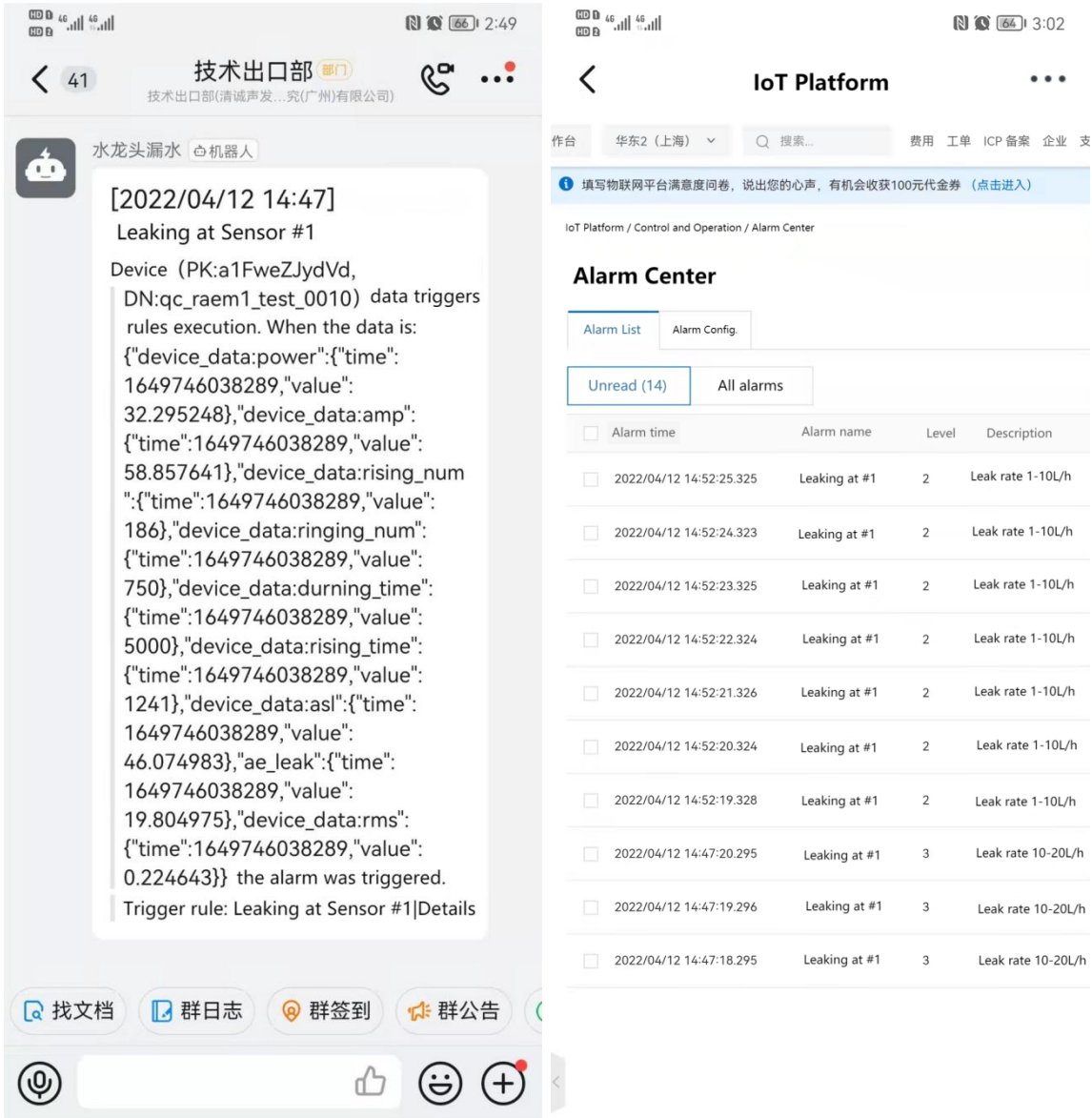
Fig. 16: Alarms on the phone or cloud server.

5. Conclusions

The AE equipment of the Internet of Things can automatically control data collection, data analysis and automatic alarm pushing through embedded software and hardware to achieve long-term unmanned quantitative leak monitoring. Through automatic data processing, massive acoustic emission data can be converted into simple and understandable leakage levels, which can eliminate the trouble that traditional acoustic emission technology relies on professionals to analyse acoustic emission data, so that users who do not understand acoustic emission can quickly get started. Moreover, the data processing is centralized in the collector, and only a small amount of data is output/uploaded, which can effectively reduce the requirements of data communication speed and equipment cost. Its advantages of long-term stable operation, automatic alarm, quantitative monitoring and low equipment/operation cost are of great significance to industrial applications.

6. References

[1] Shen, G. (2015). Acoustic emission detection technology and its application. Beijing - Science Press.

[2] Kong, D. (2010). Application of acoustic emission technology in on-line valve leakage monitoring. Beijing - Beijing University of Chemical Technology.

[3] Xie, J., Liu, S. (2019). Internet of Things Acoustic Emission: Systems and Applications.

[4] Shen, G. (2019). Advances in Acoustic Emission Technology. US - Springer, p. 19-31.

[5] Jia, N., Jiang, X., Sun, J. (2014). Research on valve Leakage Monitoring system and positioning system of gas supply pipeline based on acoustic signal. Forest Engineer, vol. 30, p. 96-98.

Measurement Equipment and Customized Solutions for Acoustic Emission Testing

We develop and produce innovative technology that makes a true difference for the safety of humans, the environment and the preservation of infrastructure. This commitment differentiates us from other suppliers and defines who we are: Vallen Systeme – The Acoustic Emission Company

AMSY-6 System

The AMSY-6 System is a fully featured, multi-channel Acoustic Emission measurement system. It forms a flexible basis that can be customized, extended and configured to the needs of an application.

The field of applications ranges from various inspection tasks such as pressure vessel testing, leakage testing to research and structural health monitoring of large objects

spotWave Device

The spotWave device is a portable single channel AE-measurement unit that can be controlled by a Laptop, Tablet PC, Smartphone or IoT device. It is a fully featured AE measurement device. The software supports the Vallen pridb and tradb data file format.

Typical applications are leakage detection, hot spot monitoring, AE research, etc.

Acoustic Emission Sensors

A wide range of sensors is offered covering any AE testing application.

Sensors are available for standard environments, explosion hazardous areas, for underwater applications, high temperature surfaces and harsh environments.

Sensors supporting the SmarLine™ protocol register themselves with an AMSY-6 system and minimize the configuration effort.

Vallen AE Suite Software

Unmatched flexibility and transparency at all times makes the Vallen AE Suite Software the preferred tool of choice for all acoustic emission applications.

Its modular architecture can be configured and extended to match any requirement of an application.

It offers everything from simple data visualization over complex analysis and pattern recognition to automation and web-based dashboards.

Measurement data is written to a database structure that complies with SQLite3 standard. It can be accessed from any application supporting SQLite3 which includes Matlab, Python and many more fast development environments.

CHARACTERIZATION AND EARLY DETECTION OF HYDROGEN EMBRRITTLEMENT IN OFFSHORE BOLTS USING ACOUSTIC EMISSION

Nokhaiz Sabir[1], Duncan Billson[1], David Hutchins[1] and Stephen Grigg[2]

[1]University of Warwick, United Kingdom;
u2096946@live.warwick.ac.uk, d.r.billson@warwick.ac.uk, d.a.hutchins@warwick.ac.uk
[2]TWI Ltd; stephen.grigg@twi.co.uk

ABSTRACT

In this project the non-destructive testing technique of acoustic emission testing will be used to determine the location of hydrogen embrittlement within offshore bolts. An initial testing plan has been provided which outlines that a fatigue test will be performed on the chosen bolt size and material. The obtained results will be used to link the fatigue data with the AE signals captured during testing and justify the choice of this NDT technique for detection of location of crack within the bolt. This will be later developed to detect cracks developed due to hydrogen embrittlement in high- strength steel bolts. To achieve this, a thorough literature review on hydrogen embrittlement and acoustic emission has been provided in this report along with the future plan for testing that will be used to gather experimental data which will justify this theory.

Keywords: Hydrogen embrittlement, acoustic emission, corrosion, cracking, fastener.

1.   Background and scope of the project

When hydrogen gets absorbed into the surface of steel, it can lead to corrosion and cracking. Therefore it has been widely investigated as it can lead to catastrophic results if not accounted for [1]. Large bolts and other connectors such as studs and fasteners, typically used in the offshore Energy and the oil and gas industries, have been reported to fail prematurely due to hydrogen induced cracking (HIC) [2].

To prevent such failures, a set of guidelines was published by the Energy Institute (an independent, not-for-profit, safe space for evidence-based collaboration) which outline the management of the integrity of bolted joints through non-destructive testing (NDT) techniques [3].

Acoustic Emission (AE) is the spontaneous release of strain energy which is emitted during a damage event (such as corrosion or cracking) [4]. By placing sensors on a structure, AE emitted from damage can be detected and located and thus, the damage can be detected, located, and characterized. By monitoring for AE over time, an assessment of a structures condition and an estimate on the useful remaining life can be made [5]. AE has been demonstrated to detect HIC and other hydrogen embrittlement mechanisms early [6-9]. Therefore, there is much interest to develop AE technology to explore the relationship between hydrogen embrittlement and AE for the monitoring of critical bolts, fastenings, and connections.

2. Project outline

The aim of this project is to use microstructural observations and experimental data to provide qualitative agreement between the embrittlement process and acoustic signals. In line with this in mind the following are the objectives of this project:

- Conduct a review of the mechanisms for hydrogen embrittlement in steel structures, along with how AE can be used to detect hydrogen-induced cracking within steel structures.
- Develop a methodology for using AE to monitor bolts for hydrogen embrittlement under representative in-service conditions
- Design an experimental test program that will aim to establish the parameters and conditions for successfully detecting AE from hydrogen embrittlement. This will include identifying sensors with appropriate sensitivity and frequency response to maximize the probability of detection.
- Develop the data handling and processing methodologies to achieve successful detection and use the results to identify the exact location of hydrogen embrittlement.
- With the help of obtained results, build a predictive model which will determine the current condition of a bolt and its remaining useful life.

3. Literature review

3.1 Introduction
In metals and alloys, hydrogen embrittlement (HE) occurs when hydrogen combined with stress, either externally or internally, leads to a permanent loss of ductility [6]. According to how hydrogen embrittlement affects the body, it falls into two categories: internal hydrogen embrittlement (IHE) and environmental hydrogen embrittlement (EHE). In an electroplating and pickling process, hydrogen is absorbed within the structure and causes IHE [1]. The hydrogen absorbed by steel structures from hydrogen-rich surroundings can cause EHE [5]. Corrosion of steel structures results in hydrogen being produced, which gets absorbed into the structure and results in embrittlement. As a result, cracks begin to form in steel structures, a process known as either stress corrosion cracking (SCC), or hydrogen induced stress corrosion cracking (HISCC).

3.2 Conditions needed for embrittlement
Before hydrogen embrittlement (HE) can occur, certain conditions must be present. As shown in Fig. 1, these include:

- A hydrogen source is present that disperses atomic hydrogen in the substance in an appropriate manner.
- There are sufficient levels of stress in the material to cause subcritical fracture through simultaneous and synergistic action with atomic hydrogen (the threshold level for damage within a hydrogen-charged, and hence embrittled, material will also be reduced).
- Certain hydrogen distribution and stress combinations can cause hydrogen embrittlement in certain materials.
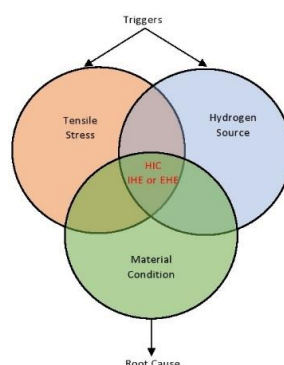

Fig. 1: Conditions contributing to the failure due to hydrogen embrittlement.

3.2.2 Damage mechanisms

A steel with a tensile strength of 1,000–2,000 MPa (150–300 ksi) is considered to be a high strength steel. When high-strength steel is tensile stressed, such as when tightening a high-strength fastener, the tension forces atomic hydrogen within the steel to diffuse (migrate) to the point of maximum stress (e.g., at the first engaged thread or at the fillet radius under the head of a bolt). Steel that is ordinarily ductile gradually turns brittle when higher concentrations of hydrogen collect at this region. A hydrogen-induced (brittle) microcrack eventually results from a concentration of tension and hydrogen in one place. As hydrogen flows to follow the tip of the developing fracture, the brittle microcrack continues to grow until the fastener is overloaded and ruptures. This hydrogen degradation mechanism can cause the fastener to fail at stresses far lower than the fastener's fundamental strength as evaluated by a typical tensile test.

Theoretical models that describe hydrogen damage mechanisms under idealized conditions have been proposed since the 1960's [1]. In the case of high strength steel, these models are based primarily on two complementary theories of decohesion, and hydrogen enhanced local plasticity (HELP) [1]. Given the complexity of HE phenomena, hydrogen damage models continue to evolve and be refined thanks to the efforts of theoretical and experimental researchers around the world. Grain boundaries, dislocations, precipitates, inclusions, and other metallurgical characteristics within the steel microstructure are examples of hydrogen "traps." As a result, hydrogen is no longer free to diffuse (i.e., travel) to locations of high stress, where it may participate in the HIC mechanism. The bonding energies of traps are used to classify them as reversible or non-reversible. Low bonding energies define reversible traps; in other words, hydrogen is more easily released from the trap. Non-reversible traps are characterized by high bonding energies; in other words, hydrogen requires a great deal of energy (e.g., heat) to be released from the trap. Hydrogen that is not trapped is called interstitial hydrogen; it is free to move in the metal lattice. Interstitial hydrogen is also called diffusible hydrogen.

3.2.3 Fracture surface

The intergranular brittle morphology is usually a good way to deduce surface of fracture that occur due to hydrogen induced cracking. This is usually the case for quenched and tempered high strength steels. It can be clearly seen in Fig. 2 below, which shows the brittle surface of the fracture which is due to hydrogen-induced cracking. The fracture surface morphology also depends on the extent to which hydrogen embrittlement has occurred and how susceptible the material is to hydrogen-induced cracking. As the Fig. 2 below shows that for a higher degree of hydrogen embrittlement, the surface has a characteristic appearance that is different to that from ductile fracture.
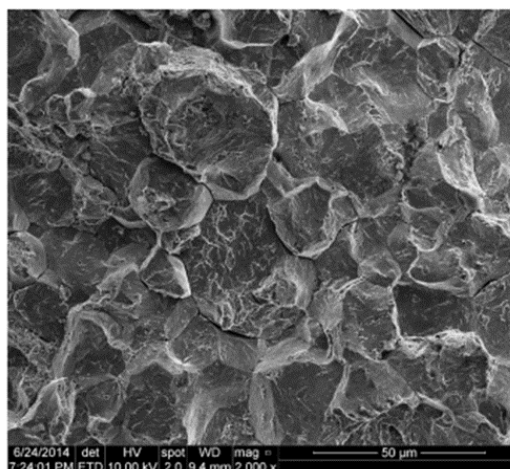
Fig. 2: Brittle fracture surface of quenched and tempered high-strength steel using electron microscope [1].

A fracture in a tensile-loaded fastener often expands to the point where the fastener's decreased cross section can no longer bear the applied stress. The fastener quickly ruptures at this location (i.e., fast fracture). A typical fracture surface related to quick rupture is ductile, as evidenced by the presence of ductile dimples. Fig. 3 below shows a fracture surface where the brittle hydrogen-induced crack propagation came to a halt (i.e., the terminal crack tip) before the fastener's ultimate quick rupture. In this case the surface shows a ductile failure instead of brittle. Some parts of structure in the figure show brittle failure and this indicates areas where hydrogen-induced cracking has occurred while the ductile failure surface shows that hydrogen-induced cracking process has ended, and material can no longer withstand the stress it is under.
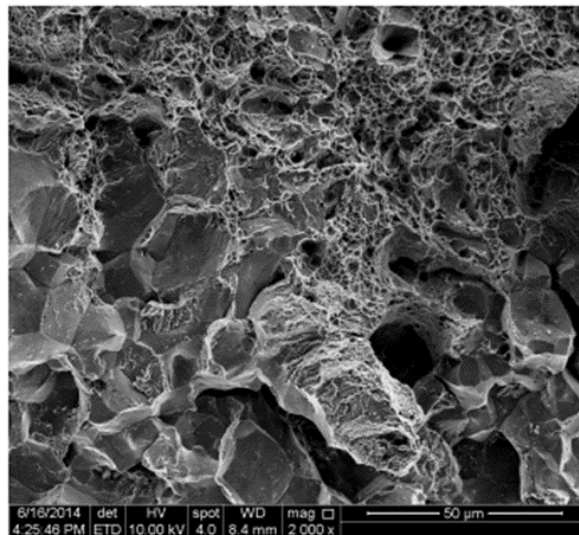
Fig. 3: Fracture surface with brittle surface showing hydrogen-induced cracking and ductile surface showing the final failure using electron microscope [1].

3.3 Acoustic emission

3.3.1 Introduction

The technique of AE is suggested in this study for detecting and monitoring hydrogen embrittlement and cracking as a non-destructive evaluation (NDE) approach for identifying active defects in materials [4]. There is an energy release when a fracture propagates (i.e., grows larger). Elastic waves propagate through the material because of the linked events, resulting in measurable AE signals. Determining the cause of AE sources is a challenge, as many people consider corrosion as mainly a manifestation of erosion and damage, where the acoustic source is not the corrosion itself, but its consequences, including bubble evolution, crack propagation, growth, and evolution of corrosion product deposits. As a matter of fact, there are good correlations between specific AE parameters and corrosion damage in various cases [7].

There are several studies that have already applied the AE technique to monitor HE. Both Cayard and Kane [8] as well as Gingell and Garat [9] showed that AE energy accumulation was greater during Stress Corrosion Cracking (SCC) tests leading to metal failure as compared to no failure tests. Weng and Chen [10] discovered a link between HIC damage as measured by the Crack Length Ratio and AE energy levels. In addition, Gingell and Garat [9] demonstrated that AE may be utilized to differentiate between the start and propagation stages of SOHIC (Stress Oriented Hydrogen Induced Cracking) growth [11].

3.3.2 AE signal detection

AE testing involves recording and evaluating AE signals to identify evolution of damage [12]. This is usually accomplished by direct coupling of piezoelectric transducers on the surface of the structure under test and loading the structure. The output of the piezoelectric sensors (during stimulus) is amplified through a low-noise preamplifier, filtered to remove any extraneous noise, and further processed by suitable electronics (as shown in Fig. 4). AE tests can non-destructively predict early failure of structures. Further, a whole structure can be monitored from a few locations with additional sensors and while the structure is in operation.
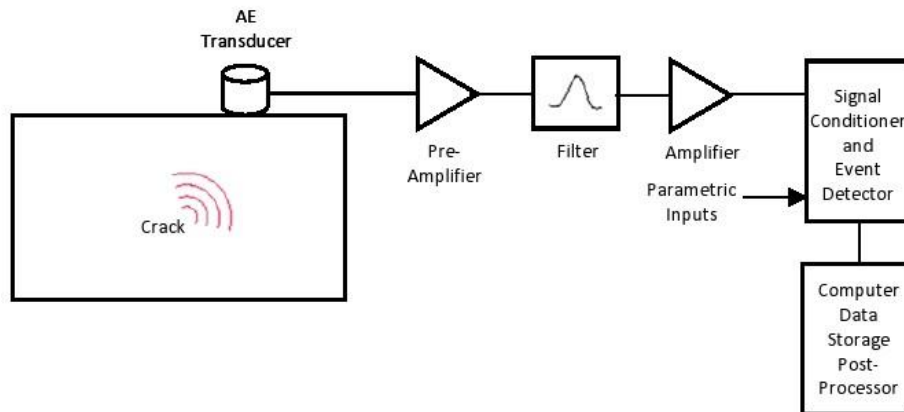
Fig. 4: A typical AE system for detection of cracks.

3.4 Experimentation

3.4.1 Initial testing plan

Most bolts are subjected to fluctuating loads when in service, leading to the well-known fatigue phenomenon which is responsible for most of the premature failure in bolts. Bolted joints are widely used for assembly of engineering structures thanks to their ease of assembly and disassembly and their low cost. Fatigue failures of bolted joints are often costly and occasionally fatal. This motivates the characterization of the fatigue strength of bolts. The testing of the axial fatigue strength of bolt and nut assemblies is the subject of international standardization, for example [13].

Fatigue failures occur primarily in the bolt, and the stresses in the nut are generally much lower. The fatigue strength of the bolt is expressed in terms of the engineering stress amplitude, e.g., force amplitude over cross sectional area, thus ignoring the stress concentrations in the thread root and in the transition from bolt shank to bolt head.

The initial testing setup will be axial fatigue testing which will be conducted on the chosen bolt grade and size following the ISO 3800 standard [13]. The aim of this axial fatigue testing to test the effect of load on the fatigue life of bolts by producing an S-N curve for different levels of load. The key feature will be to test several bolt grades to see which one will be most suitable for final testing bolt grades like AISI 4340 and property class 10.9 are the two options based on ISO 898 – 1 standard [13]. Along with axial fatigue testing, sensors will be located at appropriate parts of equipment to capture the AE signals which will then be co-related to the SN curve obtained.

3.4.2 Bolt material

Mechanical qualities like as strength and toughness, corrosion resistance, and resistance to stress corrosion cracking, also known as HE or sustained load cracking, are all important considerations when choosing bolt materials. Several materials have been considered for use in subsea fasteners, including steels, stainless steels, nickel alloys, cobalt-nickel alloys, beryllium-copper alloys, and titanium alloys. There is evidence that high-strength steels are susceptible to stress corrosion cracking and HE's [14].

As the yield strength increases, the susceptibility to cracking increases. The yield strength of steels below 827 Mega Pascals (MPa) is generally resistant to EAC. However, as strength increases, the resistance decreases. There is a possibility to find the right balance to have higher yield strength and still have the resistance to hydrogen-induced cracking. It has been found that materials become less useful in these environments if their pressure goes above 1035 MPa; similar conclusions were made by Chung and Gangloff [16, 17]. From this work, selecting materials for purposes requiring high strength becomes significantly more challenging once the strength exceeds 1035 MPa.

Steel with lesser toughness and ductility is intrinsically more brittle and vulnerable to HE than steel with higher toughness and ductility. When the required hardness is more than 39 HRC, the susceptibility of steel fasteners increases dramatically (380 HV). Steel fasteners having a specified hardness of less than 39 HRC (380 HV) are usually resistant to hydrogen embrittlement failure.

When it comes to preventing internal hydrogen embrittlement (IHE), some standards define critical hardness limits as low as 31 to 35 HRC. Based on the theory presented and the work carried out previously property class 10.9 Steel grade will be the material type for bolts as this is a high strength steel with yield strength and Hardness lying in the suggested range which is safe to consider [13].

3.4.3 Test specimens

The bolts to be tested will be M20×400 class 10.9 bolts. The bolts and nuts were all from the same series made by a single manufacturer. The mechanical properties of the bolt material are given in Table 1 below [13].

Table 1: Mechanical and Physical properties of Property Class 10.9 Bolts [13].

PARAMETER	VALUE
Tensile strength, R_m, MPa	1000 - 1040
Stress at 0,2 % non-proportional elongation, $R_{p0,2}$, MPa	900 - 940
Stress under proof load, S_p^f, MPa	830
Proof strength ratio, $S_{p,nom}/R_{p0,2\ min}$	0.88
Rockwell hardness, HRC	32 - 39
Minimum ultimate tensile loads — ISO metric coarse pitch thread	87700
Proof loads — ISO metric coarse pitch thread	70000

The M20 bolt is a very big specimen to test and for initial testing, it will be aimed to conduct a catastrophic failure. As a result of this the time of failure would be too long. Thus, to make the initial testing more simplified, a notch will be introduced into the M20 bolt, which will reduce the size of the bolt to an M12. The notching on the bolt will create an area of stress concentration which will in turn reduce loads and time required to fail the bolts. Fig. 5 below shows the measurements of bolt to be tested and the position of notch on the bolt.
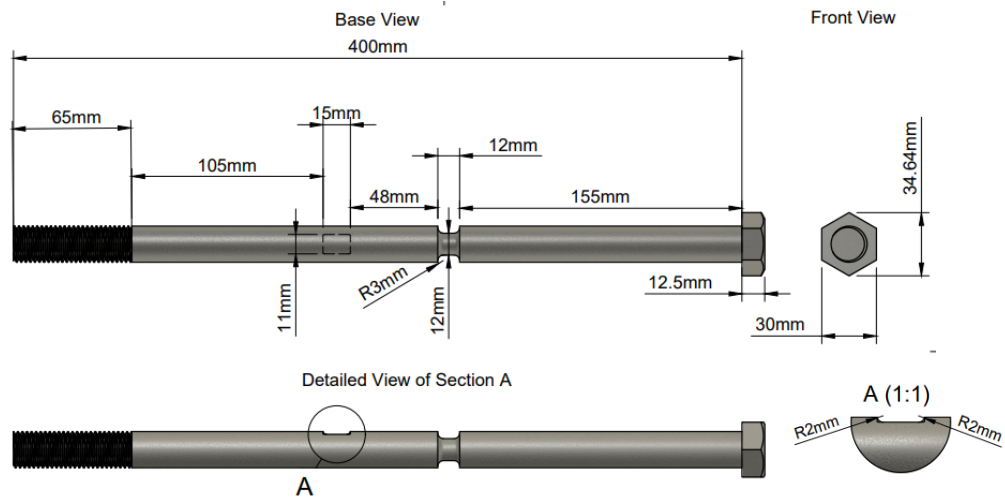
Fig. 5: Bolt Size and Measurements for testing.

It also shows that a flat surface will be created on the surface of bolt which is represented by section A in Fig. 5. This surface is created to allow space for mounting of the AE sensors on the bolt during testing. Care has been taken in sizing and location of this surface so that it does not create another stress concentrated area.

3.4.4 Test apparatus

The testing equipment will be able to keep the loads within 2% of the required values during the test and will have a device to track and record the total number of cycles each test. To achieve this precision, the testing machine will be calibrated on a regular basis. The testing machine's frequency range should be between 1 to 3 Hz. The machine must cause a sinusoidal load variation in the test item.

Fig. 6 below shows a design of the rig that will be used to test the bolts. To carry out the fatigue testing on the bolts, a rig has been designed which can hold the bolt in place and allow for the design stress amplitude to be applied on the bolt. The rig is designed to fit an M20 bolt in place and will also be used for the testing of notched bolts which will be notched down to size of M12. This means that M12 and M20 bolts will both be tested using the same rig.
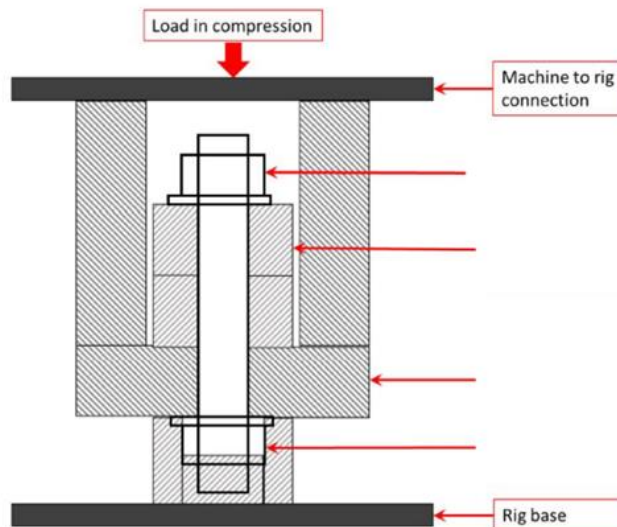
Fig. 6: Schematic of the Rig Design for Fatigue testing of M20 bolts.

3.4.5 Test procedure

For various values of mean stress in the range $0 < \sigma_{max} < Sy$, where Sy is the material's yield strength, an S-N curves will be formed. The ISO 3800 standard shall be followed to obtain the S-N curve [18]. Fatigue tests must be performed on at least four stress levels to estimate the finite life range. The stress levels should be set so that the number of stress cycles achieved is between 10^4 and 5×10^5. The stress loads at which the test will be run are calculated by estimating the stress concentration factor from Peterson's stress concentration chart shown in Fig. 7 [19]. According to this the equation for stress concentration factor is as follow:

$$K_t = \frac{\sigma_{max} \, \pi \, d^2}{4 \, P} \tag{1}$$

Where σ_{max} is maximum stress, K_t is stress concentration factor, P is maximum load and d is the diameter of the specimen after notch. The chart for grooved round bar in tension has been taken as it is most applicable to a bolt. The chart is shown in the figure below with various values of K_t against the ratio r/d and there are separate curves for each value of D/d. For this system since the original diameter of bolt is 20 mm so $D = 20$ mm and this diameter will be reduced to 12 mm so $d = 12$ mm. As a result, the ratio D/d will be equal to 1.67. Taking an estimate value of r to be 3 mm, the ratio r/d will be equal to 0.25. Looking at the graph, for $r/d = 0.25$ and $D/d = 1.5$ as an estimate, the K_t value will be 1.8 approximately.

Now using the initial value of σ_{max} to be equal to the yield strength of the material which is $\sigma_{max} = 1114 \, N/mm^2$ and putting all values in equation (1), we get the maximum load to be calculated as follow

$$P = \frac{1114 \times \pi \times 12^2}{4 \times 1.8} \tag{2}$$

$$P = 69994.68 \, N \tag{3}$$
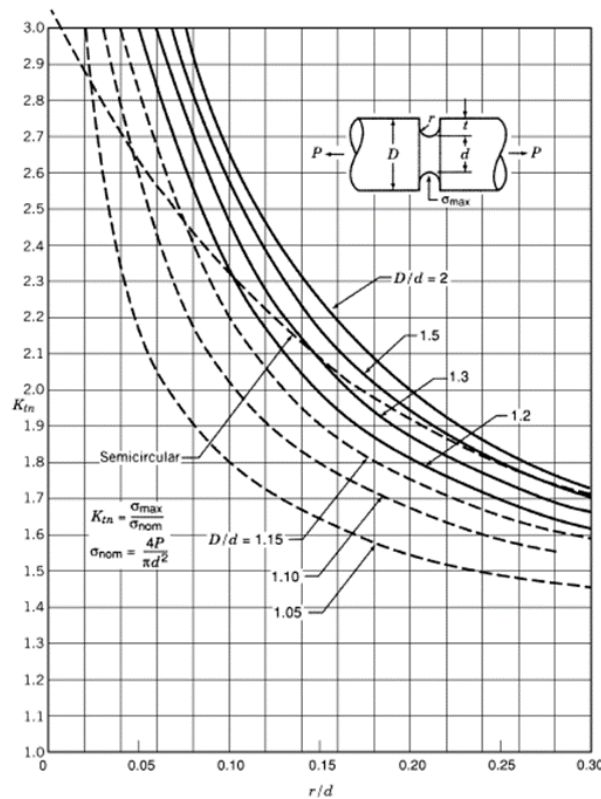
Fig. 7: Stress concentration factors for a grooved round bar in tension [19].

Therefore, the first test will be performed at stress amplitude of 1114 N/mm^2 and a stress load of 69994.68 N. Similarly, the next tests will be conducted by lowering the stress amplitude by 5% each time and calculating the corresponding stress loads for each stress amplitude in the similar manner. Table below shows the summary of the stress amplitudes and corresponding stress loads to use for the testing which were calculated in similar manner.

Table 2: Design stress amplitudes and design loads for the testing of M20 bolts.

STRESS AMPLITUDE (N/MM^2)	STRESS LOAD (N)
1114	69994.68
1058.3	66494.95
1005.4	63171.15
955.1	60010.70

4. Conclusions

The AE technique can be used to identify hydrogen induced cracking within the steel fasteners by subjecting the fasteners to axial fatigue testing and recording the AE signals emitted during the test. The main task for this project will be to conduct the initial testing proposed and to co-relate the obtained fatigue data with the AE data after testing. The next step in the project will be to introduce hydrogen blistering within the steel fasteners and to subject the fastener to load testing to distinguish the difference caused in the durability of the fasteners after introduction of hydrogen.

5. References

[1]   S. Brahimi, "Fundamentals of hydrogen embrittlement in steel fasteners," *IBECA Technology Corp,* 2014.
[2]   Y. Chung and L. Fulton, "Environmental hydrogen embrittlement of G41400 and G43400 steel bolting in atmospheric versus immersion services," *Journal of Failure Analysis and Prevention,* vol. 17, no. 2, pp. 330-339, 2017.
[3]   E. Institute and E. I. Staff, *Guidelines for the Management of the Integrity of Bolted Joints for Pressurised Systems.* Energy Institute, 2007.
[4]   R. Unnþórsson, "Hit Detection and Determination in AE Bursts. Acoustic Emission-Research and Applications. Ed. by W. Sikorski," ed: InTech, 2013.
[5]   A. Bhattacharya, N. Parida, and P. Gope, "Monitoring hydrogen embrittlement cracking using acoustic emission technique," *Journal of materials science,* vol. 27, no. 6, pp. 1421-1427, 1992.
[6]   J. Billingham, J. Sharp, and J. Spurrier, "Review of the performance of high strength steels used offshore," 2003.
[7]   V. Smanio, J. Kittel, M. Fregonese, T. Cassagne, B. Normand, and F. Ropital, "Acoustic emission monitoring of wet H2S cracking of linepipe steels: Application to hydrogen-induced cracking and stress-oriented hydrogen-induced cracking," *Corrosion,* vol. 67, no. 6, pp. 065002-1-065002-12, 2011.
[8]   M. Cayard and R. Kane, "Evaluation of various methods of reducing the duration of SSC qualification testing," in *Corrosion97*, 1997: OnePetro.

[9]   A. Gingell and X. Garat, "Observations of damage modes as a function of microstructure during NACE TM-01-77/96 tensile testing of API 5L grade X60 linepipe steels," in *CORROSION 99*, 1999: OnePetro.

[10]   C. C. Weng and R. T. Chen, "Acoustic emission characteristics of a high–strength steel subjected to corrosive hydrogen sulfide solution," *Journal of the Chinese Institute of Engineers,* vol. 16, no. 2, pp. 195-202, 1993.

[11]   N. International, *Laboratory Testing of Metals for Resistance to Specific Forms of Environmental Cracking in H2S Environments: Standard Test Method*. NACE International, 1996.

[12]   Y. Dong and F. Ansari, "Non-destructive testing and evaluation (NDT/NDE) of civil structures rehabilitated using fiber reinforced polymer (FRP) composites," in *Service life estimation and extension of civil engineering structures*: Elsevier, 2011, pp. 193-222.

[13]   E. ISO, "898-1 Mechanical properties of fasteners made of carbon steel and alloy steel–Part 1: Bolts, screws and studs with specified property classes–Coarse tread and fine pitch thread," *Belgium: CEN,* 2009.

[14]   E. National Academies of Sciences and Medicine, *Bolting Reliability for Offshore Oil and Natural Gas Operations: Proceedings of a Workshop*. National Academies Press, 2018.

[15]   A. McEvily Jr, "Atlas of stress-corrosion and corrosion fatigue curves," 1990.

[16]   Y. Chung, "Threshold preload levels for avoiding stress corrosion cracking in high strength bolts, *"Corrosion Cracking, Salt Lake City,* pp. 137-142, 1985.

[17]   R. P. Gangloff, "Hydrogen assisted cracking of high strength alloys," Aluminum Co of America Alcoa Center Pa Alcoa Technical Center, 2003.

[18]   B. S. I. Staff, *Threaded Fasteners. Axial Load Fatigue Testing. Test Methods and Evaluation of Results*. B S I Standards, 1994.

[19]   S. McGuigan, "Peterson's Stress Concentration Factors Second Edition," *Proceedings of the Institution of Mechanical Engineers,* vol. 212, no. 2, p. 145, 1998.

HYDROGEN INDUCED CRACKS MONITORED WITH ACOUSTIC EMISSION UNDER THE LABORATORY CONDITION

Dandan Liu[1,2,*], Han Yang[1,2], Bin Wang[2] and Stephen Grigg[1]

[1]TWI Ltd, Granta Park, Great Abington, Cambridge, CB21 6AL, UK;
dandan.liu@brunel.ac.uk, han.yang@brunel.ac.uk, stephen.grigg@twi.co.uk
[2]Department of Mechanical and Aerospace Engineering, Brunel University London, Uxbridge UB8 3PH,
UK; bin.wang@brunel.ac.uk
*Correspondence: dandan.liu@brunel.ac.uk

ABSTRACT

Hydrogen induced cracking (HIC) is a common form of failure in steel exposed to hydrogen rich environments, which always occurs inside material making their detection difficult. Acoustic Emission (AE) is a promising Nondestructive Evaluation technique for crack detection. However, it is challenging to distinguish the signals generated from HIC, corrosions and bubbles. In this study, these mixed AE signals were obtained by electrochemical hydrogen charging on A516 carbon steel with the solution of 0.5 mol/L H_2SO_4 and 0.5 g/L $NaAsO_2$. Microstructures of the sample's cross-section were observed to verify the existence of HIC. moreover, separate signals of bubbles and corrosions were acquired from just exposures to 0.5 mol/L H_2SO_4. After analyzing, key parameters from the AE signals, i.e. the peak frequency, the spectrum gravity, the duration and energy, were identified to differentiate the source mechanisms. Results show that the peak frequency and the spectrum gravity of corrosion signals are higher than those of HIC and bubbles, while the duration and energy of HIC signals are higher than those of the other two kinds of signals. To reduce manual operations, the unsupervised learning algorithms, Principal Components Analysis (PCA) and K-means, were used for clustering, for further understanding of these clusters and their evolution with time.

Keywords: Acoustic Emission, hydrogen induced crack, hydrogen blisters, unsupervised learning, clusters.

1. Introduction

Hydrogen embrittlement (HE) is a common phenomenon of steels exposed to hydrogen rich environment. Hydrogen induced crack (HIC) is one form of HE that can occur inside the material without external forces while Hydrogen Blisters (HB) is a special case in which the location of HIC is close to the surface of the material and part of the material is lifted up to form the blisters. HIC is a cumulative process but fracture of structure due to HIC happens suddenly and may lead to serious consequences. During the refining and transportation of petroleum, the sour conditions with Hydrogen sulfide (H_2S) are highly corrosive to steel and HIC is the most common failure form [1]. Industries such as mining and paper processing are also plagued by HIC [2]. Therefore, it is crucial to monitor HIC propagation and evaluate the remaining life of structure to avoid sudden failures. To detect internal cracks without affecting normal operations of the structure, Non-

destructive Testing (NDT) is preferred. There are various restrictions when using conventional NDT methods. For example, Ultrasonic testing (UT) has certain requirements on geometry such as shape and thickness; Radiographic Testing (RT) is involves high cost for detection and protection; Magnetic particle Testing (MT) has stringent requirements on the surface smoothness of the tested parts, with small detection range and slow detection speed. Acoustic emission (AE) is an advanced dynamic NDT method which overcomes many limitations of others. The stress wave generated by the rapid release of strain energy when the defect is active can be captured by AE sensors in real time. The activity and severity of the defect can be determined then by analyzing the electrical signal. AE technology has no requirements on the physical state of material surface and shape complexity, and the source location in complex structure can be predicted with a sensors array.

AE sensors are highly sensitive to detect defect activities, but at the same time, the chances of collecting background noise also increase. For instance, for pipeline steels in contact with hydrogen sulfide, three kinds of AE signals are generated, these are from hydrogen charging bubbles, the generation and detachment of Ferrous sulfide (FeS) films and HIC growths. Therefore, it is a challenge to extract the HIC signals from other sources accurately.

In order to simulate the working environment and state of pipeline steel in practice, most studies were based on NACE TM0284 [3], which are the standard tests to evaluate the resistance of steels to HIC. For the purpose of finding HIC signals from mixed ones, Smanio et al. [4-6] first collected signals from the hydrogen charging and FeS film processes by means of cathodic protection and anodic protection, respectively. They concluded two decisive parameters, the energy and duration, to distinguish the signals, and based on that to manual extract HIC signals from three mixed signals. For X65 and the buffered solution 50 mg/L Sodium chloride (NaCl) and 4 mg/L Sodium acetate (CH_3COONa) in distilled water under 1 bar H_2S, they found that the biggest difference between HIC and other signals is that the duration of HIC signals which is longer than 1500 us. Many other studies on extracting HIC signals are based on Smanio's work because of their detailed experimental procedures. However, some investigations have obtained different results. Attar et al. [7] also detected three different groups of signals and concluded that the duration of HIC signals is longer than 1000 us.

In the study of Li et al. [8-9] on 20R steel exposed to H_2S saturated aqueous solution, results showed that a vital parameter was the amplitude which is 72 to 75 dB attributed to HIC propagation, while Smanio's results [4-6] indicated that the amplitude of HIC signals is lower than 60 dB. The differences may be caused by the setup of experiment, such as the size of specimen, type of material, position of sensors, amplitude threshold, etc. Therefore, signals from bubbles and corrosion accompanying the HIC growth be obtained separately in advance under the same experimental setup is the premise to ensure that the separated HIC signals are correct. This study simulates the procedures of Smanio's work, the noise signals (from bubbles and corrosions) are obtained separately using the same setup except for the electrolyte and the HIC signals are then manually extracted. Nevertheless, re-collection and analysis of noise signals are required if any parameter will change, which is time-consuming. Consequently, a universal method is necessary to cluster different kinds of signals directly from the mixed results which is suitable to most experiments with various parameters.

For this study, the unsupervised learning method, Principal Components Analysis (PCA) has been combined with K-means clustering [10]. Unsupervised learning is a type of machine learning algorithm that classifies data based on commonalities present in the features of the data. For an AE signal, there are many parameters to characterize it, such as amplitude, rise time, duration, energy, counts, frequency spectrum, etc. Each parameter reflects some information of a signal to various degrees. However, these variables are not independent of each other. For example, signals with high amplitudes typically have higher durations and counts. Considering too many variables will increase the complexity of analysis due to the interaction or overlap information among them. Therefore, as few principal features as possible should be extracted to characterize as much information as possible of the signal. PCA is an important dimensionality reduction method that

uses orthogonal transformation to transform a series of possibly linearly related variables into a set of linearly uncorrelated new variables. According to the new data obtained from PCA, the simplest unsupervised learning algorithm, K-means, was then applied for clustering the signals. In this study, the electrochemical hydrogen charging method has been used for generation of HIC in steels instead of those specified by NACE TM0284 to avoid using toxic H$_2$S and to simplify the setup as well as accelerate tests, since obtaining HIC by standard methods typically requires 4 - 14 days [3]. Generally, diluted solution of Sulfuric acid (H$_2$SO$_4$) or Sodium hydroxide (NaOH) can be used as the electrolyte. For H$_2$SO$_4$, the cathodic reaction is:

$$2H^+ + 2e^- = H_2 \to H_2 \uparrow /2H \qquad (1)$$

And for NaOH, the cathodic reaction is:

$$2H_2O + 2e^- = 2OH^- + H_2 \to H_2 \uparrow /2H \qquad (2)$$
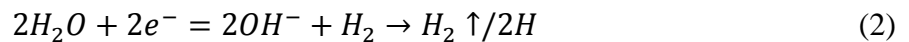
In both reactions, part of the hydrogen generated at the cathode will escape as H$_2$ gas and part will enter the specimen in the atomic form. Dunne et al. [11] successfully obtained hydrogen blisters on X70 by hydrogen charge for 2 h at 50 mA/cm^2 using 0.5N H$_2$SO$_4$ and 250 mg/L Sodium arsenite (NaAsO$_2$). Du et al. [12] completed the hydrogen charging of A537 steel plates using Devanathan's double-electrolytic cell with the electrolyte as 0.2 mol/L NaOH and 0.25 g/L As$_2$O$_3$ and calculated the effective hydrogen diffusivity. Park et al. [13] evaluated the effects of alloying elements (C, Mo) on hydrogen diffution behaviours using the electrochemical permeation experiments, using NACE + 0.05 M Na$_2$S + 0.3 wt.% NH$_4$SCN with constant cathodic current density of 1 mA/cm^2. These studies show that the electrochemical hydrogen charging can be used as an effective method for rapid assessment of susceptibility to HIC of steels.

The present paper work aims at obtaining and extracting the signals related to HIC/HB under laboratory conditions by electrochemical hydrogen charging method. Sulfuric acid is chosen as main electrolyte in this study to simulate the sour environment where H$_2$S exists as much as possible. A major challenge is to distinguish different AE sources accurately. Based on the manual clustering approach proposed by Smanio et al, a series of tests are designed to manually cluster AE signals step by step. In addition, a combined unsupervised learning method, PCA+K-means, is applied to directly cluster all the AE signals which can eliminate human intervention and possibility to become a potential universal classification method.

2. Experiments

2.1 Materials

HIC-sensitive steels should be considered to ensure that HIC can be obtained. In the light of Kane's [14] report, it is indicated that HIC susceptibility is high for a carbon steel with high Sulphur content (>0.002 %) in the as-rolled condition because MnS inclusions are the main site of HIC. In addition, Dunne et al. [11] investigated the effect of microstructure on HIC with X70 carbon steel and found that the banded ferrite-pearlite is the most suitable microstructure for HIC to produce. Therefore, rolled ASTM A516 Grade 65 carbon steel plate was purchased with high content of S and Mn from Brown Mcfarlane Ltd. for this study. The chemical compositions (%) of A516 are displayed in Table 1. The specification of specimen is 200 x 50 x 5 mm and the microstructure is also observed under the optical microstructure which is shown as Fig. 1.

Table 1: Chemical Compositions (%) of A516 carbon steel.

COMPOSITION	C	Mn	Si	P	S	Cr	Ni	Mo	Cu	Al	Ti	Nb
CONTENT (%)	0.137	1.073	0.169	0.011	0.005	0.015	0.008	0.002	0.016	0.033	0.001	0.014
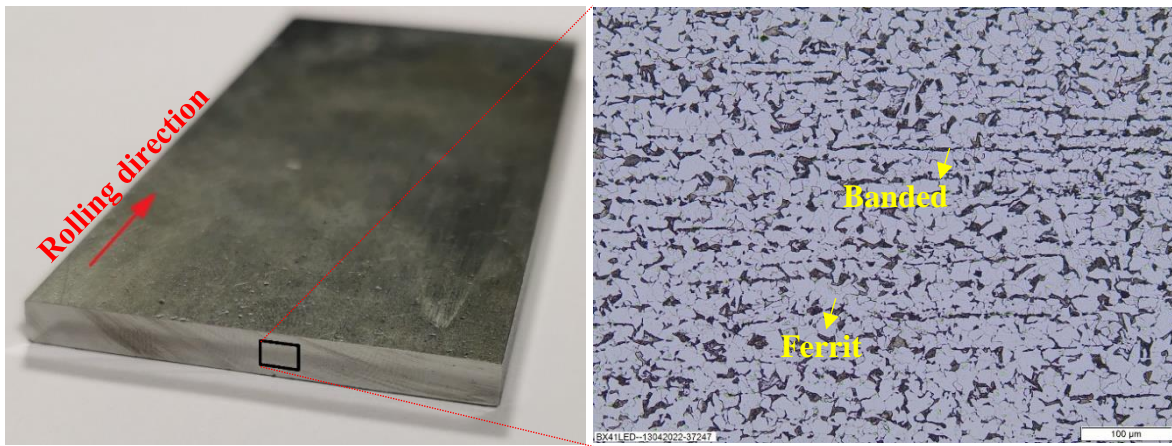
Fig. 1: The banded ferrite-pearlite microstructure of A516 carbon steel.

2.2 Hydrogen charging method

For this study, The specimen and platinum are used as cathode and anode respectively. The electrolyte 0.5 mol/L H_2SO_4 and 0.5 g/L $NaAsO_2$ dissolved in deionized water was used. The acidic solution was used to provide more H^+ while $NaAsO_2$ was used to inhibit the recombination of hydrogen atoms which plays a crucial role to promote more hydrogen atoms to enter into the sample. The A516 steel plate was polished to 2500 grit and then cleaned with alcohol. After adding current, H_2 bubbles are generated on specimen's surface, since the signals of bubble activity will also be acquired by sensors, the area where exposed to the electrolyte was reduced to a 1 cm^2 square area by covering it with Belzona 4311 coating to reduce such background noise. Similarly, the current density was chosen as 5 mA/cm^2 for the purpose of reducing the generation of bubbles. The electrolyte is held in a glass conical funnel-like container which is sealed to the specimen with silicone. The setup is shown in Fig. 2.
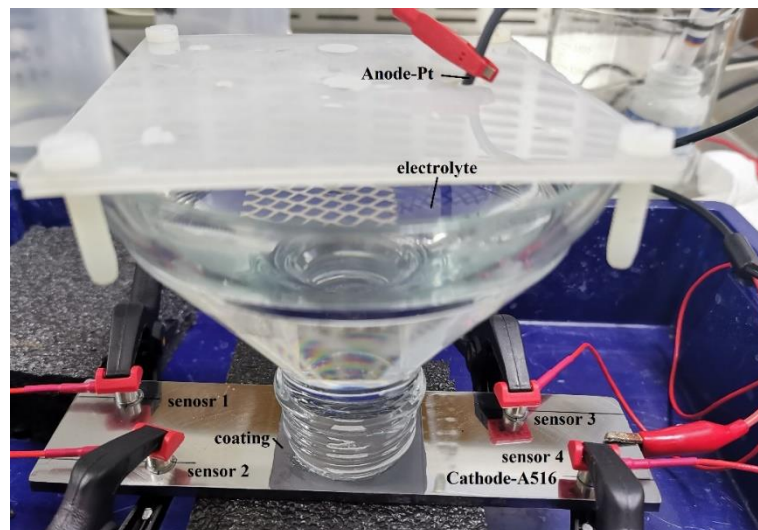
Fig. 2: Setup of electrochemical hydrogen charging test.

2.3 Acoustic emission

AE signals were collected using four nano-30 piezoelectric sensors (Mistras system) which is linked to a Vallen 4 AE-channels AMSY-6 System by AEP4 Pre-amplifiers (Vallen System GmbH). As shown in Fig. 2, working are is in the specimen center and sensors are placed near the four corners, this was to enable source localisation, however is not presented in this work. A schematic layout of the sensors is shown in Fig. 3. The tests were carried out on the ventilated bench in the lab at TWI Ltd. Bubble wrap (as shown in Fig. 2) was used to decouple the specimen

from the bench surface during the test to reduce external vibration noise. No signal was detected prior to the start of hydrogen charging. The threshold was set of 40 dB suggested by Smanio [5] to filter out most background noise. In addition, the Duration Discrimination Time, the Rearm Time and the Sample Rate were set as 400 us, 1000 us and 2.5 MHz, respectively.
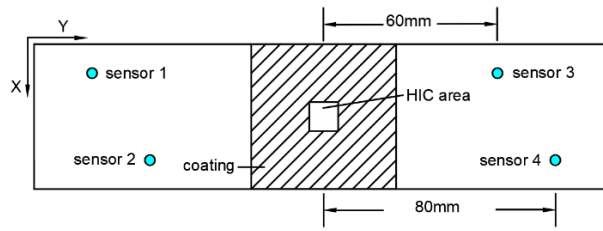
Fig. 3: The schematic layout of the sensors.

Although the cathodic protection method will make the steel not corroded so quickly in an acidic solution, a small current of 5 mA/cm^2 cannot completely eliminate the corrosion effect of sulfuric acid, and the concentration of H_2SO_4 in the solution will gradually increase with the progress of the experiment. Besides, crevice corrosion may occur at the boundary due to the presence of coating. Therefore, similar to the experiments using H_2S to generate HIC, there are still three AE sources during the electrochemical tests which are from H_2 bubbles, corrosions and HIC [13]. In order to better distinguish these 3 kinds of signals, three different tests were designed whose information are summarized in Table 2. For Test 1, the surface of specimen contacted 0.5mol/L H_2SO_4 without current which caused the reaction below:

$$Fe + H_2SO_4 = FeSO_4 + H_2 \uparrow$$
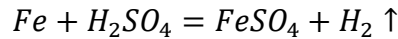
Therefore, two AE sources appeared in Test 1: H_2 bubbles and corrosion. For Test 2, there are also two sources of AE signals during this process: bubbles and corrosion. However, the signal of the bubbles is dominant while the corrosion reaction is supressed, which is due to the current density of 5mA/cm^2.

Table 2: The information of three tests.

	ELECTROLYTE	CURRENT	DURATION	AE SOURCES
Test 1	0.5 mol/L H_2SO_4	×	1 h	Bubbles + Corrosion
Test 2	0.5 mol/L H_2SO_4	5 mA/cm^2	1 h	Bubbles + Corrosion (suppressed)
Test 3	0.5 mol/L H_2SO_4 +0.5 g/L NaAsO$_2$	5 mA/cm^2	20 h	Corrosion + Bubbles + HIC

3. Results and discussion

3.1 Analysis of Test 1 and Test 2

Under these two conditions, the morphology of surface and cross-section were observed after test. No evidence of HIC/HB was observed, thus AE signals associated with the activities of H_2 bubbles and corrosions in Tests 1 and 2. The only difference is that the corrosion reaction in Test 2 was suppressed due to the specimen acting as the cathode of the electrolytic cell. From the results of

Test 1 and Test 2, it can be found that there are mainly two obvious kinds of frequency spectrums obtained with Fast Fourier Transform (FFT) which is shown in Fig. 4 with two typical cases of each. The first one is shown as Fig. 4(a), the main frequency is lower than 200 kHz with the peak frequency of around 50 kHz or 120-180 kHz. Fig. 4(b) indicates another kind of completely different frequency spectrum where frequency components above 300 kHz occupy a significant portion with wide range of frequency. According to the work of Shen et al. [8] and Smanio et al. [6], AE signals related to H_2 evolution were also detected by electrochemical method whose results exhibited the characteristics of signals with low energy, low duration and peak frequency or average frequency of 0-250 kHz. Therefore, signals with the spectrum shown in Fig. 4(a) can be considered to come from the H_2 evolution while those in Fig. 4(b) are from corrosion process.

Based on this conclusion, the Energy-Duration graph of Test 1 and Test 2 are presented in Fig. 5 (a) and (b) respectively. Corrosion on the surface of specimen in Test 2 was suppressed due to the application of cathodic protection, theoretically, the corrosion signals in Test 2 will be less than that in Test 1. Fig. 5 indicates the same result as theory, verifying the correctness of distinguishing these two kinds of signals by frequency spectrum. The characteristics of AE signals related to H_2 activities and corrosion can be summarised as follows:

Signals from H_2 activities:

- 50 kHz < Peak Frequency & Frequency Gravity < 200 kHz
- Energy < 1000 eu,
- Duration < 1000 us.

Signals from corrosion:

- Peak Frequency > 300 kHz or
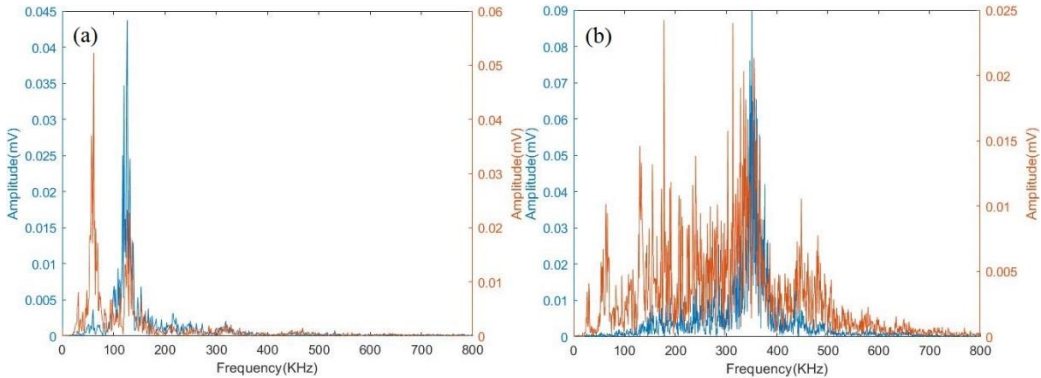- Frequency Gravity > 200 kHz with wide spectrum.

Fig. 4: Plots of the two kinds of frequency spectrum of signals from Test 1 (a) and Test 2 (b).
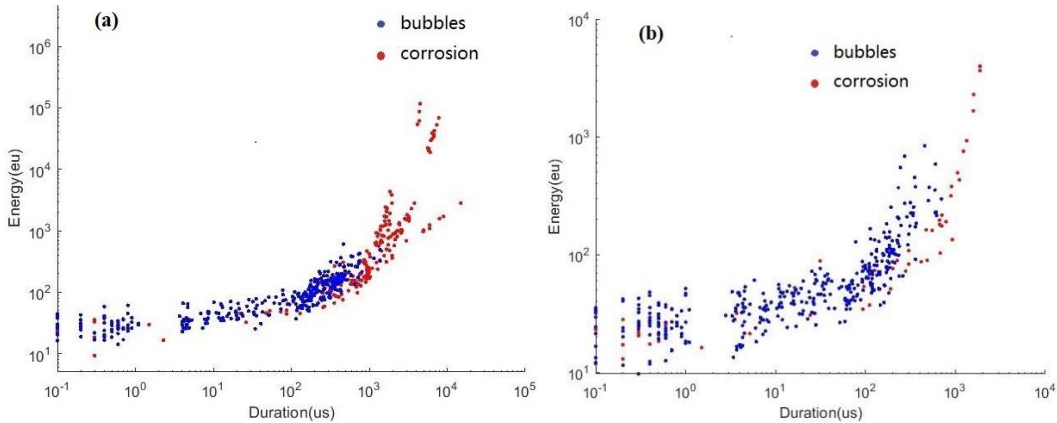
Fig. 5: Representation of the signals generated from Test 1 (a) and Test 2 (b) in Energy-Duration graph.

3.2 Analysis of Test 3

3.2.1 Hydrogen-induced blisters and cracks
After 20 hours of Test 3, the specimen was removed and the surface morphology was observed with camera as shown in Fig. 6(a). It can be seen that there are many distinct hydrogen blisters on the surface of work area. Fig. 6(b) shows the results of optical microscope (OM) on cross-section under the hydrogen blisters which demonstrates that a surface-lifting blister phenomenon consists of many small cracks underneath.
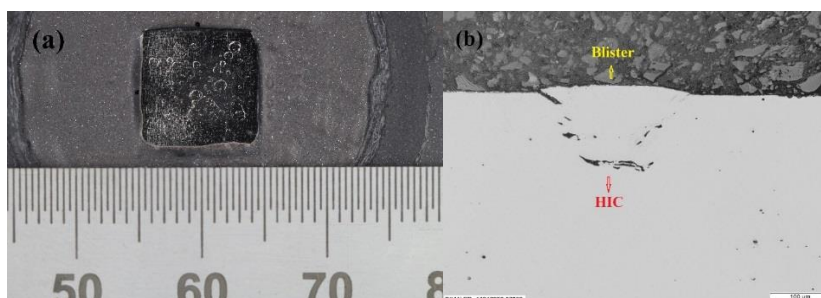
Fig. 6: Photo of surface morphology of HB (a) and OM observation on the cross-sections (b).

3.2.2 AE results
In Test 3, HIC and Hydrogen blisters were clearly observed after several hours with the catalysis of NaAsO$_2$. Signals from three different sources, H$_2$ activities, supressed corrosion and HIC, are expected to be mixed in the collected results. Compared with the signals of Tests 1 and 2, a new model of signals appeared with low frequency but high energy and high duration. Considering that this kind of signal are only detected in Test 3, the nature of those signals associated with HIC/Hydrogen blisters. Fig. 7 shows two typical cases of frequency spectrum of this model. The peak frequency of these signals generally locates between 100-200 kHz with some minor components between 50-100 kHz or 200-300 kHz. This conclusion is consistent with the results of Dmitry's study [15].

Therefore, these signals in Test 3 can be divided into 3 clusters by procedure according to the chracteristics of signals as follows: peak frequency/frequency spectrum gravity of signals from corrosion >250 kHz, the low frequency signal with duration less than 1000 us comes from hydrogen activity, thus the remaining signals are related to HIC/HB. Fig. 8 (a) demonstrates the representation of 3 clusters of signals in Test 3 about the Energy-Duration graph and the cumulate energy of these signals with time (b). It can be seen that HIC-related initial signals are generated within two hours and a large amount of HIC activity is generated in about seven hours under the electrochemical hydrogen charging conditions. Compared with the standard method of introducing H$_2$S [3], the time cost of judging whether the material is sensitive to HIC is greatly reduced.
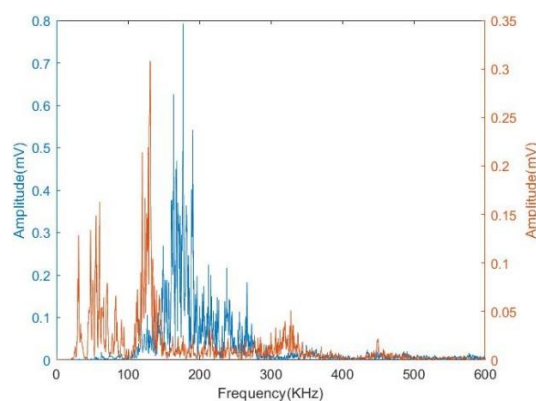
Fig. 7: Frequency spectrum of signals related to HIC/Hydrogen blisters.

Fig. 8: Representation of manual clusters of signals in Test 3 about the Energy-Duration graph (a) and the cumulate energy of these signals with time (b).

3.2.3 Clustering by Unsupervised Learning

According to the above discussion, the first step of manual classification is to divide with hard cutoff as peak frequency/gravity of frequency spectrum of 250 kHz and duration of 1000 us. However, for the critical signals of these three clusters, it is necessary to differentiate them again to improve the classification accuracy which is time-consuming and relies heavily on operator's knowledge and expertise. In order to reduce the manual intervention, unsupervised learning method was introduced for clustering. In this study, seven features were chosen as the initial components for PCA - amplitude, rise time, duration, energy, counts, peak frequency and gravity of frequency spectrum. The contribution rate of each component from high to low is shown in Table 3. From the component with the highest contribution rate, several principal components with a cumulative contribution rate greater than 90 % (most often chosen) [16-17] were finally selected for classification: spectrum gravity, peak frequency, energy, and count. According to the new data obtained from PCA, the simplest unsupervised learning algorithm, K-means, was applied for clustering the signals. Fig. 9 demonstrates the classification results in the form of Energy-Duration graph as well as the cumulate energy with. In Fig. 9(b), the cumulate energy of three clusters with time is almost identical to that of manual clustering results, which proves the validity of investigating the HIC growth process through the unsupervised learning clustering method. Moreover, Fig. 9(a) indicates that the signals of three clusters cross each other at the junction where duration is 1000 us, which provides more precise cluster results and thus better determinates the initial signal of HIC. Therefore, it is no longer necessary to separately obtain signals from bubbles and corrosion and to summarise their characteristics. To cluster signals directly through unsupervised learning methods is reliable, which simplifies the process of extracting HIC signals and reduces the time cost of experiments and data processing to verify the HIC susceptibility of steel.

Table 3: The contribution rate of each component for PCA.

COMPONENTS	SPECTRUM GRAVITY	PEAK FREQUENCY	ENERGY	COUNTS	DURATION	RISE TIME	AMPLITUDE
CONTRIBUTION RATE (%)	40.9160	26.4138	16.3414	9.5521	3.2516	1.9511	1.5740

314

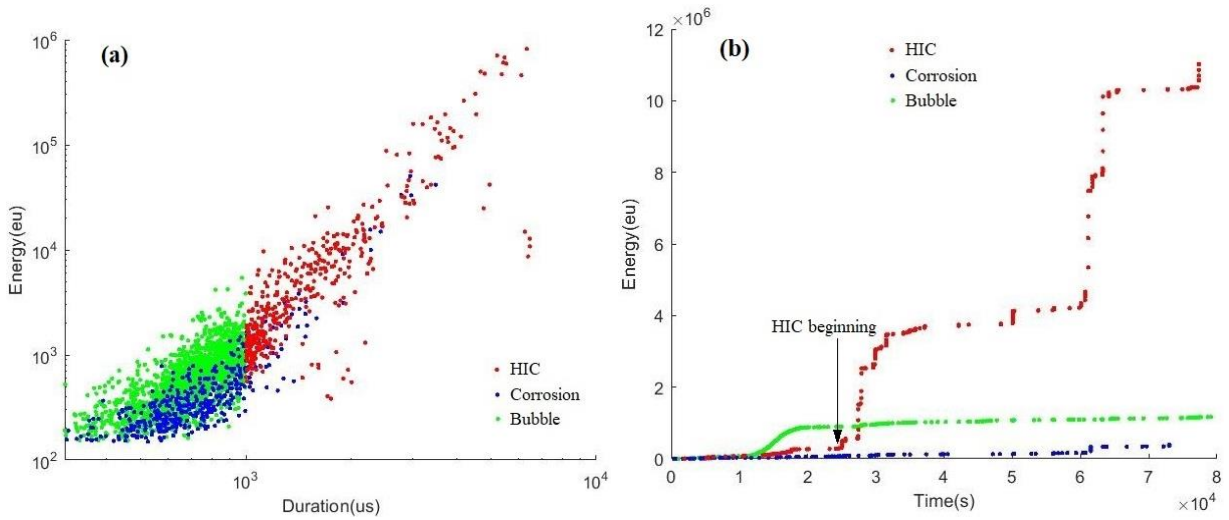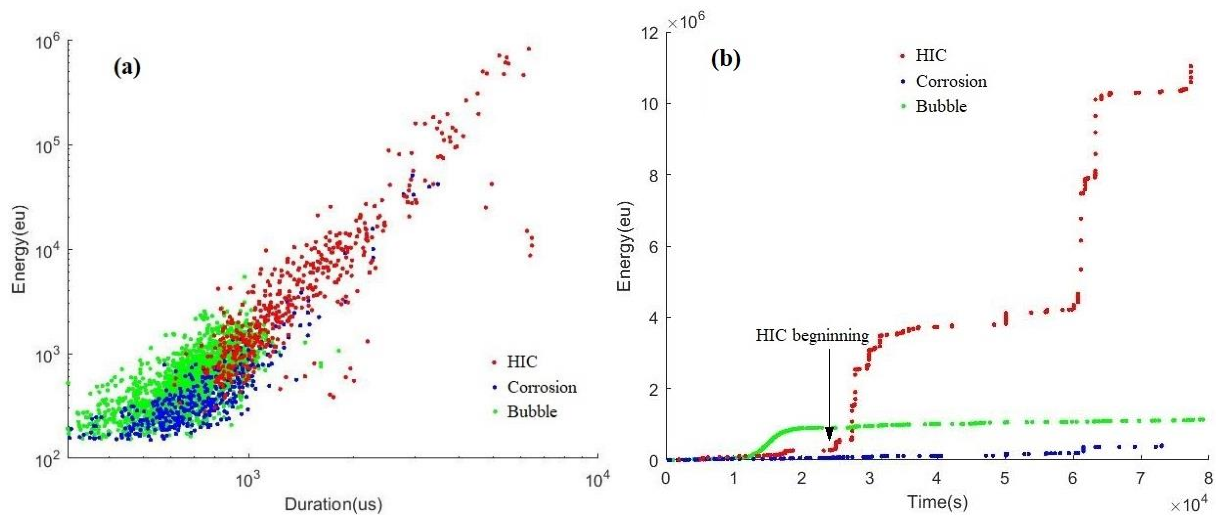Fig. 9: Representation of 3 clusters of signals in Test 3 about the Energy-Duration graph (a) and the cumulate energy of these signals with time (b) by PCA + K-means method.

4.   Conclusions

Electrochemical hydrogen charging method was carried out in this study to obtain HIC/HB which was monitored with AE. With the condition of H_2SO_4/$NaAsO_2$ mixed electrolyte and current of 5 mA/cm^2, a large amount of HIC behavior will be generated in the A516 plate after about 7 hours. Compared with the standard test with H_2S, electrochemical hydrogen charging method seems more suitable to generate HIC/HB under the laboratory conditions due to the short test duration and lower toxicity. A series of tests and features of AE signals were used to distinguish different AE sources. It is found from the manual cluster procedure that AE signals associated with corrosions have higher peak frequency/frequency gravity (>250 kHz) while signals from H_2 activities have low duration (<1000 us), low energy and low frequency. The characteristics of signals related to HIC/HB are high duration, high energy and low frequency. The artificially selected hard cutoffs do not take much consideration into the classification of critical signals. Moreover, the selected cutoff value, e.g. frequency gravity of 250 kHz, duration of 1000 us, only guarantees the correctness of the cluster results with the same experimental parameters as this study. The combined unsupervised learning method used in this work, PCA + K-means, completely eliminate human intervention and got comparable result which demonstrated that it is a potential tool to cluster signals from tests with different parameters as an universal method.

In the future, more tests with different parameters, such as material, thickness of specimen, applied current, etc., will be carried out to verify the universal applicability of the combined unsupervised learning method. If it is successfully verified, the pre-experiments to obtain the noise signals are no longer required before the formal experiment and the fixed classification boundary will be removed, which simplifies the process of experiment and data processing.

5.   References

[1]   Carneiro, R. A., Ratnapuli, R. C., & Lins, V. D. F. C. (2003). The influence of chemical composition and microstructure of API linepipe steels on hydrogen induced cracking and sulfide stress corrosion cracking. Materials Science and Engineering: A, vol. 357, no. 1-2, p. 104-110, doi:10.1016/S0921-5093(03)00217-X.

[2] Martin, M. L., & Sofronis, P. (2022). Hydrogen-induced cracking and blistering in steels: A review. Journal of Natural Gas Science and Engineering, vol. 101, 104547, doi: 10.1016/j.jngse.2022.104547.

[3] ANSI/NACE Standard TM0284-2003. Evaluation of Pipeline and Pressure Vessel Steels for Resistance to Hydrogen-Induced Cracking.

[4] Smanio, V., Kittel, J., Fregonese, M., Cassagne, T., Normand, B., & Ropital, F. (2011). Acoustic emission monitoring of wet H2S cracking of linepipe steels: Application to hydrogen-induced cracking and stress-oriented hydrogen-induced cracking. Corrosion, vol. 67, no. 6, 065002, doi:10.5006/1.3595097.

[5] Smanio, V., Cassagne, T., Ropital, F., Kittel, J., Frégonèse, M., & Normand, B. (2008, March). Evaluation of hydrogen embrittlement induced damages in steels using acoustic emission. In CORROSION 2008.

[6] Smanio, V., Fregonese, M., Kittel, J., Cassagne, T., Ropital, F., & Normand, B. (2010). Wet hydrogen sulfide cracking of steel monitoring by acoustic emission: discrimination of AE sources. Journal of materials science, vol. 45, no. 20, p. 5534-5542, doi:10.1007/s10853-010-4613-2.

[7] H. Attar, A. Traidia, A. Enezi. Acoustic Emission Monitoring of HIC Growth in Carbon Steel: Laboratory Testing.

[8] Gongtian Shen G. T., Li, L. F., Zhang, W. L. (2008). Investigation on Acoustic Emission of Hydrogen Induced Cracking for Carbon Steel Used in Pressure Vessel. 17th World Conference on Nondestructive Testing, Shanghai, China.

[9] Li, L. F., Zhang, Z., Shen, G. T., & Wu, Z. W. (2010, October). Acoustic emission as a technique to study hydrogen induced cracking behavior of low-carbon steel. In 2010 3rd International Congress on Image and Signal Processing, vol. 8, p. 4002-4005, IEEE.

[10] Ju, S., Li, D., & Jia, J. (2022). Machine- learning- based methods for crack classification using acoustic emission technique. Mechanical Systems and Signal Processing, vol. 178, 109253, doi:10.1016/j.ymssp.2022.109253.

[11] Dunne, D. P., Hejazi, D., Saleh, A. A., Haq, A. J., Calka, A., & Pereloma, E. V. (2016). Investigation of the effect of electrolytic hydrogen charging of X70 steel: I. The effect of microstructure on hydrogen-induced cold cracking and blistering. international journal of hydrogen energy, vol. 41, no. 28, p. 12411-12423, doi: 10.1016/j.ijhydene.2016.04.114.

[12] Du, X. S., Cao, W. B., Wang, C. D., Li, S. J., Zhao, J. Y., & Sun, Y. F. (2015). Effect of microstructures and inclusions on hydrogen-induced cracking and blistering of A537 steel. Materials Science and Engineering: A, vol. 642, p. 181-186, doi: 10.1016/j.msea.2015.06.085.

[13] Park, J. S., Lee, J. W., Hwang, J. K., & Kim, S. J. (2020). Effects of alloying elements (C, Mo) on hydrogen assisted cracking behaviors of A516-65 steels in sour environments. Materials, vol. 13, no. 18, p. 4188, doi:10.3390/ma13184188.

[14] Kane, R. D., & Cayard, M. S. (1998). Roles of H2S in the behavior of engineering alloys: a review of literature and experience. CORROSION 98.

[15] Merson, D., Dement'ev, S., Ioffe, A., Suvorov, P., & Vinogradov, A. (2011). Acoustic emission during hydrogen charging of a pipeline steel. ISIJ international, vol. 51, no. 10, p. 1682-1687, doi:10.2355/isijinternational.51.1682.

[16] Chen, C., Chen, X., & Ning, Y. (2022). Identification of fracture damage characteristics in ultra-high performance cement-based composite using digital image correlation and acoustic emission techniques. Composite Structures, vol. 291, 115612, doi:10.1016/j.compstruct.2022.115612.

[17] Pořízka, P., Klus, J., Képeš, E., Prochazka, D., Hahn, D. W., & Kaiser, J. (2018). On the utilization of principal component analysis in laser-induced breakdown spectroscopy data analysis, a review. Spectrochimica Acta Part B: Atomic Spectroscopy, vol. 148, p. 65-82, doi:10.1016/j.sab.2018.05.030.

IDENTIFICATION OF INTERNAL DAMAGES IN REINFORCED CONCRETE SLABS USING PROBABILITY DENSITY FIELD OF ACOUSTIC EMISSION EVENTS

Fengqiao Zhang[1,*], Yuguang Yang[1] and Max A.N. Hendriks[1,2]

[1]Department of Engineering Structures, Delft University of Technology, Delft, the Netherlands;
F.Zhang-5@tudelft.nl, yuguang.yang@tudelft.nl, M.A.N.Hendriks@tudelft.nl
[2]Department of Structural Engineering, Norwegian University of Science and Technology, Trondheim, Norway
*Correspondence: F.Zhang-5@tudelft.nl

ABSTRACT

To assess the structural capacity of reinforced concrete structures, identifying the internal cracks is important. Acoustic emission (AE) is promising to estimate the location of internal cracks. However, the localization is influenced by many factors like arrival time picking error, presence of crack, etc., resulting in localization error. The error cannot be entirely removed. Considering the inevitable localization error, a probabilistic method was recently developed by the authors. The method estimates the probability of the location of AE events, creating a probability density field of AE events (pdAE field). This method can possibly improve the identification of internal damages. This paper evaluates the performance the pdAE field in identifying internal damages in a reinforced concrete slab. The slab was loaded to failure by a point load. Compared to the conventional localization results, the pdAE field showed a clearer internal crack pattern. Moreover, calculation of the pdAE field was time efficient, thus was suitable for real-time monitoring. With these benefits, the pdAE field indicated the failure of the slab before it occurred.

Keywords: Acoustic emission source localization, probability density field, damage identification, internal damages, reinforced concrete structures.

1. Introduction

To assess the structural capacity of reinforced concrete structures, identification of the location and magnitude of the internal cracks is important. Most techniques only measure the cracks on the structural surfaces, losing the information of the internal damages. A promising technique to detect the internal damages is acoustic emission (AE). Concrete changes like cracking will release energy and generate elastic waves, which propagate to the structural surface and are detected by the AE sensors. By analysing the received signals, AE can estimate the source location (which is source localization) [1], classify the source type (which is source classification) [2] and estimate the structural damage level [3]. Among all its capabilities, the scope of this paper is within source localization.

The conventional source localization methods strive to accurately locate AE sources. However, the localization accuracy is influenced by many factors, such as arrival time picking error,

uncertainty of concrete material properties, sensor locations, etc. These uncertainties cannot be entirely removed from the localization process.

A simplified probabilistic method was developed by the authors in a previous paper [4]. Instead of aiming to accurately locate the source, the probabilistic method quantifies the uncertainties in the localization process and estimates the probability of source location. For a given AE event obtained by a localization process, the method calculates the probability of the location of the event in the 1D, 2D or 3D space, which is called probability density field of the AE event (pdAE field). The probability density field of multiple AE events is obtained by adding up the field of each event. The pdAE field method can possibly improve the identification of the internal damages.

This paper aims to evaluate the performance of the pdAE field method in identifying the internal damages in reinforced concrete slabs. A reinforced concrete slab was loaded to failure by a point load. During load testing, we calculated the pdAE field of AE events in 3D. Compared to the estimated source locations from a traditional localization process, pdAE field shows a clearer internal crack distribution. Moreover, the calculation of pdAE field is time efficient, thus suitable for real-time monitoring. With clearer and real-time identification of internal cracks, the pdAE field is able to indicate the structural failure before it occurs.

2. Probability density field of acoustic emission events

The concept of the pdAE field method is to calculate the probability of the location of AE events based on the estimated source location which contains localization error. Two important inputs are the estimated source locations and the error properties.

The source location is estimated by deterministic localization methods such as grid search method [5] or more advanced method concerning a variable velocity distribution [6]. In principle, one can use any method but the corresponding error properties may differ. To evaluate the error properties, one can refer to a previous paper by the authors which provided a method based on simulations and validated by experiments [7].

The source localization error is defined as the relative location of the estimated source location to the actual location:

$$\mathbf{\Delta} = \mathbf{x_s} - \mathbf{x_g} \tag{1}$$

where, $\mathbf{x_s}$ is the actual source location and $\mathbf{x_g}$ is the estimated source location.

The magnitude of source localization error $\|\mathbf{\Delta}\|$ is the Euclidian distance between the actual and estimated source locations:

$$\|\mathbf{\Delta}\| = \sqrt{\sum_{i=1}^{k} \Delta_i^2} \, , k \in \{1,2,3\} \tag{2}$$

where, k is the dimension of the measuring zone which could be 1D, 2D or 3D and Δ_i is the error component in the ith direction.

The error component Δ_i is assumed following a normal distribution, with zero mean and standard deviation σ, which is the same for all directions. Then the probabilistic density function of the source localization error $\mathbf{\Delta} = (\Delta_1, \cdots, \Delta_k)^{\text{T}}$ is:

$$f(\mathbf{\Delta}) = \frac{1}{(\sqrt{2\pi})^k} \frac{1}{\sigma^k} e^{-\|\mathbf{\Delta}\|^2/2\sigma^2}, k \in \{1,2,3\} \tag{3}$$

For 1D source localization, the scalar-valued error $\mathbf{\Delta}=\Delta_1$ follows a normal distribution with mean zero and standard deviation σ. For 2D and 3D source localization, the error $\mathbf{\Delta}$ follows a multivariate normal distribution with uncorrelated error components Δ_i, with mean zero and the same standard deviation σ.

With the estimated source location as the origin, we are able to calculate the probability density at any point $\mathbf{x}$ as:

$$f\left(\mathbf{x}, \mathbf{x_g}\right) = \frac{1}{\left(\sqrt{2\pi}\right)^k} \frac{1}{\sigma^k} e^{-\|\mathbf{x}-\mathbf{x_g}\|^2/2\sigma^2}, k \in \{1,2,3\} \tag{4}$$

where, $\mathbf{x_g}$ is the estimated source location, $\mathbf{x}$ is a random point in the space of k dimensions. The probability density $f(\mathbf{x},\mathbf{x_g})$ evaluates the likelihood that an AE event which is estimated at point $\mathbf{x_g}$ (from deterministic localization method) but is actually located at point $\mathbf{x}$. The probability density at points in the whole space create the probability density field of the AE event (pdAE field). The integration of probability densities over the whole space equals 1. Fig. 1a shows the pdAE field of an AE event that is estimated at location $\mathbf{S}$, when $k=2$ and $\sigma=39$ mm (the value of σ is taken from a previous simulated case [4]). The likelihood of the AE event located at p_1 is larger than that at p_2.

Regarding the source localization error magnitude $\|\mathbf{\Delta}\|$, since we assume that the error component follows a normal distribution, by definition, the error magnitude can be described by a chi distribution [8]:

$$g(\|\mathbf{\Delta}\|, k) = \frac{\|\mathbf{\Delta}\|^{k-1} e^{-\|\mathbf{\Delta}\|^2/(2\sigma^2)}}{2^{k/2-1}\Gamma(k/2)} \frac{1}{\sigma^k}, k \in \{1,2,3\} \tag{5}$$

For 1D source localization, $k=1$, the chi distribution is also known as half-normal distribution; for 2D source localization, $k=2$ leads to a Rayleigh distribution; for 3D source localization, the chi distribution with $k=3$ is Maxwell-Boltzmann distribution. Fig. 1b shows the three distributions when $\sigma=39$ mm. A higher degree of freedom k gives a larger expected value of error magnitude.
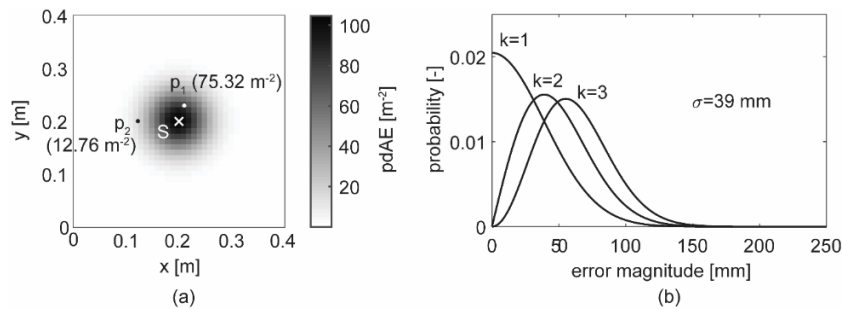
Fig. 1: Probability distribution of (a) the location of the source that is estimated at $\mathbf{S}$ (when $k=2$, $\sigma=39$ mm) and (b) the error magnitude (when $k=\{1,2,3\}$, $\sigma=39$ mm).

When more AE events occur during monitoring, the probability density field of each event is added, resulting in a probability density field of multiple AE events. For all AE events that occur in the measuring time and space range, the probability density at a random location $\mathbf{x}$ is calculated as:

$$p_{\mathbf{A}}(\mathbf{x}) = \sum_{a \in \mathbf{A}} f\left(\mathbf{x}, \mathbf{x_{g,a}}\right) = \sum_{a \in \mathbf{A}} \frac{1}{\left(\sqrt{2\pi}\right)^k} \frac{1}{\sigma^k} e^{-\|\mathbf{x}-\mathbf{x_{g,a}}\|^2/2\sigma^2}, k \in \{1,2,3\} \tag{6}$$

where, $\mathbf{A}$ is a set of all AE events that occurred in the measuring time and space range, $\mathbf{x_{g,a}}$ is the estimated location of event a, and other parameters are defined same as before. The integral of $p_{\mathbf{A}}(\mathbf{x})$ over the whole space equals the number of AE events in the set $\mathbf{A}$.

Fig. 2 illustrates the whole approach which uses the estimated source location and error properties to calculate the pdAE field which shows the probability of the locations of AE events.
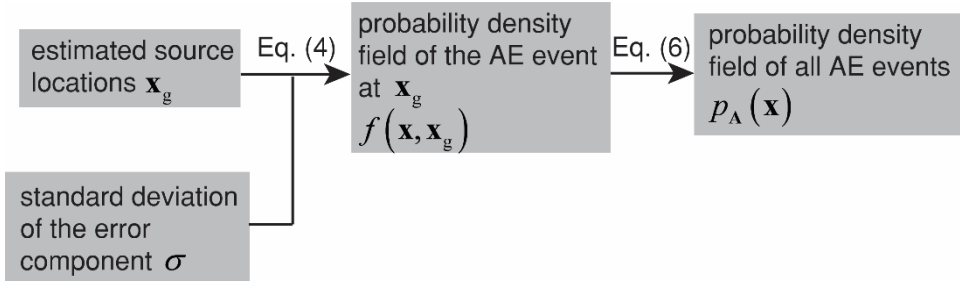
Fig. 2: Derivation of probability density field of AE events.

3. Experiments

3.1 Test setup

The dimensions of the reinforced concrete slab specimens are 5000 mm × 2500 mm × 300 mm (Fig. 3). The concrete class is C35. The specimen is reinforced with ribbed bars. The reinforcement mesh is of 21Ø20 mm bars with a spacing of 125 mm in the longitudinal direction and 41Ø10 mm bars with a spacing of 125 mm in the transverse direction. The concrete cover is 25 mm.
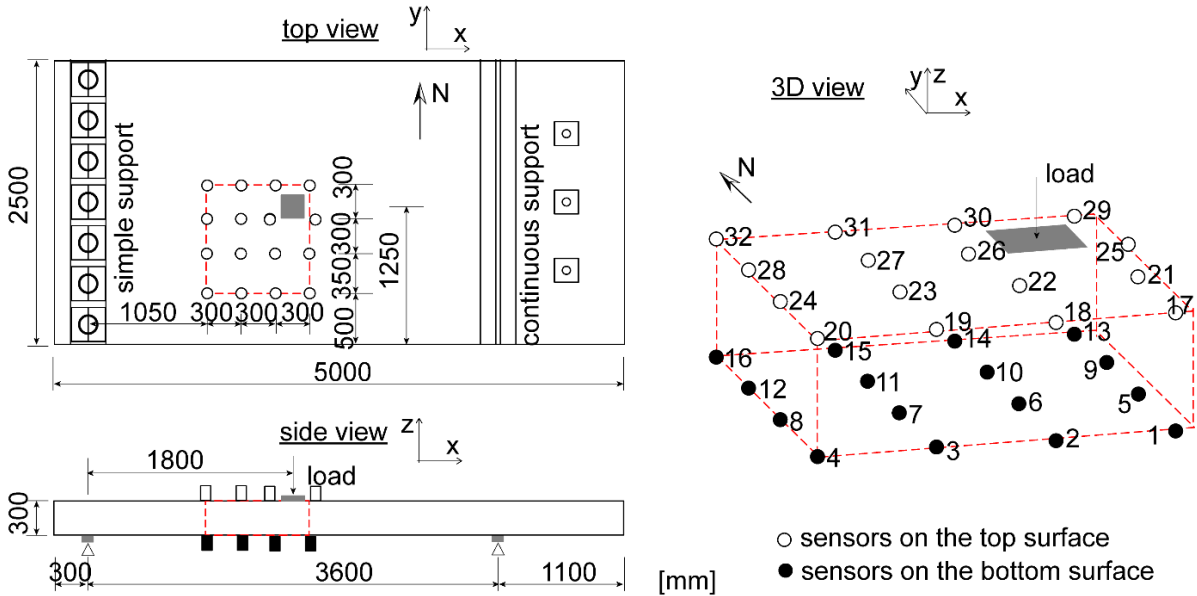
Fig. 3: A sketch of slab configuration including slab dimension, AE sensor layout and locations of supports and load.

The slab was supported at one end by seven separate bearings forming a simple support, and at the other by a line support with a cantilever of 1.1 m. At the end of the cantilever, a downward force of 45 kN was applied by three prestressing bars (15 kN each), to simulate the clamping moment at a continuous support. Fig. 4a shows a photo of the test setup.

The slab was loaded by a single point load, with shear span of 1800 mm. The load was applied through the hydraulic jack in a displacement-controlled manner. The loading speed was 0.04 mm/s. Fig. 4b shows the loading history. The loading protocol can be divided into two parts. The first part was carried out as a proof load test. The detailed considerations have been reported by Zarate

Garnica [9]. The second part included load cycles of higher load level. In the end, the slab was loaded to failure (at 1125 kN). For every load level, three or four load cycles were applied. When reading a higher load level, the load was increased in a step of around 50 kN to enable a good control of load execution. At every load step, the load was hold for a while to mark the crack patterns on the structural surface and take photos for digital image correlation (DIC).
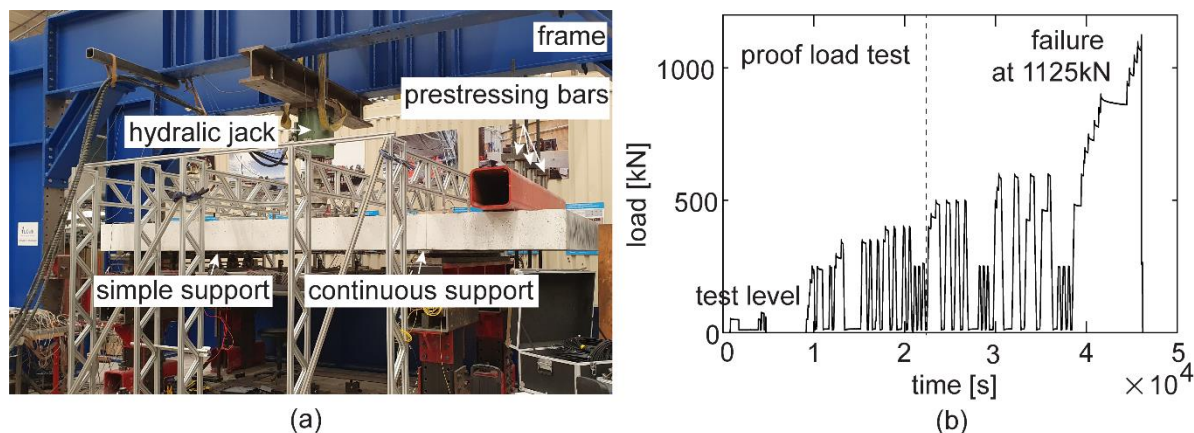
Fig. 4: (a) Photo of test setup including frame, supports and hydraulic jack, (b) loading history.

3.2 AE monitoring

AE sensors of type R6I from MISTRAS [10] were used. The central frequency is 60 kHz. The sensor was fixed to the specimen by a steel holder. Grease-like material from MOLYKOTE [11] was used as couplant between the sensor surface and structural surface. Sensors were installed both on the top and bottom surfaces. The sensor spacing in each direction was around 0.3 m, with minimum 0.25 m and maximum 0.425 m. Fig. 3 shows the sensor layout.

After installation, pencil lead break tests were carried out next to the sensor to prove sufficient coupling effect. Pencil lead with grade 2H and diameter 0.3 mm was used. The coupling was verified when the peak amplitude of the received signal was higher than 90 dB.

The data acquisition system is a 32-channel MISTRAS Express-8 system. The threshold for recording a signal was set to 45 dB. The arrival time of each signal was also automatically picked using a threshold of 45 dB.

Before loading, a preliminary measurement on wave speed was carried out (the detailed setups can refer to the thesis [12]). One sensor emitted the signal and the others received. Based on the wave travel time and distance, we estimated the wave speed. The wave speed was around 3000 m/s on the top surface and around 4000 m/s on the bottom surface. A lower wave speed on the top surface could be due to a rougher surface or more air bubble near the top. In any case, the layer that was influenced was shallow compared to the whole slab height. Therefore, we did not consider the effect of variant wave speed and used the wave speed on the bottom surface (4000 m/s) for the whole slab.

With the information of wave speed, sensor locations and arrival times of the signals, we estimated the source locations in 3D using grid search method. The grid point had a spacing of 10 mm in each direction. Source localization results outside the sensor enclosed zone were not accurate, thus were not considered.

Based on the estimated source locations, we calculated the pdAE field. The error property standard deviation of error component σ was taken as 55 mm, considering the influence from arrival time picking error and presence of cracks between source and receiver. This value is from simulated tests that have similar setups as the experiments in this paper [4].

3.3 Other measurements

Except for AE monitoring, other sensors were applied during the load testing, including laser distance finder, linear variable differential transformer (LVDT) and digital image correlation (DIC). Among them, DIC measurement is used in this paper. Photos of the bottom surface and the south surface were taken when reaching every load step. Compared to the reference (the photo that was taken before loading), the displacement field of the photo at every load level was calculated. The displacement field was then converted into the principle strain distribution, which showed the crack patterns on the bottom and side surfaces. Detailed setups can be found in the measurement report [9].

4. Results

4.1 Crack patterns on the structural surface from DIC

Fig. 5a shows the crack patterns right before failure (at 1100 kN) on the bottom and south surface obtained from DIC. The zone near loading plate was more damaged. Due to out-of-plane displacement, it is hard to estimate the crack width from DIC. The slab failed in punching at 1125 kN with a large crack opened in the north part of the bottom surface (Fig. 5b).
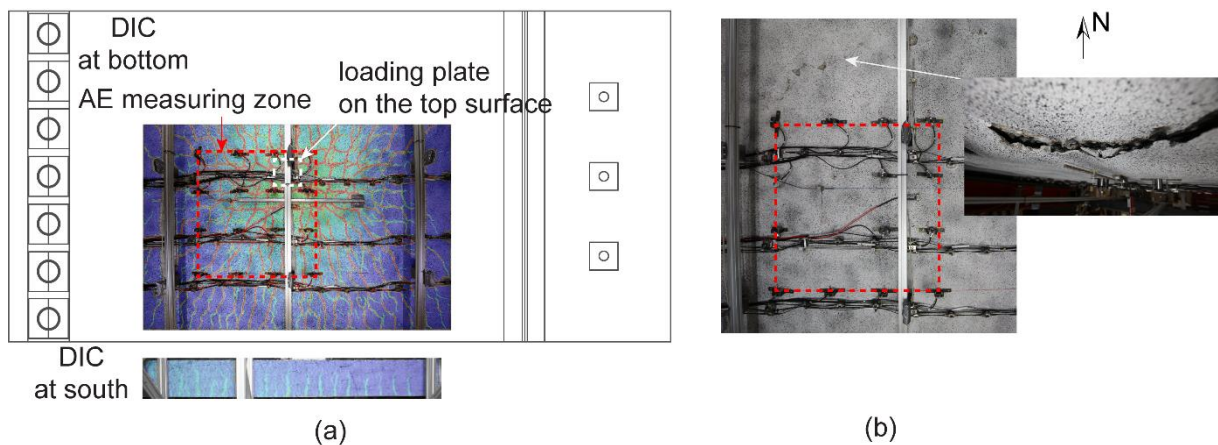
Fig. 5: Crack patterns on the bottom and the south surfaces (a) from DIC right before failure, (b) from observation after failure.

4.2 Internal crack patterns from traditional localization method

Fig. 6 shows the located AE events from the start of test to the structural failure (AE events during unloading are not included). Plot a shows the estimated locations in 3D, plot b and c respectively show the AE events in the upper and lower part of the slab in x-z plane. The estimated source locations are scattered and hard to determine the crack pattern. This is due to the larger source localization error, especially in our case when multiple cracks present between two sensors (referred to the crack patterns in Fig. 5a.
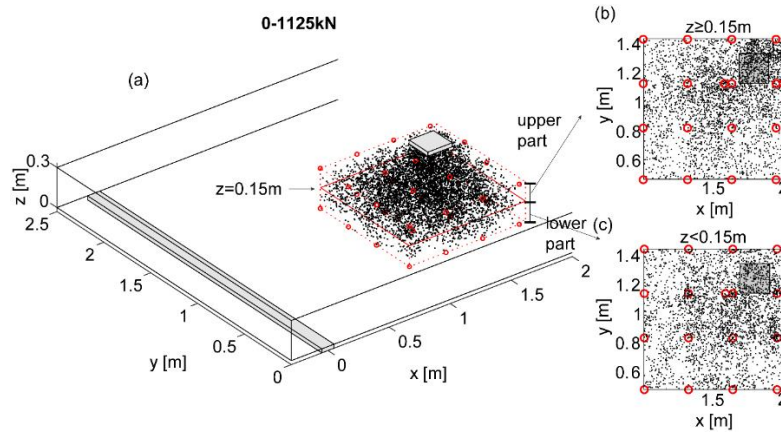
Fig. 6: Estimated source locations from grid search method until failure (0-1125 kN) excluding AE events during unloading: (a) in 3D volume, (b) in the upper part ($z \geq 0.15$ m) in x-y plane and (c) in the lower part ($z < 0.15$ m) in x-y plane.

4.3 Internal crack patterns from pdAE field method

Based on the estimated source location, we calculated the phAE field in 3D. Fig. 7 shows the sectional results from the start of test to the failure (excluding AE events during unloading). Comparing the pdAE fields at the two horizontal sections at different heights (Fig. 7b and Fig. 7c), we find that the cracks tended to concentrate to the loading plate when approaching the top section (where was the compressive zone). Comparing the pdAE fields at the vertical sections (Fig. 7d-f), we find that the section closer to the loading plate was more damaged.

To provide a 3D internal view, we plot the results in voxels (Fig. 7g). The voxel size is 20 mm × 20 mm × 20 mm. The voxel is plotted in different colours according to the pdAE value. The voxel is plotted in red, where the pdAE is over the ½ of the max pdAE. The voxel is plotted in yellow, where the pdAE is in range (¼, ½) of the max pdAE. The voxel is not plotted, where the pdAE is below ¼ of the max pdAE. The max pdAE in the detection zone is found to be 71827 m^{-3}. In 3D, the pdAE field shows a shape of punching cone under the loading plate. This meets our expectation for a punching failure. The pdAE field can more clearly detect the internal crack patterns compared to the estimated source locations using traditional method (Fig. 6).
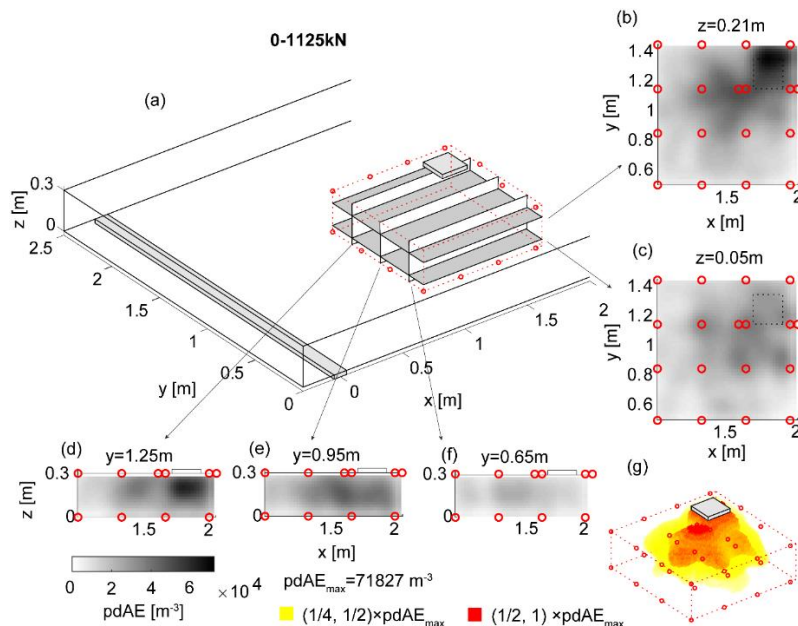
Fig. 7: The pdAE field of AE events until failure (0-1125 kN) excluding those during unloading: (a) locations of the selected cross sections, (b) sectional field at z=0.21 m, (c) sectional field at z=0.05 m, (d) sectional field at y=1.25 m, (e) sectional field at y=0.95 m, (f) sectional field at y=0.65 m and (g) voxel plot in 3D.

When new AE events occurred (excluding those during unloading), the pdAE fields from the new events were added up to the existing field. We updated the pdAE field every load step. Fig. 8 exemplifies the pdAE fields until 400 kN, 750 kN, 950 kN and 1050 kN. At 400 kN (plot a), AE events most occurred under the loading plate where the bending moment was the largest. This indicates the flexural cracking. At 750 kN (plot b), the internal cracks already formed a shape of punching cone under the loading plate, which could be a foreseen of punching failure. With further loading (until 950 kN and 1050 kN), the number of AE events increased, indicating further opening of the internal cracks that ended up as a punching cone. The results show that the pdAE field is able to indicate the punching failure before it occurs.
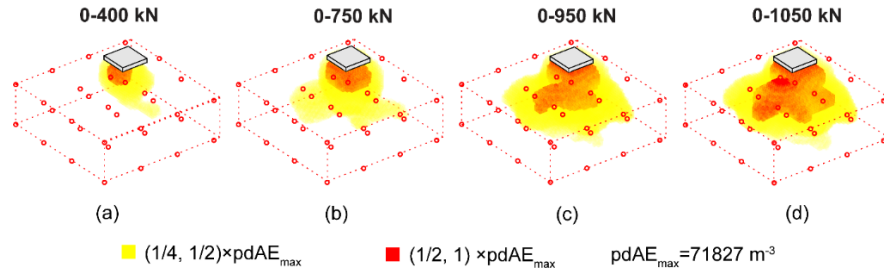

Fig. 8: The pdAE field in 3D voxels (a) until 400 kN, (b) until 750 kN, (c) until 950 kN and (d) until 1050 kN (all without AE events during unloading).

Another favourable feature of pdAE field to indicate structural failure is that the pdAE field can be computed time-efficiently. In this test, it cost less than 0.12 s to update the pdAE field when one new AE event occurred. This time was much less than other probabilistic methods in literatures (which was around 50 s) [13,14]. Moreover, updating a set of AE events together used less time than one event by another. For example, updating a set of 347 events used around 9 s, resulting in an average of 0.03 s for one event. We used Matlab to calculate, and the computational time can be improved by using faster programming language like C/C++. The effective computation of the pdAE field makes the method suitable for real-time monitoring during load testing.

5. Discussions

The above demonstration shows the benefits of using pdAE field in identifying internal damages. Firstly, compared to DIC, the pdAE field method can indicate the internal damages which are important for structural assessment. In the presented test, we detected the formation of punching cone inside the structure before the failure occurred.

Secondly, compared to traditional source localization methods, the pdAE field method can more clearly distinguish the crack patterns, by considering the source localization error in a probabilistic manner.

Thirdly, compared to other probabilistic methods in literatures [13,14], the pdAE field method significantly reduces the computational time and is suitable for a real-time monitoring.

Moreover, we found a higher pdAE in the region that was expected to be more damaged (Fig. 7 and Fig. 8). However, we were not able to build the relationship between pdAE and crack width in the presented test, since we lacked an accurate measurement of the crack width. DIC cannot measure the crack width without compensating the out-of-plane displacement. But in a previous demonstration in beams, a close relationship between pdAE and crack width has been found [4]. To implement the pdAE field method in other tests, some remarks are addressed.

- To estimate the source location, one can use any localization method. But the resultant error property needs to be adjusted correspondingly. One can use the simulations proposed in the previous paper [4] to evaluate the error property.
- For the studies that only require the crack patterns, one can directly use the source localization error property σ in range of 39-55 mm [4], without running the simulations.

- For a real-time monitoring, the pdAE field can be updated every AE event, every load step or every time interval like 60 s, depending on the users' need. The total delay of the pdAE field is the sum of time interval and calculation time.

6. Conclusions

This paper evaluated the performance of the pdAE field method in identifying the internal damages in reinforced concrete slabs. The pdAE field estimates the probability of the locations of AE events, considering the inevitable source localization errors. We demonstrated the method in the load testing of a reinforced concrete slab. A 3D pdAE field was computed and updated with increasing load. The results showed a clearer internal crack patterns compared to the traditional localization process. Moreover, the calculation of pdAE was computationally efficient, which served for a real-time monitoring. With these benefits, the pdAE field method was able to indicate the punching failure of the slab before it occurred.

7. References

[1] T. Kundu, Acoustic source localization, Ultrasonics 54(1) (2014) 25-38.
[2] M. Ohtsu, Recommendation of RILEM TC 212-ACD: Acoustic emission and related NDE techniques for crack detection and damage evaluation in concrete: Test method for classification of active cracks in concrete structures by acoustic emission, Materials and Structures 43(9) (2010) 1187-1189.
[3] M. Ohtsu, M. Uchida, T. Okamoto, S. Yuyama, Damage assessment of reinforced concrete beams qualified by acoustic emission, ACI Structural Journal 99(4) (2002) 411-417.
[4] F. Zhang, Y. Yang, M. Naaktgeboren, M.A.N. Hendriks, Probability density field of acoustic emission events: Damage identification in concrete structures, Construction and Building Materials 327 (2022) 126984.
[5] C. Grosse, M. Ohtsu, Acoustic emission testing: Basics for Research-Applications in Civil Engineering, 2008.
[6] S. Gollob, Source localization of acoustic emissions using multi-segment paths based on a heterogeneous velocity model in structural concrete, ETH Zürich, 2017.
[7] F. Zhang, L. Pahlavan, Y. Yang, Evaluation of acoustic emission source localization accuracy in concrete structures, Structural Health Monitoring 19(6) (2020) 2063-2074.
[8] M.L.L. Abell, J.P. Braselton, J.A. Rafter, J.A. Rafter, Statistics with Mathematica, Elsevier Science1999.
[9] G. Zarate Garnica, Measurement report of reinforced concrete slabs, Stevin Report, Delft University of Technology, Delft, the Netherlands, 2021.
[10] MISTRAS, R6I-AST Sensor, Product Data Sheet, MISTRAS Group Inc., Princeton Junction, NJ 08550, 2008.
[11] MOLYKOTE, MOLYKOTE 4 Electrical Insulating Compound, Product Data Sheet, DuPont de Nemours, Inc., 2018.
[12] F. Zhang, Acoustic emission-based indicators of shear failure of reinforced concrete structures without shear reinforcement, Civil Engineering and Geosciences, Delft University of Technology, Delft, the Netherlands, to be published.
[13] T. Schumacher, D. Straub, C. Higgins, Toward a probabilistic acoustic emission source location algorithm: A Bayesian approach, Journal of Sound and Vibration 331(19) (2012) 4233-4245.
[14] M.R. Jones, T.J. Rogers, K. Worden, E.J. Cross, A Bayesian methodology for localising acoustic emission sources in complex structures, Mechanical Systems and Signal Processing 163 (2022) 108143.

CRACK MODE ANALYSIS OF CEMENT MORTARS WITH SIGNAL - BASED ACOUSTIC EMISSION TECHNIQUES

Nuhamin Eshetu Deresse[1], Charlotte Van Steen[1], Mina Sarem[2], Stijn François[2] and Els Verstrynge[1]

[1]Materials and Constructions Section, Department of Civil Engineering, KU Leuven, 3001 Leuven, Belgium; nuhamineshetu.deresse@kuleuven.be, charlotte.vansteen@kuleuven.be, els.verstrynge@kuleuven.be
[2]Structural Mechanics Section, Department of Civil Engineering, KU Leuven, 3001 Leuven, Belgium; mina.sarem@kuleuven.be, stijn.francois@kuleuven.be
*Correspondence: nuhamineshetu.deresse@kuleuven.be

ABSTRACT

Determining the crack mode in structures made of brittle materials, such as concrete and masonry, is important for structural analysis and failure prediction. Fractures monitored with the acoustic emission technique (AE) are commonly classified into different modes using Rise angle (RA) – Average Frequency (AF) analysis, the simplified Green's functions for moment tensor analysis (SiGMA), and frequency spectrum analysis. However, the classification limits are dependent on the material, the test setup, and the monitoring condition. Hence, this study defines these limits by comparing the three AE-based fracture mode analysis methods on AE data collected from three test types on mortar specimens. In a direct tensile test, the peak frequencies of most of the AE events were higher (>60 kHz). While almost all of the AE events in a friction test had significantly lower peak frequency (<40 kHz). In a Brazilian splitting test, there was a shift in peak frequency from high to low value as the fracture progressed. The results of the SiGMA classification were in good agreement with the frequency analysis. AF-RA analysis also captured the tensile to shear crack mode change at progressive loading stages.

Keywords: Signal-based acoustic emission analysis, moment tensor analysis (SiGMA), frequency spectrum analysis, cement-based mortar, Brazilian splitting test, direct tensile test.

1. Introduction

When a material goes through an inelastic (irreversible) deformation, energy is dissipated and detected as an acoustic emission (AE) event. The AE technique can track material changes during the load history and is capable of localizing sources spatially and temporally. In addition, the AE technique can be used to identify the type of fracture modes. AE-based crack type classification was applied in concrete [1], cementitious mortars [2], clay brick and hydraulic lime mortar [3], reinforced concrete [4], and different types of natural rocks [5]. The fracture modes may evolve throughout the phases of the material life. Hence, identifying the fracture modes can indicate the damage stage. In quasi-brittle materials, mode-I cracks often dominate the initial damage state of the material, and mode-2 cracking (shear mode) becomes pronounced near failure [1].

Ohno and Ohtsu [1] compared the Rise angle (RA) – Average Frequency (AF) and the simplified Green's functions for moment tensor (SiGMA) analysis on cracks induced by a four-point bending test of concrete and reinforced concrete beams and also used a hydrostatic expansion test of a concrete prism. It was found that applying RA-AF analysis on only the first hit of AE events gave similar results as the SiGMA analysis. Hence, the number of AE events classified as tensile and mixed-mode by the SiGMA method were similar to the number of events classified as the tensile mode by the RA-AF method. This good agreement was found when the ratio between the RA and AF was set at 1 to 200. In addition, Ohno and Ohtsu [1] noticed a dominant tensile crack mode for the four-point bending test of the concrete beam and a dominant shear crack mode for the hydrostatic expansion test of the concrete prism. Aggelis, et al. [2] applied RA and AF analysis on AE events detected from bending and shear tests performed on cement-based mortars. The research compared the AF, the peak frequency, and the RA values of all AE events detected in the experiment. As opposed to the shear test, higher AF and peak frequency, and lower RA values were observed for the bending tests. In addition, the research revealed the sensitivity of AF, peak frequency and RA to sensor-source distance. Zhang, et al. [4] investigated AE source classification on RC beams and RC slab tests. The research found that peak frequency and partial power showed a clear boundary between signals from two types of AE sources (i.e., partial power is calculated by summing the power of the frequency spectrum in a specified range of frequencies and dividing it by the total power of all frequencies). AE sources with peak frequency above 70 kHz were identified as tensile crack mode. Du, et al. [5] performed a Brazilian splitting test, three-point bending test, modified shear test, and uniaxial compressive test on different rock types (granite, marble, and sandstone). It was found that AE from tensile crack had a peak frequency above 100 kHz, and those from shear crack had peak frequency below 100 kHz. Livitsanos, et al. [6] performed three-point bending and modified shear tests on different mortars and red clay bricks. The crack modes were monitored using AF-rise time (RT) analysis and digital image correlation (DIC). The AF-RT analysis was found powerful in identifying the fracture modes in complex tests where the crack modes would not otherwise be known. This was validated using the strain field plots obtained from the DIC.

Despite the performance of AE in crack mode analysis, defining boundaries for classification still requires dedicated investigation of the specific material, sample geometry, testing, and AE monitoring condition. This research aims at developing a method of crack type and noise classification that can be applied to small-sized cementitious mortars in the Brazilian splitting test.

2. Experimental test program

2.1 Materials and mechanical tests

A cement mortar was used for all test specimens, with a composition of 533 kg/m³ CEMII/B (S-L) 32.5 N; 1600 kg/m³ river sand with a maximum aggregate size of 4 mm and 0/2 grain size curve distribution according to EN 13139 and 266.5 l/m³ water, resulting in a 0.5 W/C ratio. Conditions of sample preparation and curing are described in [7].

For direct tensile tests, cylinders with 50 mm in diameter and 150 mm in length are cored (drilled) from a 150 mm x 150 mm x 150 mm mortar cube. At mid-height, a notch with 5 mm depth and an opening of 7 mm was sawn around the circumference, resulting a 40 mm diameter section at the notch, see Fig. 1 and Fig. 2. The top and bottom edges of the notched samples are gripped with a PVC ring with a height of 20 mm and an inner diameter of 50 mm, which is then glued to a steel plate with a two-component adhesive. The steel plates are connected to a testing machine by four bolts. The test was a displacement-controlled test with a rate of 0.1 mm/min.

Three mortar cylinders with 100 mm in diameter and length (named L_1 to L_3) and three cylinders with 27 mm in diameter and length (S_1 to S_3) are prepared in molds for the Brazilian splitting tests. During testing, the load is distributed in small strips at the top and bottom contact points to avoid excessive stress concentration and crushing at load application points. These load-bearing strips

are made of hardboard with a thickness of 3 mm and a width of 15 mm for the larger samples and 4 mm for the smaller samples, see Fig. 1 and Fig. 2. The Brazilian splitting test is a monotonic force-controlled test. The loading rate is 705 N/s for the larger samples and 45 N/s for the smaller samples (i.e. valued adopted from EN 12390-6 [8]). The loading is applied using a universal testbench (Shimadzu AG-X), with a maximum capacity of 100 kN. During the test, the load and stroke displacement of the crosshead were recorded.
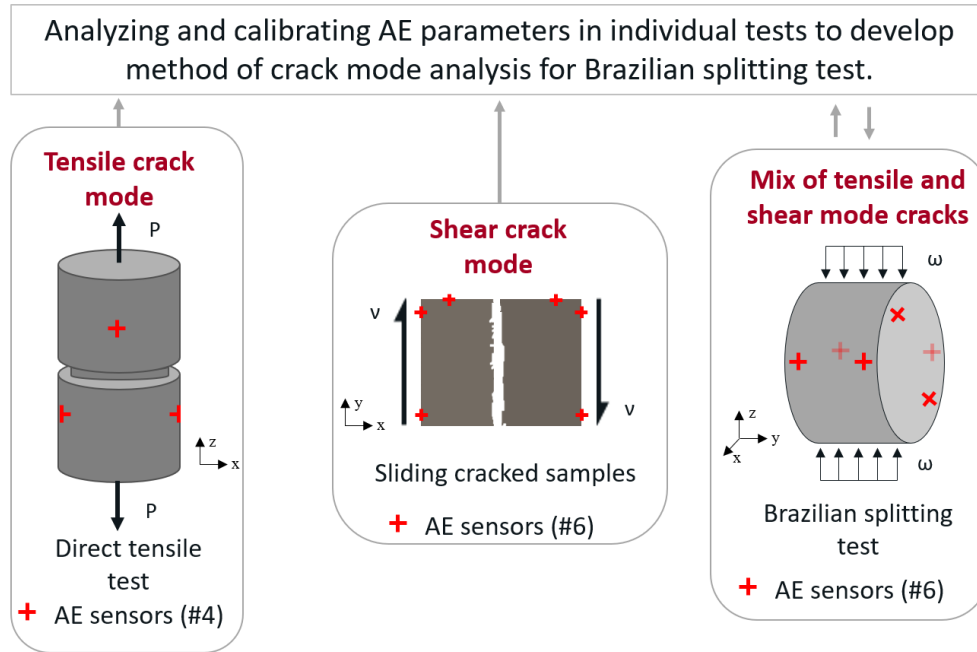
Fig. 1: Schematic representation of the different tests and their objectives.

For the friction test, one of the larger samples that broke during a Brazilian splitting test is used to generate friction noise by manually sliding the crack surfaces against each other while monitoring the noise with AE technique, see Fig. 1.

2.2 Acoustic emission setup

A Vallen AMSY-6 acquisition system with six-channel ASIP-2/S AE boards is used to monitor all the tests. Piezoelectric AE sensors (Digital Wave B1025) with a miniature size (9.3 mm diameter x 12.7 mm height) and a 50 to 2000 kHz frequency range are attached with a thin layer of hot-melt glue on the sample surface. The sensor layout for the three tests is shown in Fig. 1. The AE sensors were connected to preamplifiers with 34 dB gain (AEP5, Vallen) and subsequently to the acquisition system. The digital frequency filter was set between 25 kHz to 850 kHz. The amplitude threshold was set at 40 dB, a value determined by monitoring the environmental noise of the laboratory. AE data are recorded at a sampling rate of 10 MHz, with 4096 samples per signal and 409.6 µs in resulting signal length. The rearm time and the duration discrimination time for AE hit definition are both taken as 200 µs. Real-time data is visualized using Vallen Visual AE software. Further post-processing analysis was conducted with an in-house developed AE toolbox in MATLAB.

Fig. 2: Photograph of (a) the direct tensile test (b) the Brazilian splitting test.

3.   Results and discussion

3.1 AE peak frequency

The peak frequencies of the first AE hits in the AE events are analyzed. Fig. 3 shows the time evolution of the peak frequencies (i.e. with a moving mean of 10 data points) and loads for the Brazilian splitting tests with the two different sample sizes. It can be seen for all the cases that the peak frequen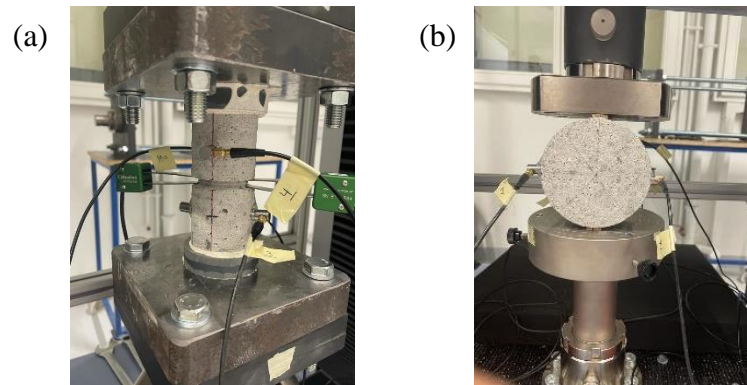cy lowers as the load approaches the peak value. This can be because of frequency attenuation due to the formation of cracks. It can also be because of the increase of crack sizes and the transformation of crack mode from tensile to shear as failure is approached [1, 9]. AE with low peak frequency are also identified at the very beginning of the test, this can be due to the local crushing of the sample at the contact surface. Such AE events due local crushing is more prominent in the larger sample, this is because of the relatively higher contact force that is generated on the larger sample. When comparing the magnitude of the peak frequencies in the small and larger samples it can be seen that the peak frequencies in the smaller samples are significantly higher than the larger sample. This is because for larger samples, there is relatively higher frequency attenuation due to longer source to sensor distance [2, 10].

Fig. 4 shows the histograms of the peak frequencies for all of the AE events detected in a Brazilian splitting test at progressive loading stages. At the pre-peak loading stage (10 to 90%) AE events with high peak frequencies (60 to 100 kHz) dominate. This is more pronounced for the smaller samples, see Fig. 4 a), c) and e), mainly because there is relatively less frequency attenuation for the smaller samples. In addition, there is also a surge of AE with low peak frequencies near the peak load (90 to 100%) and in the post peak phase (100 to 90%). This is even more significant for the larger samples, see Fig. 4 b), d) and f), where there is an increase of AE events with low peak frequencies near the peak load (90 to 100%) and almost no AE activity at the post-peak stage (100 to 90%). This is mainly because for larger samples, there is a sudden (brittle) crack propagation that will intensify the effect of attenuation and generation of shear noise [7].

Fig. 5 a) shows the histogram of the peak frequencies for all AE events detected in the direct tensile test. Fig. 5 b) shows the histogram of the peak frequencies for the AE signals detected only in the pre-peak stage (0 to 100%) of the direct tensile test. As it can be inferred when analyzing the AE recorded in the pre-peak stage (0 to 100%), most of the AE events have higher peak frequencies (60 kHz - 80 kHz). Hence, to analyze damage initiation in tensile tests such as Brazilian splitting test or direct tensile test, focus can be made on AE signals with relatively higher peak frequencies.
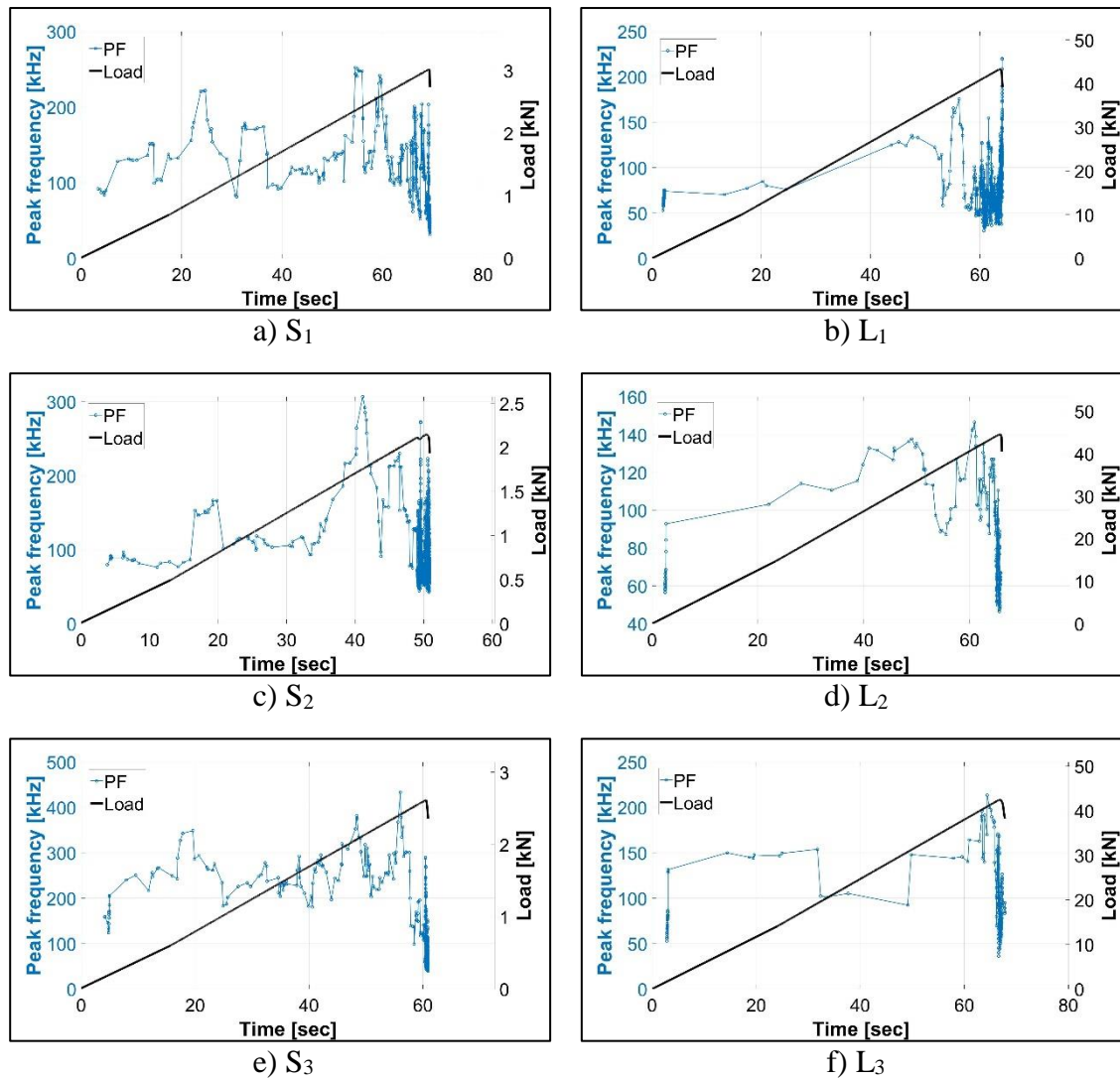
Fig. 3: Evolution of the peak frequency of the first hit of AE events and load with time in a Brazilian splitting test, (left) the small samples (right) the large samples.

The histogram of the peak frequencies of all of the AE events in the friction tests is shown in Fig. 6. Here, as expected, AE events with low peak frequencies mostly dominate the histogram. This further asserts that shear/friction induces AE events with relatively lower peak frequencies [2, 4, 11].

The limits of peak frequencies to identify tensile and shear crack modes can be defined using the AE signals detected from the different tests and also by comparing the AE events in the pre- and post-peak loading stage. Hence, AE signals with peak frequencies greater than 60 kHz can be identified as likely due to tensile crack modes. The limits are defined by considering frequency attenuation due source-sensor distance by regarding the analysis of the two sample sizes in the Brazilian splitting test.
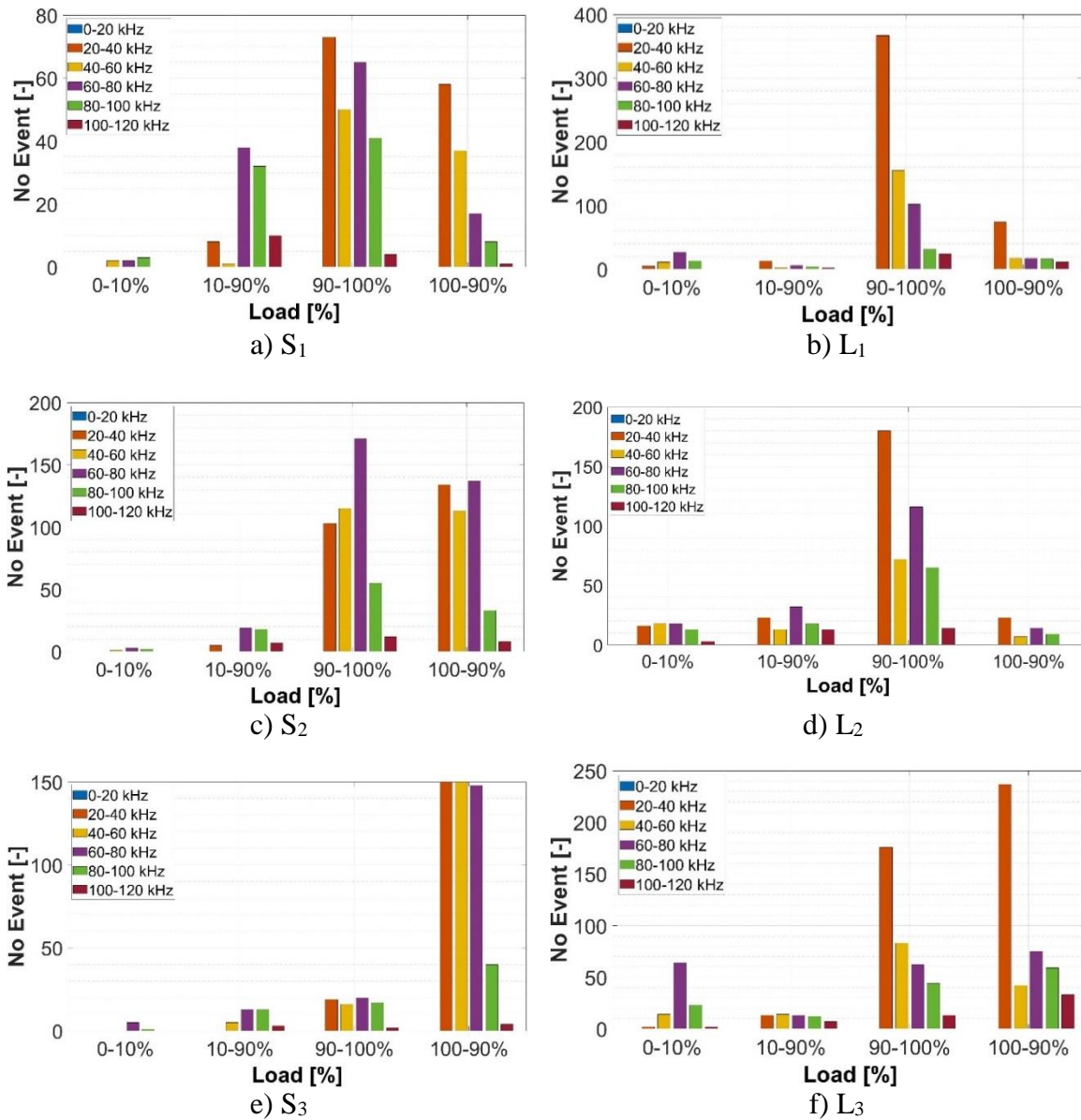
Fig. 4: Histogram of the peak frequency (with each bar having a 20 kHz range) of the first hit of AE events at progressive loading stages. (left) Small samples of Brazilian splitting test, (right) Large samples of Brazilian splitting test (the load percentage is a percentage of the peak load).
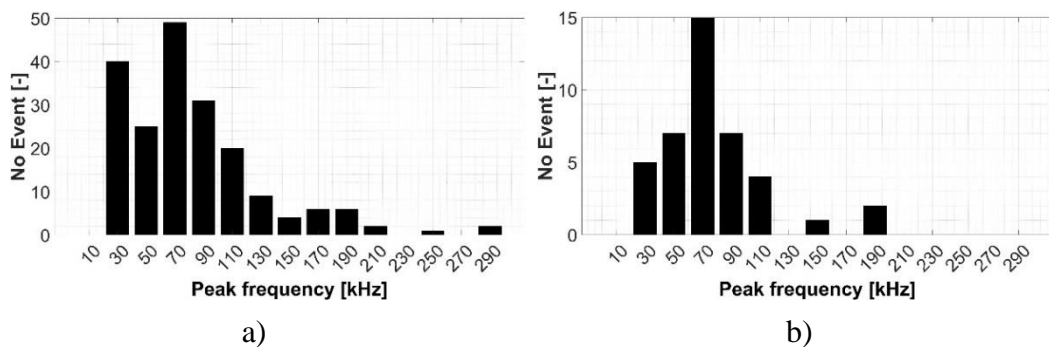
Fig. 5: Histogram of the peak frequency of the first hit of AE events of the DTT. (a) Histogram for all of the AE data detected in the test duration, (b) Histogram for the AE data detected in pre-peak loading stage (0 to 100%) (the load percentage is a percentage of the peak load).
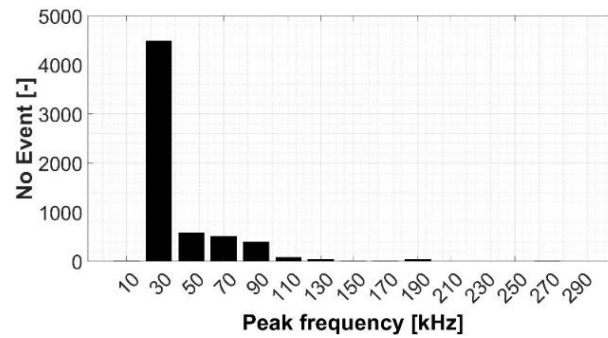
Fig. 6: Histogram of the peak frequency of the first hit of all AE events for the friction test.

3.2 *Moment tensor analysis*

Fracture modes are characterized by a specific radiation pattern of the seismic energy detected by the sensors. The radiation pattern can be visualized using stereographic projections. These are projections of the compressive wave onset amplitude on the hemisphere around the source [12]. Hence, the sign of the first arrival p-wave at different sensors (polarities of initial P-wave pulses) can be used to identify the type of fracturing mechanism. Moment tensor analysis was originally used to analyze fault motions in seismology [13]. However, Ohtsu, et al. [14] developed SiGMA (simplified Green's functions for the moment tensor analysis) for the AE inversion analysis to classify crack type and to determine crack orientation. In this paper, the algorithm for SiGMA analysis for crack mode classification was prepared following the steps stated in Ohtsu, et al. [14], Ohtsu and Aggelis [15].

Fig. 7 shows the results of AE-based fracture mode classification using SiGMA analysis in a localization plot and in a peak frequency-time plot for two representative Brazilian splitting tests and the friction test. From the SiGMA classification, it can be observed in Fig. 7 a) and b) that the Brazilian splitting test is dominated by tensile cracks (red dots), while the friction test, see Fig. 7 c) gave more mixed and shear crack modes (green and blue dots). Since these results are as expected, it demonstrates the capabilities of moment tensors analysis in crack mode classification. In addition, it can been seen in Fig. 7 a) and b) that cracks classified as tensile with SiGMA analysis have higher peak frequencies. This validates the previous observations that as peak frequency decreases, the crack mode transforms from tensile to shear. As discussed before, peak frequency is affected by signal attenuation; hence as the source-sensor distance increases or as a crack progresses, using peak frequency for crack classification can be difficult as all of the AE events will have lower peak frequencies. However, as can be seen in Fig. 7 a) and b), SiGMA analysis can classify even attenuated (lower peak frequency) AE events. This is especially useful near the peak load (90 to 100 %), where cracking intensifies.

On the other hand, as observed in Fig. 7 c), some AE events are identified by SiGMA as tensile modes in the friction test and have lower peak frequency (< 50 kHz). Hence both methods result in few false classifications and results should be considered carefully, yet in general, both have shown great potential in crack mode analysis. Main disadvantage of SiGMA analysis is that it can only be used for AE events that are detected by six or more sensors and for those that were able to be localized. These AE events are only small fractions of the overall AE data collected during the test. Hence, SiGMA can be used to understand the overall dominant crack mode in a test or a specific region of the sample. However, it has less use for applications such as AE signal filtering.

a) L_1 in a Brazilian splitting test

b) S_1 in a Brazilian splitting test

c) Friction test
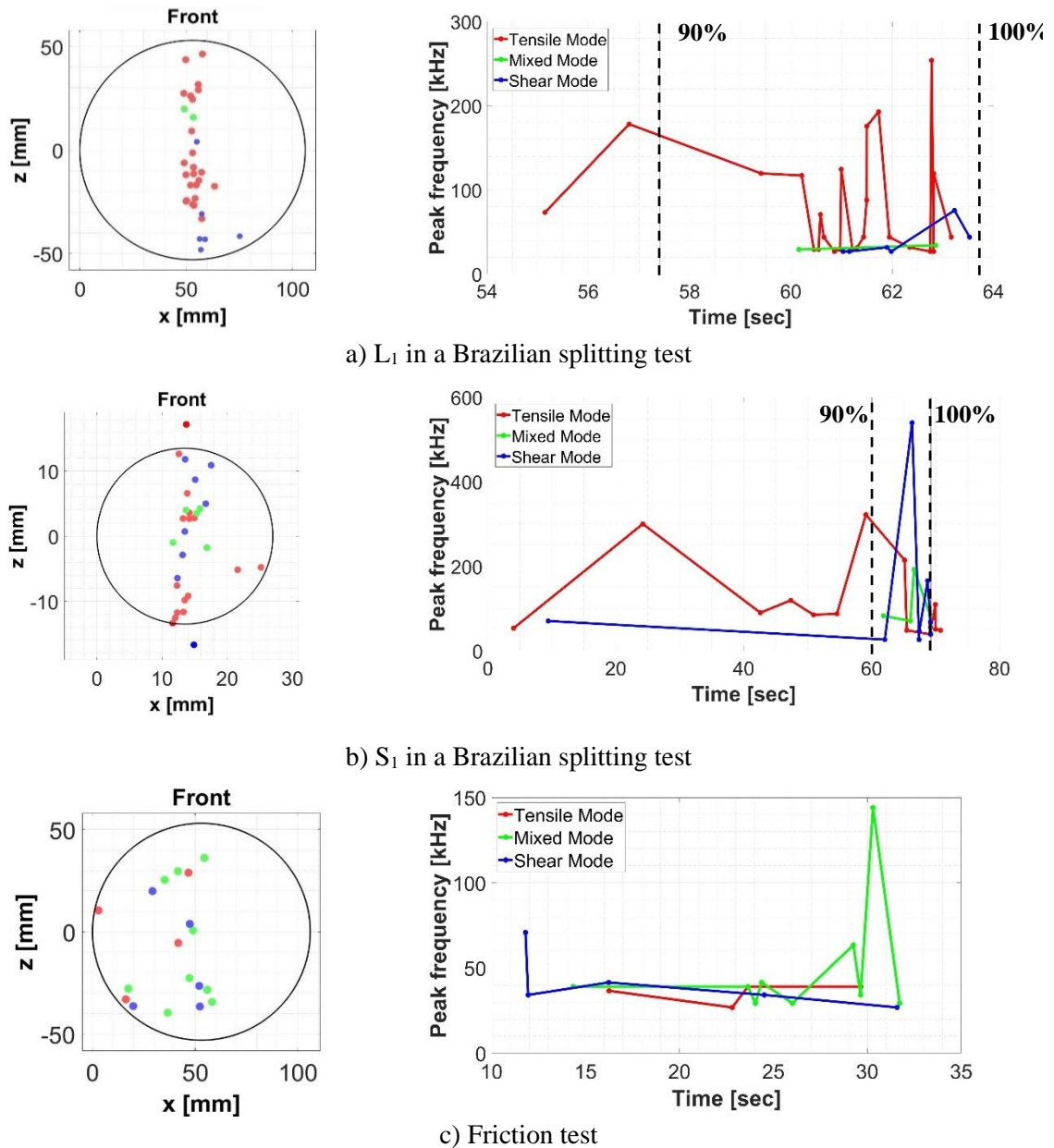
Fig. 7: SiGMA based crack mode classified AE events, (left) shown in a AE localization plot (right) shown in a peak frequncy vs time plot for different tests.

3.3 AF RA analysis

Directly measured AE parameters such as 'Count', 'Amplitude', 'Rise time' and 'Duration' are used to calculate AF and RA. AF is calculated by dividing the 'Count' by the 'Duration'. RA is calculated by dividing 'Rise time' by 'Amplitude'. Fig. 8 a) shows the AF-RA plots of the AE events for the direct tensile test and Fig. 8 b) is the AF-RA plot for all of the AE events detected in the friction test. To classify the tensile and friction events, following boundary line is proposed: $AF = 0.5 \times RA$. This line is defined by assuming that most of the AE events in the pre-peak period of the direct tensile test are tensile mode and most of the AE events in the friction test are shear mode, as was also concluded from the previous section.

Fig. 8: AF-RA plots of the AE events detected from (left) the direct tensile test at the pre- and post-peak loading stage and (right) the friction test.

Fig. 9 shows the AF-RA plots of AE events at progressive loading stages (as a percentage of the peak load) of a Brazilian splitting test. The same dividing line was used in this plot as well. It can be seen that the AF-RA plot also reflects the same results as SiGMA and peak frequency analysis. There are shear noises at the initial contact loading phase (0 to 10%), there is the dominance of the tensile crack mode in the pre-peak stage (10 to 90%), and the shear mode starts to dominate near the peak loading stage (90 to 100%) and the post-peak loading phase (100 to 90%). In literature, the AF-RA plots are often made by averaging the AE hits or AE event values due to high scatter. Here, however, AF-RA plots are made with the individual values of the first hit in AE events (without averaging). Although there are some false classifications, this analysis is still able to capture expected results and is in good agreement with SiGMA and peak frequency analysis.
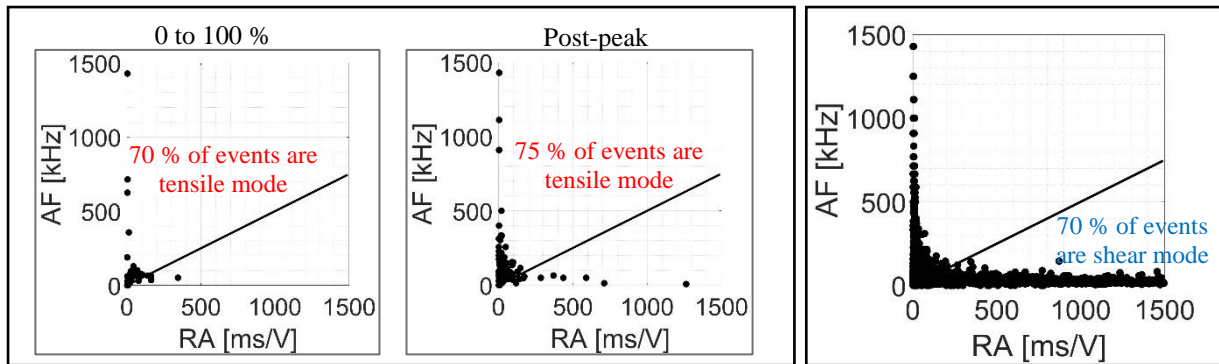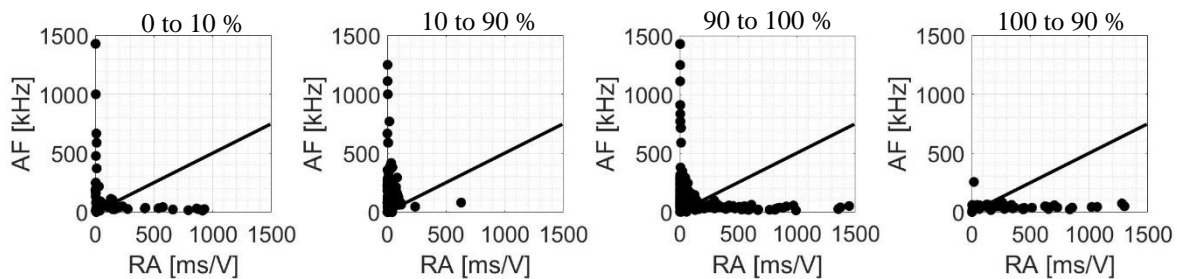

Fig. 9: AF-RA plots of the AE events detected from a representative Brazilian splitting test of a larger sample (L_2) at progressive loading stages.

4. Conclusions

The study compares three acoustic emissions (AE)-based crack mode analysis techniques on cement mortars subjected to different mechanical loading schemes: direct tensile test, Brazilian splitting test, and friction test. From the analysis, the following main conclusions are drawn:

- A significant number of AE events in the friction test have low peak frequencies (<40 kHz). On the other hand, a high number of AE events with high peak frequencies (>60 kHz) are detected during the pre-peak loading stage (0 to 100%) of the direct tensile test. Similarly, in the Brazilian splitting test, high peak frequency AE events dominate the pre-peak phase (10 to 90 %). However, near the peak (90 to 100%) and in the post-peak (100 to 90%) phase, there was an increase in the number of AE events with low peak frequencies, which was attributed to a shift in failure mode. In addition, due to attenuation AE events in the larger samples had relatively lower peak frequencies.
- SiGMA analysis-based crack classification resulted in more tensile AE events in the Brazilian splitting test than in the friction test. A strong correlation between the SiGMA and peak frequency analysis has been found.

- AF-RA analysis showed similar crack mode shift at progressive loading stages of the Brazilian splitting tests. In addition, a tensile-shear dividing line (AF = 0.5xRA) was defined using direct tensile and friction tests, and validated on the Brazilian splitting tests.

5. Acknowledgements

6. References

[1]   K. Ohno and M. Ohtsu, "Crack classification in concrete based on acoustic emission," *Construction and Building Materials,* vol. 24, no. 12, pp. 2339-2346, 2010/12/01/ 2010.

[2]   D. Aggelis, A. Mpalaskas, and T. Matikas, "Investigation of different fracture modes in cement-based materials by acoustic emission," *Cement and Concrete Research,* vol. 48, pp. 1-8, 2013.

[3]   G. Livitsanos *et al.*, "Acoustic emission characteristics of fracture modes in masonry materials," *Construction and Building Materials,* vol. 162, pp. 914-922, 2018.

[4]   F. Zhang, Y. Yang, S. A. Fennis, and M. A. Hendriks, "Developing a new acoustic emission source classification criterion for concrete structures based on signal parameters," *Construction and Building Materials,* vol. 318, p. 126163, 2022.

[5]   K. Du, X. Li, M. Tao, and S. Wang, "Experimental study on acoustic emission (AE) characteristics and crack classification during rock fracture in several basic lab tests," *International Journal of Rock Mechanics and Mining Sciences,* vol. 133, p. 104411, 2020/09/01/ 2020.

[6]   G. Livitsanos, N. Shetty, E. Verstrynge, M. Wevers, D. Van Hemelrijck, and D. G. Aggelis, "Shear failure characterization in masonry components made with different mortars based on combined NDT methods," *Construction and Building Materials,* vol. 220, pp. 690-700, 2019/09/30/ 2019.

[7]   N. E. Deresse, C. Van Steen, M. Sarem, S. François, and E. Verstrynge, "Acoustic Emission Analysis of Fracture and Size Effect in Cementitious Mortars," *Applied Sciences,* vol. 12, no. 7, p. 3489, 2022.

[8]   "NBN EN 12390-6:2009: Testing hardened concrete. Tensile splitting strength of test specimens," ed: NBN, 2010.

[9]   D. G. Aggelis, "Classification of cracking mode in concrete by acoustic emission parameters," *Mechanics Research Communications,* vol. 38, no. 3, pp. 153-157, 2011.

[10]   C. U. Grosse, M. Ohtsu, D. G. Aggelis, and T. Shiotani, *Acoustic Emission Testing: Basics for Research-Applications in Engineering*. Springer Nature, 2021.

[11]   N. E. Deresse, C. Van Steen, M. Sarem, S. François, and E. Verstrynge, "Acoustic emission-based damage monitoring to study fracture in cementitious mortars under fatigue loading," *European NDT & CM 2021,* 2021.

[12]   F. Finck, M. Yamanouchi, H.-W. Reinhardt, and C. U. Grosse, "Evaluation of mode I failure of concrete in a splitting test using acoustic emission technique," *International Journal of Fracture,* vol. 124, no. 3, pp. 139-152, 2003/12/01 2003.

[13]   C. U. Grosse, M. Ohtsu, D. G. Aggelis, and T. Shiotani, *Acoustic Emission Testing*. Springer, 2022.

[14]   M. Ohtsu, T. Okamoto, and S. Yuyama, "Moment tensor analysis of acoustic emission for cracking mechanisms in concrete," *Structural Journal,* vol. 95, no. 2, pp. 87-95, 1998.

[15]   M. Ohtsu and D. Aggelis, "Innovative AE and NDT techniques for on-site measurement of concrete and masonry structures," *RILEM State-of-the-Art Reports,* vol. 20, pp. 89-103, 2016.
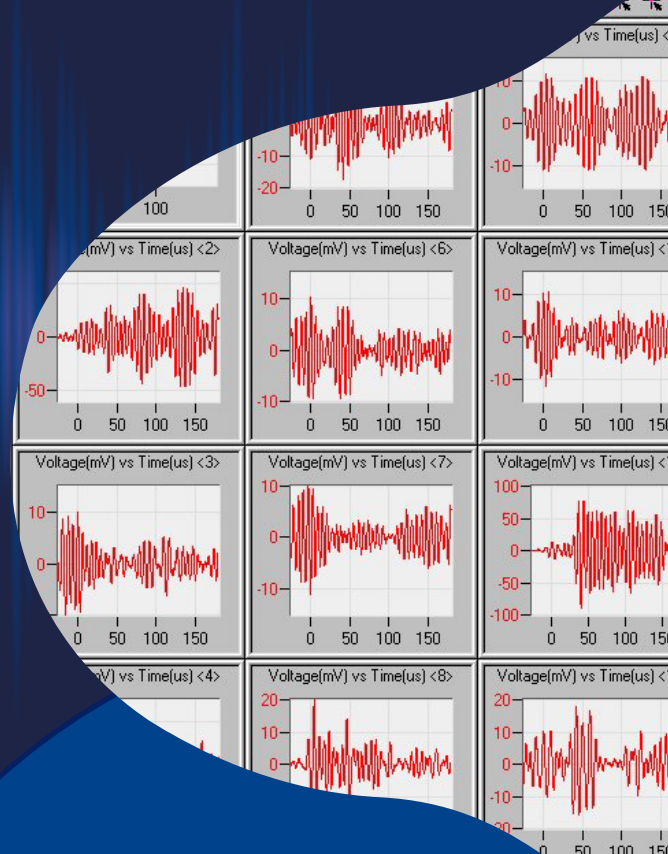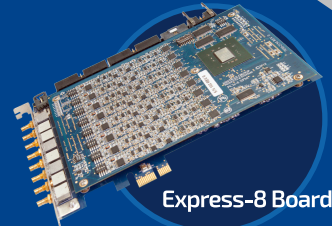
MONITORING OF FRESH CONCRETE WITH SUPERABSORBENT POLYMERS (SAPS) USING ACOUSTIC EMISSION (AE)

Eleni Korda[1,2], Eleni Tsangouri[1], Didier Snoeck[3], Geert De Schutter[2] and Dimitrios G. Aggelis[1]

[1]Vrije Universiteit Brussel, Faculty of Engineering, Brussels, Belgium;
eleni.korda@vub.be, eleni.tsangouri@vub.be, dimitrios.aggelis@vub.be
[2]Gent University, Faculty of Engineering and Architecture, Gent, Belgium;
eleni.korda@ugent.be, geert.deschutter@ugent.be
[3]Université Libre de Bruxelles, Brussels School of Engineering, Brussels, Belgium;
didier.snoeck@ulb.be
*Correspondence: eleni.korda@vub.be; tel.: +32 456155502

ABSTRACT

In fresh concrete, early-age shrinkage is affected by many factors, such as thermal deformations moisture loss and the hydration reaction. Novel admixtures for internal curing, like SuperAbsorbent Polymers (SAPs) can be used to mitigate the shrinkage phenomenon. These admixtures strongly modify the microstructure influencing the Acoustic Emission (AE) activity. Acoustic emission has been proven adequate to monitor activities during the curing of fresh cement-based materials. However, so far, it is difficult to distinguish the original mechanisms due to the overlapping nature of the processes that take place. In addition, localization of AE sources is not possible due to the heterogeneous and damping nature of the fresh material. The motivation of this study is to obtain real-time information on the different ongoing processes in fresh concrete, like settlement and shrinkage cracking, using AE and comparing the results to concrete containing SAPs. A preliminary study for 3D source localization in fresh concrete is also performed. The goal is to control concrete curing and confirm suitable final mechanical properties, resulting therefore in more sustainable materials.

Keywords: Acoustic Emission, fresh concrete, superabsorbent polymers, localization.

1. Introduction

Fresh cementitious media present complex and overlapping processes due to water evaporation and cement hydration. While concrete is in the plastic state, the cement particles' movement can lead to early shrinkage cracking which can be critical for the final mechanical properties of the material. The long-term performance of concrete is closely linked to its early age properties; hence it is important to understand and isolate the different mechanisms taking place during hydration. Therefore, monitoring the early-age concrete behavior is important. Non-destructive techniques have gained a lot of attention recently for the characterization of fresh cementitious materials [1]. Acoustic Emission (AE) is a non-invasive monitoring technique that presents a high sensitivity to recording waves released by many processes simultaneously. AE has been lately used by researchers to monitor the hydration process [2,3,4,5]. According to the cumulative activity and the AE parameters, the various curing stages and cracking modes can be detected. For example,

shear cracks are characterized by lower frequencies and longer duration, than tensile cracks, information that can be very useful when it comes to material or damage characterization.

In fresh concrete, early-age shrinkage is affected by many factors, such as thermal deformations due to the hydration reaction, moisture loss, and hardening due to changes in pore water content. Novel admixtures like SuperAbsorbent Polymers (SAPs) have been successfully used to mitigate the shrinkage phenomenon [6]. SAPs are particles that can swell by absorbing water, up to 500 times their mass, and later release it back to the cementitious matrix promoting autogenous healing [6]. According to the literature, when the action of SAPs is initiated, high bursts of AE data are observed [1]. So far, the investigation of the SAP behavior in fresh cementitious media has been limited to mortar specimens. In the present study, the behavior of a reference concrete mix is compared to that of a mix containing SAPs, to study the SAP influence on the AE behavior of fresh concrete cubes.

2. Materials and methods

2.1 Materials
A reference concrete mixture and a mixture containing SAPs were investigated for this study. Portland cement (CEM I 52.5 N Strong, Holcim, Belgium) was used, with a water-to-cement ratio of 0.35 (REF). River sand, fine stones and coarse gravel stones (sizes 4/8 and 6.3/14) were used in a proportion of 1.27:1.27:2.36 with respect to the weight of cement. The sand and the aggregates were dried in the oven for 48 hours and then let to naturally cool down at room temperature prior to mixing. Superplasticizer MasterGlenium 51 from BASF (Ludwigshafen, Germany) was added at a percentage of 0.6% by mass of cement to ensure sufficient workability.

A second composition (VP400) was made including SAPs in a percentage of 0.2% per cement weight and the same amount of aggregates and sand and cement as the reference mixture. The utilized SAP type was provided by BASF (Ludwigshafen, Germany) and is a copolymer of acrylamide and sodium acrylate with a dry particle size equal to 100 ± 21.5 µm. An additional amount of water, equal to 30 grams per gram of SAP, was added to the mix, to obtain the identical flow as the reference concrete while using the same amount of superplasticizer as the reference cube.

2.2 Specimens
The material was mixed for a total of four minutes in the laboratory concrete mixer, at 361 RPM, with one minute of dry mixing and 3 minutes of mixing with water. Then it was poured into a 150 mm x 150 mm x 150 mm (internal dimensions) metallic mold. Type-K thermocouples were used to monitor the temperature released during the hydration process. The mix was poured into the mold in two layers. Initially, the mold was filled up to the mid-height, and then the thermocouples were placed at the center of the mold. The rest of the mix was added, and the mold was vibrated at a high frequency for 20 seconds until the surface was smooth.

2.3 Acoustic emission
The AE behavior of the samples was monitored by five R15a piezoelectric sensors, with a resonance frequency of 150 kHz using the Micro-II express acquisition system by Mistras Group. Five sensors were attached in total, one on every outer side of the mold, at different heights and one at the bottom, using a coupling agent and magnetic clamps. A schematic view of the experimental setup is represented in Fig. 1.

A sensitive and low threshold was set equal to 35 dB and the AE signals were amplified using a preamplifier 1220A of 40 dB. A Pencil Lead Break (PLB) was performed near every sensor before the initiation, but also at the end of the monitoring, to ensure the coupling efficiency of the sensors to the mold. The measurements started between 10-12 minutes after water was added to the dry materials. Each cube was monitored for approximately three days.
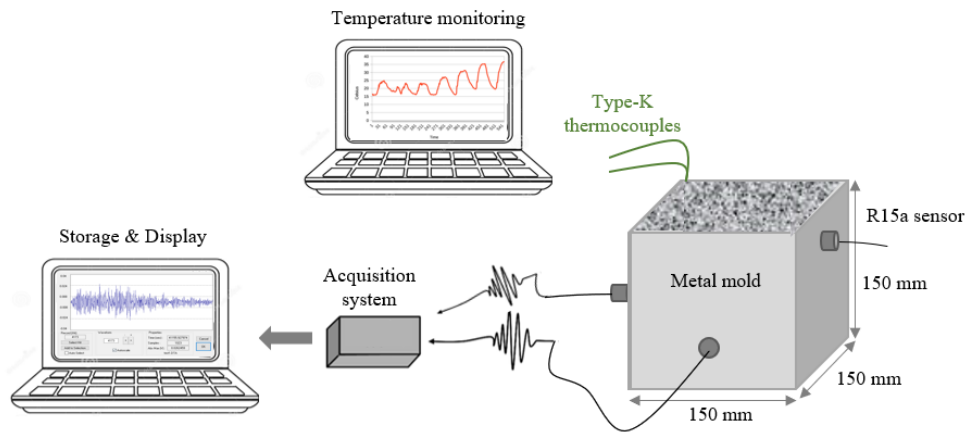
Fig. 1: Schematic view of the experimental setup.

2.4 Source localization

By considering the position of the sensors and the difference in the arrival time on each of them, the source location can be calculated, provided that the wave velocity in the medium is known. In this study, an attempt for a three-dimensional localization in fresh concrete was made for the first time, using the AE Win Software by Mistras Group. For a 3D localization, at least 4 sensors are needed for the algorithm to calculate the location coordinates. The time of the first recorded hit is considered the absolute arrival time, and it is used to calculate the delay in arrival times of the upcoming hits in the event.

Since concrete undergoes hydration and the stiffness increases, the velocity at which the elastic waves propagate changes as well. This makes the localization in the highly attenuative nature of cementitious materials complicated. To overcome this issue, different velocities were used to account for each curing stage and changing stiffness, based on ultrasonic measurements conducted by Lefever et al. [7] on mortar specimens made using the same cement as this study. Although the velocity of mortar is not the same as the one of concrete, a good approximation can be derived from the results of [7]. Early UPV measurements on concrete specimens unfortunately are not possible due to the highly attenuative nature of the material, but also due to the larger required mold thickness compared to mortar. The aforementioned factors result in a significant attenuation of the signal during the first hours of measurements when concrete is still very fresh. The three-day monitoring period was divided into four phases according to the different mechanisms of interest.

3. Results and discussion

3.1 Evolution of AE parameter and temperature during internal curing

The SAP activity was well-captured by the sensors, showing a vertical increase in the cumulative hits, as seen in Fig. 2(a). The cumulative hits for REF were approximately 5000 while for VP400 they were much higher approximately 48000. The initiation of the SAP activity took place at approximately 12 h of monitoring and lasted up to 20 h. To define the time when the SAP action was completed, the hit rate was examined. The time of the SAP activity termination was selected as the time when the hit rate dropped to 10% of the maximum hit rate. Indeed, this time is around between 20 and 21 h. As seen in Fig. 2(a), after 20 h, the slope of the cumulative hits rate starts to decrease, indicating that most of the SAP action was completed.

It is not clear if the increased AE activity is due to the SAPs releasing the entrained water or due to the consumption of the free water by the SAPs. Snoeck et al. [8] studied the release of water from the SAPs towards the cementitious matrix during the cement hydration, using the Nuclear Magnetic Resonance (NMR) method, using the same SAP and cement type as the ones used for

this study. The results showed that up to 11 h, SAPs release a little amount of the entrained water after the final setting is reached. Then, up to 22 h, the free water was consumed and a slight decrease in the SAP shape was observed, due to possible debonding of the SAP from the pore wall [9]. After that, the entrained water starts to decrease again, up to 30 h.

Fig. 2b shows the temperature development at the center of the cube. The reference cube exhibited slightly higher temperatures, although the slope of the curve during the acceleration period is the same for the two mixtures. The peak temperature for the reference specimen reached 31.2 °C, while for the specimen with SAPs the peak value was 30.8 °C. The ambient temperature during monitoring varied between 28 °C and 29 °C. The raw materials were left at room temperature before mixing. The high AE activity starts around 12 h which coincides with the end of the acceleration period of hydration (peak of the temperature curve). This could indicate that most of the free water is consumed, lowering the relative humidity, hence, causing the SAPs to release their entrained water. The end of the SAP activity seems to coincide with the end of the deceleration period of hydration.
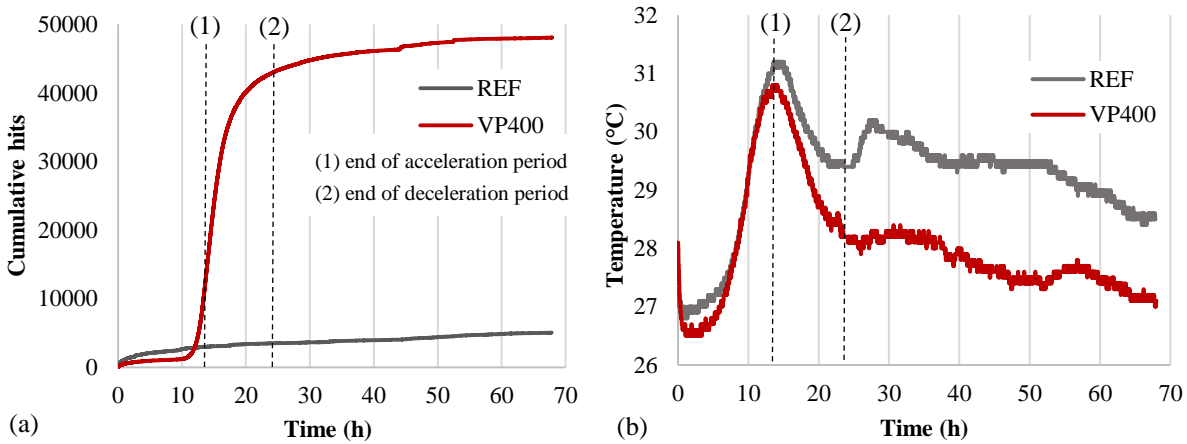
Fig. 2: (a) Cumulative activity; (b) temperature evolution.
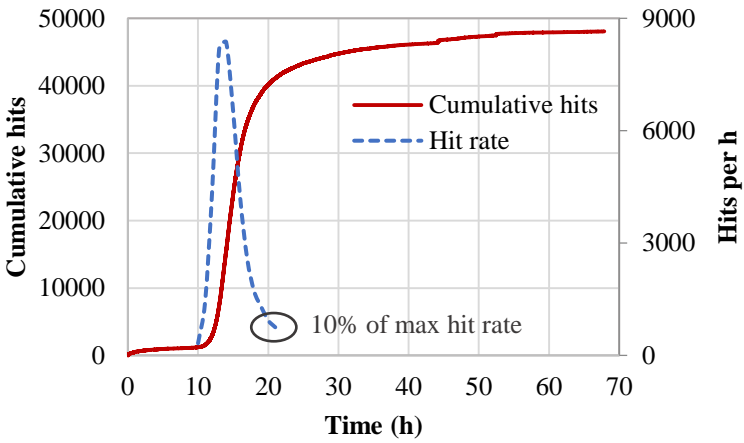
Fig. 3: Cumulative activity and hit rate of VP400.

Mechanisms such as settlement, shrinkage cracking, SAP action and detachment of the specimen from the mold can be characterized by various AE parameters. Fig. 4 shows the moving average of the amplitude and risetime of the two specimens during the monitoring period. Amplitude is one of the most important AE parameters since it is closely related to the energy that the emitted elastic waves. Risetime can be useful to characterize mechanisms such as the type of cracking. The curing process was divided into four phases, which were subsequently used to distinguish the events during localization, as shown in Table 1. The settlement, which takes place during the first

two hours after casting [2], presents higher amplitudes and a concentrated AE activity compared to the rest of the processes. The SAP activity is the denser part of the amplitude graph shown in Fig. 4a. The AE activity of the VP400 cube is generally characterized by lower amplitudes compared to the REF cube, which can be explained by the fact that SAPs mitigate the shrinkage cracking that exhibits higher amplitude bursts than the rest of the processes. This is more profound in the final stage of hardening, where shrinkage cracking is more likely to occur. The SAP cube shows again lower amplitudes, whereas the reference cube presents higher amplitude peaks, which are possibly recorded due to cracking.
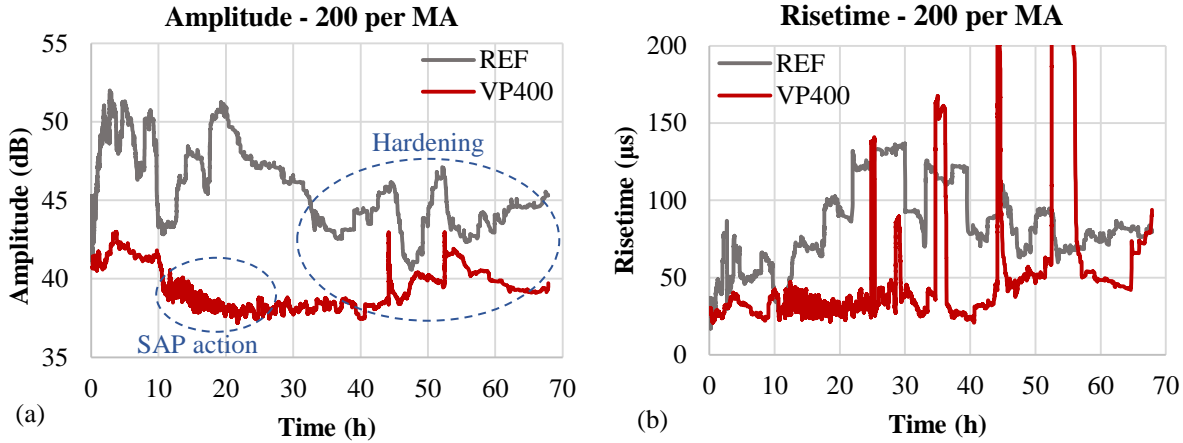
Fig. 4: 200 per moving average of (a) amplitude and (b) risetime evolution.

3.2 Source localization

3D source localization in fresh concrete was performed, using the localization algorithm implemented in the AE Win software. Since the sensors are attached to the metallic mold and not directly to the material itself, the waves propagate through two different materials and possibly exhibit a nonlinear path before they reach the sensors, something that is not considered in the localization algorithm. Still, localization gives a first impression of how the curing of concrete evolves in terms of AE events, while still being in the process of being optimized.

Table 1: Phases of the curing process, time frames & UPVs utilized for the distinction of the AE events.

CURING PHASE	MONITORING TIME (H)	UPV(M/S)
(1) Settlement	0-2	500
(2) Early hydration	1-12	1000
(3) Later hydration/SAP activity	12-20	2000
(4) Hardening	20 to end	3000

A top view of the AE events for each curing stage is depicted in Fig. 5, while Fig. 6 shows the 3D view. During settlement, most of the activity is concentrated near the center of the mold for the REF specimen. As concrete hardens, the events seem to move towards the outer sides of the specimen. Even though VP400 exhibited a considerably higher number of hits compared to REF, the number of AE events was higher for the REF specimen. This might be explained by the fact that the events in REF were of higher amplitude, and thus were more easily recorded by at least 4 sensors, resulting in reliable localization of the source. Another possibility for the low number of recorded events in the VP400 might be the increased porosity of the matrix due to the SAP

inclusion, which makes the material even more attenuative for wave propagation. It should also be mentioned that during the internal curing period, and specifically after 12 h, the recorded hit rate is quite high, implying that several sources may be active almost simultaneously and effectively being overlapped in a single waveform, making the localization even more complicated.
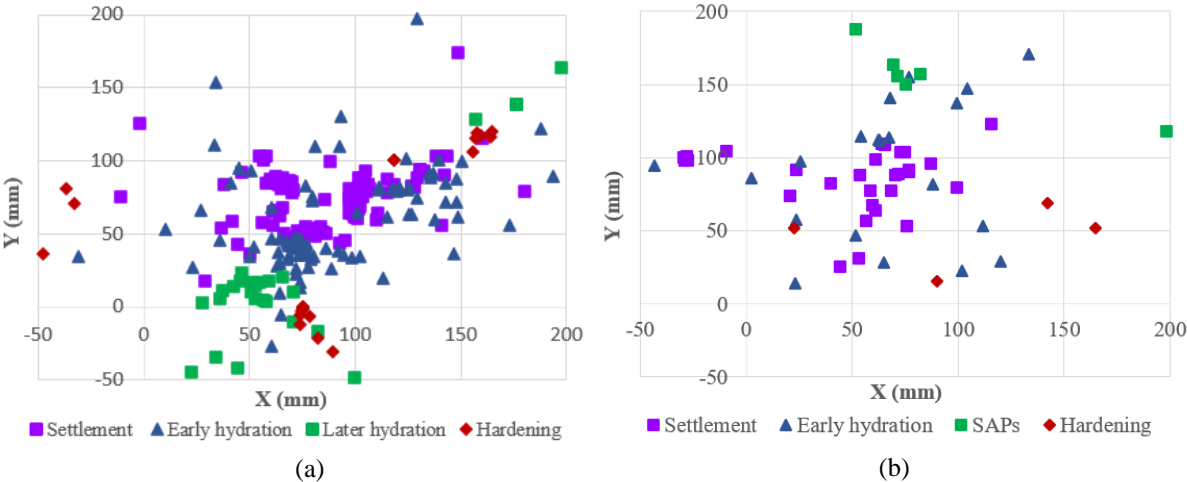
Fig. 5: Top view of AE events for (a) REF and (b) VP400.

When observing the 3D view of the events, it seems like the majority is located at the mid-height of the cube and towards the bottom. Sources occurring at the center of the mold are easier to localize since they have approximately the same distance from all the sensors. Moreover, the waves have to go through the metallic mold to reach the sensors, something that also impacts the accuracy of the localization.
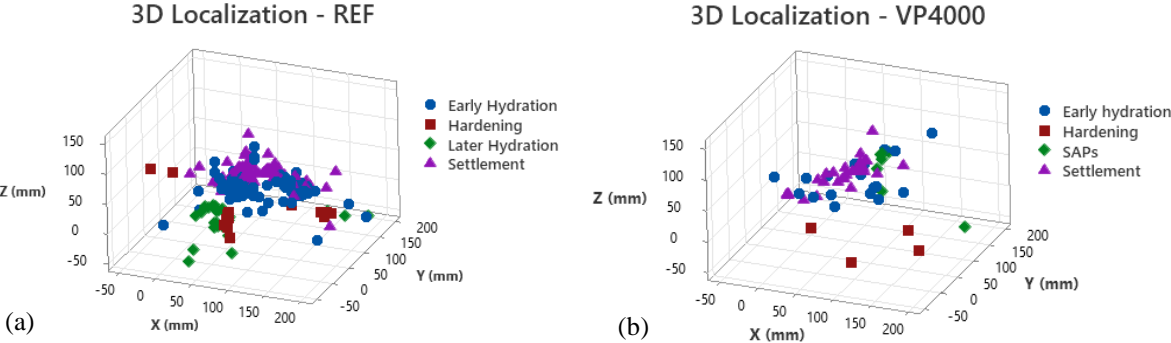
Fig. 6: 3D view of AE events for (a) REF and (b) VP400.

4. Conclusions

Acoustic emission monitoring was performed on fresh concrete cubes, with and without the presence of superabsorbent polymers to monitor the curing process. The temperature inside the specimens was also monitored. A study of three-dimensional localization in fresh concrete was done for the first time.

The specimen containing SAPs exhibited in general a lower temperature evolution, especially during the later stages of hydration, which can be linked to the delay that the SAPs cause in the hydration process. Most of the SAP activity was completed at around 20 h, although more investigation is needed to better understand the nature of the increased AE activity in SAP

concrete. The end of the SAP activity seems to coincide with the end of the deceleration period of hydration, as seen from the graph of the temperature evolution.

The SAP concrete exhibited a significantly higher number of hits compared to the reference concrete. The initiation of the SAP activity was accompanied by a rapid increase in AE hits, and the water release started approximately 12 hours after mixing and lasted up to approximately 20 hours. The concrete containing SAPs was characterized by lower amplitude values throughout the monitoring period compared to the reference concrete, which confirms that SAPs mitigated shrinkage cracking that is characterized by signals with high amplitudes.

The curing process was divided into four phases, and different wave velocities were applied to account for the changing stiffness of concrete as it undergoes hydration. The 3D localization showed a wide distribution of events for the different processes, while numerical simulations should be conducted to account for possible nonlinear paths between the source and the sensors.

5. References

[1] Lefever, G., Snoeck, D., De Belie, N., Van Vlierberghe, S., Van Hemelrijck, D., & Aggelis, D. G. (2020). The contribution of elastic wave NDT to the characterization of modern cementitious media. Sensors, 20(10), 2959.

[2] Dzaye, E., De Schutter G., and Aggelis D.G. 2020. "Monitoring early-age acoustic emission of cement paste and fly ash." Cement and concrete Research 129(105964).

[3] T.J. Chotard, A. Smith, D. Rotureau, D. Fargeot, C. Gault, Acoustic emission characterisation of calcium aluminate cement hydration at an early stage, J. Eur. Ceram. Soc. 23 (2003) 387–398.

[4] T. Chotard, R. D., S. A., Analysis of acoustic emission signature during aluminous cement setting to characterise the mechanical behaviour of the hard material, J. Eur. Ceram. Soc. 25 (2005) 3523–3531, https://doi.org/10.1016/j.jeurceramsoc.2004.09.019.

[5] A.I.S. Vladimir, V. Bardakov, Forecasting of concrete strength during the hardening process by means of acoustic emission method, Progress in Acoustic Emission XVIII, Proceedings of the 23rd International Acoustic Emission Symposium, the Inauguration Conference of International Institute of Innovative Acoustic Emission & the 8th International Conference on Acoustic Emission JSNDI, 2016.

[6] Snoeck, D., Pel, L., & De Belie, N. (2020). Autogenous healing in cementitious materials with superabsorbent polymers quantified by means of NMR. Scientific reports, 10(1), 1-6.

[7] Lefever, G., Ospitia, N., Serafin, D., Hemelrijck, D. V., & Aggelis, D. G. (2020). Chasing the bubble: Ultrasonic dispersion and attenuation from cement with superabsorbent polymers to shampoo. Materials, 13(20), 4528.

[8] Snoeck, D., Pel, L., & De Belie, N. (2017). The water kinetics of superabsorbent polymers during cement hydration and internal curing visualized and studied by NMR. Scientific reports, 7(1), 1-14.

[9] Snoeck, D., Goethals, W., Hovind, J., Trtik, P., Van Mullem, T., Van den Heede, P. & De Belie, N. (2021). Internal curing of cement pastes by means of superabsorbent polymers visualized by neutron tomography. Cement and Concrete Research, 147, 106528, 1-10.

ACOUSTIC EMISSION-BASED STRUCTURAL HEALTH MONITORING CONCEPT FOR CORROSION OF ALUMINUM AIRCRAFT STRUCTURES

Thomas Erlinger[1,*], Christoph Kralovec[1] and Martin Schagerl[1]

[1]Institute of Structural Lightweight Design, Johannes Kepler University, 4040 Linz, Austria;
thomas.erlinger@jku.at, christoph.kralovec@jku.at, martin.schagerl@jku.at
*Correspondence: thomas.erlinger@jku.at

ABSTRACT

In the aircraft industry, where highly optimized aluminum structures and most stringent safety requirements meet, corrosion of aluminum is an important issue to be controlled. To this end, several structural health monitoring (SHM) methods have already been demonstrated, including the acoustic emission (AE) method, which has shown potential for corrosion monitoring. Typically, immersion-like setups are used for demonstration. However, recent results at the authors' research group also show the potential of the AE method to monitor atmospheric corrosion of aluminum aircraft structures. This contribution presents a SHM concept for the identification, i.e., detection, localization, quantification, and typification, of corrosion of thin-walled aluminum structures by AE. The proposed monitoring concept combines time and frequency domain features of corrosion triggered AE signals and AE source localization-based imaging with a-priori knowledge of structural configuration and loading by the utilization of machine learning methods to quantify and typify corrosion. Successful detection of atmospheric corrosion of aluminum by AE is briefly presented. Furthermore, the concept is theoretically discussed for quantification and typification of corrosion forms typical for atmospheric corrosion conditions.

Keywords: Acoustic emission, structural health monitoring (SHM), corrosion, aluminum, aircraft structure.

1. Introduction

Aluminum has applications in several industries due to a variety of advantageous properties compared to other metals [1]. For example, aluminum, especially the 2XXX alloy series, is widely used for structural components in the aircraft industry due to its good mechanical properties. The main alloying element of these alloys is copper (Cu) which is responsible for the high strength properties, however, Cu also increases the susceptibility to corrosion of the alloys [1]. Most often aircrafts are attacked by so-called atmospheric corrosion, which is the type of corrosion where on a metallic surface only little electrolyte is present in the form of a thin film or small droplets [1, 2]. Such corrosive environments occur, e.g., during operation or parking in marine environments, but also when moisture from rain, fog, or snow forms together with different pollutants like dirt, exhaust gases, sulfates, chlorides, etc., electrically conductive and chemically reactive solutions

[2, 3]. Furthermore, deliquescence of soluble pollutants such as salts due to changes in relative humidity (RH) caused by operation of aircrafts in different climate zones and altitudes can also form highly concentrated electrolytes [1-3]. Corrosion of aircraft structures has to be controlled to ensure functionality and safety during operation. Typically, this is done by scheduled inspections and clear protocols on how to determine corrosion [3]. However, research has already been conducted to automatically investigate and detect corrosion issues in various industries using non-destructive testing (NDT) or structural health monitoring (SHM) methods. For example, electrochemical techniques like electrochemical noise or the electrochemical impedance spectroscopy have already been tested and show good potential for corrosion monitoring [4, 5]. Also, optical fiber based techniques have already been investigated, e.g., in civil engineering for monitoring corrosion in steel reinforced concrete [6], but also for aircrafts these techniques have already been tested [7]. Another group for corrosion detection and monitoring are acoustic methods, i.e., ultrasonic testing (UT), guided waves (GW), and acoustic emission (AE). UT is a well-developed method for offline testing, i.e., during inspections, but GW and AE are also suited for online monitoring, i.e., during operation. GW and AE are quite similar methods, both methods detect transient elastic waves propagating in the structure, typically with piezoelectric sensors. However, GW is an active method that uses an actuator to excite the structure and a sensor to measure a response signal, while AE is a passive method that directly measures the transient elastic wave caused by damage itself, e.g., corrosion. Especially AE is a promising technique for online monitoring of corrosion of metals. For steel, there are many research works and also some industrial applications for corrosion monitoring with AE. For example, in the oil and gas industry AE is used for corrosion and leakage detection in large storage tanks and pipelines [8, 9], and in civil engineering for corrosion monitoring of steel-reinforced concrete [10]. Unlike steel, there are no industrial applications and only little research for corrosion monitoring of aluminum with AE. The found research works investigate corrosion of aluminum aircraft structures, e.g., pitting and exfoliation corrosion of AA2024 and AA7449 alloys by AE in immersion-like setups and under accelerated conditions caused by potentiostatic polarization [11, 12]. However, the authors found no research work that addresses AE monitoring of atmospheric corrosion of aluminum.

Recent experimental results of the authors' research group demonstrate that AE is also capable to detect atmospheric corrosion of thin-walled aluminum aircraft structures [13]. Aluminum alloy AA2024-T351 was exposed to small droplets of a 50 g/l sodium chloride (NaCl) solution, that caused clear pitting corrosion. In addition, operating conditions of an aircraft were simulated by a controlled variation of the RH. Low RH lead to evaporation of the droplet and a stop of corrosion, subsequent increase of the RH, caused deliquescence of the remaining NaCl crystals and to progress of corrosion again, a typical periodic phenomenon that can occur during a flight. The AE monitoring detected significant AE signals during phases of high RH and no signals were detected in the low RH phases, i.e., the stop and re-onset of corrosion could be observed. The present paper continues the recent research of the authors' research group with a SHM concept for full identification of atmospheric corrosion on thin-walled aluminum aircraft structures by AE. Damage identification in SHM is commonly divided into the four levels detection, localization, quantification, and typification of the damage [14]. As described above, successful detection is already demonstrated, thus approaches for AE source localization and subsequent quantification and typification based on spatial imaging and a-priori knowledge on corrosion types and the considered structure are discussed.

2.   In situ corrosion monitoring with acoustic emission – state of the art

The AE method is a passive SHM method, that detects damages at the moment they occur. For example, due to corrosion mechanical energy is released and transient elastic waves propagate through the structure, which are measured by a sensor. The sensitive element of a commercially available AE sensor is typically a piezoelectric element, however, such sensors are expensive and

bulky, thus, not well suited for SHM. Instead, piezoelectric wafer active sensors (PWAS) are cheap, lightweight, unobtrusive and their applicability for AE monitoring is already shown [13, 15].

Corrosion of aluminum due to aqueous electrolytes always reacts under hydrogen (H_2) formation. In the case of pitting corrosion anodic oxidation takes place at the base of the pit where aluminum is dissolved and cathodic reduction occurs most likely at intermetallic particles outside the pit by H_2 evolution and oxygen reduction. The overall corrosion reaction of aluminum (Al) is

$$Al + 3\,H_2O \rightarrow Al(OH)_3 + \frac{3}{2}\,H_2, \tag{1}$$
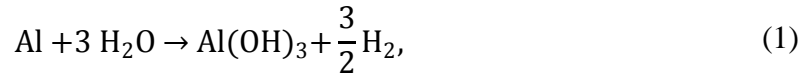
i.e., corrosion product aluminum hydroxide ($Al(OH)_3$) and H_2 are formed [1]. It is commonly concluded that bubble activity in immersion tests is the main source of the measured AE signals [12, 13] and recent results show that this is also the most likely AE source for atmospheric corrosion [13], cf. Fig. 1. However, other AE sources that are not related to corrosion cannot be fully excluded, but it is shown that such sources or effects only occur in minor quantities.
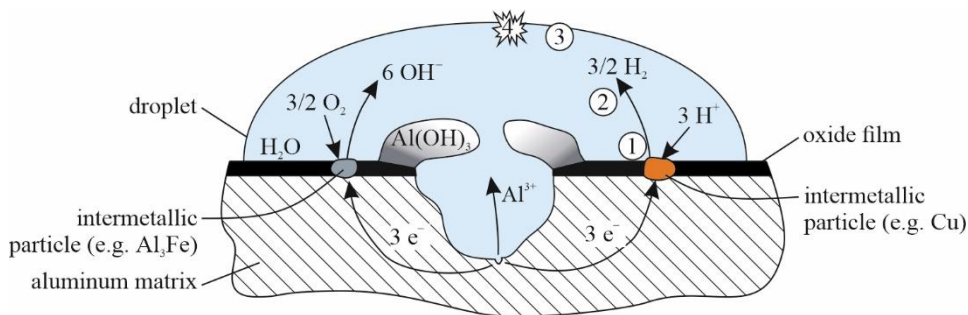
Fig. 1: Pitting corrosion due to a droplet of an aqueous electrolyte [1]. H_2 bubble activity, i.e., ① formation, ② detachment from metal surface and movement, ③ arrival at droplet surface and growth, and ④ bursting of H_2 bubbles, is the dominant AE source.

As already mentioned above SHM is commonly divided into four levels. In the following, these four levels are discussed for the present damage scenario, i.e., atmospheric corrosion of thin-walled aluminum aircraft structures.

2.1 Level 1 detection

Recent experiments of the authors' research group investigated the potential of AE to detect atmospheric corrosion on aluminum aircraft structures. A thin-walled specimen of aluminum alloy AA2024-T351 was exposed to a small droplet of a 50 g/l NaCl solution. AE was monitored continuously with a permanently bonded PWAS. Operating conditions of an aircraft were simulated by a controlled variation of the ambient RH. The progress of corrosion was additionally observed by video recording of the corrosion site. Findings of this experimental investigation are summarized in Fig. 2. Atmospheric corrosion conditions were represented by four phases. First, the application of the droplet, cf. Fig. 2a, and high RH initiated pitting corrosion. Second, gradual reduction of the RH lead to evaporation of the water of the droplet, i.e., a dry specimen surface with remaining NaCl crystals, cf. Fig. 2b, and to a stop of corrosion. Third, RH was slowly increased again, thus, the NaCl crystals deliquesced and formed several smaller droplets of electrolyte again, resulting in a re-onset of corrosion, cf. Fig. 2c and d. Fourth, rapid reduction of the RH lead again to evaporation of the droplet and to the final stop of corrosion, cf. Fig. 2e. The black dashed curve in Fig. 2 shows the prevailed RH during the experiment. AE activity was evaluated by the cumulative AE hits, cf. the orange curve in Fig. 2. Correlations between RH or the amount of electrolyte present at the specimen, progress of corrosion, and the cumulative AE hits were found. It is shown that during phases of high RH, i.e., if a sufficient amount of electrolyte

is present on the specimen, AE hits are clearly detected and during phases of low RH where no or just little electrolyte is present on the specimen no AE hits are detected. Thus, it is shown that atmospheric corrosion on aluminum can be reliably detected with today's AE measurement equipment. Further investigations concluded that H_2 bubbles, which are formed when aluminum reacts with an aqueous electrolyte, are the predominant sources for the detected AE hits.
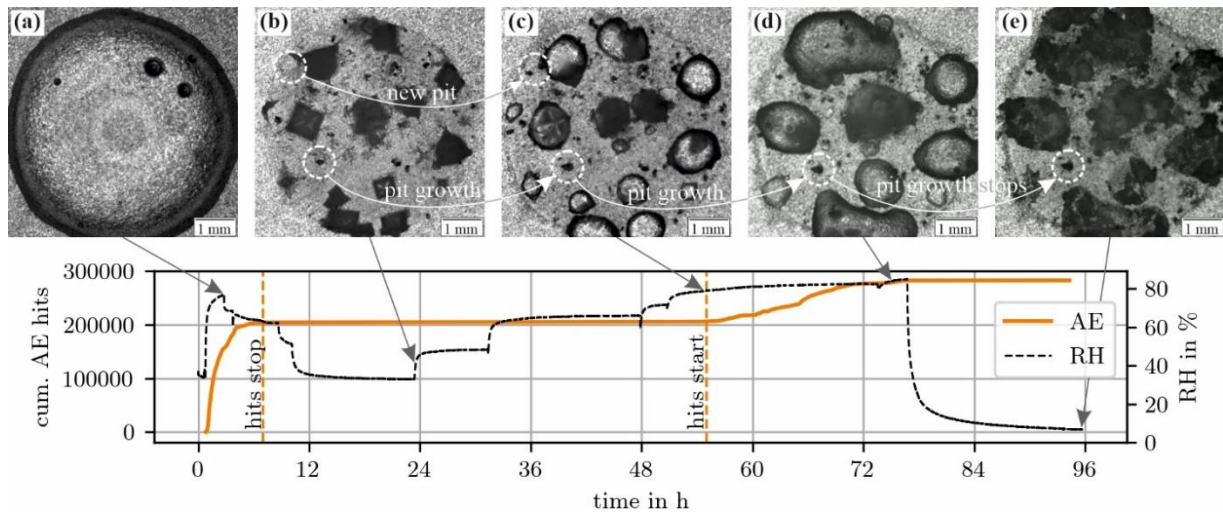

Fig. 2: Detection of atmospheric corrosion on aluminum alloy AA2024-T351 by AE [13]. The diagram shows the relative humidity (RH) during the experiment and the cumulative AE hits over time. (a) to (e) Exemplary images of the corrosion site show different atmospheric corrosion situations and the occurrence of pitting corrosion.

2.2 Level 2 localization

Classical planar AE source localization techniques require at least three PWAS and are all based on time of arrival (TOA) estimation of the sensor signals. Based on the time differences of the TOAs for all possible sensor pairs, the source location can be determined. Therefore, different approaches can be used, e.g., analytical calculation by triangulation, iterative optimization algorithms, or data-driven methods [16]. However, precise TOA estimates are always essential for an accurate localization result. The simplest method for TOA estimation is just using an amplitude threshold. Therefore, the proper value has to be found which has to be above noise level but should still detect the onset of the S0 wave [17]. However, especially for small amplitude signals this can lead to inaccurate results, as there the S0 wave often is hidden in noise. Therefore, advanced AE signal onset estimators exist, e.g., based on the Akaike information criterion (AIC). The so-called AIC-picker models the AE signal as an autoregressive process, where the AE signal is divided into two stationary segments. The first segment only contains noise and the second segment contains noise and the signal. The AIC picker searches for the separation point of these two segments which is considered to be the signal onset, i.e., TOA [17]. This TOA estimation method was already used for localizing corrosion in reinforced concrete [18]. Localization accuracy can further be increased by the use of more sensors, or by probabilistic approaches that consider uncertainties of the wave speed in the material and of the TOA estimation itself [19].

2.3 Level 3,4 quantification and typification

In the context of SHM, quantification refers to determining the size of the damage and typification refers to identifying the type of the damage [14]. AE evaluates transient elastic waves caused by the introduction or release of mechanical energy as explained above. For atmospheric corrosion of aluminum this energy introduction is predominantly caused by H_2 bubbles. Thus, direct quantification of a corrosion damage based on a single detected AE signal seems impossible. Typification of a damage is typically assessed by numerous time and frequency domain features of the AE signal [20]. This may be also well applicable for the distinction between, e.g., pitting

corrosion and stress corrosion cracking (SCC). However, for the classification of corrosion types, like e.g., uniform, pitting, or intergranular corrosion (IGC), the emitted AE signals are expected to have very similar characteristics. Thus, their classification into different types may be not or only poorly possible with today's methods. However, to access the integrity of a monitored structure the knowledge of location, type, and size of a corrosion damage are essential. In the following a potential concept for full corrosion damage identification utilizing corrosion imaging, incorporation of a-priori knowledge, and advanced statistical data evaluation methods is presented.

3.   SHM concept for corrosion damage identification

The proposed SHM concept for corrosion damage identification by AE is based on the assumption that atmospheric corrosion can be detected and a considered structure of interest is equipped with a sufficient number of PWAS to allow adequate localization of the detected hits. The first, detection, was experimentally demonstrated in [13] and results are shortly presented in Fig. 2. The latter, localization, is state of the art, although there are still issues to be solved for a sufficiently accurate localization within complex structures at ambient noise. However, the further quantification and typification of progressing corrosion damage are challenging with today's AE-based evaluation methods. Thus, a concept for the combined corrosion evaluation of multiple AE events and a-priori knowledge is proposed. An overview of the concept is given in Fig. 3. AE events potentially from corrosion are detected and localized according to the state of the art. Further evaluation is enabled by imaging the corrosion on the a-priori known geometry of the structural element of interest by plotting the AE source locations. A weighting of the plotted locations by, e.g., the AE signal energy may further improve the corrosion imaging. To conclude on the corrosions quantity and type modern machine learning approaches may be applied, that fuse time and frequency domain features of the AE signals and localization imaging with a-priori knowledge of the structure (e.g., geometry, material, loading, and relevant boundary conditions). This should be based on a comprehensive data set of known corrosion conditions and their development histories, like e.g., known AE characteristics of corrosion types, localization images and their development histories for different corrosion types at different structural configurations, and probabilities of corrosion types for structural configurations and loading.
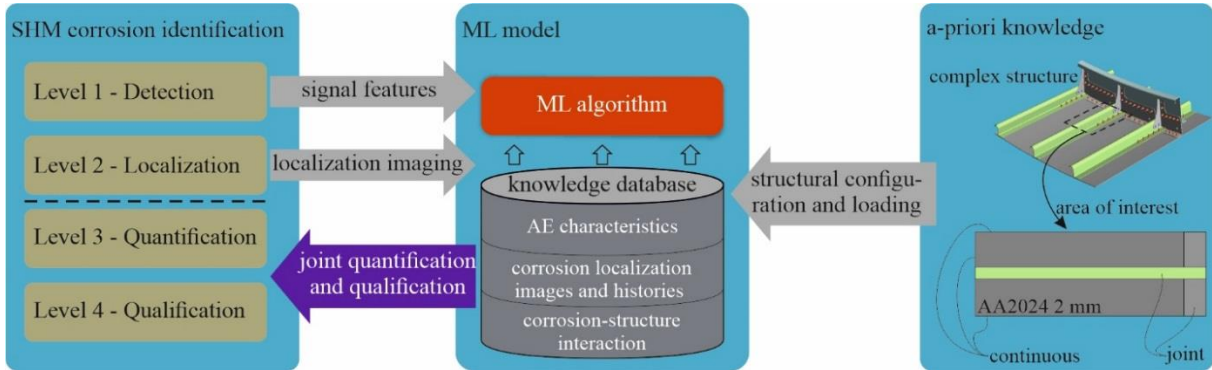
Fig. 3: SHM concept for corrosion damage identification based on time and frequency domain signal features, AE source localization-based imaging, and the a-priori knowledge of the structural configuration and loading.

So far, the proposed concept was not applied to a real corrosion event. However, possible imaging results of the presented SHM approach for different structures and corrosion types considered are illustrated in Fig. 4. Fig. 4a shows (i) 5000 nearly uniformly distributed localization results over a wider area (marked in green) which is assumed to represent uniform corrosion, and (ii) 1000 localization results accumulated in a dense cluster around a certain site (marked in orange) which

is assumed to represent localized corrosion (e.g. pitting). Localization errors cause a spread of results that are assumed to be normally distributed around the single local corrosion sites. The presented example images suggest a corrosion quantification directly by the spanned area of accumulated localization results. This may be appropriate for uniform corrosion but fails for corrosion that develops into the depth of a structure, like given for pitting corrosion. Consequently, quantification and typification of corrosion can only be realized by a joint evaluation, considering the spanned area of the accumulated localization results and the density and weight of localization results. However, it is definitely not always possible to fully identify corrosion by imaging the localization results alone. Inclusion of further a-priori knowledge like geometry features (edges, gaps, etc.), material and material combinations, joints, applied loads, etc., for the evaluation is strongly believed to provide very valuable additional information. Fig. 4b for example shows 1000 localization results in a dense, slightly asymmetric, and scattered rectangular cluster. Combined with the a-priori knowledge of the area of interest showing a riveted single-lap-shear joint, crevice corrosion can be strongly assumed.

Fig. 4: Possible corrosion imaging results by AE localizations (marked by thin crosses) on thin-walled structures. Specific accumulation of localization results can provide information about the size and type of corrosion, e.g., (a) uniform and localized corrosion or (b) crevice corrosion at a riveted single-lap-shear joint.

In the following, typical corrosion forms occurring under atmospheric corrosion conditions on thin-walled aluminum structures and the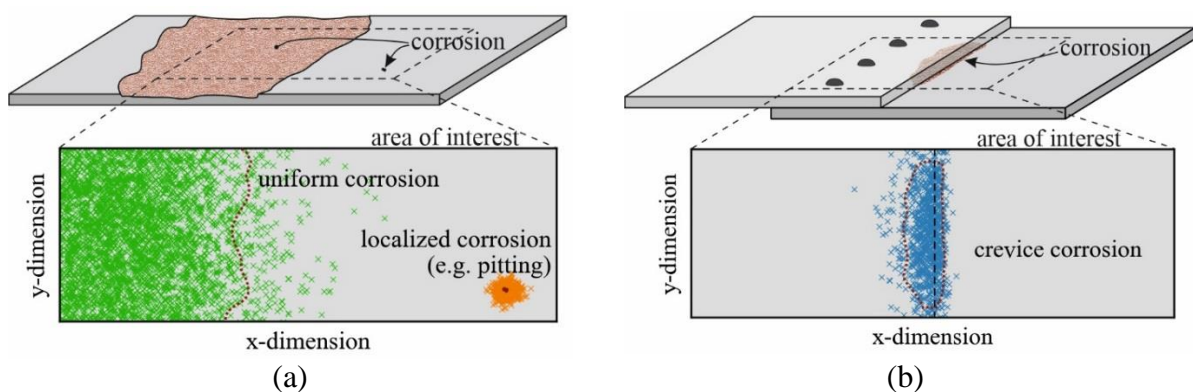ir potential identification based on time and frequency domain signal features, AE source localization imaging, and a-priori knowledge of the structural configuration and loading are discussed.

- Uniform corrosion: A corrosion form represented by localization results evenly distributed over a larger area. The size (areal extent and corroded volume) may be approximated by the spanned area of the localization results, localization density, and signal features (e.g. AE signal energy).
- Pitting corrosion: A corrosion form that is represented by a larger number of localization results that lie very close together at certain spots. Very accurate localization results can possibly provide information about the lateral extent of a pit. The depth of the pits may be estimated by localization density and signal features.
- Intergranular corrosion (IGC): A corrosion form that typically spreads from pits [1], thus, the identification is expected to be similar to pitting corrosion but the differentiation from pitting corrosion is unlikely to be possible by the proposed concept.
- Exfoliation corrosion (EFC): A corrosion form that typically spreads inter-granularly where layers of intermetallic particles are formed. Besides H_2 bubble activity, cracking phenomena occur caused by corrosion products between the layers resulting in AE signals of different characteristics, which can assist differentiation from other corrosion forms [1, 12]. Moreover, certain alloys are especially prone to EFC which can be valuable a-priori

knowledge. Precise localization results, localization density, and signal features can potentially provide size information.

- Stress corrosion cracking (SCC) and corrosion fatigue (CF): Corrosion forms where localization results accumulate at certain spots where cracks initiate and grow. Knowledge about structural features (e.g., edges) and the loading can help to differentiate from other types with similar imaging results, such as crevice corrosion. Moreover, the signals in SCC and CF are not only caused by H_2 bubble activity, but also by mechanical cracking with different AE signal characteristics [21]. Precise localization could give information on crack length.

- Crevice corrosion: A corrosion form where localization results accumulate at crevices. Knowledge of joints, material combinations, etc. of the structure is necessary for typification. The affected area can be estimated by the spanned area of the localization results. The corroded volume may be approximated by localization density and signal features.

However, it has to be mentioned that the concept described is currently theoretical and that there are several challenges to be solved before implementation. A fundamental challenge is the detection of low-amplitude corrosion signals in noisy environments and the accurate localization with multiple sensors at specific distances from the corrosion site. This problem is considered most critical for uniform corrosion, pitting, and IGC, rather than for EFC, SCC, or CF, where higher-energy AE signals caused by cracking also occur. Furthermore, an adequate and comprehensive knowledge database including AE characteristics of different corrosion forms, corrosion localization images and histories, and corrosion-structure interactions needs to be established, which is believed to be very costly.

4. Conclusions

A SHM concept for the identification of atmospheric corrosion damages on thin-walled aluminum aircraft structures by the AE method is presented. Identification in a SHM context is understood by the four levels detection, localization, quantification, and typification of a corrosion damage. Recent results of the authors' research group are shortly presented that demonstrate successful detection of atmospheric corrosion by AE. The present contribution continues with approaches for the localization of AE signals caused by corrosion and subsequent quantification and typification of the resulting corrosion damage. Today's AE evaluation methods are not expected to allow sufficient quantification and typification of corrosion directly by single detected AE signals. The proposed concept potentially solves this issue by combining imaging by high accuracy localization, time and frequency domain features of the AE signals, and a-priori knowledge on the structural configuration (geometric features, material and material combinations, joints, etc.) and loading for a joint quantification and typification of corrosion damages through statistical data evaluation, e.g., by machine learning methods. Different corrosion forms are discussed on how the type could be classified and size (areal extent and corroded volume) approximation could be provided.

Future research is planned to implement and test TOA estimation and localization algorithms for atmospheric corrosion. Experiments shall be designed to investigate the maximum distance between sensors and corrosion site so that detection and localization are still possible. Finally, the feasibility of the presented corrosion identification concept shall be experimentally demonstrated.

5. Acknowledgements

6. References

[1] Vargel, C. (Ed.). (2020). Corrosion of Aluminium (2.), Elsevier, Amsterdam. doi:10.1016/C2012-0-02741-X.

[2] du Plessis, A. (2015). Studies on Atmospheric Corrosion Processes in AA2024. Ph.D. Thesis, University of Birmingham, https://etheses.bham.ac.uk/id/eprint/5642/.

[3] Civil Aviation Authority (2017). Corrosion and Inspection of General Aviation Aircraft, available online: https://publicapps.caa.co.uk/docs/33/CAP1570_Corrosion.pdf, accessed on 22-8-2022.

[4] Obot, I. B., Onyeachu, I. B., Zeino, A., Umoren, S. A. (2019). Electrochemical noise (EN) technique: review of recent practical applications to corrosion electrochemistry research, Journal of Adhesion Science and Technology, vol. 33, no. 13, p. 1453–1496. doi:10.1080/01694243.2019.1587224.

[5] Davis, G. D., Dacres, C. M., Krebs, L. (2000). EIS-Based In-Situ Sensor for the Early Detection of Coatings Degradation and Substrate Corrosion. Conference proceedings, The 55th annual Corrosion Conference, titled: Corrosion 2000, 26-31 March, Orlando, Florida , NACE-00275.

[6] Fan, L., Bao, Y. (2021). Review of fiber optic sensors for corrosion monitoring in reinforced concrete, Cement and Concrete Composites, vol. 120, 104029. doi:10.1016/j.cemconcomp.2021.104029.

[7] Venancio, P. G., Cottis, R. A., Narayanaswamy, R., Fernandes, J. C. S. (2013). Optical sensors for corrosion detection in airframes, Sensors and Actuators B: Chemical, vol. 182, p. 774–781. doi:10.1016/j.snb.2013.03.059.

[8] Tscheliesnig, P., Lackner, G., Jagenbrein, A. (2016). Corrosion detection by means of acoustic emission (AE) monitoring, Conference proceedings, 19th World Conference on Non-Destructive Testing, titled: WCNDT 2016, 13-17 June, Munich, Germany.

[9] Bi, H., Li, H., Zhang, W., Wang, L., Zhang, Q., Cao, S., Toku-Gyamerah, I. (2020). Evaluation of the acoustic emission monitoring method for stress corrosion cracking on aboveground storage tank floor steel, International Journal of Pressure Vessels and Piping, vol. 179, 104035. doi:10.1016/j.ijpvp.2019.104035.

[10] Kawasaki, Y., Wakuda, T., Kobarai, T., Ohtsu, M. (2013). Corrosion mechanisms in reinforced concrete by acoustic emission, Construction and Building Materials, vol. 48, p. 1240–1247. doi:10.1016/j.conbuildmat.2013.02.020.

[11] Idrissi, H., Derenne, J., Mazille, H. (2000). Detection of pitting corrosion of aluminium alloys by acoustic emission technique, J. Acoust. Emiss, vol. 18, p. 409–416.

[12] Bellenger, F., Mazille, H., Idrissi, H. (2002). Use of acoustic emission technique for the early detection of aluminum alloys exfoliation corrosion, NDT & E International, vol. 35, no. 6, p.385–392. doi:10.1016/S0963-8695(02)00011-7.

[13] Erlinger, T., Kralovec, C., Schagerl, M. (2022). Acoustic Emission Monitoring of Atmospheric Corrosion on Aluminum Aircraft Structures at Varying Relative Humidity, Preprints. 2022080097, doi:10.20944/preprints202208.0097.v1.

[14] Viechtbauer, C., Schagerl, M., Schröder, K.-U. (2013). From NDT over SHM to SHC - the future for wind turbines. Conference proceedings, The 6th International Conference on

Structural Health Monitoring of Intelligent Infrastructure, titled SHMII-6 2013, 9-11 December, Hong Kong.

[15] Mei, H., Haider, M. F., Joseph, R., Migot, A., Giurgiutiu, V. (2019). Recent Advances in Piezoelectric Wafer Active Sensors for Structural Health Monitoring Applications, Sensors, vol. 19, no. 2, p.383. doi:10.3390/s19020383.

[16] Kundu, T. (2014). Acoustic source localization, Ultrasonics, vol. 54, no. 1, p. 25–38. doi:10.1016/j.ultras.2013.06.009.

[17] Kurz, J. H. (2006). Verifikation von Bruchprozessen bei gleichzeitiger Automatisierung der Schallemissionsanalyse an Stahl- und Stahlfaserbeton. Ph.D. Thesis, Universität Stuttgart, http://elib.uni-stuttgart.de/handle/11682/245.

[18] Van Steen, C., Pahlavan, L., Wevers, M., Verstrynge, E. (2019). Localisation and characterisation of corrosion damage in reinforced concrete by means of acoustic emission and X-ray computed tomography, Construction and Building Materials, vol. 197, p. 21–29. doi:10.1016/j.conbuildmat.2018.11.159.

[19] Niri, E. D., Salamone, S. (2012). A probabilistic framework for acoustic emission source localization in plate-like structures, Smart Materials and Structures, vol. 21, no. 3, 035009. doi:10.1088/0964-1726/21/3/035009.

[20] Saeedifar, M., Zarouchas, D. (2020). Damage characterization of laminated composites using acoustic emission: A review, Composites Part B: Engineering, Vol. 195, 108039. doi:10.1016/j.compositesb.2020.108039.

[21] Calabrese, L., Proverbio, E. (2021). A Review on the Applications of Acoustic Emission Technique in the Study of Stress Corrosion Cracking, Corrosion and Materials Degradation, vol. 2, no. 1, p. 1–30. doi:10.3390/cmd2010001.

ON THE EFFECT OF COATINGS AND PRE-CORROSION DURING FATIGUE TESTS OF 7075-T6 ALUMINUM ALLOY MONITORED WITH ACOUSTIC EMISSION (AE)

Théophile Vié[1], Nathalie Godin[1], Stéphanie Deschanel[1] and Bernard Normand[1]

[1]Univ Lyon, INSA Lyon, Université Claude Bernard Lyon 1, CNRS, MATEIS, UMR5510, 69621 Villeurbanne, France;
theophile.vie@insa-lyon.fr, nathalie.godin@insa-lyon.fr, stephanie.deschanel@insa-lyon.fr, bernard.normand@insa-lyon.fr

ABSTRACT

Strength hardened aluminum alloys as 7075-T6 al are widely used in aeronautical industry due to their low density and high mechanical properties. Their specific microstructural composition makes them sensitive to corrosion damage at intermetallic particles. Aeronautical parts are often submitted to corrosive environments and fatigue loadings. For safety and economic matters, it is important to be able to monitor the development of damages during application. In this context, Acoustic Emission (AE) is a useful tool to monitor the state of material damage and predict its remaining useful lifetime. This work, which is part of a larger European project (Early detection and progress monitoring and prediction of corrosion in aeronautic Al alloys through calibrated Ultrasonic-CorROSion Sensor application), has for main objective to understand, identify and quantify, via AE, how corrosion defects impact the fatigue behaviour of aluminum alloy 7075-T6 specimens and covered with different types of coatings (top coat, primer and a conversion coating obtained by anodizing process). Therefore, tensile-tensile fatigue tests ($R_\sigma = 0.1$) monitored with AE are performed at room temperature on non-corroded samples and on corroded samples. Pre-corrosion defects are generated by the complete immersion of the samples in an NaCl bath (3.5% wt). Pre-corrosion defects tend to decrease the fatigue lifetime of the material tested and create damage in the substrate and coatings generating new AE sources. For all types of coated specimens, damage indicators based on the AE activity are studied in order to find characteristic damage times giving information on the remaining useful lifetime of the material during fatigue tests. Characteristic times linked to damage initiation in the substrate and propagation the main fatigue crack in the material are defined.

Keywords: Acoustic emission, aluminum alloy, fatigue, pre-corrosion, lifetime prediction.

1. Introduction

Strength hardened aluminum alloys as 7075-T6 al are widely used in aeronautical industry due to their low density and high mechanical properties. Their specific microstructural composition makes them sensitive to corrosion damages [1]. Nevertheless, their microstructural composition makes them sensitive to localized corrosion in chloride environment. Corrosion significantly reduces the fatigue life of structures [2-6], by up to 60%. To prevent corrosion phenomena

occurring at intermetallic particles, different types of coatings are used to cover airplanes components. The majority of the coatings used in aeronautical industry are composed of simple epoxy painting layers and an oxide layer (ceramic) obtained by anodizing process [2]. It was found that anodizing process tends to reduce the fatigue life of the tested materials. This is due to the brittle nature of the ceramic coating layer which cracks rapidly during fatigue loadings and acts as stress riser on the substrate [7-8] but also due to the pitting defects created during the pickling process [9-10]. However, for safety and economic reasons, it is important to find a way to monitor, quantify and identify material damage phenomena for airplane components in order to estimate its remaining useful lifetime during application. Several non-destructive technics as US or IR thermography are commonly used in industry to assess the damage state and evolution of a material submitted to cyclic loadings. In this work, we focus on the Acoustic Emission technique to detect damage events occurring in the material. The objective is to study, via AE emission monitoring, how coatings impact crack nucleation and propagation of 7075-T6 aluminum alloy samples during fatigue tests. AE emission is a useful and suitable Prognosis and Health Management (PHM) method to monitor damage dynamics during mechanical tests [11-17]. Indeed, when an irreversible damage occurs in the material, the resulting elastic wave is recorded by piezoelectric sensors and converted by the AE acquisition system into an electrical signal. One of the main objectives of this work is to find criteria through AE in order to predict the Remaining Useful Lifetime (RUL) of specimens submitted to fatigue tests. To do so, damage indicators based on acoustic energy are proposed to estimate the damage state of a specimen and to establish characteristic damage times during the tests.

2. Material and method

2.1 Fatigue tests

The aim of the study is to perform tensile and fatigue tests on aluminum alloy 7075-T6 dog bone samples covered with different type of coatings combinations. The specific microstructure of this material is described in Fig. 1.
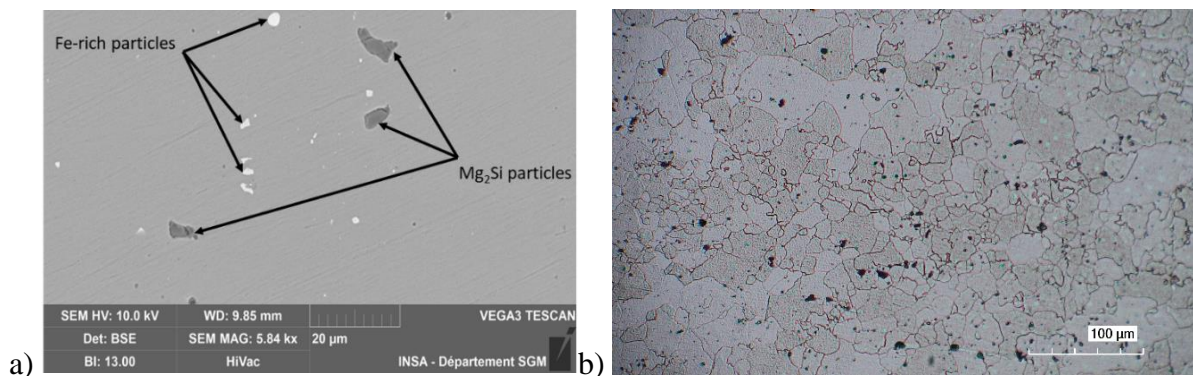
Fig. 1: Microstructure of aluminum alloy 7075-T6 a) intermetallic particles (SEM micrograph BSE) b) grain size (optical micrograph).

The studied samples are covered with coatings composed of combinations of three coating layers. The first one is a conversion coating layer (alumina) noted (A) and the two other layers are an epoxy painting primer (P) and an epoxy topcoat (T). Two types of specimens are tested in this work in order to investigate the effect of coatings on the cracking process of the material: bare samples (B) and samples coated with sulfuric acid anodization (SAA) and two epoxy painting layers (APT). Dynamic fatigue tests are performed to quantify the impact of coatings on mechanical properties (the lifetime-yield strength) and understand the different damage mechanisms at stake via AE monitoring.

Fatigue tests are carried out at room temperature on a servo-hydraulic MTS fatigue machine with a 100 kN load cell. The tests are set at imposed stress with sinusoidal loadings and a stress ratio of 0.1 (R_σ=0.1) which is common for aeronautical testing and characterization. The loading frequency is fixed at 1Hz and strain is measured with a contact extensometer. The loading values (Stress amplitude – mean stress – maximal stress) have been determined after a literature review and according to the monotonic tensile tests results. Those values are chosen for the specimens to break after about 10^4-10^5 cycles (Fig. 2). The mechanical behaviour of the material is investigated with the evolution of the strain amplitude and the secant modulus of the specimens during the tests.
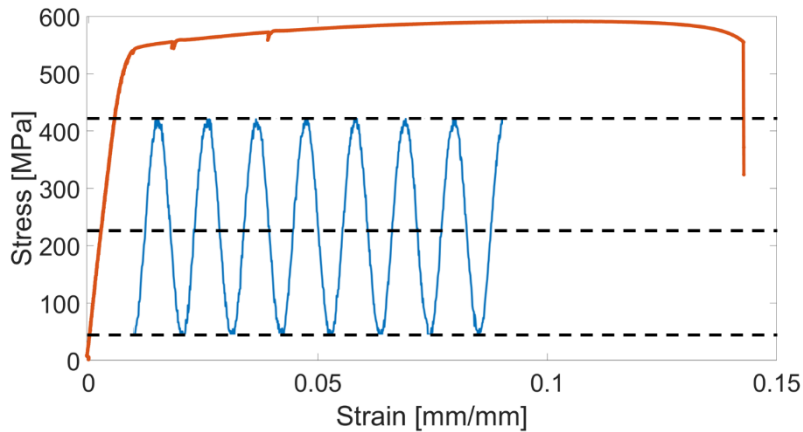
Fig. 2: Fatigue loadings during the tests in comparison with the tensile properties of the bare material.

2.2 Pre-corrosion initiation

In order to understand the coupled effect of coatings and pre-corrosion defects during fatigue tests, some samples are immersed in a corrosive bath (Fig. 3). The bath contains a solution of NaCl 3.5% wt. Open circuit potential measurements are performed between the samples and reference electrode all along the immersion. The samples were removed from the bath after 150 days. Corrosion was detected on the bare specimens but no corrosion was observed for anodized samples (AP – APT).

Fig. 3: Set up for pre-corrosion in a corrosive NaCl 3.5 wt % bath.

2.3 Acoustic emission

AE acquisition is performed with a Mistras PCI2 AE system. For all the tests, two piezoelectric sensors (micro80) are placed on the surface of the specimen. The sensors are coupled to the material with vacuum grease and maintained by clamps. For each test, the distance between the sensors is set at 65 mm. The sensors are connected to the data acquisition system via preamplifier with a 40 dB gain and 20-1200kHz bandwidth. Several AE parameters, in time and frequency domains, are recorded such as amplitude (dB), absolute energy (aJ), rise time (µs), duration (µs), centroid frequency (kHz) and peak frequency (kHz). Damage indicators based on the acoustic energy release are defined to investigate the damage dynamics. During fatigue tests, two indicators are defined based on the AE activity acquired during loading and unloading phases. R_{LU} (eq.1) is the ratio of the cumulated released energy during loading to the cumulated released energy during unloading [20]. The damage indicator R_H, (eq.2) represents the ratio between the number of hits acquired during loading and the number of hits acquired during unloading.

$$R_{LU} = \frac{\sum E_{AE\,loading}}{\sum E_{AE\,unloading}} \tag{1}$$

$$R_{H} = \frac{\sum Hits_{loading}}{\sum Hits_{unloading}} \tag{2}$$

Several types of observations (microstructure characterization-fracture surface observation) are pursued to identify the damage mechanisms occurring in the material during the mechanical tests and to interpret the AE results. Each specimen is observed with optical microscopy and SEM after failure, mainly to obtain fracture surfaces micrographs and observe crack initiation/growth areas.

3. Fatigue tests

3.1 Fatigue tests: non-immersed samples

The fatigue life of each specimen for stress imposed tensile-tensile fatigue tests is summarized in Fig. 4. The fatigue life of anodized specimens (APT) is divided by 3 compared to bare samples. This significant decrease in fatigue life demonstrates the detrimental impact of the anodization treatment on the fatigue properties of the material. The impact of the coating is noticeable from a mechanical point of view, if we consider the evolution of the secant modulus (Fig. 5).

Bare specimens exhibit a softening/hardening behaviour during the first 30% of their lifetime, then the secant modulus stabilizes during material accommodation until failure. The APT specimens show a ratcheting effect with a constant decrease of the secant modulus. This is due to the surface treatment and the presence of the brittle oxide layer. It might lead to plastic instability and early failure of the material. The disparity of results for the different specimens demonstrates the impact of coatings on crack nucleation and propagation. For bare, SEM observations appear to show that the main crack propagates from a single initiation area often related to an intermetallic failure (Fig. 6a). As for anodized samples, multiple crack initiation sites are observed and seem to be related to cracks and irregularities in the oxide layer (Fig. 6b). For each specimen, AE monitoring allowed to identify fatigue stages linked to specific characteristic damage times that could be used to quantify the remaining useful lifetime of the material.
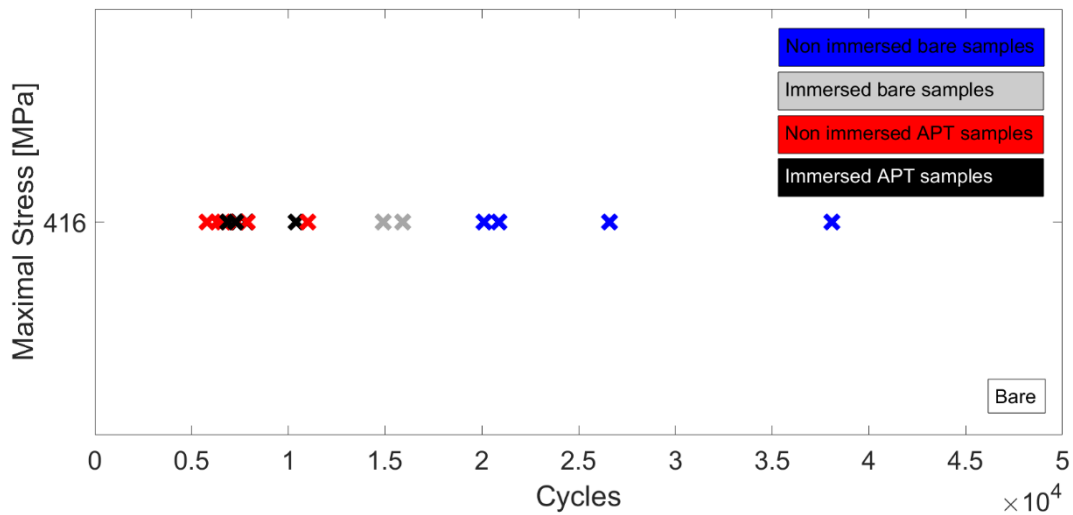
Fig. 4: Fatigue lifetimes for specimens with different type of coatings with or without immersion.
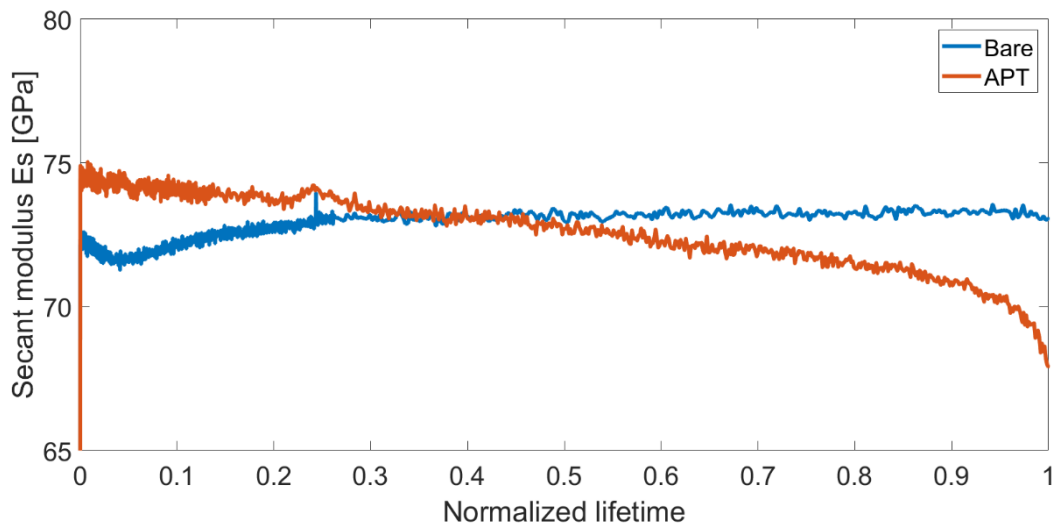
Fig. 5: Evolution of the secant modulus for all types of specimen during fatigue tests.

The acoustic activity of bare materials can be divided into 4 distinct stages (Fig. 7 – Fig. 8). The first stage (I) is linked to the initiation of micro-cracks at intermetallic particles and to the softening behaviour of the material. During this fatigue stage, dislocations movements and pileups are responsible for the incubation and nucleation of cracks in intermetallic particles and physically small crack initiations in the substrate. This is described by the acquisition of energetic AE sources during loading at high stress during the first 10% of the specimen fatigue life. After this time, the specimen enters a second fatigue stage (II), where high AE activity is acquired at low stress during unloading phases and is correlated with fretting between the surfaces of the substrate and particles after the creation of microcracks. This stage is also correlated to the hardening behaviour of the material and often occurs between 15-20% of the specimen lifetime. Then, the global AE activity stabilizes during a third stage (III) linked to the accommodation of the material where damage created during stage I and II grows to form the main fatigue crack. This stabilization of AE activity (15-20% of specimen lifetime) is repeatable for all bare specimens tested and can be considered as a characteristic damage time to characterize the RUL of the material and anticipate final

fracture. From this stabilization time (15-20% of fatigue life), damage is initiated in the material and grows to form the main crack. Finally, at 90% of the specimen's lifetime a restart of AE activity is observed during loading phases and characterized by low energetic signals. This AE is correlated to the propagation of the main crack until final failure of the material (stage IV).
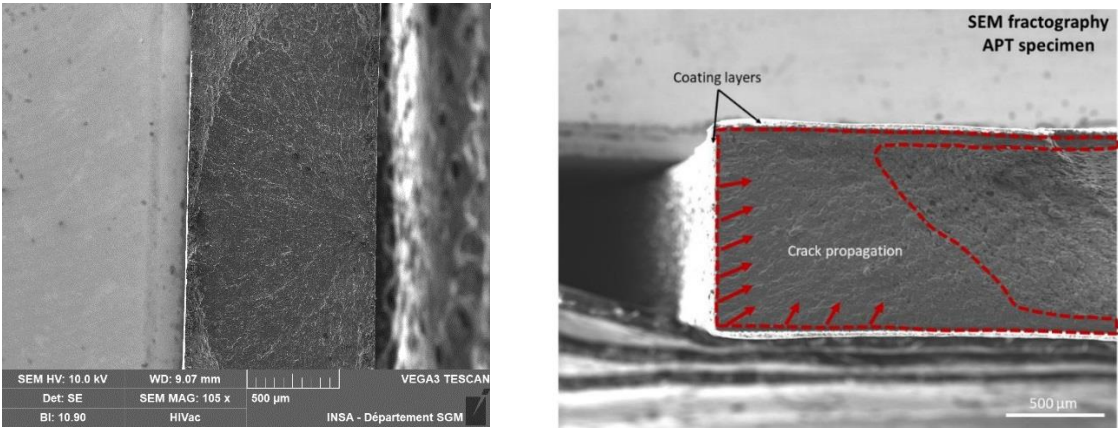

Fig. 6: SEM micrograph (SE) of the fracture surface of a) a bare specimen and b) an APT specimen after fatigue test.

Fig. 7: Occurrence of hits acquired during loading (red dots) and unloading (orange dots) for a bare specimen submitted to a fatigue test.
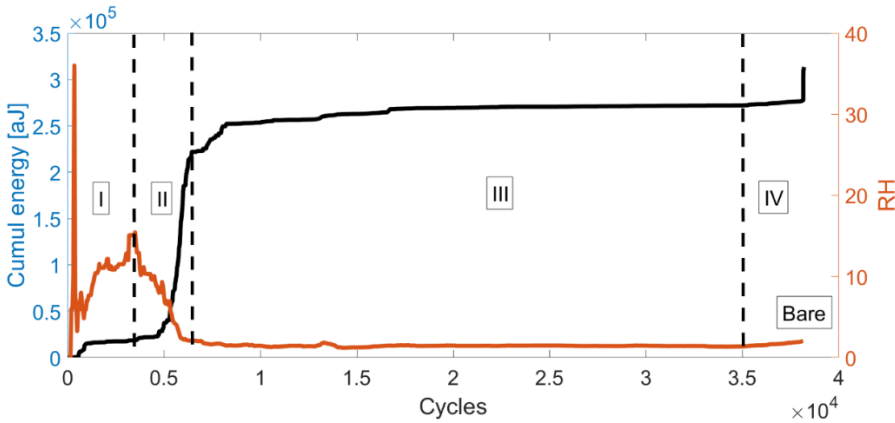
Fig. 8: Evolution of the cumulated AE energy and RH indicator vs number of cycles during a fatigue test for a bare specimen.

For anodized specimens, the AE results are divided in 3 stages (Fig. 9 – Fig. 10). The first stage is linked to the cracking of the brittle oxide layer produced by the anodizing process (large amount of AE signals acquired at high stress during loading and before the first 15% of the fatigue lifetime).

This early cracking of the alumina layer generates multiple stress concentration areas. Cracks initiated in the coating layer propagates easily in the substrate, owing to the strong adhesion between the coating and the substrate. The SEM micrograph of the fracture surface of an anodized specimen (Fig. 15) shows multiple crack initiation sites linked to irregularities and cracks in the oxide layer. The early creation of these multiple crack initiation sites is one of the reasons for the significant decrease in fatigue lifetime of anodized specimens. Stage 2 is related to the growth and propagation of the micro-cracks generated during stage 1 and almost no AE activity is acquired. At 70% of the specimen's lifetime there is an important restart of AE activity correlated with a drop of the secant modulus until failure of the specimen. This time (70% of fatigue life) is repeatable for all tests performed and can be important to consider to predict future failure of the material. It is the beginning of a third fatigue stage where the main crack propagates rapidly until final fracture of the specimen. We observe that this type of energetic AE activity acquired during loading and linked to the main crack propagation does not appear for the bare samples. We can suppose that it is related to a synergetic effect of crack growth in the substrate and cracks initiations in the coatings (alumina layer). The presence of a brittle surface near the crack tip would assist the fracture by continuous initiation process along the interface oxide/substrate. Microcracks generated in the alumina layer enhance the cracking mechanism by opening up and propagating into the substrate.
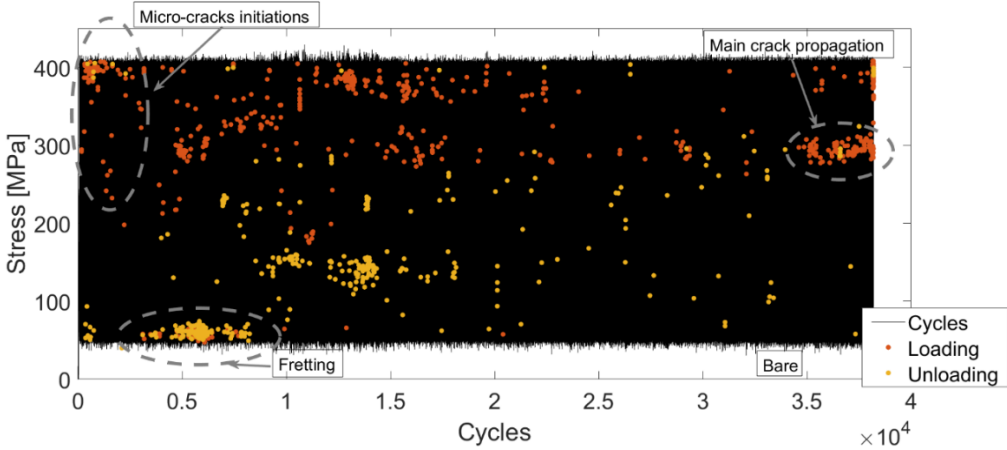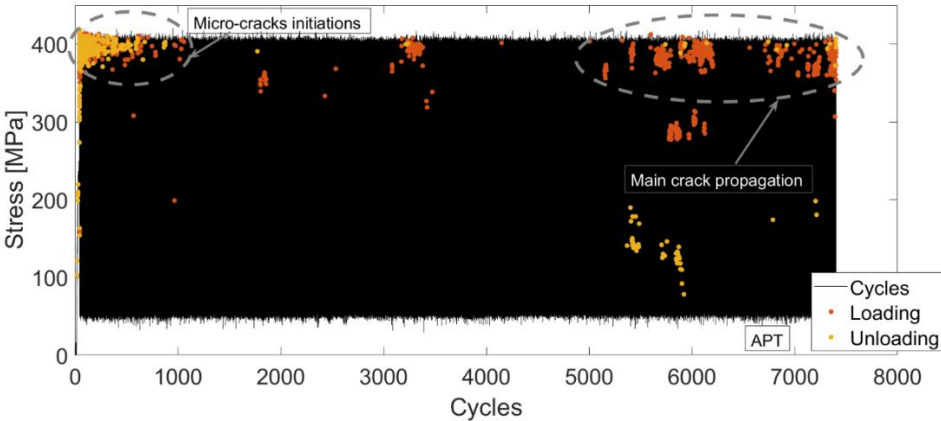

Fig. 9: Occurrence of hits acquired during loading (red dots) and unloading (orange dots) for an APT specimen submitted to a fatigue test.
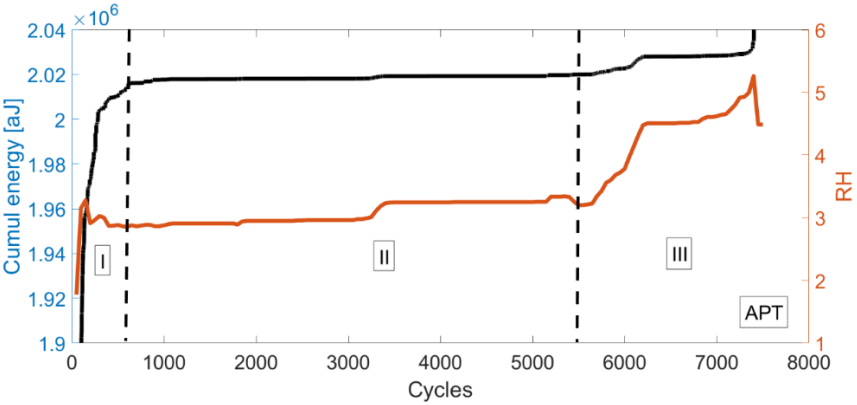
Fig. 10: Evolution of the cumulated AE energy and RH indicator vs number of cycles during a fatigue test (APT specimen).

3.2 Fatigue tests: immersed samples

This last part study the fatigue test results concerning the specimens that were immersed in a corrosive bath of 3.5% wt NaCl solution. According to the potential measurements, corrosion was mainly detected for the bare material. A decrease in fatigue lifetime is noticed concerning the immersed bare samples (bare IS) (Fig. 4), which is mainly due to the presence of corrosion defects that acted as stress raisers and produced early crack initiation sites that led to a global decrease in fatigue life (Fig. 13a). Compared to bare non-immersed samples (bare NIS), less AE hits are acquired during all fatigue lifetime of the bare immersed specimen (Fig. 11). Here, the main crack is early initiated at a corrosion defect and all the stress concentration is focussed at the crack tip, resulting in an overall decrease of intermetallic particles cracking and micro-cracks initiations along the gauge length of the specimen. This would led to a global decrease of AE activity. A minimal value of the RAE indicator is reached between 50-70% of fatigue lifetime and is repeatable for all specimens tested (Fig. 12). This specific time area could be used in order to quantity the RUL for immersed samples with corrosion defects.

Fig. 11: Cumulated AE activity for bare specimens with (grey) or without (blue) immersion.
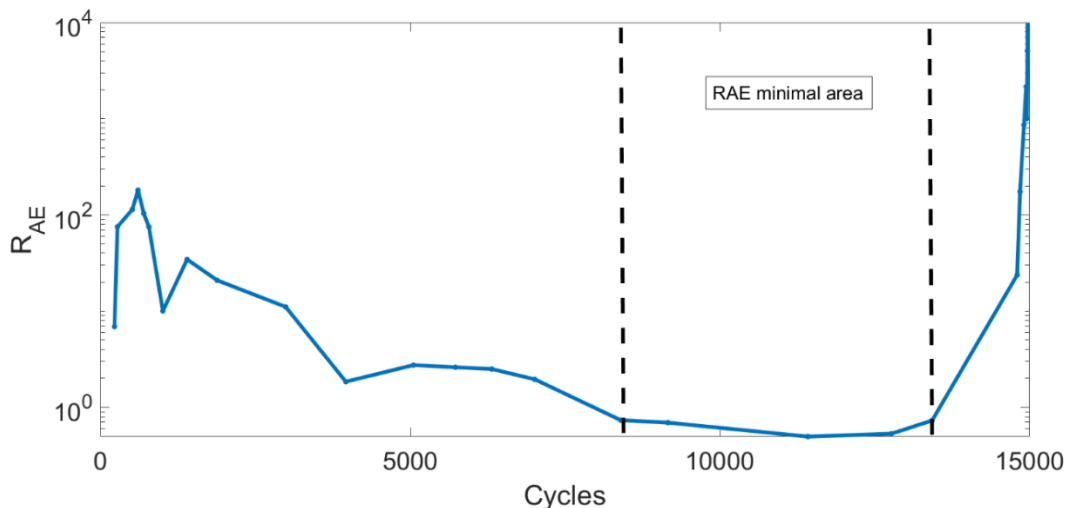
Fig. 12: RAE indicator evolution during fatigue lifetime for a bare specimen immersed in a corrosive bath.
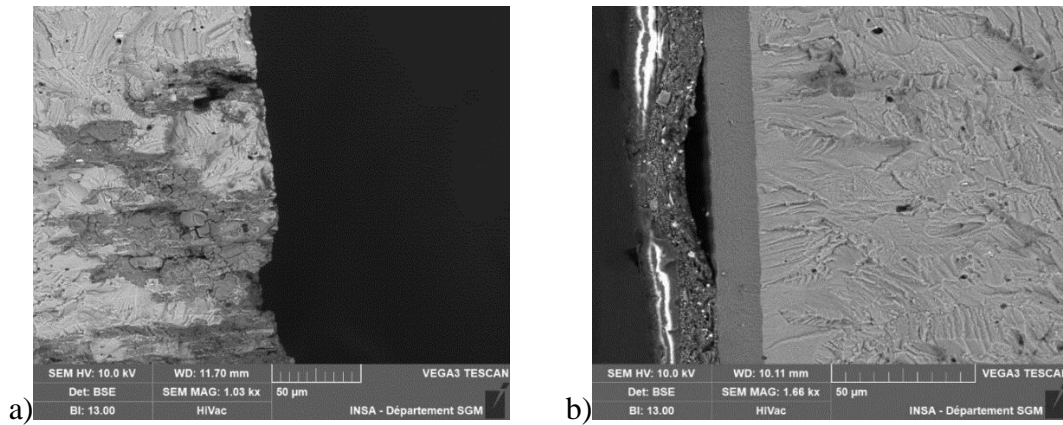
Fig. 13: Crack initiation area for a) a bare specimen and b) an APT specimen immersed in a corrosive bath: corrosion defects (SEM, BSE mode).

Concerning APT specimens, it seems that the immersion process does not impact their fatigue lifetimes (Fig. 4). This is explained by the absence of corrosion defects on the substrate. The oxide layer (SAA) provide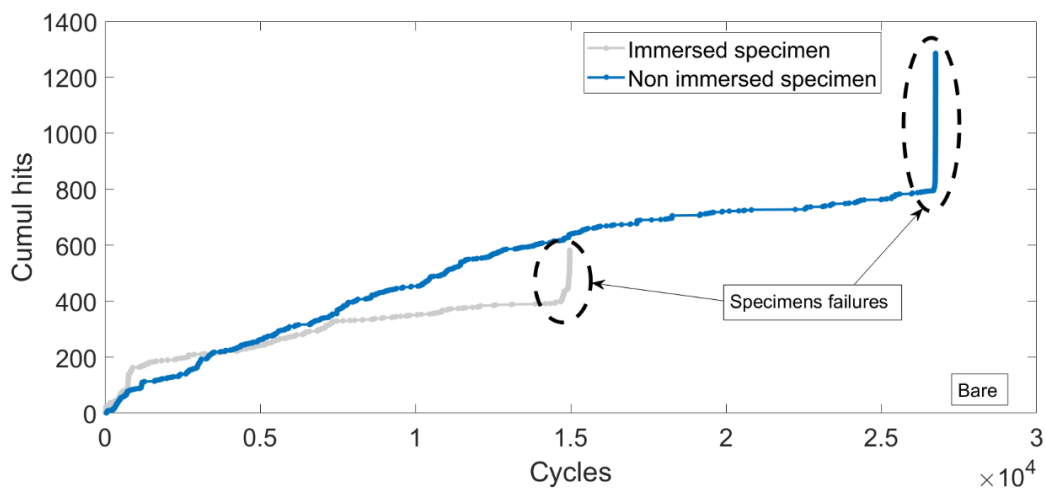s a good protection against the corrosive environment, the electrolyte was never in contact with the aluminium substrate (Fig. 13b).

In another hand, the AE activity for immersed APT samples is completely different compared to non-immersed APT samples. Indeed, much more AE signals are acquired for immersed samples (20000 hits for immersed samples and around 5000 for non-immersed samples), for a comparable fatigue lifetime (Fig. 14). The solution might change the inner microstructure of the oxide layer, this would affect the cracking process of the oxide layer during fatigue tests.

The hits acquired are highly energetic and located on all the specimen gauge length (Fig. 14 – Fig. 15). They are the signature of a diffuse damage of the oxide layer before failure of the sample.

The study of the RAE indicator allows to anticipate the failure, with an early restart of the AE activity at 30% of the fatigue lifetime until failure of the material (Fig. 16). This type of AE activity is repeatable for all specimens tested and might be used as a characteristic damage time for immersed samples.

Those results show that the environment can have significant impacts on the properties of the substrate and the coatings. This is important to consider in order to perform real time damage monitoring and perform lifetime prediction with AE. From an environment to another the AE activity related to the damage processes in the substrate and the coatings changes completely.

Fig. 14: a) Cumulated AE hits and events for an APT specimen with (black) and without (red) immersion.

Fig. 15: Location of the AE events acquired on the gauge length of an APT immersed specimen.
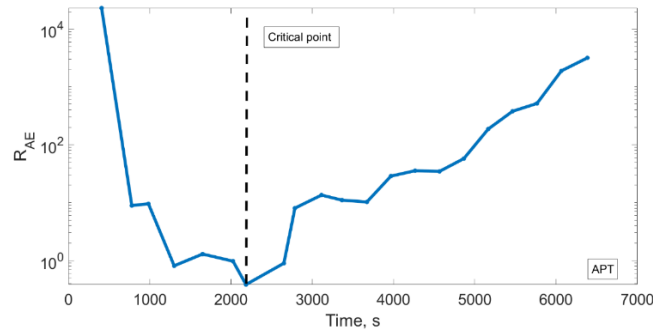
Fig. 16: Evolution of the RAE indicator during fatigue lifetime for an immersed APT specimen.

4.   Conclusions

The present article investigates via AE monitoring the impact of different coating layers on crack initiation and propagation during mechanical tests f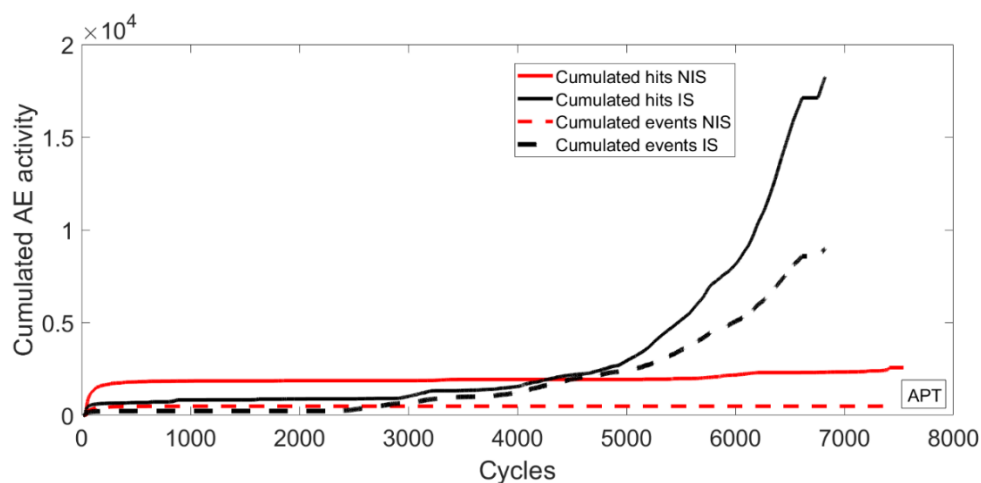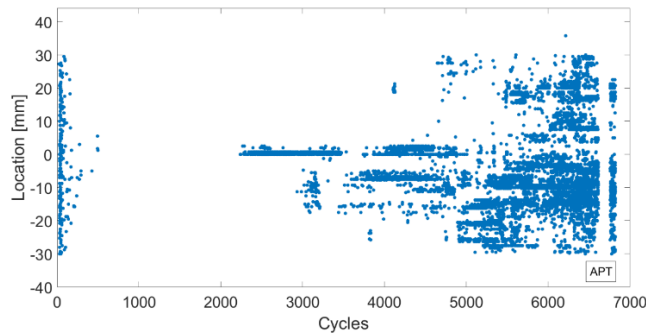or Al 7075-T6. In the last part, this work also investigates the coupled impact of coating and immersion in a corrosive environment during fatigue tests. Bare samples and samples coated with sulfuric acid anodization and the two epoxy painting layers (APT) are studied. Dynamic fatigue tests have been performed on all the specimens. Coatings are important parameters to consider when monitoring material damage, given their impact on the mechanical properties and the possible creation of additional damage mechanisms, sources of AE. For anodized specimens, the acquired AE signals mostly come from cracking of the oxide layer.

The coatings have a major impact on fatigue behaviour and lifetime of the material. The AE results are used to identify the fatigue stages of the material and understand the main characteristics of crack initiation and propagation for all types of specimens. The AE base damage indicators studied to quantify the damage state of the specimens allowed to find characteristic damage times that could be used to quantify the RUL of the material and anticipate failure. For all types of samples, those times are mainly linked to the initiation of micro-cracks in the substrate and the propagation of the main fatigue crack. The propagation of the main crack does not create energetic AE activity for 7075-T6 aluminum alloy and is only detected in the last cycles of the test. On the other hand, AE is very relevant concerning the anodized specimens, it is noticeable that the main crack growth process creates an important and energetic AE activity which is linked to a synergetic effect between the crack advancing in the substrate and the creation of cracks in the oxide layer.

AE is also used to quantify the impact of a corrosive environment (NaCl 3.5 wt%) on the damage processes in the substrate and the coatings. For specimens immersed in the corrosive bath, only the bare specimens are corroded by the solution. This induce a decrease in fatigue lifetime due to an early crack initiation at corrosion defects. For the immersed bare material, a characteristic damage time linked to the minimum value of the RAE indicator is found at around 50% of the lifetime for all specimens. Concerning the immersed anodized samples, no impact on fatigue life

is observed, the substrate is protected by the oxide layer and no corrosion defects are observed. The larger AE activity during fatigue tests for APT immersed samples are linked to changes in the oxide microstructure in contact with the corrosive solution. The study of the RAE indicator allows to anticipate failure for immersed APT specimens, with a characteristic damage reached for all samples at 30% of the fatigue lifetime. Those results underline that environment is an important parameter to consider in order to perform AE damage monitoring.

5. References

[1] T. Dursun, C. Soutis, Recent developments in advanced aircraft aluminium alloys, Mater. Des., 56 (2014), pp. 862-87.

[2] E. Cirik, K. Genel, Effect of anodic oxidation on fatigue performance of 7075-T6 alloy - Surface & Coatings Technology 202 (2008) 5190–5201.

[3] K. Genel, Environmental effect on the fatigue performance of bare and oxide coated 7075-T6 alloy, Engineering Failure Analysis 32 (2013) 248–260.

[4] PS Pao, CR Feng, SJ Gill, Corrosion fatigue crack initiation in aluminum alloys 7075 and 7050, Corrosion 2000;56:1022–31.

[5] Haipeng Song, Changchun Liu, Hao Zhang, Xudong Yang, Yajun Chen, Sean B. Leen, Experimental investigation on damage evolution in pre-corroded aluminum alloy 7075-T7651 under fatigue loading, Materials Science and Engineering: A, Volume 799, 2021, 140206, ISSN 0921-5093.

[6] Sheng Zhang, Teng Zhang, Yuting He, Xu Du, Binlin Ma, Tianyu Zhang, Long-term atmospheric pre-corrosion fatigue properties of epoxy primer-coated 7075-T6 aluminum alloy structures, International Journal of Fatigue, Volume 129, 2019,105225.

[7] Chang, Y. Z.; Tsai, P. H.; Li, J. B.; Lin, H. C.; Jang, J. S. C.; Li, C.; Chen, G. J.; Chen, Y. C.; Chu, J. P.; Liaw, P. K. Zr-Based Metallic Glass Thin Film Coating for Fatigue-Properties Improvement of 7075-T6 Aluminum Alloy. *Thin Solid Films* 2013, *544*, 331–334.

[8] Lee, C. M.; Chu, J. P.; Chang, W. Z.; Lee, J. W.; Jang, J. S. C.; Liaw, P. K. Fatigue Property Improvements of Ti–6Al–4V by Thin Film Coatings of Metallic Glass and TiN: A Comparison Study. *Thin Solid Films* 2014, *561*, 33–37.

[9] Shahzad, M.; Chaussumier, M.; Chieragatti, R.; Mabru, C.; Rezai-Aria, F. Surface Characterization and Influence of Anodizing Process on Fatigue Life of Al 7050 Alloy. *Materials & Design* 2011, *32* (6), 3328–3335.

[10] Shahzad, M.; Chaussumier, M.; Chieragatti, R.; Mabru, C.; Rezai-Aria, F. Influence of Anodizing Process on Fatigue Life of Machined Aluminium Alloy. *Procedia Engineering* 2010, *2* (1), 1015–1024.

[11] Amer, A. O.; Gloanec, A.-L.; Courtin, S.; Touze, C. Characterization of Fatigue Damage in 304L Steel by an Acoustic Emission Method. *Procedia Engineering* 2013, *66*, 651–660.

[12] Goetz, J. M. Investigation of Coating Cracking and Fatigue Strength of 7050-T74 Aluminum Alloy with Different Anodize Coating Thicknesses. 47.

[13] Dickinson, J. T.; Snyder, D. B.; Donaldson, E. E. Electron and Acoustic Emission Accompanying Oxide Coating Fracture. *Thin Solid Films* 1980, *72* (2), 223–228.

[14] Shaira, M.; Godin, N.; Guy, P.; Vanel, L.; Courbon, J. Evaluation of the Strain-Induced Martensitic Transformation by Acoustic Emission Monitoring in 304L Austenitic Stainless Steel: Identification of the AE Signature of the Martensitic Transformation and Power-Law Statistics. *Materials Science and Engineering: A* 2008, *492* (1–2), 392–399.

[15] Mazal, P.; Vlasic, F.; Koula, V. Use of Acoustic Emission Method for Identification of Fatigue Micro-Cracks Creation. *Procedia Engineering* 2015, *133*, 379–388.

[16] El May, W. Etude par émission acoustique de la plasticité et de l'endommagement de l'aluminium en fatigue oligocyclique. Matériaux, Insa de Lyon, Lyon, 2013.

[17] Racle, E.; Godin, N.; Reynaud, P.; Fantozzi, G. Fatigue Lifetime of Ceramic Matrix Composites at Intermediate Temperature by Acoustic Emission. *Materials* 2017, *10* (6), 658.

CHARACTERIZATION OF OPTICAL AE SIGNALS AT LOADING OF FIBRE REINFORCED COMPOSITES

Martin Misson[1], Primož Potočnik[2], Zoran Bergant[2], Mario Sorgente[3], Edvard Govekar[2], Roman Šturm[2] and Tomaž Kek[2,*]

[1]LTH Castings d.o.o., 4200 Škofja Loka, Slovenia; martin.misson@lthcastings.com
[2]Faculty of Mechanical Engineering, University of Ljubljana, 1000 Ljubljana, Slovenia;
primoz.potocnik@fs.uni-lj.si, zoran.bergant@fs.uni-lj.si, tomaz.kek@fs.uni-lj.si,
roman.sturm@fs.uni-lj.si, edvard.govekar@fs.uni-lj.si
[3]Optics 11, Amsterdam, The Netherlands; mario.sorgente@optics11.com
*Correspondence: tomaz.kek@fs.uni-lj.si

ABSTRACT

Characterization of acoustic emission (AE) signals in loaded materials can reveal structural damage and consequently provide early warnings about product failures. Therefore, extraction of the most informative features from AE signals is an important part of the characterization process. This study considers the characterization of AE signals obtained from bending experiments for biocomposite and glass fiber epoxy (GFE) composites at room temperature and low temperature. For the acquisition of AE signals, fiber optic sensors (FOS) are used that can outperform classical electrical sensors under challenging operational environments. In this paper, we propose the extraction of deep features using different machine learning methods. The deep features are compared with extracted standard AE features. Then, the different feature sets are analyzed through discriminant analysis, neural networks, and extreme learning machines, combined with feature selection, to estimate the predictive potential of various feature sets. The proposed signal processing structure is focused on the classification of AE signals to recognize the source material, evaluate the predictive importance of extracted features, and evaluate the ability of used FOS for evaluation of material behavior under challenging low-temperature environments.

Keywords: Polymer composites, fiber optic sensor, biocomposites, GFE composites, acoustic emission, deep feature extraction.

1. Introduction

Composite materials are increasingly used in lightweight transportation systems and civil engineering due to increasing weight constraints and installation costs. In the case of transportation systems such as in the aerospace and automobile industries, the use of composite materials reduces the weight, which is reflected in increasing the transportable load and reducing fuel consumption, and therefore the mechanical performance of the material is a very important and desired attribute. The use of fiber-reinforced polymer (FRP) composites is somewhat limited due to the possibility of sudden damage under load. Damage mechanisms in FRP are heterogeneous in that they often begin in-depth and then propagate at different length scales (micro-, meso-, or macroscales). In addition, the composite constituents (fiber, matrix, and interfacial bonding), and the applied

mechanical load (stress level of the loading sequence, stress ratio) influence the damage evolution [1,2]. This aggravates the development of damage-tolerant design procedures like those used for metallic materials. In polymer composites, this is mostly related to the development of experimental techniques that can monitor material behavior and offer real-time information about damage evolution [3].

Performance improvement is the main goal of nowadays industries. The need for efficient, competitive processes allows for clear material characterization, the development of cutting-edge technologies and, innovative scientific approaches to nowadays demands. Moving forwards means having solid foundations to face new challenges. Industries need efficient materials to operate in harsh environments and conditions and to be monitored continuously with the highest accuracy, precision, and repeatability. The acoustic emission technique has been applied to materials research, non-destructive evaluation (NDE), and structural health monitoring. AE is a non-invasive technique that allows damage detection in materials and tracks their evolution in real time. Events such as cracks, delamination, corrosion, and debonding release energy in the form of high-frequency elastic waves which travel across materials. By measuring such elastic waves, AE sensors allow detection and locate faults in complex structures. The formation of cracks in engineering structures results in the generation of transient acoustic (or elastic) waves throughout the structure. This phenomenon is called acoustic emission, and it can occur in many different types of materials, namely metal, concrete and composite structures.

Electrical AE systems use piezoelectric sensors to acquire these high-frequency acoustic waves. However, piezoelectric sensors have some limitations that narrow down their application in harsh environments. This is because a standard piezoelectric sensor has a limited operating temperature and is not usually suitable for cryogenic or high temperatures without protection, and it is not robust against, nuclear radiation and electromagnetic interferences. In such a context, fiber optic transducers have been investigated through the years as a possible solution. Thanks to their passive nature, fiber optic sensors (FOS) can outperform electrical sensors in challenging operational environments [4].

During composite loading, several damage mechanisms occur almost simultaneously, which creates a scientific challenge to assign a specific set of AE signal features to a particular damage mechanism. This is now most frequently solved with pattern recognition [5,6]. Tang et al. [7] used a sequential feature selection method based on a k-means clustering algorithm for the classification of AE signals in wind turbine blades loaded in the flap-wise direction. The visualization of clusters in peak frequency−frequency centroid features is used to correlate the clustering results with failure modes. Hamdi et al. [8] used the Hilbert–Huang transform to extract frequency descriptors based on intrinsic mode functions for k-means pattern recognition for unidirectional GFRP during three-point bending. Nair et al. [9] used an unsupervised k-means clustering method with a neural network based on a multi-layer perceptron (MLP) and support vector machine (SVM) algorithm for pattern recognition in CFRP retrofitted RC beams.

Automatic extraction of the intrinsic characteristics of signals based on deep learning is becoming increasingly popular. Extraction from the time-frequency domain enables the model to learn features, that more comprehensively reflect the intrinsic characteristics in the signal compared to features extracted from the time and/or frequency domain [10]. The clarity of high-fidelity characterization would enable an understanding of the local structural drivers of the damage response of composites [11]. In addition, a single methodology framework, which can be extended not only to various applications, conditions (i.e., industries), and configurations (test materials, data acquisition setups) but even broadly in different engineering domains, can be even more readily adopted [12]. For example, for milling tool wear condition monitoring, a stacked spare autoencoder has been utilized as a feature learning method [13]. The feature value extracted by the traditional method is obtained by manual construction and requires certain professional knowledge [14,15], while deep learning is used to establish a network model, allowing the network to automatically learn features, avoiding the loss of signals in the time and frequency domains during the manual feature extraction [16].

2. Material and methods

In the research, we used flax biocomposite specimens with a total of eight plies of twill weave flax fabrics. The specimens of $20 \times 4 \times 200$ mm in size were water-jet cut out of the plate of 300x300 mm. Besides biocomposite specimens, we used pultruded glass fiber epoxy GFE composite of the same dimension $20 \times 4 \times 200$ mm.

2.1 Experimental setup

For the loading of composites we used a 3-point bending test on a Messphysic loading machine with a span of 80 mm and the loading pin with a diameter of 8 mm. Bending tests were performed at room temperature and a low temperature of -80 °C was achieved in climatization chamber. We used a 4-channel OptimAE system with 2 optical AE sensors (version 05) with a resonance frequency of 215 kHz. An optical AE acquisition system can collect signals down to cryogenic temperatures. The operating principle of the OptimAE system is based on interferometry, where the differential change in the path length of two optical fibers due to the acoustic wave is detected with high sensitivity. The fibers in such a setup are densely coiled in a package inside the AE sensor. The sensitive coil is attached to the surface of the specimen, with the metallic mandrel in direct contact with the structure for optimum transmission of the acoustic wave to the fibers. This is causing the stretching of the fibers on the coil, and the resulting interferometric signal is transferred to the OptimAE box. This offers signal acquisition, demodulation of the AE signal, and computer communication with OptimAE software.

Fig. 1: Fiber optics sensor system OptimAE.

2.2 Feature extraction

Features used in the analysis were extracted from time and frequency domains, which are often used to classify damage mechanisms in polymer composites. These features are henceforth referred to as "standard features", whereas features extracted using CAE are referred to as "deep features". Extracted standard features with designations are: a1 - peak amplitude [nm], a2 - burst signal duration [μs], a3 - burst signal energy [au], a4 - burst signal rise-time [μs], a5 - spectral centroid [Hz], a6 – Counts [/], a7 - RMS value [μV], a8 - frequency of the max. amplitude of Fourier transformation [Hz], a9 - frequency of the max. amplitude of continuous wavelet transformation [Hz], and partial powers of Fourier spectrum in different frequency spans [/]:
a10 – 0-75 kHz, a11 – 75-150 kHz, a12 – 150-300 kHz, a13 – 300-475 kHz. The convolutional autoencoder (CAE) presented in this section is designed to extract "deep features". These features are extracted automatically during the CAE training phase. Deep features do not have physical meaning but are designed to minimize information loss of the input-output mapping of the CAE. Deep features (denoted as d1, d2, … [/]) were extracted from continuous wavelet transform (complex Morlet wavelets) scalograms using a convolutional autoencoder (CAE) [17]. Matrix-wise standardization was used in the pre-processing stage.

The structure of the convolutional autoencoder for deep feature extraction is depicted in Fig. 2. Model input is a 2-D matrix of size 48 × 432, which is, before any computations, split into four stripes of 12 × 432 matrices. The subsequent layer operations are performed separately and independently (without parameter sharing) on each of the stripes. Two convolutional layers (filter dimension 3 × 5, ReLU activation and strides 1, 3) and 2 × 2 max-pooling layers (C+P layers) with a stride of 2 were used. Then, all of the resulting output feature maps were concatenated back into one merged feature map. A single convolutional layer (filter dimension 3 × 3, ReLU activation and strides 1, 1) and a 2 × 2 max-pooling layer with a stride of 2 follow. The resulting 2-D feature map is flattened to 1-D and connected to three fully connected layers—FCL 1, FCL 2, and FCL 3. These layers complete the CAE's encoder used to extract deep features after the whole model (with decoder) has been trained. The number of neurons set in FCL 3 translates to the dimensionality of the feature vector, which encodes each scalogram as a specific series of numbers—deep features.
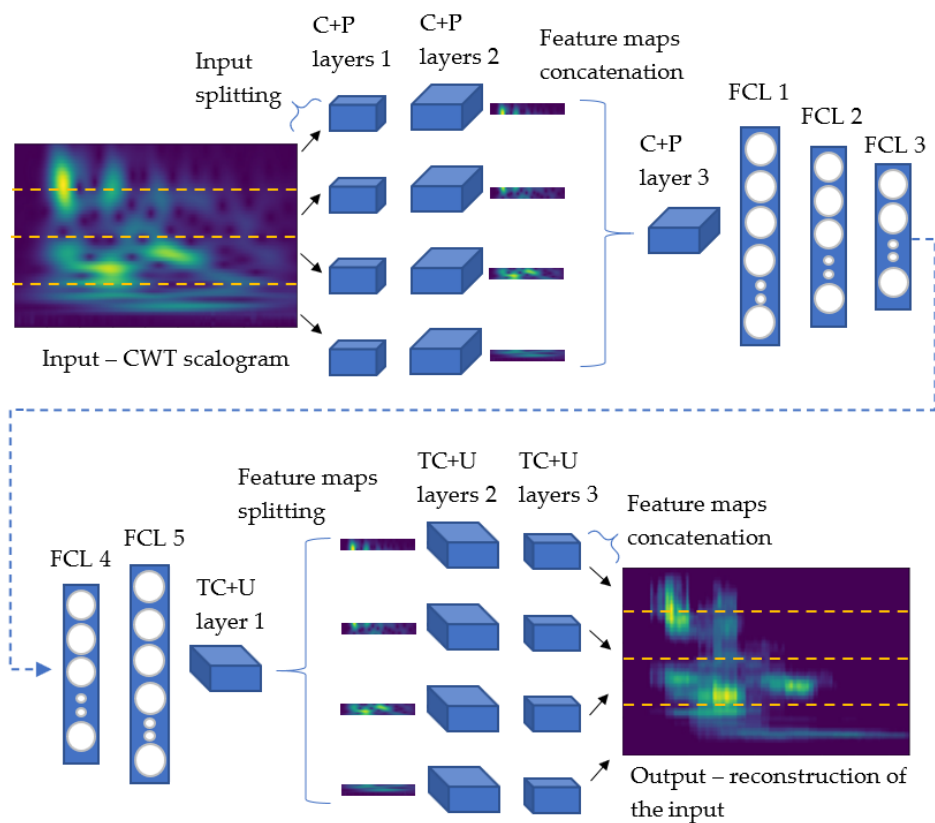
Fig. 2: Convolutional autoencoder (CAE) for deep feature extraction.

To construct the classifiers of features extracted from AE signals we used different classification methods that are neural networks (NN), discriminant analysis (DA), and extreme learning machines (ELM). To select the most informative extracted AE features and to provide an estimation of generalization performance we used the forward feature selection (FFS) procedure and 5-fold cross-validation (CV). Fig. 3 shows the classification accuracy of correctly classified samples regarding the used sample material for included features with the use of the ELM model. The results are shown separately for standard, combined, and deep features. The unsupervised extraction process shows that the combination of standard and deep features achieves better classification accuracy than standard or deep features alone. The classification accuracy of the combined features reaches up to 79,9 % while the standard and deep features up to 74 and 67,2 %.
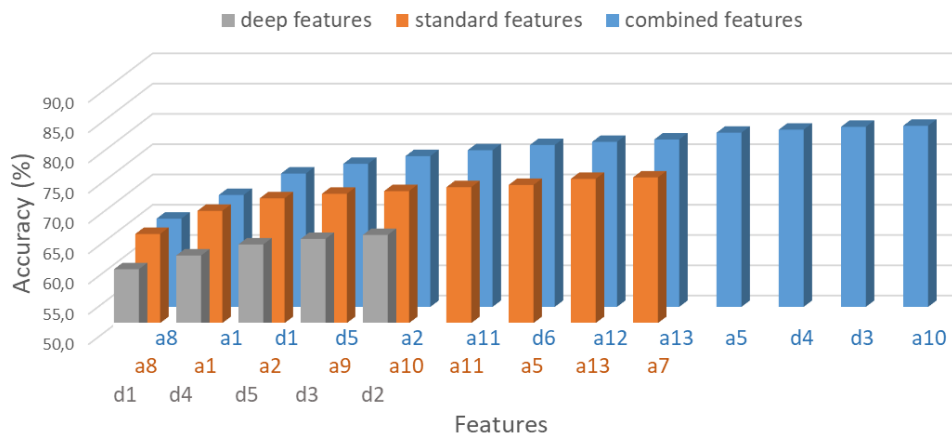
Fig. 3: Classification accuracy for the extreme learning machine (ELM) classification method.

3. Conclusions

In this paper, the research was designed to investigate the AE signals at biocomoposits and GFE composites during bending of the specimens. OptimAE sensors, developed and commercialized by Optics11, were used for the acquisition of AE signals. FOS is configured in a Michelson interferometry setup and has the ability to withstand lower temperatures than conventional PZT sensors. The evaluation of the performance of a deep convolutional autoencoder (CAE) in providing informative features for the classification and characterization of AE signals is described. For the analysis different machine learning (ML) methods were used. Among them are discriminant analysis (DA), neural networks (NN), and extreme learning machines (ELM). ML methods were used for the construction of classifiers of extracted AE features of acquired signals. The most informative extracted features were selected with the forward feature selection (FFS) procedure and 5-fold cross-validation (CV). The described processing structure for AE signals offered a classification of AE signals with the ability to classify source material of stressed specimens. The unsupervised extraction process shows that the combination of standard and deep features achieves better classification accuracy compared to standard or deep features alone. The results also confirm the ability of used FOS for predictive monitoring of FRP composites in challenging conditions with low temperatures.

4. References

[1]   Duchene, P., Chaki, S., Ayadi, A., Krawczak, P. A review of non-destructive techniques used for mechanical damage assessment in polymer composites. J. Mater. Sci. 2018, 53, 7915–7938, https://doi.org/10.1007/s10853-018-2045-6.

[2]   Hamam, Z., Godin, N., Reynaud, P., Fusco, C., Carrère, N., Doitrand, A. (2022). Transverse Cracking Induced Acoustic Emission in Carbon Fiber- Epoxy Matrix Composite Laminates. Materials (Basel). 2022, 15, 1–15, https://doi.org/10.3390/ma15010394.

[3]   Crivelli, D., Guagliano, M., Monici, A. Development of an artificial neural network processing technique for the analysis of damage evolution in pultruded composites with acoustic emission. Compos. Part B: Eng. 2014, 56, 948–959, https://doi.org/10.1016/j.compositesb.2013.09.005.

[4]   Sorgente, M., Zadeh, A.R., Saidoun, A. Performance Comparison Between Fiber-Optic and Piezoelectric Acoustic Emission Sensors. 2020, 1–9.

[5]   Sause, M., Gribov, A., Unwin, A., Horn, S. (2012). Pattern recognition approach to identify natural clusters of acoustic emission signals. Pattern Recognit. Lett. 2012, 33, 17–23, https://doi.org/10.1016/j.patrec.2011.09.018 .

[6]   Panek, M., Blazewicz, S., Konsztowicz, K.J. (2020). Correlation of Acoustic Emission with Fractography in Bending of Glass–Epoxy Composites. J. Nondestruct. Eval. 2020, 39, 1–10, https://doi.org/10.1007/s10921-020-00706-0.

[7]   Tang, J., Soua, S., Mares, C., Gan, T.-H. (2017). A Pattern Recognition Approach to Acoustic Emission Data Originating from Fatigue of Wind Turbine Blades. Sensors 2017, 17, 2507, https://doi.org/10.3390/s17112507.

[8]   Hamdi, S.E., Le Duff, A., Simon, L., Plantier, G., Sourice, A., Feuilloy, M. (2013). Acoustic emission pattern recognition approach based on Hilbert–Huang transform for structural health monitoring in polymer-composite materials. Appl. Acoust. 2013, 74, 746–757, https://doi.org/10.1016/j.apacoust.2012.11.018.

[9]   Nair, A., Cai, C., Kong, X. (2018). Acoustic emission pattern recognition in CFRP retrofitted RC beams for failure mode identification. Compos. Part B Eng. 2018, 161, 691–701, https://doi.org/10.1016/j.compositesb.2018.12.120.

[10] Gu, Y.-K., Zhou, X.-Q., Yu, D.-P., Shen, Y.-J. (2018). Fault diagnosis method of rolling bearing using principal component analysis and support vector machine. J. Mech. Sci. Technol. 2018, 32, 5079–5088, https://doi.org/10.1007/s12206-018-1004-0.

[11] Muir, C., Swaminathan, B., Almansour, A.S., Sevener, K., Smith, C., Presby, M., Kiser, J.D., Pollock, T.M., Daly, S. (2021). Damage mechanism identification in composites via machine learning and acoustic emission. NPJ Comput. Mater. 2021, 7, 1–15, https://doi.org/10.1038/s41524-021-00565-x.

[12] Kaji, M., Parvizian, J., Venn, H. (2020). Constructing a Reliable Health Indicator for Bearings Using Convolutional Autoencoder and Continuous Wavelet Transform. Appl. Sci. 2020, 10, 8948, https://doi.org/10.3390/app10248948.

[13] Ou, J., Li, H., Huang, G., Zhou, Q. (2020). A Novel Order Analysis and Stacked Sparse Auto-Encoder Feature Learning Method for Milling Tool Wear Condition Monitoring. Sensors 2020, 20, 2878, https://doi.org/10.3390/s20102878.

[14] García-Martín, J., Gómez-Gil, J., Vázquez-Sánchez, E. (2011). Non-Destructive Techniques Based on Eddy Current Testing. Sensors 2011, 11, 2525–2565, https://doi.org/10.3390/s110302525.

[15] Gao, X., Mo, L., You, D., Li, Z. (2017). Tight butt joint weld detection based on optical flow and particle filtering of magneto-optical imaging. Mech. Syst. Signal Process. 2017, 96, 16–30, https://doi.org/10.1016/j.ymssp.2017.04.001.

[16] Miao, R., Gao, Y., Ge, L., Jiang, Z., Zhang, J. (2019). Online defect recognition of narrow overlap weld based on two-stage recognition model combining continuous wavelet transform and convolutional neural network. Comput. Ind. 2019, 112, 103115, https://doi.org/10.1016/j.compind.2019.07.005.

[17] Potočnik, P., Misson, M., Šturm, R., Govekar, E., Kek, T. (2022). Deep Feature Extraction Based on AE Signals for the Characterization of Loaded Carbon Fiber Epoxy and Glass Fiber Epoxy Composites. Appl. Sci. 2022, 12, https://doi.org/10.3390/app12041867.

FIBER OPTIC SENSING SYSTEMS

State-of-the-art sensing systems for unmatched performance in the most challenging environments

Our profile

OPTICS11 is an Amsterdam based high tech company that offers state-of-the-art fiber optic sensing systems for unmatched performance.

Optics11 has extensive experience with monitoring Acoustic Emission, Temperature (including cryogenic), Strain, Acceleration, and Pressure.

All Optics11 systems embrace innovative measurement techniques that allow to overcome most of the drawbacks and limitations of classic fiber-optic sensing systems such as limited bandwidth, limited sensitivity, and bulky sensor size.

Fiber optic sensing systems for

Monitoring in Cryogenic Environment

Structural Health Monitoring

Condition Monitoring

INVESTIGATION OF BACKGROUND NOISE AFFECTING AE DATA ACQUISITION DURING TENSILE LOADING OF FRPs

Maria Gfrerrer[1,*], Johannes Wiener[1], Andreas J. Brunner[2†] and Gerald Pinter[1]

[1]Montanuniversität Leoben, Materials Science and Testing of Polymers, Leoben, Austria;
maria.gfrerrer@unileoben.ac.at, johannes.wiener@unileoben.ac.at, gerald.pinter@unileoben.ac.at
[2]Empa, Swiss Federal Laboratories for Materials Science and Technology, Dübendorf, Switzerland;
andreas.brunner@empa.ch
[†]Retired Scientist
*Correspondence: maria.gfrerrer@unileioben.ac.at; tel.: +43 3842 402 2128

ABSTRACT

The method of acoustic emission (AE) allows the detection of damage initiation and growth in composites due to its high sensitivity. However, for the same reason, AE signal acquisition can easily be disrupted by ambient noise. A significant source of noise is the testing machine itself. In this contribution, the qualification of different types of testing machines to perform material testing in combination with AE measurements is investigated. For this purpose, quasi-static tensile tests of ±45° carbon fiber-reinforced epoxy specimens are conducted on a static, an electro-dynamic and a servo-hydraulic machine. Static and electro-dynamic machines in the used setup seem to have no influence on AE data acquisition. Contrary, AE data acquisition on the servo-hydraulic machine proves difficult. Measures, such as increasing the threshold for detection or using a high-pass filter to reduce noise have a detrimental effect on data acquisition, since desired signals are discriminated as well.

Keywords*: Acoustic emission, fiber-reinforced polymers, test engineering, background noise.*

1. Introduction

Due to their composition, fiber-reinforced polymers (FRPs) exhibit a series of complex, microscopic damage mechanisms, e.g. matrix cracking, fiber-matrix debonding or fiber breakage, when being loaded. In order to be able to predict and model their behavior during service life the understanding of damage evolution is of high interest [1].

The method of acoustic emission (AE) allows the detection of damage initiation and growth. Each formation of new microscopic damage results in the generation of an elastic wave. This excited wave propagates through the material until it reaches a sensor, where it is converted into a transient AE signal. These signals then can be analyzed to gain information about the underlying damage mechanisms [2, 3].

So far, the application of AE for damage detection in FRPs mainly focused on quasi-static testing [4, 5]. Even though the characterization of damage evolution during fatigue loading is of similar importance, there are still some obstacles which need to be overcome. For one thing, AE data acquisition during fatigue loading tends to yield an excessive amount of data, which is difficult to

handle. Apart from that, noise originating from servo-hydraulic testing machines, which are mainly used for fatigue testing, disturb AE data acquisition originating from material damage [5, 6]. Usually noise is a continuous source of AE and overlaps the transient signals. If the noise exceeds the set threshold for triggering signal recording, transient signals from damage in the material can no longer be discriminated.

In this contribution AE measurements during quasi-static tensile loading of carbon fiber-reinforced polymer (CFRP) specimens on different types of testing machines were performed. The influence of background noise generated by the drive of a static, an electro-dynamic, and a servo-hydraulic testing machine on AE data acquisition is investigated. The performed tests serve as a preliminary study to investigate the qualification of each testing machine. Potential measures to minimize noise from the testing machine in order to be able to exclusively detect signals originating from damage inside the material are discussed as a further consequence.

In addition, the algorithm of HDBSCAN (hierarchical density-based spatial clustering of applications with noise) is applied to one exemplary AE dataset, followed by a simplified interpretation of the identified clusters.

2. Experimental

2.1 Material and specimen preparation

Specimens were cut from a carbon fiber-reinforced epoxy laminate with a fiber volume content of approximately 55 % and a layup of $(+45°, -45°)_{2s}$. For the matrix, EPIKOTE™ resin MGS® RIMR135 and EPIKURE™ curing agent MGS® RIMH1366 by Momentive (Esslingen am Neckar, Germany) were mixed in a ratio of 100:30 (weight proportion resin:curing agent). Carbon fibers are of type HS 15-50/250 by G. Angeloni srl (Quarto d'Altino, Italy). The laminate was manufactured in a vacuum assisted resin transfer molding process. Thereby, curing was performed at 80 °C for 5 h.

Specimen dimensions for tensile testing were 200 x 20 x 2 mm³. Shafted aluminum tabs of 1 mm thickness and 50 mm length were glued to the specimens on each side. This resulted in a gauge length of 100 mm.

2.2 Testing equipment and parameters

Quasi-static tensile tests were performed on three different testing machines. Table 1 gives an overview on the used equipment. All tensile tests were performed with a crosshead speed of 2 mm/min.

Table 1: Overview on testing machines and equipment used for the tensile tests.

TESTING MACHINE TYPE	TESTING MACHINE DESIGNATION	LOAD CELL	CLAMPING JAWS
Static (spindle drive)	Z250 by ZwickRoell GmbH & Co. KG (Ulm, Germany)	20 kN	pneumatic
Electro-dynamic	ElectroForce® 3550-AT by Bose Corporation – ElectroForce Systems Group (Minnesota, USA)	15 kN	mechanical
Servo-hydraulic	MTS 831.50 by MTS Systems Corporations (Minnesota, USA)	15 kN	mechanical

The used AE system is by MISTRAS Group Inc. (Princeton Junction, USA). For each measurement two broad band (WD) sensors were mounted to the specimen using silicone free vacuum grease as coupling medium and spring clamps for mounting. The distance between the sensors amounted to approximately 75 mm, as shown in Fig. 1. Additionally, each sensor was connected to a 2/4/6 preamplifier with a gain of 40 dB and a 20 - 1200 kHz bandpass filter. The software AEwin^{TM} by MISTRAS Group was used for data acquisition and evaluation of the amplitude over duration plots. For evaluating the rest of the features, the software nAExtor by BCMtec GmbH (Augsburg, Germany) was used.

For AE data acquisition the threshold was set to 40 dB$_{AE}$ and a sampling rate of 5 MHz was chosen. The maximum duration for one hit was limited to 100 ms. The following values were chosen for the AE timing parameters:

- Peak definition time (PDT): 50 μs
- Hit definition time (HDT): 100 μs
- Hit lockout time (HLT): 300 μs
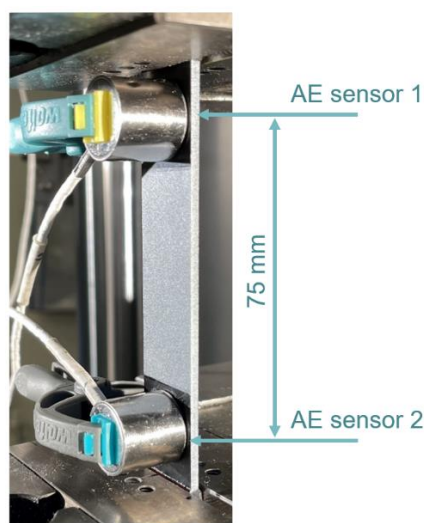
Fig. 1: Test setup for tensile tests with WD sensors mounted to the specimen.

2.3 Data treatment for clustering

Prior to clustering the selected features were normalized according to equation (1) in order to scale all feature vectors x between -1 and 1 ($\bar{x}$ represents the mean value). Normalization avoids size dependent influences, when absolute feature values have different orders of magnitude.

$$x_{norm} = \frac{x - \bar{x}}{\max(x - \bar{x})} \tag{1}$$

Clustering was performed in Python 3.8 using the "hdbscan" package [7]. Minimum number of points per cluster was set to 5 and minimum number of samples for the density evaluation was set to 20. The remaining parameters were kept at their default values. A detailed description of HDBSCAN can be found in [8]. After clustering the normalized features were rescaled to their original values.

3. Results and discussion

In this section the detected AE parameters from the tensile tests on the different types of testing machines are presented. Based on the outcome, potential measures to reduce or eliminate noise are discussed.

3.1 Presentation of AE data

Fig. 2 shows a selection of AE parameters measured during tensile loading of the ±45° CFRP specimens on the three different testing machines. Red curves or data point represent features evaluated from signals detected at sensor 1 (Channel 1) and blue curves or datapoints signal features detected at sensor 2 (Channel 2). The chosen AE parameters are the cumulative AE hits, representing AE activity, the AE signal amplitude, representing the intensity of the detected signals and moreover AE signal peak frequency. Peak frequency represents the frequency with the highest contribution in the frequency spectrum.

Cumulative AE hits detected during tensile loading of the specimens on the static and electro-dynamic testing machine show the typical exponential increase, reflecting damage growth proportional to the already existing amount of damage [3]. The onset of the cumulative hit curve in both cases correlates with a change of slope of the force-curve, indicating damage initiation. During both of the presented examples the specimen failed closer to sensor 2, which correlates with the higher amount of AE hits detected at sensor 2, respectively.

Signal amplitudes increase over the experiment, as occurring damage events intensify and finally result in catastrophic failure.
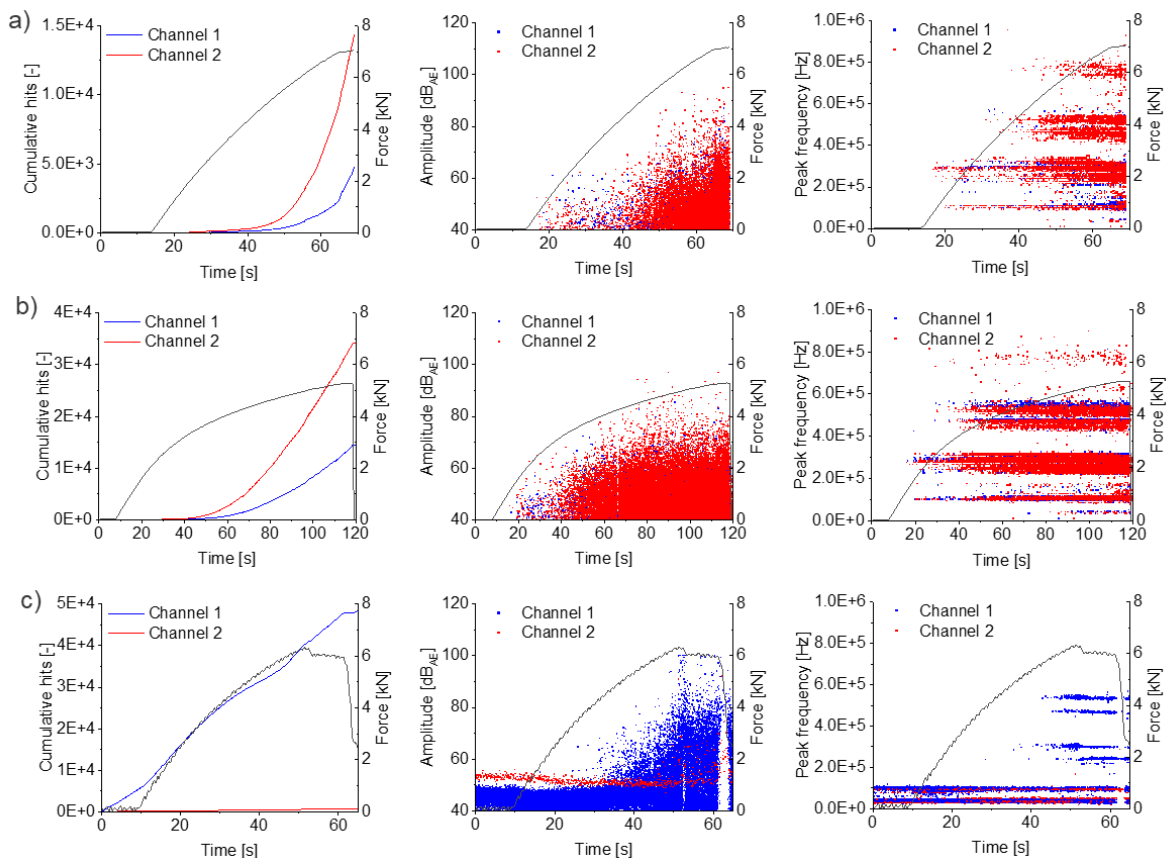
Fig. 2: Cumulative AE hits, AE signal amplitude and peak frequency acquired during tensile loading of a ±45° CFRP specimen on a) the static, b) the electro-dynamic and c) the servo-hydraulic testing machine.

During tensile loading on both, the static and the electro-dynamic testing machine, AE signal peak frequencies appeared in the same ranges. Thereby low-frequency dominated AE signals, being correlated with matrix cracking in literature [2], already arise shortly after load application. High-frequency dominated AE signals tend to arise later during the tensile test and usually are correlated with mechanisms such as interfacial failure (fiber-matrix debonding) or fiber breakage [2].

This observation is confirmed by the growth of the found clusters over the experiment. HDBSCAN was applied to the features peak frequency and partial power 2 (power percentage in the frequency region of 150 – 300 kHz in %) of the AE data acquired during tensile loading of a specimen on the static testing machine. Fig. 3 a shows the found clusters and Fig. 3 b the relative occurrence of those clusters over the experiment. Cluster 2 and 3 with the lower peak frequencies are active from a very early stage of the tensile test. Cluster 0 and 1, located at higher peak frequencies, start to grow later when approximately 40 % of the failure load is reached. All clusters show exponential growth. It has to be noted that data points marked as "not assigned" represent hits that could not be associated with a certain cluster by this specific algorithm with the selected parameters.
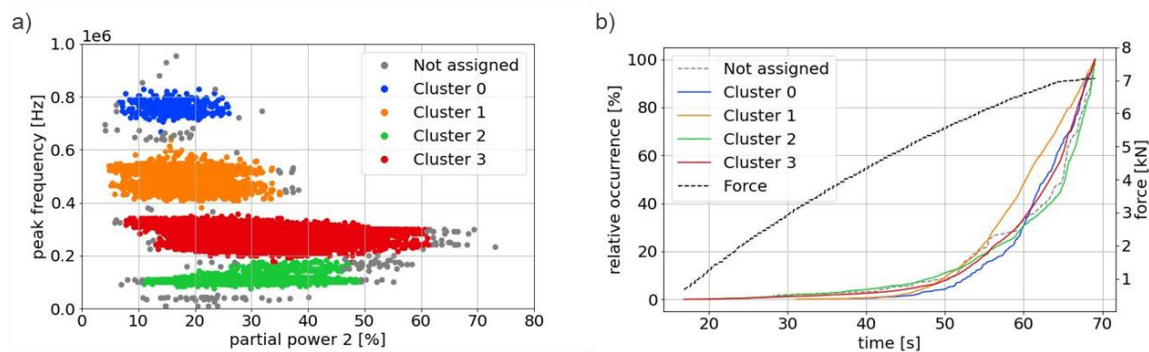
Fig. 3: Result of clustering of AE data acquired during quasi-static tensile loading of a ±45° CFRP specimen on the static testing machine with HDBSCAN a) Found clusters in the selected feature space b) Relative size of the found clusters over the experiment.

Cumulative AE hits detected during tensile loading of a representative specimen on the servo-hydraulic testing machine are clearly dominated by noise, which explains the linear increase of cumulative AE hits. Sensor 2 was located at the side of the specimen closer to the moving piston. The smaller number of AE hits detected at this sensor, is explained by the long duration of the detected signals, blocking triggering of new hits.

Fig. 4 shows the AE signal amplitude over duration plots during tensile loading of a specimen on the static and servo-hydraulic testing machine for each sensor. During loading on the static testing machine, signal duration was below 500 µs for most signals at both sensors and only a few signals exceeded this duration. At sensor 2 during tensile loading on the servo-hydraulic testing machine signal duration for most signals amounts to 100,000 µs, which is the maximum allowable duration specified for a single hit. Signals originating from the servo-hydraulic drive need to travel a longer way through the specimen to reach sensor 1 and therefore suffer more from attenuation compared to signals recorded at sensor 2. Hence, they are of shorter duration on the one hand and of lower amplitude on the other hand. The AE signal amplitude distribution depicted in Fig. 2 implies, that the average amplitude level is around 55 dB_{AE} at sensor 2 and between 40 and 50 dB_{AE} at sensor 1.

Analysis of the frequencies of the detected signals leads to the conclusion that the servo-hydraulic testing machine generates noise signals with dominating frequencies of 50 and 100 kHz. This can clearly be observed from the peak frequency over time plot (see Fig. 2 c), where data points extend over the whole experiment at these two frequency levels. There are only a few signals with higher frequencies dominating.
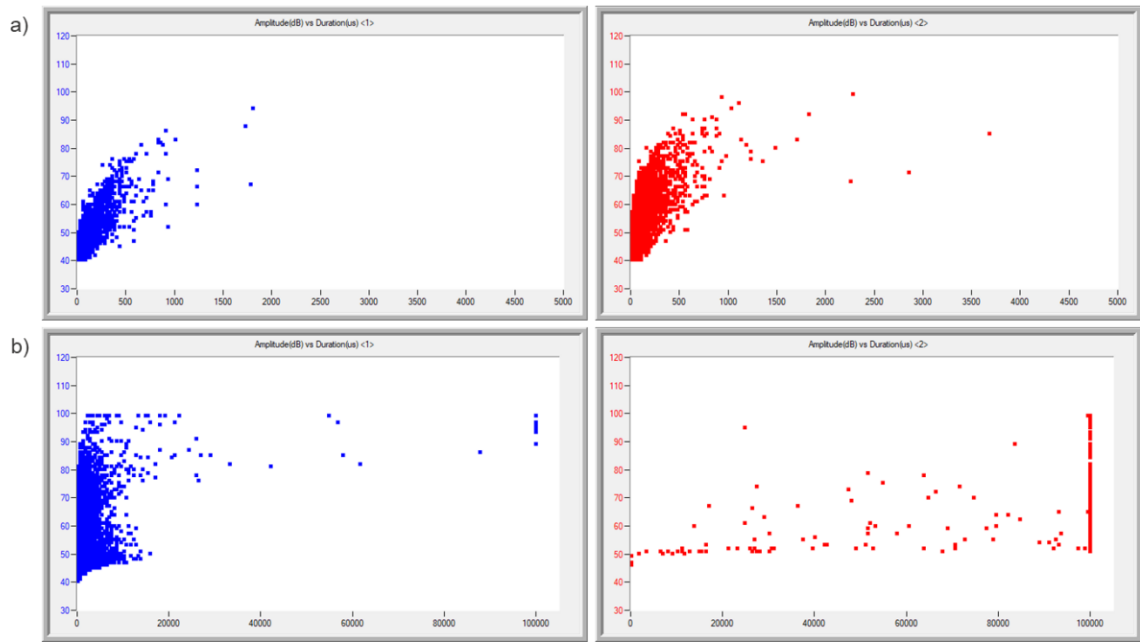
Fig. 4: AE signal amplitude over duration acquired during tensile loading of a ±45 ° CFRP specimen on a) the static and b) the servo-hydraulic testing machine (sensor 1 in blue, sensor 2 in red).

The problem with noise disturbing AE signal recording during testing observed at the servo-hydraulic testing machine clearly stands out by having a closer look at the detected waveforms. In Fig. 5 on the left side a typical waveform originating from a damage event is depicted. It was recorded during tensile testing on the static testing machine. After not exceeding the threshold for 100 µs (HDT) the waveform ends. On the right side a typical waveform detected during loading the specimen on the servo-hydraulic testing machine can be seen. There is mainly noise overlapped by five transients that are collected in one hit. The system does not "recognize" and resolve these transients because the threshold is triggered by noise at short time intervals.
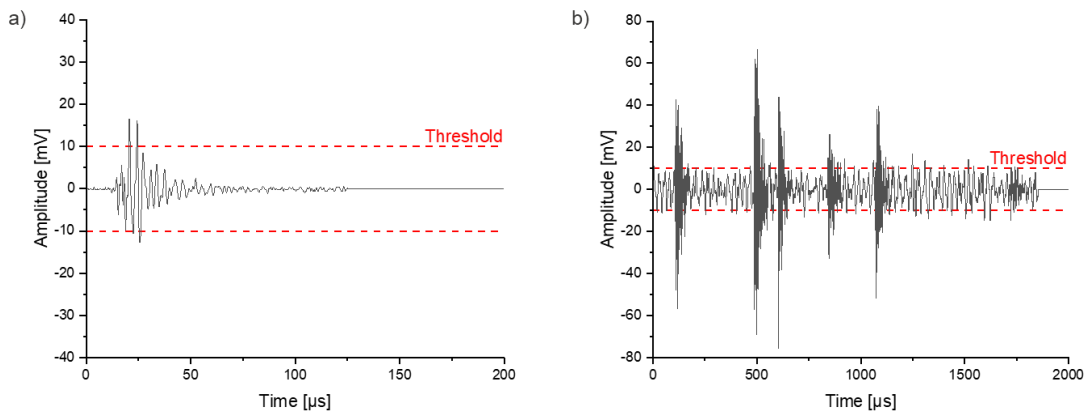

Fig. 5: Representative AE waveform acquired during tensile loading of a ±45° CFRP specimen on a) the static and b) the servo-hydraulic testing machine.

3.2 Elimination of noise

In terms of noise, one would obviously prefer the static or electro-dynamic testing machine. Nevertheless, in the following section, measures to reduce noise of the servo-hydraulic machine and their effects on detected AE parameters are discussed, since for fatigue testing this type of machine is more widely used.

In order to discriminate transient signals from noise the simplest approach is to increase the threshold level. In case of the test setup of the hydraulic testing machine, threshold would have to be set to 55 dB_{AE}. Obviously signals with a low intensity get lost in doing so.

Based on the outcome of frequency analysis, the application of a high-pass filter constitutes a further option. Since there are damage signals detected at the static and electro-dynamic machines within the same frequency ranges as the noise of the servo-hydraulic machine the application of a suitable high-pass filter will eliminate these low-frequency signals as well.

To show the effects of these two considerations, the aquired AE data was evaluated again with a threshold of 55 dB and a high-pass filter of 150 kHz. Results are presented in Fig. 6. Due to the stated problem that often more than one transient signal is contained in a hit (see Fig. 5), some signals get lost, since only one transient signal can be evaluated per hit. For that reason, the number of remaining signals is reduced, especially at sensor 2. If these considerations already are implemented during the process of acquisition, obviously each transient signal is detected separately. Regardless, the effects can be shown and are as expected. The originally linear increase of cumulative hits now shows the typical exponential increase for both evaluations, which reflects the elimination of noise.
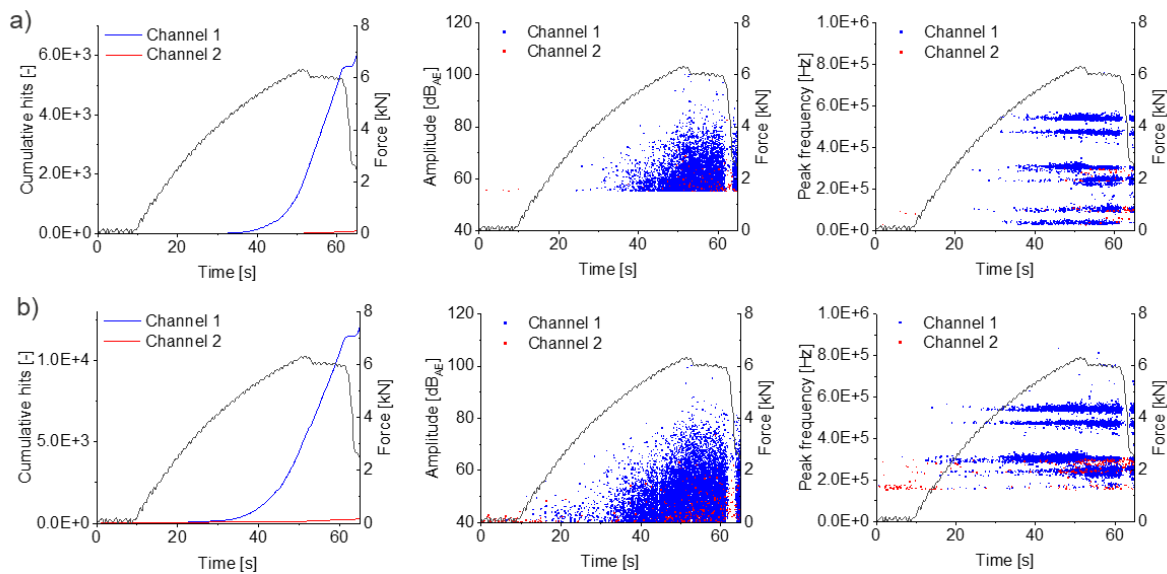
Fig. 6: Cumulative AE hits, AE signal amplitude and peak frequency acquired during tensile loading of a ±45° CFRP specimen on the servo-hydraulic testing machine a) evaluated with a threshold of 55 dB_{AE} b) evaluated with a high-pass filter of 150 kHz.

In order to preserve low-frequency and low-intensity damage signals, noise from the machine needs to be attenuated before reaching the specimen. This could be achieved by incorporating a damping element acting as a high-pass filter between the source of noise and the specimen. An easily accessible position would be the clamping jaws. Noise could be eliminated by attaching a damping material between grips and specimen. However, care must be taken that required axial loads or displacements can be introduced to the specimen properly without significant shear deformation of the damping elements or slipping of the specimen.

A common method to exclusively acquire data originating from a certain section of the specimen, that also needs to mentioned in this context, is the application of a Δt-filter. The difference in arrival time of an AE event at the sensors is used to sort out unwanted signals from outside the

region of interest [2]. For the above described example Δt-filtering is not applicable, since the unwanted signals in this case are continuously present. Transient signals originating from damage inside the specimen only occur as random overlaps and their time of arrival is not known by the system.

4. Conclusions

AE measurements during quasi-static tensile loading of ±45° CFRP specimens on a static, an electro-dynamic and a servo-hydraulic testing machine were performed to investigate the influence of machine noise on AE data acquisition. Detected AE signals during loading on the static and electro-dynamic machines had the typical shape of bursts originating from damage events. Signals detected during loading on the servo-hydraulic testing machine were dominated by noise. Burst signals could not be separated from the continuous noise signal with the selected settings for AE data acquisition. Threshold would have to be increased from the originally selected 40 dB$_{AE}$ to 55 dB$_{AE}$, having the effect of losing hits with low amplitude. The application of a high-pass filter to eliminate noise on the other hand would filter low-frequency burst signals originating from damage appearing in the same frequency range (< 150 kHz), which were observed during experiments on the static and electro-dynamic testing machines.

One approach discussed to eliminate noise without losing desired signals is the integration of a suitable damping element between the source of noise and the specimen, e.g. directly between clamping jaws and specimen.

5. References

[1] Stinchcomb, W.W., Bakis, C.E. (1991). Fatigue behavior of composite laminates: Chapter 4. Reifsnider K.L. (Ed.), Fatigue of composite materials. Elsevier, Amsterdam, New York, p. 105-178.

[2] Sause, M.G.R. (2016). Acoustic Emission: Chapter 4. Sause, M.G.R. (Ed.), In Situ Monitoring of Fiber-Reinforced Composites: Theory, Basic Concepts, Methods, and Applications. Springer International Publishing AG, Cham, p. 131-349, doi:10.1007/978-3-319-30954-5.

[3] Sause, M.G.R., Brunner, A.J. (2022). AE in Polymeric Composites. Grosse, C.U., Ohtsu, M., Aggelis, D.G., Shiotani, T (Eds.), Acoustic Emission Testing: Basics for Research – Applications in Engineering. Springer International Publishing AG, Cham, p. 621-661, doi:10.1007/978-3-030-67936-1.

[4] Brunner A.J (2018). Fiber-reinforced polymer composites test specimen design for selected damage mechanisms. Construction and Building Materials, vol. 173, p. 629-637, doi:10.1177/1464420718800347.

[5] Krummenacker, J., Hausmann, J. (2021). Determination of Fatigue Damage Initiation in Short Fiber-Reinforced Thermoplastic through Acoustic Emission Analysis. Journal of Composites Science, vol. 5, no. 221, doi: 10.3390/jcs5080221.

[6] Jüngert, A., Dugan, S., Udoh, A (2016). Acoustic emission testing under difficult conditions. Conference proceedings, The 32nd European Conference on Acoustic Emission Testing, 7-9 September, Prague, Czech Republic, p. 239-246.

[7] https://hdbscan.readthedocs.io/en/latest/how_hdbscan_works.html (last visited: 10.06.2022).

[8] Campello, R.J.G.B., Moulavi, D., Sander, J. (2013). Density-Based Clustering Based on Hierarchical Density Estimates. Pei, J., Tseng, V.S., Cao, L., Motoda, H., Xu, G. (Eds.), Advances in Knowledge Discovery and Data Mining. PAKDD 2013. Lecture Notes in Computer Science, vol 7819. Springer, Berlin, Heidelberg, p. 160-172, doi:10.1007/978-3-642-37456-2_14.

DEVELOPMENT OF NOVEL ACOUSTIC EMISSION SOURCE LOCATION METHOD UTILIZING WAVELET TRANSFORM AND AKAIKE INFORMATION CRITERION

Yoshito Suzuki[1] and Takuma Matsuo[2]

[1]Graduate School of Science and Technology, Meiji University; ce212051@meiji.ac.jp
[2]School of Science and Technology, Meiji University; matsuo@meiji.ac.jp

ABSTRACT

The acoustic emission (AE) method enables real-time monitoring of damage initiation and progression. Recently, AE analysis using machine learning has become widely popular; however, the AE source location is often located manually to ensure reliability and accuracy. It is desirable to ensure the AE source location is fully automated with high accuracy when used for machine learning and other applications, or in a situation that generates huge amounts of AE signals. This study proposes a novel AE source location method that can accurately and automatically locate AE sources. First, a wavelet transform was applied to an AE signal to extract the wavelet coefficient of a specific frequency. Then, the Akaike information criterion is applied to the time transient of wavelet coefficient to identify the initial wave arrival time. The localized AE source accuracy of the method is compared with a conventional method. The result of the verification, comparing source location error is nearly same with manual initial detection and the developed method. In addition, about 30 times faster than the conventional visual method. Thus, the developed method is an excellent AE source location method in terms of both accuracy and speed of analysis.

Keywords: Acoustic emission, source location, wavelet transform, Akaike information criterion.

1. Introduction

The acoustic emission method is a nondestructive testing technique to detect the initiation and propagation of damage in real time. The source location method is one of the methods for analyzing AE signals, which uses multiple sensors to identify the location of the AE source depending on the difference in the arrival times of the signals detected by the sensors. This analysis method enables real-time monitoring of AE signal initiation and propagation locations.. Furthermore, it is possible to correctly locate the AE sources by manually determining the initial wave arrival time of each AE waveform. However, considering it is difficult to manually check waveforms, an automatic analysis method is required in an environment that generates huge amounts of AE signals. Additionally, in recent years, AE analysis using machine learning has become popular; however, it requires full automation. Since then, several methods have been developed to automatically determine the arrival time of AE signals.
There are several ways to locate the AE source location, such as using the Akaike information criterion (AIC) [1-3], wavelet transforms [4, 5], mode or frequency wave speed differences [6-8],

machine learning [9, 10], etc. [11-13]. AIC is used in various fields to identify the initial arrival time of waveforms [14-16] and the initial arrival time of AE signals [17]. However, for small AE signal waveforms, the initial wave part is hidden in noise, owing to which the rise time cannot be measured correctly [18]. The time-frequency information of AE is essential [19-22] for both metals and composite materials [23]. However, when the wavelet transform is used, the wavelet coefficient peak is often used as a reference; however, errors are likely to occur due to reflected waves for objects with complex shapes. Additionally, methods such as machine learning require a learning process and parameter settings when used in different situations [10].

Furthermore, there are methods that can be used with anisotropic materials such as composites [24-30], although they are limited compared to isotropic materials. Many methods for calculating the source location in anisotropic materials use frequency whose propagation velocity does not depend significantly on the angle of AE source and sensor location. However, the frequency of use is limited considering the available frequency based on the situation.

This study proposes a novel AE source location method with high accuracy that functions automatically under various conditions by using AIC and wavelet transform. The proposed method was first used to evaluate the calculated location accuracy by using an artificial AE source. The accuracy of the developed method was then compared to the conventional method.

2. Experimental method for AE source location accuracy using an artificial AE source and the developed method

2.1 Experimental setup

Fig. 1 shows the experimental setup. Four AE sensors were placed in the center of a 2 mm thick aluminum plate (A1100P, L × W = 1000 × 400 mm) in a 300 × 300 mm area. Artificial sources (Hsu-Nielsen Source) were excited at 50 mm intervals between the sensors. Artificial AE signals were excited five times at each source position and selected two AE signals at random for verification. Three types of resonant AE sensors (PAC: PICO, R15α, and R50α) were used, as shown in Table 1. Herein, we evaluated the accuracy of different positioning methods and the differences in the accuracy of the sensors used.
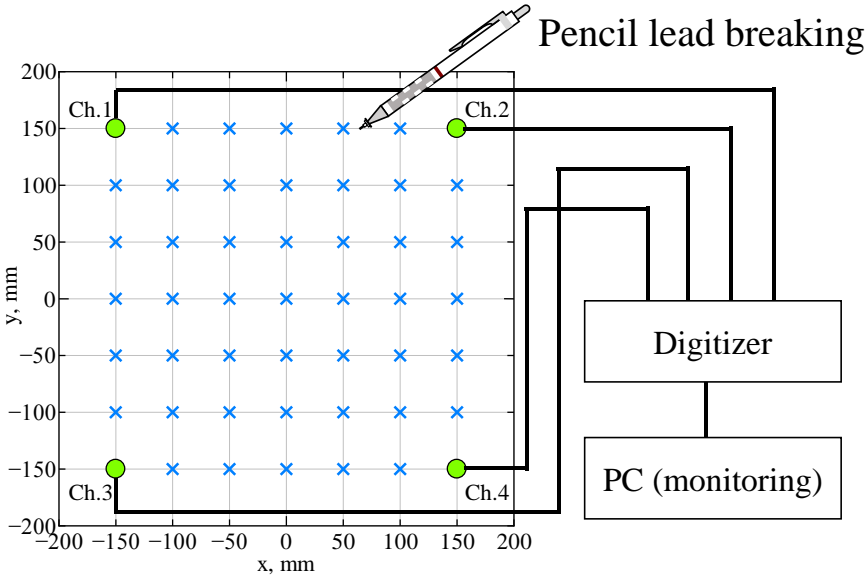

Fig. 1: Experimental setup for comparing the source location accuracy produced
by pencil lead breaking.

Table. 1: Resonant frequency and size of sensors.

MODEL	*RESONANCE FREQUENCY [KHZ]*	*CONTACT AREA (RADIUS [MM])*
PAC, PICO	450	2.4
PAC, R50α	500	8.7
PAC, R15α	150	8.7

2.2 Developed Algorithm for AE source location

Fig. 2 shows the algorithm of the proposed source location method. As an example for describing the method below, we used the pencil lead breaking AE input at (x, y) = (-50.0,50.0) with the PICO sensor locating at channel 1. First, the measured AE waveform (Fig. 2(a)) was wavelet transformed to create a wavelet contour map (Fig. 2(b)). Then, the time transient of the wavelet coefficients at a specific frequency was extracted (Fig. 2(c)). We extracted the resonance frequency of the PICO sensor, i.e., 450 kHz. Lastly, AIC was applied to automatically read the arrival time of the initial wave for the time transient of wavelet coefficient (Fig. 2(d)).
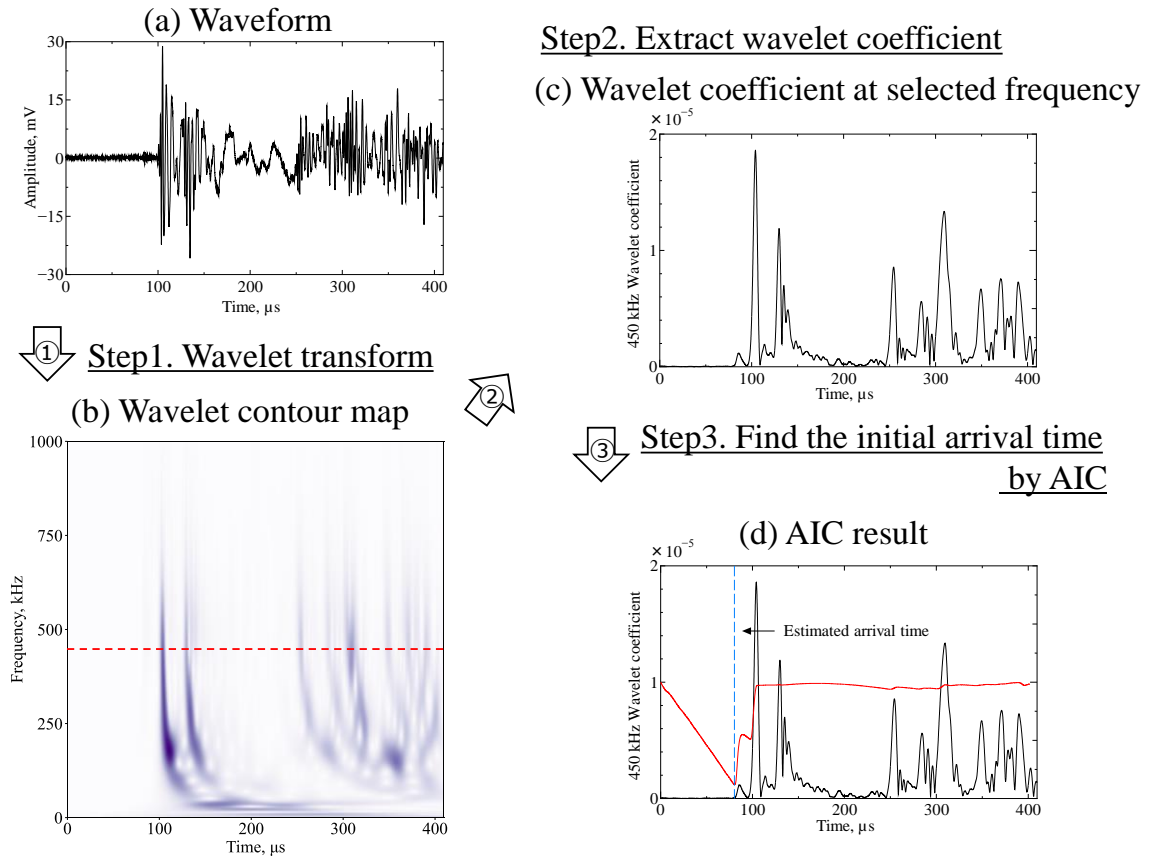

Fig. 2: Process of the proposed source location method.

The evaluation of AIC was defined by the following relation, which applies the maximum likelihood method to adjust the parameters to maximize the likelihood for the observed data [31]:

$$AIC = (-2)log(maximum\ likelihood) + 2(number\ of\ adjusted\ parameters) \quad (1)$$

Based on this equation, the formula was refined to identify discontinuities in the data, expressed as given below. AIC_k at the point $i = k$ with amplitude value $X_i (i = 1,2, \dots, N)$ was calculated for a single AE waveform recorded with N number of samples, given as [32]:

$$AIC_k = k \cdot \log\{var(X[1,k])\} + (N - k) \cdot \log\{var(X[k, N])\} \tag{2}$$

where $var(X[1,k])$ and $var(X[k, N])$ are the variance of amplitude value from X_1 to X_k and X_k to X_N, respectively. Finally, the k of AIC_k minimum value indicate arrival time of the AE signal. As shown in Fig. 2(d), the arrival time of the initial wave was calculated as 80.25 μs. Then, the arrival times at all sensors were obtained. Finally, the calculated arrival times were used to calculate the AE source location using the virtual sound source scanning method. Calculations were performed with a resolution of 0.1 mm within the range of the sensor. Fig. 3 shows an existing method that compares the accuracy of developed method with that of the manual identification of the arrival time of the initial wave [33].
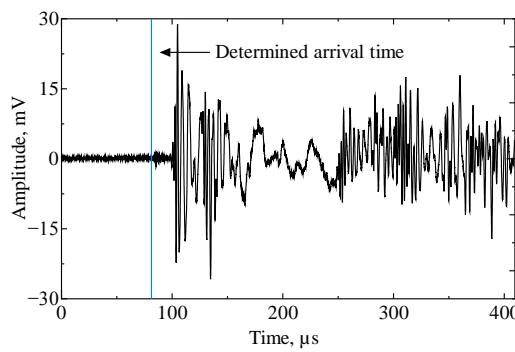

Fig. 3: Initial arrival time determination by manual identification.

3. Result and discussion

3.1 Evaluation of AE source location accuracy with conventional methods

Fig. 4 compares the results of the proposed method and conventional methods for AE source location. The left side of the figure demonstrates the results by using the PICO sensor, whereas the right side of the figure shows the error distribution of the results. On comparing the results, it was found that the result by proposed method was as same accuracy as the visually read the initial wave.

Fig. 5 shows one of the results input at (-50,100). Fig. 6 shows the identified time of the ch.4 considering ch.4 has the long-distance in the four channels at this point. The manual method (Fig. 6(a)) presumably identified the initial arrival time correctly. The developed method (Fig. 6(b)) also estimated initial arrival time correctly. The manual identification must be perfectly correct. However, the actual located source location is shifted on the opposite side of the ch.4. This is because distance between AE source and sensor of ch.1 and ch.4 is large difference. Difference of propagation distance is affected by wave attenuation, which led the small source location error by manual method. This verifies the efficiency of the proposed in situations having a long-distance between the source and sensor locations.

Fig. 7 shows the average of the source location accuracy for each sensor and the percentage of AE signals that were correctly identified for all the methods. The percentage of "correctly identified" is a targeting error of 19 mm or more equivalent to the largest sensor diameter.

Although, the developed method is not fully located correctly, correctly identified rate is almost 100 %. Comparing source location error is nearly same with manual initial detection and the developed method. Therefor, the developed method source location accuracy is enough.

Next, compares the analysis time for each method. The method of reading manually depends on the skill of the engineer. In this case, the data was obtained by an engineer with about two years of AE analysis experience. The manual method needs about 15 s per 1 signal to identify the arrival time. On the other hand, the developed method only needs about 0.5 s per 1 signal. This is about 30 times faster and does not depend on the AE analyzing skill of the operator's experience. To sum up, the developed method is an excellent AE source location method in terms of both accuracy and speed of analysis.

(a) Initial wave arrival time
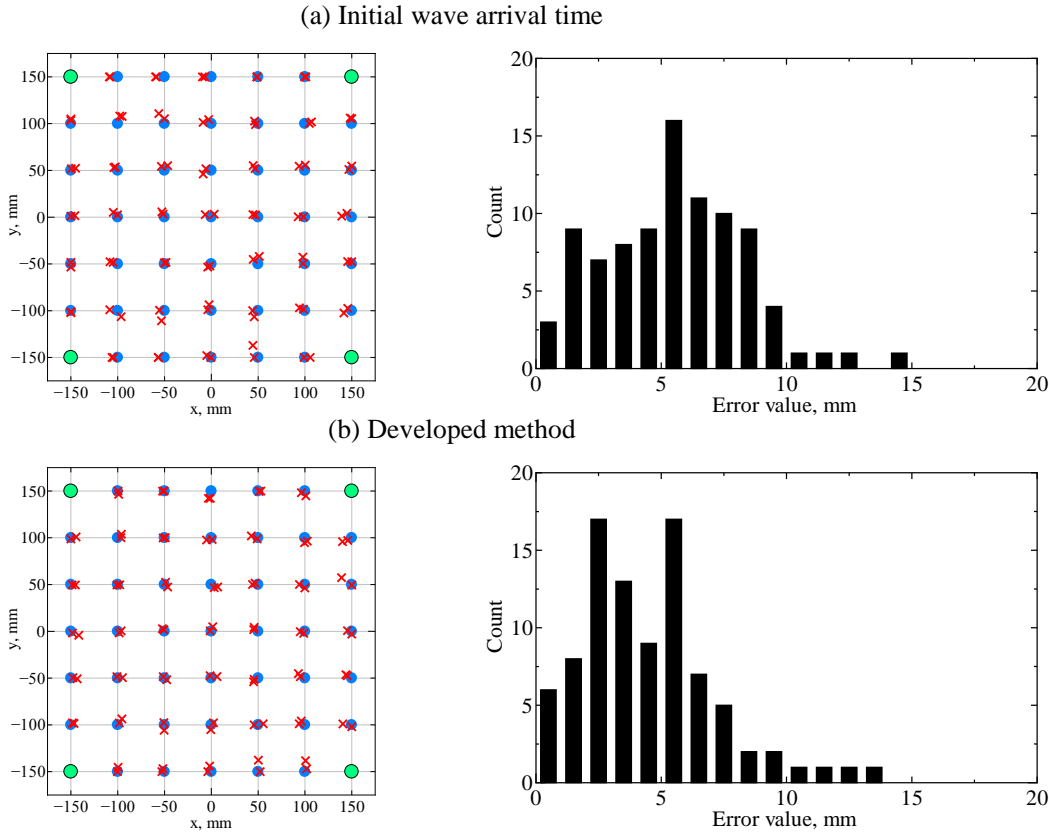
(b) Developed method

Fig. 4: Source location result by the conventional method and the proposed method (left), and the distribution of the source location error (right).
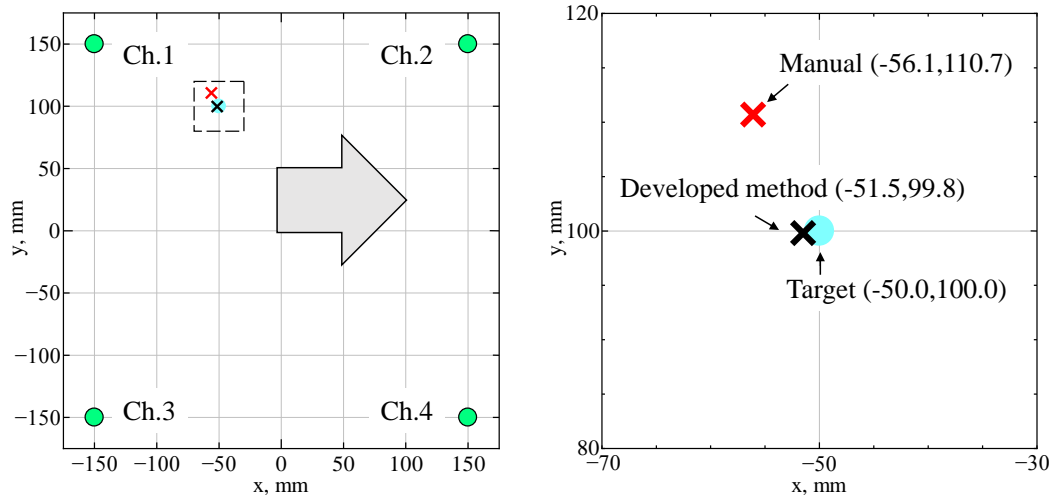
Fig. 5: Comparison of the source location error at (-50,100) detected by the PICO sensor.

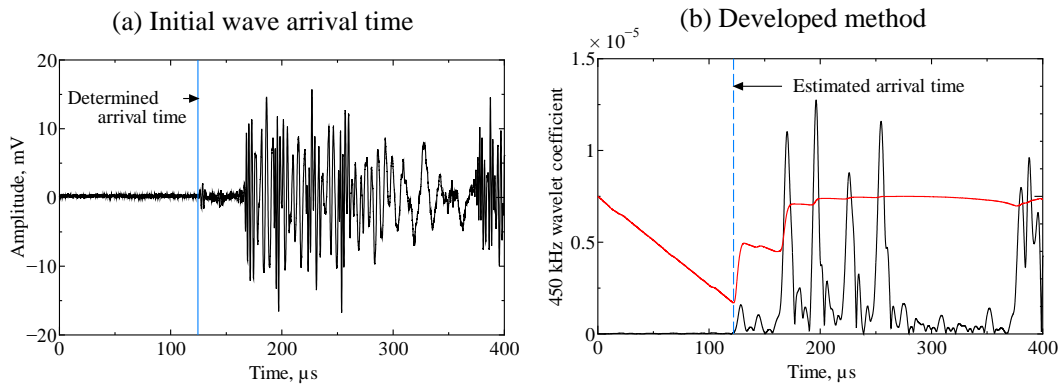(a) Initial wave arrival time (b) Developed method

Fig. 6: Comparison of the initial wave detection detected by Ch.4 of the PICO sensor at (-50,100).
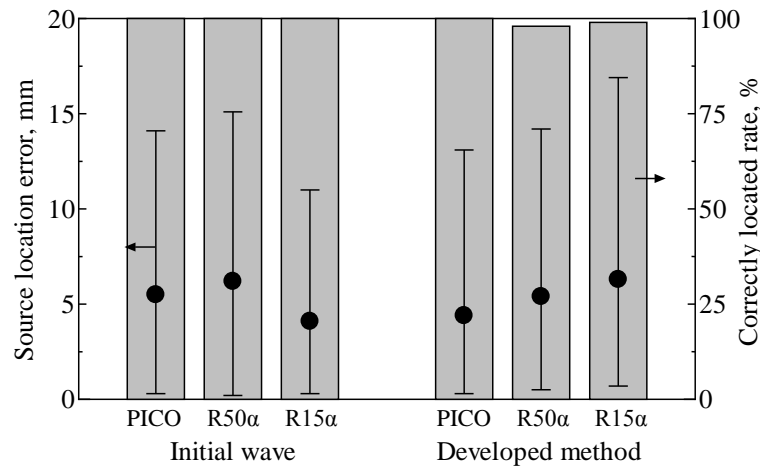
Fig. 7: Comparison of the source location error and the correct rate.

Next, we compared each sensor's source location average error. Higher frequency sensors which is PICO and R50α tend to source location average error get lower. This can be attributed to the fact that the slope of the initial wave of the wavelet coefficients in the wavelet transform becomes more gradual as the frequency decreases, making it difficult to identify discontinuities due to AIC. Therefore, when using this new method, AE sensors with resonance frequencies above 200 kHz must be used for accurate targeting or selecting the second resonance frequency above that frequency.

In this study, although we did not compare the accuracy of this method with that of machine learning and deep learning methods, we believe this method is very versatile considering it is a simple algorithm.

4. Conclusions

In this study, we proposed a novel method for AE source location with high accuracy that functions automatically by using AIC and wavelet transform. We compared the accuracy of various conventional and the proposed method using artificial AE of pencil lead breaking. Although the proposed method was not highly accurate, it was effective in fully automated localizing of the detected AE signals while considering the accuracy and AE location correctly. Furthermore, we confirmed that the accuracy of AE location detection changes depending on the frequency, and that the resonance frequency of the sensor can be used to achieve high accuracy at a frequency of 200 kHz or higher.

5. References

[1] Pearson, M.R., Eaton, M., Featherston, C., Pullin, R., Holford, K. (2017). Improved acoustic emission source location during fatigue and impact events in metallic and composite structures. Structural Health Monitoring, vol. 16, p. 382-399, doi:10.1177/1475921716672206

[2] Hensman, J., Mills, R., Pierce, S.G., Worden, K., Eaton, M. (2010). Locating acoustic emission sources in complex structures using Gaussian processes. Mechanical Systems and Signal Processing, vol. 24, p. 211-223, doi:10.1016/j.ymssp.2009.05.018

[3] Sedlak, P., Hirose, Y., Khan, S.A., Enoki, M., Sikula, J. (2009). New acoustic localization technique of acoustic emission signals in thin metal plates. Ultrasonics, vol. 49, p. 254-262, doi:10.1016/j.ultras.2008.09.005

[4] Jeong. H., Jang, Y.S. (2000). Fracture Source Location in Thin Plates Using the Wavelet Transform of Dispersive Waves. IEEE Transactions on Ultrasonics, Ferroelectrics, and Frequency Control, vol. 47, p. 612-619, doi:10.1109/58.842048

[5] Jiao, J., He, C., Wu, B., Fei, R., Wang, X. (2006). A new acoustic emission source location technique based on wavelet transform and mode analysis. Frontier of Mechanical Engineering in China, vol. 3, p. 341-345, doi:10.1007/s11465-006-0006-4

[6] Mostafapour, A., Davoodi, S., Ghareaghaji, M. (2014). Acoustic emission source location in plates using wavelet analysis and cross time frequency spectrum. Ultrasonics, vol. 54, p.2055-2062, doi:10.1016/j.ultras.2014.06.022

[7] Baxter, M.G., Pullin, R., Holford, K.M., Evans, S.L. (2007). Delta T source location for acoustic emission. Mechanical Systems and Signal Processing, vol. 21, p. 1512-1520, doi:10.1016/j.ymssp.2006.05.003

[8] Jiao, J., He, C., Wu, B., Fei, R., Wang, X. (2004). Application of wavelet transform on modal acoustic emission source location in thin plates with one sensor. International Journal of Pressure Vessels and Piping, vol. 81, p. 427-431, doi:10.1016/j.ijvp.2004.03.009

[9] Cheng, L., Xin, H., Groves, R.M., Veljkovic, M. (2021). Acoustic emission source location using Lamb wave propagation simulation and artificial neural network for I-shaped steel girder. Construction and Building Materials, vol. 273, p. 1-17, doi:10.1016/j.conbuildmat.2020.121706

[10] Pillai, M.A., Ghosh, A., Joy, J., Kamal, S., Chandran, S., Balakrishnan, A.A., Supriya, M.H. (2019). Acoustic Source Localization using Random Forest Regressor. 2019 International Symposium on Ocean Technology, p. 191-199, doi:10.1109/SYMPOL48207.2019.9005303

[11] Zárate, B.A., Pollock, A., Momeni, S., Ley, O. (2015). Structural health monitoring of liquid-filled tanks: a Bayesian approach for location of acoustic emission sources. Smart Materials and Structures, vol. 24, p. 1-10, doi:10.1088/0964-1726/24/1/015017

[12] Ebrahimkhanlou, A., Salamone, S. (2017). Acoustic emission source localization in thin metallic plates: a single-sensor approach based on multimodal edges reflections. Ultrasonics, vol. 78, p. 134-145, doi:10.1016/j.ultras.2017.03.006

[13] Ebrahimkhanlou, A. Salamone, S. (2018). Single-Sensor Acoustic Emission Source Localization in Plate-Like Structures Using Deep Learning. Aerospace, vol. 5, no. 50, doi:10.3390/aerospace5020050

[14] Maeda, N. (1985). A Method for Reading and Checking Phase Time in Auto-Processing System of Seismic Wave Data. Zisin (Journal of the Seismological Society of Japan. 2nd ser.), vol. 38, p. 365-379, doi:10.4294/zisin1948.38.3_365

[15] Sleeman, R., Eck, T.V. (1999). Robust automatic P-phase picking: an on-kine implementation in the analysis of broadband seismogram recordings. Physics of the Earth and Planetary Interiors, vol. 113, p.265-275, doi:10.1016/S0031-9201(99)00007-2

[16] Zhang, H., Thurber, C., Rowe, C. (2003). Automatic P-Wave Arrival Detection and Picking with Multiscale Wavelet Analysis for Single-Component Recordings. Bulletin of the Seismological Society of America, vol. 93 no. 5, p. 1904-1912, doi:10.1785/0120020241

[17] Kurz, J.H., Grosse, C.U., Reinhardt, H.W. (2005). Strategies for reliable automatic onset time picking of acoustic emission and of ultrasound signals in concrete. Ultrasonics, vol.43, p. 538-546, doi:10.1016/j.ultras.2004.12.005

[18] Aggelis, D.G., Matikas, T.E. (2012). Effect of plate wave dispersion on the acoustic emission parameters in metals. Computers and Structures, vol. 98-99, p. 17-22, doi:10.1016/j.compstruc.2012.01.014

[19] Niethammer, M., Jacobs, L.J., Qu, J., Jarzynski, J. (2000). Time-frequency representation of Lamb waves using the reassigned spectrogram. The Journal of the Acoustical Society of America, vol. 107, p. L19-L24, doi:/10.1121/1.428894

[20] Suzuki, H., Kinjo, T., Hayashi, Y., Takemoto, M., Ono, K. (1996). Wavelet Transform of Acoustic Emission Signals. Journal of Acoustic Emission, vol. 14, no. 2, p. 69-84,

[21] Ding, Y., Reuben, R.L., Steel, J.A. (2004). A new method for waveform analysis for estimating AE wave arrival times using wavelet decomposition. NDT&E International, vol. 37, p. 279-290, doi:10.1016/j.ndteint.2003.10.006

[22] Ambrozinski, L., Stepinski, T., Packo, P. Uhl, T. (2012). Self-focusing Lamb waves based on the decomposition of the time-reversal operator using time-frequency representation. Mechanical Systems and Signal Processing, vol. 27, p. 337-349, doi:10.1016/j.ymssp.2011.09.019

[23] Jeong, H. (2001). Analysis of plate wave propagation in anisotropic laminates using a wavelet transform. NDT&E International, vol. 34, p. 185-190, doi:10.1016/S0963-8695(00)00056-6

[24] Mizutani, Y., Miki, T., Todoroki, A., Suzuki, Y. (2016). Manual Lamb Wave Tomography Utilizing AE Technique. 32nd European Conference on Acoustic Emission Testing, p. 333-341

[25] Koabaz, M., Hajzargarbashi, T., Kundu, T., Deschamps, M. (2011). Locating the acoustic source in an anisotropic plate. Structural Health Monitoring, vol. 11, no. 3, p. 315-323, doi:10.1177/1475921711419991

[26] Kundu, T., Nakatani, H., Takeda, N. (2012). Acoustic source localization in anisotropic plates. Ultrasonics, vol. 52, p. 740-746, doi:10.1016/j.ultras.2012.01.017

[27] Jones, M.R., Rogers, T.J., Worden, K., Gross, E.J. (2022). A Bayesian Methodology for Localising Acoustic Emission Sources in Complex Structures. Mechanical Systems and Signal Processing, vol. 163, p. 1-14, doi:10.1016/j.ymssp.2021.108143

[28] Toyama, N., Koo, J.H., Oishi, R., Enoki, M., Kishi, T. (2001). Two-dimensional AE source location with two sensors in thin CFRP plates. Journal of Materials Science Letters, vol. 20, p.1823-1825, doi:10.1023/A:1012507821711

[29] Yamada, H., Mizutani, Y., Nishino, H., Takemoto, M., Ono, K. (2000). Lamb wave source location of impact on anisotropic plate. Journal of acoustic emission, p. 51-60

[30] Jeong, H., Jang, Y.S. (2000). Wavelet analysis of plate wave propagation in composite laminates. Composite Structures, vol. 49, p. 443-450, doi:10.1016/S0263-8223(00)00079-9

[31] Akaike, H. (1985). Prediction and Entropy: Chapter 1. Parzen, E., Tanabe, K., Kitagawa, G. (Eds.), Selected Papers of Hirotugu Akaike. Springer Series in Statistics. Springer, New York, NY. p. 387-410, doi:10.1007/978-1-4612-1694-0_30

[32] Ohno, K., Shimozono, S., Sawada, Y., Ohtsu, M. (2008). Automatic Detection of AE First Motion Based on AIC Picker for SiGMA Analysis. Journal of the Japanese Society for Non-destructive Inspection, vol. 57, no. 11, p. 531-536, doi:10.11396/jjsndi.57.531.

[33] Mizutani, Y., Inaba, H., Nakamura, H., Enoki, M., Ohtsu, M., Shigeishi, M., Yuyama, S., Sugimoto, S., Shiotani, T. (2016). Practical Acoustic Emission Testing. Springer Tokyo, doi:10.1007/978-4-431-55072-3

ACOUSTIC EMISSION CLASSIFICATION BY CROSS-CORRELATION

Théotime de la Selle[1], Stéphanie Deschanel[1] and Jérome Weiss[2]

[1]Univ Lyon, INSA-Lyon, MATEIS UMR CNRS 5510, F69621 Villeurbanne;
Theotime.de-la-selle@insa-lyon.fr, stephanie.deschanel@insa-lyon.fr
[2]ISTerre, CNRS and Université Grenoble-Alpes, CS 40700, 38053, Grenoble, France;
jerome.weiss@univ-grenoble-alpes.fr

ABSTRACT

Acoustic emission signals specific to the incremental advance of fatigue cracks can be detected, cycle after cycle, during crack propagation tests. They were termed acoustic multiplets in reference to repeating earthquakes. Detecting such multiplets would give information about the fracturing process and provide early warnings when monitoring industrial parts in service. We developed a clustering method to extract multiplets signals from all signals and noise of fatigue tests. This method is based on the computation of the cross-correlation function between waveforms. On the distribution of the cross-correlation matrix, signals belonging to multiplets are clearly identified and permit to automatically clustered. This paper develops the steps of the method, presents results obtained on a dataset of a fatigue test and shows its noise robustness.

Keywords: Acoustic emission, fatigue crack growth, multiplets, cross-correlation, waveform clustering.

1. Introduction

Despite many efforts over the last hundred years to understand its causes and detect its possible precursors, cyclic fatigue of materials remains one of the major causes of failure of industrial parts [1]. The problem is "How to alert in real time when a crack is likely to lead to the ruin of the part?". Acoustic emission (AE) is a key method of non-destructive testing, as it enables the recording of transient elastic waves occurring during damage of materials and structures. Numerous works carried out with this method have shown that there is a correlation between the global acoustic activity and damage, including during fatigue [2]. However, this correlation only becomes significant near the final failure and thus far too late [3]. Indeed, the monitoring of slow crack growth from a global measurement is difficult and very sensitive to the signal to noise ratio (SNR). Moreover, the non-specific nature of these AE measurements makes the identification of sources difficult [4].

A new approach, recently proposed [4, 5], allows the detection of acoustic emissions specific of fatigue crack growth, called "acoustic multiplets" in reference to the analogous phenomenon in seismology [6]. These so-called acoustic multiplets are characterized by highly correlated waveforms (Fig. 1a), signature of a unique source. They are repeatedly triggered over many successive loading cycles at almost the same stress level (Fig. 1c-e) and originate from a single location (Fig. 1a). They are considered to mark the slow, incremental propagation of a crack at each cycle (see striations on Fig. 1b), or the rubbing along its faces (fretting). Being specific to

incremental fatigue cracking, they can therefore potentially be used as early warnings of global failure of industrial parts [5].
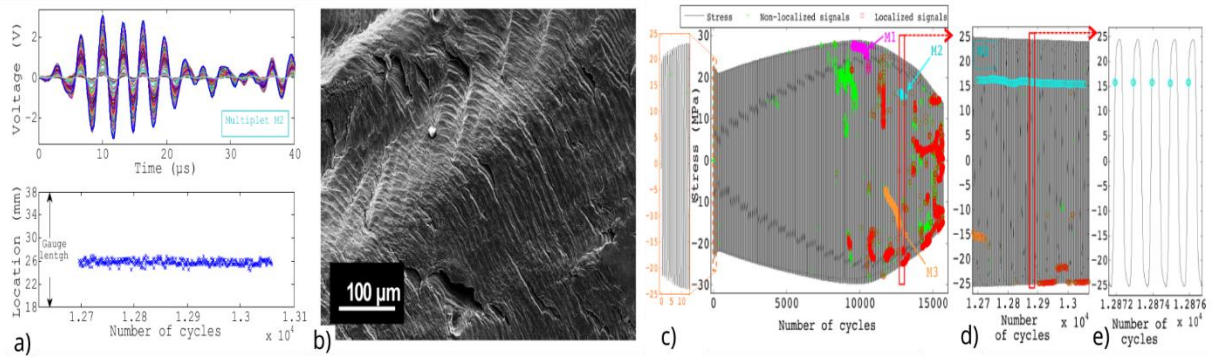

Fig. 1: Acoustic multiplets as a signature of fatigue crack growth (from [4]) - a) Waveforms of acoustic signal belonging to a multiplet during fatigue of Aluminum at 0.1 Hz, and locations of the corresponding AE signals on the specimen; b) Striations on a post-mortem SEM image of the crack face of the sample; c) Acoustic activity during a fatigue test on aluminum: stress vs number of cycles. Magenta, cyan and orange clusters correspond to typical examples of multiplets; d) Enlargement on a specific multiplet and e) on some loading cycles.

A key point in this approach is the choice of an appropriate and robust measure of waveforms similarity. Due to the classical procedure to detect acoustic bursts from threshold crossing and the noise that affect the signal, nearly identical signals can be shifted by a little time delay and are then non-aligned. It means that the method of measure needs to be able to quantify the similarity between 2 waveforms regardless of the delay.

The cross-correlation function is often chosen for this kind of problematic [7-9]. In the field of acoustic emission, the cross-correlation function has been sometimes used to improve the localisation of acoustic sources [9]. A cross-correlation matrix over all the AE signals signals of a channel recorded during a mechanical test on concrete has been used to investigate very quickly changes in the physical properties of the ray path of events from one cluster [8]. Another application of the cross-correlation matrix has been proposed to filter noise in fatigue test [10].

This article offers a robust way based on cross-correlation matrix distribution to extract highly correlated populations of signals, in order to identify multiplets in fatigue crack growth tests.

2. Method to extract highly correlated populations

2.1 Cross-correlation function

Cross-correlation consists in the displaced dot product between two signals. It is often used to quantify the degree of similarity or interdependence between two signals [7]. In the case of AE, since all measurements were recorded using digital acquisition systems, signals have been discretized, so that the cross-correlation between two signals v and w with the same N samples length is expressed by equation 1.

$$corr[v, w](t) = \sum_{n=n_0}^{N} v(n) \cdot w(t + n) \tag{1}$$

When the discrete time series v and w match, the value of $corr[v,w]$ is maximized. We called the maximizing point t_m : it corresponds to the time delay between the two waveforms. This is explained when peaks (positive areas) are aligned, making a large contribution to the summation.

In the case of AE waveforms, the two parameters n_0 and N define a cross-correlation window. Because acoustic waveforms are transient waves and contain a pre-trigger, an impulsive part and a coda, the choice of this window has to be set precisely for an adequate determination of the maximizing point.

2.2 Cross-correlation matrix

By calculating all cross-correlation functions for each pair of waveforms for a single channel, and searching for the maximum of these functions, it is possible to build a cross-correlation matrix. Hence, the coefficients contain a value in [0, 1] corresponding to the normalized measure of similarity by cross-correlation (see equation 2).

$$M_{xy} = max_t(corr[x, y](t)) \tag{2}$$

An example is presented in Fig. 2 showing a cross-correlation matrix of 198 signals compared to each others. By construction, it is a symmetrical matrix with a diagonal full of 1. Then, only half of the matrix is computed.
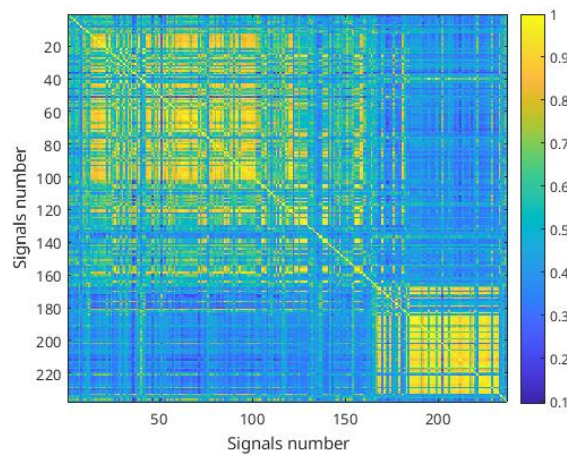

Fig. 2: Example of cross-correlation matrix calculated from a fatigue crack growth test on steel.

Since multiplets are groups of highly similar waveforms emitted close in time, multiplets appear as yellow squares on Fig. 2. In the rest of the article, for the sake of simplicity, the term 'cross-correlation' will refer to the value taken by a coefficient of the cross-correlation matrix as described in equation 2.

2.3 Distribution of cross-correlation

An operator can visually identify groups of waveforms highly similar in the cross-correlation matrix, but an automatized way is possible by calculating the distribution of the matrix. In a fatigue test characterized by acoustic multiplets, two peaks are expected in this distribution (see Fig. 3): one narrow peak close to 1 containing cross-correlations between waveforms belonging to multiplets, and a wider one corresponding to uncorrelated source signals. The remaining correlation of these uncorrelated source signals results from the resonant nature of the AE sensors. Indeed, due to the acquisition chain, and particularly to the frequency domain of the sensor, the cross-correlation between two totally different source signals is larger than zero. Nevertheless, a distribution of cross-correlations computed on a set of data from an experiment without multiplets would not exhibit the peak of large cross-correlations values.
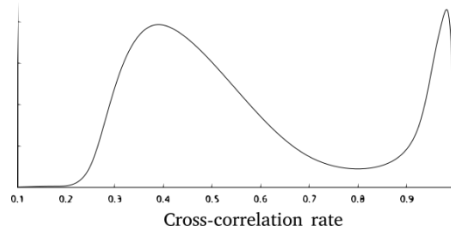
Fig. 3: Schematic cross-correlation distribution for a fatigue test emitting multiplets.

From this distribution, it is easy to extract automatically multiplets by setting a threshold on the cross-correlation , e.g. 0.8 for the schematic figure above. All waveforms implicated in cross-correlations above the threshold are collected and labelled as "multiplets".

3.   Application to a fatigue crack growth test

This method has been applied to several acoustic emission dataset recorded during fatigue crack growth tests. Here, results from a load-imposed fatigue test ($R = \sigma_{min}/\sigma_{max} = 0.1$) performed on compact tension (CT) specimen of 5083 aluminium alloy are presented.
Two nano30 sensors, from PAC, were coupled on the specimen surface as depicted on Fig. 4. The PCI2 system triggered recording waveforms sampled at 5 MHz when the signal exceeds the threshold of 43 dB. After the test, no filtering process was applied. Cross-correlation matrices and distributions were directly computed on the waveforms, independently for the both channels. We selected a part of 1000 consecutive waveforms containing 2 multiplets for this study.
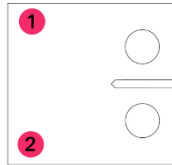
Fig. 4: Geometry of CT specimen and sensors locations.

3.1 Selection of the cross-correlation window
As explained in part 2.1, a proper window has to be set for the cross-correlation between two AE waveforms. In order to select the starting and ending point of time series, respectively n_0 and N, cross-correlation distributions are calculated for different window lengths.
The pre-trigger of 20 µs is not taken into account in the calculation: n_0 is fixed, while N takes values to select [20, 40, 60, 80, 100, 120, 160] µs of the waveforms. Fig. 5 shows an example of a waveform from the dataset and the different windows used for cross-correlations.

Fig. 5: Example of a waveform and the different cross-correlation windows. Each window starts at t = 0 µs.

390

Fig. 6: Distributions of cross-correlation for different windows. Right: Zoom around peak of high cross-correlations.

The overall shape of the expected distribution presented in section 2.3 for all 7 windows can be found in Fig. 6. By extracting signals involved in cross-correlations above 0.8, we clustered, as predicted, multiplets signals into one cluster.
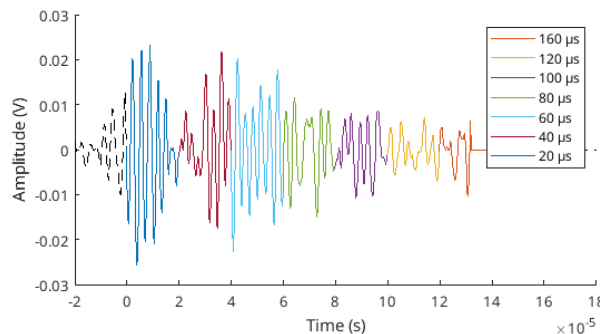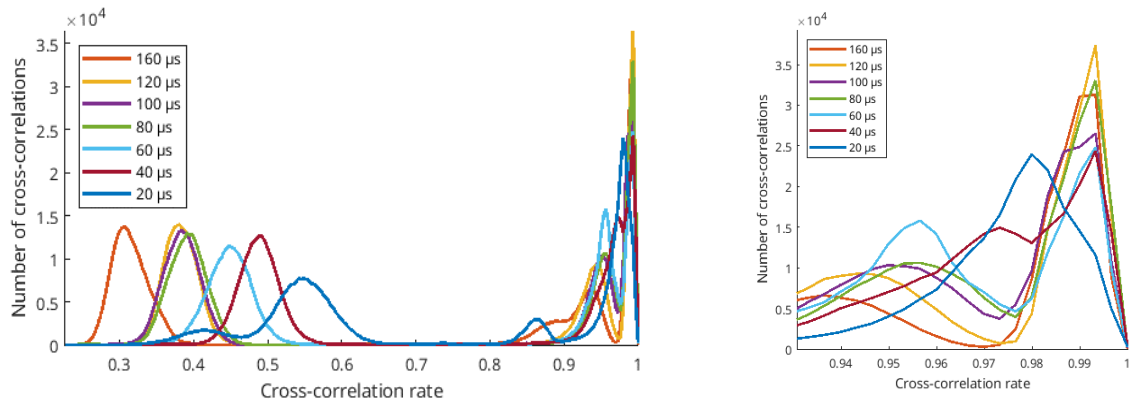
But if the window is to short or too long, some multiplets signals are miss-classified. Extending the length of the cross-correlation window shifts the low cross-correlation peak towards 0 and modifies the large cross-correlation peak level. A cross-correlation performed on too short windows raises the risk to miss the right alignement resulting in an imprecise similarity measure, e.g. distributions computed on windows of 20, 40 and 60 μs whose maximums do not exceed 25 000 cross-correlations.. On the opposite, a too long window contains a large part of the waveforms codas which are less correlated and are characterized by a lower SNR. Hence, the distribution computed on windows of 160 μs has a lower maximum than distributions computed on windows of 80 and 120 μs. That is why the choice of the window is essentially ruled by the level of the large cross-correlation peak : the best clustering performance is obtain by maximizing the number of cross-correlation in the highest cross-correlation peak. Here, the window has to be set between [80,120] μs.

In addition, one observes that all distributions exhibit three peaks. One in low cross-correlation range and two in the large cross-correlation range. The second peak in the large cross-correlation range between 0.92 and 0.97 in Fig. 6, not presented in part 2.3, contains cross-correlations performed between waveforms belonging to different multiplets emitted by the same type of sources. Selecting a threshold between these two close peaks allows to separate different multiplets thanks to an algorithm (not detailed here) by adding information of the signals emission time.

3.2 Noise effect

The noise robustness of our method is evaluated by adding white Gaussian noise to all waveforms. Distributions of cross-correlations are computed for different levels of SNR and are represented on Fig. 7.
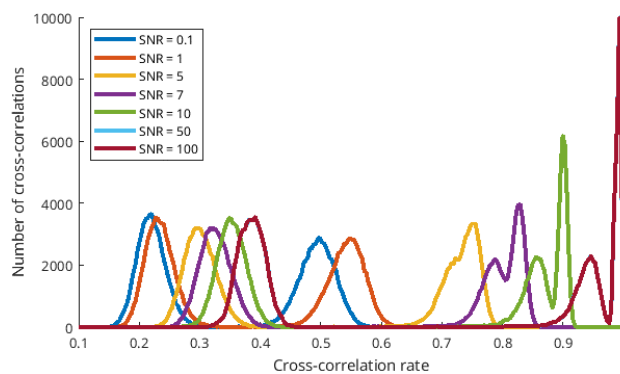

Fig. 7: Cross-correlation distributions for different SNR.

From SNR = 100 to SNR = 0.1, the global shape of the distribution including high and low cross-correlations is preserved and shifted towards lower cross-correlation values, as expected. While the shape of the peak of low cross-correlations remains essentially unchanged, the two peaks of high cross-correlations are widening and merge. The method then is still applicable for low SNR, down to 0.1, by moving the cross-correlation threshold to separate highly similar waveforms, belonging to multiplets, from uncorrelated ones. Nevertheless, below SNR = 1 many errors are reported in the classification and below SNR = 5, it is not possible to distinguish the two peaks of high cross-correlations.

4. Conclusions

This paper presents a method to automatically cluster groups of highly similar signals by computing the distribution of the cross-correlation matrix. This matrix is obtained by extracting the maximum of the cross-correlation function of each pair of waveforms from a fatigue test. The selection of the cross-correlation window is discussed and optimized by applying this method on several window lengths. And we show that this method is efficient to extract mulitplets, acoustic signature of fatigue crack growth, even if waveforms are polluted by noise.

5. References

[1]   Suresh S. (1998). Fatigue of materials, Cambridge University Press.
[2]   Harris, D.O. and Dunegan, H.L.(1974). Continuous monitoring of fatigue-crack growth by acoustic emission techniques, Experimental Mechanics, 14(2), 71-81.
[3]   Berkovits, A. and Fang, D.N. (1995). Study of fatigue-crack characteristics by acoustic emission, Engineering Fracture Mechanics, 51(3), 401-416.
[4]   Deschanel, S. and Weiss, J. (2018), Contrôle de la fatigue des matérieux par émission acoustique, Techniques de l'Ingénieur, 12, IN 226, 1-15.
[5]   S. Deschanel, W. Ben Rhouma, and J. Weiss (2017), Acoustic emission multiplets as early warnings of fatigue failure in metallic materials, Sci Rep, 7(1), 13680.
[6]   Lengliné O., and D. Marsan (2009), Inferring the Coseismic and Postseismic Stress Changes caused by the 2004, M=6 Parkfield Earthquake from Variations of Recurrence Times of Microearthquakes, J. Geophys. Res., 114, B10303.
[7]   Proakis, J.G., Manolakis, D.G. (1996). Digital Signal Processing, 3ed. Prentice Hall.
[8]   H. Kurz J., Finck F., U. Grosse C., Reinhard H. W. (2004). Similarity matrices as a new feature for acoustic emission analysis of concrete. Conference proceedings, The 26th European Conference on Acoustic Emission Testing for Non-Destructive Testing. September 15-17, 2004 - Berlin, p. 769-775.
[9]   Grabec, I. Application of correlation techniques for localization of acoustic emission sources. Ultrasonics 16, 111–115 (1978).
[10] Emamian V., Kaveh M., H. Tewfik A., Shi Z., J. Jacobs L., Jarzynski J., (2003) Robust Clustering of Acoustic Emission Signals Using Neural Networks and Signal Subspace Projections, EURASIP Journal on Applied Signal Processing 2003:3, 276–286.

EXPERIMENTAL CHARACTERIZATION, MODELLING AND SIMULATION OF AE SIGNAL DUE TO CRACK PROPAGATION IN PMMA

Xi Chen[1], Nathalie Godin[1], Aurelien Doitrand[1] and Claudio Fusco[1]

[1]INSA de Lyon, Univ. Lyon, MATEIS UMR 5510, F-69621 Villeurbanne, France;
xi.chen@insa-lyon.fr, nathalie.godin@insa-lyon.fr, aurelien.doitrand@insa-lyon.fr,
claudio.fusco@insa-lyon.fr

ABSTRACT

Acoustic Emission (AE) is a non-destructive instrumentation that allows the detection of cracking, which dissipates elastic waves resulting from local crack-induced displacement jumps within the material. However, based on the AE experiments, a link between the crack fracture mechanics and the AE features is difficult to establish quantitatively, especially under quasi-static and dynamic loading conditions. Numerical simulations have proved to be very promising for this purpose. In this study, Pencil-Lead Break (PLB) tests are carried out on PMMA plate specimens with different thicknesses in order to determine the damping characteristics of PMMA and experimentally validate the AE numerical simulations. The influence of the specimen thickness, the distance between the sensor/source and the type of sensors on the measured acoustic emission are also studied.

Keywords: Acoustic emission, crack propagation, numerical simulation, PMMA.

1. Introduction

Acoustic Emission (AE) is a non-destructive testing technique that allows to detect damage in materials and structures. The different damage mechanisms may be identified due to their different AE signature. This signature is described by temporal and frequency descriptors, such as amplitude, energy, frequency centroid and peak frequency. The descriptor-based approach is widely used to analyze the AE characteristics of signals [1]. In most studies concerning crack propagation in a plate, AE characterization tests are used as a tool for predicting fracture in a structure [2,3]. Despite the effectiveness of this analysis methods, the acquired signals may be modified by the type of sensors used, their placement on the specimen, the coupling between the sensor and the specimen or even the parameters of the acquisition system [4-7].

In the AE analysis, the role of the AE source, the propagation medium and the recording system on the detected signal is very important [8]. Thus, it is relevant to establish a link between crack propagation and the acoustic emission signatures. Based on the classic experimental test, the numerical methods are combined to go further to build a quantitative relationship between the damage mechanisms and the acquired signal [9,10]. This problem can be divided into three major steps: firstly, the Pencil-lead Break (PLB) tests are carried out to obtain the AE characteristics of PMMA, such as the damping characteristics (Fig. 1(a)) that can be used as input parameters to

the numerical simulation (Fig. 1(c)) representing a real crack initiation and propagation experiment (Fig. 1(b)). Then, the AE mechanical experiments are carried out on specimens containing a circular hole (example of sketch shown in Fig. 1 (b)) to observe the crack propagation process and record the signals with several sensors. Besides, a numerical model is established. Fig. 1(c1) shows the part of the simulation of the crack propagation in a plate containing a circular hole under such a specimen. This can be done in the framework of Finite Fracture Mechanics (FFM) using for instance the Coupled Criterion (CC). The CC combines both energy and stress criteria to predict the initiation of a crack. It has been proved that it is an effective method to predict the crack initiation and propagation, which is rarely combined with AE technique, especially considering dynamic crack propagation [11,12]. After that, the acoustic emission is simulated, and the signals are received by sensors as shown in Fig. 1(c2). The simulated signals can thus be compared to the results obtained experimentally to validate the numerical model. Finally, a link between the crack propagation and the AE features can be established.

The PLB tests are carried out on three plates with different thicknesses. Four different types of sensors are used to record the signals. The influence of the distance between the sensor and the source and of the thickness on the AE signature are investigated to illustrate the AE parameters of PMMA plate. The difference of the signatures recorded by different sensors is also showed to identify the influence of sensor effect and choose a more suitable sensor to be used in the following mechanical test of PMMA plate. In this study, we focus on the PLB test to validate the simulation setup which will be used for the crack propagation and acoustic emission analysis in a further work.
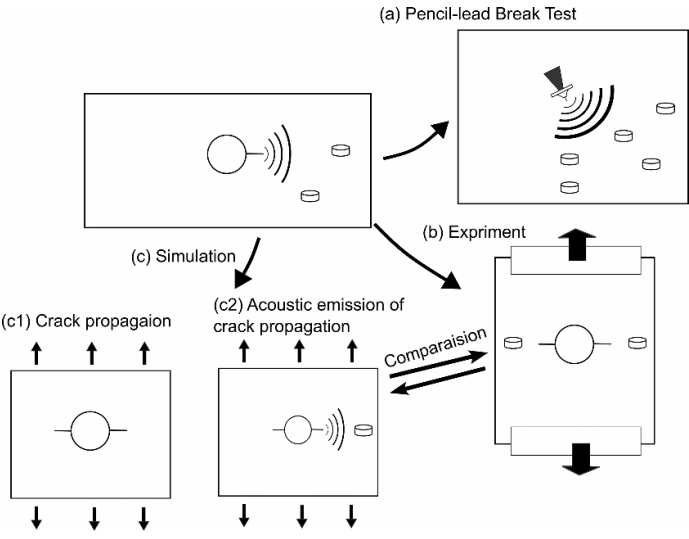
Fig. 1: Introduction of the problem.

2. Description of the experimental setup

For the validation of the FEM calculations, the experimental setup consists of a PLB procedure repeated 6 times for each configuration, on square plates with different thicknesses. The thicknesses of these specimens are 3mm, 5 mm, and 10 mm and their length are 1 m. Fig. 2 shows the sketch of the Pencil-lead break test program. To determine the acoustic parameters of PMMA and investigate the reflection from the plate boundary, two similar sensors are positioned at two points (coordinates: (-10, 0) and (0, 0) respectively). In our work, four types of sensors (nano 30, WD, micro 80 and micro 200 HF) are used to record signals. The pencil-lead used is a 2H lead of 0.5 mm diameter and 4.0 mm length. The pencil-lead breaks at all blue points on the quarter surface of the plate with different distances between the sensor/ source along two directions 0° and 45°, as shown in Fig. 2 (b).

Once the acquisition is over, signals are post-treated using MATLAB software. Firstly, the signals are pre-triggered, and the tail of each signal is cut on the basis of an energy criterion [13]. Then they are resampled with a 5 MHZ sampling rate. In our work, the main descriptors are amplitude, energy, frequency centroid (FC) and peak frequency (PF).
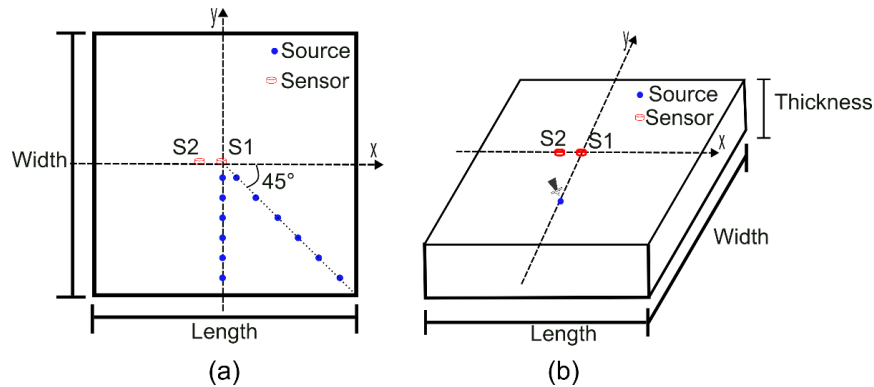

Fig. 2: Sketch of the PLB test program.

3. Results and discussions

3.1 Effect of sensor type

The nano 30 is very sensitive around 300 kHz and does not detect frequency content beyond 500 kHz. However, micro 80 and micro 200 HF are two sensors with wider pass band. In Fig. 3, we compare two signals from the same source in the temporal and frequency domain, detected by nano 30, and micro 200 HF sensors. These two sensors are equidistant from the source. Having a 27.3% correlation coefficient in the frequency domain, it is obvious that these different sensors do not detect the same information, due to their sensitivity, as shown in Fig. 3. Thus, the suitable sensor should be chosen according to the different sources with different frequency bands so that the sensor effect could be reduced, and the signals could record much more real information.
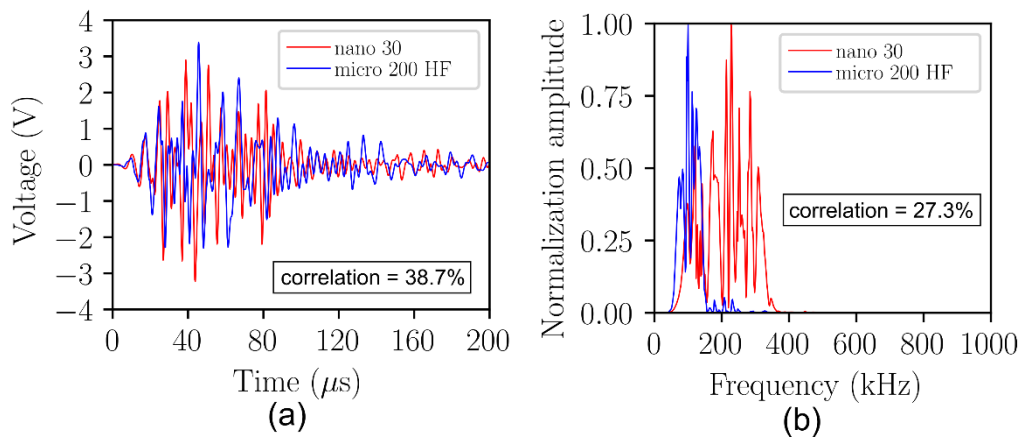
Fig. 3: Signals obtained with four types of sensors: Nano 30, WD, Micro 80 and Micro 200 HF sensors in the temporal (a) and frequency (b) domain. Pencil-lead breaks on (0, -10).

3.2 Effect of the propagation distance

The calculated descriptors display a clear dependence on distance between the lead break position and the sensor. Table 1 shows a summary of some descriptors for four tests. The values presented show that the type of sensors and the position of the AE sources substantially affect the descriptors.

Table 1: Descriptors calculated for two lead break positions ((0, 10) and (0, 40)).

Descriptors	*Nano 30*		*WD*		*Micro 80*		*Micro 200 HF*	
	Near to Sensor	Far from Sensor	Near to Sensor	Far from Sensor	Near to Sensor	Far from Sensor	Near to Sensor	Far from Sensor
(cm)	(0, 10)	(0, 40)	(0, 10)	(0, 40)	(0, 10)	(0, 40)	(0, 10)	(0, 40)
Energy (10^3 V^2)	379	1	930	6	285	1	305	5
Amplitude (dB)	89	64	92	71	87	64	89	70
Frequency Centroid (kHz)	216	143	199	129	234	148	145	111
Peak Frequency (kHz)	175	116	97	99	123	128	99	99

Fig. 4 shows the evolution of temporal and frequency descriptors with the source/sensor distance and with the different sensors. Each point on the graphs corresponds to a detected signal. The amplitude, in dB, varies linearly with distance and it loses more than 35 dB between the nearest and the furthest leak break. The energy decreases drastically with distance. The frequency centroid decreases linearly, and the decrease becomes slower with increasing distance: the reduction is almost 70 kHz with nano 30, WD and micro 80 sensor, and just 50 kHz with micro 200 HF sensor. The peak frequency undergoes slight variations in certain ranges: the peak frequency with nano 30 sensor and with a near distance is higher since it is close to the resonant frequency of the sensor, and the peak frequencies with the other three sensors are almost constant with distance.
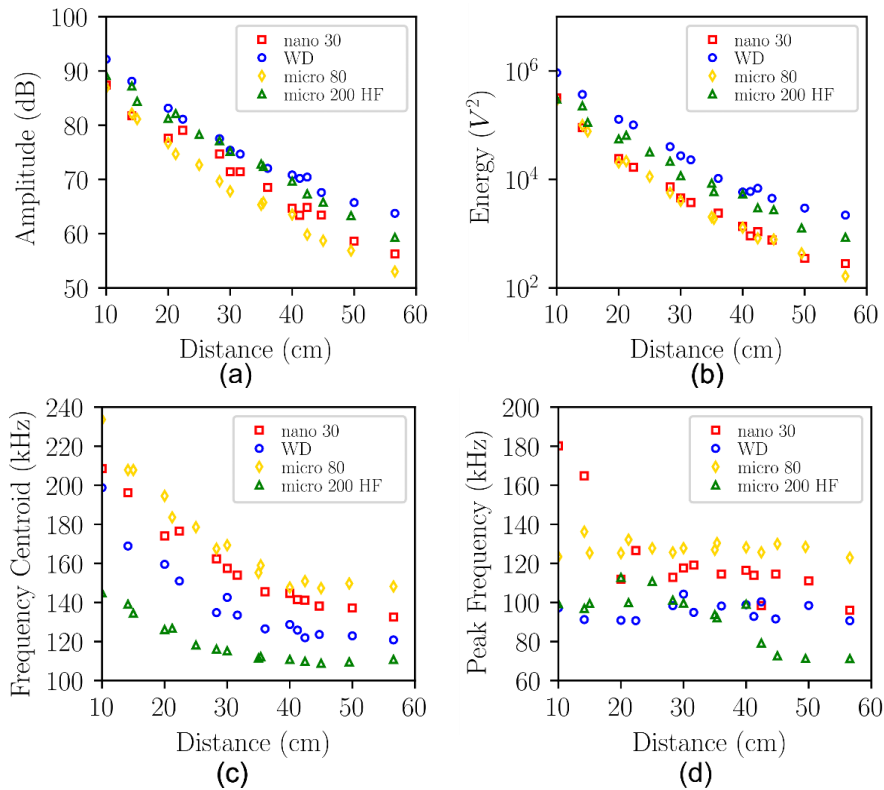

Fig. 4: Descriptors vs. distance for signals detected by nano 30 sensor, WD sensor, micro 80 sensor and micro 200 HF sensor: (a) amplitude in dB, (b) energy in V^2, (c) frequency centroid in kHz, (d) peak frequency in kHz.

Fig. 5 shows the time-frequency maps ascribed to pencil-lead break for four positions with four different distances (10, 20, 30, and 40 cm). For pencil-lead breaks near the sensors, the content of high frequency disappears progressively when the source is far.
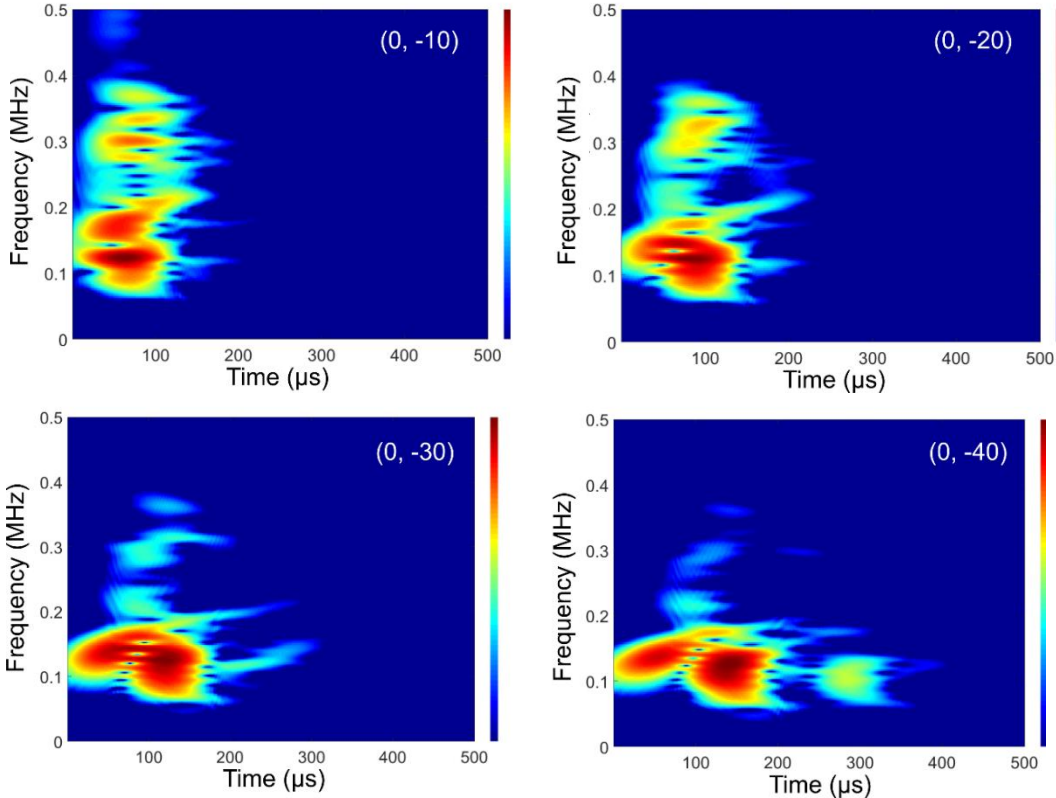

Fig. 5: Time-frequency results for four source positions for signals recorder by micro 80 sensor.

The variation of the frequency content of signals is significantly dependent on the propagation distance. The high frequency content is damped during the propagation. Thus, these results are useful to define the acoustic parameters.

3.3 Effect of the thickness

Fig. 6 shows the evolution of temporal and frequency descriptors with the distance source/sensor and with three different thicknesses. Each point on the graphs corresponds to a detected signal. The amplitude of a 10 mm thick specimen is the smallest compared to specimens with the other two thicknesses. Moreover, the values of the amplitude of 3 mm and 5 mm thick specimens are almost equivalent on the same position, except that when the source is close to the sensor, the values of a specimen with 5 mm thickness is a bit smaller than those of a 3 mm thick specimen. The variation of the energy is a similar as the variation of the amplitude. The frequency centroid close to the source is almost equivalent with three different thicknesses. With the increase of the distance, the reduction of the frequency centroid of the 5 mm thick specimen is larger, going from 220 kHz to 130 kHz, while the reductions of 3 mm and 5 mm thick specimens are from 220 kHz to about 180 kHz. The peak frequency is close to the resonant frequency of the sensor (about 300 kHz) when the source is close to the sensor. For most of the propagation distance, the peak frequency of a 5 mm thick specimen is smallest compared to the other two specimens.
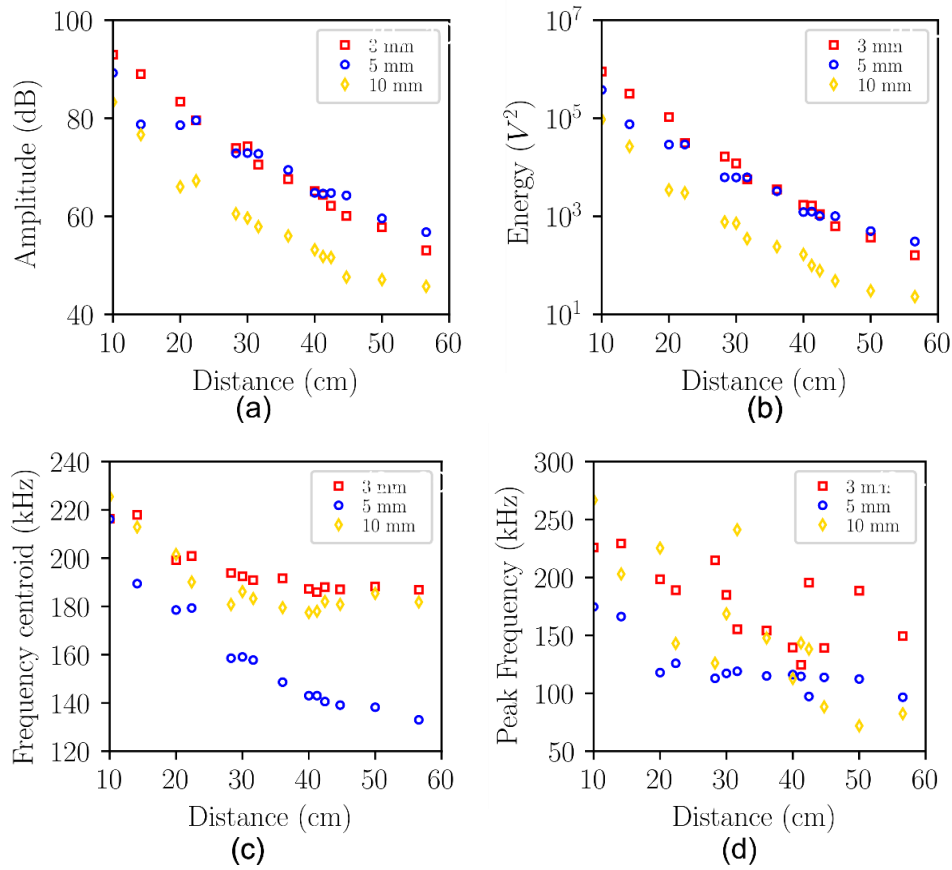
Fig. 6: Descriptors vs. distance with 3 mm, 5 mm, and 10 mm thickness for signals detected by nano 30 sensor: (a) amplitude in dB, (b) energy in V^2, (c) frequency centroid in kHz, (d) peak frequency in kHz.

4. Conclusions

The final objective of the problem is to establish a more quantitative relationship between the crack propagation as source of AE and the AE characteristic of the detected signals. To achieve this aim, pencil-lead break test of PMMA was first carried out. Concerning the different types of sensors, micro 80 sensor was more suitable to be used to receive the signals from the crack propagation due to a wider frequency band. The classical descriptors are very dependent on the propagation distance. This dependence is mainly due to the damping characteristics of PMMA. In the following numerical calculation, these damping characteristics could be described by the Rayleigh Damping ratio. Besides, theses descriptors are also dependent on the thickness of a specimen. For example, the frequency centroid of a 5 mm thick plate is smaller than that of the other two plates.

This pencil-lead break test results will be used as a basis for the further investigation of crack propagation from a circular hole in a plate. The use of the Coupled Criterion will be beneficial to determine the crack propagation stage under quasi-static or dynamic loading. Finally, a numerical model will be proposed to combine the crack propagation and the acoustic emission part.

5. References

[1] Godin N., Reynaud P., Fantozzi G. (2018). Acoustic Emission and Durability of Composite Materials. John Wiley & Sons.

[2] Sayar, H., Azadi M., Alizadeh M. (2019). Detection of Crack Initiation and Propagation in Aluminum Alloy Under Tensile Loading, Comparing Signals Acquired by Acoustic Emission and Vibration Sensors. Journal of Nondestructive Evaluation, vol. 38, no. 4: p. 100, doi: https://doi.org/10.1007/s10921-019-0639-9.

[3] Vshivkov A.N., Iziumova A.Yu., Panteleev L.A. et al. (2019). The study of a fatigue crack propagation in titanium Grade 2 using analysis of energy dissipation and acoustic emission data. Engineering fracture mechanics, vol. 210, p. 312-319, doi: 10.1016/j.engfracmech.2018.05.012.

[4] Maillet E., Christopher Baker, Gregory N. Morscher et al. (2015). Feasibility and limitations of damage identification in composite materials using acoustic emission. Composites Part A: Applied Science and Manufacturing, vol. 75, p. 77-83.

[5] Le Gall T., Monnier T., Fusco C. et al. (2018), Towards Quantitative Acoustic Emission by Finite Element Modelling: Contribution of Modal Analysis and Identification of Pertinent Descriptors. Applied sciences, vol. 8, no. 12, p. 2557, doi: 10.3390/app8122557.

[6] Aggelis D.G., Shiotani T., Papacharalampopoulos A. et al. (2011). The influence of propagation path on elastic waves as measured by acoustic emission parameters. Structural Health Monitoring, vol. 11, no. 3, p. 359-366, doi: 10.1177/1475921711419992.

[7] Carpinteri A., Lacidogna G., Accornero F. et al. (2013). Influence of damage in the acoustic emission parameters. Cement and Concrete Composites, vol. 44, p. 9–16.

[8] Sause M.G., Hamstad M.A. (2018) Numerical modeling of existing acoustic emission sensor absolute calibration approaches. Sensors and Actuators A: Physical, vol: 269, p. 294-307, doi: 10.1016/j.sna.2017.11.057.

[9] Hamam Z., Godin N., Reynaud P. et al. (2022). Transverse Cracking Induced Acoustic Emission in Carbon Fiber-Epoxy Matrix Composite Laminates. Materials, vol. 15, no. 1, p. 394, doi: 10.3390/ma15010394.

[10] Boulay, N., Lhémery A., Zhang F. (2018). Simulation of the spatial frequency-dependent sensitivities of Acoustic Emission sensors. Journal of physics. Conference series, vol. 1017, no. 1, p. 12008, doi: 10.1088/1742-6596/1017/1/012008.

[11] Morizet N., Godin N., Tang J., Maillet E., Fregonese M., Normand B. (2016). Classification of acoustic emission signals using wavelets and Random Forests: Application to localized corrosion. Mechanical Systems and Signal Processing, vol. 70, p. 1026-1037, doi: 10.1016/j.ymssp.2015.09.025.

[12] Laschuetza T., Seelig T. (2021). Remarks on dynamic cohesive fracture under static pre-stress — with a comparison to finite fracture mechanics. Engineering Fracture Mechanics, vol. 242, p. 107466, doi: 10.1016/j.engfracmech.2020.107466.

[13] Doitrand A., Molnár Gergely, Leguillon D. et al. (2022). Dynamic crack initiation assessment with the coupled criterion. European Journal of Mechanics - A/Solids, vol. 93, p. 104483, doi: 10.1016/j.euromechsol.2021.104483.

IoT–AE Remote Unattended Long–term Monitoring System

Bearings wear

4G/5G
NB–IoT

Wi-Fi

LoRa

zigbee

Pipe/Valve leakage

Bridge Wire breaking

Qingcheng IoT
Cloud Platform
or AWS or
Customized Server

4G/5G
Internet

4G/5G
Internet

Bluetooth

PC Desktop

Smart–Phone

Wind Power
Bearing /Blades
Monitoring

Products

SAEU3H AE Testing System
- Sample rate: 10MSPS, 16 bit
- 4, 20,or 48   channel
- Single USB rate: 300MB/s
- Frequency range: 1kHz 2.5MHz

RAEM1-6 Acoustic (AE) Remote Unattended Monitoring System
- 6 RAEM1 integrated
- IoT–AE system with Qingcheng IoT Cloud Platform
- Benchtop instrument: WiFi/cable to PC

RAEM1 Series (IoT–AE System)
- Single channel, triggered by signal or time
- Sensor, preamp and power internal or external
- Communications: 4G, NB IoT, LoRa, Zigbee, WiFi or wired
- Onsite test: smartphones via Bluetooth
- Wireless time synchronization
- Remote online monitoring: IoT Cloud

Acoustic Emission Sensors
- various types, ultra–high temperature, tiny size, frequency bands, preamplifier integrated, etc.

RAEM2 Series (IoT–AE System)
- Single channel, triggered by time
- Sensor, preamp and power internal or external
- Communications: 4G, NB IoT, LoRa, Zigbee, WiFi or wired
- Remote online monitoring: IoT Cloud platform
- Onsite test: smartphones via Bluetooth

QingCheng AE Institute

QingCheng AE Institute (QCAE) (previous name: Beijing SoundWel) has been a manufacturer of Acoustic Emission products from sensors to systems since 1998

+86–20–32290092

sales2@ae ndt.com

www.en.ae–ndt.com

Room 601–9,Building 3, 232 Ke Zhu Road, Huang Pu District, Guang Zhou City, Guang Dong Province, China

jessicajia

400

PROSPECTS ON APPLICATION OF ELASTIC METAMATERIALS IN ACOUSTIC EMISSION SENSING

Zbigniew Klimek[1] and Paweł Paćko[2]

[1]Office of Technical Inspection (UDT), Warsaw, Poland. Central Laboratory of Technical Inspection (CLDT), Cracow branch; zbigniew.klimek@udt.gov.pl
[2]AGH University of Science and Technology, Faculty of Mechanical Engineering and Robotics, Department of Robotics and Mechatronics, Krakow, Poland; pawel.packo@agh.edu.pl

ABSTRACT

This paper discusses challenges, limitations and problems arising in currently employed acoustic emission testing systems, sensors and signal processing algorithms. Main factors influencing and compromising accuracy and reliability of the classically used methods are briefly analyzed. Next, metamaterials and their dynamic properties are outlined with the aim and focus on their potential in manipulating energy flow. Several applications of metamaterials in acoustic emission are presented that indicate their potential in acoustic emission. Finally, possibilities of designing a new type of sensor for acoustic emission using metamaterials is discussed. As a consequence, it is expected to increase sensitivity and accuracy of source localization with smaller number of sensors used during measurements.

Keywords: Acoustic emission, metamaterials, sensors, signal processing.

1.   Introduction

Acoustic Emission (AE) is classified as one of non-destructive testing methods for structural inspection - it allows for detection, localization and, possibly, characterization of anomalies in the material. AE is commonly regarded as a passive method that detects only active defects. Depending on needs, it can be used as a tool for periodic inspection by subjecting the object to additional loading, a monitoring test, a check of previously detected discontinuities or as a continuous monitoring system, usually referred to as a structural health monitoring (SHM) system. This method of verifying structural integrity can be employed in a wide range of applications and for various types of structures and materials, which makes it very popular and appealing in many branches of industry [1-5].

In practical applications, the multi-modal and dispersive character of elastic waves, propagating in a structure upon AE event generation, induces substantial difficulties in reliable assessment of structural state. These complex properties of the wavefield originate from the existence of material boundaries, discontinuities, variation in material properties and thickness [6, 7]. In particular, wave dispersion consists in different velocity of waves depending on their frequency, resulting in waveform distortion along the propagation path [8, 9]. As a consequence, acquired complex time-domain signals contain contributions from multiple modes at various frequencies and wavelengths.

These signals are subsequently processed by AE systems and screened for damage-related features.

Currently used commercial acquisition units and sensors, among other deficiencies, prevent a single acoustic emission sensor from extracting individual wave modes of different wavelengths, at the same temporal frequency, from a single waveform. This, in turn, compromises detection, localization and characterization capabilities of an AE system. Limitations resulting from the construction of AE sensors and signal processing methods, can be improved by employing elastic metamaterials (MMs).

Metamaterials are materials of extraordinary properties. Complex topologies of metamaterials may be used for virtually arbitrary energy control, e.g. resulting in materials with a negative refraction index, negative compressibility, vanishing shear modulus, negative Poisson's ratio and other properties [10]. These specific dynamic properties can be employed for enabling spatial filtration properties of sensors, enhancing their broadband response and sensitivity, and contributing to the improvement of accuracy and reliability of structural inspection [11].

This paper aims at discussing challenges in acoustic emission, in particular those related to source localization, followed by analysis of dynamic properties of elastic metamaterials that can be potentially used to address these difficulties. Also, current applications of metamaterials in AE technologies are briefly reviewed and summarized.

2.   Challenges in acoustic emission

The primary goal of acoustic emission is to detect a signal that originates from the release of elastic energy due to the occurrence of an event in the object under investigation. AE can be used to perform different types of tests and tasks, such as monitoring, control, diagnosis and prognosis. It can be used in variety of media such as metal, wood, plastic (and other) composites, rocks, etc. Once a signal has been acquired and event detected, the next step is to localize and identify it in the inspected object. These three tasks are fundamental to acoustic emission testing [12-14]. Despite considerable research effort over last few decades, there are still some challenges in acoustic emission.

Well-known problems in AE testing arise from environment-related interferences. The method is sensitive to disturbances that can limit measurement accuracy and reliability. These can come directly from the object under test or from external sources in its immediate vicinity. With too high noise level, it is difficult to perform a reliable measurement and effectively indicate the correct source of the signal. In such a case, structural state evaluation depends on the operator experience. A number of publications describing techniques for improving the signal-to-noise ratio (SNR) can be found [15-17], proving that this problem is vital in AE testing. Indeed, the presence of high level of noise can influence localization due to misinterpretation of measurements, e.g. wrong estimation of the arrival time [18, 19]. Further difficulties arise in AE testing due to long propagation paths and high attenuation, e.g. in large and/or complex objects such as pipelines, bridges or rocks etc. For such structures it is necessary to use a large and dense networks of sensors, and complex and costly acquisition systems [20].

An acoustic emission event is typically a broadband source that generates partial elastic waves. Depending on the medium type, these can be either longitudinal or longitudinal and shear waves [21-23]. Partial waves propagate from the source to the sensor undergoing multiple reflections and refractions at material boundaries, inclusions and discontinuities. As a consequence, the signals acquired by the sensors are dispersive, i.e. the phase velocity of a given wave type is frequency-dependent, and multimodal, and therefore distorted along the propagation path [24, 25]. This makes their interpretation and use in localization and identification algorithms cumbersome.

Typical currently used industrial AE sensors are narrowband to ensure sufficient sensitivity and measurement range. Widely used AE sensors are omnidirectional, hence capture AE events regardless of the direction of arrival. This lack of information about the incidence direction, results

in the need of using several sensors for source localization. Also, sensitivity to the tested object's temperature can reduce sensor's durability and increase the risk of damage. Resonant sensors offer frequency filtering capabilities and allow for tracking of components at the pre-designed narrow frequency range. At the same time, information about the source carried by other frequency components is lost in the acquisition process.

Another important aspect of AE testing is source localization. The most common currently used localization methods are based on the wave speed for a given material as the key parameter. Methods based on estimated velocity are subject to error due to incorrect input of this value. As a result of the multimodality and dispersion of the wavefield and the corresponding different propagation velocities of different modes at different frequencies, substantial errors in the estimated source location can occur. This effect is particularly important for the time difference of arrival method (TDOA or TOA), in which it is assumed (in its classical and most basic formulation) that the wave speed in the tested object is constant, the material is homogeneous and isotropic, and that the wave propagation follows the shortest path from the source to the sensor. The method is based on the calculation of differences in the wave arrival time between the sensors, where their exact positions are known. In fact, in practice, spatial and directional variations in the wave speed due to inhomogenities, nonuniformity of the material, geometrical features and dispersion deteriorate localization accuracy [26]. Other methods that make use of the calibrated or computed constant wave speed for acoustic source localization, e.g. beamforming-based techniques [27, 28], also suffer from multimodality, dispersion and attenuation.

3. Metamaterials characteristics

Metamaterials have been intensively developed over last few decades [29, 30]. MMs are materials with unusual properties that are typically not found in nature and whose complex topologies can be used for virtually arbitrary energy control, e.g. resulting in materials with negative refractive index [31], negative compressibility, vanishing shear modulus, negative Poisson's ratio and other properties. Metamaterials may employ different physics and hence can be classified as electromagnetic, acoustic, thermal and mechanical [32]. Specific dynamic properties of mechanical MMs are obtained through proper arrangement of their (micro-)structure, by combining materials of various mechanical properties. The design process of MMs is typically supported by analytical and numerical models, e.g. the finite element method, finite difference method and other, while the manufacturing process is carried out – at least at the prototyping stage - using 3D printing technologies [33].

Elastic metamaterials' properties are determined by their mass density and elastic constants spatial distributions [34]. Proper design of MMs microstructural properties leads to achieving desired macrostructural effects in terms of elastic waves propagation through affecting waves amplitudes and phases at selected frequency and wavenumber bands, possibly in a direction-dependent way. As a consequence, MMs structure is heterogeneous and achieves the designed dynamic properties through the diffraction (and other) effects at the material level or through localized resonant structures [35]. Each approach allows for wave manipulation at a different length scale, namely the microstructural patterns typically affect waves of wavelength comparable to the characteristic mictrostructure scale, while the resonant structures can provide means for deeply subwavelength interactions [36]. As already pointed out, metamaterials display a number of intriguing dynamic properties. Some of them - with prospective applications in acoustic emission - will be briefly outlined next.

One of the most immediate consequences of periodicity, typical for phononic systems, is the occurrence of bandgaps. These are bands in which wave propagation is blocked and can be used to filter out a specific frequency range. Depending on the mechanism used to achieve a bandgap, two types can be distinguished. Similarly to the above-mentioned general classification of MMs, bandgaps can be formed due to the classical Bragg scattering mechanism or due to the wave

interaction with resonant structures. In the latter case, it was observed that low-frequency bandgaps were possible to achieve [37, 38]. This filtering effect of MMs was recently employed in structural health monitoring to remove unwanted wave components in non-linear guided waves based inspection [39].

An opposite effect, namely amplitude amplification over a certain frequency band, can be also achieved with MMs. One possible technique is the use of Gradient Refractive Index (GRIN) material [40], where the pressure field is amplified due to the compression of acoustic waves. Another application of the wave compression amplification using anisotropic acoustic MMs can be found in [41]. Amplification and multiplexing of weak signals was shown in [42] where a gradient acoustic-grating metamaterial (GAGM) that employs acoustic rainbow trapping, was used to capture series of low-amplitude periodic impulses. Signal amplitude enhancement was also achieved by the use of gradient MMs scrolls, where a gradient and a scroll structure are used simultaneously. Such a solution, as discussed in [43], resulted in signal amplification over a broad frequency range. The above approach, as stated by the authors, can be used to enhance harmonic signals and extract additional information from them. A similar technique and application can be found [44].

Controlling and directing energy flow in wave propagation problems, possible with metamaterials, can be also of interest for AE sensing applications. In particular, the direction of arrival of the wave is important in terms of locating its source based on clusters of sensors and without the need to know material properties of the structure [45]. Also, as shown in [46], it is not only possible to amplify the signal level, but to determine the direction of wave arrival by using gradient acoustic MM supplemented by space convolution structures. Metamaterials have been also used for detecting the direction of arrival of an infrasound wave, replacing large pressure sensing arrays in [47].

In recent years, substantial effort is made to control and re-configure dynamic properties of metamaterials. This research resulted in a rapid development of tunable metamaterials which properties may additionally depend on external or internal control factors. In [48] a tunable metamaterial with deformation-controlled tunable bandgaps was developed. Another example of bandgap tuning, by placing the resonators in a flexible matrix, can be found in [49], where bandgap closing and opening was presented. The tunability of acoustic metamaterials can be realized in a number of ways and allows waves to be manipulated over a wide spectrum, enhancing their performance [50].

Finally, it should be noted that other classes of metamaterials can be of interest to acoustic emission. As an example, thermal metamaterials can be mentioned as a means to control heat conduction [51, 52]. These types of structures are already used in electronics [53] and provide good thermal shielding.

Naturally, the range of possible applications of MMs is limitless and the above short overview gives only a flavor of potential directions. In the next section, the properties of MMs discussed above are paired with the challenges in acoustic emission, described in the previous section, in order to provide a prospect on application of metamaterials for the development of new types of AE sensors.

4. Use of metamaterials in acoustic emission

This section presents an outline for possible application of metamaterials in acoustic emission. As already discussed in the previous section, MMs display interesting dynamic phenomena that can be tailored to meet specific requirements. An initial attempt to defining these requirements and propose particular features of MMs that allow for their fulfillment, is presented below.

A fundamental challenge in acoustic emission testing is noise that affects the accuracy and compromises reliability of measurements. A potential improvement offered by metamaterials could be related to structurally blocking signals at undesired frequency bands by using bandgaps.

An additional advantage of employing bandgaps, in the context of acoustic emission sensing, is that the mechanical elimination of noise results in the reduction of amount of acquired data, both in the context of a single waveform and the number of events registered. This effect can be chieved by considering phononic crystals as elements of internal structure of an AE sensor. It was shown thoretically and validated experimentally that phononic crystals can be effective in blocking selected frequency bands by means of bandgaps, which allowed for canceling background noise [54]. In particular, it was shown that only one sensor can be used for monitoring cracking activity in a slab, without the need to install additional guard sensors.

Low amplitude and/or highly attenuating materials and structural components require sensors and preamplifiers able to introduce sufficient gain to acquire AE signals. Metamaterials offer solutions that may be potentially used to address that problem. As an example of use of MMs for signal amplification, a gradient-index phononic crystal lenses were proposed [55] for increasing amplitude of signals triggered by an AE event. Consequently, the distance between sensors can be increased and/or the number of sensors in the network can be limited.

Metamaterials can also facilitate acoustic emission source localization processes. Currently used AE sensors are omnidirectional, allowing for acquisition of distrubances from any direction, but not capable of distinguishing the arrival direction. Such an information on the incidence direction could be used to improve localization, make the localization process insensitive to material properties (or, equivalently, wave speed) estimates [45] and to reduce the number of AE sensors. As already mentioned, directional properties of MMs can be used to design a sensor that can capture waves arriving from certain directions only or employ feature-coding of the direction of arrival, e.g. frequency-coding [56]. The localization process, as well as source characterization can be also improved by the spatial filtering capabilities of MMs. Possibility of application of spatial filters, thus selectivity in the wavenumber domain, could help

in resolving the wave masking problem in multimodal systems. It should be noted that such an approach would require adapting sensor's characteristics to particular measurement conditions, as it is a standard approach for nowadays AE testing. In this respect, tunable MMs can offer a potential of using a single tunable sensor that could be adjusted to the test conditions.

Other metamaterial types can also provide benefits to AE testing, for instance electromagnetic MMs can be used for reducing electrical interferences while thermal MMs can be employed for thermal insulation when a sensor must be used in hot environment.

5. Conclusions

In this article, current challenges in acoustic emission testing were outlined. In particular, interferences, noise, complex wave dispersion characteristics, signal propagation issues in large and/or highly attenuating objects were briefly discussed. Next, fundamental dynamic properties and phenomena associated with a new class of materials - metamaterials - were discussed along with their applications. Finally, prospects on applying MMs and employing some of their properties to address acoustic emission testing challenges were given.

By analyzing current challenges in acoustic emission on one side and capabilities of elastic, and other, metamaterials it was hypothesized that MMs can be used to address at least some of the problems. In particular, it seems feasible to apply metamaterials in the acoustic emission sensor structure to facilitate temporal and spatial filtering, signal amplification and possibly induce its directional properties in order to simplify and improve accuracy of AE source localization methods. Also, other types of MMs can provide potential for reducing the negative influence of electromagnetic noise and improving thermal resistance of the sensors, hence allowing their applications in even more demanding harsh environments.

6. Acknowledgements

7. References

[1]   Cai, X., Shi, C., Chen, X., & Yang, J. (2021). Identification of damage mechanisms during splitting test on SFP at different temperatures based on acoustic emission. Construction and Building Materials, 270, 121391, doi: 10.1016/j.conbuildmat.2020.121391.

[2]   Holford, K. M., Eaton, M. J., Hensman, J. J., Pullin, R., Evans, S. L., Dervilis, N., & Worden, K. (2017). A new methodology for automating acoustic emission detection of metallic fatigue fractures in highly demanding aerospace environments: An overview. Progress in Aerospace Sciences, 90, 1-11, doi: 10.1016/j.paerosci.2016.11.003.

[3]   Jia, Z., Xie, H., Zhang, R., Li, C., Wang, M., Gao, M., ... & Zhang, Z. (2020). Acoustic emission characteristics and damage evolution of coal at different depths under triaxial compression. Rock Mechanics and Rock Engineering, 53(5), 2063-2076, doi: 10.1007/s00603-019-02042-w.

[4]   Kishawy, H. A., Hegab, H., Umer, U., & Mohany, A. (2018). Application of acoustic emissions in machining processes: analysis and critical review. The International Journal of Advanced Manufacturing Technology, 98(5), 1391-1407, doi: 10.1007/s00170-018-2341-y.

[5]   Sengupta, S., Datta, A. K., & Topdar, P. (2015). Structural damage localisation by acoustic emission technique: A state of the art review. Latin American Journal of Solids and Structures, 12, 1565-1582, doi: 10.1590/1679-78251722.

[6]   Hernandez Crespo, B., Courtney, C. R., & Engineer, B. (2018). Calculation of guided wave dispersion characteristics using a three-transducer measurement system. Applied Sciences, 8(8), 1253, doi: 10.3390/app8081253.

[7]   Nazarchuk, Z., Skalskyi, V., & Serhiyenko, O. (2017). Propagation of elastic waves in solids. In Acoustic Emission (pp. 29-73). Springer, Cham, doi: 10.1007/978-3-319-49350-3_2.

[8]   Jothi Saravanan, T. (2022). Investigation of guided wave dispersion characteristics for fundamental modes in an axisymmetric cylindrical waveguide using rooting strategy approach. Mechanics of Advanced Materials and Structures, 29(4), 495-505, doi: 10.1080/15376494.2020.1777601.

[9]   Lašová, Z., & Zemčík, R. (2017). Determination of group velocity of propagation of Lamb waves in aluminium plate using piezoelectric transducers, doi: 10.24132/acm.2017.346.

[10] Askari, M., Hutchins, D. A., Thomas, P. J., Astolfi, L., Watson, R. L., Abdi, M., ... & Clare, A. T. (2020). Additive manufacturing of metamaterials: A review. Additive Manufacturing, 36, 101562, doi: 10.1016/j.addma.2020.101562.

[11] Zhang, X., Xing, J., Liu, P., Luo, Y., & Kang, Z. (2021). Realization of full and directional band gap design by non-gradient topology optimization in acoustic metamaterials. Extreme Mechanics Letters, 42, 101126, doi: 10.1016/j.eml.2020.101126.

[12] Scruby, C. B. (1987). An introduction to acoustic emission. Journal of Physics E: Scientific Instruments, 20(8), 946, doi: 10.1088/0022-3735/20/8/001.

[13] Gholizadeh, S., Leman, Z., & Baharudin, B. H. T. (2015). A review of the application of acoustic emission technique in engineering. Structural Engineering and Mechanics, 54(6), 1075-1095, doi: 10.12989/sem.2015.54.6.1075.

[14] Kaphle, M., Tan, A., Thambiratnam, D., & Chan, T. (2011). Acoustic emission technique-Opportunities, challenges and current work at QUT. In Proceedings of the First International

Conference on Engineering, Designing and Developing the Built Environment for Sustainable Wellbeing (pp. 312-317). Queensland University of Technology.

[15] Zhou, C., & Zhang, Y. (2012). Particle filter based noise removal method for acoustic emission signals. Mechanical systems and signal processing, 28, 63-77, doi: 10.1016/j.ymssp.2011.08.004.

[16] Grosse, C. U., Reinhardt, H. W., Motz, M., & Kroplin, B. (2002). Signal conditioning in acoustic emission analysis using wavelets. NDT. net, 7(9), 1-9

[17] Ruiz-Cárcel, C., Hernani-Ros, E., Cao, Y., & Mba, D. (2014). Use of spectral kurtosis for improving signal to noise ratio of acoustic emission signal from defective bearings. Journal of Failure Analysis and Prevention, 14(3), 363-371, doi: 10.1007/s11668-014-9805-7.

[18] Zhou, Z., Cheng, R., Rui, Y., Zhou, J., Wang, H., Cai, X. I. N., & Chen, W. (2020). An improved onset time picking method for low SNR acoustic emission signals. IEEE Access, 8, 47756-47767, doi: 10.1109/ACCESS.2020.2977885.

[19] Chacon, J. L. F., Kappatos, V., Balachandran, W., & Gan, T. H. (2015). A novel approach for incipient defect detection in rolling bearings using acoustic emission technique. Applied Acoustics, 89, 88-100, doi: 10.1016/j.apacoust.2014.09.002.

[20] Ono, K. (2018). Review on structural health evaluation with acoustic emission. Applied Sciences, 8(6), 958, doi: 10.3390/app8060958.

[21] Meleshko, V. V., Bondarenko, A. A., Dovgiy, S. A., Trofimchuk, A. N., & Van Heijst, G. J. F. (2009). Elastic waveguides: History and the state of the art. I. Journal of Mathematical Sciences, 162(1), 99-120, doi: 10.1007/s10958-009-9623-8.

[22] Royer, D., & Dieulesaint, E. (1999). Elastic waves in solids I: Free and guided propagation. Springer Science & Business Media.

[23] Pao, Y. H. (1983). Elastic waves in solids. ASME Journal of Applied Mechanics, 50, 1152-1164.

[24] Hamstad, M., O'GALLAGHER, A., & Gary, J. (2002). A wavelet transform applied to acoustic emission. J. Acoust. Emiss, 20, 39-61.

[25] Aggelis, D. G., & Matikas, T. E. (2012). Effect of plate wave dispersion on the acoustic emission parameters in metals. Computers & structures, 98, 17-22, doi: 10.1016/j.compstruc.2012.01.014.

[26] Aljets, D., Chong, A., Wilcox, S., & Holford, K. (2012). Acoustic emission source location on large plate-like structures using a local triangular sensor array. Mechanical Systems and Signal Processing, 30, 91-102, doi: 10.1016/j.ymssp.2012.01.012.

[27] McLaskey, G. C., Glaser, S. D., & Grosse, C. U. (2010). Beamforming array techniques for acoustic emission monitoring of large concrete structures. Journal of Sound and Vibration, 329(12), 2384-2394, doi: 10.1016/j.jsv.2009.08.037.

[28] He, T., Pan, Q., Liu, Y., Liu, X., & Hu, D. (2012). Near-field beamforming analysis for acoustic emission source localization. Ultrasonics, 52(5), 587-592, doi: 10.1016/j.ultras.2011.12.003.

[29] Boardman, A. (2010). Pioneers in metamaterials: John pendry and victor veselago. Journal of optics, 13(2), 020401, doi:10.1088/2040-8978/13/2/020401.

[30] Engheta, N., & Ziolkowski, R. W. (2005). A positive future for double-negative metamaterials. IEEE Transactions on microwave theory and techniques, 53(4), 1535-1556.

[31] Smith, D. R., & Kroll, N. (2000). Negative refractive index in left-handed materials. Physical review letters, 85(14), 2933, doi: 10.1103/PhysRevLett.85.2933.

[32] Fan, J., Zhang, L., Wei, S., Zhang, Z., Choi, S. K., Song, B., & Shi, Y. (2021). A review of additive manufacturing of metamaterials and developing trends. Materials Today., doi:10.1016/j.mattod.2021.04.019.

[33] Surjadi, J. U., Gao, L., Du, H., Li, X., Xiong, X., Fang, N. X., & Lu, Y. (2019). Mechanical metamaterials and their engineering applications. Advanced Engineering Materials, 21(3), 1800864, doi: 10.1002/adem.201800864.

[34] Liu, J., Guo, H., & Wang, T. (2020). A review of acoustic metamaterials and phononic crystals. Crystals, 10(4), 305, doi: 10.3390/cryst10040305.

[35] Craster, R. V., & Guenneau, S. (Eds.). (2012). Acoustic metamaterials: Negative refraction, imaging, lensing and cloaking (Vol. 166). Springer Science & Business Media., doi: 10.1007/978-94-007-4813-2.

[36] Norris, A. N., & Packo, P. (2019). Non-symmetric flexural wave scattering and one-way extreme absorption. The Journal of the Acoustical Society of America, 146(1), 873-883, doi: 10.1121/1.5087133.

[37] Zhu, R., Liu, X. N., Hu, G. K., Yuan, F. G., & Huang, G. L. (2015). Microstructural designs of plate-type elastic metamaterial and their potential applications: a review. International Journal of Smart and Nano Materials, 6(1), 14-40, doi: 10.1080/19475411.2015.1025249.

[38] Liu, J., Guo, H., & Wang, T. (2020). A review of acoustic metamaterials and phononic crystals. Crystals, 10(4), 305., doi: 10.3390/cryst10040305.

[39] Shan, S., Wen, F., & Cheng, L. (2021). Purified nonlinear guided waves through a metamaterial filter for inspection of material microstructural changes. Smart Materials and Structures, 30(9), 095017, doi: 10.1088/1361-665X/ac1955.

[40] Chen, T., Yu, D., Wu, B., & Xia, B. (2021). Weak Signals Detection by Acoustic Metamaterials-Based Sensor. IEEE Sensors Journal, 21(15), 16815-16825, doi: 10.1109/JSEN.2021.3076860.

[41] Chen, Y., Liu, H., Reilly, M., Bae, H., & Yu, M. (2014). Enhanced acoustic sensing through wave compression and pressure amplification in anisotropic metamaterials. Nature communications, 5(1), 1-9., doi: 10.1038/ncomms6247.

[42] Chen, T., Jiao, J., & Yu, D. (2021). Broadband acoustic enhancement and weak signals detection within a gradient acoustic-grating metamaterial. Measurement, 171, 108817., doi:10.1016/j.measurement.2020.108817.

[43] Chen, T., Jiao, J., & Yu, D. (2020). Enhanced broadband acoustic sensing in gradient coiled metamaterials. Journal of Physics D: Applied Physics, 54(8), 085501., doi: doi.org/10.1088/1361-6463/abc6d7.

[44] Chu, Y., Chen, T., & Yu, D. (2020). Acoustic enhancement and weak signal detection based on the space-coiling gradient acoustic grating. Applied Physics Express, 13(9), 097002, doi: 10.35848/1882-0786/abb0a4.

[45] Sen, N., Gawroński, M., Packo, P., Uhl, T., & Kundu, T. (2021). Square-shaped sensor clusters for acoustic source localization in anisotropic plates by wave front shape-based approach. Mechanical Systems and Signal Processing, 153, 107489., doi: 10.1016/j.ymssp.2020.107489.

[46] Chen, T., Wang, C., & Yu, D. (2022). Pressure amplification and directional acoustic sensing based on a gradient metamaterial coupled with space-coiling structure. Mechanical Systems and Signal Processing, 181, 109499, doi: 10.1016/j.ymssp.2022.109499.

[47] Rouse, J. W., Bowman, D., & Walsh, T. F. (2021). Directional infrasound sensing using acoustic metamaterials. The Journal of the Acoustical Society of America, 150(1), 367-375, doi: 10.1121/10.0005594.

[48] Ning, S., Yang, F., Luo, C., Liu, Z., & Zhuang, Z. (2020). Low-frequency tunable locally resonant band gaps in acoustic metamaterials through large deformation. Extreme Mechanics Letters, 35, 100623, doi: 10.1016/j.eml.2019.100623.

[49] Wang, P., Casadei, F., Shan, S., Weaver, J. C., & Bertoldi, K. (2014). Harnessing buckling to design tunable locally resonant acoustic metamaterials. Physical review letters, 113(1), 014301, doi: doi.org/10.1103/PhysRevLett.113.014301.

[50] Chen, S., Fan, Y., Fu, Q., Wu, H., Jin, Y., Zheng, J., & Zhang, F. (2018). A review of tunable acoustic metamaterials. Applied Sciences, 8(9), 1480, doi: 10.3390/app8091480.

[51] Sklan, S. R., & Li, B. (2018). Thermal metamaterials: functions and prospects. National Science Review, 5(2), 138-141, doi: 10.1093/nsr/nwy005.

[52] Peralta, I., Fachinotti, V. D., & Alvarez Hostos, J. C. (2020). A brief review on thermal metamaterials for cloaking and heat flux manipulation. Advanced Engineering Materials, 22(2), 1901034, doi: 10.1002/adem.201901034.

[53] Dede, E. M., Zhou, F., Schmalenberg, P., & Nomura, T. (2018). Thermal metamaterials for heat flow control in electronics. Journal of Electronic Packaging, 140(1)., doi: 10.1115/1.4039020.

[54] Kabir, M., Mostavi, A., & Ozevin, D. (2018). Noise isolation with phononic crystals to enhance fatigue crack growth detection using acoustic emission. Journal of Civil Structural Health Monitoring, 8(3), 529-542, doi: 10.1007/s13349-018-0291-6.

[55] Okudan, G., Danawe, H., Zhang, L., Ozevin, D., & Tol, S. (2021). Enhancing Acoustic Emission Characteristics in Pipe-Like Structures with Gradient-Index Phononic Crystal Lens. Materials, 14(6), 1552, doi: doi.org/10.3390/ma14061552.

[56] Senesi, M., & Ruzzene, M. (2011). A frequency selective acoustic transducer for directional Lamb wave sensing. The Journal of the Acoustical Society of America, 130(4), 1899-1907, doi: 10.1121/1.3626165.

FIELD-EXPERIENCES OF TRACKING PLANT'S XYLEM EMBOLISM FORMATION WITH EMBEDDED ACOUSTIC EMISSION SENSORS

Dinko Oletić[1], Sabine Rosner[2] and Vedran Bilas[1]

[1]University of Zagreb, Faculty of Electrical Engineering and Computing, Zagreb, Croatia;
dinko.oletic@fer.hr, vedran.bilas@fer.hr
[2]BOKU Vienna, Institute of Botany, Vienna, Austria; sabine.rosner@boku.ac.at
*Correspondence: dinko.oletic@fer.hr; tel.: +385 1 6129 536

ABSTRACT

Plant physiology, forestry, and agriculture require novel field-deployable instruments for tracking plant's hydraulic status, to enhance understanding of the strategies plants developed to cope with drought stress, enable tracking of damages caused by seasonal droughts, and to rationalize water expenditure used for precision-irrigation. Acoustic emission sensing (AE) is a promising indirect method of non-invasively tracking the cavitation-induced xylem embolism. We developed a low-power embedded system enabling in-field 2,5 MHz AE acquisition, real-time sensor-response equalization, time-, and frequency-domain feature extraction, micro-SD storage and Sigfox wireless communication. The system is solar-powered and operates with commercial miniature piezoelectric transducers (Vallen). In this paper we show early results of our work-in-progress on outdoor testing on grapevine plants.

Keywords: Drought stress, xylem embolism, AE signal features, embedded sensors, outdoor experiments.

1. Introduction

In plants, water is transported against the force of gravity from roots to leaves through plant's xylem system of capillary conduits by a passive hydraulic mechanism, described in plant physiology as a "cohesion-tension" theory [1]. When exposed to drought stress, tension increases in xylem capillaries, leading to nucleation of microscopic gas-bubbles [2]. Aggregation of gas-bubbles in xylem conduits can lead to embolization of portions of xylem tissue, leading to loss of its hydraulic conductivity. This may consequently cause wilting of leaves, desiccation of branches or even draught-induced death of the whole plant [3]. However, monitoring progression of xylem embolism requires either destructive reference hydraulic methods, or costly laboratory equipment such as X-ray μCT, which is non-applicable in the field, and may induce cellular damage [4], [5], [6]. Therefore, plant physiology, forestry, and agriculture require novel field-deployable instruments for tracking plant's hydraulic status. They would enhance understanding of plants' strategies to cope with drought stress, enable tracking of damages caused by seasonal droughts, and help rationalize water expenditure used for precision-irrigation.

Tension-induced nucleations of gas-bubbles in xylem conduits (also referred as cavitation) create mechanical waves [2] observed by piezoelectric transducers placed on plant's trunk surface as

acoustic emission (AE) in ultrasonic frequency range [7]. AE testing has been evaluated by plant-physiologists as a non-invasive indirect alternative to reference methods for measurement of hydraulic vulnerability on living plants under laboratory conditions [8], [6], [9]. Despite great potential, several challenges still need to be addressed, for AE testing to became field-worthy in the long-term e.g., season-scale unattended monitoring of plant's drought-related symptoms.

The challenge related to analysis and interpretation of AE signals is that multiple AE signal sources exist, apart from xylem gas-bubble nucleation. They include stem-shrinkage, fractures in xylem-structure and bark, water drainage in porous tissue (Haines jumps) [6]. Outdoors, additional sources of interferences may be present, like sensor movement caused by wind- or stem-shrinkage, raindrops [10], temperature-variations [11]. In addition, effects of wave propagation through anisotropic wooden medium distorting AE signal waveforms [12], combined with typically resonant, non-flat frequency response of piezo-electric sensors are to be considered. Data-driven attempts have been made for selection of time and frequency-domain AE signal features [6], [9] suitable for differentiation of physiological AE source type based on natural clustering of [13], [14]. Finally, portable embedded systems are needed, capable of acquiring AE waveforms at high sample-rate and high precision, real-time on-board processing, storage, and communication [15].

In our previous work, a low-power, portable, embedded sensor system specifically designed for acquisition [16], and processing of plant physiological AE signals was presented. A set of time-frequency signal features was proposed [17] for detection of xylem cavitation-related ultrasonic signatures, implementable on the embedded sensor system. The sensitivity of the technique was verified on the developed sensor system in laboratory conditions, against reference xylem water potential measurements [18]. This paper presents results of preliminary testing of the sensor system's performance in outdoor conditions. The specific goal is to verify the occurrence of AE signatures specific for drought-induced hydraulic processes under field conditions during multiple days. Additionally, practical challenges of outdoor AE monitoring are discussed.

2. Methods and materials

2.1 Embedded AE hardware for monitoring of drought symptoms

The sensor system is designed to accommodate a wide range of commercial piezoelectric AE transducers. VS600-Z1 (Vallen) was used for testing on small branches, due to small contact surface area (4.75 mm diameter), and a wide usable bandwidth around its 570 kHz resonance frequency. In the current implementation, sensors are attached to embedded electronics via SMA connector.

Two-stage analog front-end (AFE) electronics interfaces sensor to analog-to-digital converter (ADC). AFE consists of a cascade of a charge-amplifier, and a voltage-amplifier, providing in total 34 dB (50 V/V) of voltage-gain equivalent across the 100-600 kHz passband. Given that AFE needs to be always-on listening for incoming AEs, operational amplifiers implementing the AFE were selected to balance between sufficient gain-bandwidth and a minimal power consumption, consuming 3.5 mW. A triggering circuit with an adjustable voltage-threshold is implemented to conserve power of ADC and digital signal processor, by waking them up only upon detecting the presence of an AE emission. Sensor system's total wake-up latency (including the AFE, ADC and the processor) is around 700 ns, to timely capture the beginning of the AE signal's waveform.

Signal acquisition is performed by a sequential approximation ADC (AD9120, Analog devices) running at the sample rate of 2 MHz, at 16-bits. With a 2.5 V external voltage reference, resolution is 38 μV. The voltage amplifier stage and ADC are fully-differential, helping to reduce common-mode interference. Signal acquisition process is controlled by a 120 MHz ARM Cortex-M4 microcontroller (STM32L4 family, ST Microelectronics). The microcontroller stores AE waveforms in internal SRAM memory for digital signal processing. Raw waveforms, as well as the processing results with their timestamps are logged in a non-volatile Flash memory on the SD-card. In addition, a microcontroller periodically takes environmental measurements from a

temperature and humidity sensor SHT31 (Sensirion). Sigfox digital radio is used for low-power wireless communication.

The sensor system is powered by a 400 mAh 3.7 V Li-Ion battery, recharged externally by a micro-USB plug, or by an embedded 44 x 22 mm monocrystalline silicon solar panel, generating 180 mW at its maximal power point. The total active-state power consumption while performing signal acquisition is around 15 mW, and 5.7 mW while listening.
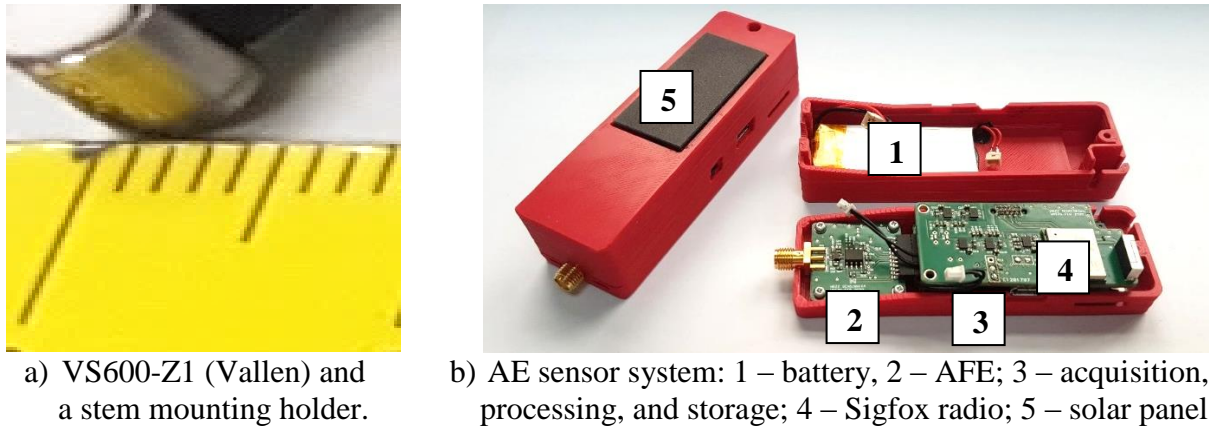

a) VS600-Z1 (Vallen) and a stem mounting holder.

b) AE sensor system: 1 – battery, 2 – AFE; 3 – acquisition, processing, and storage; 4 – Sigfox radio; 5 – solar panel.

Fig. 1: Embedded AE sensor system hardware.

2.2 Embedded AE signal analysis

Simultaneously with signal acquisition, the embedded digital signal processor enables real-time analysis of AE waveforms onboard the sensor system. Currently implemented signal analysis steps are aimed at automated extraction of AE signal features proposed in [17]. They entail logging of AE arrival-time, frequency-decomposition, correction of the sensor's frequency response, and extraction of frequency-domain signal features.

Frequency-decomposition of the initial 128 µs of AE signal (duration of most of our AE signals) is performed by 256-point Fast Fourier Transform (FFT). FFT was implemented in 32-bit complex-number floating-point arithmetic using CMSIS signal processing library for ARM Cortex. Then, amplitude spectrum is calculated for 128 positive frequencies, resulting in 7.8 kHz/bin frequency resolution. The amplitude spectrum is corrected for the sensor's frequency response (Fig. 2). The correction (equalization) is performed by dividing the signals' raw amplitude spectrum with the transducers' amplitude-frequency response, while retaining the scaling at the resonance. Such correction method breaks-down to computationally fast single vector multiplication with correction curve coefficients stored in a sensor-specific look-up table.

a) AE's amplitude spectrum before correction.

b) VS600-Z1 response (blue), correction curve (orange).

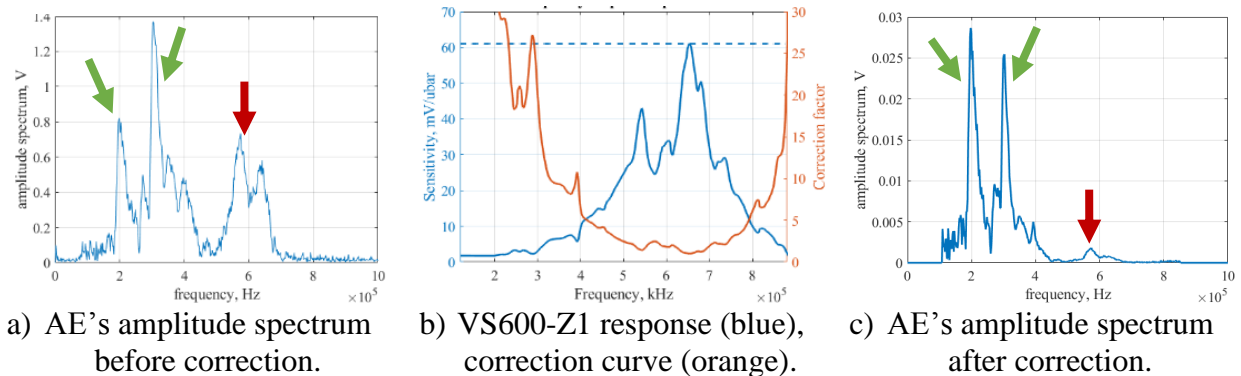c) AE's amplitude spectrum after correction.

Fig. 2: Correction of sensor's frequency response characteristics.

From the equalized amplitude spectrum, frequency-domain features are extracted. In previous laboratory climate chamber on living plants experiments [17], it was observed that specifically, in conditions of elevated drought stress corresponding to -0.7 to -1.2 MPa of leaf water potential, in addition to an increased overall AE activity, characteristic time-frequency signatures (patterns) occur. They contain three main characteristic groups of AEs, differentiated by their spectral composition: "single-component", "multi-component", and "broadband" AEs (Fig. 3).

Hence, amplitude spectrum is on the embedded sensor system analyzed for existence of outstanding frequency components, by calculating the prominence for each peak (maximum) appearing in the amplitude spectrum. AEs with a single prominent frequency-peak are considered "single-component" (Fig. 3, black). In case more than one prominent peak is found in AE amplitude spectrum, they are sorted by their descending amplitude (Fig. 3, orange, blue, green). If no prominent peaks are found, AE is considered "broadband" (Fig. 3, yellow). Number of prominent peaks are counted, and their amplitudes and frequencies are stored.
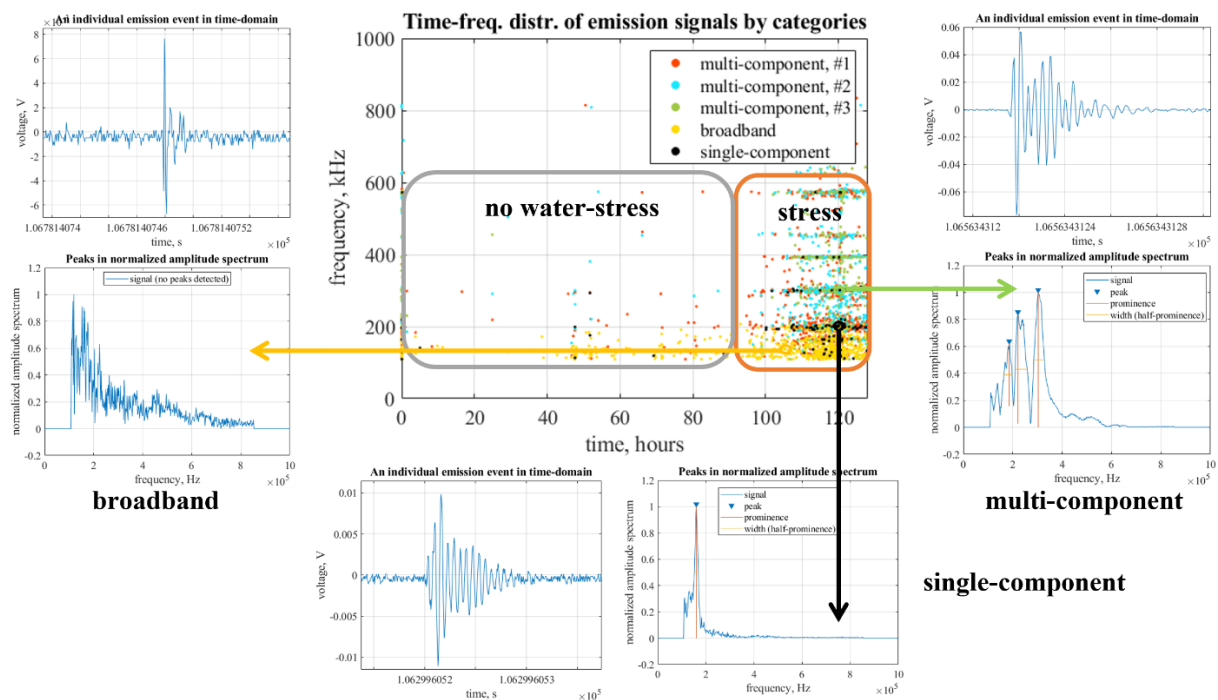
Fig. 3: Characteristic AE signatures observed during water-stress.
Three main groups of recorded AEs, and their spectral composition.

2.3 Outdoor AE experiments

With the sensitivity of the proposed AE feature-set to detect drought stress conditions as verified on the developed sensor system in laboratory conditions [18], the sensor system was tested outdoors for its reliability. The goals of the experiments were: (1) to verify occurrence of AE signatures in environmental drought stress conditions, and (2) to test robustness of hardware and signal acquisition.

A multi-day AE experiment was performed over 92 hours, from 30/07/2021 to 03/08/2021. The experiment was performed during the summer season (Central Europe, continental climate), with wide daily temperatures, ranging from 16°C at night, up to 34°C at mid-day. Measurements were conducted by two AE embedded sensor systems, attached to stems of two 2-years old grapevine seedlings held in 1 dm^3 pots (*Vitis vinifera*, cultivar Victoria). Plants were well watered before the start of the experiment they were not watered during the experiment.

A flat, 5 mm in diameter, contact-surface with the piezoelectric transducer (VS600-Z1) was formed, by shallowly debarking the stem 1-2 cm below main branching. Silicon grease (OKW) was used to seal the wound, stopping the air ingress, and to ensure good ultrasonic coupling.

Transducers were held against the grapevine stem (8-12 mm in diameter) using plastic enclosures attached with zip-ties. The contact pressure was adjusted with screws. The embedded AE sensor system ran the described signal acquisition, feature extraction, and logging results on the SD-card. Sensor system electronics were enclosed in a plastic box for extra protection against water ingress in case of rain (Fig. 4).
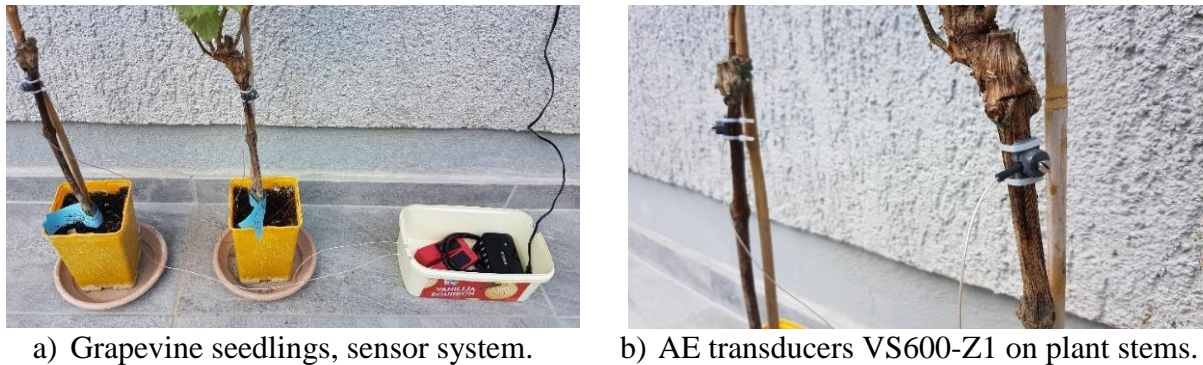

a) Grapevine seedlings, sensor system. b) AE transducers VS600-Z1 on plant stems.

Fig. 4: Experimental setup for outdoor testing of the embedded AE sensor system.

3. Results and discussion

Results of outdoor AE testing are shown in Fig. 5 and 6. Appearance of drought stress specific AE signatures is observed mid-day during the hottest days (30/07, 02/08, 03/08), coinciding with the expected maximums in evapotranspiration. Comparable responses were obtained on both plants, exposed to identical environmental conditions. Variability of environmental conditions enabled us to demonstrate the sensitivity of the sensor system. Absence of AE activity is seen during the colder, cloudy day (01/08) on both plants, indicating absence of drought stress at ambient temperatures 16-22°C.

The experiment has confirmed that due to plant-to-plant variability of absolute AE number (hourly rate, Fig. 5a, 6a), time-frequency AE features provide a better basis for detection and monitoring of progression of drought stress processes. It has been verified that the AE time-frequency signatures obtained outdoors are comparable to the signature from Fig. 3, obtained in the controlled laboratory environment [18]. In both cases, single-component emissions were observed to group most frequently around 200 kHz.
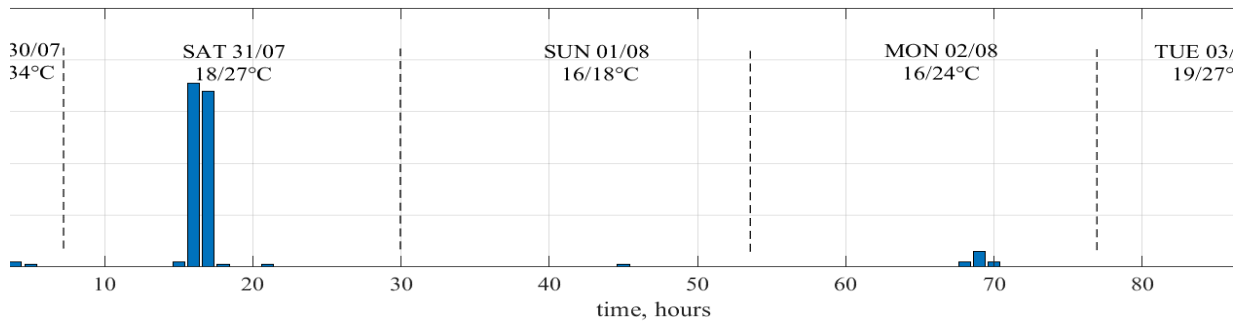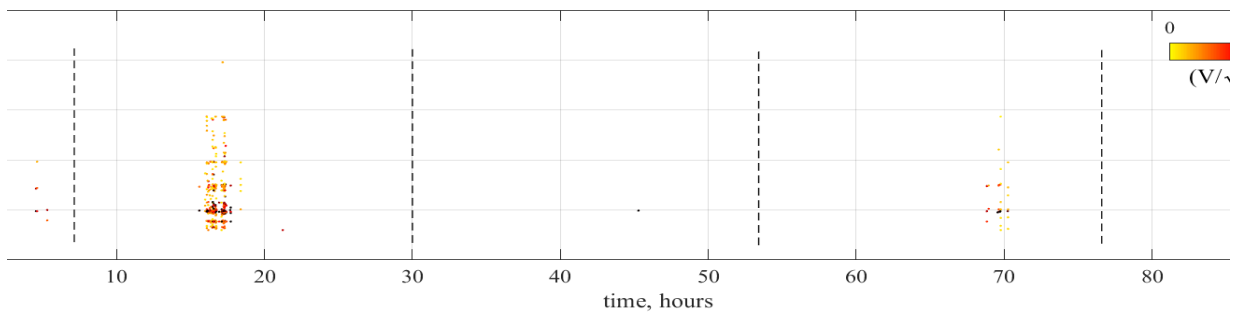
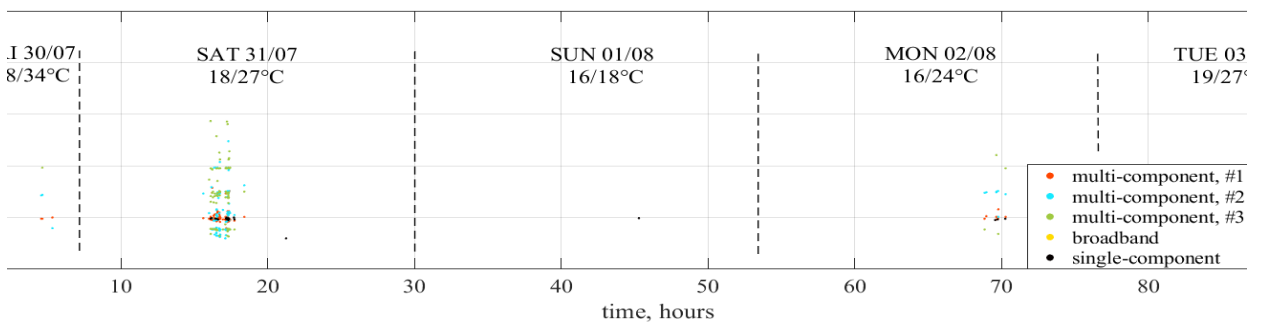a) Hourly AE rate.
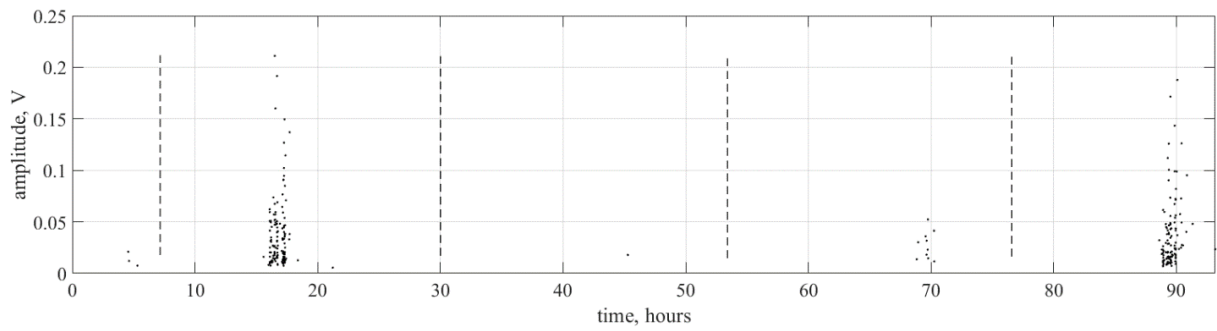
b) Distribution of time-domain AE amplitudes.
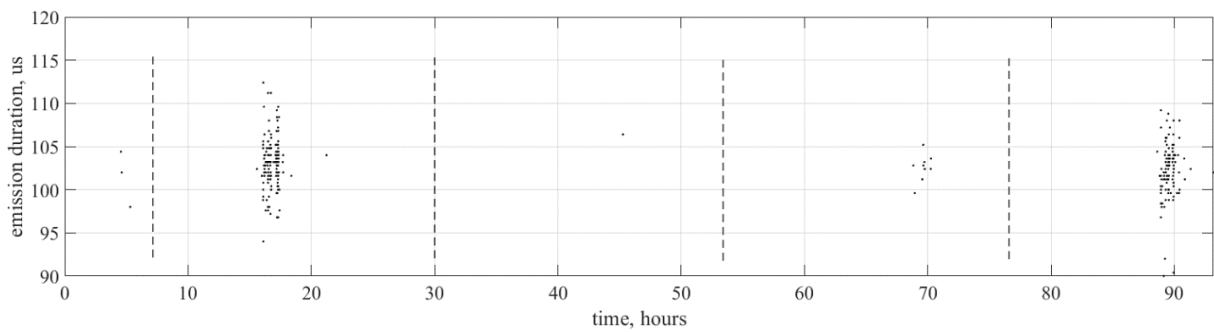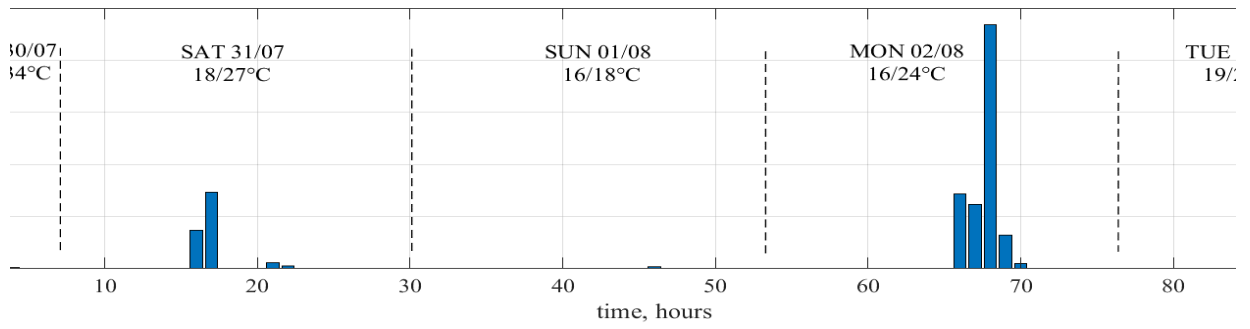

c) Distribution of AE durations.

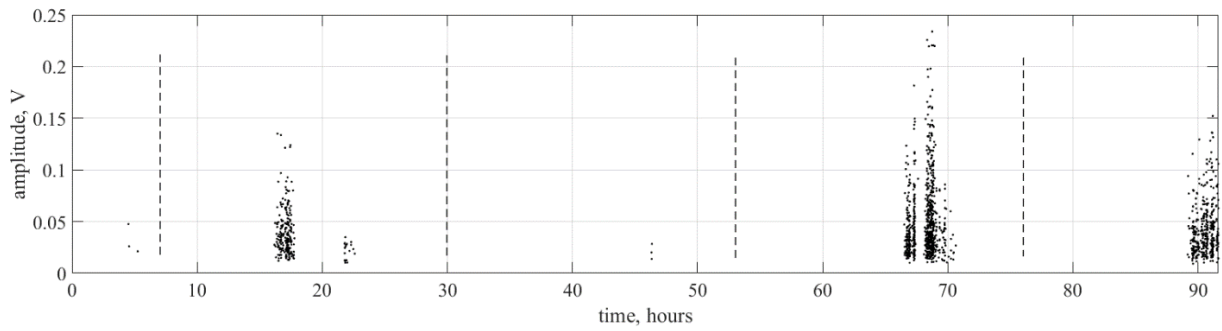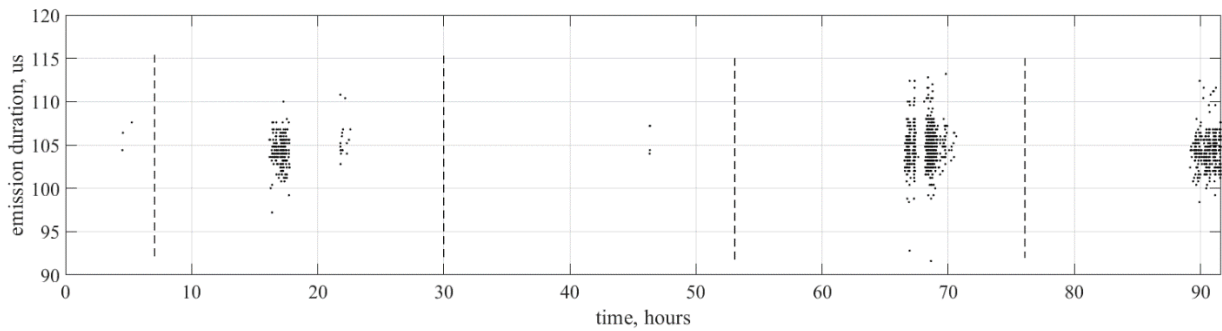d) Time-frequency distribution of amplitude spectrum peaks.

e) AE types differentiated by their spectral composition.

Fig. 5: AE signals during outdoor measurements, recorded by sensor system #1.
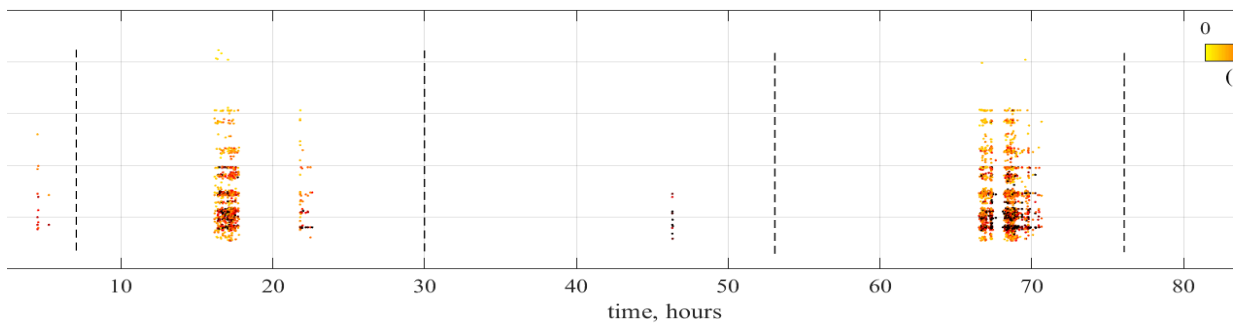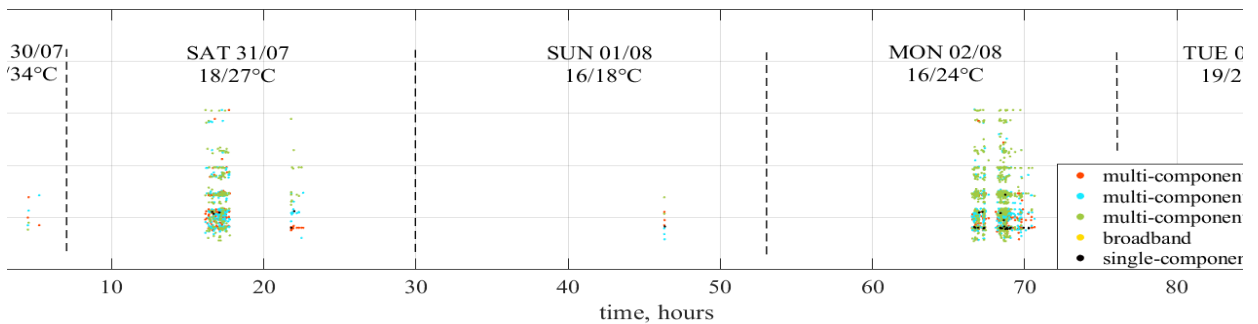
a) Hourly AE rate.

b) Distribution of time-domain AE amplitudes.

c) Distribution of AE durations.

d) Time-frequency distribution of amplitude spectrum peaks.

e) AE types differentiated by their spectral composition.

Fig. 6: AE signals during outdoor measurements, recorded by sensor system #2.

AE in this frequency range is related to drought stress induced nucleation of air-bubbles in xylem [6], [14]. Also, multi-component emissions, grouping between 200 and 600 kHz, are present. It is also observed, that among most of the acquired multi-component emissions (Fig. 3, 5e, and 6e, orange, blue, green), the frequency of the peak with the highest-amplitude (Fig. 5, orange) most likely coincides with 200 kHz single-component peaks [17], [18] (Fig. 5e, black).

Analog frontend's gain of 35 dB was found sensitive enough to detect and amplify naturally occurring physiological emissions up to 250 mV (Fig. 5b, 6b). In outdoor experiments, duration of most emissions was between 90 and 120 µs (Fig. 5c, 6c). Only a very small number of short (µs), impulse AEs were found (broadband emissions in Figs. 3, 5e, 6e, yellow). Such emissions are considered to originate from diurnal sap-flow related contractions of stem. Absence of such emissions indicates good mechanical coupling of the transducer, with no loss of contact pressure throughout the experiment. Hence, no emissions related to sensor sliding were found.

4.   Conclusions

A design of an embedded sensor system for acquisition, onboard processing, and storage of physiological AE signals was presented. The preliminary outdoor tests have confirmed the suitability of the proposed hardware design for field-measurement campaigns. Also, the drought stress specific time-frequency feature-set [17] proposed by earlier controlled laboratory tests [18] was verified in naturally occurring conditions.

Aiming at differentiation among multiple physiological AE sources, our future efforts are focused on feature-selection, and embedded implementation of automated unsupervised machine-learning AE clustering algorithms on the embedded sensor system. In addition to the currently implemented feature-set, described in the Section 2.2, the embedded system houses sufficient processing power and memory for extraction of additional common time-domain features, like duration, amplitude, rise-time, decay, root-mean-square (RMS), and energy. Also, successive, long-term experiments are planned to assess the influence of possible environmental interference sources.

5.   References

[1]   Venturas, M.D., Sperry, J.S., Hacke, U.G. (2017). Plant xylem hydraulics: what we understand, current research, and future challenges. Journal of integrative plant biology, vol. 59, no. 6, p. 356-389.

[2]   Vincent, O., Marmottant, P., Quinto-Su, P. A., and Ohl, C.-D. (2012). Birth and growth of cavitation bubbles within water under tension confined in a simple synthetic tree. Physical Review Letters, vol. 108, no. 18, p. 184502.

[3]   Choat, B., Brodribb, T.J., Brodersen, C.R., Duursma, R.A., Lopez, R., (2018). Triggers of tree mortality under drought. Nature, vol. 558, no. 7711, p. 531-539.

[4]   Cochard, H., Delzon, S., Badel, E. (2015). X-ray microtomography (micro-CT): a reference technology for high-resolution quantification of xylem embolism in trees. Plant, Cell & Environment, vol. 38, no. 1, p. 201–206.

[5]   Nolf, M., Lopez, R., Peters, J.M.R., Flavel, R.J., Koloadin, L.S., Young, I.M., Choat, B. (2017). Visualization of xylem embolism by X-ray microtomography: a direct test against hydraulic measurements. New Phytologist, vol. 214, no. 2, p. 890–898.

[6]   De Baerdemaeker, N.J., Stock, M., Van den Bulcke, J., De Baets, B., Van Hoorebeke, L., Steppe, K. (2019). X-ray microtomography and linear discriminant analysis enable detection of embolism-related acoustic emissions. Plant Methods, vol. 15, no. 1, p. 1-18.

[7]   De Roo, L., Vergeynst, L.L., De Baerdemaeker N.J.F., Steppe, K. (2016). Acoustic Emissions to Measure Drought-Induced Cavitation in Plants. Applied Sciences, vol. 6, no. 3, p. 71.

[8]   Nolf, M., Beikircher, B., Rosner, S., Nolf, A., Mayr, S. (2015). Xylem cavitation resistance can be estimated based on time- dependent rate of acoustic emissions. New Phytologist, vol. 208, no. 2, p. 625-632.

[9]   Vergeynst, L., Sause, M. G., Steppe, K. (2014). Acoustic emission signal detection in drought-stressed trees: beyond counting hits. The 31st conference of the European Working Group on Acoustic Emission (EWGAE), 3-5 Sep. 2014, Dresden, Germany.

[10]   Zweifel, R., Zeugin, F. (2008). Ultrasonic acoustic emissions in drought- stressed trees–more than signals from cavitation?. New Phytologist, vol. 179, no. 4, p. 1070-1079.

[11]   Steppe, K., Zeugin, F., Zweifel, R. (2009). Low-decibel ultrasonic acoustic emissions are temperature-induced and probably have no biotic origin. New Phytologist, vol. 183, p. 928-931.

[12]   Vergeynst, L. L., Sause, M. G., Hamstad, M. A., Steppe, K. (2015). Deciphering acoustic emission signals in drought stressed branches: the missing link between source and sensor. Frontiers in plant science, vol. 6, p. 494.

[13]   Sause, M. G., Gribov, A., Unwin, A. R., Horn, S. (2012). Pattern recognition approach to identify natural clusters of acoustic emission signals. Pattern Recognition Letters, vol. 33, no. 1, p. 17-23.

[14]   Vergeynst, L. L., Sause, M. G., De Baerdemaeker, N. J., De Roo, L., Steppe, K. (2016). Clustering reveals cavitation-related acoustic emission signals from dehydrating branches. Tree physiology, vol. 36, no. 6, p. 786-796.

[15]   Ito, K., Enoki, M. (2018). Continuous recording and wireless transmission of AE waveforms by battery powered sensor nodes. The 33rd conference of the European Working Group on Acoustic Emission (EWGAE), 12-14 Sep. 2018, Senlis, France.

[16]   Oletic, D., Bilas, V. (2019). Piezoelectric sensor front-end for energy-efficient acquisition of ultrasonic emissions related to water-stress in plants. The 2019 IEEE Sensors Conference, Oct. 2019, Montreal, Canada, p. 1-4.

[17]   Oletic, D., Rosner, S., Zovko, M., Bilas, V. (2020). Time-frequency features of grapevine's xylem acoustic emissions for detection of drought stress. Computers and electronics in agriculture, vol. 178, p. 1-19. doi:10.1016/j.compag.2020.105797.

[18]   Oletic, D., Rosner, S., Bilas, V. (2021). Verifying sensitivity of a sensor system for logging xylem's acoustic emissions related to drought stress. The 2021 IEEE International Workshop on Metrology for Agriculture and Forestry (MetroAgriFor), 3-5 Nov. 2021, Trento-Bolzano, Italy, p. 125-129.

Acoustic emission generated by alternating magnetic field

Gabor Por[1], Szebasztián Szabó[1], Tibor Morvai[1], Laszló Koroknai[1] and Ottó Szabados[1]

[1]University of Dunaújváros, Institute of Mechanical Engineering, Dunaújváros, Hungary.
porg@uniduna.hu, cn6ynx@uniduna.hu, morvait@uniduna.hu, koroknail@uniduna.hu,
Szabados.otto@uniduna.hu

Keywords: Acoustic emission, alternating magnetic field, steel plate, anisotropy.

Abstract

Stresses born in the solid state may trigger acoustic emission (AE). Stresses are traditionally caused by mechanical forces and/or pressures implemented to the surface of the material. However, inner stresses in solid state may be born due to changing of magnetic field or due to temperature changes especially when cooling down the material, for example in structure changing. It is also well known that elongation of material structures due to rolling may lead to different AE bursts, which may be used for characterization of the structure of material due to cold forming.

In the presentation we show in experiments that alternating magnetic field leads to AE burst, which have larger magnitude where the gradient of the changes of magnetic field is larger in absolute value. We also demonstrate correlation of the RMS of AE signals with the direction of the elongation of steel structure. This opens the way to investigate anisotropy in steel sheets. We also investigated the dependence of the measure of acoustic emission on frequency and on different sinus, triangle and rectangle forms in alternating magnetic field.

Filtering approaches of AE data in damage severity assessment of highly emissive concrete structures under loading

Giuseppe Scionti[1], Luigi Calabrese[1,*] and Edoardo Proverbio[1]

[1]University of Messina, Dept. of Engineering, Messina, Italy.
pepi_scionti@hotmail.com, lcalabrese@unime.it, eproverbio@unime.it

Abstract

The application of the AE technique in the field of civil engineering requires overcoming various issues related to several factors such as structure complexity, material non-homogeneity, signal attenuation, environmental noise. In this concern, multivariate statistical analysis was successfully applied to manage AE data and discriminate relevant features related to main damage mechanisms in concrete. Principal component analysis (PCA) and artificial neural networks (ANN) were applied with promising results. However, a fundamental limitation of these numerical methods is that they are not user-friendly and their application requires suitable scientific expertise. In such a context, the development of an easy de-noising protocol, able to simplify the AE data analysis for damage structure assessment and failure prediction, is a fundamental improvement toward the applicability of this technology on real-scale concrete structures.

In the present paper, the analysis of AE data collected during loading and unloading cycles up to the failure on a real scale post-tensioned concrete beam is reported. Different de-noising approaches were adopted to remove a large incoherent AE population originating from the friction of hydraulic actuator steel plate on concrete surface and friction on beam supports during loading/unloading steps. Filtered data were then synchronized with the beam deformation and crack width opening. De-noising algorithms have then been validated by structure damage severity assessment using statistical indexes such as calm ratio, load ratio, severity, and historical index. The procedure was tested with interesting results on PT concrete beams characterized by different pre-existing damages on steel tendons.

AE localization issues in heavy reinforced post-tensioned concrete beams

Giuseppe Scionti[1], Luigi Calabrese[1] and Edoardo Proverbio[1,*]

[1]University of Messina, Dept. of Engineering, Messina, Italy.
pepi_scionti@hotmail.com, lcalabrese@unime.it, eproverbio@unime.it

Keywords: Acoustic emission, concrete, source localization, damage assessment.

Abstract

Damage localization is a relevant issue in structural health monitoring (SHM) of concrete structures. A greater level of insight into the structure can be so reached enabling more informed maintenance decisions and reducing operation and maintenance costs. The basic approach to acoustic emission localization, which is often referred to as the Time of Arrival (TOA) method, is based on detecting an AE source at a number of spatially-distributed sensors. However, in anisotropic media such as reinforced concrete, the basic assumptions for the TOA method become largely invalid. Different robust methods suitable to anisotropic media, incorporating an angular-dependent velocity term into the minimization process have been developed in the past. However, the wave-velocity profile is not always known. More recently a number of other authors have adopted various Bayesian approaches as part of AE localization strategies, including the use of a Markov chain Monte Carlo inference scheme as well as nonlinear Kalman filters. The use of a probabilistic approach in source location has become increasingly applied for AE source localization in complex large structures. In heavy reinforced post-tensioned concrete structures acoustic wave path can be significantly influenced by rebars as well as metallic post-tensioning ducts. Cracks opening can further influence acoustic propagation paths and greatly influence the reliability of AE source localization algorithms. In the present paper, different localization procedures have been developed and tested on post-tensioned concrete beams during loading and unloading cycles as well as on small homogeneous concrete blocks. In a highly emissive environment, significant difficulties have been reported also in event identification thus further reducing localization procedure reliability.

An acoustic emission approach to the structural health monitoring of historical metallic tie-rods

Francesco Muscolino[1], Michele Carboni[2] and Roberto Felicetti[1]

[1]Politecnico di Milano, Department of Civil Engineering, Milano, Italy.
francesco.muscolino@polimi.it, roberto.felicetti@polimi.it
[2]Politecnico di Milano, Department of Mechanical Engineering, Milano, Italy.
michele.carboni@polimi.it

Keywords: Historical metallic tie-rods, fracture mechanics, acoustic emission, ultrasonic phased-array, magnetic particles.

Abstract

The application of Non-Destructive testing and Structural Health Monitoring systems in historical buildings is of great interest and actuality due to the need to guarantee safety and conservation. The present memory focuses on the case study of the historical wrought iron tie-rods of Duomo di Milano, Italy. In recent years, two of these elements presented critical failures, making necessary the replacement. Consequently, a monitoring methodology, based on acoustic emission, was defined. First, the fracture toughness of historical wrought iron was experimentally characterized by employing standard small scale specimens taken from one of the failed tie-rods. At the same time, acoustic emission was acquired to define a methodology for detecting and localizing the events due to damage in the material, separating those due to background noise by applying suitable pattern recognition algorithms. Subsequently, a tensile test was performed on a full scale section of the same tie-rod. Before and after the test, phased-array ultrasonic testing and magnetic particles inspections were carried out to identify and map defects and their possible development due to load application. From the analysis, it was possible to conclude that magnetic inspections allow identifying the presence of surface defects effectively, phased-array ultrasonic testing allows to estimate the geometry of the defect accurately and acoustic emission has proved to be a promising technique for monitoring the structural integrity of in-service historical metallic tie-rods.

Artificial intelligence-based corrosion sensing and prediction for aircraft applications (AICorrSens)

Christoph Kralovec[1]

[1]Johannes Kepler University Linz, Altenberger Straße 69, Science Park I, MT0220, 4040 Linz, Austria.
christoph.kralovec@jku.at

Keywords: Acoustic emission, artificial intelligence, corrosion, aircraft.

Abstract

Corrosion causes enormous damage to mechanical structures in many industrial sectors, and the aviation industry is no exception. To extend the lifetime of airframes without compromising safety, it is very important to have a clear picture of the state of corrosion (SoC) of the aircraft. Thus, it is essential to develop methodologies suitable for real-time monitoring of the SoC and subsequent reliable notification when a structure has been compromised by corrosion. Published results so far suggest that the ultrasonic (e.g. acoustic emission, guided waves) as well as electrochemical sensors (e.g. electrochemical noise, impedance spectroscopy) are suitable for monitoring aircraft-relevant corrosion but lack the technological readiness to be applied in commercial aircraft yet. A huge issue in achieving reliable monitoring systems is the correlation between corrosive phenomena and (typically) noisy sensor data. The AICorrSens project addresses these issues by developing a multi-sensor setup for monitoring the SoC based on ultrasonic, electrochemical, and environmental sensors coupled with AI algorithms. Training data shall be generated by performing accelerated corrosion tests with coupons and demonstrator parts equipped with sensors. Using AI for the subsequent data analysis, one can overcome operational noise, and thus, allow today's corrosion detection methods onboard real- time evaluation of the SoC in terms of detection, localization, quantification, and typification. The ambition of the project is to transform the created continuous stream of data into classifications of the SoC that are intuitively understandable through a human-machine interface, including a qualified corrosion prediction by the AI models generated from test campaigns. The project results shall lead to increased aircraft safety and reliability and deliver a clear economic benefit for aircraft operators as it allows a switch from regular inspection intervals to condition-based maintenance.

Valve inspection with acoustic emission – What are the boundaries, what are new opportunities for predictive maintenance?

Michael Hettegger[1] and Christoph Altmann[1]

[1]Senseven GmbH, Montlearstrasse 1B/7/14, 1140 Vienna.
michael.hettegger@senseven.ai, christoph.altmann@senseven.ai, https://senseven.ai

Keywords: Acoustic emission, valve leakage, artificial intelligence, AE inspection platform.

Abstract

Studies show that 5-10% of industrial valves are suffering from internal leakage which can lead to economic losses, health and safety issues or potentially to contamination or environmental pollution. Acoustic emission is an established technology to inspect valves for internal leakage.

Despite the successful establishment of the acoustic emission technology, current solutions have shown some limitations. These are e.g. their complexity of use, the need of trained and experienced personnel, the time required to perform analyses and the use of solely proprietary and closed devices. Experts performing inspections in the field are facing challenges such as using the right measuring points, flow noise from nearby processes, finding the right duration of measurement and interpreting the results. Research has shown that interpretation of results depends very much on experts' know-how and reproducible results have thus been difficult to achieve. This causes difficulty for companies to use the data for further purposes, such as predictive maintenance.

In order to tackle that problem, Senseven has taken over 1000 measurements in laboratories together with more than 10 different valve manufacturers during the last year. To replicate real production situations, leakages were also simulated in the field, taking into account different media/pressures/different valve sizes/nominal diameters and valve types. The experience gained and the data collected were used to build a digital and smart inspection system based on an artificial neural network. The challenge was to build a system that could generate reproducible results, analyze data automatically and store it in such a way that companies could use it for predictive maintenance purposes.

In our technical paper session, we would like to discuss the advantages of using acoustic emission for valve inspection as well as outline the current challenges companies and inspection service providers face when performing measurements. We will discuss our findings from the field simulations and present our artificial intelligence approach for automatic leak detection and leak rate estimation. In addition, we will demonstrate our Acoustic Emission Platform and how it helps companies collect and store acoustic emission data in a structured and organized manner, taking another step towards a more efficient testing process.

A computational study of AE signal due to fiber break and fiber matrix debonding in model composite

Zeina Hamam[1], Nathalie Godin[1], Aurelien Doitrand[1], Claudio Fusco[1] and Thomas Monnier[2]

[1]INSA de Lyon, Univ. Lyon, MATEIS UMR 5510, F-69621 Villeurbanne, France.
zeina.hamam@insa-lyon.fr, claudio.fusco@insa-lyon.fr, aurelien.doitrand@insa-lyon.fr
[2]INSA-Lyon, Univ. Lyon, LVA EA677, F-69621 Villeurbanne, France.
thomas.monnier@insa-lyon.fr

Keywords: Acoustic emission, composite, modelling, sensor effect, F/M debonding.

Abstract

Acoustic emission monitoring is a useful method to deal with detection and identification of damage in composite materials during mechanical tests. From an experimental point of view, it is not straightforward to establish a quantitative link between the damage sources and AE signals. Modeling and numerical simulations appear as a promising way to reach this objective. In this study, Finite Elements Modeling (FEM) was used to simulate AE signals due to fiber break and fiber/matrix debonding in a model carbon fiber composite. A specimen made of a single carbon fiber and epoxy matrix was used to experimentally validate the simulated fiber break AE signals. The objective was to compare the AE signals from a validated fiber break simulation (Fig. 1a) to the AE signals obtained from fiber/matrix debonding (with several models) and fiber break obtained in several media and to discuss the capability to detect and identify each source (Fig. 1b). The influence of the type of sensor, specimen geometry and AE source location were also studied. The proposed model was extended to identify the main parameters that influence the acoustic emission signatures. These validated results open the way to combine the experimental and the simulated data to generate a library in order to identify real-time damage mechanisms.
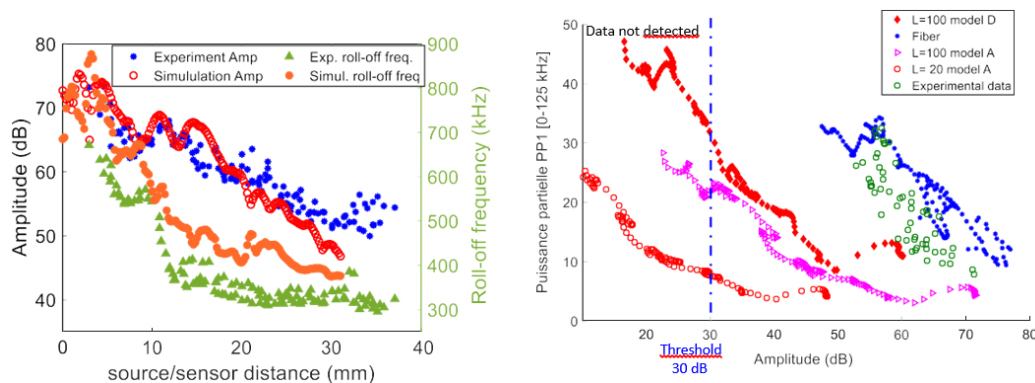
Fig. 1: (a) Amplitude and roll-off frequency vs. source/sensor distance for experimental signals and numerical signals. (b)Evolution of Partial Power PP1 [0–125 kHz] as a function of amplitude obtained with a nano 30 sensor for several sources. Fiber break and debonding (L = 20 μm or 100 μm).

Multimodal NDT monitoring of TRC sandwich under bending and early detection of interlaminar debonding

Nicolas Ospitia[1], Eleni Tsangouri[1], Ali Pourkazemi[2], Johan H. Stiens[2] and Dimitrios G. Aggelis[1]

[1]Department of Mechanics of Materials and Constructions (MeMC), Faculty of Engineering, Vrije Universiteit Brussel (VUB), Brussels, Belgium.
nicolas.ospitia.patino@vu.be, eleni.tsangouri@vub.be, dimitrios.aggelis@vub.be
[2]Department of Electronics and Informatics (ETRO), Faculty of Engineering, Vrije Universiteit Brussel (VUB), Brussels, Belgium.
apourkaz@etrovub.be, jstiens@etrovub.be

Keywords: Acoustic emission, digital image correlation, MMW spectrometry, TRC sandwich, damage monitoring.

Abstract

Textile Reinforced Cementitious (TRC) sandwich composites provide a load-bearing, non-corrosive, lightweight, and durable alternative for steel-reinforced sandwich elements, and/or traditional steel-reinforced concrete. However, the composite nature of the material and slender nature of the facings render the fracture behavior complex. Insufficient interlaminar bond can cause premature debonding, substantially reducing the loadbearing capacity of the composite. Non-Destructive Testing (NDT) techniques seem the obvious choice to monitor the damage progression of the material without affecting, nor compromising the behavior of the composite, and predict their service life.

In this study, TRC sandwich composites, subjected to quasistatic four-point bending, are monitored with three NDTs. Digital Image Correlation (DIC) allows to measure the surface strains and displacements. MMW Spectrometry, used for the first time in bending damage monitoring, allowed to detect damage such as cracking, or debonding, while Acoustic Emission (AE) allowed to localize and characterize internal cracking.

In order to simulate premature debonding, the bond between the tensile TRC facing and the insulation, in the central zone, where the bending moment is maximum, was artificially destroyed. Results show that a weak interlaminar bond reduced the ultimate load of the composite by more than 50%. Additionally, DIC, AE and MMW Spectrometry proved useful to monitor and characterize damage. Multimodal data gathered from the multimodal NDTs showed to be complementary. DIC allowed to interpret AE and MMW Spectrometry data from a surface viewpoint, while AE parameters permit predictions at low load conditions, and detect internal cracking. For instance, the AE behavior at early load stage (less than 15% of the maximum load) of the TRC sandwich with destroyed bond showed significant differences than for the reference TRC sandwich. Specifically, it showed higher RA values, and lower AF than the reference TRC sandwich, suggesting more shear related early activity for, promoted by the damaged bond. Results were corroborated with DIC, while MMW Spectrometry seemed to follow closely the level of damage of TRC sandwich composites under quasi-static four-point bending.

Simulation of acoustic emission in carbon fiber-epoxy matrix composite laminates due to transverse cracking: effect of ply stacking sequence

Aurélien Doitrand[1], Zeina Hamam[1], Nathalie Godin[1], Pascal Reynaud[1], Claudio Fusco[1] and Nicolas Carrère[2]

[1]INSA de Lyon, Univ. Lyon, MATEIS UMR 5510, F-69621 Villeurbanne, France.
[2]IRDL, CNRS UMR6027, Brest, France.

Keywords: Acoustic emission, composite, modelling, matrix cracking, effect of ply stacking sequence.

Abstract

This work focuses on the numerical simulation of the AE due to transverse cracking in laminate composites. The objective of the work is the experimental characterization and numerical simulation of the influence of the ply thickness and stacking sequence on transverse matrix cracking induced acoustic emission. AE signals induced by transverse matrix cracking are simulated numerically using finite elements (FE) for composite laminates exhibiting different number of plies and stacking sequences. 3D FE models of the specimens are set-up using Abaqus™ Standard. Either $[0_n/90_n/0_n]$ or $[90_n/0_n/90_n]$ (n=1 or 3) composite laminates are modeled, one ply thickness is 0.3 mm. Matrix transverse cracking in 90 deg. inner or outer ply is simulated. The influence of the ply thickness on acoustic emission signals recorded at the crack epicenter is significative only for inner ply transverse cracking, whereas similar signals are obtained for outer ply cracking. The frequency content of signals induced by outer ply transverse cracking does not depend on the ply thickness. Contrary to outer ply cracking, the influence of the ply thickness on inner ply transverse cracking induced signals is significative, especially on the frequency content, and on the frequency centroid only close to the crack (Fig. 1). Outer ply cracking rather exhibits signals with a low frequency content, not depending much on the ply thickness, contrary to inner ply cracking, for which the frequency content is higher and more dependent on the ply thickness.
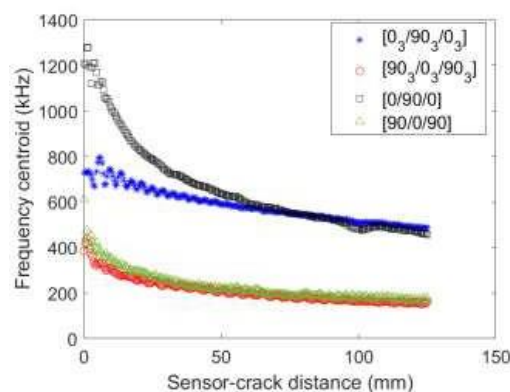
Fig.1: Frequency centroid as a function of distance between the source and the sensor obtained numerically for $[0_n/90_n/0_n]$ and $[90_n/0_n/90_n]$ stacking sequences (n=1 or 3). Results obtained without sensor effect, with a virtual perfect sensor.

Study of dislocation dynamics of copper single crystals under cycling loading through acoustic emission and microstructural characterizations

Gabriel L'hôte[1], S. Cazottes[1], M. Montagnat[2] and S. Deschanel[1]

[1]Univ Lyon, INSA-Lyon, MATEIS UMR CNRS 5510, F69621 Villeurbanne.
gabriel.l-hote@insa-lyon.fr, sophie.cazottes@insa-lyon.fr, stephanie.deschanel@insa-lyon.fr
[2]Univ. Grenoble Alpes, CNRS, IGE, F-38000 Grenoble, France.
maurine.montagnat@univ-grenoble-alpes.fr

Keywords: Acoustic emission, plasticity, fatigue, dislocation avalanches.

Abstract

During plastic deformation of crystalline materials, a *soft* plasticity, made of numerous uncorrelated dislocation movements coexists with a *wilder* plasticity, in the form of collaborative movements: dislocation avalanches. The coexistence of the two plasticities depends on the establishment of a dislocation structure, which is supposed to hinder the propagation of avalanches. We propose to study the correlation between the microstructural evolution of the dislocation arrangements and the nature of the dislocation dynamics, during cyclic loading of pure copper single crystals. Different fatigue tests with imposed stress amplitude are performed to study the influence of (i) the loading path, (ii) the loading ratio and (iii) the crystallographic orientation on the plasticity phenomena. The acoustic emission (AE) technique is used to study both types of plasticity : the continuous AE is associated with *soft* plasticity and the discrete AE with *wild* plasticity. The dislocation microstructures are studied using EBSD (crystal disorientation) and ECCI (Electron Channeling Contrast Imaging) techniques at the end of each fatigue stage. The AE-ECCI coupling gives valuable information about the dislocation dynamics of dislocations. This study shows a certain universality, with (i) the existence of dislocation avalanches, produced during a more or less deep reorganization of the structures, (ii) a progressive evolution, during the cycles, of the dislocation mean free path, associated with the emergence of a dislocation structure and (iii) an inhibition of avalanches during the emergence of a dislocation arrangement.
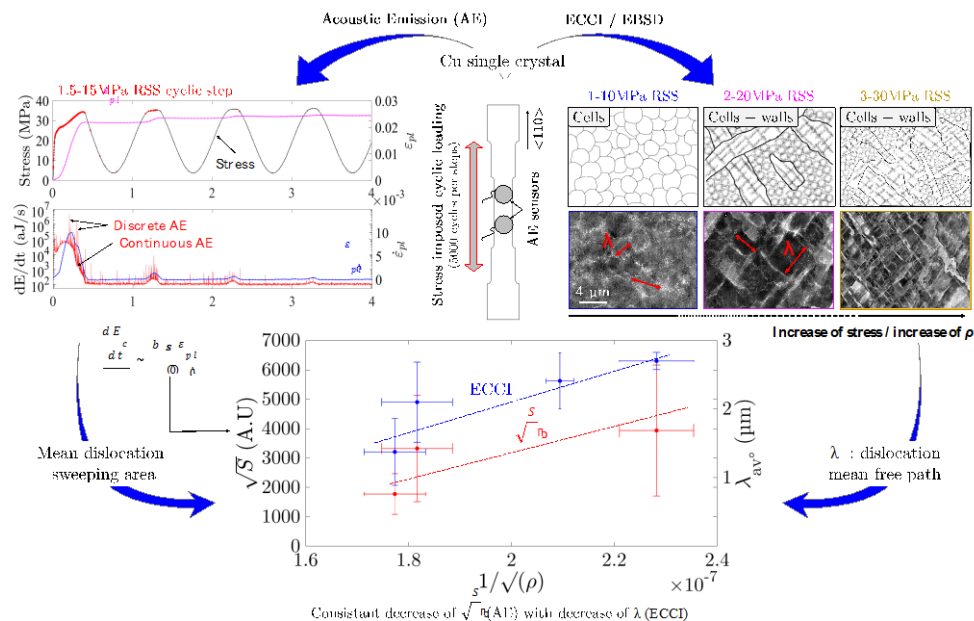
Development of new AE technology to detect and characterize leak on nuclear shielding building from inside during integrated leakage rate test

Alain Proust[1], Jean Marie Henault[2] and Benoît Masson[3]

[1]MISTRAS Group SA, 27 rue Magellan, Paris Cedex 94370 France.
[2]EDF – R&D PRISME - Développement Mesures Physiques 6 quai Watier 78400 Chatou.
[3]Responsable domaine Génie Civil Nucléaire pour DPN, Expert Enceinte de confinement et 3ème barrière Département Composants Mécaniques et Génie Civil (CMG) EDF - DIPNN – Direction Technique 19, rue Pierre Bourdeix – 69007 Lyon.

Keywords: Acoustic emission, leak detection, pre-stressed concrete.

Abstract

French Projects of Investment for the Future, called "Research for Nuclear Safety and Radiation Protection" have been initiated to further research on the causes, the management, the impact of the observed nuclear accidents and to propose and validate solutions to limit the risk and the consequences. In this context the "Non Destructive Evaluation of nuclear plants containment" project" (ENDE) with eight partners (six research institutes and two industrials) supported by the "National Agency of Research", proposes a methodology for the Non Destructive Evaluation of the containment capacity. The two major functions to be assess are strength and leak tightness. Under the frame of the VeRCoRs project EDF has developed and build a containment mock-up on the 1/3 scale (diameter 20m, height 20m, wall thickness 40cm) which has been used for some partners of ENDE project.

Mistras has been involved in characterisation of concrete cracking during pneumatic proof tests either in ENDE and VeRCoRs programs. Since some leaks occurs in the area of monitoring we use AE to characterized them.

The mockup has been used to develop and characterized an instrumentation and technology for leak detection with a major challenge leak detection has to be performed from this inside of the containment building with all the contingences of operating of full scale operating nuclear plant. This paper describe the steps of development and validation of the methodology up to the application this measurement on site help the leak characterisation during pneumatic ten year Integrated Leakage Rate Test at 4,2 bar.

Measurement Equipment and Customized Solutions for Acoustic Emission Testing

We develop and produce innovative technology that makes a true difference for the safety of humans, the environment and the preservation of infrastructure. This commitment differentiates us from other suppliers and defines who we are: Vallen Systeme – The Acoustic Emission Company

AMSY-6 System

The AMSY-6 System is a fully featured, multi-channel Acoustic Emission measurement system. It forms a flexible basis that can be customized, extended and configured to the needs of an application.

The field of applications ranges from various inspection tasks such as pressure vessel testing, leakage testing to research and structural health monitoring of large objects

spotWave Device

The spotWave device is a portable single channel AE-measurement unit that can be controlled by a Laptop, Tablet PC, Smartphone or IoT device. It is a fully featured AE measurement device. The software supports the Vallen pridb and tradb data file format.

Typical applications are leakage detection, hot spot monitoring, AE research, etc.

Acoustic Emission Sensors

A wide range of sensors is offered covering any AE testing application.

Sensors are available for standard environments, explosion hazardous areas, for underwater applications, high temperature surfaces and harsh environments.

Sensors supporting the SmarLine™ protocol register themselves with an AMSY-6 system and minimize the configuration effort.

Vallen AE Suite Software

Unmatched flexibility and transparency at all times makes the Vallen AE Suite Software the preferred tool of choice for all acoustic emission applications.

Its modular architecture can be configured and extended to match any requirement of an application.

It offers everything from simple data visualization over complex analysis and pattern recognition to automation and web-based dashboards.

Measurement data is written to a database structure that complies with SQLite3 standard. It can be accessed from any application supporting SQLite3 which includes Matlab, Python and many more fast development environments.